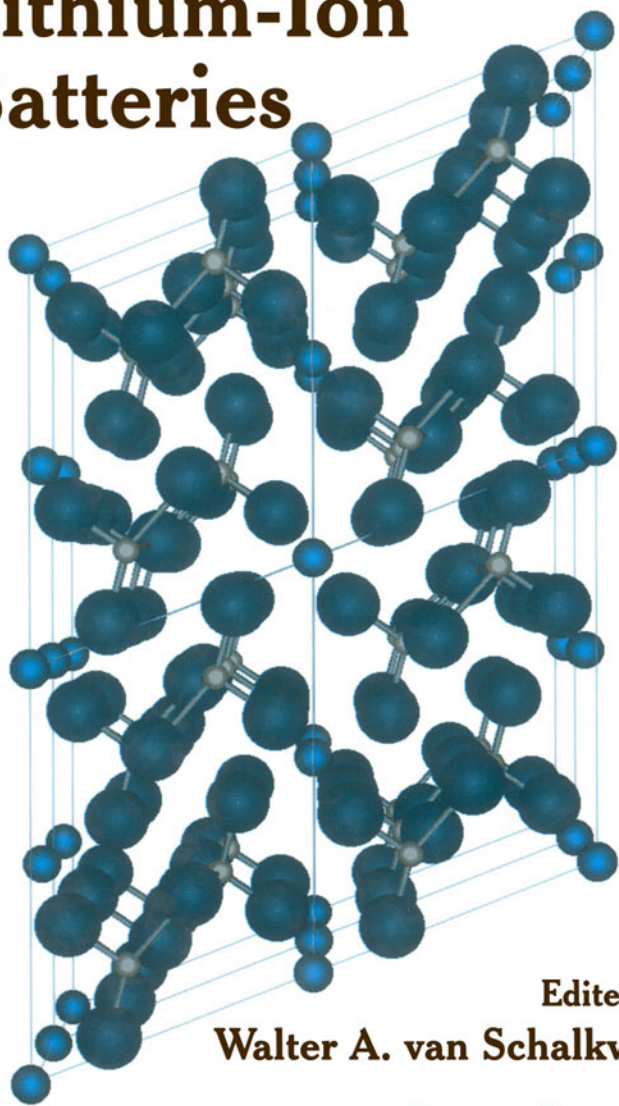# Advances in Lithium-Ion Batteries

Edited by
Walter A. van Schalkwijk
and
Bruno Scrosati

Advances in Lithium-Ion Batteries

Edited by

Walter A. van Schalkwijk

SelfCHARGE, Inc.
Redmond, Washington
Department of Chemical Engineering
University of Washington
Seattle, Washington, U.S.A.

and

Bruno Scrosati

Department of Chemistry
University of Rome
"La Sapienza"
Rome, Italy

Visit Kluwer Online at: http://kluweronline.com
and Kluwer's eBookstore at: http://ebooks.kluweronline.com

Acknowledgment

Contributors

Caria Arbizzani University of Bologna, Dip. Chimica "G. Ciamician", Via F. Selmi 2, 40126 Bologna, Italy

Doron Aurbach Department of Chemistry, Bar-Ilan University, Ramat-Gan 52900, Israel

George F. Blomgren Blomgren Consulting Services Ltd., 1554 Clarence Ave., Lakewood, Ohio 44107, U.S.A.

Ralph J. Brodd Broddarp of Nevada, Inc., 2151 Fountain Springs Drive, Henderson, Nevada 89074, U.S.A.

Michael Broussely SAFT, F-86060 Poitiers, France

Robert M. Darling International Fuel Cells, South Windsor, Connecticut, U.S.A.

John B. Goodenough Texas Materials Institute, ETC 9.102, University of Texas at Austin, Austin, Texas, U.S.A.

Mary Hendrickson U.S. Army CECOM RDEC, Army Power Division, AMSEL-R2-AP-BA, Ft. Monmouth, New Jersey 07703-5601, U.S.A.

H. Ikuta Department of Applied Chemistry, Tokyo Institute of Technology, 2-12-1 Ookayama, Meguro-ku Tokyo 152-8552, Japan

Minoru Inaba Department of Energy & Hydrocarbon Chemistry, Graduate School of Engineering, Kyoto University, Sakyo-ku, Kyoto 606-01, Japan

Hsiu-ping Lin MaxPower, Inc., 220 Stahl Road, Harleysville, Pennsylvania 19438, U.S.A.

Marina Mastragostino University of Bologna, UCA Scienze Chimiche, Via San Donato 15, 40127 Bologna, Italy

John Newman Department of Chemical Engineering, University of California at Berkeley; and Lawrence Berkeley National Labs, Berkeley, California, U.S.A.

Yoshio Nishi Sony Corporation, 1-11-1 Osaki, Shinagawa-ku, 141-0032 Tokyo, Japan

Zempachi Ogumi Department of Energy & Hydrocarbon Chemistry, Graduate School of Engineering, Kyoto University, Sakyo-ku, Kyoto 606-01, Japan

Edward J. Plichta U.S. Army CECOM RDEC, Army Power Division, AMSEL-R2-AP-BA, Ft. Monmouth, New Jersey 07703-5601, U.S.A.

Mark Salomon MaxPower, Inc., 220 Stahl Road, Harleysville, Pennsylvania 19438, U.S.A.

Bruno Scrosati Department of Chemistry, University of Rome "La Sapienza", 00185 Rome, Italy

Francesca Soavi Univeristy of Bologna, UCI Scienze Chimiche, Via San Donato 15, 40127 Bologna, Italy

Robert Spotnitz Battery Design Company, Pleasanton, California, U.S.A.

Kazuo Tagawa Hoshen Corporation, 10-4-601 Minami Senba 4-chome, Chuo-ku, Osaka 542-0081, Japan

Karen E. Thomas Department of Chemical Engineering, University of California at Berkeley; and Lawrence Berkeley National Labs, Berkeley, California, U.S.A.

Y. Uchimoto Department of Applied Chemistry, Tokyo Institute of Technology, 2-12-1 Ookayama, Meguro-ku Tokyo 152-8552, Japan

Walter A. van Schalkwijk SelfCHARGE, Inc., Redmond, Washington; and Department of Chemical Engineering, University of Washington, Seattle, Washington, U.S.A.

M. Wakihara Department of Applied Chemistry, Tokyo Institute of Technology, 2-12-1 Ookayama, Meguro-ku Tokyo 152-8552, Japan

Andrew Webber Energizer, 23225 Detroit Rd., P.O. Box 450777, Westlake, Ohio 44145, U.S.A.

Jun-ichi Yamaki Institute of Advanced Material Study, Kyushu University, Kasuga 816-8580, Japan

Contents

ix

Advances in Lithium Ion Batteries

Introduction

Walter van Schalkwijk
SelfCHARGE Inc., Redmond, WA
Department of Chemical Engineering,
University of Washington, Seattle, WA
USA

Bruno Scrosati
Universita "La Sapienza"
Dipartimento di Chimica
Opiazza Aldo Moro 5, 00185 Rome
Italy

Portable power applications continue to drive research and development of advanced battery systems. Often, the extra energy content and considerations of portability have outweighed economics when a system is considered. This has been true of lithium battery technologies for the past thirty years and for lithium ion battery systems, which evolved from the early lithium battery development. In recent years, the need for portable power has accelerated due to the miniaturization of electronic appliances where in some cases the battery system is as much as half the weight and volume of the powered device.

Lithium has the lightest weight, highest voltage, and greatest energy density of all metals. The first published interest in lithium batteries began with the work of Harris in 1958 [1]. The work eventually led to the development and commercialization of a variety of primary lithium cells during the 1970s. The more prominent systems included lithium/sulfurdi-oxide (Li/SO_2), lithium-thionylchloride $(Li/SOCl_2)$, lithium-sulfurylchloride (Li/SO_2Cl_2), lithium-polycarbon monofluoride $(Li/(CF_x)_n)$, lithium-manganese dioxide (Li/MnO_2), and lithium-iodine $(Li/(Poly-2-vinyl\ pyridine)I_n)$. Apologies to any chemistries that were not mentioned, but were studied and developed by the legions of scientists and engineers who worked on the many lithium battery couples during those early days.

The 1980s brought many attempts to develop a rechargeable lithium battery; an effort that was inhibited by difficulties recharging the metallic lithium anode. There were occasional unfortunate events pertaining to safety (often an audible Δp with venting and flame). These events were often due to the reactivity of metallic lithium (especially electrodeposited lithium with electrolyte solutions, but events were also attributed to a variety of other reactive conditions. Primary and secondary lithium batteries use non-aqueous electrolytes, which are inherently orders of magnitude less conductive than aqueous electrolytes. The reactions of the lithium electrode were studied extensively and this included a number of strategies to modify the reactivity of the Li-solution interface and thus improve its utility and safety [2].

Studies of fast ion conduction in solids demonstrated that alkali metal ions could move rapidly in an electronically conducting lattice containing transition metal atoms in a mixed valence state. When the host structure is fully populated with alkali metal atoms - lithium ions in the most common context – the transition metal atom is in the reduced state. The structure is fully lithiated. As lithium ions are removed from the host, the transition metal (and host structure) is oxidized. A host structure is a good candidate for an electrode if (1) it is a mixed ionic-electronic conductor, (2) the removal of lithium (or other alkali metal ion) does not change the structure over a large range of the solid solution, (3) the lithiated (reduced) structure and partially lithiated (partially oxidized) exhibit a suitable potential difference versus lithium, (4) the host lattice dimension changes on insertion/removal of lithium are not too large, and (5) have an operational voltage range that is compatible with the redox range of stability for an accompanying electrolyte.

This led to the development of rechargeable lithium batteries during the late 1970s and 1980s using lithium insertion compounds as positive electrodes. The first cells of this type appeared when Exxon and Moli Energy tried to commercialize the Li/TiS_2 and Li/MoS_2 systems, respectively. These were low voltage systems operating near 2 volts. In a large compilation of early research, Whittingham [3] reviewed the properties and preparation of many insertion compounds and discussed the intercalation reaction. The most prominent of these to find their way into batteries were V_2O_5, V_6O_{13}, and MnO_2. All of these systems continued to use metallic lithium anodes. The safety problems, real or perceived, limited the commercial application of *rechargeable* batteries using metallic lithium anodes.

During that era Steele considered insertion compounds as battery electrodes and suggested graphite and the layered sulfide TiS_2 as potential candidates for electrodes of a lithium-ion battery based on a non-aqueous liquid electrolyte [4].

After the era of the transition metal chalcogenides came the higher voltage metal oxides (Li_xMO_2) (where M = Ni, Co, or Mn) [5,6]. These materials are the basis for the most commonly used cathodes in commercial lithium-ion cells. At about that time the concept of a lithium-ion cell was tested in the laboratory with two insertion electrodes cycling lithium ions between them, thus eliminating the use of a metallic lithium anode [7,8]. The next decade saw substantial research and development on advanced battery systems based upon the insertion and removal of lithium ions into host compounds serving as **both** electrodes. Much of the work was associated with finding a suitable material to host lithium ions as a battery negative. As mentioned before, the concept is not new: Steele and Armand suggested it in the 1970s [4,9,10]. Eventually, in 1991, Sony introduced the first commercial lithium-ion cell based on $C/LiCoO_2$. The cells had an open circuit potential of 4.2 V and an operational voltage of 3.6 V.

Since then, there has been an extraordinary amount of work on all aspects of the lithium-ion chemistry, battery design, manufacture and application. Indeed, the mention of a lithium-ion battery can imply dozens of different chemistries, both commercial and developmental as illustrated in Figure 1.
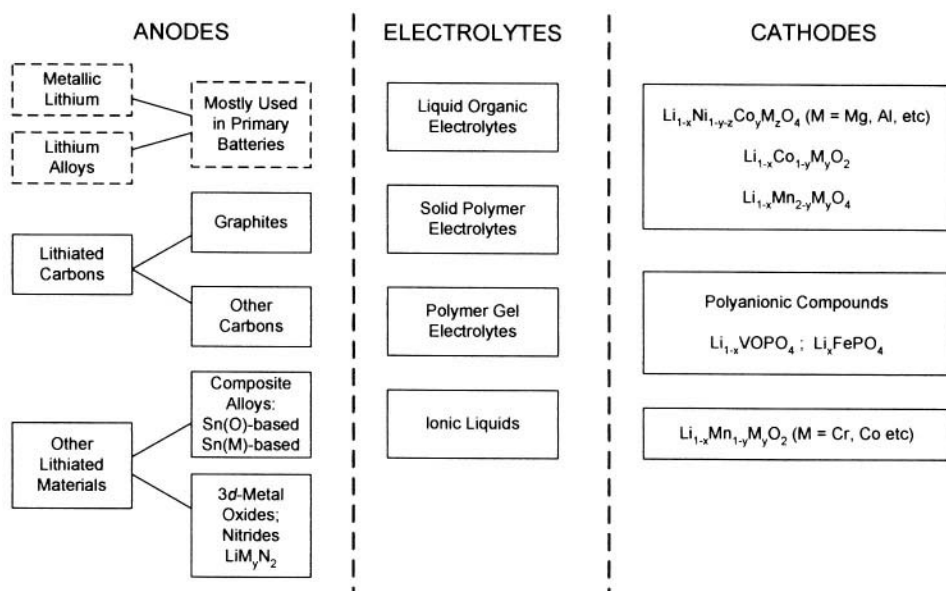
Figure 1. Numerous combinations of positives, electrolytes, and negatives combine to be called "lithium-ion", "lithium-ion-polymer," or "lithium-polymer." There are more than twenty commercially available "chemistries" and an equal number of combinations under development. Metallic lithium is mentioned because solving the problem of dendrite growth is attractive since metallic lithium has about an order of magnitude greater capacity than the "safer" materials now in use.

This book opens with an exhaustively complete chapter by Aurbach on the role of surface films in the stability and operation of lithium-ion batteries. His discussion lays the groundwork for the rest of the book because it puts many of the required properties of anode, cathode, solvent, salt, or polymer electrolyte into perspective in regards to their reactivity and passivation. Development of new electrolytes, anodes, and cathodes must account for this reactivity and indeed some new and promising electrode materials may continuously lose capacity due to their inability to passivate with the electrolytes employed.

The discussion of materials' reactivity is followed by chapters on carbon (Ogumi & Inaba) and manganese vanadate and molybdate anode materials for lithium-ion batteries. A brief chapter on oxide cathode materials by Goodenough gives a brief overview of current work on "traditional" lithium metal oxide materials and polyanionic compounds.

Yamaki presents an extensive review of the extensive efforts in various laboratories to improve the electrolyte solvent systems and studies of their reactivity with anodes and cathodes. This chapter, combined with Aurbach's opening chapter, the chapter on temperature effects in lithium-ion batteries (Salomon, Lin, Plichta, and Hendrickson) and Broussely's chapter on aging mechanisms and calendar life predictions gives a comprehensive insight into the reactivity of the systems that constitute commercial *cells*.

The chapters by Salomon, et al., and Broussely illustrate the limitations of the present commercial systems – limitations that are often ignored by application engineers using lithium-ion batteries in their appliances. Highlighting these operational limitations, which are functions of age, and operational and storage temperature, signals those working on materials and systems the type of shortcomings that must be overcome to improve the safety, reliability and utilization of lithium-ion batteries.

Many think the future moves toward solvent free systems: Scrosati presents a chapter on polymer electrolytes, most of which are solvent-containing gel-polymers in practical systems, and Nishi discusses gel-polymer battery properties and production. Webber and Blomgren give extensive treatment of ionic liquids (otherwise known as ambient-temperature molten salts) and their use in lithium-ion and other battery systems.

Scrosati's second chapter is on low-voltage lithium-ion cells: a variant of the chemistry which uses lower voltage couples (partially solving the anode material problem at the expense of system voltage and power. Several advantages are highlighted which illustrate the potential of these cells as replacements for 1.5 V systems. The final "material and chemistry" chapter is on electrochemical supercapacitors by Mastragostino, Soavi, and Arbizzani.

The remaining chapters are "system" or "engineering" chapters.

Thomas, Newman, and Darling present a thorough chapter on mathematical modeling of lithium batteries; Brodd and Tagawa describe Li-Ion cell production processes; Spotnitz explains the non-trivial nature of scale-up of Li-Ion cells; and van Schalkwijk explains the intricacies of charging, monitoring and control.

This book, while intended for lithium-ion scientists and engineers, may have parts that are of interest to scientists from other fields: polymer electrolytes and ionic liquids are useful materials in systems other than batteries. Intercalation electrodes, perhaps not as we know them, but more as fluidized beds are finding use in sequestering contaminants from the environment. Researchers in those fields will benefit from much of the knowledge gleaned by those in search of a better battery.

The editors realize that not every area of advanced research on lithium-ion batteries is represented in this book. However, it is hoped that

this book provides a timely snapshot of the current situation and with chapters extensively references, will serve as a reference volume that lasts comparatively long in this rapidly changing field.

REFERENCES

1. W.S. Harris, Ph.D. Thesis UCRL-8381, University of California, Berkeley.
2. KM Abraham and S.B. Brummer in *Lithium Batteries,* J-P. Gabano, ed., Academic Press, New York, 1983.
3. M.S. Whittingham, *Prog. Solid State Chem.,* **12**, 41-111.
4. B. C. H. Steele in *"Fast ion transport in solids: solid-state batteries and devices"* (North-Holland/American Elsevier, Inc., Amsterdam-London/New York, 1973), p. 103.
5. K. Mizushima, P.C. Jones, P.J. Wiseman, and J.B. Goodenough, *Mat. Res. Bull.,* **15**, 783, 1980.
6. M.M. Thackeray, W.I.F. David, P.G. Bruce, and J. B. Goodenough, *Mat. Res. Bull.,* **18**, 461, 1983.
7. M. Lazzari and B. Scrosati, *J. Electrochem. Soc.,* **127**, 773, 1980.
8. D.W. Murphy, F.J. DiSalvo, J.N. Carides and J.V. Waszczak, *Mat. Res. Bull.,* **13**, 1395, 1978.
9. M. Armand in *"Fast ion transport in solids: solid-state batteries and devices"* (North-Holland/American Elsevier, Inc., Amsterdam-London/New York, 1973),, p 665.
10. M. Armand in *Materials for Advanced Batteries,* D.W. Murphy, J. Broadhead, and B.C.H. Steele, eds., Plenum Press, New York, 1980.

1

The Role Of Surface Films on Electrodes in Li-Ion Batteries

Doron Aurbach

Department of Chemistry
Bar-Ilan University
Ramat-Gan 52900
Israel

1.0   INTRODUCTION

1.1   *Passivation Phenomena in Electrochemistry*

Surface film formation on electrodes is a very common phenomenon in electrochemical systems. Most metal electrodes in both aqueous and nonaqueous solutions are covered at a certain range of potentials with surface films that control their electrochemical behavior [1]. Most of the commonly used metals in electrochemical studies, as well as electrochemical devices, are naturally covered by oxide layers that may be formed spontaneously during their casting, due to the reaction of the bare metal with air oxygen [2]. Hydration of oxide films forms an outer layer of hydroxide, while reactions of oxides with air CO_2 form an outer layer of carbonates. Surface films formed on metals comprised of oxides, hydroxides, and carbonates are electronically insulating, as they reach a certain thickness, but may be able to conduct ions: oxygen anions, protons and/or metal cations [3]. In spite of the huge diversity in the properties of metals, we can find a similarity in some properties of surface films formed on metals in terms of mechanisms and kinetics of growth, as well as transport phenomena and kinetics of ion migration through surface films.

When a fresh active metal is exposed to a polar solution whose components may be reduced on the active surface to form insoluble metal salts, a surface film grows via a corrosion process. The driving force for this process is the difference between the redox potentials of the active metal and the solution species $\Delta V_{M\text{-}S}$. As a first approximation, we can assume a homogeneous surface film and Ohm's law, connecting the corrosion current density i_{corr} and $\Delta V_{M\text{-}S}$. Hence

$$i_{corr} = \Delta V_{M-S} / \left(\rho(\text{film}) \cdot l(t) \right) \tag{1}$$

where ρ(film) is the surface film's resistivity for electron tunneling (assuming homogeneous condition), and *l(t)* is its thickness (which grows in time). Assuming that all the reduction products precipitate on the active metal surface, then

$$\frac{dl}{dt} = K \cdot i_{corr} \tag{2}$$

K is the proportionality constant that depends on the molecular size of the surface species and their density of packing on the surface. Combining Equations 1 and 2, and integrating them with the boundary condition $t \rightarrow 0$, $l = 0$ yields:

$$l = \left(\frac{2K\Delta V_{M-S}t}{\rho(film)} \right)^{\frac{1}{2}} \tag{3}$$

which is the well-known parabolic growth of the surface films [4]. When the active metal exposed to solution is already covered by initial surface films, and hence at $t = 0$, $l = l_o$, then:

$$l = \left(l_o^2 + \frac{2K\Delta V_{M-S}t}{\rho(film)} \right)^{\frac{1}{2}} \tag{4}$$

We can assume that as the surface films formed on active surfaces in solutions reach a certain thickness, they become electronic insulators. Hence, any possible electrical conductance can be due to ionic migration through the films under the electrical field. The active surfaces are thus covered with a solid electrolyte interphase (the SEI model [5]), which can be either anionic or cationic conducting, or both.

For a classical SEI electrode, the surface films formed on it in polar solutions conduct the electrode's metal ions, with a transference number (t_+) close to unity. In most cases, the surface films on active metals are reduction products of atmospheric and solution species by the active metal. Hence, these layers comprise ionic species that are inorganic and/or organic salts of the active metal. Conducting mechanisms in solid state ionics have been dealt with thoroughly in the past [6-10]. Conductance in solid ionics is based on defects in the medium's lattice. Two common defects in ionic lattices are usually dealt with: interstitial (Frenkel-type) defects [7], and hole (Schottky-type) defects [8].

In the former case, the ions migrate among the interstitial defects, which may be relevant only to small metal ions. This leads to a transference number close to unity for the cation migration. In the other case, the lattice contains both anionic and cationic holes, and the ions migrate

from hole to hole [9]. The dominant type of defects in a lattice depends, of course, on its chemical structure, as well as on its formation pattern [10]. In any event, it is possible that both types of defects exist simultaneously and contribute to conductance. It should be emphasized that this description is relevant to single crystals. Surface films formed on active surfaces are much more complicated and may be of a mosaic and multilayer structure. Hence, ion transport along the grain boundaries between different phases in the surface films may also contribute to, or even dominate, conductance in these systems.

The kinetics of the simplest solid electrolyte interphase (SEI) electrode should include three stages: charge transfer across the solution-film interface, ion migration through the surface films, and charge transfer in the film-metal interface. It is reasonable to assume that the ion migration is the rate-determining step. Thus, it may be possible to use the basic Equation 5 for ionic conductance in solids as the starting point [4,6,11]:

$$i = 4zFan\upsilon \cdot \exp(-W/RT) \cdot \sinh(azFE/RT) \qquad (5)$$

where a is the jump's half distance, υ is the vibrational frequency in the lattice, z is the ion's charge, W is the energy barrier for the ion jump, n is the ion's concentration, E is the electric field, and F is the Faraday number.

When all of the potential falls on the surface films, then

$$\eta = \eta_{SEI} = El \qquad (6)$$

where l is the film's thickness. At equilibrium $\eta = 0$, so the net current is zero, the exchange current is

$$i_o = 2zFa\upsilon n \cdot \exp(-W/RT) \qquad (7)$$

In a high electrical field, $azF\eta > RTl$, and thus a Tafel-like behavior is obtained:

$$i = i_o \cdot \exp(azF\eta/RTl) \qquad (8)$$

In a low electrical field, Equation 8 can be linearized, and thus an Ohmic behavior is obtained:

$$i \approx 4.6\, i_o \eta/b \qquad (9)$$

where b is the analog of the Tafel slope extracted from Equation 8:

$$b = 2.3RTl/azF \qquad (10)$$

Hence, the average resistivity of the surface films can be extracted as

$$\rho/A = R_{film}/l = b/4.6\, i_o l = RT/2azFi_o \quad \text{A = the electrode's surface area} \qquad (11)$$

where $R_{film} = \eta/I$ is the surface film resistance for ionic conductance, extracted from Equation 9, and $I = iA$.

For example, the average resistivity values of surface films formed on active metals such as lithium magnesium and calcium in nonaqueous solutions are in the order of 10^8, 10^9, and 10^{10} $\Omega \cdot cm^2$, respectively [4].

Hence, it appears that metal electrodes in solutions (which are covered by surface films) may behave electrochemically, similar to the usual classical electrochemical systems (Butler-Volmer type behavior. [12]).

1.2   *Surface Films on Active Metal Electrodes Related to the Battery Field: Li, Ca, Mg*

It is worthwhile and important to mention surface film phenomena related to Li, Ca, and Mg electrodes when dealing with the role of surface films in lithium ion batteries, because there are some similarities in the surface phenomena on active metal electrodes and lithium insertion electrodes in the electrolyte solutions commonly used in nonaqueous batteries. The surface chemistry of lithium, calcium, and magnesium electrodes in a large variety of polar aprotic electrolyte systems has been largely explored during the past three decades, and hence, the knowledge thus obtained may help in understanding the more complicated cases of the surface chemistry and surface film phenomena on lithium insertion electrodes used in Li-ion batteries. Figure 1 illustrates typical surface phenomena, which characterize active metal electrodes [13]. Initially, lithium, calcium, and magnesium are covered by a bilayer surface film comprised of the metal oxide in its inner part, and metal hydroxide and carbonates in the outer side, due to the inevitable reactions of the active metals with atmospheric components during their production (Figure 1a). As these active metals are introduced into commonly used polar aprotic solutions, there are replacement reactions in which part of the original surface films are dissolved or react nucleophilically with solution species. Solution species also percolate through the original surface films and react with the active metal (Figure 1b). This situation forms highly complicated and non-uniform surface films that have a vertical multilayer structure and a lateral mosaic-type structure on a sub-micronic, and even nanometric, scale (Figure 1c). The unavoidable presence of trace water in nonaqueous solutions further complicates the structure of these surface films (Figure 1d). Water hydrates most of the surface species such as oxides, hydroxides, halides, and active metal organic salts that percolate through the surface films and react with the active metal to form metal hydroxide, metal oxide, and possibly metal hydride, with hydrogen gas as the co-product (which evolves away from the surface) [14]. In the case of lithium, all of the relevant lithium salts formed as surface species and deposited as thin layers, in ***all*** relevant nonaqueous polar aprotic electrolyte solutions (e.g.,

Li halides, hydroxide, oxides, carbonate, Li alkyl carbonates, carboxylates, Li nitride, Li sulfide, etc.) conduct lithium ions. Hence, Li-ion can migrate through the surface films under an electrical field (see the SEI model [4,5]). As a result, lithium can be dissolved and deposited through the surface films, which cover the lithium electrodes, while their basic structure can be retained.

In contrast, the surface films formed on calcium [15] and magnesium [16] in most of the commonly used aprotic electrolyte solutions cannot conduct the bivalent cations. Hence, dissolution of calcium and magnesium occurs via a breakdown of the surface films at relatively high over-potentials (Figure 1e [15,16]), and Ca or Mg deposition in a large variety of commonly used non-aqueous electrolyte solutions is impossible. In fact, there is no evidence of possible electrochemical calcium deposition from any nonaqueous solution. In the case of magnesium, it is possible to achieve a situation in which Mg electrodes are not passivated by stable, robust surface films. This is the case of ether solutions containing Grignard salts (RMgX) or complexes of the $Mg(AX_{4-n}R_n)_2$ type (A = Al, Br, X=halide, R=an organic group such as alkyl) [17]. In the latter solutions, Mg can be dissolved and deposited reversibly.

However, generally speaking, even in the case of Li electrodes, intensive active metal dissolution processes lead to the breakdown and repair of the surface films. The non-uniformity of the surface films leads to non-uniform secondary current distribution, which leads to a very non-uniform electro-chemical process. Hence, when metal is dissolved selectively at certain locations, the surface films are broken down and fresh active metal is exposed to solutions species, with which it reacts immediately (which leads to the "repair" of the surface films and increases further non-uniformity). The expected non-uniform structure of the surface films leads to the dendritic deposition of lithium in a large variety of electrolyte solutions, as illustrated in Figure 1f.

The surface chemistry of lithium electrodes in a large variety of electrolyte solutions has been intensively explored in recent years [18-24]. These studies have definitely paved the way for understanding the surface chemistry of lithiated carbon anodes for Li-ion batteries and for the identification of important surface species, which are formed on Li-C electrodes. The surface chemistry of calcium and magnesium was also explored [15, 16], but these studies are, in fact, irrelevant to the field of Li-ion batteries.

Intensive studies of lithium electrodes by impedance spectroscopy [25] and depth profiling by XPS [26,27] have clearly indicated the multilayer nature of the surface films formed on them. It is assumed that the inner part, close to the active metal, is compact, yet has a multilayer structure, and that the outer part facing the solution side is porous. Some evidence for this assumption was found by *in situ* imaging of lithium deposition-dissolution processes by atomic force microscopy (AFM) [28]. There is also evidence that the inner part of the surface films is more inorganic in nature, comprised of

species of a low oxidation state (due to the highly reductive environment, close to the active metal surface), while the outer parts of the surface films on lithium comprise organic Li salts [18,19,16,27,29]. These studies also serve as an important background for a better understanding of the electrochemical behavior of lithiated carbon electrodes.
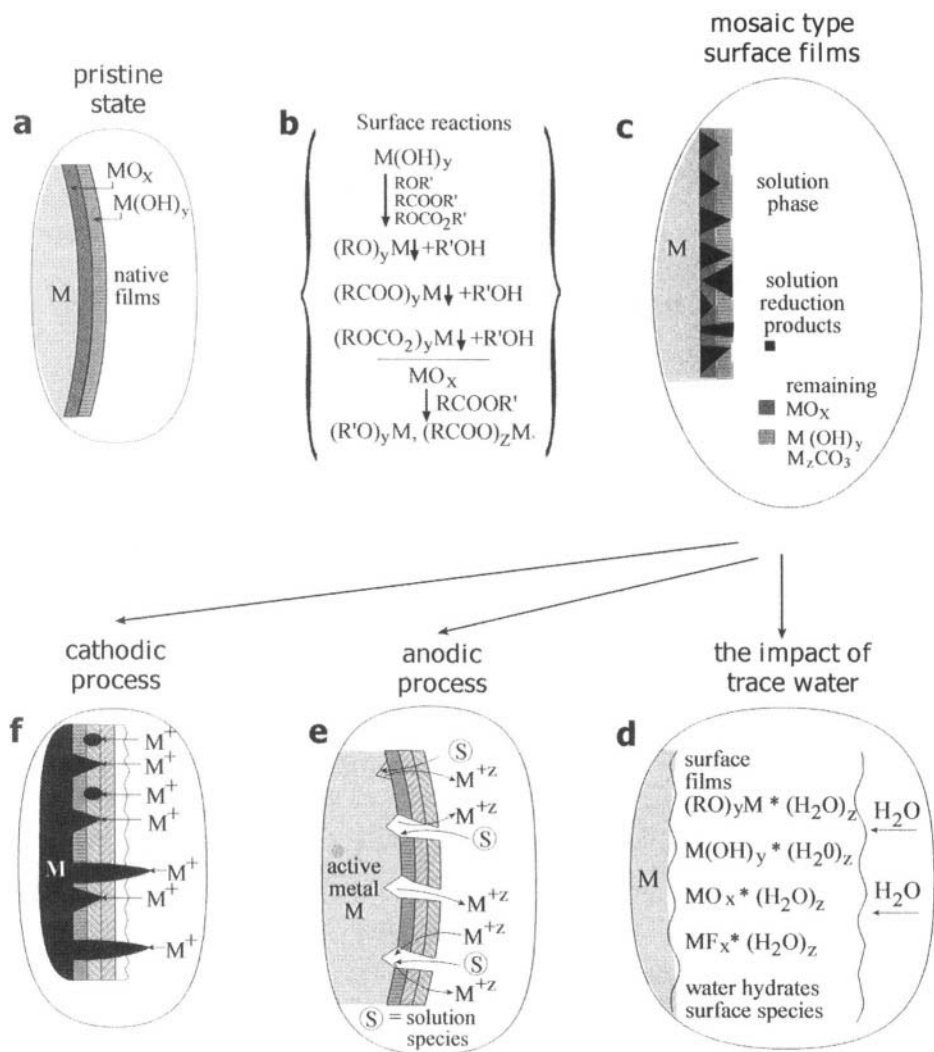
Figure 1. Schematic presentation of surface films on active metals in aprotic solutions. The pristine surface film (1a) interacts with solution species and is partially replaced by metal oxides, hydroxides, and salts, thus forming mosaic-type surface films (1b,c). Water hydrates most of the surface species. Its presence in solutions further complicates the surface chemistry (1d). Anodic processes (metal dissolution) may occur via breakdown of the films (1e). Metal deposition may be dendritic due to non-uniform secondary current distribution because of the non-uniform structure of the surface films (1f).

1.3 *Noble Metal Electrodes Polarized to Low Potentials in Lithium Salt Solutions*

We found that noble metal electrodes (e.g. Au, Pt) polarized to low potentials in nonaqueous Li salt solutions develop surface chemistry, surface films, and passivation phenomena, which are very similar to those developed on lithium electrodes in the same solutions [30,31]. In fact, when the noble metal electrodes are polarized to sufficiently low potentials in solutions of alkyl carbonates, esters, and ethers that contain lithium salts, the solvents, the atmospheric contaminants (O_2, H_2O, CO_2), and the salt anions (ClO_4^-, AsF_6^-, PF_6^-, $N(SO_2CF_3)_2^-$, etc.) are reduced to form insoluble Li salts (e.g., $ROCO_2Li$, $RCOOLi$, $ROLi$, Li_2CO_3, $LiOH$, Li_2O, LiF, $LiCl$), quite similar to the Li salts formed by reduction of these solution species by Li metal. However, the scenario of the surface film formation on noble metals may be different than that related to lithium metal. When a lithium electrode is in contact with the solution, the solution components are exposed to a very non-selective, highly reducing power of the Li surface. As the surface films grow, they progressively block the possibility of electron transfer from Li to the solution species, and hence, the selectivity of the reduction of solution species and the build-up of the surface films increases gradually as the surface films grow. This obviously leads to the multilayer structure of the surface films formed on Li electrodes in solutions. In the case of noble metal electrodes, their polarization to low potentials, either potentiostatically or galvanostatically, leads to a gradual and highly selective reduction of solution species, depending on the potentials that the electrode reaches. Figure 2 shows a typical example of the various processes that take place when a noble metal electrode is polarized cathodically and anodically in a polar aprotic solution containing a Li salt [32].

It should be noted that the study of noble metal electrodes in nonaqueous Li salt solutions is even more relevant to the understanding of the behavior of lithiated carbon anodes because, in the latter case, the carbon electrodes that are initially nearly surface film-free, are also polarized from OCV (≈ 3 V *vs.* Li/Li$^+$, see also Figure 2) to low potentials in the course of Li intercalation, and surface films are gradually formed on the carbon electrode as it reaches lower potentials. Hence, the order of surface reactions may be similar to that described in Figure 2, except for the Li under potential deposition and stripping processes, which are irrelevant to carbon electrodes (into which lithium is inserted at potentials higher than that of Li deposition).
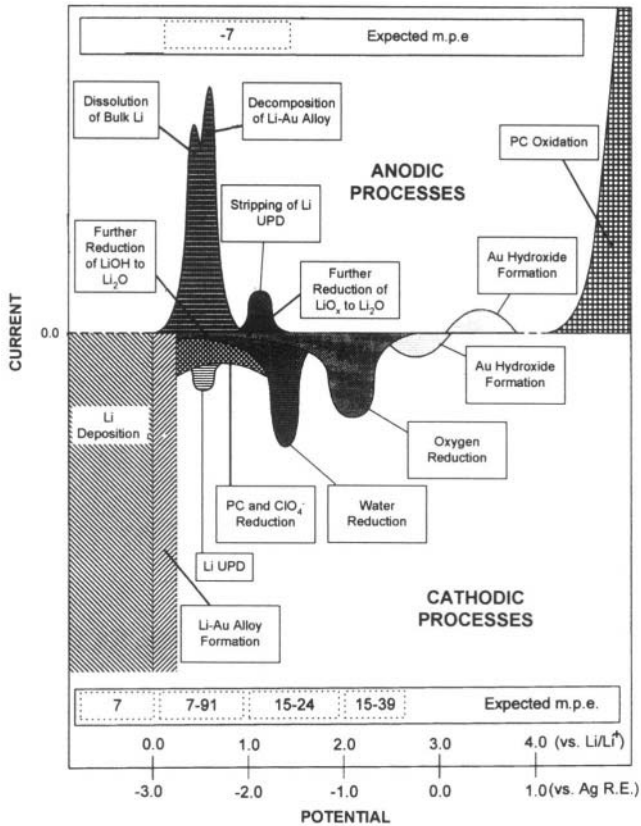
Figure 2. A schematic presentation of the electrochemical window of a Li salt/alkyl carbonate solution with a noble metal electrode. The various processes corresponding to the relevant voltammetric peaks are presented. Derived from reference 32, reproduced by permission of The Electrochemical Society, Inc.

2.0   THE SURFACE CHEMISTRY OF Li, Li_xO, CATHODICALLY POLARIZED NOBLE METALS IN Li BATTERY ELECTROLYTE SOLUTIONS

2.1   *Classification of Reactive Components: Solvents, Salts, Atmospheric Contaminants and Additives*

The nonaqueous solvents that are commonly used in electrochemistry can be classified as follows [33]:

1. Ethers

These include diethyl ether; members of the 'glyme' family, namely, polyethers of the $CH_3O(CH_2CH_2O)_nCH_3$ type (e.g., dimethoxyethene for n=1), cyclic ethers such as tetrahydrofuran (THF) and 2-methyl tetrahydrofuran; and cyclic acetals such as 1-3 dioxolane.

2. **Esters**

These include methyl formate, methyl and ethyl acetate, and **γ-buty-rolactone.**

3. **Alkyl carbonates**

These include cyclic compounds such as butylene, propylene, and ethylene carbonates (BC, PC, EC), and linear compounds such as dimethyl, diethyl carbonates, ethyl-methyl carbonate, etc. (DMC, DEC, EMC).

4. **Inorganic Solvents**

The most common inorganic solvents used in batteries were SO_2, Cl_2SO (thionylchloride), and SO_2Cl_2 (sulfuryl chloride). The former solvent was used in both secondary and primary Li battery systems, while the latter could only be used in primary Li batteries [34].

5. **Miscellaneous**

Solvents such as acetonitrile, nitromethane, N,N-dimethyl formamide, dimethyl sulfoxide, sulfolane, and methyl chloride are also often used in nonaqueous electrochemical studies.

It should be noted that the solvents in groups 2, 4 and 5 are irrelevant to the field of Li-ion batteries due to the limited electrochemical windows of some of them, problems of electrode surface reactivity with them, and the lack of electrode passivity in some of these solvents. The ethers (group 1) are also problematic, since their oxidation potentials are too low for 4 V Li-ion batteries.

Hence, the most suitable solvents for Li-ion batteries remain the alkyl carbonate (group 3 above) [3]. However, the high polarity of the alkyl carbonate solvents automatically means high reactivity at low potentials. These solvents are indeed readily reduced at potentials below 1.5 V *(vs.* Li/Li^+) in the presence of Li-ions [30,32]. The apparent stability of lithium or lithiated carbon electrodes in alkyl carbonate solutions is because of passivation phenomena of these electrodes, as described later. Solvent and electrolyte properties are discussed further in Chapter 5, Liquid Electrolytes.

In recent years, there has been an increasing interest in the use of solid electrolyte matrices for Li and Li-ion batteries. From the point of view of surface chemistry and surface film formation, we can divide the polymeric matrices connected to the field of Li batteries into two categories:

1. **Gel electrolytes** [35].

The polymeric matrix includes base polymers that do not interact with Li salts such as polyacrylonitrile, polyvinylidene-difluoride (PVdF), etc.; plasticizers that are usually alkyl carbonate solvents (e.g., EC, PC); and lithium salts. It should be noted that compounds with C-F bonds such as PVdF react with both Li and lithiated carbons to form carabides and LiF. However, in the case of the commonly used gel electrolytes, the reactions of the alkyl carbonates in the matrices dominate the electrodes' surface chemistry.

2. Solvent-free matrices

Here, the polymeric species are designed to interact with Li salts, leading to the necessary ionic separation for electrolyte systems, and therefore, the presence of liquid solvents can be avoided. In order to obtain dissolution of Li salts, the polymers have to contain ethers, ester or other polar groups. Indeed, the most important polymeric electrolytes of this kind are based on polyethylene oxide and its derivatives [36-40]. These polymers have the reactivity of ethers towards Li and lithiated carbon surfaces, which is much lower as compared with that of alkyl carbonates. However, since battery systems with solid-state electrolyte matrices are usually operated at elevated temperatures (>60 °C), it is obvious that there are surface reactions between the polyethers and the lithiated carbons which form of surface films. We should also mention problems of limited electrochemical windows when using solvent-free polymeric electrolytes, since the oxidation potentials of polyethers are similar to those of ethers which are usually in the 4-5 V range (*vs.* Li/Li^+).

Polymer and gel electrolyte systems are discussed in Chapters 7 and 8 by Nishi and Scrosati, respectively. Ionic liquids (ambient temperature molten salts) are discussed in Chapter 6.

The second component is, of course, the Li salts. The list includes $LiClO_4$, $LiAsF_6$, $LiBF_4$, $LiSO_3CF_3$, $LiN(SO_2CF_3)_2$, $LiC(SO_2CF_3)_3$, $LiN(S-O_2C_2F_5)_2$, $LiPF_6$, and, recently, the new salt from Merck, $LiPF_3(C_2F_5)_3$ (LiFAP) [41]. On examining the various Li salts available, we find that $LiPF_6$ is the most commonly used salt, so far, in Li-ion batteries because it is non-toxic, non-explosive, and highly soluble in nonaqueous solvents, thus forming highly conductive electrolyte solutions. In addition, it is apparently stable with both cathode and anode materials at a wide temperature range. All the other salts in the above list have disadvantages that make them less attractive than $LiPF_6$ for use in Li-ion batteries. For instance, $LiClO_4$ may be explosive, $LiAsF_6$ is considered to be too poisonous (arsenic), $LiSO_3CF_3$ solutions have too low a conductivity, and the salts containing the -SO_2R (fluorinated) groups may be too expensive and their thermal stability limited. It should be noted that **all** the anions of the above salts are reactive with lithium and lithiated carbons, and hence, their reaction with the electrodes may influence their surface chemistry considerably.

The third group of active components is obviously the reactive atmospheric gases. All nonaqueous solutions contain unavoidable traces of O_2, N_2, H_2O, and CO_2. All of these gases are reactive with lithium and lithiated carbon. Their surface reactions form Li oxides, Li nitrides, Li hydroxide, and Li carbonate, respectively [42]. We should add to this list of contaminants the decomposition products of $LiPF_6$. This salt decomposes to LiF and PF_5 (an equilibrium reaction) [43]. The latter compound readily hydrolyzes to form HF and PF_3O. Hence, $LiPF_6$ solutions **always** contain HF. HF reacts with both electrodes and basic surface species to form surface LiF as a major solid product.

The last group of reactive components to be mentioned is the various solution additives which were suggested for improving solution properties, electrode passivation, and for obtaining unique features such as overcharge protection and enhanced safety. In this respect, we can mention solvents such as halogenated alkyl carbonates, [44,45] sulfur-containing solvents (e.g., ethylene sulfite) [46,47], polymerizing agents such as vinylene carbonate [48], organo boron complexes [49], and inorganic compounds (CO_2 [50], SO_2 [51], nitrates [52],). The use of additives for the modification of the surface chemistry of electrodes in Li-ion batteries will be dealt with in depth later in this chapter (see Section 5.3).
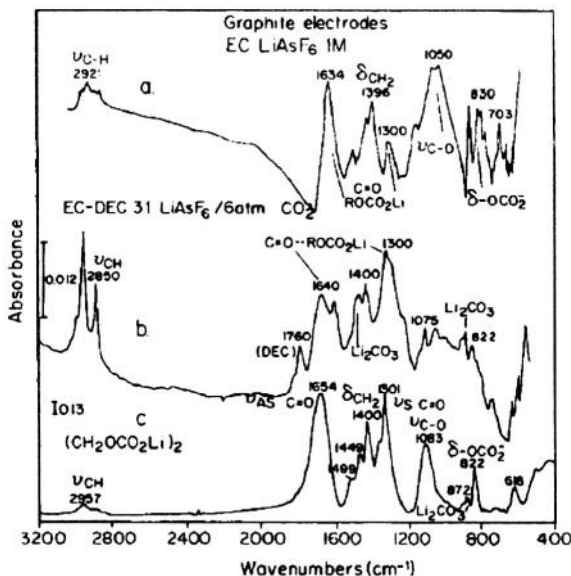
2.2 Basic Reactions of Nonaqueous Electrolyte Solutions on Li and Li-C Surfaces and on Carbon and Noble Metal Electrodes Polarized to Low Potentials

A great deal of effort has been invested in recent years in the study of the surface chemistry of lithiated carbon anodes in Li battery electrolyte solutions. Fortunately, the basic surface reactions of a large variety of nonaqueous Li salt solutions on Li, Li-C, and noble metal electrodes polarized cathodically are very similar. The tools for the study of the surface chemistry of these systems included XPS [53], AES [54], FTIR [55], Raman [56], EDAX [57], and, recently, SIMS-TOF [58]. The study of the surface chemistry of the composite electrodes used in Li-ion batteries is difficult. Hence, a previous study of the surface chemistry developed on noble metal and Li electrodes in the solutions of interest may be very helpful. It should be emphasized that the use of XPS, AES, Raman (laser beam needed), and SIMS-TOF may lead to changes in the surface species during the measurements due to further surface reactions induced by X-rays, laser beams, or bombardment by ions.

Surface sensitive FTIR spectroscopy is, so far, the best non-destructive surface-sensitive technique that can provide useful and specific information. While the study of the surface chemistry of Li or noble metal electrodes requires the use of methods such as external or internal reflectance, the study of the composite electrodes used in Li-ion batteries requires the use of the highly problematic diffuse reflectance mode (DRIFT) [59]. Because of that, the study of surface films formed on carbon electrodes can benefit so much from preceding studies of the surface films formed on lithium or noble metal electrodes in the same solutions.

Figure 3 shows a typical FTIR analysis of the surface films formed on graphite electrodes in a methyl-propyl carbonate(MPC)solution, which is based on FTIR spectra of a higher resolution obtained from lithium electrodes treated in the same solution and some reference solutions (external reflectance mode) [60]. Spectrum 3a relates to surface films on a graphite electrode cycled in an MPCsolution. Spectrum 3b relates to surface films formed on lithium in the

same solution. This spectrum (external reflectance mode) is of a higher resolution than that of the graphite particles (3a, diffuse reflectance mode). With the aid of two more reference spectra, from surface films formed on lithium in DMC solutions containing methanol (3c), and from a thin film of $LiOCH_3$ on lithium (3d), it was possible to conclude that the surface films formed on graphite in MPC are composed of all the possible reduction products of the solvent. These include CH_3OLi, CH_3OCO_2Li, C_3H_7OLi, and $C_3H_7OCO_2Li$. Figure 4 shows FTIR spectra measured from graphite electrodes treated in EC-based solutions (including CO_2 as an additive in one case), and an FTIR spectrum of the major expected surface species formed, $(CH_2OCO_2Li)_2$ [61]. The latter species was isolated by electrolysis of EC in a $THF/(C_4H_9)_4NClO_4$ solution followed by precipitation in a Li salt solution. These spectral studies clearly show that in EC-based solutions, $(CH_2OCO_2Li)_2$ is a major surface species formed on carbon electrodes. When the solutions contain CO_2, Li_2CO_3 is also formed as a major surface species. Figures 3 and 4 demonstrate that surface-sensitive FTIR spectroscopy serves as a very useful tool for the analysis of surface reactions of Li-ion battery electrodes, as well as the importance of the use of reference measurements (e.g., studies of Li and noble metal electrodes treated in the same solutions).

Figure 3. (a) FTIR spectra of graphite particles taken from an electrode which was lithiated-delithiated (one cycle) in a MPC/1 M LiAsF₆ solution (diffuse reflectance mode). (b) FTIR spectra measured *ex situ* (external reflectance mode) from a lithium electrode freshly prepared in a MPC/1 M LiAsF₆ solution and stored in it for 3 h. (c) Same as (b). Li electrode, DMC/CH₃OH 0.1 M solution. (d) A reference FTIR spectrum of a thin film of CH₃OLi on a reflective Li surface (external reflectance mode). Derived from reference 64 and reprinted with permission from Elsevier Science.

Figure 4. (a) FTIR spectra measured from synthetic graphite particles (palletized with KBr) taken from an electrode that was lithiated and delithiated in an EC/LiAsF$_6$ 1 M solution (transmittance mode); (b) Same as for (a). The solution was EC-DEC 3:1/LiAsF$_6$ 1 M under 6 atm of CO$_2$; (c) The FTIR spectrum of the EC cathodic electrolysis product in a THF/(C$_4$H$_9$)$_4$NClO$_4$ 0.2 M solution, isolated as a Li salt, identified as (CH$_2$OCO$_2$Li)$_2$. Derived from Reference 64.
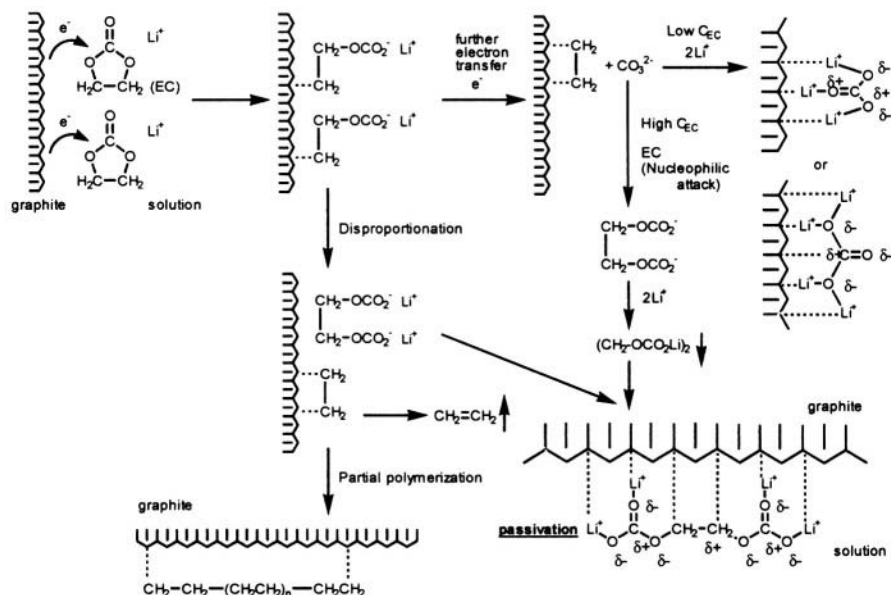
Figure 5. The various reduction patterns of EC on graphite and the relevant product distribution. The chemical structure of the expected major PC reduction product is also shown for comparison. Adapted from reference 64.

Table 1. Reaction products of solvents, salts, and atmospheric contaminants with lithium and lithiated carbon surfaces

Solvent Type	Specific Solvent	Uncomtaminated Solutions	Contaminants/Additives			
			H_2O	O_2	CO_2	HF
Alkyl Carbon-ates	PC	$CH_3CH(OCO_2Li)CH_2OCO_2Li$ & Propylene	$ROCO_2Li$, Li_2CO_3 (reaction of $ROCO_2Li$ + H_2O) LiOH-Li_2O	$ROCO_2Li$, Li_2O Li_2O_2	$ROCO_2Li$, + Li_2CO_3	LiF + H_2CO_3 $ROCO_2M$
	EC	$(CH_2OCO_2Li)_2$ & Ethylene				
	DMC	$ROCO_2Li \downarrow (CH_3OCO_2Li)$ + CH_3Oli				
	DEC	$CH_3CH_2OCO_2Li$ + CH_3CH_2OLi				
	EMC	CH_3OLi, CH_3OCO_2Li				
	PMC	CH_3OLi, CH_3OCO_2Li, $CH_3CH_2CH_2OLi$, $CH_3CH_2CH_2OCO_2Li$				
Esters	MF	Mostly HCO_2Li, ROLi (CH_3OLi?)	HCO_2Li	Li oxides+ HCO_2Li	HCO_2Li + Li_2CO_3	LiF
	γ-BL	$CH3(CH2)2COOLi$, cyclic β-keto ester anion, di-Li salt	$LiO(CH_2)_3COOLi$	Lioxides + $ROCO_2Li$ species	RCOOLi + Li_2CO_3	LiF
Ethers	THF	ROLi ($CH_3(CH2)_3OLi$)	LiOH Li_2O Li alkoxides	Li oxides RoLi species	Li_2CO_3 ROLi species $ROCO_2Li$	Ethers May Polymer-ize
	2Me-THF	Li pentoxides				
	DME	ROLi (CH_3OLi)				
	1,3-DN	HCO_2Li, $CH_3CH_2OCH_2OLi$, Poly DN species				
	DEE	$CH_3CH2OLi$, $(CH_2OLi)_2$				
	Diglyme (DG)	CH_3OLi, $CH_3OCH_2CH_2OLi$, $(CH_2OLi)_2$				

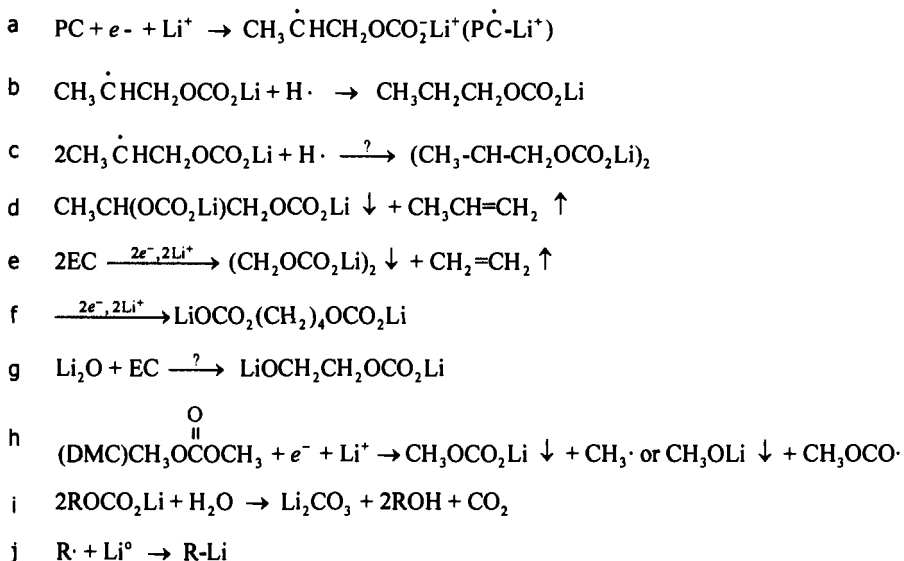| Solvent Type	Specific Solvent	Uncomtaminated Solutions	Contaminants/Additives			
			H_2O	O_2	CO_2	HF
Mixtures	EC-PC	EC Reduction products dominate	$ROCO_2Li$, Li_2CO_3, HCO_2Li, $LiOH$-Li_2O	Li_2O, $ROCO_2Li$	Li_2CO_3, $ROCO_2Li$	LiF
	EC-EC					
	EC-DMC					
	EC-DEC					
	MF-EC	HCO_2Li, $ROCO_2Li$ species	$ROCO_2Li$, Li_2CO_3, HCO_2Li, $LiOH$-Li_2O	Li_2O $ROCO_2Li$ HCO_2Li	$ROCO_2Li$ HCO_2Li Li_2CO_3	LiF
	MF-PC					
	MF-DMC	HCO_2Li dominates, $ROCO_2Li$ Li minor				
	MF-DEC	HCO_2Li, CH_3CH_2OLi, $CH_3CH_2OCO_2Li$	HCO_2Li, Li_2O-$LiOH$		Li_2CO_3+ solvent red- uction products	LiF
	MF-Ethers	ROLi ($CH_3(CH_2)_3OLi$)	$LiO(CH_2)_3COOLi$			Ethers may polymer -ize
	EC or PC with Ethers	$ROCO_2Li$ species dominate, ROLi (minor)	Li_2CO_3, $ROCO_2Li$ $LiOH$-Li_2O			
	THF-2MeTHF	THF reduction products dominate				
Salts						
$LiAsF_6$	LiF, Li_XAsF_Y		$LiPF_6$	LiF, Li_XPF_Y, $Li_XPF_YO_Z$?		
$LiClO_4$	Li_2O, LiCl, $LiClO_3$, $LiClO_2$, etc.		$LiSO_3CF_3$	$Li_XS_YO_Z$, LiF, RCF_YLi_Z, etc		
$LiBF_4$	LiF, Li_XBF_Y, $Li_XBF_YO_Z$?		$LiN(SO_2CF_3)_2$	LiF, $Li_XS_YO_Z$, Li_3N, RCF_YLi_Z, $Li_2NSO_2CF_3$		

PC=propylene carbonate; EC=ethylene carbonate; DMC=dimethyl carbonate; DEC=diethyl carbonate; MF=methyl formate; γ-BL=γ-butyrolactone; THF-tetrahydrofuran, 2Me-THF=2-methyltetrahydrofuran; DME=dimethoxyethane; 1,3-DN=1,3-dioxolane; EMC=ethyl methyl carbonate;PMC=propyl methyl carbonate; DEE=diethoxyethane; DG=$CH_3OCH_2CH_2OCH_2CH_2OCH_3$.

Figure 5 is a schematic representation of major aspects of the surface chemistry of graphite electrodes in electrolyte solutions containing EC as a major component, based on rigorous FTIR and XPS spectroscopic studies [62].

Table 1 provides surface analysis of graphite and lithium electrodes in a large variety of commonly used electrolyte solutions. The major surface species that comprise the surface films formed on the active electrodes in the solutions specified, are presented. Schemes 1 and 2 describe the surface chemistry of Li and Li-C electrodes in EC- and PC-based electrolyte solutions. Scheme 3 describes the surface reactions of the Li and Li-C electrodes in ester-based solutions. Scheme 4 relates to the surface reactions of ethers with Li and Li-C electrodes. Scheme 5 describes selected surface reactions of commonly used salt anions in Li and Li-ion batteries. Finally, Scheme 6 shows possible surface reactions of CO_2 on Li and Li-C electrodes. Table 3 (at the end of the chapter) provides a list of references for the various surface studies described in Figures 2-5, Table 1, and Schemes 1-6 [29,42,50,53,58, 60-73].

We should note that in addition to the above-described surface chemistry, there are reports in the literature on the formation of polymeric species on lithiated carbon electrodes in alkyl carbonate solution. These polymers may include polyethylene (due to polymerization of the ethylene formed by EC reduction), and polycarbonates (due to polymerization of cyclic alkyl carbonates such as EC) [58,63].

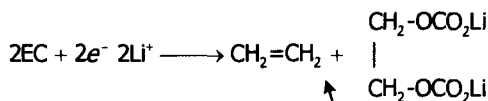**Scheme** 1: Possible reduction patterns of alkyl carbonates on Li

a $PC + e- + Li^+ \rightarrow CH_3\dot{C}HCH_2OCO_2^-Li^+ (P\dot{C}\text{-}Li^+)$

b $CH_3\dot{C}HCH_2OCO_2Li + H\cdot \rightarrow CH_3CH_2CH_2OCO_2Li$

c $2CH_3\dot{C}HCH_2OCO_2Li + H\cdot \xrightarrow{?} (CH_3\text{-}CH\text{-}CH_2OCO_2Li)_2$

d $CH_3CH(OCO_2Li)CH_2OCO_2Li \downarrow + CH_3CH=CH_2 \uparrow$

e $2EC \xrightarrow{2e^-,2Li^+} (CH_2OCO_2Li)_2 \downarrow + CH_2=CH_2 \uparrow$

f $\xrightarrow{2e^-,2Li^+} LiOCO_2(CH_2)_4OCO_2Li$

g $Li_2O + EC \xrightarrow{?} LiOCH_2CH_2OCO_2Li$

h $(DMC)CH_3\overset{\overset{O}{\|}}{O}COCH_3 + e^- + Li^+ \rightarrow CH_3OCO_2Li \downarrow + CH_3\cdot \text{ or } CH_3OLi \downarrow + CH_3OCO\cdot$

i $2ROCO_2Li + H_2O \rightarrow Li_2CO_3 + 2ROH + CO_2$

j $R\cdot + Li^o \rightarrow R\text{-}Li$

Scheme 2. EC (PC) reduction mechanisms (nudeophilic paths).

The expected reaction

$$EC + 2e^- + 2Li^+ \not\longrightarrow Li_2CO_3 + CH_2{=}CH_2$$
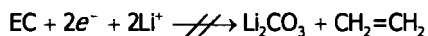
Has no evidence from surface studies

<u>Surprisingly</u>

$$2EC + 2e^- \; 2Li^+ \longrightarrow CH_2{=}CH_2 + \begin{array}{l} CH_2\text{-}OCO_2Li \\ | \\ CH_2\text{-}OCO_2Li \end{array}$$

<u>A possible mechanism:</u> $2(EC + e^- \; Li^+) \rightarrow 2\begin{bmatrix} OCO_2Li \\ | \\ CH_2 \; \overset{\cdot}{C}H_2 \end{bmatrix}$ — Disproportionation on the Li or Li-C surface

In a separate study, a nucleophilic attack on EC:

$$ROLi + EC \xrightarrow{\text{DMC, THF}} Li_2CO_3 \text{ and } (CH_2OCO_2Li)_2 \; !! + \text{other products}$$

<u>A possible mechanism:</u>

$$\begin{array}{c} CH_2 - O \\ \quad \quad \quad \diagdown \\ \quad \quad \quad \quad C{=}O \\ \quad \quad \quad \diagup \\ CH_2 - O \end{array} \xrightarrow{Li^+} ROCH_2\text{-}CH_2\text{-}OCO_2Li \quad \text{Poor nucleophile}$$

(RO⊖ attacks)

$$\begin{array}{c} RO - CH_2 \\ | \\ CH_2 - OCO_2Li \end{array} \xrightarrow[\text{attack}]{\text{second nucleophilic}} ROCH_2CH_2CH_2OR + \quad \text{nucleophile}$$

(RO⊖; carbonate anion with $\delta - \; O \cdots Li^+ \cdots O \; \delta -$)

carbonate anion:
$$Li^+ \rightarrow Li_2CO_3 \downarrow \underline{\text{Ion Pairing}}$$
competition
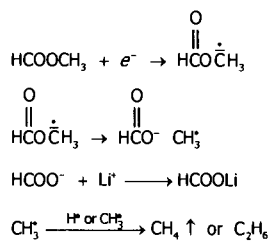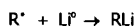$$EC \rightarrow \begin{array}{l} CH_2\text{-}OCO_2Li \\ | \\ CH_2\text{-}OCO_2Li \end{array} \downarrow \; \text{Nucleophilic attack}$$
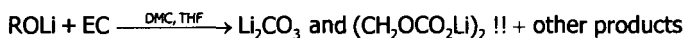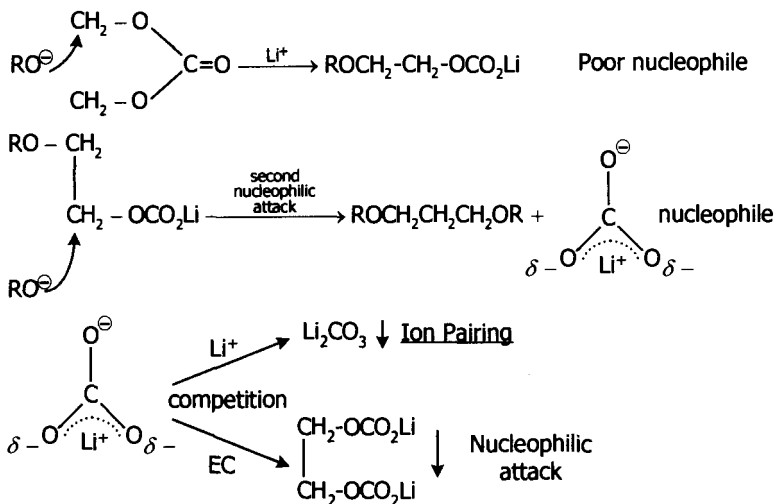
Hence, another reduction mechanism of EC (or PC) on active electrodes can be:
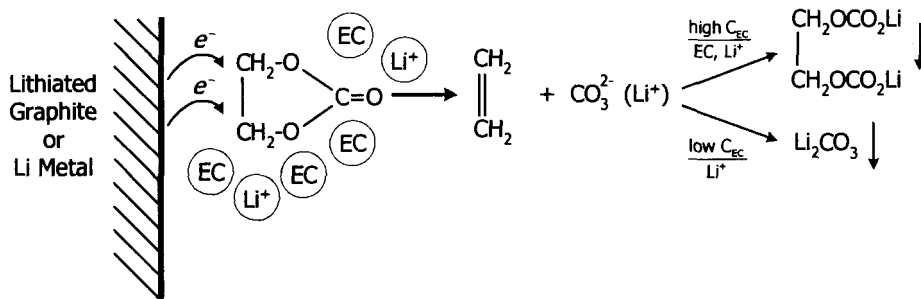
Scheme 3. Ester reaction schemes

γ-Butyrolactone

Longer Chain Formation

Methyl Formate

$$HCOOCH_3 + e^- \rightarrow HCO\overset{\cdot}{C}H_3$$

$$HCO\overset{\cdot}{C}H_3 \rightarrow HCO^- \; CH_3^\bullet$$

$$HCOO^- + Li^+ \longrightarrow HCOOLi$$

$$CH_3^\bullet \xrightarrow{\;H^\bullet \text{ or } CH_3^\bullet\;} CH_4 \uparrow \text{ or } C_2H_6$$

General

$$R^\bullet + Li^o \rightarrow RLi$$
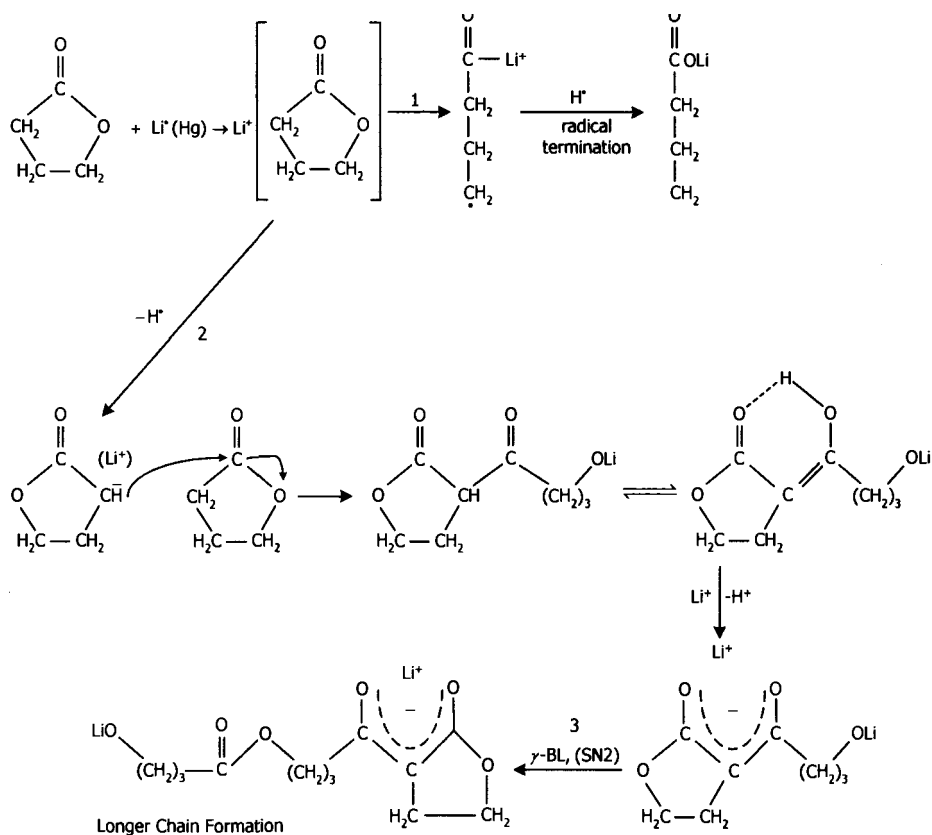
Scheme 4: Ether reaction patterns

a $R\text{-}O\text{-}R' + e^- + Li^+ \rightarrow R'O\overset{\bullet}{R}Li^{\oplus}$

b $R'O\overset{\bullet}{R}Li^{\oplus} \rightarrow ROLi + R'$ or $R'OLi + R$

c $R\bullet \xrightarrow{H\bullet} RH$ *or* $2R\bullet \rightarrow R_2$ *or* $R\bullet \xrightarrow{Li^0} RLi$

d   For example, (EC) $CH_3CH_2OCH_2CH_2OCH_2CH_3 + Li^+ + e^-$

$$CH_3CH_2OLi\downarrow + \bullet CH_2CH_2\text{-}OCH_2CH_3 \; \underline{and}$$

$$CH_3CH_2\bullet + CH_3CH_2\text{-}OCH_2CH_2OLi \downarrow$$

e   (DME) $CH_3OCH_2CH_2OCH_3 + 2Li^+ + 2e^- \rightarrow 2CH_3OLi\downarrow + H_2C{=}CH_2\downarrow$

f   THF $\xrightarrow{Li^0} CH_3CH_2CH_2CH_2OLi$ (and/or) $Li\text{-}(CH_2)_4OLi$

g   2Me-THF $\xrightarrow{Li^0} CH_3(CH_2)_4OLi + CH_3\overset{\overset{\displaystyle CH_3}{|}}{C}HCH_2CH_2OLi$
                       (and/or) $Li\text{-}ROLi)$
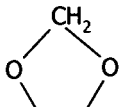
h   (DN) $H_2\overset{\overset{\displaystyle CH_2}{\diagup \;\; \diagdown}}{C}\text{-}\underset{O \diagdown\;\;\diagup O}{CH_2} + e^- + Li^+ \rightarrow \overset{\bullet}{C}H_2\,CH_2OCH_2OLi$ (major)

                  or $\overset{\bullet}{C}H_2\,OCH_2CH_2OLi$

i $CH_2CH_2OCH_2OLi \xrightarrow{H\bullet} CH_3CH_2OCH_2OLi\downarrow$
                          $CH_3CH_3\uparrow + HCO_2Li$

j $\bullet CH_2CH_2OCH_2OLi \xrightarrow{Li^0} LiCH_2CH_2OCH_2OLi$

k $ROLi + nDN \xrightarrow{polymerization} R\text{-}(OCH_2CH_2\text{-}OCH_2)_nOLi\downarrow$

Scheme 5. Surface reactions of commonly used Li salts.

a $LiAsF_6 + 2Li^+ + 2e^- \rightarrow 3LiF \downarrow + AsF_3 \text{ (sol)}$

b $AsF_3 + 2_xLi^+ + 2xe^- \rightarrow Li_xAsF_{3-x}^- + xLiF \downarrow$

c $PF_6^- + 3Li^+ + 2e^- \rightarrow 3LiF \downarrow + PF_3$

d $LiPF_6 \rightleftarrows LiF + PF_5$

e $PF_5 + H_2O \rightarrow PF_3O + 2HF$

f $PF_5 + 2_xLi^+ + 2xe^- \rightarrow Li_xPF_{5-x} \downarrow + xLiF \downarrow$

g $PF_3O + 2_xLi^+ + 2xe^- \rightarrow Li_xPF_{3-x}O \downarrow + xLiF \downarrow$

h $BF_4^- \xrightarrow{Li^+, e^-} LiF \downarrow, Li_xBF_y \downarrow \text{ (in general)}$

i $LiClO_4 + 8Li^+ + 8e^- \rightarrow 4Li_2O + LiCl$

j $LiClO_4 + xLi^+ + xe^- \rightarrow LiClO_{(4-\frac{1}{2}x)} + \frac{1}{2}xLi_2O \ (x = 2, 4, 6)$

k $LiN(SO_2CF_3)_2 + ne^- + nLi^+ \rightarrow Li_3N + Li_2S_2O_4 + LiF + C_2F_xLi_y$

l $LiN(SO_2CF_3)_2 + 2e^- + 2Li^+ \rightarrow Li_2NSO_2CF_3 + CF_3SO_2Li$

m $Li_2S_2O_4 + 10e^- + 10Li^+ \rightarrow 2Li_2S + 4Li_2O$

n $LiC(SO_2CF_3)_3 + 2e^- + 2Li^+ \rightarrow Li_2C(SO_2CF_3)_2 + LiSO_2CF_3, \text{ etc.}$

o $Li_2S_2O_4 + 4e^- + 4Li^+ \rightarrow Li_2SO_3 + Li_2S + Li_2O$

p $2LiSO_3CF_3 + 2Li^+ + 2e^- \rightarrow 2Li_2SO_3 + C_2F_6$

q $R\text{-}CF_3 + 2Li^+ + 2e^- \rightarrow RCF_2Li + LiF$

r $Li_2SO_3 + 6Li^+ + 6e^- \rightarrow Li_2S + 3Li_2O$

Scheme 6. Possible CO_2 reaction patterns

a $CO_2 + e^- + Li^+ \rightarrow \overset{\bullet}{C}O_2Li$

b $\overset{\bullet}{C}O_2Li + CO_2 \rightarrow O=\overset{\bullet}{C}\text{-}O\text{-}CO_2Li$

c $O=\overset{\bullet}{C}\text{-}O\text{-}CO_2Li + e^- + Li^+ \rightarrow CO \uparrow + Li_2CO_3 \uparrow$

d $2LiOH \downarrow + CO_2 \rightarrow Li_2CO_3 \downarrow + H_2O$

e $Li_2O \downarrow + CO_2 \rightarrow Li_2CO_3 \downarrow$

f $ROLi \downarrow + CO_2 \rightarrow ROCO_2Li \downarrow$
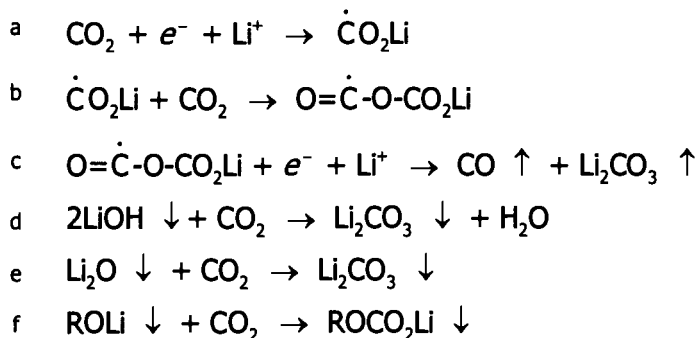
3.0   SURFACE CHEMISTRY OF CARBON ELECTRODES

3.1   *Classification of Carbon Materials in Terms of Li Insertion*

There are a large variety of carbonaceous materials that can interact with lithium ions in solutions and serve as Li insertion anodes in Li-ion batteries. The behavior of the lithium insertion processes into carbons in terms of capacity, stability, kinetics, and potential profile, depends very strongly on their 3D structure and morphology. Indeed, this chapter deals with the surface chemistry of electrodes, and hence, cannot deal in depth with structural aspects of carbonaceous materials. However, it was found and clearly demonstrated that the surface chemistry of carbons, and especially their surface film related stability, depends very strongly on their 3D structure. Therefore, in this section we deal with some structural aspects of carbonaceous materials.

Figure 6 presents a scheme of major classes of carbons, which are currently studied in connection with Li-ion battery systems. These include graphite materials that are highly ordered and are composed of graphene planes packed in parallel, [74] between which Li-ions are intercalated. Another type of ordered carbon that was recently studied in connection with Li insertion was the carbon nanotube (either single or multiwall structure) [75,76]. The other two major classes are disordered carbons that may be either soft and graphitizable [77-80] or hard and non-graphitizable [81-85]. The graphitic materials suggested as anode materials appear as flakes [86,87], beads [88-90], fibers [91-92], and chopped fibers [93]. Figure 7 presents SEM micrographs of selected carbonaceous materials of different 3D structure and morphology. Figure 8 shows illustrations of the morphology of several types of graphitic materials that are currently used as anode materials in Li battery systems.

We should emphasize some points regarding the 3D structure and morphology of carbonaceous materials that are important to the field of Li-ion batteries:

1. Graphitic carbons can insert Li up to a stoichiometry of LiC_6, corresponding to $372 \ mAh \cdot g^{-1}$. The process is intercalation: Li-ions occupy sites between graphene planes.

2. Graphitic carbons can appear in a variety of shapes and morphologies, as demonstrated in Figures 7 and 8 (flakes, beads, fibers, etc.). The morphology of the graphitic materials may have a strong impact on their electrochemical behavior.

Graphite

basal plane surface

graphene layers

layer plane spacing ($\frac{C}{2}$ = 0.3354 nm)

outline of unit cell

0.246 nm   0.142 nm

Carbon Nanotubes

SWNT

MWNT

Disordered Carbons

cluster

void

(a) soft carbon

Lc

La

(b) hard carbon

Lc

La

Li in nanopores

Li adsorbed on carbon layer surfaces

Li storage in disordered carbons
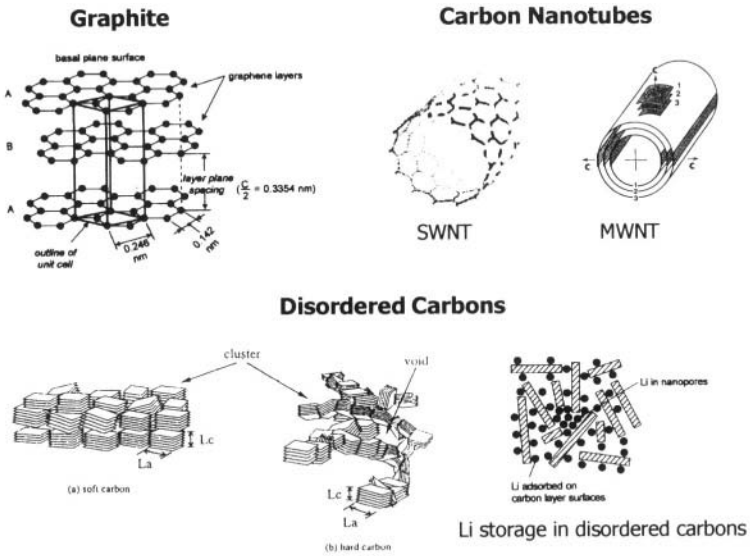
Figure 6. A schematic presentation of various types of carbons that can insert lithium reversibly.

Graphite flakes

MCMB

Graphite fibers

1 μm

Disordered carbon
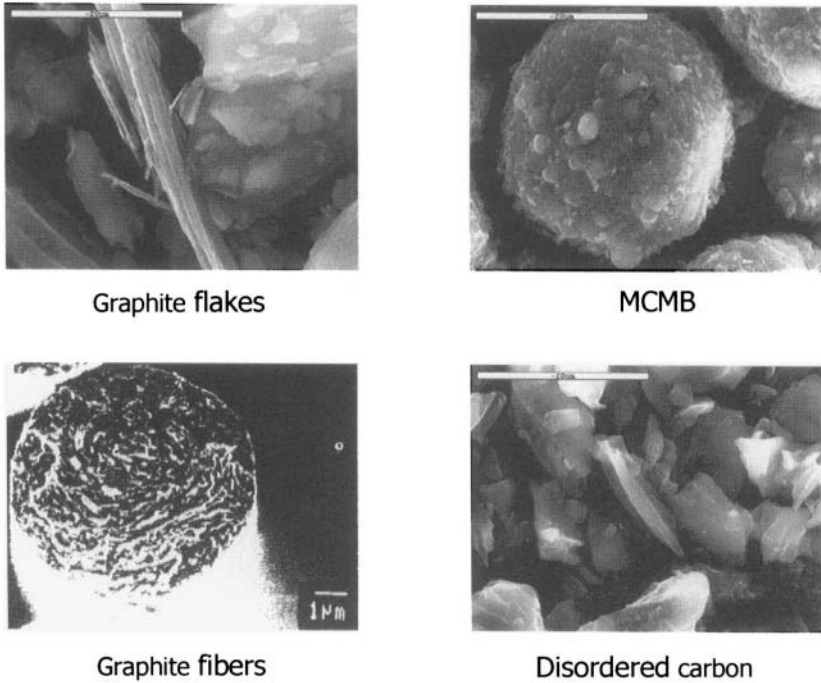
Figure 7. SEM micrographs of four types of carbon particles that may be used as anode materials in Li-ion batteries. A scale appears in each micrograph.
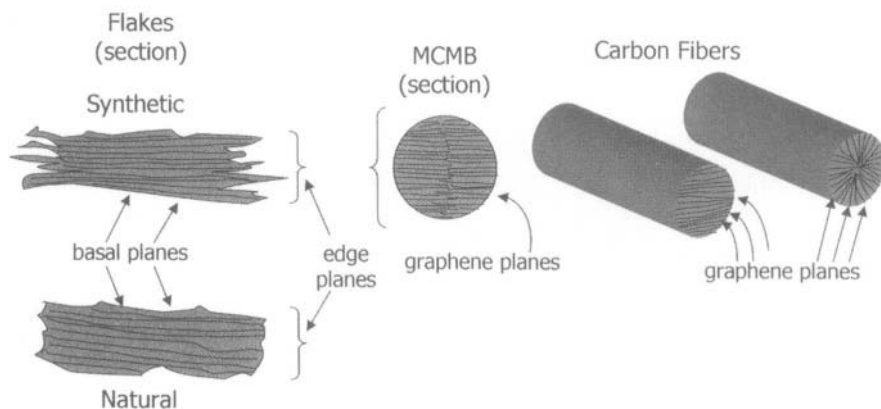
Figure 8. A schematic presentation of the morphology of various types of graphites used in anodes for Li-ion batteries.

In general, graphites are the carbon material most sensitive to the solution composition, in terms of reversibility and stability (in Li insertion processes). As discussed in depth in the next section, the stability of graphite electrodes in Li insertion processes depends on surface film formation and passivation phenomena. The morphology of the graphite particles strongly influences critical stages in the precipitation of the surface films and their passivation properties. In general, when the graphite particles have some degree of disorder (either turbostratic or in orientation of the crystals comprising the particles), their reversibility and stability in Li insertion processes is higher and their performance is less dependent on the solution composition, as compared with highly ordered materials.

3. Disordered carbons may insert lithium at a higher capacity than that of graphite. The mechanisms for Li insertion into disordered carbons are complicated and cannot be considered as a simple intercalation [94-95]. There are several types of Li insertion sites in disordered carbons [96]. Part of the capacity is due to adsorption type processes [97], and part of the Li insertion may involve interactions with C-H bonds [98-99]. These complications may lead to intrinsic irreversibility in Li insertion processes into disordered carbons.

4. The impact of the surface chemistry on the performance of disordered carbons is much less important as compared with the case of graphite. Some destruction mechanisms that relate to surface reactions of the carbons with solution species that exist in graphitic materials [64] are irrelevant to disordered carbons. This is because the existence of disorder in carbonaceous materials adds some intrinsic stability to their structure (as compared with the highly ordered graphitic carbons).

3.1   *The Anodes and Cathodes in Li-Ion Batteries Are Composite Electrodes*

The cathodes are dealt with in depth in Section 7 of this chapter. However, there are some common morphological features of both anodes and cathodes that justify a comparative discussion. As such, some of their properties related to their morphology are dealt with in this section.

Both the anodes and the cathodes used in Li-ion batteries are composite electrodes. Carbon anodes include the active mass, which may comprise more than one type of carbon particle; (>90%) polymeric binder such as Teflon, or polyvinylidene difluoride PVdF (<10%), and a metallic current collector (usually copper foil or grid). The cathodes also include the active mass (lithiated transition metal oxide, >85%), and a polymeric binder (<10%). However, it also has to contain conductive additives, which are usually high surface area carbon powders (<10%). The current collectors for cathodes are usually aluminum foils or grids. The choice of current collectors for the above electrodes definitely relates to their reactivity and surface chemistry. Although copper does not dissolve electrochemically in nonaqueous Li salt solutions in the potential range to which the anodes are exposed (0-3 V *vs.* Li/Li$^+$), it is definitely reactive in the Li battery electrolyte solutions [100]. For instance, there are possible redox reactions between the copper and salt anions, which are oxidizers. However, the surface species thus formed allow electron transfer to the active mass. On a thermodynamic basis, aluminum is electrochemically unstable at the potentials of the Li-ion battery cathodes (>3 V *vs.* Li/Li$^+$). Its apparent stability is due to passivation [101]. For instance, in solutions containing the commonly used salt, $LiPF_6$, which have obvious HF contamination, aluminum fluoride formation passivates the aluminum. These passivation phenomena prevent electrochemical Al dissolution, but allow a smooth charge flow between the active mass and the aluminum current collector. The composite electrodes are usually prepared under some pressure in order to obtain a compact active mass, and their morphology is critical to their performance. On the one hand, the formation of a compact active mass means better electrical contact among the electrode´s components and better passivation by the surface films formed at the electrode-solution interface, and a lower irreversible capacity consumed in the formation of the surface films. On the other hand, too compact a structure and morphology also means that there is worse contact between the solution and the entire active mass.

Figure 9 shows typical schemes and SEM micrographs of a carbon anode composed of graphite flakes and a $LiCoO_2$ cathode comprised of irregularly shaped micrometric particles. Figure 10 shows AFM images of pressurized graphite and $LiCoO_2$ cathodes, and compares the slow scan rate cyclic voltammograms of pressurized and unpressurized electrodes (same active mass, same electrolyte solutions). AFM images of the pressed electrodes

after cycling are also presented, and clearly show morphological changes on both anodes and cathodes that are related to surface film formation [102]. This figure demonstrates several important points related to the morphology of electrodes for Li-ion batteries and its impact on their performance.

1. In the case of graphite electrodes, the active mass is relatively soft. When the active mass is comprised of flakes, even application of mild pressure orients the particles in such a way that contact of solution species and part of the active mass is blocked. This is well reflected in the cyclic voltammograms presented in Figure 10: the pressurized graphite electrodes have slower kinetics and a less capacity.

2. In the case of cathodes, their active mass usually comprises relatively hard and irregularly shaped particles. Thereby, application of pressure increases the quality of the electrical contact of the particles, but not at the expense of solution-active mass contact. This is well reflected in the voltammograms presented in Figure 10, which show that pressurized $LiCoO_2$ electrodes have faster kinetics than non-pressurized ones.

3.2   The Electrochemical Response of Carbon Electrodes

It is impossible to deal with surface films on carbon electrodes and their impact on the degree of reversibility and stability of Li insertion processes without looking at the broader view, namely, the overall electrochemical response of lithiated carbon electrodes, to which the formation and existence of surface films contribute a great deal. Figure 11 presents the typical electrochemical response of graphite and disordered carbon electrodes in galvanostatic Li insertion-deinsertion processes (a, b, respectively). The chronopotentiograms of Figure 11 relate to the first, constant current, Li insertion-deinsertion cycle of the pristine carbon electrodes in $LiAsF_6$ 1M/methylformate solutions under CO_2 atmosphere. Both electrodes behave highly reversibly in this solution [50]. Both chronopotentiograms show a plateau ranging between 1.6 V and 1 V *vs.* Li/Li^+. This plateau relates to the surface reactions of the electrodes when polarized cathodically. Solvent, salt anions, atmospheric contaminants and active additives are reduced at potentials, which are usually much higher than those of Li insertion. As explained in previous sections, these reduction processes form surface films because part, most, or all of the reduction products, which are inorganic or organic Li salts, are insoluble in the mother solutions. As the solubility of the solution reduction products is lower, their adhesion to the electrode surface stronger, and their cohesion better, so the resultant surface species formed lead to better and more efficient passivation of the electrode.

Composite graphite electrode (high orientation)   ## Composite cathode
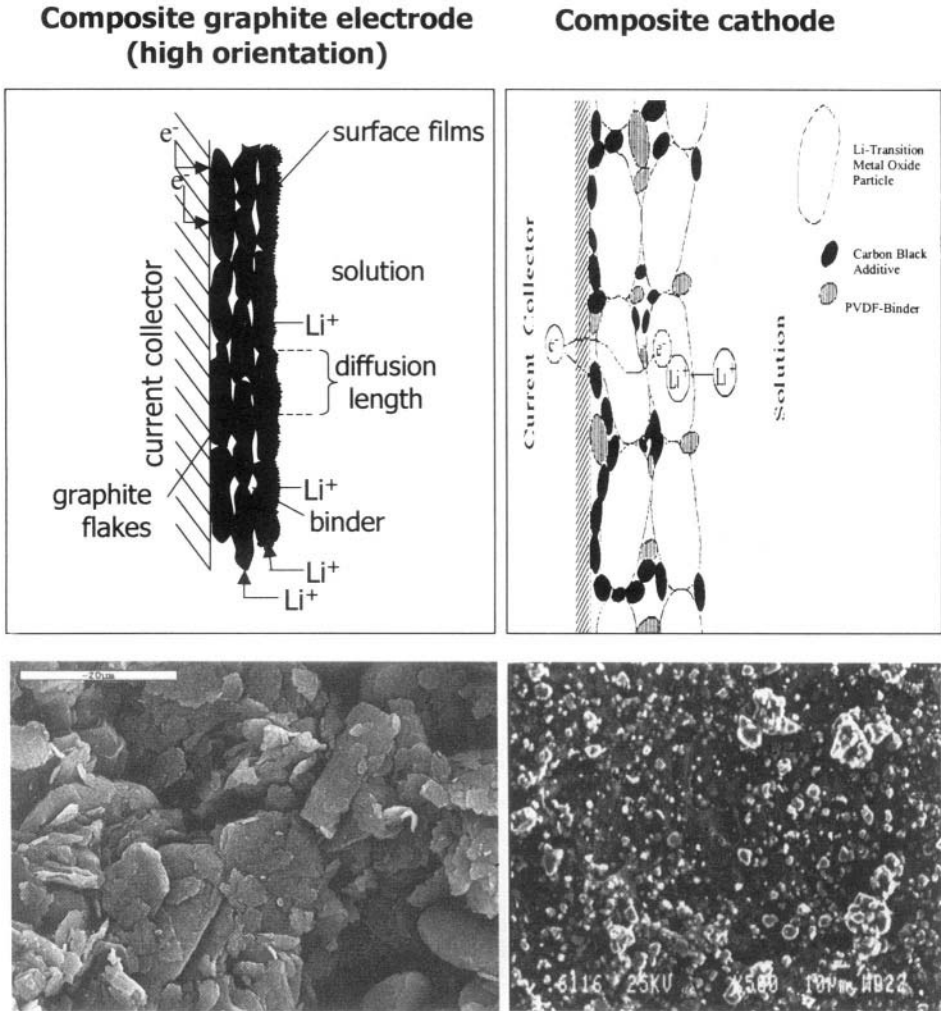
Figure 9. Schematic presentations and typical SEM micrographs of a composite graphite electrode (comprised of synthetic graphite flakes, Timrex, Inc. KS-6), and a composite LiCoO₂ electrode. A scale appears in each micrograph.

Good passivation of a carbon anode means that:

1. A minimal irreversible capacity is involved, i.e., the reduction of solution species during the first cathodic polarization of the electrode consumes as small an amount as possible of the charge involved in the reversible Li insertion-deinsertion processes.

2. The irreversible processes take place only once, during the first polarization of the electrode. Then, the surface films remain stable and invariant.
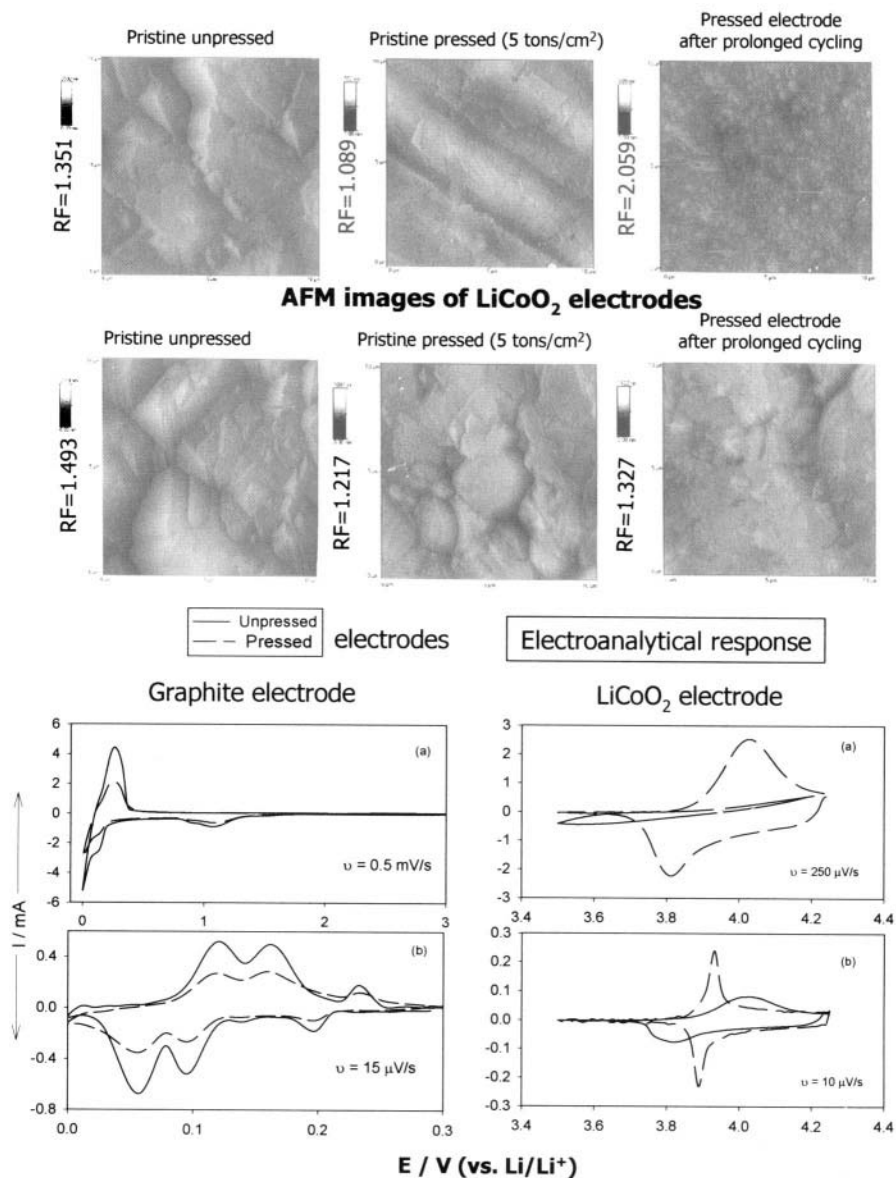
Figure 10. ***Top:*** 2D (*ex situ*) AFM images of pressed and unpressed composite graphite (synthetic flakes, Timrex KS-6), and LiCoO₂ electrodes. AFM images of cycled, pressed graphite, and LiCoO₂ electrodes are also presented for a comparison. Surface film formation on these electrodes is clearly seen. ***Bottom:*** Comparison between cyclic voltammograms of the pressed and unpressed graphite and LiCoO₂ electrodes at two potential scan rates, as indicated. EC-DMC/LiAsF₆ 1M solution. The adverse effect of pressure on these electrodes is clearly seen: more sluggish kinetics of the pressed graphite electrodes and faster kinetics of the pressed LiCoO₂ electrode. From reference 94 reproduced by permission of The Electrochemical Society, Inc.
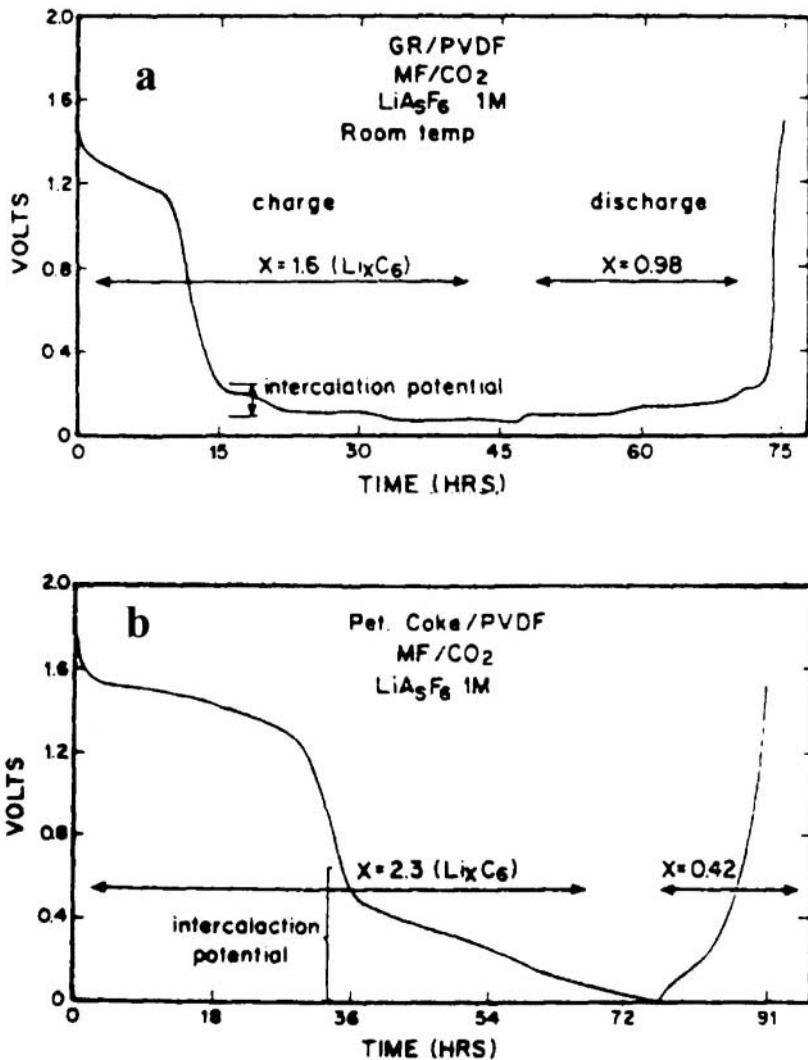
Figure 11. Typical chronopotentiometric profiles of composite graphite and petroleum coke electrodes (**a**, **b**, respectively), in a methyl formate-LiAsF$_6$ 1 M solution under CO$_2$ (6 atm). The first galvanostatic Li insertion-deinsertion cycle; C/33 h, 0.5 mA·cm^{-2}. From reference 66 reproduced by permission of The Electrochemical Society, Inc.

As discussed in the first sections, the surface films formed in these systems, which comprise insoluble Li salts, allow Li-ion migration through them, but block electron transfer from the Li-C electrode to the solution species. In general, the irreversible capacity of carbon electrodes depends on many factors, including the type of carbon, its morphology, its surface area, and, of course, the solution composition. This highly important issue is dealt with in depth in the next section related to failure and stabilization

mechanisms of carbon electrodes (Section 4). The chronopotentiograms in Figure 11 clearly reflect (in addition to the irreversible capacity discussed above) the nature of the Li insertion processes of the two electrodes. As discussed below, Li insertion into graphite forms intercalation stages, and as a result, the chronopotentiogram in Figure 11a has three distinctive plateaus at potentials around 0.25 V, 0.1 V, and 0.05 V (Li/Li⁺), reflecting the phase transition between the various intercalation stages [86-93]. The chronopotentiogram in Figure 11b, related to the disordered carbon electrode, appears as a sloping E *vs.* *t* curve in a potential range between 0.8 - 0 V (Li/Li⁺), which means that Li insertion into this carbon occurs over a wide potential range by mechanisms different from that of graphite. (See discussion below and references 77-85.)

In general, it is clear that Li insertion into carbon electrodes is a multistage, serial process. It includes Li-ion transport in solution, Li-ion migration through the surface films, charge transfer between the surface films and the active mass, solid state diffusion of Li ions (compensated by a parallel electron flow) into the carbon, and, finally, the capacitive behavior of the insertion electrode, namely, the accumulation of lithium into the bulk of the active mass. This accumulation process may involve phase transitions, as is the case for graphitic materials [74], or the formation of solid solutions with no distinctive phase transitions, as is the case for disordered carbons [97]. This serial nature of Li insertion processes into carbons (Figure 11 and related discussion) is nicely reflected by impedance spectroscopy (EIS). Using sufficiently thin electrodes, it is possible to obtain by EIS a separation of the various time constants related to the stages in the overall, serial Li insertion processes.

The surface films formed on the carbon electrodes may be similar to those formed on Li and noble metal electrodes (polarized to low potentials) in the same solutions, as discussed in sections 1 and 2 above. Hence, it is possible to describe Li-ion migration through the surface films formed on carbon electrodes by electrical models (i.e., equivalent circuit analogs) similar to those used to describe the behavior of Li and noble metal electrodes (covered by surface films) in Li salt solutions [25,31].

Figure 12 compares typical Nyquist plots obtained from a noble metal electrode covered by surface films (deposited at low potentials in a Li salt solution), Li metal, and lithiated graphite electrodes. The figure also shows the expected structure of surface films formed on these electrodes and the relevant equivalent circuit analogs for the impedance behavior of the three electrodes. The surface films formed on all three types of electrodes should have a multilayer structure, and they comprise the compact inner part and a porous outer (solution side) part. Hence, the simplest analog for describing ion transport under an electrical field through different

conducting layers in series is the 'Voight-type' analog: R-C circuits in series [103], as seen in the figure. Consequently, the impedance models of the three electrodes in Figure 12 contain common 'Voight-type' analogs that precisely simulate the high frequency semicircles that are typical of Nyquist plots of carbon, noble metal, and Li electrode, and reflect Li-ion migration through multilayer surface films (resistance elements coupled with surface layer capacitance). As seen in Figure 12, in the medium-low frequency, the impedance behavior of the three electrodes diverges. For Li electrodes, the major impedance relates to Li migration through the compact part of the surface films [25]. The charge transfer resistance of both interfaces of the surface films (metal and solution sides) is negligible compared with that of Li migration through the surface films. The effect of the porous part of the surface films may be taken into account by an analog containing capacitance in parallel with resistance and a 'Warburg'-type element for the Li electrodes, as seen in Figure 12 [104].

For the noble metal electrodes covered by surface films, the low frequency behavior of the impedance spectra reflect a huge charge transfer resistance for a further reduction of solution species on passivated electrodes (see Figure 12, top). For the carbon electrodes, the low frequency domains in the impedance spectra reflects several elements that are not relevant to the other two electrodes:

1. There is a potential-dependent charge transfer between the surface films and the active mass, which usually appears as a separate, medium frequency (small) semicircle.
2. At low frequencies, a 'Warburg'-type element is seen in the spectra, related to the slow, solid-state (potential-dependent) diffusion of lithium in the active mass.

At very low frequencies, the impedance behavior is capacitive (steep $Z_{imagin.}$ *vs.* Z_{real} line in the Nyquist plot). It should be noted that if the measurements are properly conducted, at the very low frequencies the differential Li insertion capacity of the electrode, C_{int}, can be calculated from the imaginary part, Z'':

$$C_{int} = \frac{1}{Z''} \cdot \omega, \quad \omega \to 0; \quad \omega = 2\pi f$$

Hence, we suggest a simple, serial equivalent circuit analog that describes the impedance behavior of carbon electrodes as seen in Figure 12. It contains a 'Voight-type' analog in series with R-C, which reflects the charge transfer, a potential-dependent 'Warburg'-type element (solid state diffusion of Li-ions), and, finally, a capacitive potential-dependent element that reflects the accumulation of lithium. This relatively simple model has already been discussed in depth [105-107].
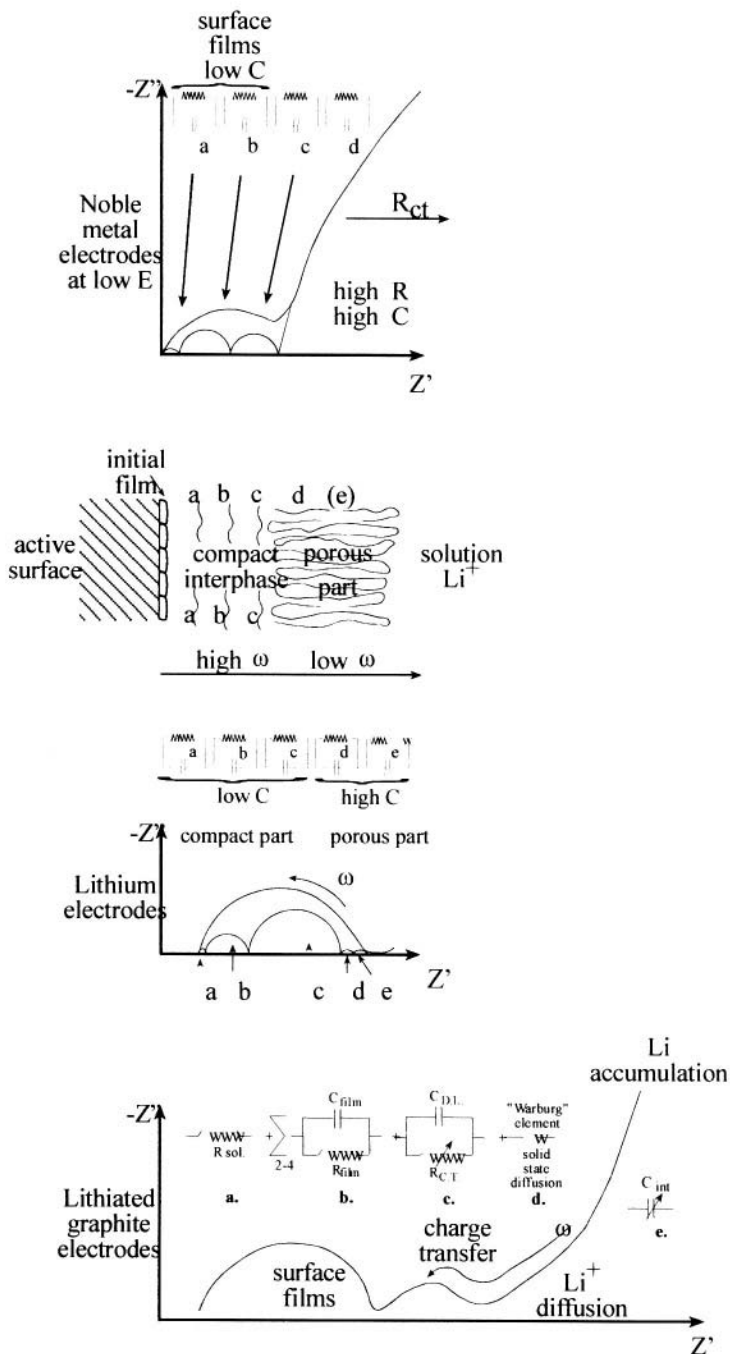
Figure 12. A schematic illustration of impedance spectra, relevant equivalent circuit analogs, and the structure of the surface films for lithium, lithiated graphite electrodes, and noble metal electrodes polarized to low potentials in Li salt, nonaqueous solutions. Reprinted from reference 219 with permission from Elsevier Science.

Figure 13 shows a typical electrochemical response of graphite and dis-ordered carbon electrodes (a, b, respectively), related to the diffusion and accumulation of lithium in the bulk carbon particles. The differential capacitance of these electrodes is nicely reflected by slow scan cyclic voltammetry. As already discussed in detail [105-107], the peaks in the CV of Figure 13a (4 sets of redox peaks) reflect phase transition between Li-graphite intercalation stages (indicated in the figure), and they correspond to the plateaus in Figure 11a. Their shape depends on the resolution of these experiments. The resolution of the voltammetric response of these electrodes depends on the thickness of the electrode, the resistance of the surface films, and the potential scan rate [108]. The best resolution in electrochemical studies of these systems is obtained in experiments with single particles [109-110]. Such experiments, however, are difficult and require special apparatus. Using composite electrodes, a condition for meaningful results, is a situation in which the electrodes are thin and the solution reaches the entire active mass, and, in fact, all the particles interact in parallel with both the current collector and solution species. In such a situation, the composite electrodes can be considered as an array of microelectrodes, and then the resolution of the measurements and their reliability are high.

A first potentiostatic polarization of carbon electrodes always shows an irreversible voltammetric peak related to the surface film formation in the potential range of 1.8 to 0.8 V (*vs.* Li/Li^+, depending on the solution composition), which corresponds to the plateaus at similar potentials in Figure 11. At scan rates that are too high, the intercalation-deintercalation processes of graphite electrodes appear as a pair of featureless peaks, because the potentiostatic Li insertion processes are interfacial-impedance or solid-state-diffusion controlled. At a sufficiently slow scan rate (as is the case for Figure 13a), it is possible to drive the Li insertion process slowly enough, beyond diffusion control, and then the typical potential-dependent Li accumulation processes of the graphite electrodes are well resolved; i.e., the phase transitions appear as distinctive voltammetric peaks. The peaks are sharper and have a smaller hysteresis with their corresponding anodic (deintercalation) peaks, as the electrodes are thinner and the surface impedance is low (depending on the properties of the surface films). The behavior of the disordered carbon seen in Figure 13b, namely, monotonous C_{int} *vs.* E (the differential capacity increases as the potential is lower), reflects a Li adsorption-type mechanism and the formation of a solid Li-C solution [96]. The chemical diffusion coefficient (D_{Li}) of Li into the carbons could be calculated by both PITT or EIS (the 'Warburg'-type, low frequency domain) [105-108]. D_{Li} *vs.* E is a peak-shaped function for graphitic materials, with sharp minima at the peak potentials (i.e., the potentials of phase transition between intercalation stages), while D_{Li} *vs.* E for disordered carbons is a function with maxima, as clearly seen in Figure 13.

As already discussed in detail [96,105-107], the variations of D *vs.* E for Li insertion processes reflect the nature of the insertion mechanisms and the interactions among Li-intercalation sites. In general, the existence of strong, attractive interactions among the intercalation sites leads to minima in D *vs.* E at the potentials of maximal inter-site interactions. Repulsion interactions among Li insertion sites lead to maxima in D *vs.* E, as we see for disordered carbons. (See the relevant discussion in Ref. 96).

It should be noted that in recent years we have seen a number of publications on Li insertion mechanisms into carbons in general, and the use of impedance spectroscopy as a tool for mechanistic studies in particular [109-118]. Other models, different from those represented in Figure 12 and the related discussion above, have been suggested for describing Li insertion into carbons [115-118]. However, in general, most of these studies also converge into a description of Li insertion into carbon electrodes as a serial, multi-stage process.

In conclusion, Li migration through surface films and charge transfer between the surface layer and the active mass are necessary stages in the overall Li insertion processes into carbon, which strongly influence the electrochemical response of Li-carbon electrodes.
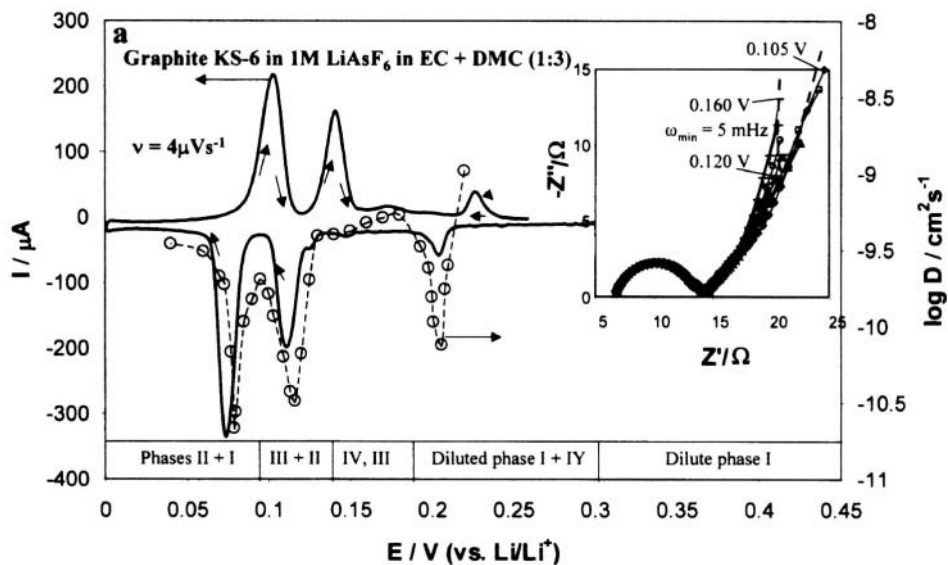
Figure 13a. The typical electrochemical response of graphite electrodes. See complete description with **Figure 13b.**
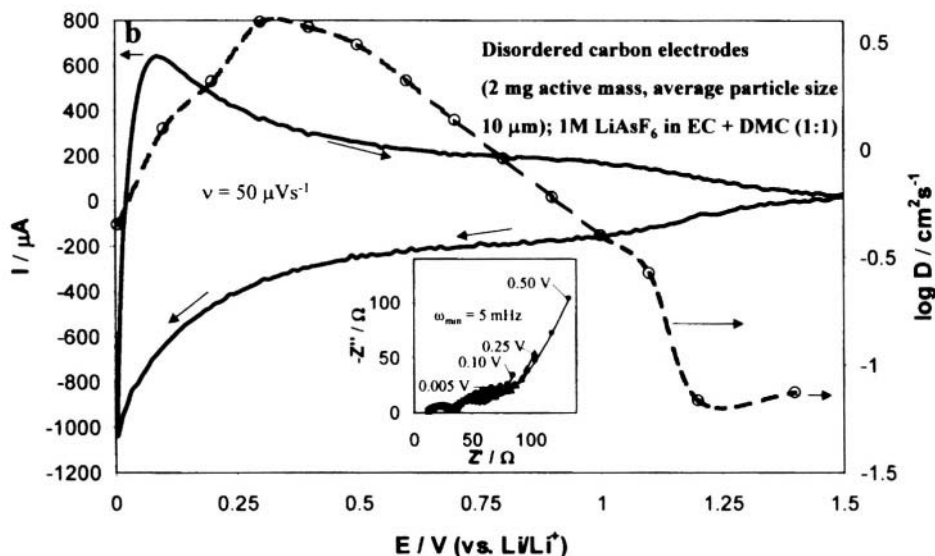
Figure 13. The typical electrochemical response of graphite and hard carbon electrodes (**a**, **b**, respectively). Slow scan CV, the variation of the diffusion coefficient *vs.* potential (log D *vs.* E), and selected impedance spectra (Nyquist plots at several potentials, as indicated) are presented. The various phases of the lithiated graphite that correspond to the various CV peaks (**13a**) are also presented. The dashed line that connects the points of the lowest frequency in the Nyquist plots of the graphite electrodes correspond to the CV peak around 0.12 V (Li/Li$^+$). The intercalation capacity corresponding to the phase transition between stages III and II can be calculated from this dashed line according to the formula $C_{int} = 1/Z''\cdot\omega$ (as $\omega \rightarrow 0$). See text and references 96, 105-107.

4.0   FAILURE AND STABILIZATION MECHANISMS OF CARBON ELECTRODES

When dealing with failure or stabilization of carbon electrodes, we can distinguish between factors that relate directly to surface reactions and those that relate to the nature of the Li insertion mechanism into the carbon. However, it should be noted that the factors related to the surface phenomena are also definitely connected to the 3D structure of the carbons. As already mentioned, Li insertion into either soft or hard disordered carbons, and the failure or stability of lithiated disordered carbon electrodes are much less dependent on their surface chemistry as compared with graphitic materials. This is due to the fact that graphites are much softer and weaker than disordered carbons. Hence, failure and stability of disordered carbon electrodes are mostly determined by structural factors, the type of Li insertion sites available, the number of C-H bonds, and the existence of sites to which Li is inserted irreversibly [81-85,94,95,97-99]. Discussion of these structural impacts on the behavior of the electrodes is beyond the scope of this chapter.

Hence, we concentrate mainly on graphite electrodes, whose surface chemistry plays a major role in determining their stability or failure. Here, we can distinguish among four general cases:

1. Graphite electrodes that behave reversibly and have an initial irreversible capacity of only a few percent of their steady state reversible capacity (and can approach 370 mAh·g^{-1}, corresponding to LiC_6).
2. Graphite electrodes that behave reversibly, but also have a relatively high irreversible capacity.
3. Graphite electrodes that fail upon charge-discharge cycling.
4. Cases in which a reversible Li insertion into graphite electrodes cannot be obtained at all.

It is very important to note that the four cases noted above depend on both the type of graphite used and the solution composition. Highly reversible behavior and low irreversible capacity are achieved when the surface species formed are adhesive to the carbon surface (as described in terms of the sticky fingers model [119]), and cohesive. In addition, they should be formed at high enough potentials so that as the electrode reaches Li insertion potentials, it is already passivated, and hence, solvent co-intercalation is avoided.

Highly reversible behavior and excellent passivation are obtained in solutions containing EC or CO_2. This can be attributed to the highly adhesive and cohesive properties of $(CH_2OCO_2Li)_2$ or Li_2CO_3 formed by reduction of these species, respectively, on the carbon surfaces [119]. In solutions based on opened chain alkyl carbonates (e.g., DMC, EMC, PMC) and esters (e.g., MF, γ-BL), graphite electrodes can insert lithium reversibly, but the irreversible capacity is high and the stability upon prolonged cycling is limited [50,65,66]. In ethers and propylene carbonate solutions, graphite electrodes fail [120]. Their failure mechanisms in propylene carbonate solutions and in ethereal solutions differ, and deserve special discussion. In any event, the presence of additives/contaminants in solutions, even at the *ppm* level, may completely change the above picture, in the direction of improved stability. The natural failure mechanisms suggested for Li graphite electrodes are attributed to co-intercalation of solvent molecules that migrate with the Li-ions which they solvate. The co-intercalating solvent molecules are expected to be reduced within the graphite, and their reduction products should block Li-ion entry into the graphite lattice. Further co-intercalation of solvent molecules may lead to a completed exfoliation of the graphite and its amorphization [121-123].

This explanation sounds very logical in light of the fact that PC may be a better donor than other alkyl carbonates such as EC (due to the effect of the methyl group). Hence, Li-ions are strongly solvated by PC, and thus, co-intercalation of PC molecules together with Li-ion into graphite is so significant when graphite electrodes are polarized cathodically in PC-containing solutions [122]. However, there is some experimental evidence

against this explanation, as discussed below. Since this subject is important, and has also been the focus of many studies and discussions in the literature, we describe below in details some experimental results related to the behavior of graphite (flake) electrodes in selected electrolyte solutions.

Figure 14 shows typical voltage profiles (*E vs.* capacity curves in galvanostatic Li insertion into pristine graphite electrodes) of graphite electrodes polarized cathodically in diglyme and propylene carbonate solutions, as indicated, together with XRD patterns obtained *ex situ* from graphite electrodes whose galvanostatic processes in these solutions were stopped at different stages, as marked on the voltage profiles. From both the chronopotentiograms and the XRD patterns in Figure 14, it is clear that different failure mechanisms are relevant to the two-electrolyte solutions [64, 120]. In the ethereal solution, the failure mechanism involves a completed exfoliation of the graphite and amorphization. In ethereal solutions, the solvents are not very reactive at the Li-C carbon surfaces, and hence, there is no massive formation of passivating surface films, even at low potentials. As a result, solvent molecules can co-intercalate with Li-ions. Indeed, phenomena such as THF intercalated graphite are known [124]. This co-intercalation may indeed split the graphene planes from each other, leading to exfoliation of the graphite and its amorphization, which was suggested as being the major destruction mechanism for graphite electrodes [125]. In our opinion, the failure mechanism of graphite electrodes in PC solutions may be different. Here, the failed electrode retains its graphitic active mass, although its polarization to low potentials leads to its deactivation as a Li insertion anode. Especially striking is the pronounced antagonistic difference in the behavior of graphite electrodes in EC- and PC-based solutions, although both molecules are very similar, the only difference being the methyl group of PC.

Our studies lead to the following conclusions regarding the failure mechanism of graphite electrodes in PC solutions [64,120,126]. Reduction of PC forms both $ROCO_2Li$ surface species that may precipitate as passivating surface films and propylene gas [61]. The fact that the $ROCO_2Li$ formed by PC reduction has methyl groups is a great disadvantage in terms of cohesion (in contrast to the case of Li_2CO_3 or the EC reduction product $(CH_2OCO_2Li)_2$, which are both very adhesive and cohesive). This disadvantage interferes badly with a **fast** formation of cohesive surface films when PC is reduced on graphite. In the case of graphitic carbons, particularly when the particles are synthetic graphite flakes, their edge planes have many crevices and they can be easily split between basal/graphene planes. Reduction of PC molecules inside crevices leads to the formation of internal pressure, due to propylene gas formation, which splits the particles. Hence, the surface area of the particles increases as reduction of solution species proceeds. Solvent molecules are reduced between split fractions of graphite particles, and a great part of the active mass loses electrical contact with the current collector

due to isolation by surface films. This scenario explains both the inactivation of graphite electrodes polarized cathodically in PC solutions and the fact that they do not lose their graphitic structure (i.e., no completed exfoliation and amorphization occur, as seen in ethereal solutions, Figure 14). It should be noted that in cases of graphitic materials with smooth edge planes or some turbostratic or polycrystalline disorder, the above destructive scenario is less important, because splitting of the particles is more difficult. Indeed, carbon electrodes comprised of graphite fibers or beads are more stable than electrodes comprised of graphite flakes [126].

Over the years, it has been clearly demonstrated how strongly the reversibility and stability of graphite electrodes depend on their surface chemistry. Moreover, even in solutions in which graphite electrodes behave reversibly, the surface chemistry could be easily attenuated by slight changes in the solution composition, examples of which are listed below:

1. Addition of crown ether (12 Cr 4) to PC solutions leads to the reversible behavior of graphite electrodes, because when the Li-ions reaching the electrodes are complexed by the crown ether, fast and efficient passivation by $ROCO_2Li$ is obtained, and hence, the detrimental processes that usually occur in PC solutions are largely avoided [127].
2. As described above, graphite electrodes fail in both PC and THF. However, in THF solutions containing 0.5 - 1.5 M PC, graphite electrodes behave highly reversibly because the dominant surface reactions in these solutions form Li_2CO_3 as an important component in the surface films (see Scheme 2 and Figure 5) [120].

In pure DMC solutions, the irreversible capacity of graphite electrodes is pronounced, and the electrodes develop high impedance upon cycling and fail. Addition of a few hundred *ppms* of water leads to the highly reversible behavior of graphite electrodes in DMC because trace water reacts with the $ROCO_2Li$ formed by DMC reaction. The solid product of this secondary reaction is Li_2CO_3, which is one of the best passivation agents for carbon electrodes [119,128].

The irreversible capacity of graphite electrodes depends not only on the solution composition, but also on the structural and morphological parameters of the particles. In solutions in which there are no specific failure mechanisms of graphite electrodes (i.e., highly reversible behavior is observed, as in EC-DEC, EC-DMC, EC-EMC solutions, etc.), the irreversible capacity depends on the average particle´s surface area [129].

There are a number of recent publications on the impact of structural and morphological parameters of graphitic materials on their performance as anode materials in general, and on their irreversible capacity in particular [130-135].

Ex-situ XRD of composite graphite electrodes (95% Synthetic graphite flakes (Timrex KS25 + 5%PVDF) on copper net.
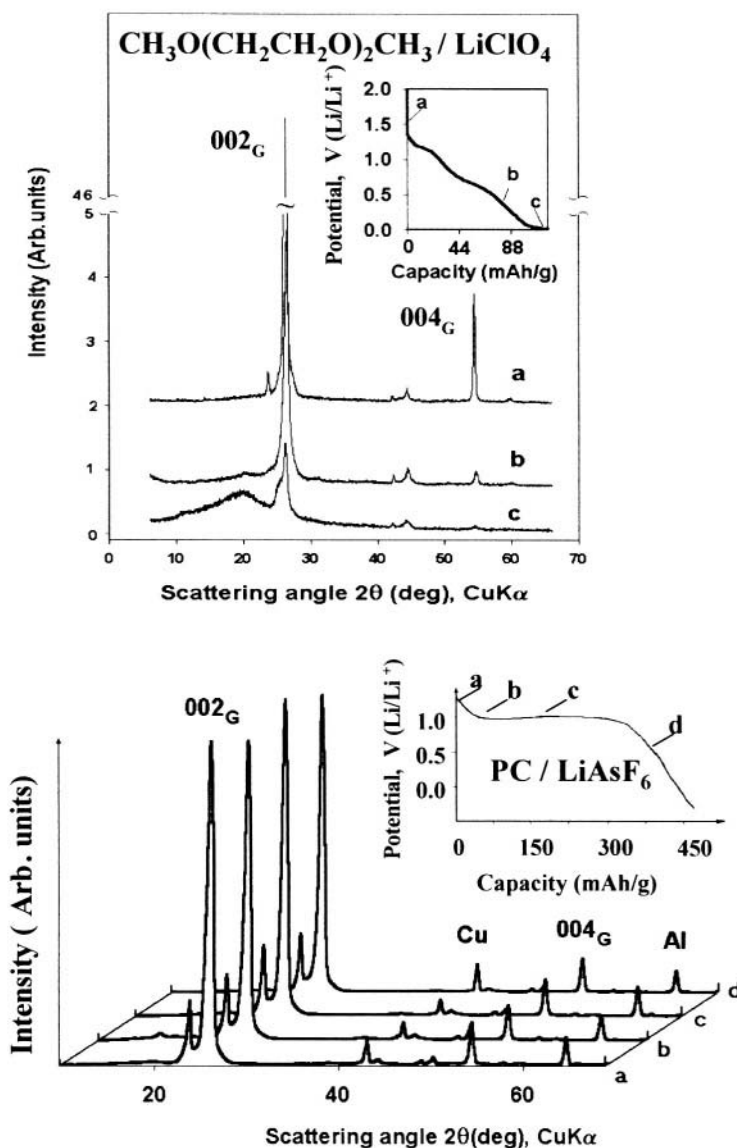
Figure 14. Typical XRD patterns and chronopotentiograms (galvanostatic experiments) of graphite electrodes in $CH_3(CH_2CH_2O)_2CH_3/LiClO_4$ 0.5 M and $PC/LiAsF_6$ 1M solutions, as indicated. In both solutions, reversible Li insertion into graphite can not be obtained. The XRD patterns were measured *ex situ.*, from electrodes whose galvanostatic processes in these solutions were stopped at points **a**, **b**, **c,** etc., as marked near the relevant voltage profiles presented in this figure. Patterns in **a** relate to the pristine electrodes. Reprinted from reference 64 with permission from Elsevier Science.
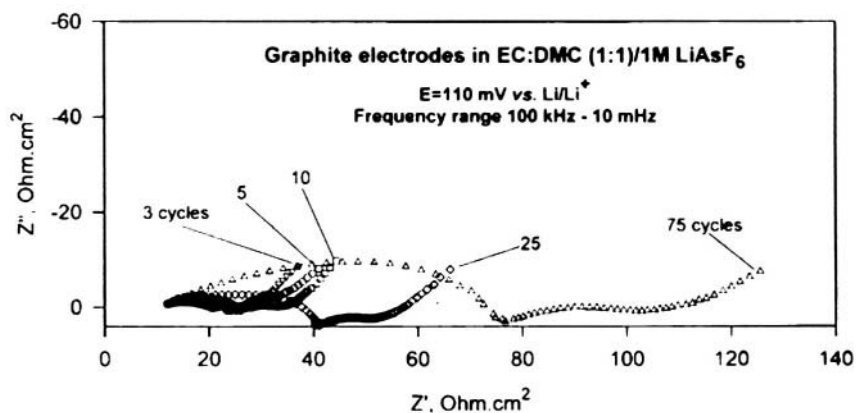
Figure 15. Impedance spectra measured from a composite graphite electrode (synthetic flakes, Timrex KS 25, 5% PVdF) during cycling in an EC-DMC 1:1/LiAsF$_6$ 1 M solution. The relevant cycle numbers are marked. Reprinted from reference 140 with permission from Elsevier Science.
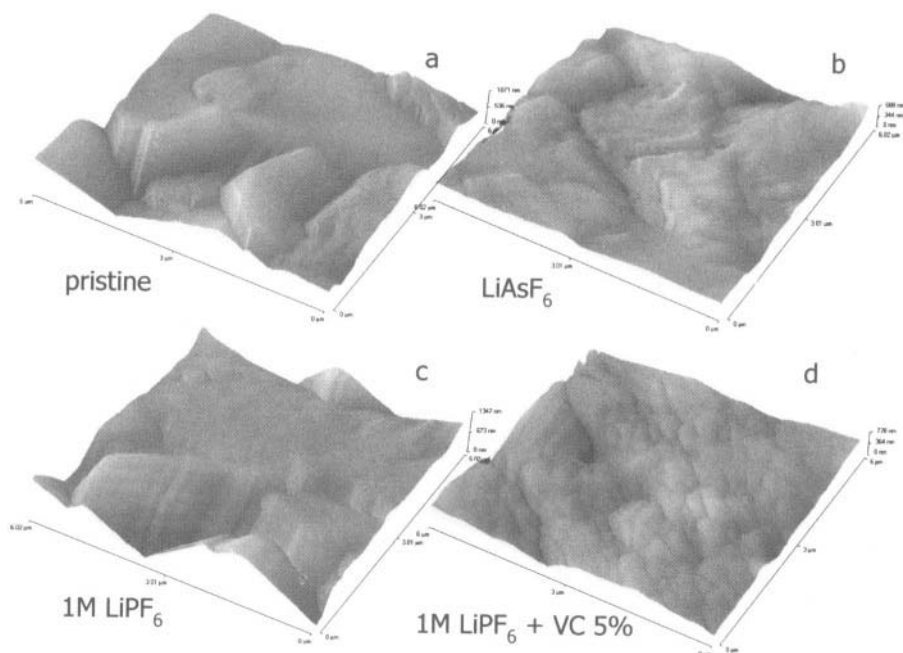
Figure 16. Typical 3D AFM images of composite graphite electrodes (synthetic flakes, Timrex KS-6, 5% PVdF) measured *in situ* in various EC-DMC solutions at 0.9 V (Li/Li$^+$), as indicated. Image a relates to the pristine electrode. Various morphologies of surface films formed at the different solutions can be seen in images b-d. Editor's Note: Image scale: In plane = about 6μm per side; vertical scale **a** = 1071 nm, **b** = 688 nm, **c** = 1347 nm, **d** = 728 nm. Reprinted from reference 140 with permission from Elsevier Science.

The last point to be dealt with in this chapter relates to the behavior of stable graphite electrodes upon prolonged charge-discharge cycling. As an example, we present typical data related to electrodes comprised of synthetic graphite flakes.

Figure 15 shows typical impedance spectra of a composite graphite electrode comprised of synthetic graphite flakes during cycling in a solution in which highly stable and passivating surface films are formed (EC-DMC/LiAsF$_6$). The electrodes develop increasing impedance upon cycling, while the capacity of the active mass is basically retained. In order to understand these electrode impedance changes during cycling, the use of *in situ* imaging by scanning probe (SPM) techniques may be very helpful. Indeed, in recent years we have increasingly seen the application of atomic force microscopy (AFM) to the study of both monolitic (HOPG) and composite graphite electrodes and their surface phenomena [136-140]. In this section, we describe some data from AFM imaging of composite graphite electrodes, which can explain their behavior during cycling, especially the increase in their impedance.

Figure 16 shows typical *in situ* AFM images of these composite electrodes measured at a low potential (0.9 *vs.* Li/Li$^+$) after surface films were formed by reaction of solution species. The formation of surface films is clearly seen by *in situ* imaging with AFM at potentials below 1.2 V (Li/Li$^+$). It is also spectacular in the images presented in Figure 16 that different salts or the presence of an additive such as VC lead to a different morphology of the surface films. It is possible to concentrate in these *in situ* imaging experiments on a specific micrometric size area and to follow morphological changes in single particles during Li insertion-deinsertion cycles. Figure 17 is a collection of AFM images and height profiles (marked on the images) measured from a composite graphite electrode comprised of synthetic flakes, during entire Li insertion-deinsertion cycles, at selected constant potentials (specified near each image and profile). The solutions selected for these experiments were EC-DMC/LiAsF$_6$ or EC-DMC/LiPF$_6$, in which graphite electrodes comprised of synthetic graphite flakes behave highly reversibly due to efficient passivation by surface films. These imaging experiments indeed reflect the stability of these electrodes upon Li intercalation-deintercalation cycling. In general, no destructive processes could be observed. However, as seen in Figure 17, which presents images and height profiles of the same area (a gap between two graphite flakes) at selected potentials, there are some slight morphological changes visible during an entire Li insertion-deinsertion cycle. From EIS and *in situ* imaging by AFM of graphite electrodes during charge-discharge cycling, we come to the conclusions described schematically in Figure 18. When Li is inserted into the graphite particles, their volume increases (due to an increase in the space between the graphene planes). Hence, the surface films on the edge planes, through which Li-ions are inserted into the graphite, are stretched. Since the surface films on lithium are usually comprised of Li salts, their flexibility is limited. Thus, they may be damaged during Li insertion (due to the increase in the particle's

volume), and thus, the passivation is limited. This allows continuous small scale reactions between the lithiated carbon and solution species, i.e., the breakdown and repair of the surface films that increase their thickness, and hence, the electrode's impedance upon cycling. As explained above, the behavior of carbon electrodes depends very strongly on the nature of the particles, as well as their morphology. Thus, the extent of the phenomena described in Figures 15-18 depends strongly on the type of carbon used.

5.0 MODIFICATION OF CARBON ANODE SURFACE CHEMISTRY

The previous sections presented several problems in the use of carbon anodes in Li-ion batteries. We mentioned the capacity limitation of graphite electrodes and their extreme sensitivity to the solution composition, a limited access of the entire active mass to solution species in thick, composite electrodes, a variety of failure mechanisms based on surface phenomena, an increase in the electrodes' impedance during charge-discharge cycling, etc. It should be emphasized that all the capacity-fading and irreversible phenomena described in the previous sections, as well as impedance increase upon cycling, become increasingly pronounced at elevated temperatures. It is, therefore, very important to develop surface modifications that increase the stability of the electrodes and modify their surface chemistry towards better passivation, especially at elevated temperatures, but not on the account of fast transport phenomena (e.g., Li-ion migration through surface films).

In this section, we review two basic approaches that relate to the modification of the surface chemistry of carbon electrodes, namely, surface pretreatment of carbon particles and modification of solution species using specially designed additives and new solvents and salts.

5.1 *Surface Modification of Graphite Electrodes*

There have been several interesting attempts to modify the surface of graphite particles before electrode construction.

1. *Removal of surface layers*

All carbon particles have surface groups whose reduction during the first cathodic polarization of electrodes may contribute to their irreversible capacity. There are reports on the removal of such surface groups using reducing atmosphere (e.g., Ag/H_2) at elevated temperatures [141]. We should also mention that mesopores in carbonaceous materials may contain active atmospheric gases such as H_2O, CO_2, and O_2, which may be easily reduced during polarization of the carbon electrodes, and in that way contribute a great deal to their irreversible capacity [142]. Hence, the

careful treatment of carbon particles in a way that removes these trapped gases before introduction into the solutions may be important for the reduction of the irreversible capacity of carbon anodes.
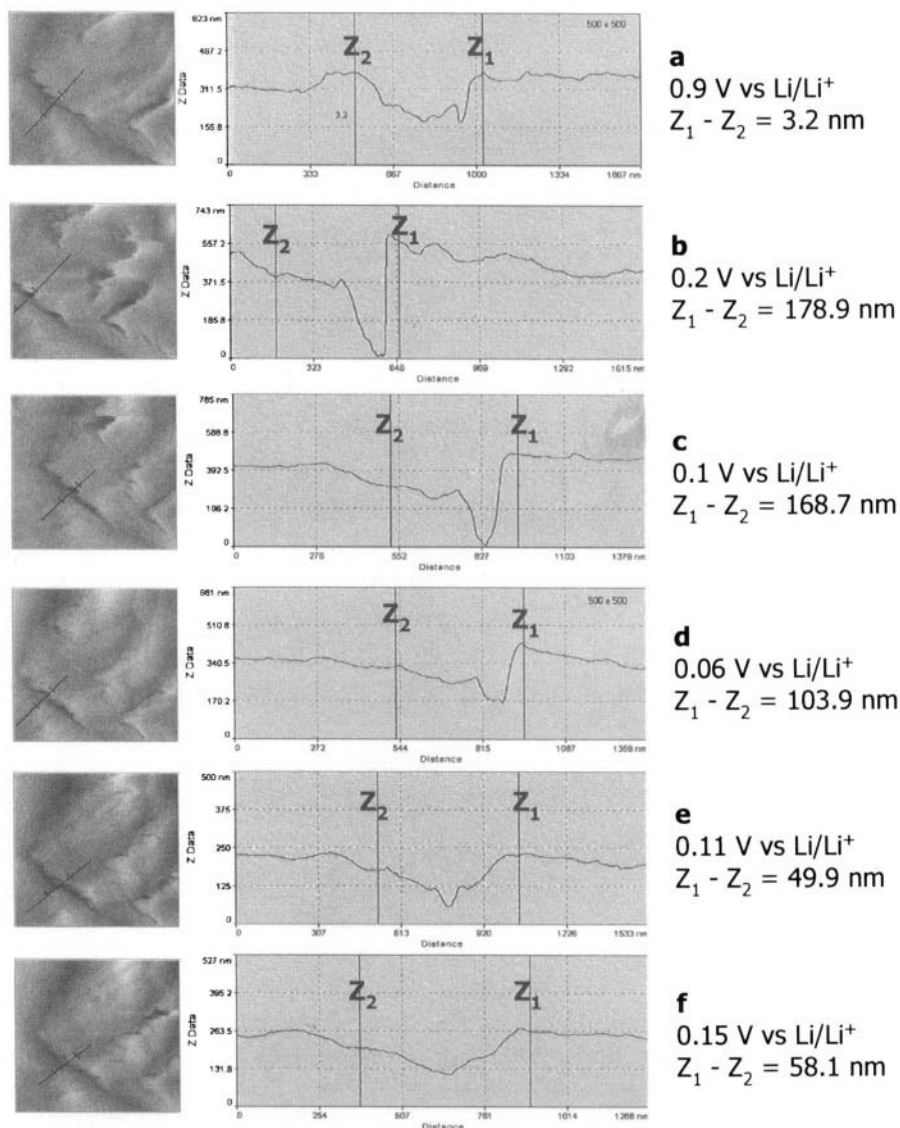
Figure 17. AFM images (2D) and profiles of a composite graphite electrode obtained *in situ* during a completed Li insertion-deinsertion cycle in EC-DMC/1 M LiAsF$_6$ solution. The various potentials at which the images were obtained are indicated. The profiles are marked on the 2D AFM images. Reprinted from reference 140 with permission from Elsevier Science.

Fading mechanisms of graphite electrodes in any "good" electrolyte
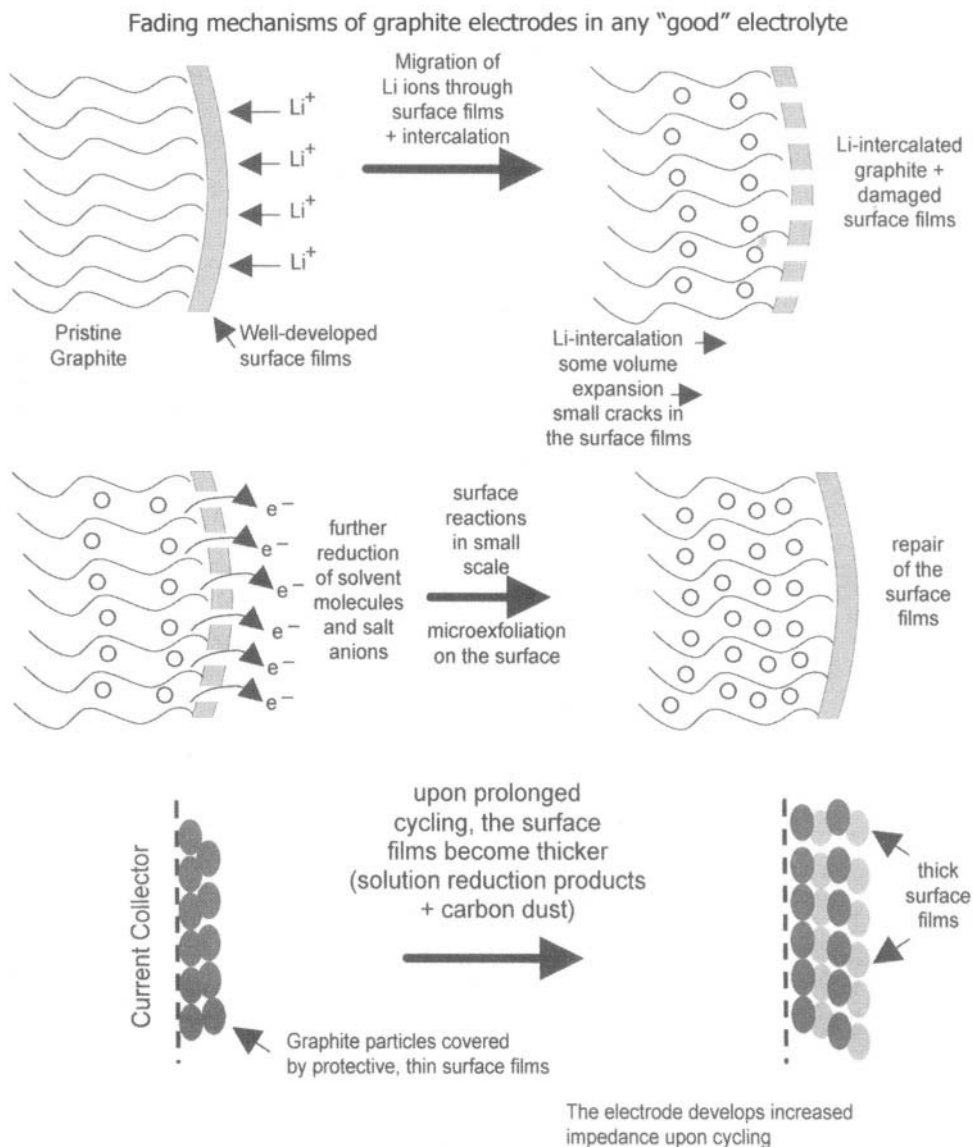
Figure 18. A schematic illustration of changes in the surface films on composite graphite electrodes upon prolonged cycling, even in solutions in which the surface films provide good passivation. Reprinted from reference 219 with permission from Elsevier Science.

2. *Formation of surface layers by oxidation and other methods*

In contrast to the approach described above, namely, removal of surface layers in order to enable surface film formation by reduction of solution species only, there is the opposite approach: developing surface films of unproved passivating properties on carbon particles, *ex situ,* (before any electrochemical treatment).

There have been several reports on the preparation of surface films on graphite particles by mild, controlled surface oxidation [143-144]. It is possible to control the build-up of surface groups on carbon particles using aqueous HNO_3 solutions at a temperature range between R.T. and 80°. It is also possible to cover the surface area of graphite particles (especially the edge planes) by oxygen-containing surface groups, by a controlled burnoff of the carbon in air at elevated temperatures.

As described in reference 144, oxidation of graphite forms a variety of surface groups, including carboxylic and hydroxylic groups, C=O double bonds, and anhydride-types groups. Cathodic polarization of electrodes comprised of these carbon particles in nonaqueous Li salt solutions forms surface Li alkoxy and Li carboxylate groups. In this way, a strongly adherent surface layer is obtained, which further influences the reduction of solution species on the carbon surface. By this approach, it is possible to achieve a very good electrode passivation, reduce their irreversible capacity, and increase their stability upon cycling. Another approach that should be mentioned here is the pretreatment of carbon particles with polymeric species that cover the particles with protective films before being in contact with the electrolyte solution. For instance, pretreatment of graphite flakes with gelatine [145] considerably reduced the irreversible capacity of anodes comprised of the pretreated particles. We should also mention that mechanical milling of carbon particles in air also forms a highly reactive surface that reacts readily with active atmospheric gases (O_2, H_2O, CO_2) to form a variety of surface groups [146]. Since mechanical milling is often used in order to obtain small size particles, it is possible to modify the surface chemistry of carbon particles by milling them in a reactive or inert atmosphere.

It is also possible to increase the reversible capacity of graphite electrodes by mild oxidation/burnoff pretreatment of the graphite particles [144,147], which form surface nanopores than can insert Li-ions reversibly, beyond the intercalation capacity related to Li insertion between graphene planes.

3.   *Surface modification by dispersion of metallic particles*

We should mention another approach for surface modification of graphite electrodes by pretreatment of the active mass, using metallic nanoparticle dispersion. Several metals, including Ni, Al, Pt, and Ag were recently mentioned in the literature in this respect. For instance, it was reported that spreading nanoparticles of Ni [148] or Ag [149] on the graphite particles improved their behavior as anode materials in terms of lowering surface impedance, enhancing passivation, reducing irreversible capacity, and increasing stability. These effects can be explained by the positive impact of the presence of metallic nanoparticles on the surface on the precipitation of adhesive and cohesive surface films. It is assumed that the presence of nanoparticles on the carbon's surface does not drastically change the basic surface chemistry of these systems, but rather changes the morphology and physical structure of the surface films.

5.2   *Improvement Carbon Anodes by Solution Modifications*

Continuous innovative efforts are underway towards the development of new solvents and salts which improve the performance of Li-ion batteries. Special attention is being paid to the increase of the electrochemical windows of the solutions (in order to prevent their oxidation on the cathodes), to the increase of their thermal stability, to obtaining positive impacts on the electrodes' surface chemistry, and to reducing undesirable contamination. In parallel, there is intensive ongoing work on the development of additives that modify the surface chemistry of the electrodes in commonly used electrolyte solutions (e.g., EC + linear alkyl carbonates and $LiPF_6$), and improve the safety features of the battery systems. Typical examples of the development of new solvents for Li-ion batteries are derivatives of propylene carbonates in which graphite electrodes behave reversibly, e.g. chlorinated PC [44], *trans* butylene carbonate [122], and fluorinated alkyl carbonates [45]. The enhanced stability of graphite electrodes in these new solvents, compared with the poor behavior in PC solutions, is well understood in light of the failure mechanism of graphite electrodes in PC solutions described in the previous section [120]. Testing other new solvents such as pyrocarbonates [150], cyclic and acyclic sulfites [151], and fluorinated organic solvents (e.g., N, N-dimethyl trifluoracetamide) [152] should also be mentioned.

As an important example of the innovative development of new salts for lithium-ion batteries, we can mention the development of $LiPF_3(CF_2CF_3)_3$ as a substitute for $LiPF_6$ [41,153]. The use of the former salt as an electrolyte minimizes the contamination of the solutions by HF, which has a detrimental impact on the performance of both anodes and cathodes in Li-ion batteries. This new salt is less reactive than $LiPF_6$ on the carbon electrodes, and its solutions seem to be more thermally stable than $LiPF_6$ solutions. It is clear that the potential use of the above-described new components of electrolyte solutions in practical Li-ion batteries depends primarily on their impact on the electrodes' surface chemistry. However, at present there is no solid information regarding the surface chemistry of Li-ion battery electrodes in all of the new solvents and salts mentioned above. Work in these directions is definitely in progress.

Table 2 summarizes a list of additives that have been tested in commonly used electrolyte solutions for Li-ion batteries, based on recent publications (patents and papers). The information in this table includes major impacts, the relevant mother solutions, and representative references for the various additives.

The true impact of most of the additives described in the table on the surface chemistry of the electrodes is not yet understood, although it is assumed that their positive effects on electrode performance relate to surface modifications induced by their presence. However, based on recent studies, we will present some ideas about how these additives can improve the performance of Li-ion batteries.

As already stated in this chapter, critical properties of surface films are their adhesion to the electrode´s surface and cohesion. The first property is a condition for stability, while the second one determines the ability of the surface films to withstand volume changes of the particles upon Li insertion, and to prevent transport of solvent molecules with Li-ions through the surface films. Our previous studies on the positive impact of CO_2 [60,65], SO_2 [51,174], and even trace water, in some cases [120,128], revealed that some inorganic Li salts and oxides may form highly passivating surface films on both Li-graphite and Li metal surfaces. Species such as Li_2CO_3, Li_2S, $Li_2S_2O_4$, and Li_2O formed in the presence of the above additives are very good passivating agents in the Li-ion conducting surface films. Tentatively, we attribute this to the ability of these species to form surface structures with strong intermolecular electrostatic interactions, with very good adhesion to the electrode′s surface. (See the sticky fingers´ model, reference 119.) Hence, additives such as nitrates, sulfites, sulfates, phosphates, and phosphonates (see Table 2, first 9 items) may be reduced on carbon surfaces in the presence of Li-ions to the corresponding inorganic Li salts. We found that the use of pyrocarbonates as additives contributes to the liberation of CO_2 by spontane- ous decomposition of these species, which further reacts on the active surface to form Li_2CO_3 (see Scheme 6). The use of Li_2CO_3 or $CaCO_3$ as additives (Table 2, item 10) partly neutralizes the trace HF in solution phase.

Recently, *trans* butylenes carbonate was suggested as a suitable solvent or co-solvent for Li-ion batteries (see Table 2, Ref. 163.) It appears that graphite electrodes are highly stable in these solutions. The authors [163] suggest that with this solvent, co-intercalation of solvent molecules with Li- ions into graphite is largely avoided. We suggest that with this solvent, the formation of passivating surface films by solvent reduction competes well with possible destructive processes in the crevices of the edge planes, such as splitting the graphite particle due to gas formation (butylenes).

The impact of VC as an additive [168] is extremely interesting. Our recent studies on the use of VC-containing electrolyte solutions [175] provided some evidence that VC reacts predominantly on graphite electrodes in EC-based solutions and forms polymeric species. Our recent studies on Li organo boron complexes as additives in electrolyte solutions for Li-ion batteries [172] also indicated that these additives probably form polymers on graphite electrodes, which contribute considerably to their stabilization, especially at elevated temperatures, and lower their impedance [176]. We can therefore conclude that the formation of polymeric species on graphite surfaces may contribute to the improved stability and low impedance of the graphite anodes. In both cases of VC and Li organo-boron complexes as additives in solutions, it was clearly seen that in their presence, the impact of salt reduction (e.g., formation of LiF surface species) on the electrode's surface chemistry is much lower than in the additive-free solutions.

Table 2

Concentration of data from recent literature on the use of additives in lithium-ion battery electrolytes in order to improve their performance.

No	ADDITIVE	SOLVENT SYSTEM	MAJOR IMPACTS	Ref.
1	Alkyl pyrocarbonates	Mixture of alkyl Carbonates, $LiPF_6$	Hi charge/discharge capacity, long cycle life, reduced first cycle Irreversible capacity; satisfactory charging/discharging cyclic performance at high temp; superior discharging at low temp.	150, 154-156
2	Biphenyl (and other aromatic monomers)	Alkyl carbonates, $LiPF_6$	Overcharge protection	157-159
3	Sulfite. Preferred: allyl Or benzyl sulfite	EC+DMC+EMC+ DEC, $LiPF_6$	High charge/discharge capacity, long cycle life, reduced first cycle irreversible capacity	160
4	Silyl sulfate, tin ulfate, orAn organic sulfate	EC+DMC+EMC+ DEC, $LiPF_6$	High charge/discharge capacity, long cycle life, reduced first cycle irreversible capacity	161
5	Alkyl nitrite	EC+DMC+EMC+ DEC, $LiPF_6$	High charge/discharge capacity, long cycle life, reduced first cycle irreversible capacity	162
6	Nitrate. Preferred: Organic alkyl nitrate	EC+DMC+EMC+ DEC, $LiPF_6$	High charge/discharge capacity, long cycle life, reduced first cycle irreversible capacity	52
7	Alkyl Phosphonate	EC+DMC+EMC+ DEC, $LiPF_6$	High charge/discharge capacity, long cycle life, reduced first cycle irreversible capacity	164
8	Alkyl phosphate	EC+DMC+EMC+ DEC, $LiPF_6$	High charge/discharge capacity, long cycle life, reduced first cycle irreversible capacity	165
9	Substituted alkyl carbonates	EC+DMC+EMC+ DEC, $LiPF_6$	High charge/discharge capacity, long cycle life, reduced first cycle irreversible capacity	166
10	Lithium carbonate or calcium carbonate	EC:DMC 2:1 $LiPF_6$	Neutralizing acid contaminants (e.g., HF), enhancing thermal stability, Improving performance and cycle life.	167
11	Vinylene carbonate (VC) 5%	PC/EC/DMC $LiPF_6$	Reduce gas evolution during the first charge and the formation of surface fims	168

Table 2 (Continued)
Concentration of data from recent literature on the use of additives in lithium-ion battery electrolytes in order to improve their performance.

No	ADDITIVE	SOLVENT SYSTEM	MAJOR IMPACTS	Ref.
12	Vinylene carbonate (VC) to enable graphite discharge, vinyl benzoate (VB) or dimethyl fumarlate (DMF) to raise coulombic efficiency	Trimethyl phosphate (TMP) Non-flammable Solvent), $LiPF_6$	The chosen electrolyte: 1 M $LiPF_6$ / TMP+HFE+VC+DMF (44:40:8:8) HFE = a fluorinated ether and its purpose is to avoid a thermal runaway at elevated temperatures.	169
13	Fluorinated solvent	Mixtures of alkyl carbonates or alkyl carbonates with ethers, $LiPF_6$	Increases diffusivity of Li ions, improves load performance	170
14	*N,N*-dimethyltrifluoro-acetamide (DTA)	PC, $LiPF_6$	Good performance at low temperatures	152
15	*Trans* butylenes carbonates	As single solvents or in mixtures with other alkyl carbonates, $LiPF_6$	Avoids co-intercalation of solvent molecules with lithium into Graphite. High stability and low irreversible capacity of graphite electrodes	163
16	Compounds based on BF_3	Mixtures of alkyl carbonates, $LiPF_6$	Lowering rate of capacity fading	171
17	Lithium chelating compounds with boron	PC or EC with DME or THF, 2-MeTHF or 2,5-DiMeTHF, $LiPF_6$	High cycling efficiency	172
18	Fluorinated boronate compounds	DME or EC/DMC, $LiPF_6$	Better conductivity, high electrochemical stability up to 5 V	173
19	Dimethyl sulfite and diethyl sulfite	EC-based electrolyte solution	Low viscosity co-solvents, good low temperature performance	151
20	SO_2	MF, PC, DEC, DMC, $LiAsF_6$, $LiPF_6$	High degree of Li intercalation into graphite and stable cycle life. Formation of surface films comprised of $Li_2S_2O_4$, Li_2S, Li_2O	51, 174
21	CO_2	MF, BL, $LiClO_4$, $LiAsF_6$, DMC	Formation of surface films comprising Li_2CO_3, good passivation of lithiated carbon electroes	65, 66

To conclude this section, it can be said that the field of electrolyte solutions for Li-ion batteries in very dynamic and paves the way for a great deal of innovative work. While is it very difficult to develop solvents and salts that can compete with the commonly used alkyl carbonate mixtures (with EC as a key component) and $LiPF_6$ as the electrolyte, it is definitely possible to develop a variety of additives that can attenuate the surface chemistry of both anodes and cathodes for Li-ion batteries, and thus improve their stability and electrical properties. The work described in Table 2 is obviously a good start.

6.0 SURFACE CHEMISTRY OF ALTERNATIVE, NON-CARBONACEOUS ANODES

For many years now we have seen intensive, on-going studies of Li alloys as anodes for rechargeable Li batteries. The use of alloys instead of Li metal as anodes in rechargeable batteries may suppress dendrite formation. However, the use of host materials, which alloy with lithium, opens the door for other problems, such as irreversible phenomena due to volume changes when Li is inserted-deinserted into/from the host metallic matrix [177]. In general, Li alloys that are formed at potentials below 1.5 V in nonaqueous Li salt solutions should develop surface films similar to those formed on Li metal, and noble metals polarized to low potential in Li salt solutions [30] and, in fact, their stability towards solution species depends on passivation by surface films. Therefore, the volume changes that occur during formation and decomposition of Li alloys induces surface instability, lack of efficient passivation, and irreversible charge consumption by surface reactions between the active alloy and solution species. The change in volume of the Li alloy anodes during charge-discharge cycling leads to deactivation of the active mass, not merely as a result of surface reactions, but also as a result of destructive bulk changes. These problems in the use of Li alloys instead of Li metal anodes led to a further development of anodes based on oxides such as SnO, SnO_2, etc. [178]. Cathodic polarization of such oxides in Li salt solutions forms Sn-Li alloys embedded in a Li_2O matrix [179], which considerably increases the intrinsic stability of the active mass compared with an active mass that comprises Li-Sn alloys only. As expected, polarization of SnO_x electrodes is accompanied by the formation of surface films that were found to be very similar to those formed in the same solutions on carbonaceous anodes [180].

In general, the field of alternative anodes for rechargeable Li batteries based on tin alloys is extensive and dynamic, and cannot be covered even briefly in this chapter. However, it is important to mention a unique phenomenon found in these systems that definitely relates to their surface chemistry and the formation of surface films. In recent work by Dahn *et al.* on Li insertion-deinsertion into SnSi films studied by *in situ* AFM imaging [181], it was found that after lithium insertion into these films, deinsertion

of lithium is accompanied by the formation of cracks. Li insertion leads to the disappearance of the cracks, and they reappear during Li deinsertion. Upon repeated cycling the cracks appear and disappear periodically at the same locations. This behavior can be explained by the fact that when the cracks appear for the first time, surface reactions with solution species take place, and the surface films formed cover all the surface that is exposed to solution. Hence, the cracks formed initially become marked by surface films, which are probably sufficiently flexible to accommodate the morphological changes of the electrodes upon cycling. Therefore, we see here periodic cracking, which is preserved by passivating surface films.

Other interesting alternative anodes for rechargeable Li batteries are matrices containing nanoparticles of CoO. It appears that cathodic polarization of CoO electrodes forms metallic cobalt and Li_2O, and this process is highly reversible and promises high capacity [182]. During cathodic polarization of these electrodes in alkyl carbonate solutions, Tarascon *et al.* [183] discovered very interesting surface phenomena: reversible formation of gel on the electrode's surface, which contributes to its reversible capacity. This was the first time that anyone discovered reversible surface phenomena related to reduction of solution species in Li salt, polar aprotic solutions. As described throughout this chapter, when any metallic or carbon electrode is polarized in Li salt nonaqueous solutions, irreversible reduction processes usually take place, and cover the electrodes with surface films that can not be re-oxidized at any potential in which the solutions are stable (up to 4.5 V). Hence, in the case described herein, on matrices containing Co and Li_2O nanoparticles, electron transfer to alkyl carbonate solutions at low potentials forms some kind of polymeric species that can be re-oxidized during the reverse process (that forms both CoO and Li-ions in solution). These new and interesting phenomena definitely deserve further study, and we believe that the appropriate analytical work is currently in progress.

7.0   SURFACE FILMS: THE CATHODE SIDE

7.1   *Classification of Li Insertion Cathodes*

When dealing with surface film formation and related phenomena in Li-ion batteries, attention is usually focused on the anode side. This is due to the fact that the redox potentials of most of the anodes relevant to these batteries are sufficiently low to drive intensive reduction processes, whose products precipitate on the electrode surfaces (as described in the previous sections). Hence, surface film formation on anodes functioning at potentials below 1.5 V (Li/Li$^+$) is spontaneous. Thus, the cathodic stability of all electrolyte solutions relevant to Li-ion batteries is due to passivation phenomena.

The case of the cathode materials is apparently different. The electrolyte solutions are always selected to be anodically stable at the redox potentials of the cathode materials. Replacing Li metal by lithiated carbon anodes means two losses: the capacity is lowered by an order of magnitude and the anode´s redox potential is also higher. Thus, cathode materials of the **highest** redox potential available are chosen in order to obtain the highest energy density possible. Both solutions and cathodes for Li-ion batteries are chosen so there are no apparent oxidation reactions between the cathode materials at any state of charge and the electrolyte solutions. The most important cathode materials for Li-ion batteries are $LiCoO_2$, $LiMn_2O_4$, and $LiNiO_2$ and their derivatives (e.g., $LiCo_xNi_{(1-x)}O_2$, $LiMn_{(2-x)}M_xO_2$, M=another metallic element: Li, Mg, Al, Cr, Ni, Cu), all of which have their major redox activity around 4 V (Li/Li^+) [184-187]. In fact, this potential window of the cathode materials has caused the alkyl carbonates to become the most commonly used solvents for Li-ion batteries, because their apparent anodic stability is high and their major oxidation occurs at potentials >5 V (Li/Li^+). Their high anodic stability enables the use of alkyl carbonate solutions even with $LiMn_{(2-x)}M_xO_2$ cathodes (e.g., M=Cu), whose redox potential reaches 5 V (Li/Li^+) [188]. The anodic behavior of alkyl carbonate solutions was studied very recently, using both electro-chemical and spectral techniques [189-191]. While these studies confirmed the high anodic stability of alkyl carbonate solutions, as described above, we nevertheless found that some small scale oxidation of alkyl carbonate solvents on noble metal electrodes (Pt, Au) can occur at potentials below 4 V (Li/Li^+) [191]. However, from recent reports on the performance of practical Li-ion batteries [192], it is clear that the commonly used electrolyte solutions are not oxidized on the cathodes in Li-ion battery systems. Hence, from our studies it appears that the composite cathodes used in Li-ion batteries are passivated and, in fact, inhibit oxidation reactions of solutions that may occur on noble metal electrodes at potentials below 4 V [191].

This brings us to a conclusion that is well supported by recent studies [193,194]: there are important surface phenomena related to surface film formation on commonly used cathodes, which play a critical role in determining their performance.

7.2 *Electrochemical Response of Common Li Insertion Cathodes*

Li insertion processes into the most important cathode materials for Li-ion batteries, namely $LiCoO_2$, $LiNiO_2$, and $LiMn_2O_4$, have several important denominators. Li intercalation into these host materials occur via phase transitions [195], and include the obvious necessary stage of solid state diffusion of Li-ions inside the active mass. Figure 19 demonstrates some aspects of the similar electroanalytical response of $LiCoO_2$, $LiNiO_2$, and

$LiMn_2O_4$ electrodes as reflected by slow scan rate voltammetry and the variation of the chemical diffusion coefficient (D) as a function of potential. As discussed in detail [107,193,194,196], the pairs of narrow CV peaks with intrinsic hysteresis (the hysteresis appears due to the nature of the intercalation process and not because of kinetic/diffusion limitation), and the minima in D *vs.* E at the peak potentials reflect attractive interactions among the Li intercalation sites and phase transitions (as marked in Figure 19). Each peak in the CV plots of Figure 19 reflects the coexistence of two phases. At sufficiently slow potential scan rates, the electrochemical processes are no longer diffusion controlled, and they thus behave like adsorption processes perturbed by some kinetic limitations [107,196]. As mentioned in the previous section, the cathodes are also covered by surface films, and thus, their electrochemical processes include the necessary stages of Li ion migration through surface films and charge transfer across the film/solution and the film/active mass interfaces. These processes contribute a major part to the impedance of these electrodes. Hence, Li insertion into the cathodes is quite similar in principle to the above-described Li insertion processes into graphite, in its sequential stages, and their order. This is clearly reflected by the impedance spectra of these electrodes. When thin enough electrodes are measured, highly resolved impedance spectra can be obtained, which clearly show all the relevant time constants of the various stages of Li insertion into the cathodes. This is demonstrated in Figure 20, which compares typical impedance spectra (Nyquist plots) measured at selected potentials (as indicated) from $LiNiO_2$, $LiCoO_2$, $LiMn_2O_4$, and lithiated graphite electrodes. All four spectra show a high frequency semicircle, which is usually potential-invariant for the cathodes, and is attributed to Li-ion migration through surface films (coupled with film capacitance). In the case of graphite electrodes, the high frequency semicircle may depend on the electrode's potential, as discussed in reference 108. At medium-low frequencies, these spectra show another semicircle that is strongly dependent on the potentials. This semicircle may be the dominant feature in the impedance spectra of the cathodes, at certain potentials (usually at low, <3.9 V and high, >4.1 V potentials), and is attributed to charge transfer into the bulk active mass (i.e., it reflects both electron transfer to the active mass from the current collector and Li-ion transfer across the surface film/active mass interface). At the low potentials a 'Warburg'-type element appearing in these spectra reflects solid-state diffusion, and at the very low frequencies (in the mHz region), the impedance behavior reflects a capacitive behavior which is, in fact, the accumulation of lithium inserted into the bulk host materials. Indeed, when the electrodes are sufficiently thin and the frequency reached is low enough, the differential intercalation capacity can be calculated quite accurately from these impedance spectra ($C_{int} = 1/\omega Z''$, $\omega \rightarrow 0$, $Z'' = $ the imaginary part) [196]. Hence, all the Li insertion processes into the four electrodes, whose spectra are presented in Figure 20, can be precisely simulated by the relatively simple

equivalent circuit analog presented in Figure 20 [105-107,196]. (See also Figure 12 above and related discussion.) It should be noted that changes in the structure of the cathode materials, e.g., partial substitution and replacement of the transition metal by another metal, may result in a considerable change in the electroanalytical response of these electrodes. A typical example is $LiNi_{1-x}Co_xO_2$ electrodes whose electroanalytical response differs from that of both $LiNiO_2$ and $LiCoO_2$. Li insertion into $LiNi_{1-x}Co_xO_2$ involves both stages of phase transitions and formation of solid solutions [197]. This is reflected by less sharp peaks in slow scan rate CV and maxima in the D *vs.* E curves [198]. However, the formation of surface films and their impact on the electrodes´ behavior is quite similar for substituted $LiM_{1-x}M'_xO_2$ electrodes as for the $LiMO_2$ electrodes described above.

7.3   *Surface Films on Li-Insertion Cathodes*

In the previous sections, we described the importance of surface film formation on the cathodes. They influence the electrode´s impedance and kinetics, and may inhibit oxidation of solution species on the cathode surfaces. A surface reaction that is common to all cathode materials in $LiPF_6$ solutions is the acid-base reaction between the basic $LiMO_2$ compounds and unavoidably present trace HF. In fact, trace HF may also be present in $LiBF_4$ and $LiAsF_6$ solutions. Thereby, $LiMO_2$ cathodes always contain LiF on their surfaces in solutions of the above three salts [194]. As is well known from previous studies of lithium surfaces in $LiPF_6$ solutions, surface films that contain a high concentration of LiF are highly resistive (by more than two orders of magnitude compared with surface films comprised of Li_2O, LiOH, Li_2CO_3, $ROCO_2Li$, etc.) [25]. The impact of the presence of LiF films when formed on the cathode impedance is demonstrated in Figure 21. This figure shows impedance spectra (Nyquist plots) of $LiMn_2O_4$ and $LiNiO_2$ electrodes measured at 4.02 V (Li/Li^+) in $LiAsF_6$, $LiPF_6$, and $LiC(SO_2CF_3)_3$ solutions in EC-DMC mixtures [194]. Except for the spectrum of the $LiNiO_2$ electrode in the $LiPF_6$ solution, which reflects a highly resistive system, all the other spectra in Figure 21 contain two semicircles and a 'Warburg'-type element (low frequencies) that belong to the surface films, charge transfer, and solid state diffusion. The differences in the impedance spectra of Figure 21 are very significant and typical. $LiNiO_2$ electrodes develop a much higher surface resistance than $LiMn_2O_4$ electrodes. We indeed find that $LiNiO_2$, $LiCoO_2$ and $LiNi_{1-x}Co_xO_2$ electrodes are more reactive towards solution species than $LiMn_2O_4$ electrodes. In addition, the surface resistance of both $LiNiO_2$, and $LiMn_2O_4$ electrodes is considerably higher in $LiPF_6$ than in any other salt solution due to the relatively high concentration of HF in $LiPF_6$ solutions, which means a formation of highly resistive LiF surface films. The cathodes´ surface chemistry in solutions also includes interactions with atmospheric components and solvent molecules.
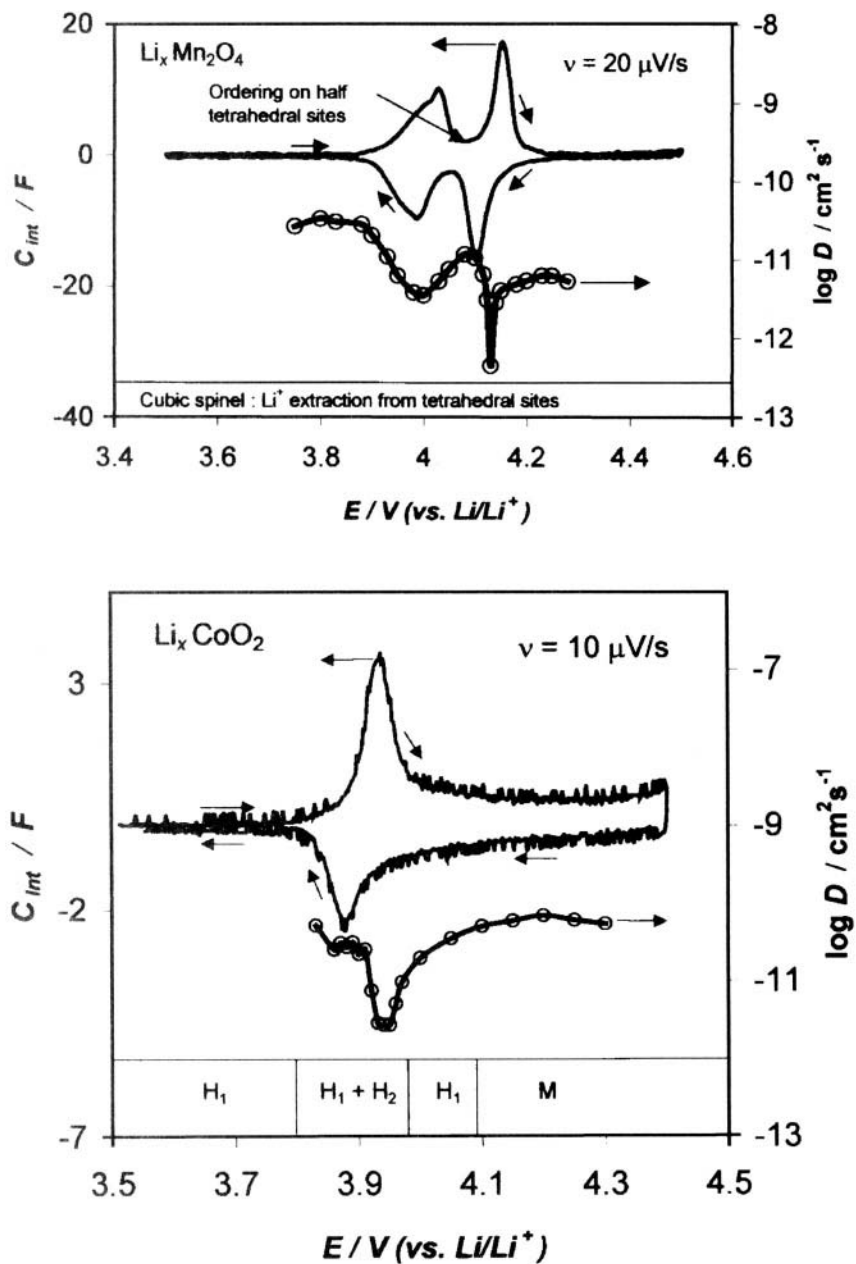
Figure 19. The typical electro-analytical response of thin composite LiMn$_2$O$_4$ and LiCoO$_2$ and LiNiO$_2$ electrodes in EC-DMC-LiAsF$_6$ solutions, as indicated. Slow scan CV (the scan rate is indicated on each chart) and log D *vs.* E are presented, as well as the corresponding phase transitions. (See references 193-199). LiNiO$_2$ on opposite page.
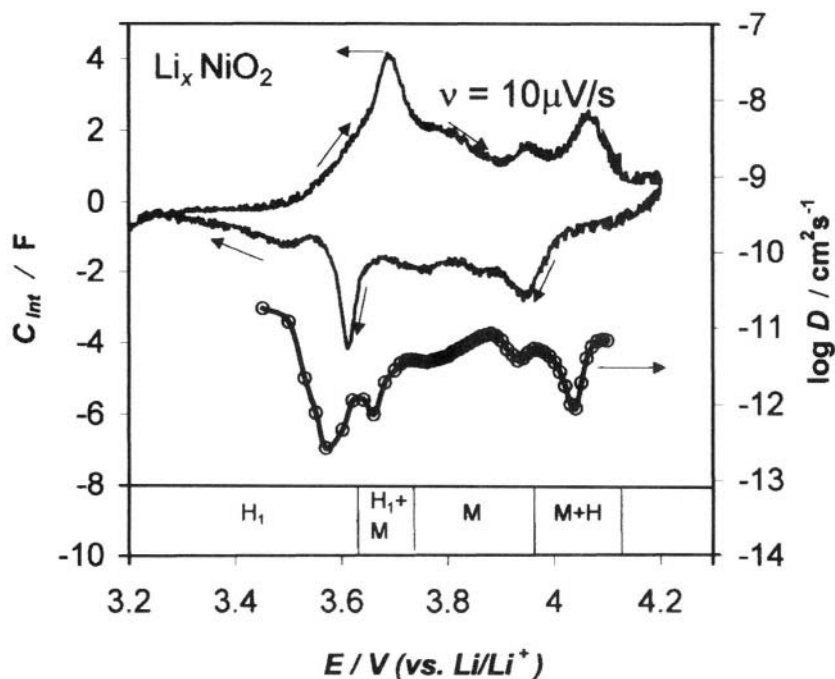
Figure 19 (Continued). Full description on opposite page.

Figure 22 shows typical FTIR spectra measured from pristine and cycled $LiMn_2O_4$, $LiNiO_2$, and $LiCoO_2$ electrodes (diffuse reflectance mode, particles scraped from the electrodes) [24]. The pristine spectra of $LiCoO_2$ and $LiNiO_2$ show pronounced Li_2CO_3 peaks (indicated) that we attribute to Li_2CO_3 surface species formed by reactions of the slightly basic $LiMO_2$ compounds with atmospheric CO_2. FTIR spectra of cycled $LiNiO_2$ and $LiCoO_2$ are very rich in absorption bands of organic species, which closely resemble the spectra of $ROCO_2Li$ species usually formed by reduction of alkyl carbonate solvents. Formation of surface $ROCO_2Li$ species on the cathodes may result from nucleophilic reactions between the lithiated oxides and the solvents, which are all electrophiles. Compared with the spectra of $LiNiO_2$ and $LiCoO_2$, the IR spectra of $LiMn_2O_4$ contain much less identifiable features. We can conclude from the above-described spectral studies that $LiMn_2O_4$ is less basic and nucleophilic than $LiCoO_2$ and $LiNiO_2$.

Figure 23 schematically summarizes several types of surface reactions of cathode materials in solutions, which lead the formation surface films. These include the following three possibilities:
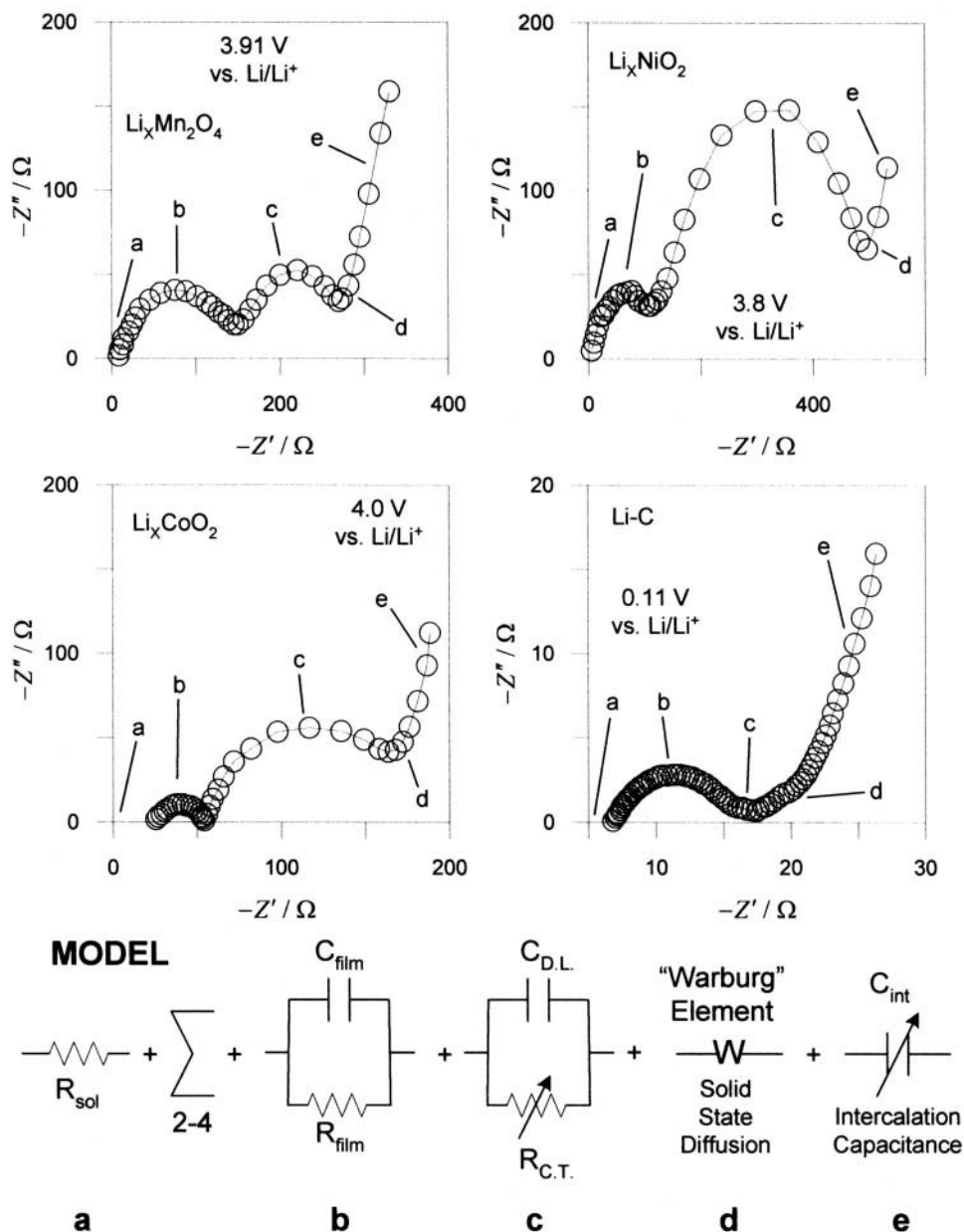
Figure 20. Typical impedance spectra measured from LiNiO₂, LiCoO₂, LiMn₂O₄, and lithiated graphite electrodes in EC-DMC/LiAsF₆ solutions (Li R.E. and C.E. electrodes). The potential of the measurements is indicated near each spectrum. A model that provides an excellent fit with these spectra is also presented. The assignment of its various elements to features of the experimental spectra is also shown. Adapted from reference 24 and reproduced with permission from Elsevier Science.
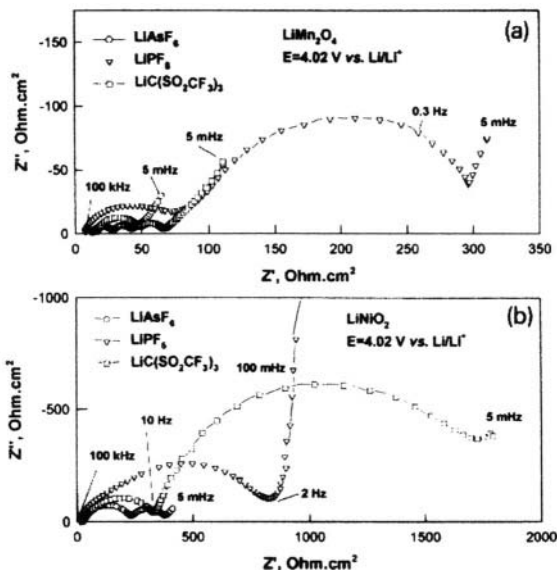
Figure 21. Typical impedance spectra measured with LiMnO$_2$ and LiNiO$_2$ electrodes (indicated) at 4.02 V (Li/Li$^+$) in LiAsF$_6$, LiPF$_6$, and LiC(SO$_2$CF$_3$)$_3$ solutions (1 M) in EC-DMC 1:1 mixtures, as indicated. From reference 219 reproduced with permission from Elsevier Science.

1. Nucleophilic reactions between LiMO$_2$ and solvent molecules, which may form ROCO$_2$Li species (relevant to LiNiO$_2$, LiCoO$_2$, and LiNi$_{1-x}$Co$_x$O$_2$, Figure 23, top. [194]).

2. Exchange reactions (e.g. M^{2+} *vs.* H$^+$ and Li$^+$), which lead to structural changes and the formation of inactive mass on the cathode particles. (May be relevant to LiMn$_2$O$_4$ cathodes, Figure 23, middle. [199]).

3. Structural changes close to the surface, which change the nature of the active mass. This was found for Li$_x$MnO$_2$ (0.3 <x<1) compounds with a major redox activity around 3 V (Li/Li$^+$), whose structure near the surface changes to a Li$_x$Mn$_2$O$_4$ spinel during repeated Li insertion-deinsertion cycling. Figure 23, bottom [200].

8.0   AGING AND SAFETY AS RELATED TO SURFACE FILM FORMATION

8.1   Aging Scenarios in Li-Ion Batteries

The combined spectral, morphological, and impedance studies described in the previous sections and the analyses of various surface film formation processes on both anodes and cathodes in Li-ion batteries, enables us to understand the possible scenarios of the aging of Li-ion batteries. The reader is referred to Chapter 13, for a thorough treatment of aging mechanisms in Li-

Ion batteries. In the commonly used LiPF$_6$-alkyl carbonate solutions, the surface films formed on the anodes may be dominated by solvent reduction, while the surface films formed on the cathodes may be dominated by LiF formation due to reactions of Li$_x$MO$_y$ with HF. Thereby, the overall impedance of Li-ion batteries may be determined mostly by the cathode´s surface resistance (due to its coverage by highly resistive LiF films). Upon cycling, the impedance of both anodes and cathodes may change:

1. In the anode side, when graphite is the active mass, the periodic changes in its volume during charge-discharge cycling may lead to continuous, small-scale surface reactions, which thicken the surface films and increase their impedance.

2. In the cathode side, continuous acid-base reactions, ionic exchange, and possible dissolution of the transition metal ions also lead to an increase in the impedance (in addition to capacity-fading due to the structural changes [201]). Highly critical in this respect is the contamination level in solutions, especially the HF concentration.

Storage at elevated temperatures completely change the passivation status. Hence, surface films stabilized on lithiated carbon electrodes at room temperature may lose their passivity at higher temperatures, allowing some electron transfer, and thus, further reduction of solution species on the active surface. Hence, the surface films are thickened, and, as the system returns to room temperature, the electrode´s impedance is much higher as compared with its pristine state.

In general, our studies show that upon cycling, a Li battery may lose capacity not because of destruction of the electrodes´ active mass, but rather due to surface film formation and their consequent thickening, which increases the overall impedance. We also analyzed surface film formation during cycling that leads to capacity-fade, because some part of the active mass in the composite electrodes becomes electronically isolated by surface films [202]. At present, aging and capacity-fade of Li-ion batteries are being intensively explored [203-205]. Of particular importance is the ability to model precisely the aging processes of Li-ion batteries, based on the understanding achieved by basic studies of the electrode reactions, as recently demonstrated [206].

8.2   The Effect of Surface Films on the Thermal Behavior of Anodes and Cathodes in Li-Ion Batteries

The subject dealt with in this section relates to safety features of Li-ion batteries that are strongly influenced by the surface films formed on both anodes and cathodes. In recent years, we have seen intensive work on the thermal behavior of Li-ion batteries using differential scanning (DSC) and accelerated rate (ARC) calorimetry [207-216]. Of special importance are calorimetric measurements of electrodes at different charge states with controlled amounts of

electrolyte solutions. Scanning the recent literature related to Li and Li-ion battery systems reveals that the most intensive and careful work in this area was carried out by Dahn *et al.* [211-218]. This group studied separately the thermal behavior of various carbonaceous electrodes at different degrees of lithiation in contact with commonly used electrolyte solutions [211-213], and partially charged cathode materials in electrolyte solutions (Li_xCoO_2, [214-215] $Li_xMn_2O_4$ [216]). These studies provided a solid basis for modeling the expected thermal behavior of practical Li-ion batteries [217, 218]. The results of the thermal studies of Li-C and Li_xMO_2 (M=Co, Mn) with the electrolyte solutions cited above converge nicely with the studies of the surface films on both anodes and cathodes described in the previous sections.
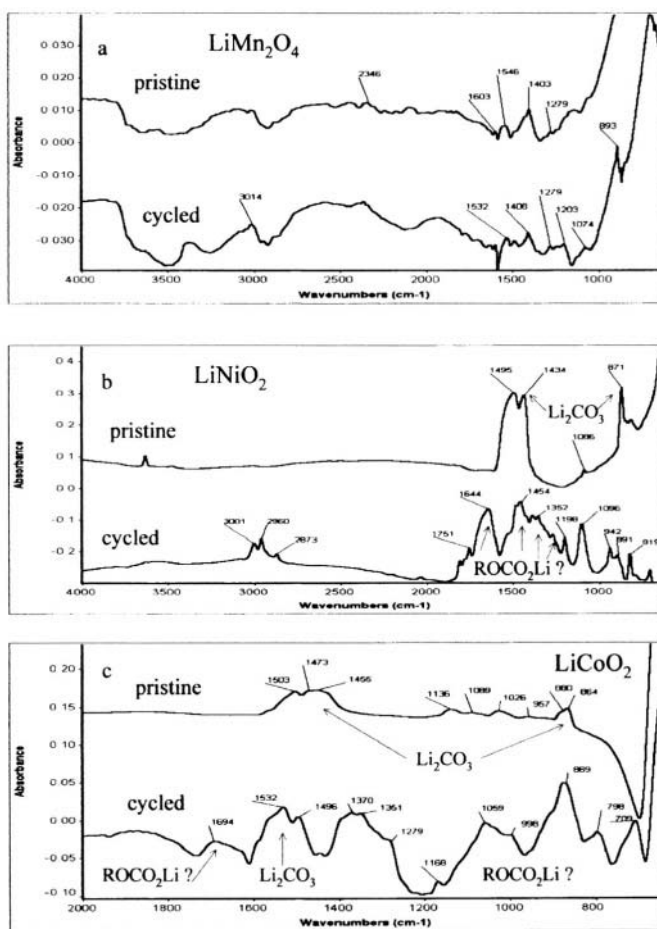
Figure 22. FTIR spectra measured from pristine and cycled $LiMn_2O_4$, $LiNiO_2$, and $LiCoO_2$ electrodes (a-c, respectively). EC-DMC/$LiAsF_6$ 1 M solutions. Diffuse reflectance mode. Some peak assignments are also presented near the spectra. Adapted from references 24 and 194 and reproduced with permission from Elsevier Science and by permission of The Electrochemical Society, Inc.
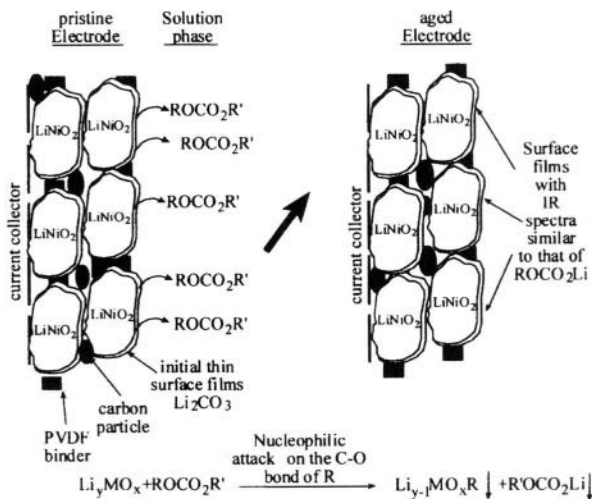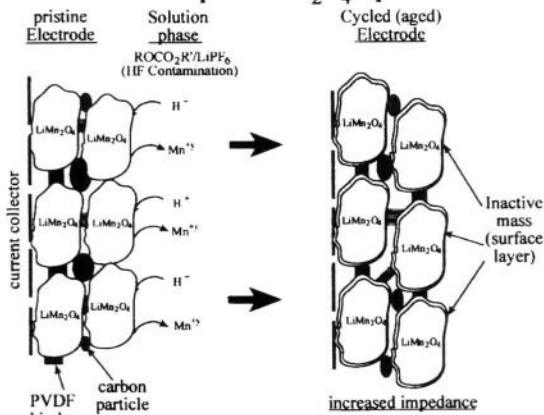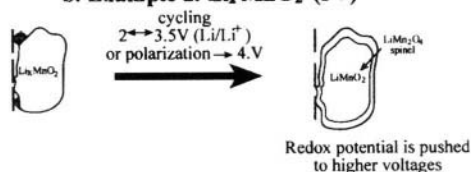
Figure 23. Schematic illustration and suggestions for surface film formation on various cathode materials. Top – nucleophilic materials ($LiNiO_2$); Middle – exchange reactions ($LiMn_2O_4$); Bottom – phase transitions ($Li_{0.3-1}MnO_2$). Reproduced from reference 219 with permission from Elsevier Science.

The following points of interest should be highlighted:

1. Following the thermal behavior of lithiated carbons in electrolyte solutions clearly shows that there are three stages in the reactions developed in these systems as the temperature is raised.

    i. The first stage is always a reaction in which the surface films are involved. This correlates well with the identification of the surface films formed in alkyl carbonate solutions, which contain $ROCO_2Li$ as major components. $ROCO_2Li$ can further react with the lithium contained in the lithiated carbon at elevated temperatures to form LiR, Li_2CO_3, Li_2O, etc. Such further reactions are indeed exothermic, as already seen in ARC measurements [211-213].

    ii. The second stage occurring at elevated temperatures involves reactions of residual lithium stored within the carbon and solution components. At high enough temperatures, the surface films lose their passivation and protection ability (e.g., due to partial dissolution, mechanical breakdown, and nucleophilic reactions with solution species). For example, RLi or Li_2O can react nucleophilically with alkyl carbonates to form soluble organic Li salts. Hence, the highly reactive Li-C intercalation compounds reach physical and electrical contact with solution species, which leads to intensive reduction reactions of solvent molecules.

    iii. At sufficiently high temperatures (>200 °C), there are redox reactions between the solvent molecules (alkyl carbonates) and the salt anion (e.g., PF_6^-), which acts as an oxidizer.

2. Cathode materials such as Li_xCoO_2 decompose at elevated temperatures to form $LiCoO_2$, Co_3O_4, CoO, and O_2 (disproportionation) [214-215]. In the presence of electrolyte solutions at elevated temperatures, the Li_xCoO_2 oxidizes the solvents. CO_2 is formed and reacts with the cobalt oxides and lithiated cobalt oxides to form lithium and cobalt carbonates. The presence of $LiPF_6$ in solutions impedes the exothermic redox reactions between Li_xCoO_2 and alkyl carbonate solvents at elevated temperature. Moreover, the redox reactions of Li_xCoO_2 and the solvents at elevated temperatures are less intense in the presence of $LiPF_6$, as compared with other salts (e.g., $LiBF_4$) [214,215]. This correlates with the spectral and impedance studies of cathode materials in the solutions containing different salts [194]. In $LiPF_6$ solutions, the cathode develops highly resistive surface films comprised of LiF as a major component. This passivating surface film, developed especially in $LiPF_6$ solutions, to some extent inhibits the thermal redox reactions of cathodes with the alkyl carbonate solvents at elevated temperature.

11:03 am, Jan 20, 2005

Another significant result that should be mentioned is the higher thermal stability of Li_xCoO_2, as compared with $LiMn_2O_4$, in electrolyte solutions [216]. This finding correlates with the study of these electrodes by FTIR, XPS, and EIS, which revealed that $LiMn_2O_4$ is less reactive than $LiCoO_2$ or $LiNiO_2$ with solution species [24,194]. Hence, $Li_xMn_2O_4$ electrodes are less passivated in solutions than $LiCoO_2$ or $LiNiO_2$, and thus, their redox reactions with solution species at elevated temperatures ($Li_xMn_2O_4$ is the oxidizer) are less impeded and can occur more readily, as compared with the better-passivated $LiCoO_2$ electrodes.

9.0   CONCLUDING REMARKS

This chapter describes highly important phenomena of Li and Li-ion batteries, namely, basic electrode-solution interactions, surface film formation, passivation, and the correlation among 3D structure, morphology, surface chemistry, electronic properties, and electrochemical behavior of anodes and cathodes for Li-ion batteries. It was found that surface films are formed in both Li-C anodes and Li_xMO_y cathodes, control their stability, influence their kinetics, and have a significant impact on the degree of capacity fading upon cycling. The safety features of the electrodes, (and, in fact, the batteries) at elevated temperatures are also determined by the surface films that cover them.

In the case of the cathodes, surface films are formed by acid-base reactions (e.g., HF + Li_xMO_y to form LiF and protonated oxides), nucleophilic reactions (e.g., $LiNiO_2$ + alkyl carbonates to form $ROCO_2Li$ species), and polymerization (e.g., formation of polycarbonates by polymerization of EC initiated by Lewis acids). These surface films increase the cathodes´ impedance, and also increase their passivation, which may lead to a better thermal stability. The anode side is, of course, more complicated. Surface films are always formed due to the inevitable reduction of solvent molecules, salt anions, and reactive contaminants, at the low potential to which the anodes are polarized during Li insertion. The surface films formed on the anodes precipitate as a result of a very delicate balance among several competing surface reactions of the various solution components. In the case of alkyl carbonates, these reduction processes are accompanied by formation of gases. When the solvents are not too reactive, as is the case with ethers, surface film formation may be accompanied by co-intercalation of solvent molecules, migrating together with the Li-ions, which they solvate. The surface reactions of the solution components on graphite electrodes at low potentials may be very destructive to the graphite structure due to co-intercalation processes (ethers) that lead to amorphization, or splitting of graphite particles, due to the formation of internal pressure (propylene carbonate), which in turn leads to the electrical isolation of the active mass by surface films.

The precipitation of passivating surface films, which can protect the carbon anodes´ active mass and prevent detrimental processes such as co-intercalation and exfoliation, depends on several factors. These include the degree of cohesion and adhesion of the Li salts formed by reduction of the solvents, and to what extent their precipitation in thin cohesive/adhesive films is not perturbed by gas formation (the co-product of solvent reduction). Here, the morphology of the graphite particles plays an important role (e.g., the smoother the edge planes of the particles, the better is the passivation that can be achieved by surface film precipitation). Hence, here we observe the very interesting correlation between surface chemistry and 3D structure and morphology. The surface films formed on the anodes determine their imped-ance, stability and capacity fading upon cycling.

In conclusion, the above-described phenomena open the door for extremely interesting studies at the forefront of surface science, whose research deserves application of the most novel spectroscopic and electrochemical tools. The importance of these surface phenomena makes the entire field of Li and Li-ion batteries dependent on prerequisite fundamental studies of acomplicated surface chemistry.

10.0   REFERENCES

Table 2. List of references for surface studies of lithium and lithiated carbon electrodes

	ELECTROLYTE SYSTEMS	REFERENCE
1	Alkyl carbonate solvents in general	53,58,62-66
2	PC	29,50,61,65,66
3	EC	50,61,65
4	DMC	62,66
5	EMC	67
6	PMC	60
7	Ethers in general	29,65,68,69
8	1,3-Dioxolane	65
9	Cyclic ethers (THF, 2Me-THF)	29,65
10	Glymes	70
11	γ-Butyrolactone	50,64-66
12	Methyl Formate (MF)	50,64-66,73
13	Salt Reactions	50,64-66,71,72
14	CO_2 reactions	50,65,66,73
15	Atmospheric contaminants	42,50,65,66

1.   A.K. Vijh, "Electrochemistry of Metals and Semiconductors: The Application of Solid State Science to Electrochemical Phenomena," Marcel Dekker, Inc., New York, N.Y. 1973, J.W. Diggle, A.K. Vijh, Editors "The Anodic Behavior of Metals and Semiconductors Series: Oxides and Oxide Films," Marcel Dekker, Inc., New York, N.Y. 1976. *Vol. 4.*

2.   N. Sato, "Electrochemistry at Metal and Semiconductor Electrodes," Elsevier, Oxford, U.K. . Ch. 2, pp. 15-59, Ch. 3, pp. 61-86, Ch. 5, pp. 119-199, Ch.11, pp.373-389, 1998

3.   I. Riess, In "CRC Handbook Solid State Electrochemistry," R.J. Gellings, and H.J.M. Bouwmeester, Eds., CRC Press, Boca Raton and New York, 1997, Ch. 7, 223-268.

4.   E. Peled, in "Lithium Batteries," J.P. Gabano, Ed., Academic Press, London, 1983, Ch. 3, p. 43.

5.   E. Peled, *J. Electrochem. Soc.,* **126**, 2047, 1979.

6.   L. Young, "Anodic Oxide Films," 1961, Academic Press, London, N.Y.

7.   J. Frenkel, *Z. Physik* **35,** 652, 1926.

8.   N.W. Ashcroft, and N.D. Mermin, "Solid State Physics," 1976, Ch. 30, Saunders Co., USA, p. 616.

9.   C. Wagner, and W. Schottky, *Z. Physik. Chem.,* **10**, 163, 1930.

10.   D.O. Ralegh, in "Electroanalytical Chemistry," A.J. Bard, Ed., Marcel Dekker, Inc., N.Y., 6, 1973.

11.   A.D. Holding, D. Pletcher, and R.V.H. Jones, *Electrochimica Acta,* **34**, 1529, 1989.

12.   A.J. Bard, and L.R. Faulkner, "Electrochemical Methods, Fundamentals and Applications", John Wiley and Sons, N.Y., Ch. 3, p. 86, 1980.

13.   D. Aurbach, Y. Gofer, A. Schechter, O. Chusid, H. Gizbar, Y. Cohen, M. Moshkovich, and R. Turgeman, *J. Power Sources,* **97-98**, 269, 2001.

14.   G. Zhuabg, P.N. Ross, Jr., F.-P. Kong, F. McLarnon, *J. Electrochem. Soc.,* **145**, 159, 1998.

15.   D. Aurbach, R. Skaletsky, and J. Gofer, *J. Electrochem. Soc.,* **138,** 3536, 1991.

16.   Z. Lu, A. Schechter, M. Moshkovich, and D. Aurbach, *J. Electroanal. Chem.,* **466**, 203, 1999.

17.   D. Aurbach, A. Schechter, M. Moshkovich. and Y. Cohen, *J. Electrochem. Soc.,* **148**, A1004, 2001.

18.   K. Kanamura, H. Tamura, S. Shiraishi, and Z-I. Takehara, *Electrochimica Acta,* **40**, 7, 913, 1995.

19.   K. Kanamura, H. Tamura. and Z-I. Takehara, *J. Electroanal. Chem.,* **333**, 127, 1992.

20.   K. Wang, P.N. Ross,Jr., F. Kong, F. McLarnon, *J. Electrochem. Soc.,* **143**, 422.1996.

21.   L. J. Rendek, G.S. Chottiner, and D.A. Scherson, *Langmuir,* **17**, 849, 2001.

22.   D. Aurbach, A. Zaban, Y. Gofer, Y. Ein-Eli, I. Weissman, O. Chusid, O. Abramson, and B. Markovsky, *J. Power Sources,* **54**, 76, 1995.

23.   D. Aurbach, A. Zaban, Y. Ein-Eli, I. Weissman, O. Chusid, B. Markovsky, M.D. Levi, E. Levi, A. Schechter, and E. Granot, *J. Power Sources,* 86, 91, 1997.

24.   D. Aurbach, B. Markovsky, M.D. Levi, E. Levi, A. Schechter, M. Moshkovich, and Y. Cohen, *J. Power Sources,* **81-82**, 95, 1999.

25.   D. Aurbach, E. Zinigrad, and A. Zaban, *J. Phys. Chem.,* **100**, 3089, 1996.

26.   K. Kanamura, S. Shiraishi, and Z.-I. Takehara, *J. Electrochem. Soc.,* **143**, 7, 2187, 1996.

27.   K. Kanamura, S. Shiraishi, H. Tamura, and Z.-I. Takehara, *J. Electrochem. Soc.,* **141**, 9, 2379, 1994.

28.   D. Aurbach, and Y. Cohen, *J. Electrochem. Soc.,* **143**, 3525, 1996.

29.   A. Schechter, and D. Aurbach, *Langmuir,* **15**, 3334, 1999.

30.   D. Aurbach, M.L. Daroux, P. Faguy, and E. Yeager, *J. Electroanal. Chem.* **297**, 225, 1991.

31. D. Aurbach, and A. Zaban, *J. Electrochem. Society,* **141**, 1808, 1994.
32. D. Aurbach, M. Moshkovich, and Y. Gofer, *J. Electrochem. Soc.,* **148**, E155, 2001.
33. D. Aurbach and I. Weissman in *"Nonaqueous Electrochemistry",* D. Aurbach, Ed., Marcel Dekker, Inc. New-York, Basel, Ch. 1, p. 1, 1999.
34. C.R. Schlaikjer, in *"Lithium Batteries,"* J.P. Gabano, Ed., Academic Press, New York and London, Ch. 13, p. 303, 1983.
35. T. Osaka, in: *"Energy Storage Systems for Electronics."* T. Osaka, and M. Datta, Eds., Gordon and Breach Science Publishers, Amsterdam, Ch.12, p. 431, 2000.
36. B. Scrosati, in *"Lithium Ion Batteries. Fundamentals and Performance.* "M. Wakihara, and O. Yamamoto, Eds., Wiley-VCH, New York, Ch. 10, p. 218, 1998.
37. D.F. Shriver, and P.G. Bruce, in "*Solid State Electrochemistry.* "P.G. Bruce, Ed., Cambridge University Press, Cambridge, England, Ch. 5, p. 95, 1995; P.G. Bruce, and F.M. Gray, *ibid,* Ch. 6, p. 119.
38. C. Julien, and G.-A. Nazri, Kluwer, *"Solid State Batteries: Materials Design and Optimization,"* Kluwer Academic Publishers, New York, Ch. 5, p. 347, 1994.
39. F. Gray, and M. Armand, in *" Handbook of Battery Materials,"* J. O. Besenhard, Ed., Wiley-VCH, New York, Ch. 8, p. 499, 1999.
40. W.H. Meyer, *Adv. Mater.,* **10**, *6,* 439, 1998.
41. M. Schmidt, U. Heider, A. Kuehner, R. Oesten, M. Jungnitz, N. Ignat´ev, and P. Sartori, *J. Power Sources, 97-98,* 557, 2001.
42. D. Aurbach, *J. Electrochem. Soc.,* **136**, 1610, 1989.
43. S. E. Sloop, J. K. Pugh, S. Wang, J.B. Kerr, K. Kinoshita, *Electrochem. Solid-State Lett.* **4**, A42, 2001.
44. X. Z. Shu, R.S. McMillan, J.J. Murray, and J.J. Davidson, *J. Electrochem. Soc.,* **142**, L161, 1995.
45. M. Inaba, Y. Kawatate, A. Funabiki, S.K. Jeong, T. Abe, and Z. Ogumi, *Electrochimica Acta,* **45**, 99, 1999.
46. G.H. Wrodnigg, J.O. Besenhard, and M. Winter, *J. Electrochem. Soc.,* **146,** 470, 1999.
47. G.H. Wrodnigg, T.M. Wrodnigg, J.O. Besenhard, and M. Winter, *Electrochem. Comm.,* **1**, 148, 1999.
48. B. Simon, J.P. Boeuve, B. Spigai, and M. Broussely, *The Electrochem. Soc. Fall Meeting,* Paris 1997. Extended abstracts Vol. 97-2, p. 184; B. Simon, and J.P. Boeuve, SAFT Patents, FR 94 04889 (1994) EP 0683537, US 5,626,981.
49. Y. Sasaki, M. Handa, K. Kurashima, T. Tonuma, and K. Usami, *J. Electrochem. Soc.,* **148**, A999, 2001.
50. D. Aurbach, Y. Ein-Eli, B. Markovsky, Y. Carmeli, H. Yamin, and S. Luski, *Electrochimica Acta,* **39**, 2559, 1994.
51. Y. Ein-Eli, S.R. Thomas, and V.R. Koch, *J. Electrochem. Soc.,* **143**, L195, 1996.
52. H. Gan, and E.S. Takeuchi, "Nitrate additives for nonaqueous electrolyte rechargeable cells," (Wilson Greatbatch Ltd., USA): Application for US. Patent, An. 2000:752090.
53. K. Kanamura, H. Tamura, S. Shiraishi, and Z.-I. Takehara, *J. Electroanal. Chem.,* **394**, 49, 1995.
54. D. Aurbach, M. Daroux, G. McDougal, and E.B. Yeager, *J. Electroanal. Chem.,* **358**, 63, 1993.
55. E. Goren, O. Chusid, and D. Aurbach, *J. Electrochem. Soc.,* **138**, L6, 1991.
56. J.-C. Panitz, P. Novák and O. Haas *Appl. Spectrosc.,* **55**, 1131, 2001.
57. D. Aurbach, I. Weissman, H. Yamin, and E. Elster, *J. Electrochem. Soc.,* **145**, 1421, 1998.

58.   E. Peled, D. Bar Tow, A. Merson, A. Gladkich, L. Burstein, and D. Golodnitsky, D. *J. Power Sources.* **97-98,** 52, 2001.
59.   M.P. Fuller, and P.R. Griffiths, *Anal. Chem.,* **50,** 1906, 1978.
60.   Y. Ein-Eli, S.F. McDevitt, B. Markovsky, A. Schechter, and D. Aurbach, *J. Electrochem. Soc.,* **144**, L 180, 1997.
61.   D. Aurbach, Y. Gofer, M. Ben-Zion, and P. Aped, *J. Etectroanal. Chem.* **339,** 451, 1992.
62.   D. Aurbach, B. Markovsky, A. Schechter, Y. Ein-Eli, and H. Cohen, *J. Electrochem. Soc.,* **143**, 3809, 1996.
63.   R. Yazami, *Electrochimica Acta,* **45,** 87, 1999.
64.   D. Aurbach, B. Markovsky, K. Gamolsky, E. Levi, and Y. Ein-Eli, *Electrochimica Acta,* **45**, 67, 1999.
65.   D. Aurbach, O. Youngman Chusid, Y. Carmeli, M. Babai, and Y. Ein-Eli, *J. Power Sources,* **43**, 47, 1993.
66.   D. Aurbach, Y. Ein-Eli, O. Chusid, M. Babai, Y. Carmeli, and H. Yamin, *J. Electrochem. Society,* **141**, 603, 1994.
67.   D. Aurbach, A. Schechter, B. Markovsky, Y. Ein-Eli, and V. Koch, *J. Electrochem. Soc.,* **143**, L273, 1996.
68.   D. Aurbach, A. Zaban, Y. Gofer, O. Abramson, and M. Ben-Zion, *J. Electrochem. Soc.,* **142**, 687, 1995.
69.   D. Aurbach, M.L. Daroux, P. Faguy, and E. Yeager, *J. Electrochem. Soc.,* **135**, 1863, 1988.
70.   D. Aurbach, and E. Granot, *Electrochimica Acta,* **42**, 697, 1997.
71.   D. Aurbach, O. Chusid, and I. Weissman, *Electrochimica Acta,* **41**, 747, 1996.
72.   D. Aurbach, and Y. Ein-Eli. *Langmuir,* **8**, 1845, 1992.
73.   D. Aurbach, and O. Chusid, *J. Electrochem Soc.,* **140**, L155, 1993.
74.   J.R. Dahn, A.K. Sleigh, H. Shi, B.M. Way, W.J. Weydanz, J.N. Reimers, Q. Zhong and U. von Sacken, *Lithium Batteries – New Materials, Developments and Perspectives,* G. Pistoia, Ed. Elsevier-North Holland, Amsterdam 1993, p. 1.
75.   J.E. Fischer, *Chem. Innov.,* **30**, 21, 2000.
76.   Z.H. Yang, and H.Q. Wu, *Mater. Chem. and Phys.,* **71**, 7, 2001.
77.   N. Takami, A. Satoh, M. Hara, and T. Ohsaki, *J. Electrochem. Soc.,* **142**, 371, 1995.
78.   R. Fong, U. von Sacken, and J.R. Dahn, *J. Electrochem. Soc.,* **137,** 2009, 1990.
79.   D. Fauteux, *J. Appl. Electrochem.,* **23**, 1, 1993.
80.   M. Jean, A. Tranchant, and R. Messina *J. Electrochem. Soc.,* **143**, 391, 1996.
81.   E. Buiel, and J.R. Dahn, *Electrochimica Acta,* **45**, 121, 1999.
82.   A.M.Wilson, and J.R. Dahn, *J. Electrochem. Soc.,* **142**, 326, 1995.
83.   Y.S. Han, J.S. Yu, G.S. Park, and J.Y. Lee, *J. Electrochem. Soc.,* **146**, 3999, 1999.
84.   S. Gautier, F. Leroux, E. Frackowiak, A.M. Faug, J.N. Rouzaud, and F. B´Guin, *J. Phys. Chem.,* A**105,** 5794, 2001; G. Sandi, K.A. Carrado, R.E. Winans, C.S. Johnson, and R. Csencsits, *J. Electrochem. Soc.,* **146**, 3644, 1999.
85.   I. Mochida, C.H. Ku, and T. Korai, *Carbon,* **39,** 399, 2001.
86.   H. Huang, W.F. Liu, X.J. Huang, L.Q. Chen, E.M. Kelder, and J. Schoonman, *Solid State Ionics,* **110**, 173, 1998.
87.   A. Naji, P. Willmann, and D. Billaud, *Carbon,* **36**, 1347, 1998.
88.   R. Al Cantera, J.L. Tirado, J.M.J. Mateos, C.G. De Salazar, R. Stoyanova, and E. Zhechera, *Carbon.* **38**, 1031, 2000.
89.   Y.C. Chang, H.J. Sohn, C.H. Ku, Y.G. Wank, Y. Korai, and I. Mochida, *Carbon,* **37**, 1285, 1999.

90. C. Kim, T. Fujino, K. Miyashita, T. Hayashi, M. Endo, and M.S. Dresselhaus, *J. Electrochem. Soc.,* **147**, 1257, 2000.
91. K. Yamaguchi, J. Suzuki, Saito, M.; K. Sekine, and T. Takamura, *J. Power Sources,* **97-8**, 159, 2001.
92. K. Suzuki, T. Iijima, and M. Wakihara, *Electrochimica Acta,* **44**, 2185, 1999.
93. K. Zagib, K. Tatsumi, H. Abe, T. Ohsaki, Y. Sawada, and S. Higuchi, *J. Electrochem. Soc.,* **145**, 210, 1998.
94. P. Zhou, P. Papanek, R. Lee, J.E. Fischer, and W.A. Kamitakahara, *J. Electrochem. Soc.,* **144**, 1744, 1997.
95. H. Azuma, H. Imoto, S.J. Yamada, and K. Sekei, *J. Power Sources,* **81-82**, 1, 1999.
96. D. Aurbach, J.S. Gnanaraj, M.D. Levi, E. Levi, G. Salitra, J.F. Fischer, and A. Claye, *J. Electrochem. Soc.,* **148**, A525, 2001.
97. E. Buiel, A.E. George, and J.R. Dahn, *J. Electrochem. Soc.,* **145**, 2252, 1998.
98. A. Claye, and J. E. Fischer, *Electrochimica Acta,* **45**, 107, 1999.
99. P. Papanek, M. Radosavljevic, and J.E. Fischer, *Chem. of Mater.,* **8,** 1519, 1996.
100. J. Kawakita, and K. Kobayashi, *J. Power Sources,* **101**, 47, 2001.
101. J.W. Braithwaite, A. Gonzales, G. Nagasubramanian, S.J. Lucero, D.E. Peebles, J.A. Ohlhausen, and W.R. Cieslak, *J. Electrochem. Soc.,* **146**, 448, 1999.
102. J.S. Gnanaraj, Y.S. Cohen, M.D. Levi, and D. Aurbach, *J. Electroanal. Chem.,* **516**, 89, 2001.
103. M.E. Orazem, P. Agarwal, and L.H. Garcia Rubio, *Electroanal. Chem.,* **378**, 51, 1994.
104. D. Aurbach, and A. Zaban, *J. Electroanal. Chem.,* **367**, 15, 1994.
105. D. Aurbach, and M.D. Levi, *J. Phys. Chem.* B., **101**, 4641, 1997.
106. D. Aurbach, and M.D. Levi, *J. Phys. Chem.* B., **101**, 4630, 1997.
107. M.D. Levi, and D. Aurbach, *Electrochimica Acta,* **45**, 167, 1999
108. D. Aurbach, and B. Markovsky, *Electrochimica Acta,* **43**, 2287, 1998.
109. M. Nishizawa, H. Koshika, R. Hashitani, T. Itoh, T. Abe, and I. Uchida, *J. Phys. Chem. B,* **103**, 4933, 1999.
110. M. Umeda, K. Dokko, Y. Fujita, M. Mohamadi, I. Uchida, and J.R. Selman, *Electrochimica Acta,* **47**, 885, 2001.
111. A. Martinent, B. Le Gorrec, C. Montella, and R. Yazami, R. *J. Power Sources,* **97-8**, 83, 2001.
112. Q. Wang, H. Li, X. Huang, and L. Chen, *J. Electrochem. Soc.,* **148**, A737, 2001.
113. J.R. Dahn, T. Zheng, Y. Liu, and J.S. Xue, *Science,* **270**, 590, 1998.
114. A. Mabuchi, H. Fujimoto, K. Tokumitsu, and T. Kasuh, *J. Electrochem. Soc.,* **142**, 3049, 1995.
115. Y.O. Kim, and S.M. Park, *J. Electrochem. Soc.,* **148**, A194, 2001.
116. A. Funabiki, M. Inoda, S. Ogumi, J. Yuasa, J. Otsuji, and A. Tasaka, *J. Electrochem. Soc.,* **145**, 172, 1998.
117. P. Novak, F. Joho, M. Lanz, B. Rykart, J.C. Panitz, D. Alliata, R. Kotz, and O. Haas, *J. Power Sources,* **97-8,** 39, 2001.
118. R. Yazami, *J. Power Sources,* **97-8,** 33, 2001.
119. Y. Ein-Eli, *Electrochem. and Solid State Lett.,* **2,** 212, 1999.
120. D. Aurbach, M.D. Levi, E. Levi, and A. Schechter, *J. Phys. Chem. B.,* **101**, 2195, 1997.
121. M. Winter, J.O. Besenhard, M.E. Spahr, and P. Novak, *Adv. Mater.,* **10**, 725, 1998.

122. G.C. Chung, S.H. Jun, K.Y. Lee, and M.H. Kim, *J. Electrochem. Soc.,* **146**, 1664, 1999; G.C. Chung, H.J. Kim, S.H. Jun, J.W. Choi, and M.H. Kim, *J. Electrochem. Soc.,* **147**, 4398, 2000.

123. M. Winter, G.H. Wrodnigg, J.O. Besenhard, W. Biberacher, and P. Novák, *J. Electrochem. Soc., ***147,** 2427, 2000.

124. A. Herold, in "*Intercalated Layered Materials,* "F. Levy, Ed., D. Riedel Publishing Co., Boston and London, p. 365, 1979.

125. M. Winter, and J.O. Besenhard. in *"Handbook of Battery Materials,* "J.O. Besenhard, Ed., Wiley-VCH, Weinheim, New York, Ch. 5, p. 383, 1999.

126. D. Aurbach, H. Teller, and E. Levi, *J. Electrochem. Soc..* In press. 2002.

127. Z.X. Shu, R.S. McMillan, and J.J. Murray, *J. Electrochem. Soc.,* 140, 922, 1993.

128. D. Aurbach, and Y. Ein-Eli, *J. Electrochem. Soc.,* **142**, 1746, 1995.

129. M. Winter, P. Novak, and A. Monnier, *J. Electrochem. Soc.,* **145**, 428, 1998.

130. F. Joho, B. Rykart, A. Blome, P. Novak, H. Wilhelm, M.E. and Spahr, *J. Power Sources,* ***97-8,*** 78, 2001.

131. C.H. Dahn, H.S. Kim, and S.I. Moon, *J. Power Sources,* **101**, 96, 2001.

132. C. Lampe-Onnerud, J. Shi, P. Onnerud, R. Chamberlain, and B. Barnett, *J. Power Sources,* **97-8**, 133, 2001.

133. J. Oliver, and M. Winger, *J. Power Sources,* **97-8**, 151, 2001.

134. F. Joho, B. Rykart, A. Blome, P. Novák, H. Hilkelm, and M.E. Spahr, *J. Power Sources,* **97-8**, 78, 2002.

135. M.E. Spahr, H. Wilhelm, F. Joho, and P. Novak, *ITE Letters on Batteries, New Technologies & Medicine,* **2**, 370, 2001.

136. D. Alliata, R. Kotz, P. Novak, and H. Siegenthaler, *Electrochem. Comm.,* **2**, 436, 2000.

137. S.K. Jeong, M. Inaba, T. Abe, and Z. Ogumi, *J. Electrochem. Soc.,* **148**, A989, 2001.

138. M. Inaba, Z. Siroma, A. Funabiki, T. Abe, Y. Mizutani, M. Asano, and Z. Ogumi, *Langmuir,* **12**, 1535, 1996.

139. K. Morigaki, T. Fujii, and A. Ohta, *Denki Kagaku,* **66**, 1122, 1998.

140. M. Koltypin, Y.S. Cohen, Y. Cohen, B. Markovsky, and D. Aurbach, *Electrochem. Comm.,* **4**, 17, 2002.

141. T. Takamura, M. Kikuchi, and Y. Ikezawa, in: *"Rechargeable Lithium-ion Batteries,"* S. Megahed, B.M. Barnett, and L. Xie, Eds., The Electrochemical Society, Soft Bound Series PV 94-28, The Electrochem. Soc. Inc., Pennington, N.J., p.213, 1998.

142. W. Xing, and J.R. Dahn, *Abstr. 190th Electrochemical Soc. Meeting, San Antonio, TX, E*xtended abstract, Vol. 96-2, p. 1062, 1999.

143. C. Menachem, D. Golodnitsky, and E. Peled, *J. Solid State Chem.,* **5**, 81, 2001.

144. E. Peled, D. Golodnitsky, and J. Penciner, in *"Handbook of Battery Materials,"* J.O. Besenhard, Ed., Wiley-VCH, New York, 1999, Ch. 6, p. 419.

145. M. Gaberscek, M. Bele, J. Drofenik, R. Dominko, and S. Pejovnik, *J. Power Sources,* **97-98**, 67, 2001.

146. F. Chevallier, L. Aymard, and J.M. Tarascon, *J. Electrochem. Soc.,* **148**, A1216, 2001.

147. Y. Ein-Eli, and V.R. Koch, *J. Electrochem. Soc.,* **144**, 2968, 1997.

148. J.A. Ritter, R.E. White, and B.N. Popov, *Proc. Electrochem. Soc.,* PV 99-25, The Electrochemical Society Inc., pp. 86-98, 2000.

149. H. Honbo, S. Takeuchi, H. Momose, K. Nishimura, T. Horiba, Y. Muranaka, and Y. Kozono, *Denki Kagaku,* **66**, 939, 1998.

150. H. Gan, and E.S. Takeuchi, "Dicarbonate additives for nonaqueous electrolyte rechargeable cells," (Wilson Greatbatch Ltd., USA), Application for US. Patent, An. **2001**:45110.

151. G.H. Wrodnigg, J.O. Besenhard, and M. Winter, *J. Power Sources,* **97-98**, 592, 2001.

152. K. C. Moller, T. Hodal, W.K. Appel, M. Winter, and J.O. Besenhard, *J. Power Sources,* **97-98**, 595, 2001.

153. F. Kita, H. Sakata, A. Kawakami, H. Kamizori, T. Sonoda, H. Nagashima, N.V. Pavlenko, and Y. Yagupolskii, *J. Power Sources,* **97-98,** 581, 2001.

154. F. Coowar, A.M. Christie, P.G. Bruce, and C.A. Vincent, C. A. *J. Power Sources,* **75**, 144, 1998.

155. M.C. Smart, B.V. Ratnakumar, and S. Surampudi, *Proc. Electrochem. Soc.* 2000. The Electrochemical Society Softbound Series PV 99-25, The Electrochem. Soc. Inc., Pennington, NJ, p. 423, 2000.

156. N. Sugeno, "Secondary Nonaqueous-Electrolyte Batteries," (Sony Corp., Japan): *Eur. Pat. Appl.;* Ep./**1994**, An. **1995**:522701.

157. H. Mao, "Polymerizable Aromatic Additives for Overcharge Protection in Secondary Nonaqueous Lithium Batteries," (Moli Energy (**1990**) Limited, Can.): *Eur. Pat. Appl.;* Ep./**1997**, An. **1997**:257375.

158. H. Mao, and D.S. Wainwright, "Polymerizable Additives for Making Secondary Nonaqueous Lithium-Ion Batteries Safe After Overcharge," (Moli Energy Limited, Can.): *Eur. Pat. Appl.;* Ep./**1998**, An. **1998**:764156.

159. H. Mao, and U. von Sacken, "Aromatic Monomer Gassing Agents for Protecting Nonaqueous Lithium Batteries Against Overcharge," (Moli Energy Limited, Can.): *Eur. Pat. Appl.;* Ep./**1997**, An. **1997**:443251.

160. H. Gan, and E.S. Takeuchi, "Sulfite Additives for Nonaqueous Electrolyte Rechargeable Batteries" (Wilson Greatbatch Limited, USA): *Eur. Pat. Appl.;* Ep./**2000**, An. **2000**:513428.

161. H. Gan, and E.S. Takeuchi, "Sulfate Additives for Nonaqueous Electrolyte Rechargeable Cells," (Wilson Greatbatch Ltd., USA): *Eur. Pat. Appl* Ep./**2001**, An. **2001**:451045 7.

162. H. Gan, and E.S. Takeuchi, "Nitrite Additives for Nonaqueous Electrolyte Rechargeable Electrochemical Cells," (Wilson Greatbatch Ltd., USA): US patent application, US **2001**, An. **2001**:241686.

163. G.C. Chung, H.J. Kim, S.H. Jun, and M.H. Kim, *Electrochem. Com.,* **1**, 493, 1999.

164. H. Gan, and E.S. Takeuchi, "Phosphonate Additives for Nonaqueous Electrolyte in Rechargeable Electrochemical Cells," (Wilson Greatbatch Ltd., USA): US patent application, US. **2001**, An. **2001**:453468; U.S. patent 6,200,701.

165. H. Gan, and E.S. Takeuchi, "Phosphate Additives for Nonaqueous Electrolyte in Rechargeable Lithium Ion Batteries," (Wilson Greatbatch Ltd., USA), *Eur. Pat. Appl.;* Ep./**2000**, An. **2000**:790241.

166. H. Gan, and E.S. Takeuchi, "Organic Carbonate Additives for Nonaqueous Electrolyte Rechargeable Cells," (Wilson Greatbatch Ltd., USA). *Eur. Pat. Appl.*: Ep./**2000**, An. **2000**:277807.

167. A.M. Stux, and J. Barker, "Carbonate Additive for Inhibiting Decomposition of Lithium Salts in Nonaqueous Battery Electrolyte and Electrolytes Containing this Additive," (Valence Technology, Inc., USA). US patent application, US, **1998**, An. **1998**:44815.

168. C. Jehoulet, P. Biensan, J.M. Bodet, M. Broussely, C. Moteau, and C. Tessier-Lescourret, C. *Proc. -Electrochem. Soc., 97-18,* 974, 1997.

169. N. Shinoda, J. Ozaki, F. Kita, and A. Kawakami, *Proc. - Electrochem. Soc.* **2000**, *99-25,* 440.

170. J. Arai, H. Katayama, and M. Kobayashi, "Nonaqueous and Polymer Electrolytes for Lithium Battery and Electrochemical Capacitor," (Hitachi, Ltd., Japan). Eur. Pat. Appl. Ep./**2001**, An. **2001**:208040.

171. Y. Wang, M. Zhang, U. von Sacken, and B.M. Way, "Boron Trifluoride as an Electrolyte Additive for Improving Cycle Life of Nonaqueous Rechargeable Lithium Batteries," (Moli Energy Limited, Can.). *Eur. Pat. Appl.*; Ep./1999, An. 1999:213180.

172. Y. Sasaki, M. Handa, S. Sekiya, K. Kurashima, and K. Usami, *J. Power Sources,* **97-98**, 561, 2001.

173. H.S. Lee, X.Q. Yang, X. Sun, J. McBreen, *J. Power Sources,* **97-98**, 566, 2001.

174. Y. Ein-Eli, S.R. Thomas, V.R. Koch, *J. Electrochem. Soc.,* **144**, 1159, 1997.

175. D. Aurbach, K. Gamolsky, B. Markovsky, Y. Gofer, M. Schmidt, and U. Heider, *Electrochimica Acta.* In press. 2002.

176. D. Aurbach, B. Markovsky, K. Gamolsky, M. Koltypin, U. Heider, and M. Schmidt, *ITE Battery Letters,* **2**, B46, 2001.

177. M. Winter, and J.O. Besenhard, *Electrochimica Acta,* **45**, 31, 1999.

178. R. A. Huggins, *Solid State Ionics, 113-115,* 57, 1998.

179. I.A. Courtney, and J.R. Dahn, *J. Electrochem. Soc.,* **144**, 2045, 1997.

180. J. Li, H. Li, Z. Wang, X. Huang, and L. Xhen, *J. Power Sources,* **81-82**, 346, 1999.

181. L.Y. Beaulieu, K.W. Eberman, R.L. Turner, L.J. Krause, and J.R. Dahn, *Electrochem. and Solid State Lett.,* **4**, A137, 2001.

182. P. Polzot, S. Laruelle, S. Grugeon, L. Dupont, and J.M. Tarascon, *Nature (London).* **407**, 496, 2000.

183. A. Debart, L. Dupont, P. Poizot, J.B. Leriche, and J.M. Tarascon, *J. Electrochem. Soc.,* **148**, A1266, 2001.

184. C. Delmas, M. Menetrier, L. Croguennec, I. Saadoune, A. Rougier, C. Pouillerie, G. Prado, M. Grune, and L. Fournes, *Electrochimica Acta, 45,* 243, 1999.

185. H. Kawai, M. Nagata, H. Kageyama, H. Tukamoto, and A.R. West, *Electrochimica Acta,* **45**, 315, 1999.

186. T. Ohzuku, A. Veda, M. Nagayama, Y. Iwakoshi, and H. Komori, *Electrochimica Acta,* **38**, 1159, 1993.

187. M. Wakihara, G. Li, and H. Ikuta, "Li-ion Batteries, Fundamental and Performance", M. Wakihara, and O. Yamamoto, Eds. Wiley-VCH, New York, Ch. 2, p. 26, 1998.

188. Y. Ein-Eli, W.F. Howard, S.H. Lu, S. Mukerjee, J. McBreen, J. Vaughey, and M.M. Tackeray, *J. Electrochem. Soc.,* **145**, 1238, 1998.

189. K. Kanamura, *J. Power Sources,* **81-82**, 123, 1999.

190. F. Joho, and P. Novak, *Electrochimica Acta,* **45**, 3589, 2000.

191. M. Moshkovich, M. Cojocaru, H.E. Gottlieb, and D. Aurbach, *J. Electroanal. Chem.,* **497**, 84, 2001.

192. Tarascon, J.-M. and Armand, M. *Nature,* **144**, 359, 2001.

193. D. Aurbach, M.D. Levi, E. Levi, H. Teller, B. Markovsky, G. Salitra, L. Heider, and U. Heider, *J. Electrochem. Soc.,* **145**, 3024, 1998.

194. D. Aurbach, K. Gamolsky, B. Markovsky, G. Salitra, and Y. Gofer, *J. Electrochem. Soc.*, **147**, 1322, 2000.

195. D. Guyonard, ("Advanced Cathode Materials for Li-ion Batteries"), in "*Energy Storage Systems for Electronics,*" T. Osaka, and M. Datta., Eds. Gordon and Breach Science Publishers, Amsterdam, Ch. 9, p 253, 2000.

196. D. Aurbach, M.D. Levi, B. Markovsky, H. Teller, G. Salitra, U. Heider, and L. Heider, *J. Electrochem. Soc.*, **146**, 1279, 1999.
197. D. Aurbach, E. Levi, M.D. Levi, G. Salitra, B. Markovsky, K. Gamolsky, R. Oesten, U. Heider, and L. Heider, *J. Solid State Ionics* **126,** 97, 1999.
198. M.D. Levi, E. Levi, D. Aurbach, M. Schmidt, R. Oesten, and U. Heider, *J. Power Sources*, **97-98**, 525, 2001.
199. D. Aurbach, M.D. Levi, K. Gamolsky, B. Markovsky, G. Salitra, and E. Levi, U. Heider, L. Heider, and R. Oesten, *J. Power Sources*, **81-82**, 443, 1999.
200. E. Mengeritsky, E. Elster, E. Granot, P. Dan, H. Yamin, E. Levi, E. Zinigrad, H. Teller, M.D. Levi, and D. Aurbach, *J. Electrochem. Soc.*, **144**, 4133, 1997.
201. R. Koksbang, J. Barker, H. Shi, and M.Y. Saidi, *Solid State Ionics*, **84**, 1, 1996.
202. D. Aurbach, B. Markovsky, A. Rodkin, M. Cojocaru, E. Levi, and H.J. Kim, *Electrochimica Acta.* In press. 2002.
203. K. Amine, C.H. Chen, J. Liu, M. Hammond, A. Jansen, D. Dees, I. Bloom, D. Vissers, and G. Henriksen, *J. Power Sources*, **97-8**, 684, 2001.
204. D. Zhang, B.S. Haran, A. Durairajan, R.E. White, Y. Podrazhanski, and B.N. Popov, *J. Power Sources*, **91**, 122, 2000.
205. X. Zhang, P.N. Ross, R. Kostecki, F. Kong, S. Sloop, J.B. Kerr, J. Striebel, E.J. Cairns, and F. McLarnon, *J. Electrochem. Soc.*, **148**, A463, 2001.
206. M. Broussely, S. Herreyre, P. Biensan, P. Kasztejna, K. Nechev, and R.J. Staniewicz, *J. Power Sources*, **97-8**, 13, 2001.
207. Y. Saito, K. Takano, K. Kanari, A. Negishi, K. Nozaki, and K. Kato, *J. Power Sources*, **97-8**, 688, 2001.
208. Z. Zhang, D. Fouchard, and J.R. Rea, *J. Power Sources*, **70**, 16, 1998.
209. H. Maleki, S.A. Hallij, J.R. Selman, R.B. Dinwiddie, H. and H. Wang, *J. Electrochem. Soc.*, **146**, 947, 1999.
210. M. Inaba, M. Fujikawa, T. Abe, and Z. Ogumi, *J. Electrochem. Soc.*, **147**, 4008, 2000.
211. M.N. Richard, and J.R. Dahn, *J. Electrochem. Soc.*, **146**, 2068, 1999.
212. M.N. Richard, and J.R. Dahn, *J. Electrochem. Soc.*, **146**, 2078, 1999.
213. D.D. MacNeil, D. Larcher and J.R. Dahn *J. Electrochem. Soc.*, **146**, 3596, 1999.
214. D.D. MacNeil. L. Christensen, J. Landucci, J.M. Paulsen, and J.R. Dahn, *J. Electrochem. Soc.*, **147**, 970, 2000.
215. D.D. MacNeil, and J.R. Dahn, *J. of Phys. Chem. A*, **105**, 4430, 2001.
216. MacNeil, D. D. and Dahn, J. R. *J. Electrochem. Soc.*, *148*, A663, 2001.
217. T.D. Hatchard, D.D. MacNeil, A. Basu, and J.R. Dahn, *J. Electrochem. Soc.*, **148**, A755, 2001.
218. M.N. Richard, and J.R. Dahn, *J. Power Sources*, **79**, 135. 1999.
219. D. Aurbach, *J. Power Sources*, *89,* 206, 2000.

2

Carbon Anodes

Zempachi Ogumi
Minoru Inaba
Department of Energy & Hydrocarbon Chemistry
Graduate School of Engineering
Kyoto University
Sakyo-ku, Kyoto 606-01
Japan

1.0   INTRODUCTION

Lithium metal is the most attractive material for use as an anode in rechargeable batteries because of its anode potential (–3.045 *vs.* standard hydrogen electrode) and its high specific capacity (3,860 mAh·g^{-1}) [1,2]. In fact, lithium metal has been widely used as an anode in primary lithium cells for more than two decades. However, prolonged deposition/dissolution cycling causes dendrite formation of the lithium metal, which brings about serious problems in safety and cycleability for rechargeable (secondary) batteries. In spite of extensive efforts of many researchers, it will be some time before rechargeable lithium metal batteries are placed on the market. Recent developments in rechargeable lithium-ion batteries (LIBs) were achieved by the use of carbonaceous materials as lithium reservoirs at the anodes [3,4]. The charge and discharge reactions are described simply as:

$$C + xLi^+ + xe^- \underset{\text{Discharge}}{\overset{\text{Charge}}{\rightleftarrows}} Li_xC \tag{1}$$

Lithium ion can be intercalated, more or less, into most kinds of carbon, and the resulting lithiated carbons show extremely negative electrochemical potentials close to that of the metallic lithium electrode. The reversible intercalation/deintercalation reactions overcome the problem of dendrite formation of lithium and provide dramatic improvements in safety and cycleability. The carbon anodes are combined with non-aqueous electrolyte solutions and lithium-transition metal oxides such as $LiCoO_2$ as cathodes to fabricate 4 V-class LIBs. Only lithium ion moves back and forth between the cathode and the anode upon charging and discharging, which give rise to a potential difference of about 4 V between the two electrodes. The name, "lithium-ion" batteries came from this simple mechanism.

Electrochemical lithium intercalation properties of carbonaceous materials greatly depend on the crystallinity, morphology, and orientation of crystallites, *etc*. Many kinds of carbonaceous materials, from crystalline to strongly disordered carbon, have been tested as anodes in LIBs over the past decade. As a result, graphite is now most widely used as an anode in commercially available LIBs because of its relatively high specific capacity (theoretically **372 mAh·g⁻¹**), small irreversible capacity, and good cycleability. However, the rapid development of electronic devices today demands a much higher energy density for carbon anodes as well as a higher power density and a smaller irreversible capacity. To answer these demands, fundamental understanding of the lithium intercalation/deintercalation reactions of carbons is essential. In this chapter, the authors focus on three fundamental aspects of carbon anodes, intercalation/deintercalation mechanisms, kinetics, and surface film formation, and summarize the results of recent studies on carbon anodes.

2.0   STRUCTURE OF CARBONACEOUS MATERIALS

Although carbon has several allotropes, graphite and its disordered forms are used as practical anode materials for LIBs. Graphite is a typical layered compound that consists of hexagonal graphene sheets of sp^2-carbon atoms (called graphene sheets), weakly bonded together by van der Waals forces into an ABAB.... stacking sequence along the *c*-axis as shown in Figure 1 [5]. The lattice belongs to a space group of *P6₃/mmc*, and the *a*- and *c*-axis lengths of the hexagonal unit cell are $a_0 = 0.246$ nm and $c_0 = 0.6708$ nm, respectively, at room temperature. Graphite crystal thus has two kinds of characteristic surfaces, normal and parallel to its *c*-axis, which are called the basal and the edge plane, respectively. This anisotropic structure is an important feature that determines the properties of lithium intercalation within graphite as described later.

Although graphite exists in nature, it can be synthesized artificially by treating a pyrolyzed carbon at high temperatures around 3000°C. In addition to graphite, many kinds of carbonaceous materials such as carbon black, activated carbon, carbon fiber, cokes are manufactured. These artificial carbons are more or less disordered, and have some imperfection within them, such as stacking disorder of neighboring graphene sheets, called "turbostratic disorder", and unorganized or buckled layers. Carbonaceous materials heat-treated at lower temperatures have low crystallinity and are further classified into two categories: "soft carbons" (graphitizable carbons) and "hard carbons" (non-graphitizable carbons) [6]. Structural models proposed for soft and hard carbons are shown in Figure 2 [6]. In soft carbons, small crystallites are stacked nearly in the same direction, and thereby subtle diffusion induced upon heating results in graphitization. In contrast, the crystallites of hard carbons do not have such distinct orientation and hence are difficult to develop even when heat-treated at high temperatures > 2000°C.
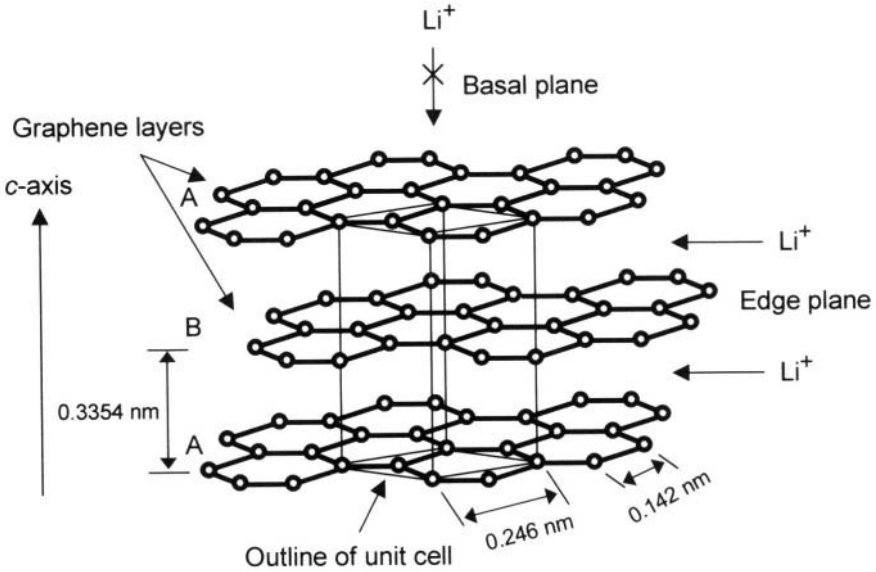
Figure 1. Crystal structure of hexagonal graphite showing the ABAB...stacking of graphene sheets and the unit cell.
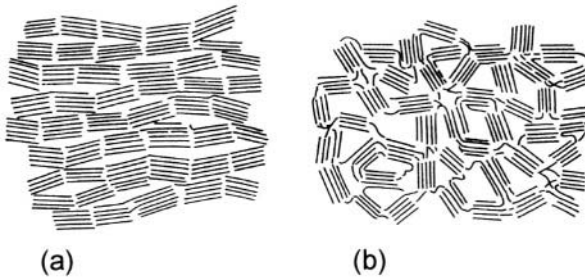
Figure 2. Models for the structures of (a) soft and (b) hard carbons [discussed in reference 6].

3.0   INTERCALATION/DEINTERCALATION MECHANISMS OF VARIOUS CARBONS

Many kinds of carbonaceous materials have been tested as anodes in LIBs so far. The electrochemical characteristics of carbonaceous materials strongly depend on the morphology, crystallinity, orientation of crystallites, *etc*. To systematically understand the electrochemical properties of carbonaceous materials, it is convenient to classify them, first, into the two categories, soft and hard carbons, and then to consider the effects of heat-treatment temperature (HTT). Figure 3 shows the relationships between the specific capacity and HIT

of soft and hard carbons, which was summarized by Dahn *et al.* [7]. As shown in Figure 3, soft and hard carbons show different variations with HTT. Highly graphitized carbons, which are prepared from soft carbons at temperatures > 2400°C, have specific capacities in the range **300-370 mAh·(g-carbon)$^{-1}$** (Region A in Figure 3) [8-10,15,16]. With decreasing HTT from 2400°C, the specific capacity decreases, gives the minimum at HTT = 1800–2000°C, and then increases again (Region B in Figure 3) [16-18,20]. It has been reported that soft carbons heat-treated at temperatures below 1000°C have extremely high specific capacities in the range **500-1000 mAh·g^{-1}** (Region C in Figure 3) [16,22-28]. Hard carbons generally have specific capacities lower than those of soft carbons; however, they have recently attracted much attention of many researchers because some hard carbons heat-treated at around 1000°C exhibit high specific capacities in the range **500-700 mAh·g^{-1}** (Region D in Figure 3) [28-30]. The electrochemical characteristics and intercalation/deintercalation mechanisms of these four types of carbons are described below.
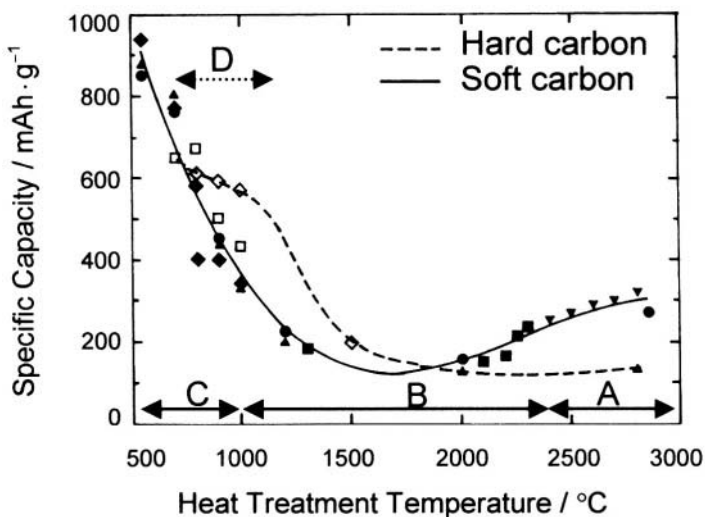
Figure 3. Relationships between reversible specific capacity and HTT [Derived from reference 7]. Closed and open circles shows data obtained for soft and hard carbons, respectively. Regions A-D correspond to those used in the text.

Natural graphite and synthetic graphite heat-treated above 2400°C belong to Region A. Figure 4 shows charge and discharge characteristics of natural graphite (NG-7, The Kansai Coke and Chemicals Co., Ltd.). During the first charging (intercalation), the potential drops rapidly after subtle retardation at ca. 0.8 V. The main intercalation and deintercalation of lithium take place at potentials < 0.25 V vs. **Li$^+$/Li,** accompanied by three potential plateaus. The charge consumed upon the first charging (ca. **400 mAh·g^{-1}**) is not fully recovered upon the following discharging (ca. **335 mAh·g^{-1}**). The capacity that cannot be recovered is called the "irreversible

capacity" (Q_{irr}), which is more or less observed in the first charge/discharge cycle of any carbonaceous materials. At the second and subsequent cycles, graphite shows good reversibility (rechargeablility) with a Coulombic efficiency of ~100%. The reversible specific capacity (Q_{rev}) typically ranges from 300 to **370 mAh·g⁻¹**.

Plot: Potential / V vs. Li⁺/Li on the y-axis (0 to 2), Specific capacity / mAh g⁻¹ on the x-axis (0 to 400). $Q_{re} = 335\,mAh\cdot g^{-1}$ and $Q_{irr} = 65\,mAh\cdot g^{-1}$.
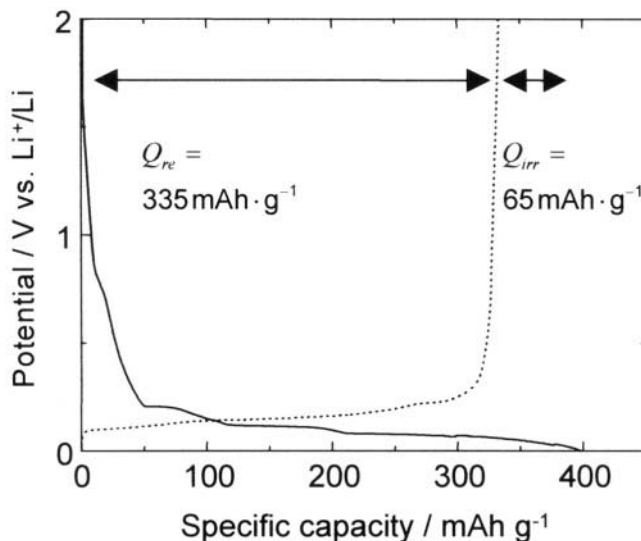
Figure 4. Charge and discharge characteristics of natural graphite powder (NG-7, Region A) at the first cycle in 1 M LiClO₄/EC + DEC (1:1 by volume).

Lithium ion is intercalated within graphite to form lithium-graphite intercalation compounds (Li-GICs) [8-10]. GICs are layered compounds that atomic or molecular layers of a different chemical species called the intercalate are inserted between the graphene sheets of host graphite [11]. The most important and characteristic property of GICs is the staging phenomenon, which is characterized by intercalate layers that are periodically arranged in a matrix of graphene sheets. Schematic illustrations for the stage structures of GICs are shown in Figure 5a. These stage structures are designated in terms of stage index *n,* which denotes the number of graphene sheets between adjacent intercalate layers as shown in Figure 5a. Another important feature of GICs is the in-plane ordering of the intercalate with respect to the adjacent graphene sheets called the "superlattice structure". The superlattice structure of stage-1 Li-GIC is shown in Figure 5b, in which lithium ion exhibits a √3 x √3 structure [12]. The structure of stage-1 Li-GIC thus gives a composition of **LiC₆**.

It has been known for a long time that lithium ion can be intercalated within graphite to form Li-GIC since the discovery by Herold [13] in 1955. (The first success in electrochemical lithium intercalation was reported in a patent of Sanyo in 1981 [14].) The phase diagram of Li-GIC, which was obtained by an

electrochemical process, is shown in Figure 6 [8]. Four different stage struc-
tures (n = 1–4) are known for Li-GICs, depending on the concentration of
lithium. The mechanism of lithium intercalation within graphite has been
studied so far using X-ray diffraction (XRD) [8-10] and Raman spectroscopy [15-
17]. The stage structure changes successively from a higher to a lower stage
during electrochemical lithium intercalation, and in the opposite direction
during lithium deintercalation [Equations. 2-4].

Dilute stage-1	↔ Stage-4	(ca. 210 mV)	**(2)**
Stage-2L	↔ Stage-2	(ca. 120 mV)	**(3)**
Stage-2	↔ Stage-1	(ca. 90 mV)	**(4)**
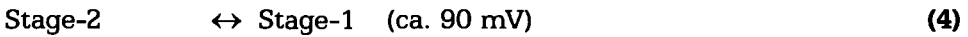
where dilute stage-1 (1') denotes a phase where lithium ion is intercalated
randomly within graphite and stage-2L denotes a liquid-like stage-2 phase
that has no in-plane ordering. As shown earlier, graphite allows lithium
intercalation up to a composition of LiC_6. This restricts the specific capacity
of graphite to **372 mAh·g^{-1}**. Because of the low and flat discharge profile
and high reversibility of the reaction, natural and synthetic graphites have
been widely used as anode materials in commercially available LIBs.
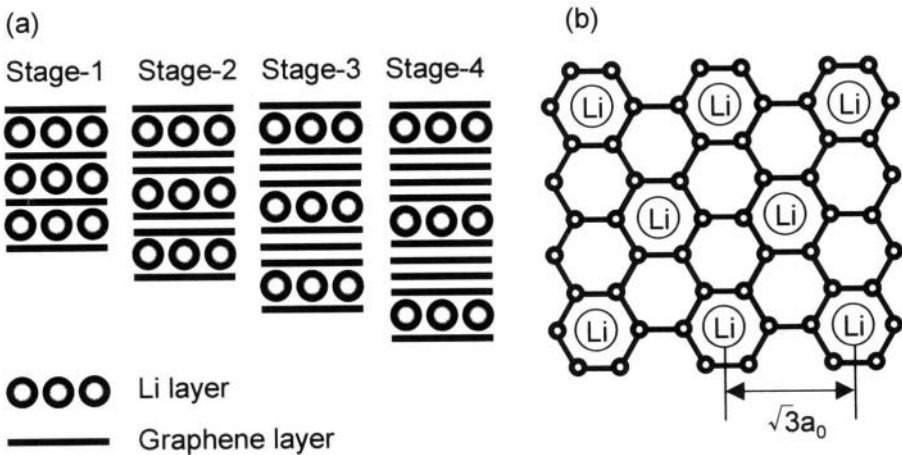
Figure 5. (a) Stage structures of GICs and (b) in-plane structure of stage-1 Li-GIC.

In Region B in Figure 3, the reversible capacity decreases with a decrease in
HTT from 2400°C, and reaches the minimum at about 2000°C, and then
increases again [18]. Figure 7 shows charge and discharge curves of
mesocarbon microbeads heat-treated at 1800°C (MCMB1800, Osaka Gas). HTT
affects not only the reversible capacity, but also the shape of charge and
discharge curves. Soft carbons heat-treated at temperatures below 2000°C

exhibit monotonous charge and discharge profiles without any potential plateaus as shown in Figure 7. These monotonous profiles indicate that lithium ion is intercalated randomly between graphene sheets without the formation of any stage structures [16].
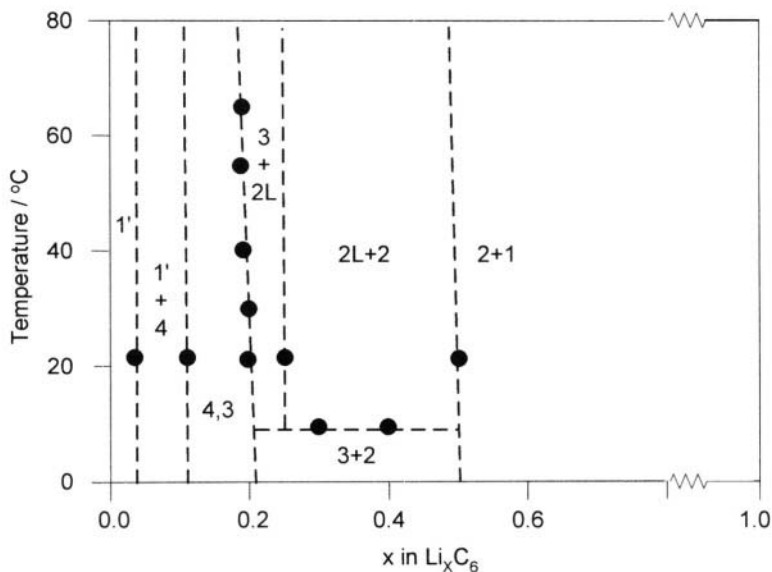
Figure 6. Phase diagram of Li_xC_6 obtained by an electrochemical method [Derived from reference 8]. The phase designations are described in the text.
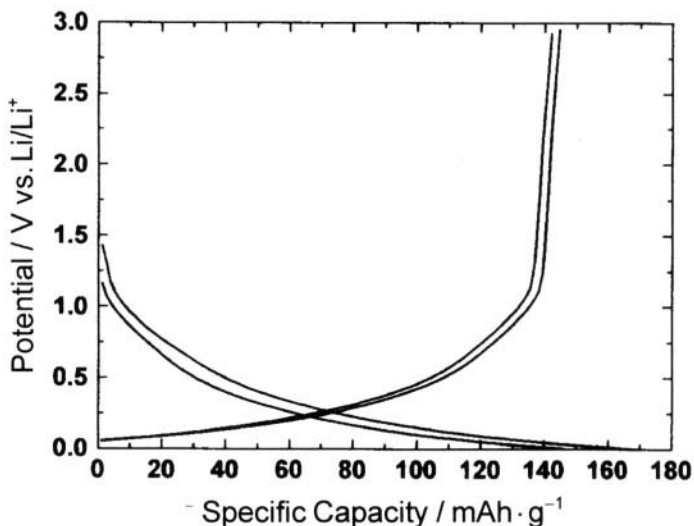
Figure 7. Charge and discharge characteristics of mesocarbon microbeads heat-treated at 1800°C (MCMB1800, Region B) at the first and second cycles in 1 M $LiClO_4$/EC + DEC (1:1 by volume).

The soft carbons in this region contain many imperfections such as turbostratic disorder and unorganized part in their crystallites. Dahn *et al.* [18] reported that the maximum reversible capacity (x_{max}) in this region can be well described by the following expression:

$$x_{max} = g\{(1\text{-}P)1 + Px_r\} + (1\text{-}g)x_u \qquad (5)$$

where g, P, x_r, and x_u denote the fraction of low strain part, the probability of finding turbostratic disorder, the reversible capacity of unstrained graphene sheets with turbostratic disorder (random shifts or rotations), and that of highly strained unorganized carbon, respectively. For soft carbons, reversible capacities calculated from Equation 5 are in good agreement with experimental ones when $x_r = 0.3$ and $x_u = 0.9$ are assumed as shown in Figure 8 [18]. When lithium ion is intercalated between adjacent parallel graphene sheets, these sheets shift from ABAB.... into AAAA....stacking [19]. Therefore, graphene sheets with turbostratic disorder will most likely be pinned and hence be unable to shift into the AAAA....stacking arrangement, resulting in a lower capacity ($x_r = 0.3$). On the other hand, the presence of unorganized carbon leads to lower density and gives more space for lithium ion to accommodate. This results in a relatively high capacity of the unorganized carbon ($x_u = 0.9$). The unorganized part disappears upon heat-treatment up to 2000°C, but turbostratic disorder is gradually removed by heat treatment at temperatures above 2000°C; hence, the reversible capacity shows the minimum at ~ 2000°C. Tatsumi *et al.* [20] obtained a similar relationship between the reversible capacity and the probability of finding ordered stacking sequence, called the P_1 parameter [20].
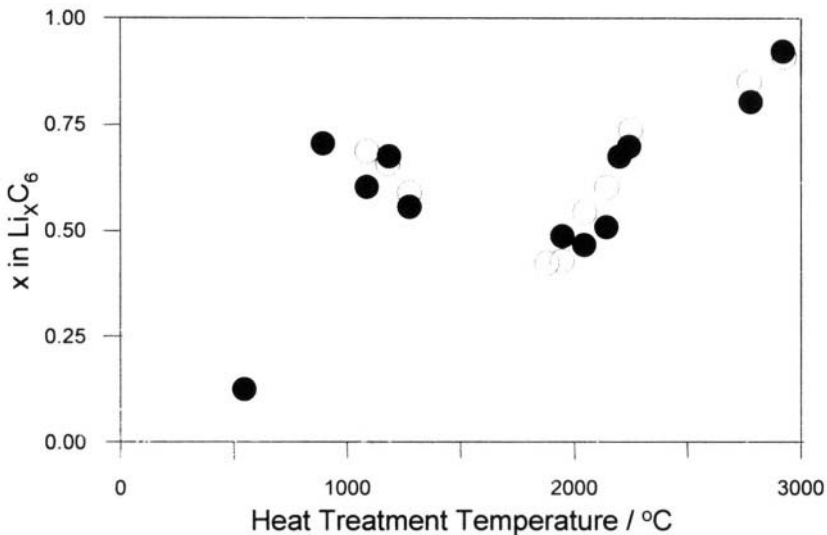
Figure 8. Variations of the reversible capacity of soft carbons with heat-treatment temperature. Derived from reference 18 and reproduced with permission from Elsevier Science. Solid circles: experimental values; open circles: values calculated using Eq. (2) with $x_r = 0.3$ and $x_u = 0.9$.

It has been recently reported that two categories of disordered carbons have much higher capacities than the theoretical capacity of graphite [16,22-28]. One type of these high-capacity carbons are soft carbons heat-treated at temperatures below 1000°C (Region C in Fig. 3), which show specific capacities in the range **500-1000 mAh·g^{-1}** [16,22]. Typical charge/discharge profiles of the Region C carbons are shown in Figure 9(a) [16]. Some hard carbons heat-treated below 1000°C showed similar behavior as well [23]. This kind of soft (and hard) carbon is characterized by a large hysteresis in their potential profiles. The presence of the hysteresis leads to a loss of stored electrical energy, which is dissipated as heat during charge/discharge cycles [22]. Another drawback is poor cycleability, and the capacity decreases to a half of the initial capacity in several cycles. Because their reversible capacities are much higher than the theoretical capacity of graphite, their insertion mechanism is not explained by the simple intercalation/deintercalation mechanism described earlier for natural and synthetic graphites. Various models explaining their high capacities have been suggested so far. These include lithium intercalation between graphene sheets with an in-plane LiC_2 structure [24], lithium doping within nanoscopic cavities [25], formation of ionic complexes like lithium naphthalene [26], a chemical reaction between inserted lithium atoms and the hydrogen-terminated edges of hexagonal carbon fragments [27], etc. However, the mechanism for their high capacities is still controversial. The mechanism should explain the hysteresis in the potential profiles as well as the high reversible capacity. The presence of hysteresis indicates that the reaction is not a simple lithium insertion shown by Equation 1, but a complicated process that involves a kind of following chemical reactions associated with large activation energies, as pointed out by Zheng *et al.* [28] and by the authors [22]. The energy diagram proposed by Zheng *et al.*[28] is shown in Figure 10. Although the region C carbons show high reversible capacities, they have serious drawbacks, such as their low density **(~1.5 g·cm^{-3})**, large irreversible capacity at the first cycle, and poor cycleability, to be solved for practical use.

The other type of the high-capacity carbons are hard carbons heat-treated at ~1000°C (Region D in Figure 3), which exhibit specific capacities in the range **500-700 mAh·g^{-1}** [29-31]. Hard carbons prepared from petroleum pitch, poly(furfuryl alcohol), and phenolic resins belong to this class. This type of hard carbons are characterized by the presence of a low and large potential plateau at about 0.05 V in their charge/discharge profiles as shown in Figure 9(b) [29]. It seems that the high capacity is brought about by Li-cluster formation in nanopores formed by small graphene sheets (~2.5 nm) in the hard carbons [30], which is called the "house of card" model [31]. The region D carbons are very promising candidates as anodes in high-capacity LIBs in the near future. Their drawbacks are high hygroscopicity, low density **(1.5-1.8 g·cm^{-3})**, degradation of the capacity at high current densities, and the risk of lithium metal deposition during charging.
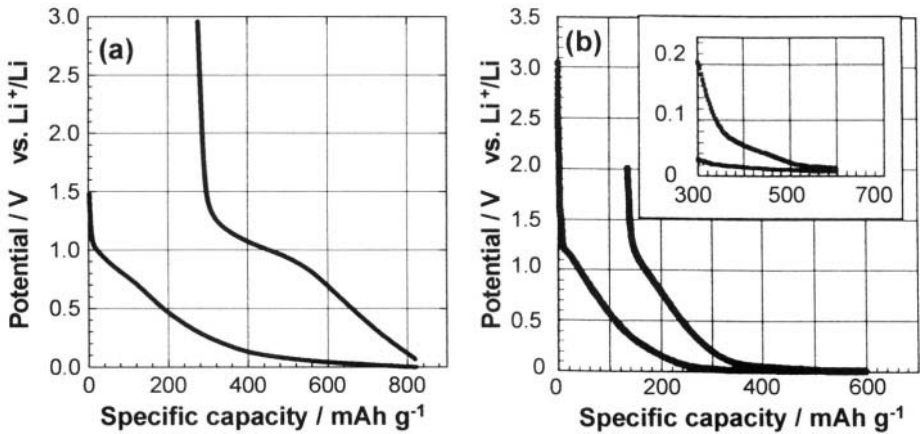
Figure 9. Charge and discharge characteristics of (a) MCMB700 (Region C) in 1 M LiClO₄/EC + DEC (1:1 by volume). From reference 16 reproduced by permission of The Electrochemical Society, Inc. and (b) petroleum-pitch-based pseudo-isotropic carbon (PIC, Region D) in 1 M LiClO₄/EC+dimethoxyethane (DME) (1:1 by volume) [data from 29].
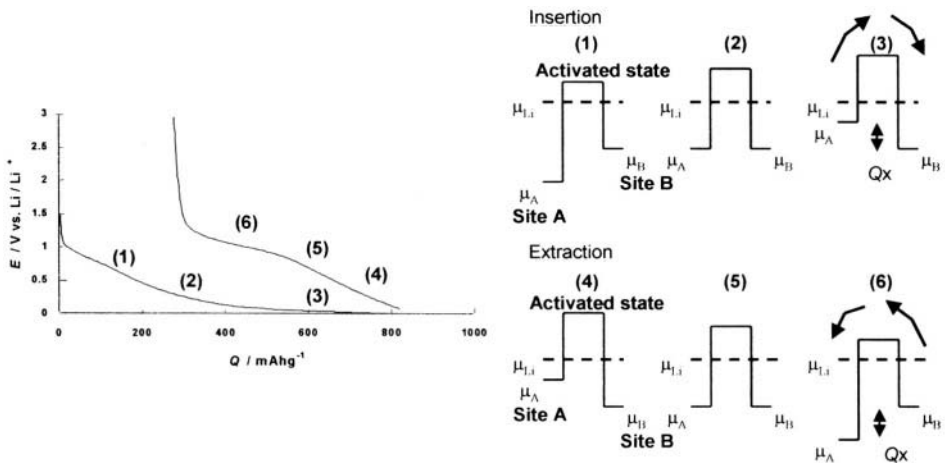
Figure10. An energy state model to explain voltage profiles of the Region C soft carbons. Sites A and B denote the intercalation and bonding sites, respectively. From reference 28 reproduced by permission of The Electrochemical Society, Inc.

4.0   SURFACE FILM FORMATION ON CARBON ANODES

This topic is treated extensively in the chapter by Aurbach. It is discussed here from the standpoint of the different carbons, their structure and reactivity. High stability against reduction is one of the required conditions for solvents in LIBs, because lithium intercalation and deintercalation take place at extremely negative potentials close to Li⁺/Li. Aqueous solutions cannot be used for this

reason; instead, nonaqueous solutions containing lithium salts, such as $LiClO_4$, $LiPF_6$, and $LiBF_4$, as electrolytes are used in LIBs. As nonaqueous solvents, mixtures of ethylene carbonate (EC) with less viscous linear alkyl carbonates such as dimethyl carbonate (DMC), diethyl carbonate (DEC), and ethyl methyl carbonate (EMC) are used in commercially available LIBs. However, even non-aqueous solvents should not be thermodynamically stable at such negative potentials. It has been widely believed that a protecting surface film, which is conductive for lithium ion but electronically insulating, is formed on graphite anode *via* reductive decomposition of electrolyte solution in the initial stage of charging [32,33]. The passivating film, often called the solid electrolyte inter-face (SEI) [32], suppresses further solvent decomposition and plays a beneficial role in improving the safety and cycleability of LIBs. The SEI formation on carbon anodes thus a prerequisite for their stable charging and discharging; however, it is the primary cause for bringing about the irreversible capacity through consumption of a considerable amount of charge. Many researchers have made efforts in search for good solvent systems that give superior SEI with a minimal consumption of charge. For this purpose, understanding of the SEI composition, stability, and its influence on the battery performance is very important, and has been a focus of many researches over the past decade. For example, the composition of SEI formed on carbon anodes has been extensively studied with a variety of analytical tools [34-64]. Aubach *et al.* [34-43] have investigated surface reactions occurring at graphite anodes in various nonaqueous solutions by *in situ* Fourier-transform infrared spectroscopy (FT-IR) and impedance spectroscopy, and suggested that the major constituent of the SEI formed in ethylene carbonate (EC)-based solutions is a lithium alkyl carbonate $(CH_2OCO_2Li)_2$, which is a reduction product of EC. The reaction scheme proposed by them is shown in Figure 11 [43]. Yoshida *et al.* [44] detected carbon monoxide and ethylene from LIBs after being cycled by gas chromatography (GC), and suggested the presence of a lithium alkoxide $(CH_2OLi)_2$ and Li_2CO_3 in the SEI. X-ray photoelectron microscopy (XPS) [45] and transmission electron microscopy (TEM) analysis [46,47] revealed that the film contains inorganic compounds such as LiOH and Li_2CO_3. The authors detected oligomers that have repeated oxyethylene units from the SEI formed on graphite anodes by pyrolysis-gas chromatography-mass spectroscopy (Py-GC-MS), and suggested that the SEI consists of polymerized compounds similar to poly(ethylene oxide) (PEO) [48]. The presence of polymers in the SEI on carbon anodes has been also proposed by other researchers [49,50]. Peled *et al.* [51-54] have analyzed reaction products formed on the basal and the edge planes of highly oriented pyrolytic graphite (HOPG) that was cycled in EC-based solutions by XPS, time-of-flight secondary ion mass spectrometry (TOF-SIMS), etc. They have reported that the surface film on the edge plane is rich in inorganic compounds, whereas that formed on the basal plane is rich in organic compounds (mainly polymers).
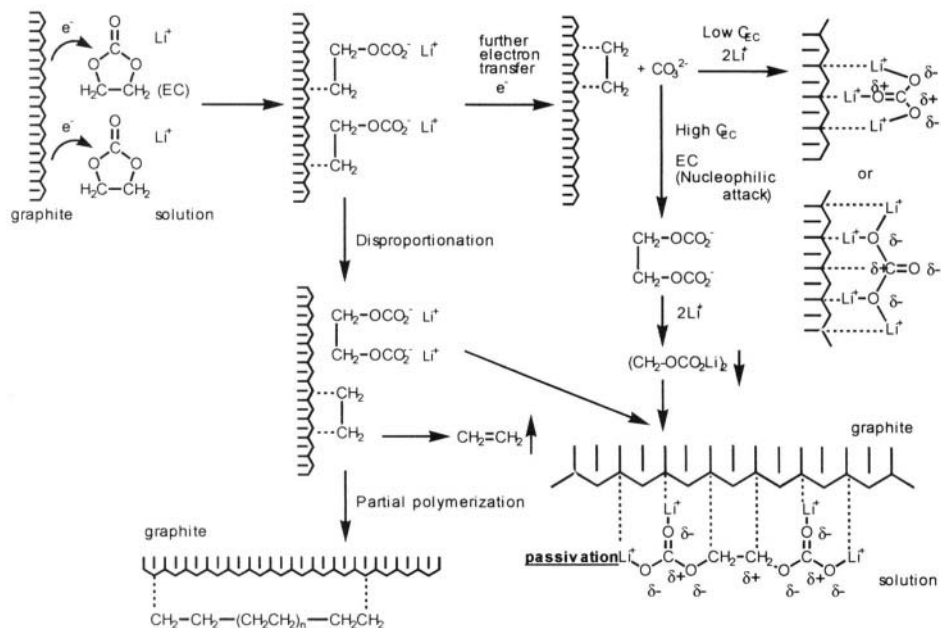
Figure 11. Reduction mechanisms of EC on graphite proposed by Aurbach et al. Reproduced from reference 43 with permission from Elsevier Science.

As mentioned above, the chemical composition of SEI has been extensively studied, but it seems that the role of solvent co-intercalation have been underestimated. Besenhard et al. [55,56] studied the crystal expansion of HOPG during electrochemical reduction in an EC-based solution by dilatometry, and observed a drastic expansion of the graphite matrix (> 150%) at potentials more negative than 1.0 V vs. Li^+/Li. They attributed this expansion to solvent co-intercalation, and concluded that the intercalated solvent further decomposes to form an immobile product remaining between the graphene sheets and that this reduction product prevents further solvent intercalation and the exfoliation of the graphene sheets as shown schematically in Figure 12 [55]. The authors have employed electrochemical scanning tunneling microscopy (STM) [56-61] and atomic force microscopy (AFM) [62-64] to clarify the mechanism of the surface film formation on HOPG. Panel (a) in Figure 13 shows a cyclic voltammogram of the HOPG basal plane in 1 M $LiClO_4$/EC + DEC [62]. Cathodic peaks at 1.0, 0.8, and 0.5 V, and a large cathodic current at potentials more negative than 0.3 V are related to solvent decomposition and SEI formation. The surface morphology changes are shown in images (b)-(f) in Figure 13. The results in Figure 13 revealed that two different processes are involved in the SEI formation on graphite anodes. One is the intercalation of solvated lithium ion at potentials just below 1 V, followed by its decomposition between graphene sheets. The complicated pattern observed in Figure 13(d), which consists of atomically flat surfaces

raised by 1-2 nm overlapping with one another, is evidence for the intercalation of solvated lithium ion [56-58,62]. The other process is direct reductive decomposition of solvent on the surface of the graphite electrodes at lower potentials. The particle-like precipitates observed at potentials more negative than 0.65 V in Figsures 13 (e) and (f) are direct decomposition products of the solvents on the surface [62]. Figure 14 shows an expanded (10 x 10 μm) image and a height profile after the 5 x 5 μm area in Figure 13 was completely scraped off by repeated AFM scanning [62]. The thickness of the precipitate layer is about 40 nm after one cycle of cyclic voltammetry in Figure 13(a). The SEI layer hence has two important roles: (i) suppressing cointercalation of solvent molecules from the edge plane and (ii) suppressing direct solvent decomposition on the whole surface (both the basal and edge planes).
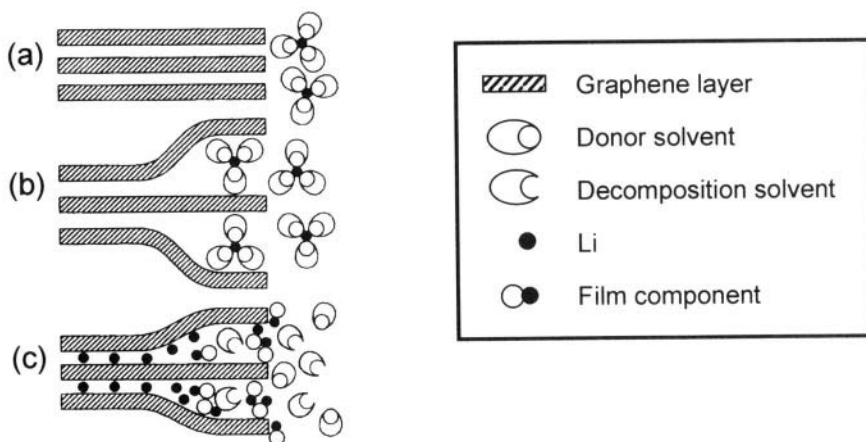
Figure 12. Solvent cointercalation model for surface film formation on/in graphite proposed by Besenhard et al. (a) before reaction, (b) formation of ternary GIC, $Li_x(solv)_yC_n$, and (c) film formation by decomposition of $Li_x(solv)_y$. Reproduced from reference 55 with permission from Elsevier Science.

The SEI formation processes and the properties of the resulting SEI greatly depend on the kind of solvent. The most important and interesting fact is that propylene carbonate (PC), which has been used as a solvent in primary lithium cells, has a poor compatibility with graphite anodes [65-68]. When graphite is polarized in PC-based electrolyte solution, ceaseless solvent decomposition and intensive exfoliation of graphene sheets take place, and does not give an effective surface film. It seems that co-intercalation of PC is much more vigorous than that of EC. This is the reason why EC-based solutions are exclusively used in commercially available LIBs. Nevertheless, PC-based solutions are attractive as electrolyte solutions for LIBs because of

their superior ionic conductivity at low temperatures [69]. It has been reported that the addition of certain kinds of organic molecules (typically 5% by volume) to PC-based solutions greatly suppresses solvent decomposition and graphite exfoliation, and enables lithium ion to be intercalated within graphite. These include chloroethylene carbonate (Cl-EC) [70-72], vinylene carbonate (VC) [73], ethylene sulfite (ES) [74], propylene sulfite (PS) [74], fluoroethylene sulfite (FEC) [76], α-bromo-γ-butyrolactone [77], methyl chloroformate [77], *t*-butylene carbonate *(t*-BC) [78,79], and 12-crown-4 (12-C-4) [80-81]. In addition to these additives, some co-solvents, such as dimethyl-sulfoxide (DMSO), diethoxymethane (DEM), dimethoxymethane (DMM), and diethoxyethane (DEE) are also effective for stable surface film formation in PC-based solutions [82]. The authors studied the effects of VC, ES, and FEC additives in PC by *in situ* AFM, and found that these additives decompose to form an effective SEI layer at potentials more positive than 1 V before PC-solvated lithium ion begins to be intercalated within graphite [63].
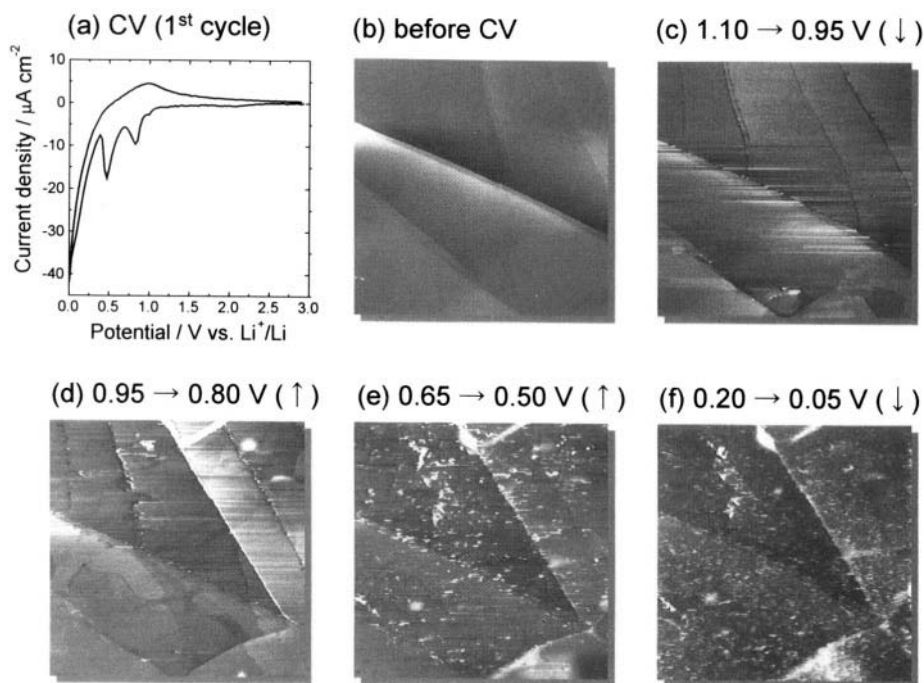
Figure 13. Cyclic voltammograms (a) and AFM images (5 x 5 μm) of the HOPG basal plane surface obtained at (b) 2.9 V before CV, (c) 1.10-0.95 V, (d) 0.95-0.80 V, (e) 0.65-0.50 V, and (f) 0.20-0.05 V during the first cycle at 0.5 mV s^{-1} in 1 M LiClO$_4$/EC+DEC (1:1). Reproduced from reference 62 with permission of The Electrochemical Society, Inc.
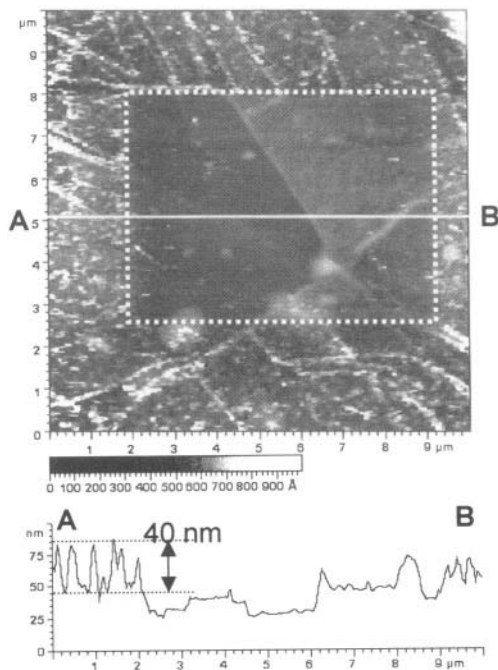
Figure 14. AFM image of an expanded area (10 x 10 μm) and a height profile of the HOPG basal plane surface obtained at 2.9 V after the first cycle of CV in Figure 13. The dotted square shows the area observed during the first cycle. Reproduced from reference 62 with permission of The Electrochemical Society, Inc.

5.0 INTERCALATION/DEINTERCALATION KINETICS OF CARBON ANODES

Electrochemical lithium intercalation within a carbon anode involves a variety of processes such as diffusion in the electrolyte solution, migration through the surface film, charge transfer at the carbon/electrolyte interface, and diffusion within the carbon electrode. The positive charge of lithium ions within the carbon is compensated by the negative charge of electrons injected in the carbon host [83]. Because the mobility of electrons is much higher than that of lithium ions, migration by an electric field within the carbon is negligible. Thus, the mass transport of lithium ions within the carbon can be regarded as a diffusive process. Because diffusion in a solid is generally a slow process, the diffusion rate would dominate the overall reaction rate. The diffusion coefficient of lithium ion within carbonaceous materials (D_{Li}^+) is thus a critical parameter that determines the power density (*i.e.* rate-capability) of a lithium-ion cell. The values of D_{Li}^+ have been determined by several methods including galvanostatic intermittent titration technique (GITT) [84], current pulse relaxation (CPR) [85,86], potential step chronoamperometry (PSCA) [85-89], AC impedance spectroscopy [89-94], and electrochemical

permeation [95]. Typical data determined by these techniques are summarized in Table 1. The values of D_{Li}^+ are rather scattered over a wide range of 10^{-6}-10^{-13} cm$^2 \cdot$s^{-1} depending on the kind of carbon and on the technique employed. To obtain $D_{Li}+$ by using these methods, one has to know the accurate surface area of the sample, *A,* and in some techniques, the variation of the open-circuit potential with lithium composition. *dE$_{oc}$/dx.* However, precise determination of *A* and *dE$_{oc}$/dx* is difficult in general, which is one of the reasons for the scattering of the data.

Table 1. Diffusion coefficients of lithium ion (D_{Li}^+) in various carbonaceous materials

Sample	Morphology	D_{Li}^+ Method (cm$^2 \cdot$s^{-1})	Reference
Petroleum coke powder	$2 \times 10^{-7} - 1 \times 10^{-8}$	GITT[a]	84
Pitch-based coke powder	$3 \times 10^{-8} - 1 \times 10^{-9}$	CPR[b], PSCA[c]	85
Synthetic graphite powder	$1 \times 10^{-7} - 1 \times 10^{-11}$	Impedance, PSCA	87-89, 92
Natural graphite powder	$2 \times 10^{-8} - 1 \times 10^{-9}$	Impedance	92
Natural graphite powder	$10^{-5} - 10^{-8}$	Impedance	93,94
Carbon fiber	$2 \times 10^{-7} - 4 \times 10^{-13}$	CPR[b], PSCA[c]	86,91,92
Glassy carbon plate	$\sim 10^{-8}$	ECP[d]	95

[a] Galvanostatic intermittent titration technique. [b] Current pulse relaxation. [c] Potential step chronoamperometry. [d] Electrochemical permeation.

The anisotropic structure of carbonaceous materials is another factor to determine the diffusional behavior of lithium ion. Imanishi *et al.* [96] reported that the microtexture (onion-like, radial, or random) of carbon fibers greatly affects the charge and discharge characteristics such as reversible capacity, although it is not the sole factor. The effect of anisotropy of carbon is made clearer by comparison of the two cyclic voltammograms of HOPG in Figure 15 [93]. Curve (a) in Figure 15 shows a voltammogram when only the basal plane of HOPG was in contact with the electrolyte solution, whereas curve (b) was obtained when the whole piece of HOPG was soaked in the solution. In the latter case [curve (b)], the intercalation and deintercalation current was two orders of magnitude larger than that in the former case [curve (a)]. This fact indicates that lithium ion is intercalated predominantly at the edge plane, and then diffuses to the interior in the direction parallel to the basal plane [93].

It should be noted that the intercalation is accompanied by a series of stage formations in the case of natural and synthetic graphites (Region A in Figure 3). Figure 16 shows the variation of D_{Li}^+ within a natural graphite with electrode potential, which was obtained by the authors using AC impedance spectroscopy [94]. D_{Li}^+ tends to decrease with a drop in electrode potential, that is, with an increase in lithium content, as is generally observed for other carbonaceous materials. Two characteristic features are seen in Figure 16. One is that D_{Li}^+ in staged GICs is one or two orders of magnitude smaller than that in the dilute stage-1 phase, which does not have a distinct stage structure. This fact clearly shows that the ordering of the host and intercalate layers affects the diffusivity of the mobile ion in GICs. The other feature is that D_{Li}^+ abruptly drops at 0.21, 0.12,

and 0.09 V vs. Li$^+$/Li. As mentioned earlier, the stage transformations (Equations, 2, 3, and 4, respectively) occur at these potentials; that is, two different phases coexist at these potentials. Under such conditions, lithium-ion movement is not well described by a single value of D_{Li}^+ because it is a parameter defined in a uniform medium. In two-phase co-existence regions, stage transformation is accompanied by the movement of phase boundaries [97-99]. An example for the phase-boundary movement observed with an optical microscope is shown in Figure 17 [100]. Because more than 80% of the reversible capacity is given by the two-phase coexistence regions for graphite, not only the diffusion constant in a single phase, but also the rate of phase-boundary movement is an important factor to determine the maximum current densities for charge and discharge.
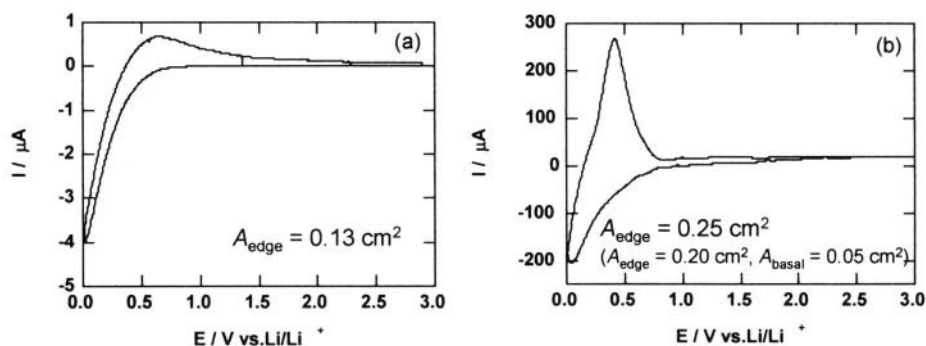
Figure 15. Cyclic voltammograms at the second cycle of (a) basal plane (0.13 cm^2) of a HOPG block and (b) the whole surface of a HOPG piece (0.25 cm^2) in 1 M LiClO$_4$/EC+DEC (1:1). Sweep rate = 0.1 mV·s^{-1}. Reproduced from reference 93 with permission from Elsevier Science.
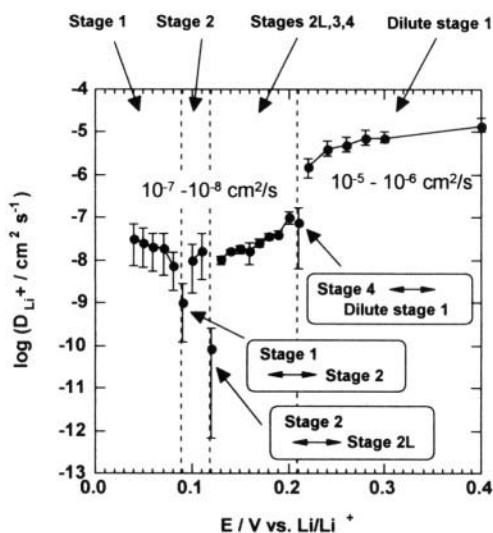
Figure 16. Chemical diffusion coefficients of lithium within graphite plotted against electrode potential. Reproduced from reference 94 by permission of The Electrochemical Society, Inc.
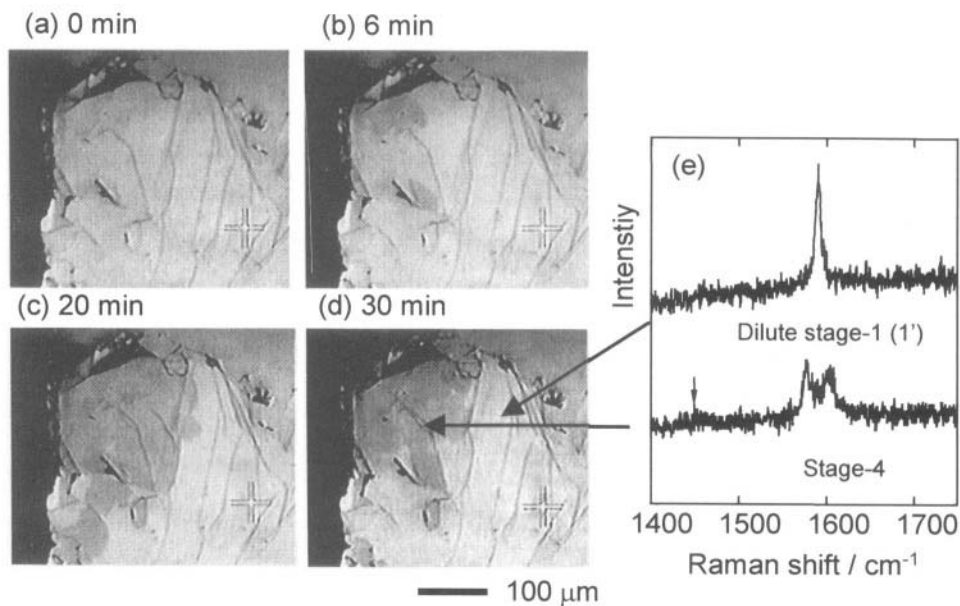
Figure 17. Optical microscope images of the basal plane of HOPG obtained at (a) 0, (b) 6, (c) 20, and (d) 30 min after the potential was stepped from 0.22 to 0.20 V. Raman spectra (e) of a bright part and a dark part in the images. Reproduced from reference 100 with permission from Elsevier Science.

Although the data are rather scattered, the diffusivity of lithium ion within carbonaceous materials reported in the literature seems to be higher ($\sim 10^8$ $cm^2 \cdot s^{-1}$) [94] than that within the cathode material, $LiCoO_2$, (10^{-10}–10^{-11} $cm^2 \cdot s^{-1}$) [101]. Hence, the interfacial charge-transfer reaction can be the rate-determining step as well under some experimental conditions that the diffusional flux of lithium ion is high in the host carbon. This problem was first pointed out by the authors in their potential step studies [102]. Takamura et al. [103] have also reported that the interfacial reaction of carbon fibers is slow and can be improved by coating the fibers with thin layers of metals such as Pd, Ag, Zn, etc. High power density is required for large-scale LIBs, and improvement of the kinetics of the interfacial reaction may be a key factor for realizing hybrid electric vehicles employing LIBs in the near future.

6.0   SUMMARY AND OUTLOOK

In this chapter, the authors focused on three fundamental aspects of electrochemical lithium intercalation, *i.e.* intercalation/deintercalation mechanisms, kinetics, and surface film formation. Since the commercialization if 1991, much effort has been devoted to improve the performance of LIBs, and actually the capacity of 18650-type cells has increased to about 1800 mAh, which is about twice that of the cells in 1991, for the past decade. However, rapid

development of portable electronic devices imposes us a demand for even lighter-weight and smaller-sized rechargeable batteries. Development of large-scale LIBs for hybrid electric vehicles and energy storage systems is also a matter of great urgency in the twenty-first century. The reversible capacity of graphite, which is now most widely used in commercially available LIBs, is theoretically limited to 372 mAh·g^{-1} at maximum. The high-capacity disordered carbons have several problems remained to be solved as described in the text, and the key is how we use these high-capacity carbons in practical cells. In addition, modification of carbon anodes with alloy-forming materials such as tin [104-106] and silicon [107-111] would be another promising method to increase the reversible capacity in the near future.

In spite of numerous research efforts, details on the SEI composition, stability, and its influence on the battery performance are still controversial. Careful analysis and discussion are necessary to understand the nature of the SEI on carbon anodes. Theoretical considerations for solvent decomposition, which just started to appear in the literature [112,113], will be of a great help. It was also reported that the formation of SEI is the primary reason for long-term degradation of large-scale LIBs because of continuous growth of the SEI layer.

The kinetics of lithium intercalation/deintercalation has been underesti-mated despite of its importance for practical use. To increase the power density of LIBs, *e.g.* for use in hybrid electric vehicles, the diffusivity of lithium ion in various carbonaceous materials should be accurately evaluated, and for this purpose we need to develop a method that can precisely give the diffusivity of lithium ion not only in carbon anodes, but also in cathode materials in LIBs. As described in the text, not only the diffusivity, but also the rate of the interfacial charge-transfer reaction may be the rate-determining step, and further investigation is necessary on this issue.

7.0   REFERENCES

1. J. Yamaki and S. Tobishima, in *Handbook of Battery Materials,* J. O. Besenhard, ed., Wiley-VCH, Weinheim, pp. 339-357, 1999
2. M. Inaba and Z. Ogumi, *IEEE Electr. Insul. M.,* **17**, 6, 2001.
3. 3.M. Inaba and Z. Ogumi, Bull. Chem. Soc. Jpn., **71**, 521, 1998.
4. 4.M. Winter and J. O. Besenhard, in *Handbook of Battery Materials,* J. O. Besenhard, ed., Wiley-VCH, Weinheim, pp. 339-357.383-418, 1999
5. I. Mochida, *Tansozai no Kagaku to Kogaku, Asakura,* Tokyo (1990) p.10 (in Japanese).
6. R. E. Franklin, *Proc. Roy. Soc. (London),* **A209**, 196, 1951.
7. J. R. Dahn, T. Zheng, Y. Liu, and J. S. Xue, *Science,* **270**, 590, 1995.
8. J. R. Dahn, *Phys. Rev.,* B44, 9170, 1991.
9. T. Ohzuku, Y. Iwakoshi, and K. Sawai, *J. Electrochemical. Soc.,* **140**, 2490, 1993.

11. Z. Jiang, M. Alamair, and K. M. Abraham, *J. Electrochemical Soc.,* **142**, 333, 1995.
12. Tanso Zairyo Gakkai, ed., *Kokuen Sokan Kagoubutu (Graphite Intercalation Compounds),* Realize, Tokyo, p. 91 (in Japanese), 1990.
13. A. Herold, *Bull. Soc., Chim. Fr.,* **187**, 999, 1955.
14. H. Ikeda, S. Narukawa, and H. Nakajima, Japanese Patent 1769661, 1981.
15. M. Inaba, H. Yoshida, Z. Ogumi, T. Abe, Y. Mizutani, and M. Asano, *J. Electrochem. Soc.,* **142**, 20, 1995.
16. M. Inaba, H. Yoshida, and Z. Ogumi, *J. Electrochem. Soc.,* **143**, 2572, 1996.
17. M. Inaba and Z. Ogumi, *Denchi Gijyutu (Battery Technology),* **8**, 3, 1996.
18. J. R. Dahn, A. K. Sleigh, H. Shi, J. N. Reimers, Q. Zhong, and B. M. Way, *Electrochim. Acta,* **38**, 1179, 1993.
19. N. Kambe, M. S. Dresselhaus, G. Dresselhaus, S. Basu, A. R. McGhie, and J. E. Fischer, *Mater. Sci, Eng.,* **40**, 1, 1979.
20. K. Tatsumi, A. Mabuchi, N. Iwashita, H. Sakaebe, H. Shioyama, H. Fujimoto, and S. Higuchi, *J. Electrochem. Soc.,* **142**, 716, 1995.
21. C. R. Houska and B. E. Warren, *J. Appl. Phys.,* **25**, 204, 1954.
22. A. Mabuchi, K. Tokumitsu, H. Fujimoto and T. Kasuh, *J. Electrochem. Soc.,* **142**, 1041, 1995.
23. M. Inaba, M. Fujikawa, T. Abe and Z. Ogumi, *J. Electrochem. Soc.,* **147**, 4008, 2000.
24. K. Sato, M. Noguchi, A. Demachi, N. Oki and M. Endo, *Science,* **264**, 556, 1994.
25. K. Tokumitsu, H. Fujimoto, A. Mabuchi and T. Kasuh, *Carbon,* **37**, 1599, 1999.
26. N. Takami, A. Satoh, T. Ohsaki and M. Kanda, *J. Electrochem. Soc.,* **145**, 478,1998.
27. T. Zheng, Y. Liu, E. W. Fuller, S. Tseng, U. von Sacken and J. R. Dahn, *J. Electrochem. Soc.,* **142**, 2581, 1995.
28. T. Zheng, W. R. McKinnon, and J. R. Dahn, *J. Electrochem. Soc.,* **143**, 2137, 1996.
29. N. Sonobe, M. Ishikawa and T. Iwasaki, *Extended Abstracts of 35th Battery Symposium in Japan,* Nagoya, Japan, pp. 47-48, 1994
30. M. Ishikawa, N. Sonobe, H. Nakauma and T. Iwasaki, *Extended Abstracts of 35th Battery Symposium in Japan,* Nagoya, Japan, pp. 49-50, 1994
31. Y. Liu, J. S. Xue, T. Zheng and J. R. Dahn, *Carbon,* **23**, 193, 1996.
32. E. Peled, *J. Electrochem. Soc..* **126**, 2047,1979.
33. E. Peled, in *Handbook of Battery Materials,* J. O. Besenhard, ed., Wiley-VCH, Weinheim, 1999 pp. 419-458, 1999.
34. Y. Ein-Eli, B. Markovsky, D. Aurbach, Y. Carmeli, H. Yamin, and S. Luski, *Electrochim. Acta,* **39**, 2559, 1994.
35. D. Aurbach, Y. Ein-Eli, O. Chusid (Youngman), Y. Carmeli, M. Babai, and H. Yamin, *J. Electrochem. Soc.,* **141**, 603, 1994.
36. D. Aurbach, Y. Ein-Eli, B. Markovsky, A. Zaban, S. Luski, Y. Carmeli, and H. Yamin, *J. Electrochem. Soc.,* **142**, 2882, 1995.
37. Y. Ein-Eli, S. R. Thomas, V. Koch, D. Aurbach, B. Markovsky, and A. Schechter, *J. Electrochem. Soc.,* **143**, 1273, 1996.
38. D. Aurbach, B. Markovsky, A. Schechter, and E. Ein-Eli, *J. Electrochem. Soc.,* **143**, 3809, 1996.
39. Y. Ein-Eli, S. F. McDevitt, D. Aurbach, B. Markovsky, and A. Schechter, *J. Electrochem. Soc.,* **144**, 1180, 1997.

40. D. Aurbach, A. Zaban, Y. Ein-Eli, I. Wessman, O. Chuid, B. Markovsky, M. Levi, E. Levi, A. Schechter, and E. Granot, *J. Power Sources,* **68**, 91, 1997.
41. D. Aurbach, M. D. Levi, E. Levi, and A. Schechter, *J. Phys. Chem. B.,* **101**. 2195, 1997.
42. D. Aurbach, M. D. Levi, E. Levi, H. Teller, B. Markovsky, and G. Salitra, *J. Electrochem. Soc.,* **145**, 3024, 1998.
43. D. Aurbach, B. Markovsky, I. Weissman, E. Levi, and Y. Ein-Eli, *Electrochim. Acta.* **45**, 67, 1999.
44. H. Yoshida, T. Fukunaga, T. Hazama, M Terasaki, M. Mizutani, and M. Yamachi, *J. Power Sources,* **68**, 311, 1997.
45. K. Kanamura, S. Shiraishi, H. Takezawa, and Z. Takehara, *Chem. Mater.,* **9**, 1797, 1997.
46. A. Naji, J. Ghanbaja, B. Humbert, P. Willmann, and D. Billaud, *J. Power Sources,* **62**, 141, 1996.
47. M. Dolle, S. Grugeon, B. Beaudoin, L. Dupont, J-M. Trascon, *J. Power Sources,* **97-98**, 104, 2001.
48. Z. Ogumi, A. Sano, M. Inaba, and T. Abe, *J. Power Sources,* 97-98, 156, 2001.
49. R. Yazami, *Electrochim. Acta,* **45**, 87, 1999.
50. P. Novak, F. Joho, M. Lanz, B. Rykart, J. C. Panitz, D. Alliata, R. Kotz, and O. Haas, *J. Power Sources,* **97-98**, 39, 2001.
51. C. Menachem, E. Peled, L. Burstein, and Y. Rosenberg, *J. Power Sources,* **68**, 277, 1997.
52. E. Peled, D. Golodnitsky, C. Menachem, and D. Bar-Tow, *J. Electrochem. Soc.,* **145**, 3482, 1998.
53. D. Bar-Tow, E. Peled, and L. Burstein, *J. Electrochem. Soc.,* **146**, 824, 1999.
54. E. Pled, D. Bar-Tow, A. Merson, A. Gladkich, L. Burstein, and D. Golodnitsky, *J. Power Sources,* **97-98**, 52, 2001.
55. J. O. Besenhard, M. Winter, J. Yang, and W. Biberacher, *J. Power Sources,* **54**, 228, 1995.M
56. M. Winter, G. H. Wrodingg, J. O. Besenhard, W. Biberacher, and P. Novak, *J. Electrochem. Soc.,* **147**, 2427, 2000.
57. M. Inaba, Z. Siroma, Z. Ogumi, T. Abe, Y. Mizutani, and M. Asano, *Chem. Lett.,* 661, 1995.
58. M. Inaba, Z. Siroma, A. Funabiki, Z. Ogumi, T. Abe, Y. Mizutani, and M. Asano, *Langmuir,* **12**, 1535, 1996.
59. M. Inaba, Z. Siroma, Y. Kawatate, A. Funabiki and Z. Ogumi, *J. Power Sources,* **68**, 221, 1997.
60. M. Inaba, Y. Kawatate, A. Funabiki, S.-K. Jeong, T. Abe, and Z. Ogumi, *Electrochim. Acta,* **45**, 99, 1999.
61. M. Inaba, Y. Kawatate, A. Funabiki, S.-K. Jeong, T. Abe, and Z. Ogumi, *Electrochemistry,* **67**, 1153, 1999.
62. S.-K. Jeong, M. Inaba, T. Abe, and Z. Ogumi, *J. Electrochem. Soc.,* **148**, A989, 2001.
63. S.-K. Jeong, M. Inaba, R. Mogi, Y. Iriyama, T. Abe, and Z. Ogumi, *Langmuir,* **17**, 8281, 2001.
64. Z. Ogumi, M. Inaba, T. Abe, and S.-K. Jeong, in *Studies in Surface Science and Catalysis,* Vol. 132, Y. Iwashita, N. Oyama, and H. Kunieda, eds., Elsevier Science B.V., Amsterdam, pp. 929-934, 2001.

65. A. N. Dey and B. P. Sullivan, *J. Electrochem. Soc.,* **117**, 222, 1970.
66. J. O. Besenhard and H. P. Fritz, *J. Electroanal. Chem..* **53**, 329, 1974.
67. G. Eichinger, *J. Electroanal. Chem.,* **74**, 183, 1976.
68. M. Arakawa and J. Yamaki, *J. Electroanal. Chem.,* **219**, 273, 1987.
69. J. T. Dudley, D. P. Wilkinson, G. Thomas, R. LeVae, S. Woo, H. Blom, C. Horvath, M. W. Juzkow, B. Denis, P. Juric, P. Aghakian, and J. R. Dahn, *J. Power Sources,* 35, 59, 1991.
70. Z. X. Shu, R. S. McMillan, and J. J. Murray, *J. Electrochem. Soc.,* **142**, L161, 1995.
71. A. Naji, P. Willmann, and D. Billud, *Carbon,* **36**, 1347, 1998.
72. Z. X. Shu, R. S. McMillan, J. J. Murray, and I. J. Davidson, *J. Electrochem. Soc.,* **143**, 2230, 1996.
73. P. Biensan, J. M. Bodet, F. Perton, M. Broussely, C. Jehoulet, S. Barusseau, S. Herreyre, and B. Simon, *Extended Abstracts of The 10th International Meeting on Lithium Batteries,* Como, Italy (2000) Abs. No. 286.
74. G. H. Wrodnigg, J. O. Besenhard, and M. Winter, *J. Electrochem. Soc.,* **146**, 470, 1999.
75. G. H. Wrodnigg, T. M. Wrodnigg, J. O. Besenhard, and M. Winter, *Electrochem. Commun.,* 1, 148, 1999.
76. R. McMillan, H. Slegr, Z. X. Shu, and W. Wang, *J. Power Sources,* **81-82**, 20, 1999.
77. A. Naji, J. Ghanbaja, P. Willmann, and D. Billaud, *Electrochim. Acta,* **45**, 1893, 2000.
78. G.-C. Chung, H.-J. Kim, S.-H. Jun, and M.-H. Kim, *Electrochem. Commun.,* **1**, 493, 1999.
79. G.-C. Chung, H.-J. Kim, S.-H. Yu, S.-H. Jun, J.-W. Choi, and M.-H. Kim, *J. Electrochem. Soc.,* **147**, 4391, 2000.
80. Z. X. Shu, R. S. McMillan, and J. J. Murray, *J. Electrochem. Soc..* **140**, 922, 1993.
81. Z. X. Shu, R. S. McMillan, and J. J. Murray, *J. Electrochem. Soc.,* **140**, L101, 1993.
82. T. Abe, Y. Mizutani, N. Kawabata, M. Inaba, and Z. Ogumi, *Synthetic Metals,* **125**, 249, 2002.
83. J. Conard and H. Estrade, *Mater. Sci. Eng.,* **31**, 173,1977.
84. M. Jean, C. Menachem, D. Bar-Row, and A. Melman, *J. Electrochem Soc.,* **142**, 2122, 1995.
85. T. Uchida, T. Itoh, Y. Morikawa, H. Ikuta, and M. Wakihara, *Denki Kagaku,* **61**, 1390, 1993.
86. T. Uchida, Y. Morikawa, H. Ikuta, M. Wakihara, and K. Suzuki, *J. Electrochem Soc.,* **143**, 2606, 1996.
87. M. D. Levi and D. Aurbach, *J. Phys. Chem. B,* **101**, 4641, 1997.
88. M. Nishizawa, R. Hashitani, T. Itoh, T. Matsue, and I. Uchida, *Electrochem. Solid State Lett.,* **1**, 10, 1998.
89. M. D. Levi, E. A. Levi, and D. Aurbach, *J. Electroanal. Chem.,* **421**, 89, 1997.
90. B. Markovsky, M. D. Levi, and D. Aurbach, *Electrochim. Acta,* **43**, 2287, 1998.
91. M. Morita, N. Nishimura, and Y. Matsuda, *Electrochim. Acta,* **38**, 1721, 1993.
92. N. Takami, A. Satoh, M. Hara, and T. Ohsaki, *J. Electrochem Soc.,* **142**, 371, 1995.
93. A. Funabiki, M. Inaba, and Z. Ogumi, *J. Power Sources,* **68**, 227, 1997.
94. A. Funabiki, M. Inaba, Z. Ogumi, S. Yuasa, J. Otsuji, and A. Tasaka *J. Electrochemical Soc.,* **145**, 172, 1998.
95. M. Inaba, S. Nohmi, A. Funabiki, T. Abe, and Z. Ogumi, in *Materials for Electrochemical Energy Storage and Conversion II-Batteries, Capacitors and*

Fuel Cells. D. S. Ginley, D. H. Doughty, B. Scrosati, T. Takamura, and Z. Zhang, eds., Mat. Res. Soc. Symp. Proc. Vol. 496, Materials Research Society, Warrendale, PA, pp. 493-498, 1998

96. N. Imanishi, H. Kashiwagi, T. Ichikawa, Y. Takeda, O. Yamamoto, and M. Inagaki, *J. Electrochem.Soc.,* **140**, 315, 1993.

97. P. C. Eklund, C. H. Olk, F. J. Holler, J. G. Spolar, and E. T. Arakawa, *J. Mater. Res.,* **1**, 361, 1986.

98. R. Nishitani, Y. Sasaki, and Y. Nishina, *J. Phys. Soc. Jpn.,* **56**, 1051, 1987.

99. R. Nishitani, Y. Sasaki, and Y. Nishina, *Phys. Rev.,* **B37**, 3141, 1988.

100. A. Funabiki, M. Inaba, T. Abe, and Z. Ogumi, *Carbon,* **37**, 1591, 1999.

101. Y. Iriyama, M. Inaba, T. Abe, and Z. Ogumi, *J. Power Sources,* **94**, 175, 2001.

102. A. Funabiki, M. Inaba, T. Abe, and Z. Ogumi, *Carbon,* **37**, 1591, 1999.

103. T. Takamura, K. Sumiya, J. Suzuki, C. Yamada, and K. Sekine, *J. Power* Sources, **81-82**, 368, 1999.

104. Y. Idota, T. Kubota, A. Matsufuji, Y. Maekawa, and T. Miyasaka, *Science,* **276**, 1395, 1997.

105. M. Wachtler, J. O. Besenhard, and M. Winter, *J. Power Sources,* **94**, 189, 2001.

106. I Rom, M. Wachtler, I. Papst, M. Schmied, J. O. Besenhard, F. Hofer, and M. Winter, *Solid State Ionics,* **143**, 329, 2001.

107. S. Bourderau, T. Brousse, and D. M. Schleich, *J. Power Sources,* **81-82**, 223, 1999.

108. H. Li, X. J. Huang, L. Q. Chen, Z. G. Wu, Y. Liang, *Electrochem. Solid State Lett.,* **2**, 547, 1999.

109. H. Li, X. Huang, L. Chen, G. Zhou, Z. Zhang, D. Yu, Y. J. Mo, and N. Pei, *Solid State Ionics,* **135**, 181, 2000.

110. S. B. Ng, J. Y. Lee, and Z. L. Liu, *J. Power Sources,* **94**, 63, 2001.

111. B. Gao, S. Sinha, L. Fleming, and O. Zhou, *Adv. Mater.,* **13**, 816, 2001.

112. T. Li, P.B. Balbuena, *Chem. Phys. Lett.,* **317**, 421, 2000.

113. Y. Wang, S. Nakamura, M. Ue, and P. Balbuena, *J. Am. Chem. Soc.,* **123**, 11708(2001).

3

Manganese Vanadates and Molybdates as Anode Materials for Lithium-Ion Batteries

M. Wakihara
H. Ikuta
Y. Uchimoto
Department of Applied Chemistry
Tokyo Institute of Technology
2-12-1 Ookayama, Meguro-ku
Tokyo 152-8552
Japan

1.0   INTRODUCTION

The explosive demand for portable electronic devices has brought about an increase in the importance of compact, lightweight and reliable power sources. One of the most probable candidates for such requirements is Li-ion rechargeable battery due to its high capacity and energy density. The Li-ion rechargeable battery constitutes of two intercalation compounds as electrode materials. One is a lithiated transition metal oxide as cathode and the other graphite anode. However, it is well known that the quantity of active material per unit weight or volume determines the capacity density of the battery. In such a viewpoint, the graphite anode material commonly used in Li-ion rechargeable batteries restricts on the capacity of the cell per unit weight (theoretically $372 \ \mathrm{mAh \cdot g^{-1}}$) and/or per unit volume due to its low density. To overcome these disadvantages, considerable amounts of attempts have been made by several workers to find out alternative anode materials such as tin based oxide glasses [1] and metal oxides (MO; M=Co, Ni, Fe) [2] in place of graphite anodes.

Recently, it has been reported that vanadium-based compounds like RVO_4 (R:In,Cr,Fe,Al,Y) undergo amorphization during low potential electrochemical lithiation [3] and much emphasis has been placed over the remarkable difference in the charge-discharge profile that occur before and after amorphization. Piffard *et al.* [4] reported on the synthesis of amorphous and crystalline manganese vanadate $MnV_2O_{6+\delta}$ $(\delta>0.5)$ with various amount of crystalline water by a 2-step method, which consists of precipitation followed by ozonation procedure. They also showed that the

anode material with amorphous structure is capable of delivering high capacity compared to crystalline one and indicated a smooth voltage variation with lithiation except around 2.4V region. Generally, synthesis procedure of vanadium based metal oxide reported up to now except co-precipitation method requires heat-treatment at temperature above 500°C for a few days. In this experiments, we report on simple synthesis procedure of crystalline stoichiometric MnV_2O_6 without crystalline water through the use of solution route using polymer resin as gelling agent followed by heat-treatment at 450°C [6]. In addition to MnV_2O_6, we focused on the $Mn_{1-x}Mo_{2x}V_{2(1-x)}O_6$ that has the same brannerite structure as MnV_2O_6.

In addition to vanadates, molybdenum oxides should also attract an attention as anode material for Li-ion rechargeable battery because they also have various oxidation states like vanadium. Related molybdenum compounds, Auborn *et al.* [5] have proposed molybdenum oxide MoO_2 as anode material for lithium secondary battery more than ten years ago. However, their study was limited by experimental conditions such as poor stability of the electrolyte at low potential. Here, we prepared $MnMoO_4$ using solid-state reaction [7,8].

The electrochemical properties of MnV_2O_6, $Mn_{1-x}Mo_{2x}V_{2(1-x)}O_6$ and $MnMoO_4$ were examined as anode properties. Furthermore, we discuss the mechanism of underlying electrode process and its relevance over the existing anode materials for Li-ion rechargeable battery.

2.0   ANODE PROPERTIES OF BRANNERITE-TYPE OXIDES

2.1   *Brannerite Structure*

Mineral brannerite $(U,Ca,Ce)(Ti,Fe)_2O_6$ is named after the American geologist, J.C. Branner (1850-1922). Ruh and Wadsley analyzed the crystal structure of $ThTi_2O_6$ instead of UTi_2O_6 [9]. In the AB_2O_6 brannerite structure, six oxygen atoms octahedrally coordinate both cations A and B. All the A and B cations are in equivalent positions, respectively. The brannerite itself contains both tetravalent Th^{4+} and Ti^{4+} cations in A and B positions, respectively, a number of divalent metal metavanadates, $M^{2+}V^{5+}_2O_6$ (M=Mg,Mn,Co,Zn,Cd,Hg,Co) [10-14], form brannerite structure.

In these metavanadates, the crystal structure of MgV_2O_6 has been investigated using X-ray diffraction of its single crystal [13]. The schematic figure of crystal structure for MV_2O_6 in a direction perpendicular to *a-c* plane is shown in Figure 1. MgV_2O_6 crystallizes in the monoclinic space group C2/m with lattice parameter a=9.279 X *b*=3.502 A, c=6.731 A and β=111.77° with Z=2. In this structure, the Mg^{2+} (isolated small spheres) situated at a site with

2/m symmetry and coordinated octahedrally by six oxygen atoms (large spheres) with slight distortion with average bond length of 2.140 Å. All the remaining atoms lie in the crystallographic mirror planes with the V ion (small spheres) coordinated to six oxygen atoms with bond length from 1.666 to 2.671 Å, which is represented by sticks in the figure. These VO_6 octahedra are largely distorted like VO_5 pyramid in shear structured V_2O_5 and share opposite corners forming chains running parallel to the *b-axis*. Octahedra in adjacent chains share edges involving two oxygen atoms on one side of the chain. On the other side, chains interleaf such that one octahedron shares two edges with two adjacent octahedral in a neighbouring chain. Mg^{2+} ions lie in the octahedral interstices sharing oxygen atoms with six different V^{5+} ions. MgO_6 groups form chains paralleling the *b*-axis by edges with two translation equivalent MgO_6 groups. The Mg-O bonding in MgO_6 octahedron shows an angular distortion consistent with a repulsive interaction between vanadium ions separated by a b-axis translation and sharing an oxygen atom with the Mg^{2+} ion.
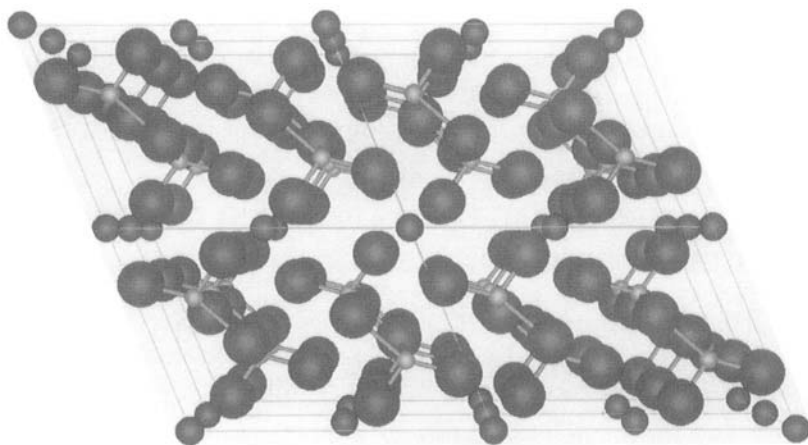
Figure 1. Schematic figure of brannerite structure for MV_2O_6

Kozlowski *et al.* [15] have reported observed and calculated peaks for MnV_2O_6 and $Mn_{1-x}Mo_{2x}V_{2(1-x)}O_6$ based on the assumption that it forms the same crystal structure as MgV_2O_6. They prepared MnV_2O_6 to investigate its catalytic behaviour. Although they did not refine the structural parameters of each element, the intensity of the calculated peaks is almost consistent with that of the observed ones. They have reported the lattice parameter values as a=9.315Å, *b*=3.536Å, c=6.754Å, and β=112.66° for MnV_2O_6 and *a*=9.378Å, *b*=3.613Å, *c*=6.751Å, and β=112.18° for $Mn_{0.6}Mo_{0.8}V_{1.2}O_6$.

2.2   Experimental

2.2.1   Preparation and Characterization of Crystalline MnV$_2$O$_6$

Crystalline MnV_2O_6 was synthesized by the method similar to that described for the preparation of $LiMn_2O_4$ and $LiCoO_2$ [16,17]. Starting materials used were $Mn(CH_3COO)_2 \cdot 4H_2O$ (99.9% Soekawa Chemicals Ltd.), V_2O_5 (99.9% Soekawa Chemicals Ltd.) and PVA (PolyVinyl Alcohol, Reagent grade, Wako Pure Chemical Industries Ltd. molecular weight 1500~1800). Stoichiometric amount of V_2O_5 and $Mn(CH_3COO)_2 \cdot 4H_2O$ were separately dissolved in distilled water and mixed, then stirred until a clear solution formed. Appropriate polymer/metal ratio of PVA solution (P/M ratio=2.5) was added to the stoichiometric mixed metal solution. Upon mixing PVA, the color of total solution was turned from opaque orange to translucent yellowish brown. The mixed solution was heated on a hot plate around 80°C with moderate stirring which underwent water evaporation, eventually leading to brown viscous gel. Throughout this process, the solution was stirred to keep homogeniety. Then, the viscous gel was heated at around 300°C for 2h in a furnace in air. The viscous mass on further oxidative decomposition leads to the formation of a precursor, which on decomposition eventually gave rise to brownish black fluffy powdered precursor. The prepared precursor was ground well and re-calcined at 450°C for 24h in air. A chemical reaction, assuming complete thermal decomposition of starting material up to 450°C, may be written as:

$$2V_2O_5(aq) + 2Mn(CH_3COO)_2 \cdot 4H_2O(aq) + 15CH_3CHOH + 45.5O_2(air) \rightarrow$$
$$2MnV_2O_6 + 38CO_2 + 44H_2O$$
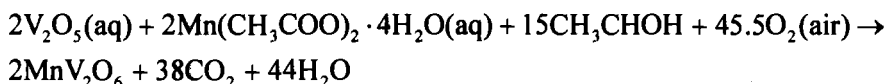
The calcination temperature for the precursor was set at 450°C in order to execute a complete decomposition of the residual organic moiety and eventual crystallization of brannerite type MnV_2O_6.

TG/DTA measurement was carried out by Shinku-riko TGD 9600 at a heating rate of 5°C/min in air to understand thermal reaction process such as weight loss and phase formation temperature of precursor. The Infrared spectra of the precursor and re-calcined powder were measured by JASCO FT/IR 350 between 2000 and 400 cm^{-1} with KBr method. The particle size and morphology features were collected by employing a scanning electron microscope (JEOL JSM 5200). The phase identification and lattice parameter measurement were carried out by powder X-ray difrractometry using Rigaku RINT2500V with CuKα radiation. The K-edge value of Mn and V were obtained by XANES measurements by Rigaku R-EXAFS Super, and it gives the information of oxidation state of Mn and V.

The samples for the electrochemical measurement were prepared by mixing crystalline MnV_2O_6, acethylene black and polytetra-flouro-ethylene (PTFE) binder

(50-45-5wt%, respectively) in an agate mortar and made in the form of film (100 μm thickness). The film was then cut into a disk form (5.4mm diameter). Cells were fabricated by coupling this disc with lithium foil of same area as counter electrode using Celgard as separator. 1M $LiClO_4$ dissolved in EC/DEC (vol ratio=1:1) was used as the electrolyte as received from Tomiyama Pure Chem. Ind. The electrochemical measurement was carried out galvanostatically at various current densities at room temperature in a glove box under argon atmosphere. The cut-off voltage was set at 0.0 and 3.5V. The electrodes removed at different depths of lithiation during the first cycle, were covered with polyethylene film, and subjected to ex-situ XRD measurements in order to understand the crystal structure change. Also, fully lithiated electrode was examined by ^7Li NMR measurement. For this, the electrode charged to 0V at the rate of 0.2C, was washed in PC solution and dried in argon atmosphere for more than 30 minutes. After drying, the electrode was put into zirconia rotors and set into NMR spectrometer (Chemagnetics, CMX-300 infinity) operating at ^7Li resonance frequency of 116.2MHz and magic angle spinning (MAS) with spin rate of 10kHz. Aqueous LiCl solution was employed as chemical-shift reference.

2.2.2   Preparation and Characterization of $Mn_{1-x}Mo_{2x}V_{2(1-x)}O_6$

$Mn_{1-x}Mo_{2x}V_{2(1-x)}O_6$ (x=0.1,0.2,0.3,0.4 and 0.5) powders were prepared by reacting a stoichiometric mixture of Mn_2O_3, V_2O_5 and MoO_3. Mn_2O_3 was first prepared by the decomposition of $MnCO_3$ at 600°C. The mixture was pressed into a pellet using a hand-press machine, then heated in air at appropriate temperature around 600°C with intermittent grindings, followed by slow cooling at a rate of 1°C/min. In order to compare the electrochemical properties, we prepared MnV_2O_6 (designated also as $Mn_{1-x}Mo_{2x}V_{2(1-x)}O_6$ (x=0)) by the same solid-state reaction as x=0.4. The phase identification and the evaluation of the lattice parameter of prepared samples were carried out by powder X-ray diffraction using $CuK\alpha$ radiation.

The samples for electrochemical measurements were prepared by following procedure. The working electrode were fabricated by doctor-blade technique on a copper-foil, spreading paste consisted of 10wt% polyvinylidenefluoride (PVDF) binder, 20 wt% acethylene black (conductive agent), 70 wt% active material of $Mn_{1-x}Mo_{2x}V_{2(1-x)}O_6$ and appropriate amount of 1-metyl-2-pyrrolidenone (NMP) as solvent. After drying of NMP solvent in a furnace at 110°C in air atmosphere for 1 day, the electrodes were roll-pressed and cut into disks. Lithium metal was used as counter electrode. The electrolyte was 1M $LiClO_4$ dissolved in Ethylene Carbonate (EC) / Diethyl Carbonate (DEC) (volume ratio 1:1) (received from Tomiyama pure chemical industries LTD.). The working electrode, counter electrode, separator and electrolyte were

fabricated in CR2032 coin type cell. The cell assembly was operated in a glove box filled with argon gas. The electrochemical measurements were carried out galvanostatically at various current densities at 30°C under air atmosphere. Relaxation time between each charge-discharge was set at 20 minutes. To measure the ex-situ XRD, beaker-type cell was selected for charge discharging. The working electrode was prepared similarly as mentioned above, Li foil was used as counter and reference electrode. Ni mesh (100mesh Niraco) was used for current conductor. 1M $LiClO_4$ dissolved in EC/DEC was used as electrolyte. In this case, assembling cells and electrochemical measurements were carried out in the glove box under an argon atmosphere at room temperature. The electrodes removed after the first lithium insertion and extraction were covered with polyethylene film to prevent the moisture in air. For beaker-type cells, the electrochemical measurements were carried out galvanostatically at current density of 0.2 C (0.07 $A \cdot g^{-1}$ of active materials) and relaxation time was set at 20 minutes.

2.3   *Results and Discussion*

2.3.1   *Synthesis and Characterization*

PVA was used to enhance the homogeneous mixing of the metal ions and suppress the precipitation of impurities. Since PVA has hydroxyl side groups in its chains, it can interact with metal ions. This interaction and random arrangement of polymer chain possibly enhance the mixing of metal ions. Therefore, the precursor can form a homogeneous single phase of precise stoichiometry at low temperature in short time relatively.
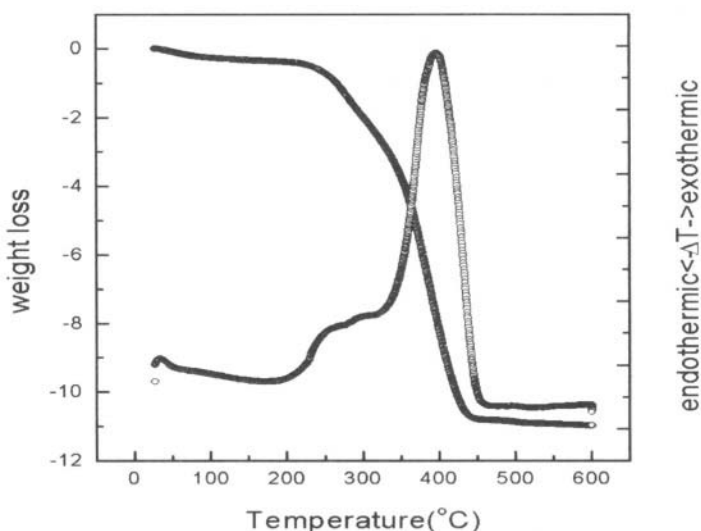
Figure 2. TG-DTA curves of MnV$_2$O$_6$ precursor powder

In order to obtain the complementary information on the phase formation temperature of the brannerite crystalline compound MnV_2O_6, the precursor material was subjected to TG/DTA thermal analysis from a room temperature to 600°C. The curves obtained are presented in Figure 2. The TG measurement in the curve predicts that weight-loss occurs between ca. 200 and 400°C. The DTA curve exhibits two exothermic peaks in it and a smaller shoulder peak that is then followed by a well-defined peak. An exothermic reaction observed around 250°C is indicative of onset of decomposition reaction, which is followed by oxidative elimination of remaining moiety of organic components in precursor. As the process of heating continues, huge exothermic reaction begins to appear at around 380°C and this process eventually leads to the formation of crystallization of brannerite structure. We can infer from the TG/DTA curves that about 20% of weight loss accounts for crystallization and decomposition of organic material, which remained even after preliminary heat- treatment during the preparation of precursor.

FT-IR spectra of precursor and crystalline MnV_2O_6 recorded at room temperature are depicted in Figure 3(a) and (b), respectively. The irregular pattern of IR spectra that exists between wavelength region of $1700 \ cm^{-1}$ and $1200 \ cm^{-1}$ is indicative of the presence of residual organic material in the precursor powder. This is also supported by the decomposition reaction accompanied by the weight loss, which is observed in the TG/DTA measurement. These bands disappear with heat treatment of the precursor powder beyond their decomposition temperature of the organic materials.

Figure 4 shows the SEM photographs of (a) precursor and (b) heat-treated crystalline powder of MnV_2O_6. The particles of precursor containing partially decomposed polymer shows large irregular surface area whereas the final products after heat-treatment leading to oxidation and removal of organic material shows a well-defined picture with the particle size less than 1 μm.

The crystal structure of the synthesized powder was examined by X-ray diffractometry analysis. The well-defined peak obtained confirms that the compound MnV_2O_6 formed with brannerite structure as already explained above section and the JCPDS data (card number 35-139) provides the exact match without any impurity phases. Figure 5 shows the measured powder diffraction profile for MnV_2O_6 and is compared with the simulated pattern, assuming the brannerite structure that was reported by Kozlowski *et al.* [15] as already described in the preceeding section. Furthermore, the measured data shows fair agreement with the simulated one and the position of the every peak matches perfectly. Kowzlowski *et al.*[15] have reported that lattice parameter values as 9.315Å(*a*), 3.536Å (*b*), 6.754Å(*c*), and 112.66° (*β*) which agree relatively with the data 9.303Å (a), 3.522Å (*b*), 6.756Å (*c*) and 112.38° (*β*) obtained for our material. It can be considered that these observed differences caused by the slight change of oxygen content. Therefore we carried out XANES and investigated the oxidation state of Mn and V in synthesized compound to verify the chemical formula.
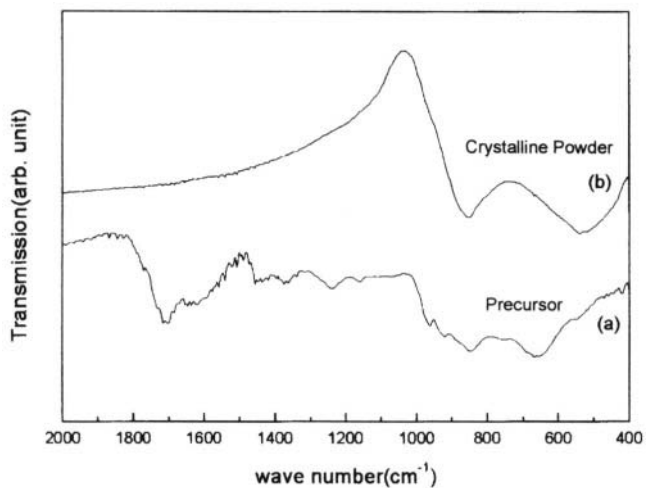
Figure 3. IR spectra for (**a**) precursor (**b**) heat treated at 400°C
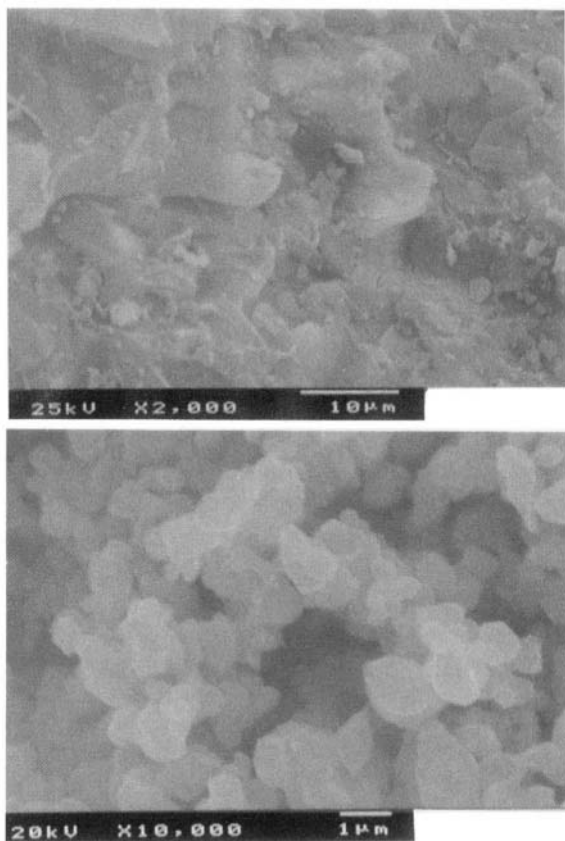
Figure 4. SEM images of (top) precursor (bottom) crystalline MnV_2O_6 heat treated at 400°C
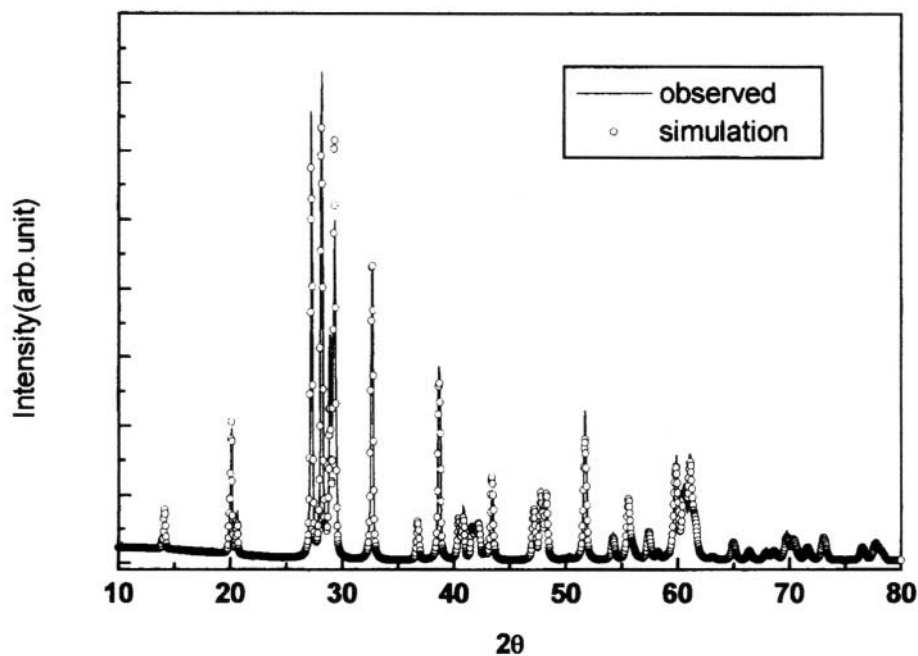
Figure 5. The powder XRD pattern for MnV_2O_6 and the calculated pattern assuming brannerite structure.
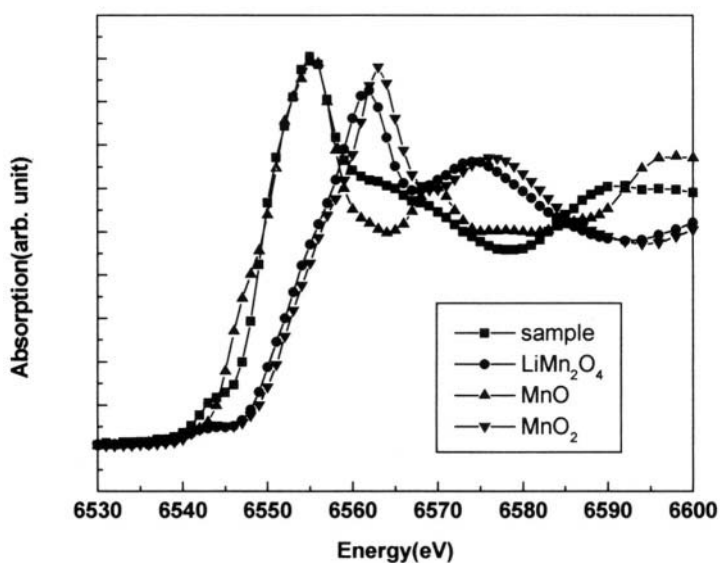
Figure 6. Mn K-edge XANES of the prepared MnV_2O_6 sample and MnO, MnO_2, $LiMn_2O_4$ as reference.
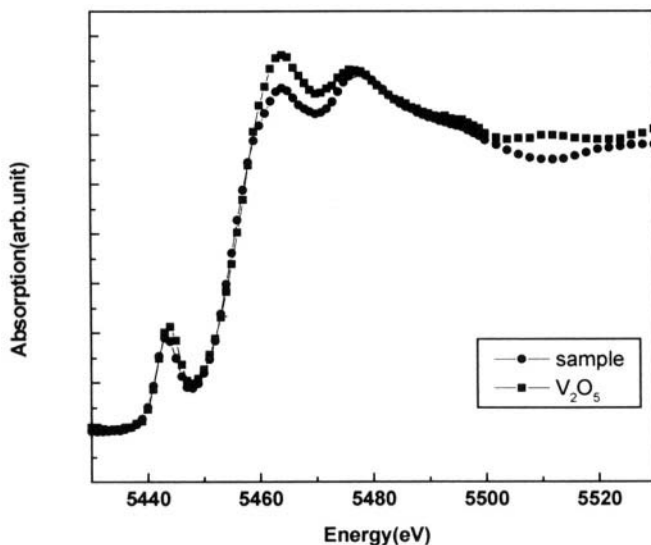
Figure 7. V K-edge XANES of the prepared MnV₂O₆ sample and V₂O₅ as reference.

The Mn K-edge XANES spectra of synthesized MnV_2O_6 and other reference material MnO, MnO_2 and $LiMn_2O_4$ are represented in Figure 6. As the spectra for the edge jumps for MnO and MnV_2O_6 are very close to each other, we can assume that Mn exists as Mn^{2+} in MnV_2O_6. Similar comparison of XANES spectra of MnV_2O_6 and V_2O_5 presented in Figure 7 illustrate that the valence of V in MnV_2O_6 is +5. The oxidation state arrived from the XANES spectra and well-defined XRD pattern obtained for the prepared sample confirm beyond doubt that the compound is stoichiometric MnV_2O_6 with brannerite crystalline structure.

2.3.2   *Electrochemical Properties*

In order to obtain charge-discharge profile of MnV_2O_6, cell was subjected to several cycles at constant current mode. The initial five charge-discharge profiles obtained are depicted in Figure 8. The difference between the first charge profile and the rest of charge curves is indicative of the two different mechanism operating in the lithium insertion process. Lithium ions inserted into MnV_2O_6 at the end of first charge corresponds to more than 12 lithium ions per MnV_2O_6 unit (1400 mAh·g⁻¹) whereas the subsequent discharge amounts only 7.6 lithium ions per MnV_2O_6 unit (800 mAh·g⁻¹) de-intercalated. For $LiNiVO_4$ compound, similar irreversible capacity has also been observed by Orsini *et al.* [4]. They have found that the compound with higher surface area (35m²·g⁻¹) has larger irreversible capacity compared to the compound with

lower surface area. In the present study we observed that MnV_2O_6 prepared by polymer gellation method which is devoid of water molecule with relatively small surface area of about $2m^2 \cdot g^{-1}$, also exhibits high irreversible capacity. During the first charge, the lithium intercalation process exhibited a plateau around 0.7 V versus Li/Li^+, which is not observed in the following cycles.

Guyomard *et al.* [18] have explained that the irreversible capacity in $LiMVO_4$ (M:Ni, Co, Zn, Cd) is due to the formation of a new type of lithiated amorphous material. With a view to understand electrode process undergoing during the first charge of the electrode, electrodes with different depth of charge were removed from the cell and subjected to XRD measurement. The X-ray diffractogram obtained for the fresh electrode as well as for the electrode charged up to different cut-off voltages such as 0.4 V, 0.7 V and 1.0 V are depicted in the Figure 9. The principal peaks appearing around $2\theta=28°$, characteristics of brannerite crystalline MnV_2O_6 gradually decreased with lithiation, the peaks disappeared completely at 0.4V. When the discharged electrodes were charged again, we could not observe the recovery of crystalline peaks, suggesting that an irreversible phase transformation into amorphous lithiated material occurred during the first lithium insertion.
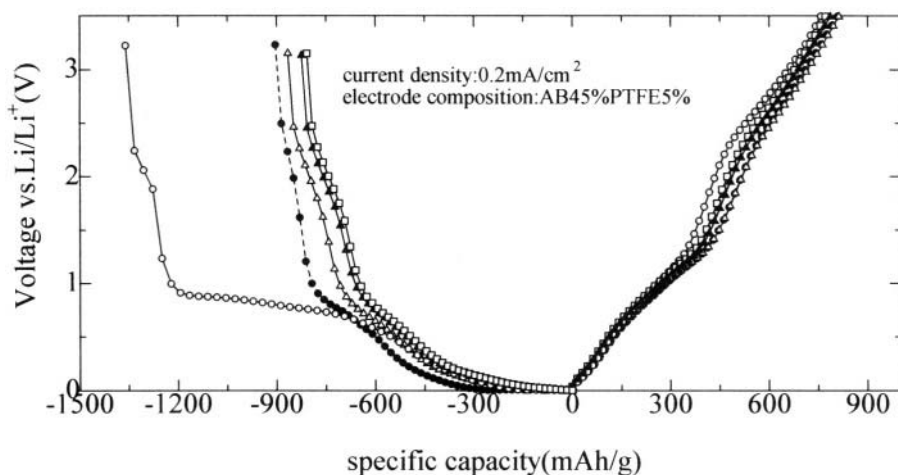
Figure 8. A typical charge-discharge curves of Li|MnV_2O_6 cell at initial five cycles. The arrow mark shows the potential point, which measured the ex-situ XRD of the electrode.

In addition, the reactivity of crystalline MnV_2O_6 with large amount of lithium cannot be explained by simple displacement of Mn and V by lithium, as given by following reactions.

$$MnV_2O_6 + xLi \rightarrow Li_xV_2O_6 + Mn \text{ or}$$

$$MnV_2O_6 + xLi \rightarrow Li_xMnO_6 + V \text{ or}$$

$$MnV_2O_6 + 2xLi \rightarrow xLi_2O + Mn + 2V$$
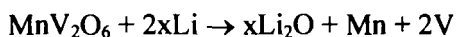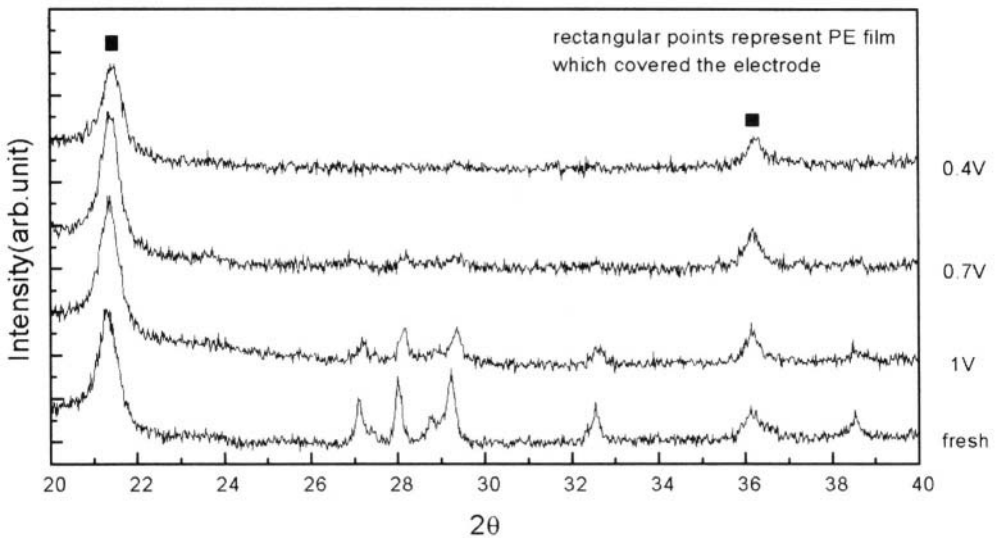
Figure 9. XRD patterns of the composite electrode at several potentials during the first lithium insertion. The symbol (■) indicates the peak of polyethylene film, which covered the electrode.

We could not detect any metallic Mn or V element in XRD measurement, which is not in agreement with the results of Takeda *et al.* [19] who pointed out the displacement of Cu by lithium in copper vanadate. This means that the interpretation of this high capacity of MnV_2O_6 must be interpreted by another mechanism for Li insertion.

Again, contrary to the present idea that the insertion process is largely due to the involvement of transition metal cation such as Mn in $LiMn_2O_4$, Denis *et al.*[3], to account for the abnormal insertion of lithium into vanadium-based oxide electrode material, proposed that in addition to the involvement of vanadium, there proceeds a parallel insertion process due to participation of oxygen leading to formation of "Li-O bonds" and explained the interactions of non-coordinated oxygen to lithium. Although there are differences in material (component, composition and crystal structure) of ours with those of Denis *et al.*, we can also consider the role of oxygen in manganese vanadate during electrochemical lithiation process. However it requires further investigation to understand the exact mechanism underlying the electrode process, and an attempt was made to understand the exact nature of lithium present in the structure to throw light on the abnormal high capacity of this compound.

The chemical status of lithium measured by ^{7}Li NMR spectra for the fully lithiated MnV_2O_6 composite electrode is shown in Figure 10. Two bands clearly appear at 1-2ppm and 40-41ppm, and other peaks can be assigned to spinning side bands. The band at *ca.* 40ppm can be attributed to the incorporated lithium in carbonaceous material as conductive agent of the composite electrode. It is well known that the shift value around 40ppm is

"signature" of lithiated carbonaceous material [19]. The other band at around 2ppm indicates that lithium accommodated in MnV_2O_6 is strong ionic character. Recent ^{7}Li NMR studies [20-22] on the low temperature synthesis carbon material whose capacity is higher than LiC_6 also showed ionic character of stored lithium. To explain the high capacity for carbon at low temperature, three mechanisms have been proposed. The first one is cavity mechanism, which explains that intercrystallite spaces are capable of lithium accommodation [23]. Secondly, Sato *et al.*[24] have proposed the existence of Li_2 covalent molecules. Finally, Hara *et al.* [25] suggested an ionic complex composed of lithium ions and aromatic rings with negative charge. Of these mechanisms, the formation of ionic complex mechanism is the relevant one to explain the role of oxygen in MnV_2O_6 and the formation of "Li-O bond". To understand the high capacity of MnV_2O_6, we can assume the formation of "Li-O bond" with ionic character. Accordingly, it can be stated that the oxygen present in the crystalline MnV_2O_6 with its high coordination possibility is responsible for the large intake of lithium. The first lithiation process disrupts the crystallinity into a more stable amorphous state with the formation of irrecoverable lithium strongly bonded to oxygen, is mainly responsible for the irreversibility and limited delithiation process $(800mAh \cdot g^{-1})$. However, more studies are needed to elucidate the mechanism responsible for the high capacity anode and irreversibility of vanadium-based oxides including MnV_2O_6.
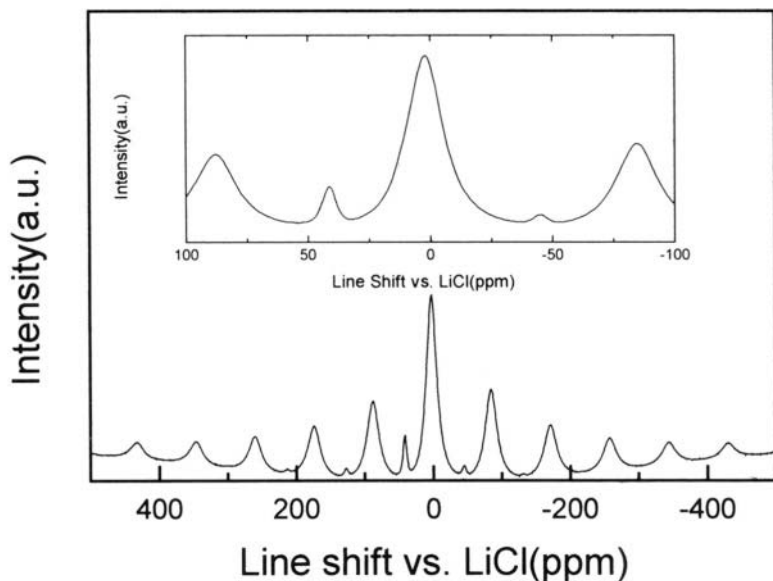
Figure10. ^{7}Li NMR spectra of the fully lithiated MnV_2O_6 electrode.

Figure 11 shows the discharge capacity with current density of MnV_2O_6, $SnSO_4$ [26] and natural graphite. For all the samples [6], each electrode fabricated with same mixing ratio (sample, conductive agent and binder were 50wt%, 45wt% and 5wt%, respectively). Each measured point in the figure corresponds to the discharge capacity of the first cycle. From these results, MnV_2O_6 shows reasonable rate capability compared to the other anode materials.
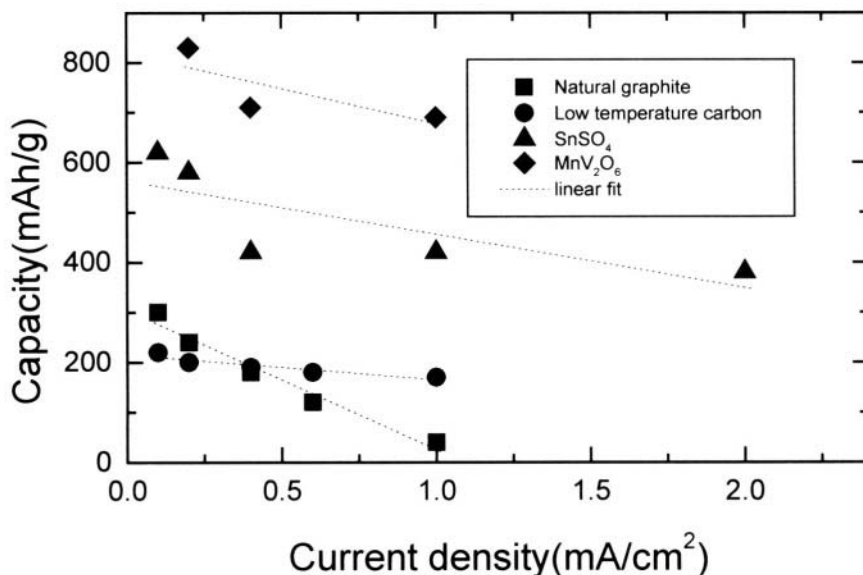
Figure 11. The discharge capacity variation of MnV_2O_6, $SnSO_4$, pitch-based carbon heated around 850°C and natural graphite with current density.

The cycling behavior over several tens of cycles is shown in Figure 12. As mentioned above, we can observe the large irreversible capacity caused by drastic structure transformation to amorphous at the first cycle and then capacity fading drops to levels of few percent per cycles. Piffard and Guyomard [3,18] have reported that "electrochemical grinding effect" in amorphous vanadium compounds, the phenomena of capacity increase with continuing the cycles due to the pulverization of active material. However, in present study, we could not find out this kind of effect. Hence it needs intensive further investigation to understand the lithium intercalation mechanism underlying it so as to improve cycle life to make it a commercially available material.

2.3.3   Synthesis and characterization of $Mn_{1-x}Mo_{2x}V_{2(1-x)}O_6$

The crystal structure of the synthesized powder was examined by XRD analysis. Almost all the diffraction peaks of $Mn_{1-x}Mo_{2x}V_{2(1-x)}O_6$ ($0<x\leq0.5$) samples coincide with the data for MnV_2O_6 in JCPDS card (35-139). In the case of the compound with x=0.5, trace of MoO_3 was observed at around

$2\theta=26°$. Figure 13 shows the lattice parameters of $Mn_{1-x}Mo_{2x}V_{2(1-x)}O_6$ (x=0, 0.1, 0.2, 0.3, 0.4, 0.5). Lattice parameters *a* and *b* increase with the value of x. From the measurement of Mn *L*-edge XANES, the valence of Mn is mainly +2. However, the minor peaks, which correspond to *L*3 absorption edge of Mn^{3+}, are observed in each samples around 642 eV, a small amount of Mn^{3+} would also be coexisted. V and Mo *L*-edge XANES reveal that the valence state of each cation is derived to be V^{5+} and Mo^{6+}, respectively. Mo *L*-edge spectra of $Mn_{0.7}Mo_{0.6}V_{1.4}O_6$ are almost consistent with those of MoO_3. In the absorption of Mo *L*-edge, the observed splitting due to the t_{2g} and e_g orbital indicates that Mo is coordinated octahedrally with oxide ions in Brannerite type structure $Mn_{1-x}Mo_{2x}V_{2(1-x)}O_6$.
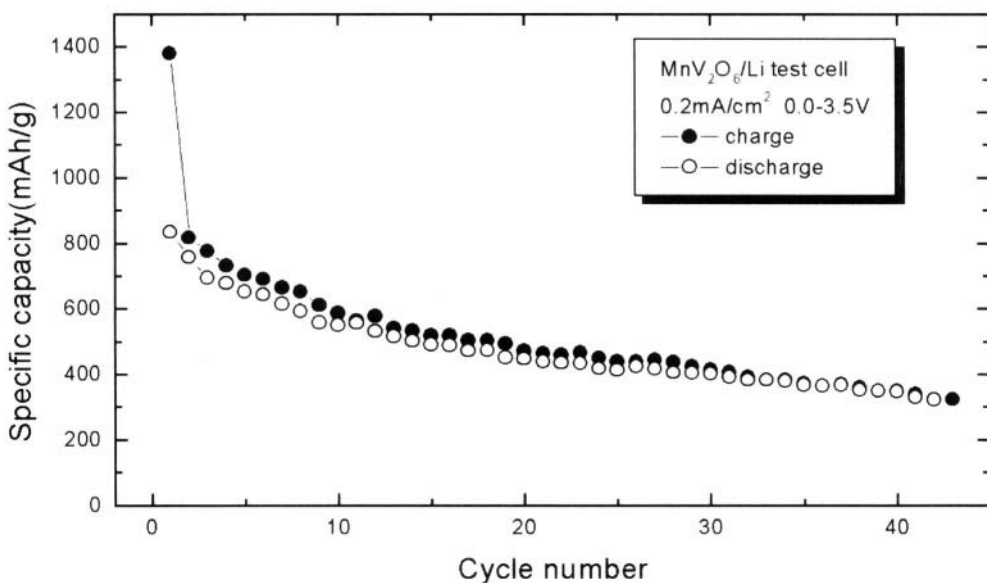
Figure 12. The specific capacity variation with the cycle number of the $Li|MnV_2O_6$ cell.

2.3.4   *Electrochemical properties of $Mn_{1-x}Mo_{2x}V_{2(1-x)}O_6$*

The first charge-discharge curves for $Li|Mn_{1-x}Mo_{2x}V_{2(1-x)}O_6$ (x=0.4) cell are shown in Figure 14 compared with that of $Li|MnV_2O_6$ ($Mn_{1-x}Mo_{2x}V_{2(1-x)}O_6$ (x=0)) cell. All the materials have rather large capacity compared with graphite. The lithium intercalation process into $Mn_{1-x}Mo_{2x}V_{2(1-x)}O_6$ (x=0.4) exhibits three plateaus around the voltages of 0.8, 0.5 and 0.2V. To evaluate the source of reversible capacity, cutoff voltages were set at several volts as shown in Figure 15. No reversible capacity could be obtained for the discharge at the cutoff voltages at 0.65 and 0.50 V, whereas the large reversible capacity was obtained for the discharge at the

cutoff voltages below 0.5V. The large reversible capacity arises from the third plateau at around 0.23V in the first discharge, and the capacity of the later charge coincides with that of the plateau at the discharge. This phenomenon is also applied to the non-substituted Brannerite $Mn_{1-x}Mo_{2x}V_{2(1-x)}O_6$ ($x=0$). Therefore, larger reversible capacity of substituted Brannerite $Mn_{1-x}Mo_{2x}V_{2(1-x)}O_6$ ($x=0.4$) than that of non-substituted Brannerite $Mn_{1-x}Mo_{2x}V_{2(1-x)}O_6$ ($x=0$) is due to the larger capacity of the third plateau than that of the non-substituted Brannerite. $Mn_{1-x}Mo_{2x}V_{2(1-x)}O_6$ at $x=0$ and 0.4 react with nearly 15 and 13 Li per mol, respectively, which cannot be explained even if each transition metal ion was completely reduced to metallic state. To compensate the electric charge, the oxide ions may be reduced with lithiation at low voltage region.
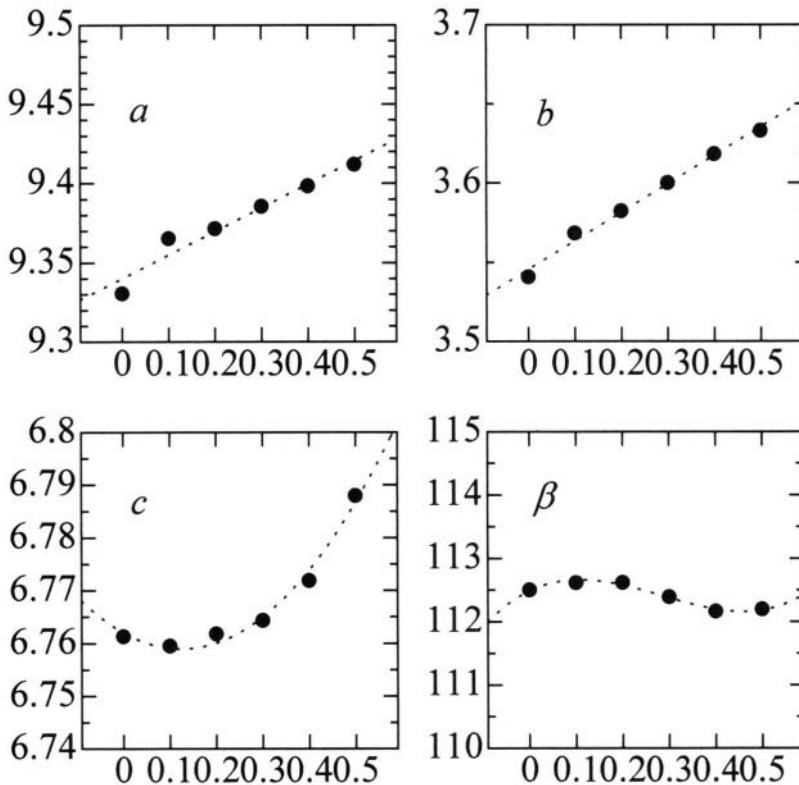
Figure 13. The lattice parameters of $Mn_{1-x}Mo_{2x}V_{2(1-x)}O_6$.
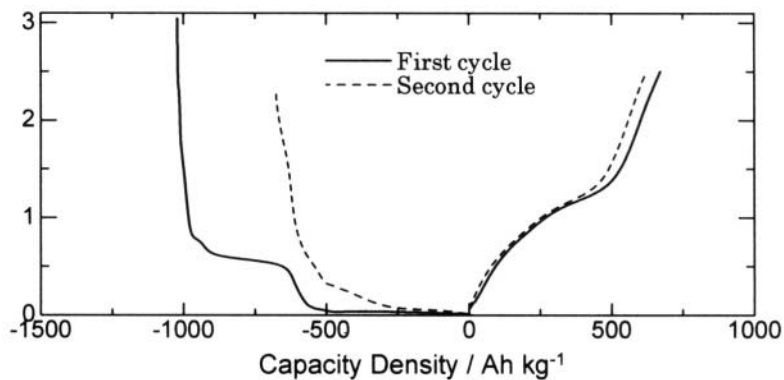
Figure 14(a). Charge-discharge curves for Li | $Mn_{1-x}Mo_{2x}V_{2(1-x)}O_6(x=0)$ cell.
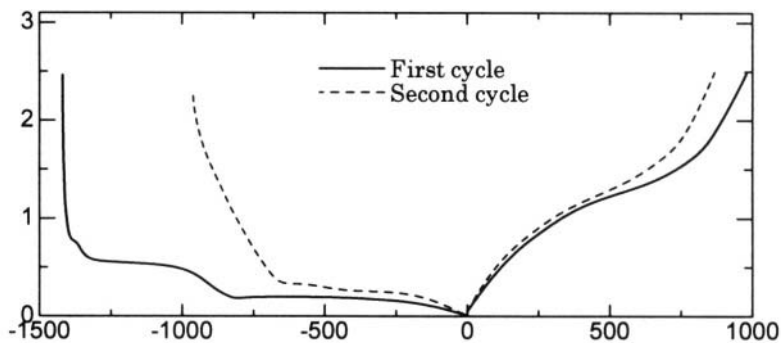
Figure 14(b). Charge-discharge curves for Li | $Mn_{1-x}Mo_{2x}V_{2(1-x)}O_6(x=0.4)$ cell.
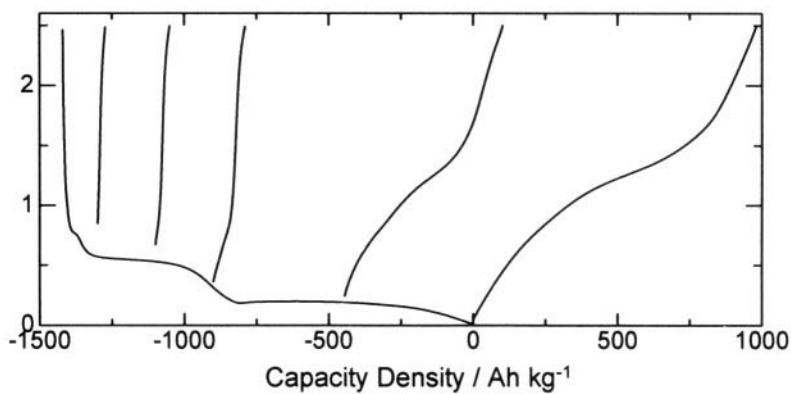
Figure 15. Charge-discharge curves for Li | $Mn_{1-x}Mo_{2x}V_{2(1-x)}O_6(x=0.4)$ cell at various cutoff voltages.

From the XRD patterns for $Mn_{1-x}Mo_{2x}V_{2(1-x)}O_6$ (x=0.4) electrodes at several cutoff voltages, the principal peaks gradually decreased with the progress of lithiation at the first discharge, and the peaks disappeared completely at 0.15V vs. Li/Li^+. After the first discharge, the charge-discharge process proceeds through this amorphous phase. The amorphization during the fist lithiation is the same phenomena as MnV_2O_6 that is already described above.

The discharge capacities of $Li|Mn_{1-x}Mo_{2x}V_{2(1-x)}O_6$ (x=0.4) cells versus cycle number are depicted in Fig. 16. It is clear that substituted brannerite $Mn_{1-x}Mo_{2x}V_{2(1-x)}O_6$ have larger reversible capacity than non-substituted brannerite MnV_2O_6. The cycleability of the $Mn_{1-x}Mo_{2x}V_{2(1-x)}O_6$ is almost the same as the value of x increases.
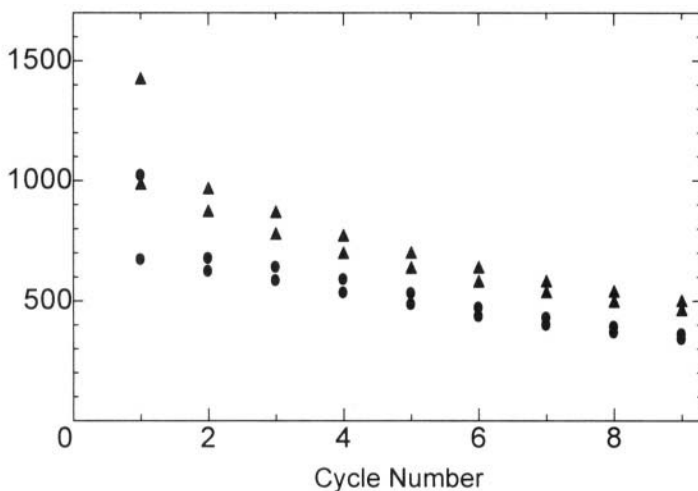
Figure 16. Capacity density against cycle numbers for Li |$Mn_{1-x}Mo_{2x}V_{2(1-x)}O_6$ (x=0($\bullet$) and x=0.4($\blacktriangle$)) cells.

2.4   Summary

Brannerite type MnV_2O_6 and $Mn_xMo_{1-x}V_{2(1-x)}O_6$ were prepared by polymer gellation method and conventional solid-state reaction. Although amorphization was occurred during the fist lithiation of these materials with relatively large irreversible capacity, these materials showed large reversible capacity at relatively low voltage in subsequent cycles. Since these materials show moderate capacity degradation with cycling, it needs intensive further investigation to understand the lithium intercalation mechanism underlying it so as to improve cycle life to make it a commercially available material.

3.0   ANODE PROPERTIES OF $MnMoO_4$

3.1   *Crystal Structure of $MMoO_4$*

Transition metal molybdates $MMoO_4$ (M=transition metals) have been focused on their catalytic activities and magnetic properties. The $MMoO_4$ takes three kinds of structures; α-$MnMoO_4$, α-$CoMoO_4$ and $NiWO_4$ type, and each molybdate can form several polymorphs depending on temperature and pressure. For example, $MgMoO_4$ and $MnMoO_4$ form α-$MnMoO_4$ structure [27], while $FeMoO_4$, $CoMoO_4$ and $NiMoO_4$ form α-$CoMoO_4$ structure [28]. However, $FeMoO_4$, $CoMoO_4$ and $NiMoO_4$ transform to α-$MnMoO_4$ structure at high temperature [29]. Moreover, all these molybdates transform to $NiWO_4$ structure at high pressure [30].

The crystal structure of α-$MnMoO_4$ has been reported by Abrahams *et al.* [27] α-$MnMoO_4$ belongs to monoclinic with space group C2/m, and its lattice parameters are a=10.469Å, b=9.516Å, c=7.143Å, β=106.3°. A shown Figure 17, Mn atoms are octahedrally coordinated by oxygen atoms while Mo atoms are tetrahedrally coordinated in this α-$MnMoO_4$ structure. Two crystallographically independent Mn atoms are surrounded by six oxygen atoms with large distortion. The average distances for each Mn-O bonding are 2.166Å and 2.162Å, respectively. The distance of Mn-O bonding changes from 2.091Å to 2.252Å. Two crystallographically independent. Mo atoms are surrounded by slightly distorted oxygen tetrahedral, with Mo-O distances ranging from 1.724Å to 1.85lÅ, the average being 1.76lÅ.

In order to compare α-$MnMoO_4$ structure [27] with other molybdates, α-$CoMoO_4$ structure [28] is shown in Figure 18. The α-$CoMoO_4$ structure also belongs to monoclinic with space group C2/m, and the general arrangement of metal atoms in the two structures is the same. However the position of the oxygen atoms considerably changes as following manner. In α-$CoMoO_4$, the Mo atoms locate at highly distorted octahedral positions in contrast to tetrahedral positions in α-$MnMoO_4$ structure. As Smith *et al.* [28] pointed out, each of the two crystallographycally independent Mo atoms is displaced by about 0.4Å from the center of its octahedron. The Mo-O distances range from about 1.72Å to 2.33Å. The average Mo-O distances are 1.991Å and 1.992Å in the two octahedral in $CoMoO_4$. The distorted octahedral radius of Mo is thus about 0.23Å greater than the tetrahedral value. Slight *et al.* [29] have reported that the molybdates with α-$CoMoO_4$ structure are 6% denser than the corresponding ones with α-$MnMoO_4$ structure. The occurrence of tetrahedral or octahedral Mo in $AMoO_4$ molybdates would thus appear to depend on the size and electronegativity of the A cations. Since the two of most electronegative cations are Mg and Mn in the series of Mg and the first transition metals

that form $AMoO_4$ compounds, Mg and Mn molybdates are the only materials that from α-$MnMoO_4$ structure with tetrahedral molybdenum at high temperature under atmospheric pressure. $MnMoO_4$ has the largest unit cell volume in the molybdates that form α-$MnMoO_4$ structure.
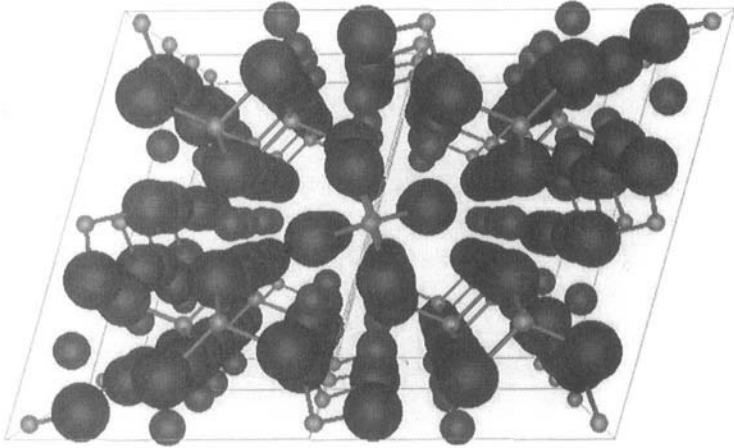
Figure 17. Schematic figure of crystal structure for α-MnMoO$_4$ structure.
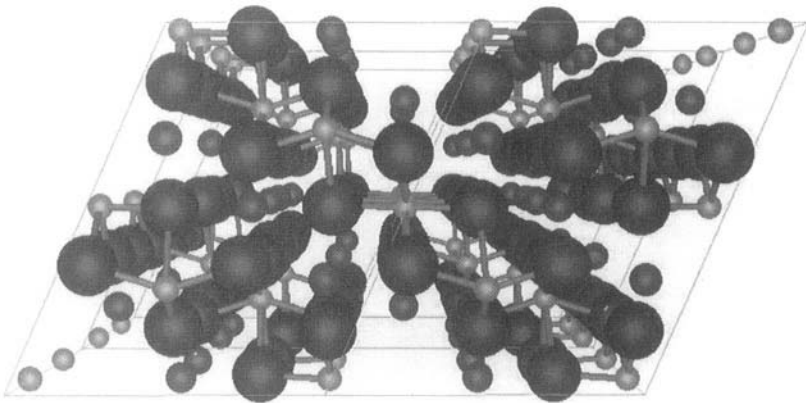
Figure 18. Schematic figure of crystal structure for α-CoMoO$_4$ structure.

3.2   Experimental

MnMoO$_4$ powder was prepared by solid state reaction. Starting material used were **MnCO$_3$** (99.9%, Soekawa chemicals) and **MoO$_3$** (99.9%, Soekawa chemicals). These reagents at stoichiometric ratio were mixed in agate mortar and heated at 600°C for 24, 72 and 264h in air. The phase identification of the prepared samples was carried out by powder X-ray diffractiometry using Rigaku RINT2500V with **CuKα** radiation. The samples for the electrochemical measurement were prepared by mixing crystalline **MnMoO$_4$,** acetylene black (conductive agent) and PTFE binder with 50:40:5 at weight ratio and pressed into a film. A sample electrode with a disk form was cut from the film. Cells were fabricated by coupling this disk as working electrode with lithium foil of same area as counter electrode. 1M **LiClO$_4$** dissolved in ethylene carbonate (EC) / diethyl carbonate (DEC) was used as the electrolyte as received from Tomiyama Pure Chem. Ind. The electrochemical measurements were carried out galvanostatically at various current densities. The cutoff voltage was set at 0.0 and 2.0V vs. **Li/Li$^+$**. To estimate valence state of the individual atoms in **MnMoO$_4$,** Mo **L$_{23}$-edge,** Mn **L$_{23}$-edge** and O K-edge XANES spectra were obtained at BL7A and BL8B1 beam line at UVSOR.

3.3   Results and Discussion

3.3.1   Synthesis and Characterization

The phase identification of the prepared powder was carried out by X-ray diffractometry. Figure 19 shows the measured powder diffraction profile for **MnMoO$_4$**. The well defined peak obtained confirms that the synthesized compound is **MnMoO$_4$** without any impurity phases even 24h heating. The obtained peaks shows exact match with the JCPDS data (card number 27-1280), which is known as **α-MnMoO$_4$** structure [27]. As already shown in above section, the Mn ion locates at octahedral site and the Mo ion at tetrahedral site in this **α-MnMoO$_4$** structure.

Mn and Mo XANES measurements for the synthesized powder were carried out to investigate the oxidation states of Mn and Mo. The obtained peaks are shown in Figure 20 with various reference materials at several oxidation states. The Mn L-edge XANES shows two strong absorption features due to the spin-orbit splitting of the Mn $2p$ core hole. The absorption peaks at about 640-645eV in Figure 16 show the $2p_{3/2}$ **(L$_3$)** edge. In Figure 20(a), the edge of the spectra for **MnMoO$_4$** is well coincident with that for **MnCO$_3$**. Accordingly, the Mn exists as **Mn^{2+}** in **MnMoO$_4$**. MoL-edge XANES spectra of **MnMoO$_4$** and **MoO$_3$** presented in Figure 20(b) illustrate that the valence of Mo in **MnMoO$_4$** is +6. The oxidation states derived from the XANES spectra and the well-defined XRD pattern obtained for the prepared sample confirm that the compound is completely stoichiometric

$MnMoO_4$. Furthermore, the spectra of Mo L-edge XANES of $MnMoO_4$ and MoO_3 show two separated peaks, which indicate the transition from the $2p$ core level to the empty $4d$ orbital. Generally, in octahedrally coordinated metals, the d orbitals are split into triply degenerate t_{2g} and doubly degenerate e_g orbitals. The electrons in e_g orbitals are repelled more strongly by the negative charge since electrons are located along the bonding axes than those of t_{2g} orbitals that point between axes. Thus the t_{2g} orbitals lie lower in energy than the orbitals. Whereas in tetrahedral coordination, triply degenerate t_2 orbitals lie higher in energy than doubly degenerate e orbitals. The Mo atoms in MoO_3 are in an octahedral environmental and Fig.20(b) indicates the typical $4d$ split into two sets of e_g and t_{2g} symmetry. On the other hand, the Mo atoms in $MnMoO_4$ are in a tetrahedral environment and Fig.20(b) shows ligand field splitting parameter is about 1.6eV. The difference in d orbital splitting for tetrahedral and octahedral coordinations has been reported for several molybdates previously [31].
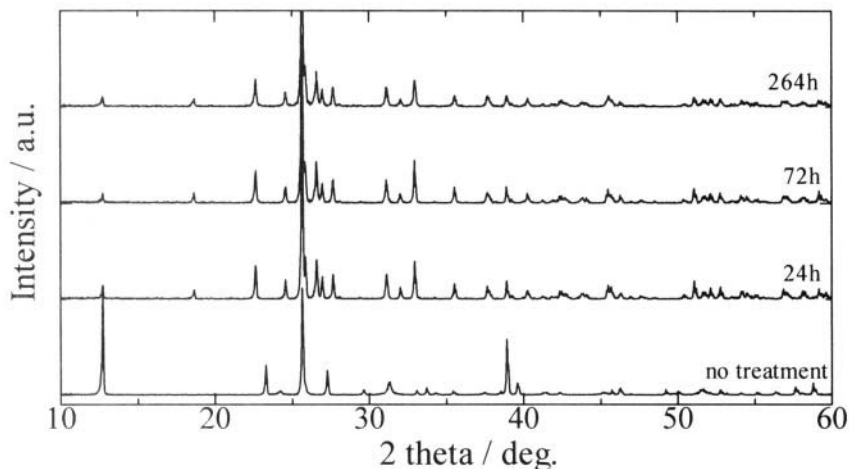
Figure 19. The XRD patterns for $MnMoO_4$ prepared at 600°C for 24, 72 and 264h.

3.3.2   *Electrochemical Properties*

In order to obtain charge-discharge profile of $MnMoO_4$, the cell was subjected to several cycles at constant current mode. The charge-discharge profiles obtained are depicted in Figure 21. The initial charge capacity was about 1800 mAh·g^{-1} and the reversible capacity in consequent discharge process was around 1000 mAh·g^{-1}. During the first charge, the lithium intercalation process exhibited a plateau around 0.8 V vs. Li/Li^+, which is not observed in the following cycles. The X-ray diffraction patterns obtained for the fresh electrode as well as for the electrode charged up to different cut-off voltages are shown in Figure 22. The principal peaks gradually decreased with lithiation and the peaks disappeared completely at 0.29 V vs. Li/Li^+. When the

discharged electrodes were charged again, we could not observe the crystalline peaks, suggesting that an irreversible phase transformation into amorphous lithiated material occurred during the first lithium insertion. This phenomenon of amorphization during the first lithiation was reported previously in several vanadates and molybdates [3,6,32]. The difference between the first charge profile and the second charge curves is also indicative of the two different mechanisms operating in the lithium insertion process. Furthermore, a series of new Bragg peaks appeared between 0.5 and 0.25 V during the first lithiation and disappeared at full lithiated electrode. The XRD patterns of electrode between 0.5 and 0.25 V together with the Bragg peak of NaCl-type compound VO are shown in Figure 23. Although these peaks were too broad to be identified exactly, it was enough to assume that the amorphization process of **MnMoO$_4$** has an intermediate state of Nad-type structure that has equal amounts of anion and cation by the appearance of new peaks of NaCl-type compound. The lattice constant calculated from the new Bragg peaks of NaCl-type compound observed at 0.29 V was 4.30 Å and this value agrees fairly with the theoretical lattice constant of **Li$_2$MnMoO$_4$** (4.27 Å) which was calculated by using the ionic radii of Shannon [33]. The similar behaviour of vanadium redistribution with lithiation was observed in vanadate or molybdenum substituted vanadate, which was prepared by electrochemical or chemical methods [34].
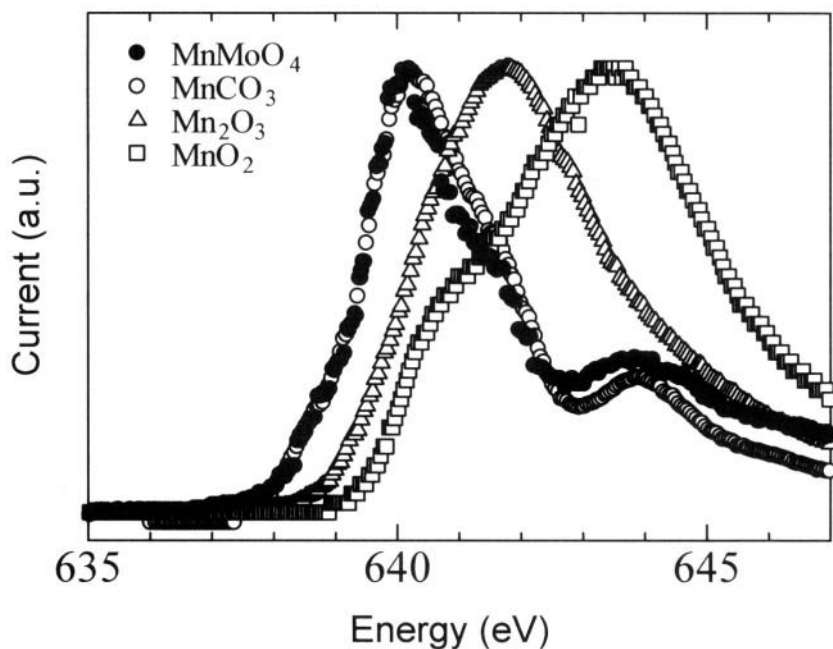
Figure 20(a). Mn L_{III} edge XANES spectrum of MnMoO$_4$ and various Mn compounds as reference.
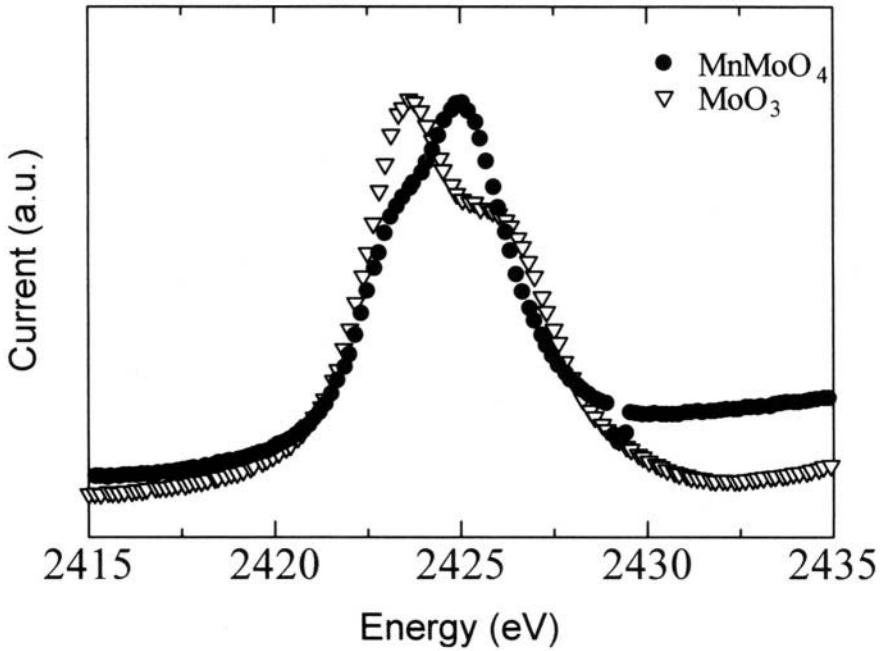
Figure 20(b). Mo L_{III} edge XANES spectrum of MnMoO$_4$ and MoO$_3$.
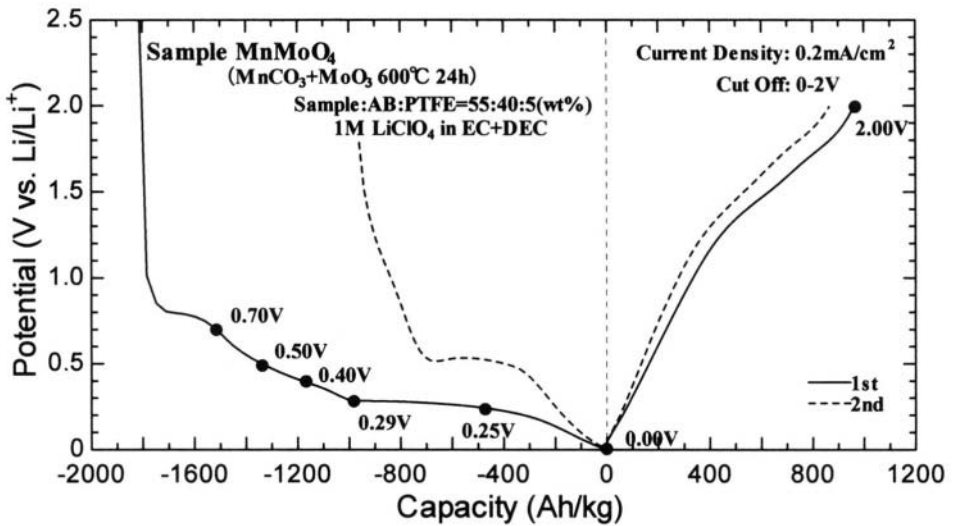
Figure 21. Charge-discharge curves for a Li|MnMoO$_4$ cell. The point represents the potential that measured the XRD of the electrode.
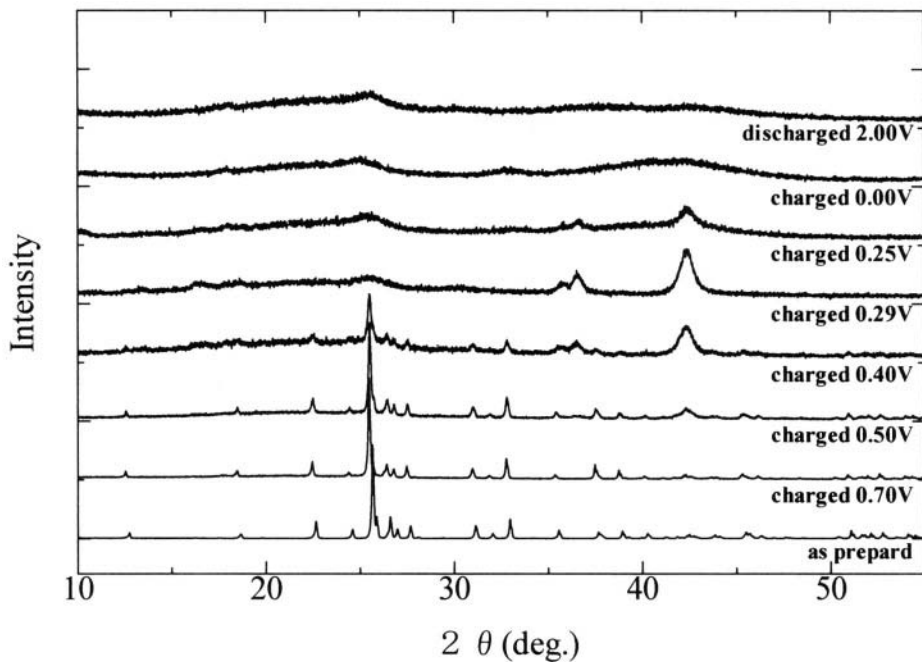
Figure 22. XRD patterns of the MnMoO4 electrode at various potentials.
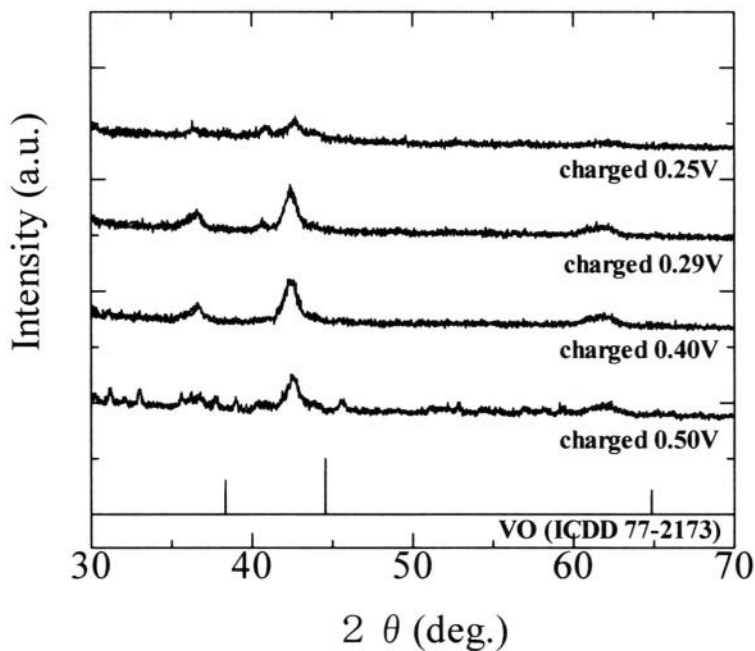
Figure 23. XRD patterns of MnMoO₄ electrode at several discharge voltages compared with VO.

The Mo L-edge XANES spectra variation during the first Li insertion and Li removal process is shown in Figure 24(a) and (b), respectively. The lines represent the energy positions of Mo^{6+} and Mo^{0}, which were determined by the measurements of Mo L-edge XANES spectrum of MoO_3 in this work and metallic Mo in previous report [35], respectively. Figure 24(a) shows that peak shift of Mo^{6+} to reduced state with lithium insertion into $MnMoO_4$ and Figure 24(b) shows re-oxidation of Mo to +4 at 2.0 V vs. Li/Li^+ during the lithium removal process. In Figure 24(a), we can observe that the valence of Mo is +5 in the spectrum at 0.8 V and the separated peak shape is not changed, though it is not enough to conclude that Mo remained in tetrahedral coordination. Furthermore, this result consists of XRD patterns up to 0.7 V during lithium insertion, which does not show amorphization as mentioned above (in Figure 22). Considering the disappearance of peak separation at 0.6 V during Li insertion, it implies crystal structure transformation to amorphous. In addition to the structural transformation, multiplets of electronic structure can also be assumed for the disappearance of peak separation. In the case of low oxidation number of Mo, $4d$ orbitals after electron promotion by X-ray absorption have more than two electrons. Therefore, the $4d$ orbitals should be multiplied by the electron-electron repulsion integrals. The valence change of Mo in $MnMoO_4$ with lithium insertion by the Mo L-edge XANES measurement is presented in Figure 25. We assumed that Mo was reduced from +6 to +1 or +2 at full lithiation and oxidized to +4 by removal of lithium according to the results of Mo L-edge XANES. Notice that the presented potentials which show measuring points of XANES in Figure 25 are not open circuit voltage (OCV). Therefore, there is a difference in the valence of Mo between Li insertion and removal, since these potentials ignore the overpotential.

The valence change in Mo is not enough to explain the capacity of $MnMoO_4$. Furthermore, the state of Mn more reduced than Mn^{2+} is difficult to imagine. Thus, it is conceivable that there is the contribution of oxygen besides the reduction of molybdenum during lithium insertion. Previously, the role of anions in the lithium insertion/removal process was suggested in anode materials such as nitride [36] or vanadium oxide material [3]. The N K-edge EELS study, whose spectra are essentially the same as XANES, on the new anode material $Li_{2.6}Co_{0.4}N$ have showed that the lithium extraction decreases the occupancy of the nitrogen $2p$ orbitals [37]. This means that nitrogen orbitals besides those of Co play an important role in keeping the charge balance. Accordingly, it can be expected that there are similar anion contributions to charge compensation for our material.
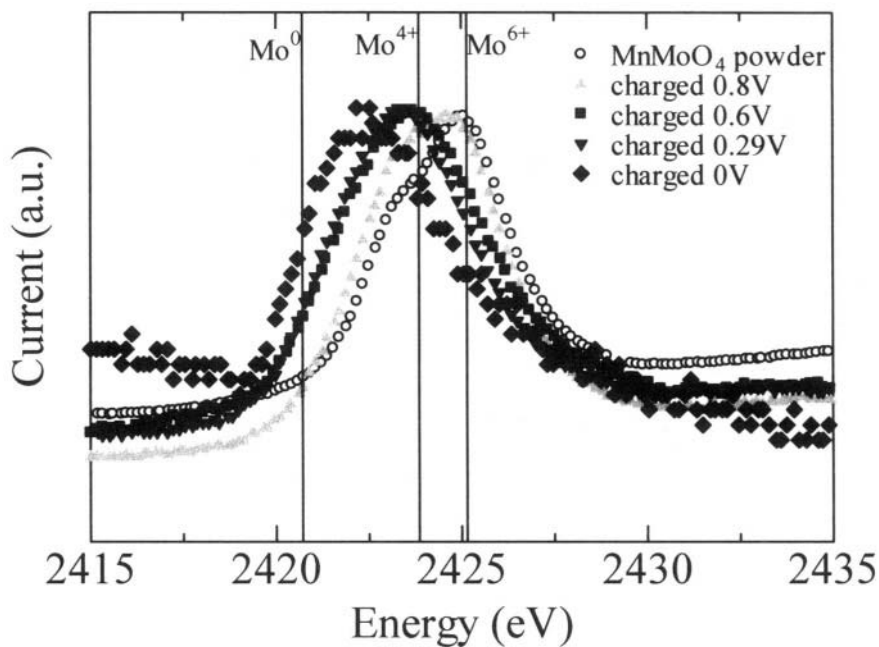
Figure 24(a). Mo L_{III} edge XANES of MnMoO$_4$ electrode during the first lithium insertion.
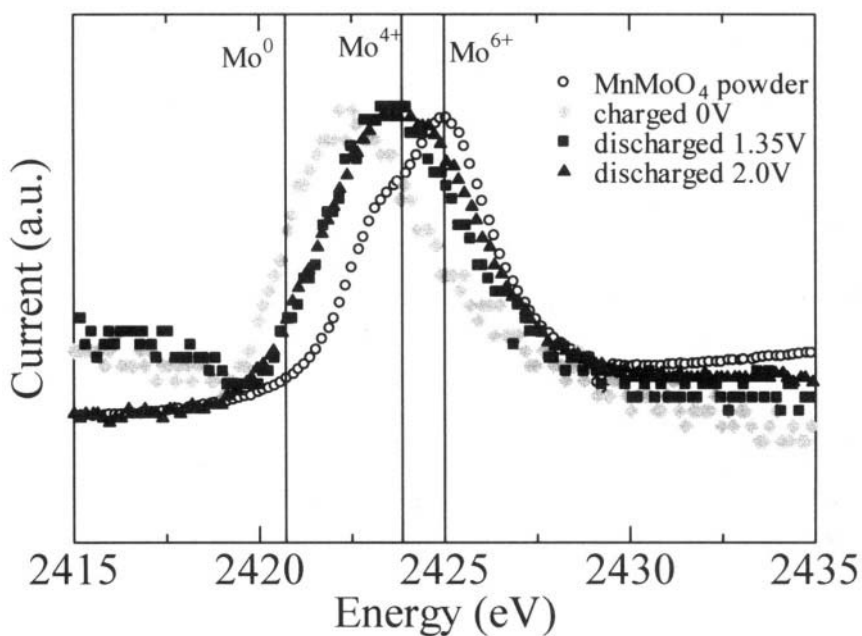
Figure 24(b) Mo L_{III} edge XANES of MnMoO$_4$ electrode during the first lithium removal.
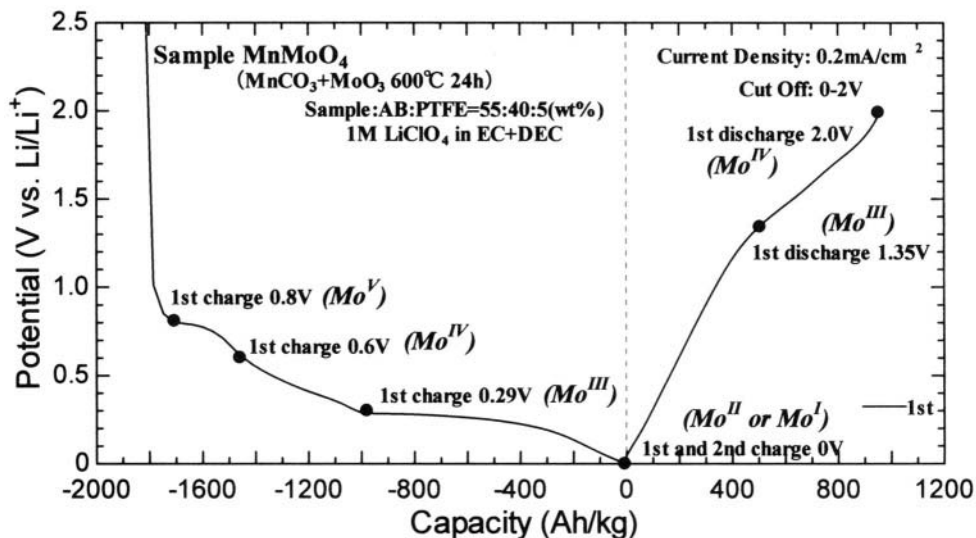
Figure 25. Variation of valence of Mo in MnMoO₄.

To investigate the role of oxygen, O K-edge XANES was measured (Figure 26). We could observe two peaks around 530 eV (o) which can be attributed to transition to the unoccupied band derived from the mixing of the Mo $4d$ with oxygen $2p$ states [38] and a broad peak around 535-545 eV (●) which can be assigned to that which originated from the mixing of the Mo $5sp$ or Mn $4sp$ with O $2p$ orbital, respectively. The peak with a high energy side is broad, so that the peak is difficult to be divided into two characters (Mo $5sp$ and Mn $4sp$). The peak splitting at 530 eV can be explained by the hybridization of tetrahedral-coordinated Mo e orbital and t_2 orbital with O $2p$ orbital and the gap of these peaks was 1.5 eV, which shows fair agreement with the result of the splitting gap (1.6 eV) of Mo e and Mo t_2 orbital in Mo L-edge XANES shown in Figure 20(b). Rodriguez *et al.* [38] have also reported consistent results on NiMoO₄ that has the same structure as α-MnMoO₄. This indicates that the Mo $4d$ band strongly hybridized with the oxygen $2p$ band, *i.e.,* Mo-O bond has strong covalent character. This result implies that there is contribution of oxygen, as previously suggested by Denis [3] and Poizot [39] through the hybridization of Mo $4d$ and O $2p$ orbitals during lithium insertion. Consequently, it can be thought that the reduction also occurs in oxygen $2p$ orbital and that the oxidation by lithium removal partly takes place using oxygen $2p$ orbital as well as Mo $4d$ orbital.
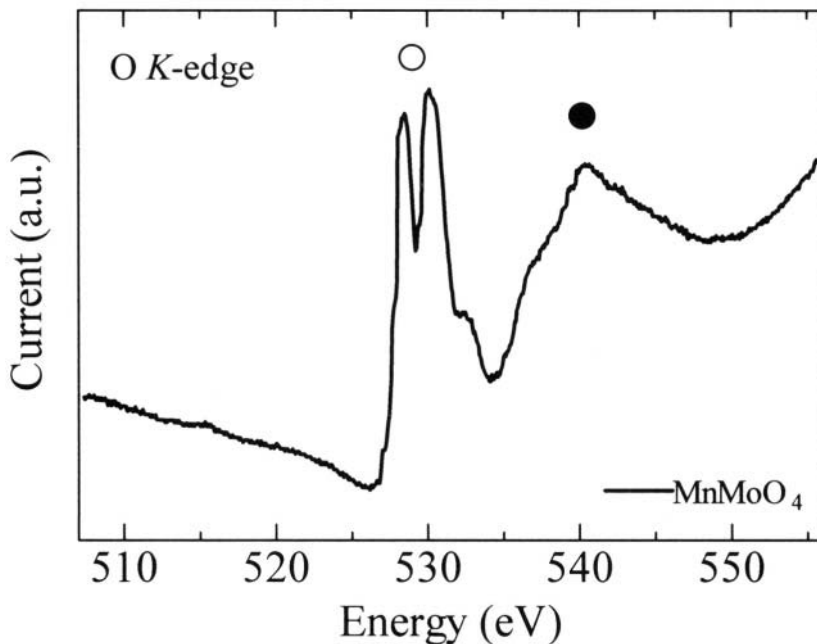
Figure 26. O *K*-edge XANES of MnMoO₄.

3.4   *Summary*

We reported the electrochemical properties of **MnMoO₄** as a new type of anode material for lithium secondary battery. This high capacity anode, realized during the first lithiation (1800 mAh·g⁻¹) and in the subsequent lithiation (1000 mAh·g⁻¹), could be attributed to the oxygen contribution to lithium insertion by the accommodation of electrons in the hybridization orbital. During the first lithiation, amorphization, which has an intermediate state of NaCl structure, was observed in XRD measurement of the electrode. The valence of Mo and Mn in **MnMoO₄** measured by XANES was +6 and +2, respectively. The valence of Mo during lithium insertion/removal investigated by XANES is not enough to explain the Li amount that is inserted and removed into/from this material. Through the O K-edge XANES measurement, we can observe the role of the anion to charge compensation in the electrochemical Li insertion/removal. Although this anode material delivers high capacity, it exhibits large irreversibility and amorphization at the first cycle. It needs further intensive investigation to understand the lithium insertion mechanisms underlying it, so as to improve cycle life to make it a commercially available material.

4.0   CONCLUSIONS

In this chapter, we summarized the synthesis procedure and the electrochemical properties of MnV_2O_6, $Mn_{1-x}Mo_{2x}V_{2(1-x)}O_6$ and $MnMoO_4$ as anode materials for Li-Ion batteries. The initial discharge capacity exceeds $800 \ mAh \cdot g^{-1}$ for all the synthesized compounds. These large charge-discharge capacities would be appeared mainly by the charge variation of vanadium or molybdenum ion. In addition, the role of oxide ion is important for the compensation of the total charge of compounds through the intercalation of lithium ion from the interpretation of the results of NMR and XANES measurements. We proceed with the investigation of other anode materials related to these compounds in order to elucidate the origin of the large capacity at relatively low voltage in the vanadates and molybdates.

5.0   ACKNOWLEDGEMENTS

6.0   REFERENCES

1.   Y. Idota, T. Kubota, A. Matsufuji, Y. Mekawa, T. Miyasaka, *Science,* **276**, 1395, 1997.
2.   P. Poizot, S. Laruelle, S. Grugeon, L. Dupont, J.-M. Tarascon, *Nature,* **407**, 469, 2000.
3.   Y. Piffard, F. Leroux, D. Guyomard, J.-L. Mansot and M. Tournoux, *J. Power Sources*, **68**, 698, 1997.
4.   S. Denis, E. Baudrin, M. Touboul and J.-M. Tarascon, *J. Electrochem. Soc.,* **144**, 4099, 1997.
5.   J. J. Auborn, Y. L. Baberio, *J. Electrochem. Soc.,* **134**, 638, 1987.
6.   S.-S. Kim, H. Ikuta, M. Wakihara, *Solid State Ionics,* **139**, 57, 2001.
7.   S.-S. Kim, S. Ogura, H. Ikuta, Y. Uchimoto, M. Wakihara, *Chem. Lett.,* 760-761, 2001.
8.   S.-S. Kim, S. Ogura, H. Ikuta, Y. Uchimoto, M. Wakihara, *Solid State Ionics,* in press
9.   R. Ruh and A. D. Wadsley, *Acta Cryst.,* **21**, 974, 1966.
10.   M. Quarton, J. Angenault, A. Rimsky, *Acta Cryst.,* **B29**, 567, 1973.
11.   J. Angenault, *Rev. Chim. Minerale,* **7**, 651, 1970.
12.   J. C. Bouloux, J. Galy, *Bull. Soc. Chim. France,* 736, 1969.
13.   H. Hg, C. Calvo, *Canad. J. Chem.,* **50**, 3619, 1972.
14.   M. Gondrand, A. Collomb, J.C. Joubert, R. D. Shannon, *J. Solid State Chem.,* **11**, 1974.
15.   R. Kozlowski, J. Ziolkowski, K. Mocala, J. Haber, *J. Solid State Chem.,* **35**, 1980.

16. Y.-K.Sun, I.-H.Oh, S.-A.Hong, *J. Mat. Sci.,* **31**,3617, 1996.
17. H.-J. Kweon, S.S. Kim, G.B. Kim and D.G. Park, *J. Mat. Sci. Lett.,* **17**,1697, 1998.
18. D. Guyomard, C. Sigala, A. Le Gal La Salle, Y. Pffard, *J. Power Sources,* **68,**692, 1997.
19. Y. Takeda, R. Kanno, M. Noda and O. Yamamoto, *Mater. Res. Bull.,* **20**, 71, 1985.
20. K. Tatsumi, T. Akai, T. Imamura, K. Zaghib, N. Iwashita, S. Higuchi and Y. Sawada, *J. Electrochem. Soc.,* **143**, 1923, 1996.
21. N. Takami, A. Satoh, T. Ohsaki and M. Kanda, *Electrochim. Acta,* **42**, 2537, 1997.
22. Y.Dai, Y. Wang, V. Eshkenazi, E. Peled and S.G. Greenbaum, *Electrochim. Acta,* 145, 1179, 1998.
23. A. Mabuchi, K. Tokumitsu, H. Fujimoto and T. Kasuh, *J. Electrochem. Soc.,* **142**, 1041, 1995.
24. K. Sato, M. Noguchi, A. Demachi, N. Oki, M. Endo, *Science,* **264**, 556, 1994.
25. M. Hara, A. Satoh, N. Takami, T. Ohsaki, *J. Phys. Chem.,* **99**, 16338, 1995.
26. M. Nagayama, T. Morita, H. Ikuta, M. Wakihara, M. Takano, S. Kawasaki, *Solid State Ionics,* **106**, 33, 1998.
27. S. C. Abrahams, J. M. Reddy, *J. Chem. Phys.,* **43**, 2533, 1965.
28. G. W. Smith, J. A. Ibers, *Acta Cryst*., **19**, 269, 1965.
29. A. W. Sleight, B. L. Chamberland, *Inorg. Chem.,* **7**, 1673, 1968.
30. A. P. Young, C. M. Schwarts, *Science,* **141**, 348, 1963.
31. J.A. Rodriguez, J.C. Hanson, S. Chaturvedi, A. Maiti, J.L.Brito, *J. Phys. Chem.,* **B 104**, 8145, 2000.
32. F. Leroux, G.R. Goward, W.P. Power, L.F. Nazar, *Electrochem. Solid-State Lett.,* **1**, 255, 1998.
33. R.D. Shannon, *Acta Cryst.,* **A 32**, 751, 1976.
34. C. Delmas, *Lithium Batteries;* G. Pistoia (Ed.), Chap.12, p.475, 1994.
35. F.F. Ferreira, T.G.S. Cruz, M.C.A. Fantiti, M.H. Tabacniks, S.C. Castro, J. Morais, A. Siervo, R. Landers, A. Gorenstein, *Solid State Ionics,* **136-137**, 357, 2000.
36. T. Shodai, Y. Sakurai, T. Suzuki, *Solid State Ionics,* **85**, 122, 1999.
37. S. Suzuki, T. Shodai, J. Yamaki, *J. Phys. Chem. Solids,* **59**, 331, 1998.
38. J.A. Rodriguez, J.C. Hanson, S. Chaturvedi, A. Maiti, J.L.Brito, *J. Chem. Phys.,* **112**, 935, 2000.
39. P. Poizot, E. Baudrin, S. Laruelle, L. Dupont, M. Touboul, J.-M.Tarascon, *Solid State Ionics,* **138**, 31, 2000.

4

Oxide Cathodes

John B.Goodenough
Texas Materials Institute, ETC 9.102
University of Texas at Austin
Austin, Texas
USA

1.0   INTRODUCTION

Before 1970, commercial batteries used aqueous electrolytes, which have a small "window" $E_g \approx 1.23$ eV between the H^+/H_2 LUMO and the O_2/H_2O or O_2/OH^- HOMO Although the lead-acid battery has a $V_{oc} = 2$ V because of slow reaction kinetics between the electrodes and the electrolyte, it is not thermodynamically stable and has a poor shelf life in both the charged and discharged state. Therefore, the discovery [1] of fast Na^+-ion conduction in the β-aluminas and the invention [2] of the Na/S battery at the Ford Motor Company in 1967 stimulated a world-wide interest in the development of rechargeable alkali-ion batteries operating with a non-aqueous electrolyte.

If fast alkali-ion conduction can occur in a solid electrolyte, it can also occur in a solid with an electronically conducting framework containing transition-metal ions in a mixed-valent state. Insertion of "guest" alkali ions into such a "host" framework would reduce the framework; extraction of the guest ions would oxidize the framework. If these reactions do not change the structure over a large solid-solution range of the guest species, the mixed electronic-ionic conductor is known as an insertion compound and is a candidate electrode material. This concept had been illustrated by the layered $NiO_{1-x}(OH)_{1+x}$ cathode and the metal-hydride (MeH_x) anode of a Ni/MeH_x battery; it was applied by Whittingham and Huggins [3] who used the 1D tunnel framework of hexagonal tungsten bronze with Na^+ ions in the tunnels, *i.e.* hexagonal Na_xWO_3, as a non-blocking electrode for testing Na^+-ion transport in solid Na^+-ion electrolytes. However, to be useful as an electrode of a battery, the redox energy of the host transition-metal ion should be matched to the "window" of the electrolyte so as to allow a maximum V_{oc}.

A number of groups, led first by Whittingham (first at Stanford and then at Exxon) proposed and investigated the use of TiS_2 as a cathode in lithium batteries. Whittingham demonstrated fast Li insertion at room temperature into the empty octahedral sites of the layered TiS_2 cathode host at *ca.* 2 V vs. Lithium over the solid-solution range $0 < x < 1$ [4]. The TiS_2/Li battery is thermodynamically stable and has a voltage-composition (V-x) curve for Li_xTiS_2 that is described by the Nernst equation

$$V = V^\circ - (RT/F)\ln\left[x/(1-x)\right] \qquad (1)$$

with $V^\circ \approx 2$ V. The increase in overpotential $\eta(I)$ with current I is not excessive, but the capacity of the electrode (*i.e.* the maximum x before the cathode becomes diffusion-limited) decreases noticeably with increasing current I. This is a reversible capacity loss reflecting the relatively low mobility of the Li in the cathode material. In order for the Li^+ ions to enter the Van der Waals gap where their charge is compensated by electrons from the external circuit that reduce the host TiS_2 layers, the Van der Waals S-S bonds must be broken to be replaced by Li-S bonds; at the front between Li-rich and Li-vacant galleries, there is a strain associated with prizing apart the gap and the mobility of the front is slowed. Nevertheless, the concept of a Li-insertion compound as a battery electrode was established. However, the $Li//TiS_2$ battery encountered safety problems; formation of a passivating layer on the Lithium anode can result in dendrite formation on recharge.

From this experience, it became clear that the anode must also be an insertion compound having a lower Fermi energy (ε_F) than that of Lithium, which would reduce the voltage of a cell with a TiS_2 cathode. This realization motivated a search for a Li-insertion cathode material having a lower Fermi energy than that of TiS_2.

A number of studies were made on other layered disulfides not only in an attempt to lower ε_F, but also because they exhibited other properties of interest such as the stabilization of charge density waves below an insulator-metal transition. However, the Ti^{4+}/Ti^{3+} redox energy lies just above the top of the $S^{2-}:3p^6$ bands. It follows that attempts to lower ε_F significantly is frustrated by an inability to lower it below the top of the $S^{2-}:3p^6$ bands at E_V; either the operative redox couple becomes pinned at E_V or it falls so far below E_V that ε_F lies in states of primarily sulfur character and the holes in the $S^{2-}:3p^6$ bands condense into S-S bonds to create disulfide ions $(S_2)^{2-}$. Redox-level pinning is an important concept in the design of Li-insertion cathodes.

Pinning of redox energies at the top of a primarily ionic anion p^6 band is illustrated in Figure 1 for an oxide. The O^-/O^{2-} redox energy lies above

the vacuum level; the affinity for the second electron is negative. The successive ionization energies for removing electrons from a transition-metal cation are all positive. Let E_I be the energy required to transfer the last electron from the cation to the O^-/O^{2-} level at infinite separation and E_M the electrostatic Madelung energy of an oxide containing transition-metal ions M^{3+}, as in a layered $LiMO_2$ oxide for example. The M^{3+}/M^{2+} and M^{4+}/M^{3+} redox energies of the free atom are separated by an electrostatic electron-electron coulomb energy U; this separation corresponds to the difference in the ionization energies for removal of the fourth and the third electron, respectively, from M. Conservation of energy causes the O^-/O^{2-} level to fall and the $M^{m+/(m-1)+}$ levels to rise in the crystalline fields created by bringing the ions together to form an ionic solid. In the example of Figure 1, an $E_M > E_{I1}$ raises the M^{3+}/M^{2+} level above the O^-/O^{2-} level, which stabilizes the valence state M^{3+} and O^{2-} in a point-charge model of the solid. However, the M^{4+}/M^{3+} level of our example is not raised above the O^-/O^{2-} level, so the energy gap between empty and filled states is between the O^{2-} level and the M^{3+} level. This Zaanen, Sawatzky, Allen [5] charge-transfer gap Δ is to be distinguished from the Hubbard gap U between the M^{3+}/M^{2+} and M^{4+}/M^{3+} couples in this point-charge model. But this model needs to be modified by the introduction of the covalent contribution to the bonding, *viz.* by the virtual electron transfer from the O^{2-} ions back to the M^{3+} ions that is treated in second-order perturbation theory. This charge transfer reduces U. It also lowers the effective charges on the ions, which reduces E_M; but the attendant lowering of E_M-E_I, is compensated by the lifting of the antibonding M^{3+}/M^{2+} redox couple and lowering of the bonding admixed O-2p states. On the other hand, covalent mixing of the O-2p and the M^{4+}/M^{3+} couple introduces antibonding states at the top of the $O^{2-}:2p^6$ bands that have the symmetry of the d orbitals of the M^{4+}/M^{3+} couple. The antibonding states of this covalent interaction reside at the top of the $O^{2-}:2p^6$ bands where they act like a pinned redox couple, but the ratio of O-2p to (O-2p + M-3d) character of these states increases sharply at the crossover from $E_M > E_{I2}$ to $E_M < E_{I2}$; and where $E_{I2}-E_M$ is large enough, oxidation of the host by removal of Li creates holes of largely O-2p character that may condense as pairs in O-O bonds to form peroxide ions $(O_2)^{2-}$. Formation of $(O_2)^{2-}$ may be followed by loss of O_2 and reduction of the host framework.

The situation for the sulfides is similar, but the top of the $S^{2-}:3p^6$ bands is higher in energy than that of the $O^{2-}:2p^6$ bands because the larger sulfide ion reduces E_M and the more negative electron affinity of the S^-/S^{2-} couple increases E_I. It follows from these considerations that to lower significantly the ε_F of a cathode from that of the Ti^{4+}/Ti^{3+} couple in TiS_2, it is necessary to go to a transition-metal oxide.
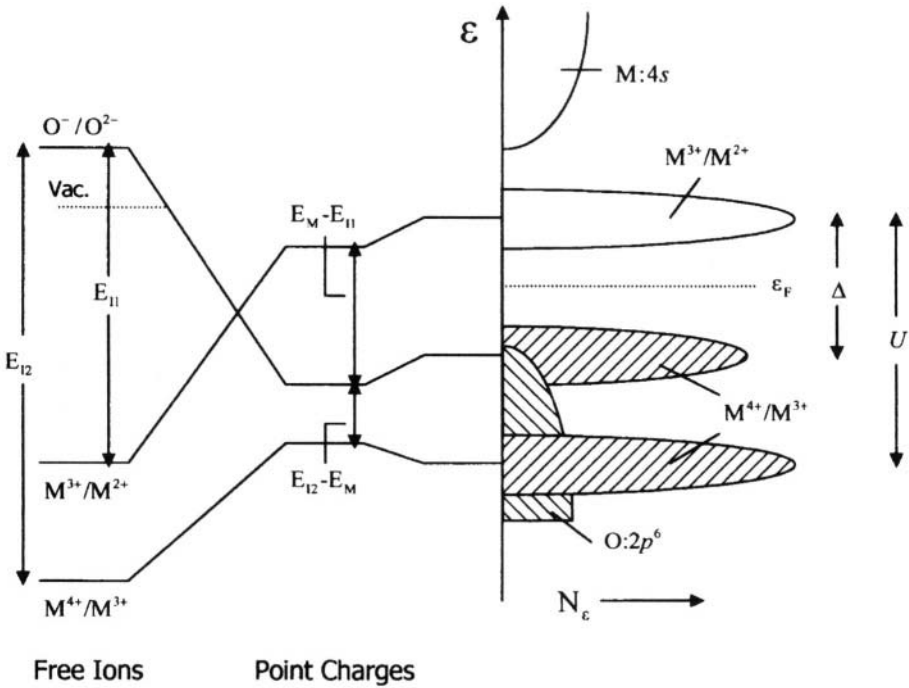
Figure 1. Illustration of pinning of an M^{4+}/M^{3+} redox couple at the top of the $O^{2-}:2p^6$ bands.

2.0   METAL OXIDES

2.1   *Layered Oxides*

In layered oxides, the coulombic repulsion between oxide-ion planes is greater than the Van der Waals bonding between them unless the transition-metal atom M forms a double bond to an apical oxygen perpendicular to the layers as in V_2O_5 or MoO_3. Consequently, layered MO_2 oxides do not exist. However, $LiMO_2$ oxides are layered; the oxide ions form a cubic-close-packed array with close-packed (111) octahedral-site planes alternately filled with Li^+ and M^{3+} ions, Figure 2. How much Li can be extracted from an $LiMO_2$ material before the M atoms move into the Li planes depends on the M atom. Displacement of a cation from one octahedral-site plane to another is via a tetrahedral site and extraction of Li from $LiMO_2$ places ε_F in the M^{4+}/M^{3+} redox couple. Therefore, both the M^{4+} and M^{3+} ions should have a strong octahedral-site preference, and the M^{4+}/M^{3+} couple should lie close to the top of the $O^{2-}:2p^6$ bands for a good cathode material. These considerations narrow the candidate M atoms to Cr, Ni, and Co since Cooperative Jahn-Teller distortions at the Mn^{3+} ions of $LiMnO_2$ give it a different structure. Moreover, the low energy required for

two Mn^{3+} ions to disproportionate into Mn^{4+} and Mn^{2+} provides Mn^{2+} with a tetrahedral-site stability to migrate to the Li-deficient Li layers. Similarly, the disproportionation $3\ Cr^{3+} + Cr^{6+}$, where the Cr^{6+} occupy tetrahedral sites, allows an irreversible structural change to occur on removal of a fraction of the Li. It was known [6] that it is difficult to prepare stoichiometric $LiNiO_2$, so $LiCoO_2$ was chosen for the initial experiment; it gave the open-circuit voltage curve of Figure 2 [7]. A similar curve, but with a little lower voltage vs. Lithium was obtained with $Li_{1-\delta-x}Ni_{1+\delta}O_2$ [8]. Once delithiation has been initiated, the Li^+-ion mobility in the oxides is higher than that in the sulfides since it is not necessary to prize apart the CoO_2 layers [9]. However, although Figure 2 shows that most of the Li can be extracted from $LiCoO_2$, only about half can be extracted reversibly; on removal of greater amounts of Li, voltages in excess of 4.2 V *vs* Lithium induce the evolution of oxygen [10] via the reaction

$$2Co^{4+} - O^{2-} = 2Co^{3+} - O^- = 2Co^{3+}(O_2)^{2-} = 2Co^{3+} + O_2 + 2e^- \tag{2}$$
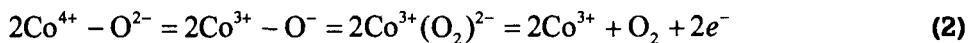
because of a large O-2p character of the holes.
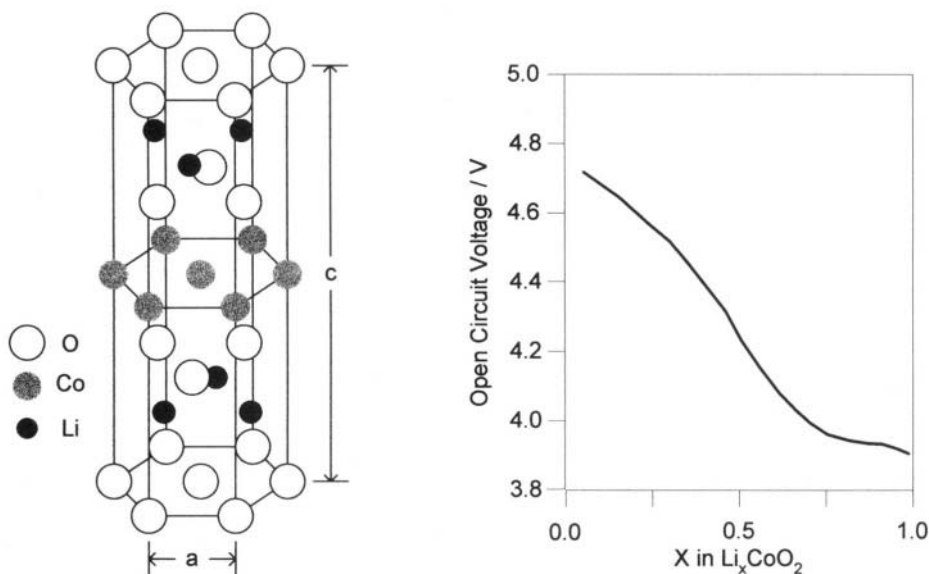
Figure 2. Initial V_{oc} *vs* x curve on charging for $Li_{1-x}CoO_2$.

In the case of $Li_{1-\delta}Ni_{1+\delta}O_2$, most of the Li can be extracted before oxygen loss occurs, but the NiO_2 layers slide with respect to one another to change the stacking of the oxygen layers from cubic (O3 referring to three octahedral-site sandwiches per unit cell) to hexagonal (O1) stacking of octahedral-site planes via planes of trigonal prismatic sites (P3) if more than about 0.7 Li

atoms per formula unit are removed [11, 12]. The origin of this difference in behavior is illustrated schematically in Figure 3. Both the low-spin Ni^{4+}/Ni^{3+} and Co^{4+}/Co^{3+} are pinned at the top of the $O^{2-}:2p^6$ bands, but the Ni^{4+}/Ni^{3+} couple lies a little above the Co^{4+}/Co^{3+} couple because the former corresponds to a **σ-bonding** couple of e-orbital parentage whereas the latter to a **π-bonding** couple of t-orbital parentage. The bonding **O-2p$_σ$** orbitals of the 90° Ni-O-Ni bridges are orthogonal to one another; the **π-bonding** t orbitals of neighboring Co of the CoO_2 array are not orthogonal, and a transition from polaronic to itinerant holes occurs in the CoO_2 array over the flat portion of the V-x curve of Figure 2 [13]. A flat V-x curve in the range **$0.07 \leq x \leq 0.25$** indicates, from the Gibbs phase rule, the existence of a two-phase region. A polaronic to itinerant electronic transition is normally first-order [14]. Although the reversible solid-solution range of $Li_{1-x}CoO_2$ is limited to **$0 \leq x \leq 0.5$**, it is nevertheless large enough to be useful.
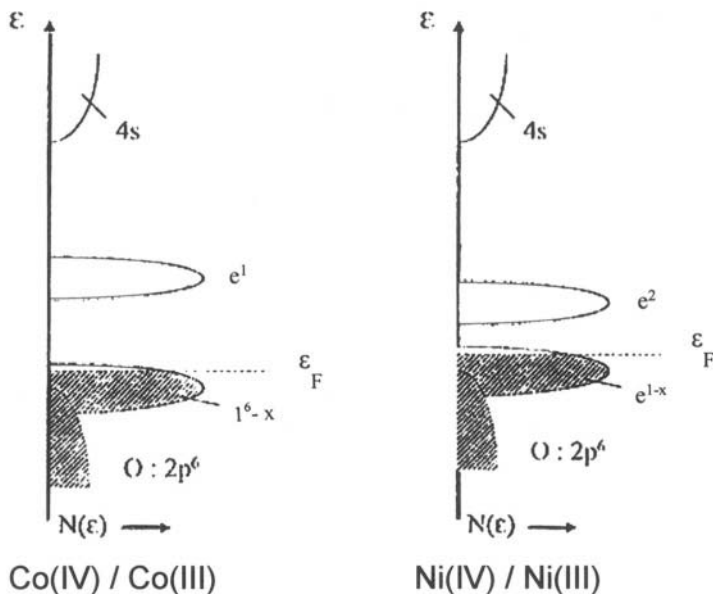
Figure 3. Schematic placement of Co(IV)/Co(III) and Ni(IV)/Ni(III) redox energies pinned at the top of the $O^{2-}:2p^6$ bands, which is isostructural with $NaFeO_2$.

In the early 1980s, no battery company in Britain or the U. S. would entertain beginning with a discharged cathode. Consequently earlier efforts with oxide cathodes had concentrated on Li insertion into vanadium oxides such as V_2O_5 and V_6O_{13}. With the exception of V_6O_{13}, the results were disappointing, V_6O_{13} accepts up to 1 Li/V if prepared with a stoichiometric V:O ratio, but the discharge curves exhibited a series of steps [15]. Workers in the SONY Corp. of Japan, on the other hand, had developed a graphite anode and realized the advantage of charging their anode from the discharged cathode. They have

commercialized with great success the $LiC_6/Li_{1-x}CoO_2$ battery [16]. Commercialization of the Li-ion battery has stimulated an extensive search for alternative cathode materials that contain a less expensive and environmentally more benign transition-metal atom than cobalt. At the present time, about 20% of the world's production of cobalt is used in Li-ion batteries.

Delmas and Saadonne [17-19] and Zhecheva and Stoyanova [20] pioneered investigation of $LiCo_{1-y}Ni_yO_2$ cathodes. The Delmas group has shown that $Li_{1-x}[Ni_{1-y}Co_y]O_2$ can be prepared with essentially no transition-metal ions in the interslab Li^+-ion galleries for $0.2 \leq y \leq 1.0$ [21] and that the extraction of Li from $Li_{1-x}[Ni_{0.8}Co_{0.2}]O_2$ is reversible over the range $0 \leq x \leq 0.6$ without long-range order of the Li^+ ions within the Li planes at x = 0.5 as occurs for $Li_{0.5}NiO_2$. In this cathode material, the Fermi energy remains located in the Ni^{4+}/Ni^{3+} couple and the discharge curve slopes monotonically over the range $4.0 V \leq V_{oc} \leq 3.5 V$ [22]. In $Li_{1-x}Ni_{0.1}Co_{0.9}O_2$, on the other hand, an increase of about 0.2 V occurs in the discharge curve on passing from the Ni^{4+}/Ni^{3+} to the Co^{4+}/Co^{3+} couple as anticipated from Figure 3 [23].

The lower cost and increased capacity of the $Li_{1-x}[Ni_{0.8}Co_{0.2}]O_2$ material would appear to make this oxide an attractive cathode candidate. However, these cathodes have two problems: the capacity fades on repeated cycling or holding in the charged state, especially at 60°C, and they generate flammable gases during charging that create safety problems [24,25]. The capacity fade is due to migration of Ni^{3+} ions into the interslab space on removal of Li^+ ions. The smaller Ni^{3+} ions bind the slabs together, thereby reducing the free volume between them and lowering the Li^+-ion mobility. This problem does not arise with $Li_{1-x}CoO_2$ because the Co atoms do not migrate to the Li layers. Substitution of a small amount of Mg^{2+} for Ni^{3+} results in a preferential transfer of the larger, more electropositive Mg^{2+} ions since Mg^{2+} moves easily into tetrahedral sites; the Mg^{2+} ions inhibit the collapse of the interstitial space on removal of Li and reduce fading of the capacity as is illustrated in Figure 4 [26]. The introduction of the larger Sr^{2+} ion directly into the Li layers with a Sr/Li mole ratio of only 10^{-8} increased the capacity of a $LiNi_{0.8}Co_{0.2}O_2$ cathode [27] and overcoating the surface of Sr-doped $LiNi_{0.9}Co_{0.1}O_2$ diminished substantially the probability of explosion of a cylindrical battery, but not sufficiently to meet safety standards [28].

Preparation of layered $LiMnO_2$ can be by ion exchange from $NaMnO_2$ [29] However, it transforms to a $Li_x[Mn_2]O_4$ spinel phase on cycling; the disproportionation reaction $2 Mn^{3+} = Mn^{4+} + Mn^{2+}$ with Mn^{2+} traversing the tetrahedral site to enter the Li planes plagues the $LiMn_{1-x}Ni_xO_2$ system with x < 0.5. However, $LiMn_{0.5}Ni_{0.5}O_2$ contains Ni^{2+} and Mn^{4+}; the strong octahedral-site preference of a Mn^{4+} ion prevents migration through a tetrahedral site to the partially occupied Li planes. On the other hand, $LiMn_{0.5}Ni_{0.5}O_2$ is stable to higher temperatures [30]; it contains Ni^{2+} and Mn^{4+} ions, each of which have a strong

octahedral-site preference. Moreover, the Ni^{3+}/Ni^{2+}, like the Ni^{4+}/Ni^{3+}, couple appears to be pinned near the top of the $O^{2-}:2p^6$ band in the presence of Mn^{4+} ions, which allows removal of at least 0.5 Li atoms per formula unit at a $V^o \approx 4.0$ V from the Ni^{3+}/Ni^{2+} redox energy [31]. However, the mixed-valent Ni^{3+}/Ni^{2+} electronic conductivity is polaronic and is further reduced by the relatively low concentration of Ni atoms, which is why the discharge curves of Figure 5 were taken at low current densities. Coating small $LiNi_{0.5}Mn_{0.5}O_2$ particles with amorphous carbon can improve the capacity at higher current densities; the carbon coat not only improves interparticle electronic contact, it also provides electron tunneling from the carbon coat into the bulk of the particle to provide charge balance for the inserted Li^+ ions [32].
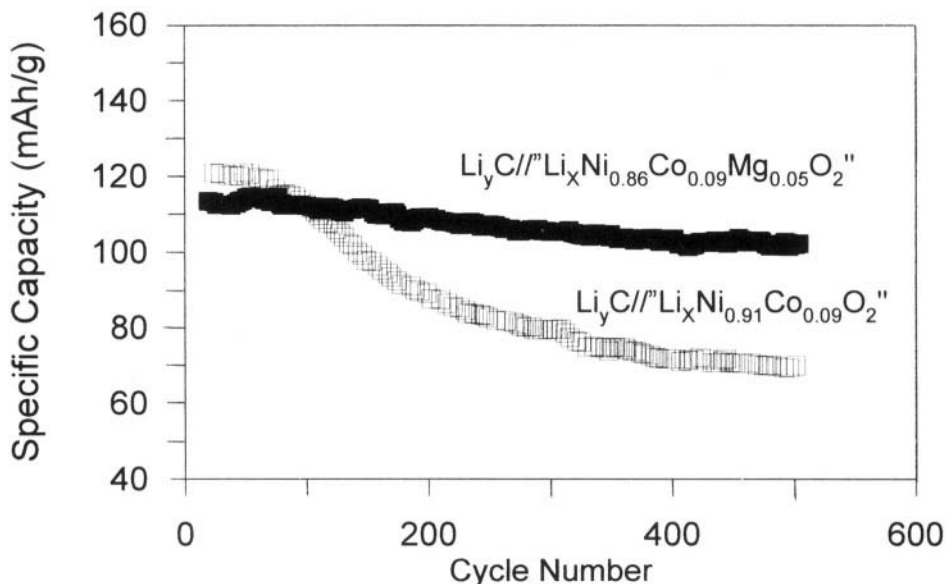
Figure 4. Evolution of the specific capacity recovered on discharge for $Li_{1-x}Ni_{0.91-y}Co_{0.09}Mg_yO_2$ (y = 0.00 and 0.05) cathodes over a 500-cycle test at C rate and 60° C. Reprinted from reference 26 with permission from Elsevier Science.

2.2   Spinels

Realization of reversible Li extraction from $LiCoO_2$ and of Li insertion into V_6O_{13} led to a search for oxide cathodes containing a cheaper and environmen- tally more benign transition-metal atom than cobalt. Moreover, the early search was governed by the prejudice of the battery community that initially Li should be inserted into, not extracted from, the cathode material. In 1981, Scrosati in Rome and Thackeray in South Africa were investigating Li insertion into magnetite, the spinel Fe_3O_4. Thackeray came to my laboratory in Oxford at that time, and I was surprised that one should attempt insertion of Li into the spinel structure of Figure 6 since it was known that the spinel structure does not

tolerate interstitial cations. As can be seen from Figure 6, Li would be inserted into the 16c octahedral sites where it would share two faces with cations at the tetrahedral 8a sites. The fact that Li can be inserted into Fe_3O_4 immediately told me that the inserted Li^+ ions must force the neighboring Fe^{3+} ions in 8a sites into the 16c sites also, thereby creating a cascade from 8a to 16c sites to give an ordered rock-salt structure. The cations in 16d octahedral sites and the oxide ions act as a spinel $[M_2]O_4$ host with a 3D interstitial space of 16c octahedral and 8a tetrahedral sites [33]. Therefore, I suggested to Thackeray that we should investigate Li insertion into the spinel $Li[Mn_2]O_4$ [34]. The V-x curve of $Li_{1+x}[Mn_2]O_4$, Figure 7, is flat over a wide solid-solution range $0 < x \le 0.8$ because of a first-order cubic-tetragonal structural change that is induced by a cooperative ordering of twofold-degenerate σ-bonding e orbitals on the Mn(III): t^3e^1 ions [35]. Global distortions due to cooperative local distortions that remove a localized-electron orbital degeneracy are known as cooperative Jahn-Teller distortions.
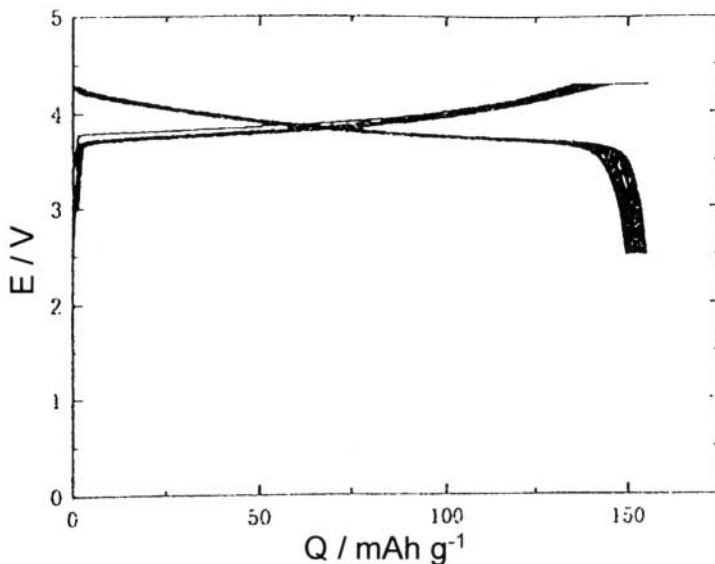
Figure 5. Charge/discharge curves of a $LiNi_{0.5}Mn_{0.5}$/Li cell operated at 0.1 mA·cm^{-2} for 30 cycles with 1 M $LiPF_6$ in EC/DMC electrolyte, Reprinted with permission from reference 31.

With the realization that a Li-ion (rocking-chair) cell containing an insertion cathode is better fabricated with a discharged cathode, as was done by the SONY Corp. with the $LiCoO_2$/C battery, Tarascon and Guyomard [36] championed use of the $Li_{1-x}[Mn_2]O_4$ compositional range, which had been shown [37] to give a V_{oc} *vs.* Li of about 4 V in contrast to the plateau at 3 V for $Li_{1+x}[Mn_2]O_4$, Figure 7. Although the theoretical capacity of each plateau is limited to 0.5 Li/Mn, it is comparable to the practical capacity of $Li_{1-x}CoO_2$ and contains the inexpensive, environmentally benign manganese atom. These

developments aroused great interest, but commercial realization of both the 3-V and the 4-V plateaus was frustrated by an irreversible capacity fade on repeated charge-discharge cycling, especially at the higher temperatures required for greater Li^+-ion mobility. At room temperature, the Li^+-ion mobility in $Li_{1+x}[Mn_2]O_4$ is much smaller than that in the layered $Li_{1-x}CoO_2$ because strong 3D bonding of the host $[Mn_2]O_4$ structure limits the free volume of the interstitial space. On the other hand, the 3D spinel framework prevents unwanted species from the electrolyte from entering the interstitial space.
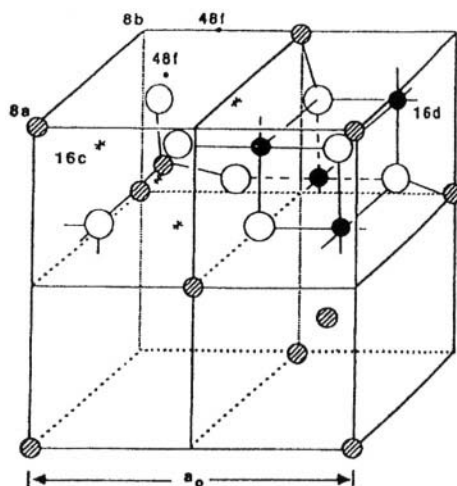
Figure 6. Two quadrants of the cubic $A[M_2]O_4$ spinel structure.
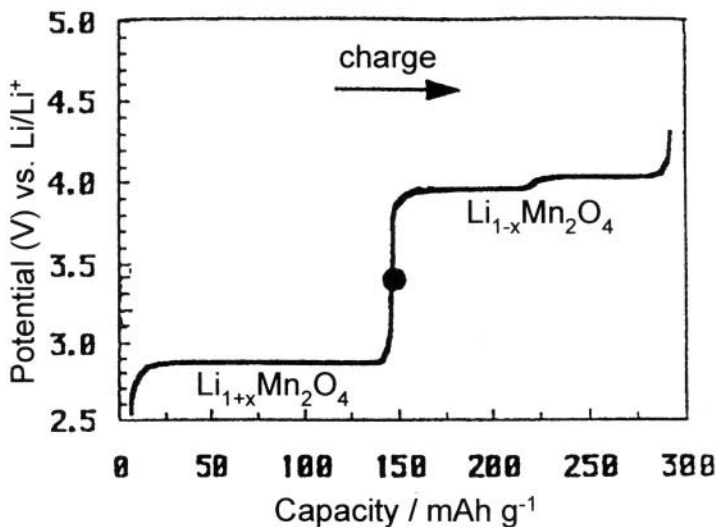
Figure 7. Open-circuit voltage V_{oc} *vs* x for $Li_{1+x}[Mn_2]_4$ and $Li_{1-x}[Mn_2]O_4$ for a Li anode.

Although stable thiospinels are restricted to $A[M_2]S_4$ compositions containing an A cation having a strong tetrahedral-site preference, *e.g.* $A = Cu^+$, Zn^{2+}, or Cd^{2+}, the spinel framework $[Ti_2]S_4$ was prepared by low-temperature chemical extraction of Cu from $Cu[Ti_2]S_4$ [42,43]. Li insertion into $Li_xCu_{0.07}[Ti_2]S_4$ gave a V-x curve over the range $0 < x < 2$ nearly identical to that of $LiTiS_2$ and a Li^+-ion mobility comparable to that in the layered compound [44]; in the thiospinel the Li^+ ions enter the 16c octahedral sites for all values of x and the larger, more polarizable S^{2-} ions offer the Li^+ ions a greater free volume than is found in $Li_x[Ti_2]O_4$.
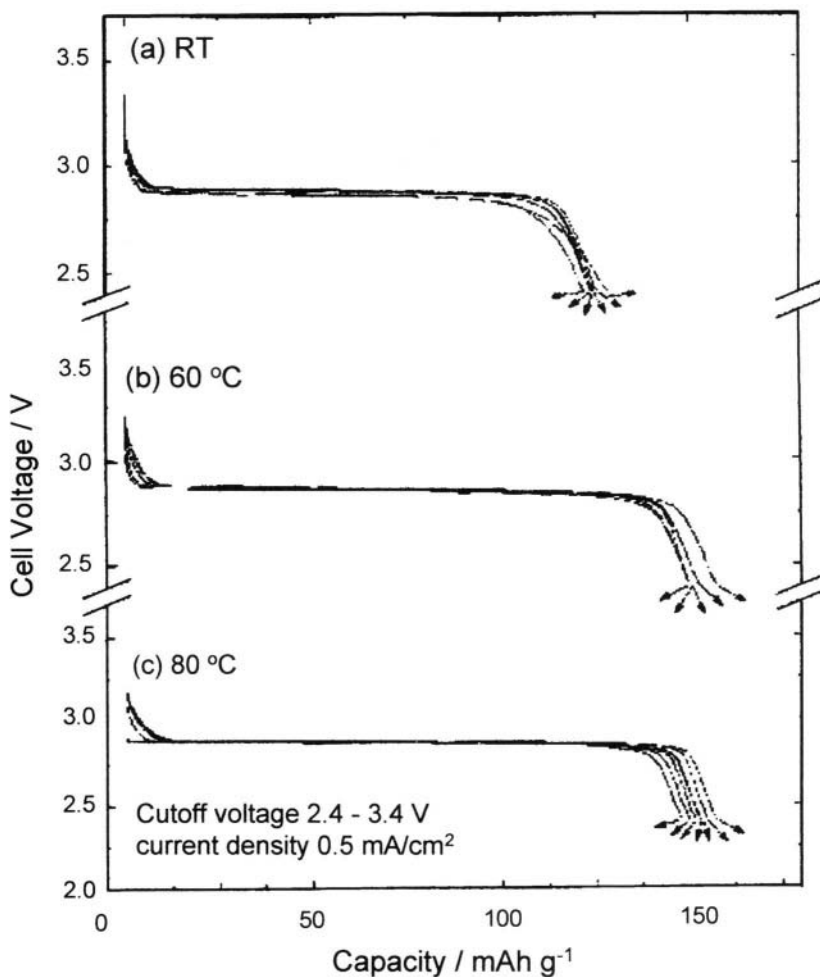
Figure 8. Discharge curves for $Li_{1+x}[Mn_2]O_4$ cathodes ball-milled for 1 h taken over the voltage range 2.4–3.4 V vs Li at a current density of 0.5 mA/cm² (a) at room temperature (RT), (b) at 60°C, and (c) at 80°C. Reprinted with permission from reference 43. Copyright 2001 The American Chemical Society.

In the 3-V range of $Li_{1+x}[Mn_2]O_4$, it is not necessary to use $LiPF_6$ as the electrolyte salt, so the problem of HF inducing a surface disproportionation reaction does not arise. Therefore, the irreversible capacity fade is primarily due to the structural distortion on Li insertion; these distortions appear to crack larger particles and/or to break the interparticle electronic or ionic contacts. An initial attempt to solve this problem was to begin with $Li[Li_yMn_{2-y}]O_4$, $0 < y \leq 1/3$ [41]. Another was to make small particles by a low-temperature synthetic route; but the resulting amorphous material [42] gave a discharge curve with voltage V varying nearly linearly with x as for a supercapacitor cathode rather than a flat V-x curve suitable for a battery cathode. The solution to this problem appears to be a simple ball-milling of the particles for more than half an hour [43]. Ball milling breaks up the larger particles into microdomains of different crystallographic orientation; it also introduces strains and stacking faults. As a result, the average distortion of the entire particle on Li insertion is suppressed even though a flat V-x curve, Figure 8, indicates a distortion of the individual microdomains. The ball-milled particles showed no capacity fade even at elevated temperature.

The $Li_{1-x}[Mn_2]O_4$ spinel phase exhibits two distinguishable regions in the V-x curve vs Li in Figure 7, a 4.2-V plateau in the range $1 > x > 0.5$ and a continuous, gradual change centered at 4.0 V in the range $0.5 > x > 0$. The 4.2-V plateau is due to the coexistence of two cubic phases, one with Li in octahedral sites for $x < 0.9$ and the other with Li ordered on one of the interpenetrating face-centered-cubic arrays of 8a sites; the Li^+ ions occupy the 8a sites randomly in the 4.0-V range. The capacity fade of $Li_{1-x}[Mn_2]O_4$ was not alleviated by ball milling. This capacity fade reflects a chemical interaction at the electrode-electrolyte interface either on charging to a high voltage or at the end of discharge. Reducing the particle surface area alleviates, but does not eliminate, the problem [44]. With voltages in excess of 4.2 V vs Li, as occurs on charging the $Li_{1-x}[Mn_2]O_4$ spinel, it is necessary to use $LiPF_6$ as the salt in the electrolyte, and any water in the electrolyte attacks $(PF_6)^-$ to create HF [45,46], which induces charge disproportionation in the $Li_{2-\delta}[Mn_2]O_4$ surface phase formed on deep discharge; the Mn^{2+} ions thus created dissolve in solution and a surface rock-salt phase Li_2MnO_3 is left on the surface. Efforts to inhibit these reactions have included coating the surface of the particles with a substance that would block them and substitution for some of the Mn atoms of a cation that suppresses the surface disproportionation reaction $2Mn^{3+} = Mn^{2+} + Mn^{4+}$.

Amatucci *et al* [46,47] have demonstrated that the capacity fade in the 4-V range of $Li_{1-x}[Mn_2]O_4$ occurs primarily at the end of discharge. A poor Li-ion mobility results in a build-up of the tetragonal $Li_{2-\delta}[Mn_2]O_4$ phase at the surface at the end of discharge, and the high Mn^{3+}-ion concentration in this phase allows it to be attacked by any HF in the electrolyte via a surface disproportionation reaction $2Mn^{3+} = Mn^{4+} + Mn^{2+}$ followed by Mn^{2+} dissolution into the electrolyte. As a result, the rock-salt phase Li_2MnO_3 is also formed at the surface [48]. In

addition, Amatucci *et al* [46,47] observed that the spinels with a cubic lattice parameter $a \leq 8.21$ Å were more stable against irreversible capacity loss, but they were unable to find a satisfactory explanation for this phenomenon. Their finding suggests that the disproportionation reaction is suppressed by a smaller lattice parameter; reducing the lattice parameter may increase the energy required to create a larger Mn^{2+} ion. In any event, these authors reduced the irreversible capacity loss by substituting a smaller Al^{3+} ion for Mn^{3+} and compensating for the resultant loss in capacity by substitution of F^- for O^{2-} ions to the extent allowed for a lattice parameter $a \leq 8.21$ Å. The maximum solid solution of Al^{3+} was 0.2 per formula unit, which led to the starting composition $Li[Al_{0.2}Mn_{1.8}]O_{3.8}F_{0.2}$. This spinel gave a superior performance at elevated temperatures and led the authors to speculate that the introduction of "getters" in the electrolyte to remove HF and other acids could solve the problem of capacity loss in the 4-V range. They added zeolites to getter the HF.

Other workers have also tried to inhibit the irreversible capacity loss in the 4-V range by substituting other cations for some of the manganese. Thirunakaran *et al* [45] investigated Mg-doped $Li_{1-x}[Mn_2]O_4$, Sun *et al* [49] also claimed to incorporate some S^{2-} ions in $Li_{1-x}[Al_{0.24}Mn_{1.76}]O_{3.98}S_{0.02}$, Shigala *et al* [50] substituted Cr^{3+} in $Li_{1-x}[Cr_yMn_{2-y}]O_4$, Kawai *et al* [51] and Shigemura *et al* [52] substituted Fe in $Li_{2-x}[FeMn_3]O_8$ and $Li_{1-x}[Fe_yMn_{2-y}]O_4$, respectively, Kawai *et al* [53] studied $Li_{1-x}[Co_yMn_{2-y}]O_4$, and Ein-Eli *et al* [54] $Li_{1-y}[Cu_yMn_{2-y}O_4$ $(0.1 \leq y \leq 0.5)$. Of particular interest are substitutions that give voltage plateaus in the range 4.5 to 5.0 V *vs* Li such as Co and Ni. Sun *et al* [55] have coated the surface of $Li[Ni_{0.5}Mn_{1.5}]O_4$ spinel particles with 1.5% of ZnO, an HF "getter," to achieve a reversible discharge capacity of 137 $mAh \cdot g^{-1}$ at *ca*. 4.7 V *vs* Li with a current density of 0.4 $mA \cdot cm^{-2}$ at 55°C. In $Li[Ni_{0.5}^{2+}Mn_{1.5}^{4+}]O_4$, the initial operative redox couple on Li removal is the Ni^{3+}/Ni^{2+} couple, which appears to be pinned near the top of the O^{2-}:$2p^6$ bands since the voltage change at x = 0.5 in $Li_{1-x}[Ni_{0.5}Mn_{1.5}]O_4$ is small. For x > 0.5, the principal operative redox couple would appear to be Ni^{4+}/Ni^{3+}, but this couple may be overlapped by a Mn^{5+}/Mn^{4+} couple that is also pinned at the top of the O^{2-}:$2p^6$ band. However, this cathode is restricted to modest current densities in its present form. It should be noted that although the initial composition is $Li[Ni_{0.5}Mn_{1.5}]O_4$, the surface of a particle after discharge contains tetragonal $Li_{2.8}[Ni_{0.5}Mn_{1.5}]O_4$ as a result of the poor Li^+-ion mobility. Nevertheless, the surface disproportionation reaction is suppressed by the ZnO coating that getters the HF.

2.3 *Polyanion Structures*

The poor Li^+-ion mobility at room temperature in the 3D oxospinel framework is due to the relatively small interstitial free volume associated with a close-packed oxide-ion array. Substitution of polyanions for oxide ions can open up the interstitial free volume, but at the expense of both weight and volume

energy density. Although electronic conduction across a polyanion is lower than that across an oxide ion, the reduction in electronic conductivity need not be critical so long as the electronic mobility is at least as large as the Li^+-ion mobility. Early studies of 3D Na^+-ion conductivity in framework structures had identified fast alkali ion conduction in the $M_2(XO_4)_3$ NASICON framework structure in which the octahedral-site M cation shares corners with the tetrahedral polyanions SiO_4 and PO_4 [56]. The hexagonal phase of $Fe_2(SO_4)_3$ has the NASICON framework of Figure 9 and therefore invited investigation of an open 3D framework containing $(SO_4)^{2-}$ polyanions. Initial experiments [57] compared Li insertion into hexagonal $Fe_2(SO_4)_3$ with that for isostructural $Fe_2(MO_4)_3$ and $Fe_2(WO_4)_3$. Each compound contains Fe^{3+} ions in the octahedral sites, and insertion of two Li per formula unit converts the Fe^{3+} ions to Fe^{2+}. $Li_xFe_2(SO_4)_3$ had an open-circuit voltage $V_{oc} = 3.6$ V whereas $Li_xFe_2(MoO_4)_3$ and $Li_xFe_2(WO_4)_3$ each had a $V_{oc} = 3.0$ V. The V_{oc} vs x curve of $Li_xFe_2(SO_4)_3$ was flat due to a small, displacive structural change between the hexagonal $Fe_2(SO_4)_3$ and the orthorhombic $Li_2Fe_2(SO_4)_3$ phases, which are both insulating. Consequently a low mobility of the front between the Li-rich and Li-poor phases gave a reversible capacity loss that increased with the current density. Nevertheless the overvoltages remained acceptably low. This experiment demonstrated three things: (1) mixed-valent electronic transport across a polyanion is not prohibitively low, (2) the position of the Fe^{3+}/Fe^{2+} redox energy is lowered significantly not only by the lower Madelung energy of the structure, but also by the counter cation of the $(XO_4)^{n-}$ polyanion, and (3) the redox energy of the octahedral-site cation can be tuned over a considerable energy range by the choice of the counter cation X. The more acidic the (XO_4) group, the weaker the covalent component of the Fe-O bond and the lower the energy of the Fe^{3+}/Fe^{2+} couple, which translates to a larger V_{oc}.
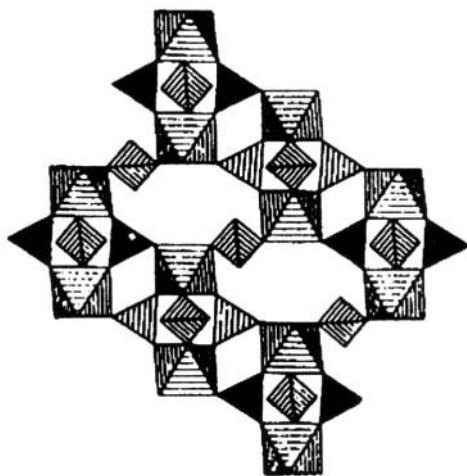

Figure 9. The NASICON framework.

With two different cations in the octahedral sites and the possibility of introducing up to five Li atoms per formula unit into the interstitial space of the NASICON framework, it was possible to map out the relative redox energies of several 3d-block transition-metal ions and how these energies shift on changing the polyanion from $(PO_4)^{3-}$ to $(SO_4)^{2-}$ [58]. The greater acidity of the $(SO_4)^{2-}$ anion uniformly raised all the voltages relative to their position with the $(PO_4)^{3-}$ anion by 0.8 V. Unlike the spinels, the redox energies in the NASICON structure do not vary with the location of the Li^+ and/or Na^+ ions in the interstitial space. Except for an overlap of the redox energies of two different octahedral-site cations M and M' in the same structure, successive redox energies gave steps in the curve of voltage *vs* Li concentration, each step corresponding to a Nernst profile centered around the standard voltage $V°$ of a particular redox couple of a given ion. Moreover, comparison of the redox energies with only one or with two different octahedral-site cations in $M_2(XO_4)_3$ and $MM'(XO_4)_3$ frameworks showed that the standard voltage $V°$ was not changed significantly by the presence of a different M cation, but it did shift significantly with a change of the tetrahedral-site cation X. For example, Figure 10 shows three redox energies for $Li_{1+x}FeNb(PO_4)_3$ with $0 \le x \le 3$; they correspond successively to $V°(Fe^{3+}/Fe^{2+}) \approx 2.8$ V, $V°(Nb^{5+}/Nb^{4+}) \approx 2.2$ V and $V°(Mb^{4+}/Nb^{3+}) \approx 1.8$ V all *vs.* Li. A $V°(Fe^{3+}/Fe^{2+}) \approx 2.8$ V was also found in $Li_{3+x}Fe_2(PO_4)_3$ with $0 \le x \le 2$. These experiments gave, for the phosphates, the redox energies relative to the Fermi energy of Lithium that are shown in Figure 11. A similar series of experiments with $(SO_4)^{2-}$ as the polyanion showed the relative positions of the redox energies remained the same, but the voltages were all increased by 0.8 V signaling a uniform decrease in energy of 0.8 eV because of the greater acidity of the $(SO_4)^{2-}$ ion. Access to the $V°(V^{4+}/V^{3+}) \approx 3.8$ V couple in $Li_{2+x}NaV_2(PO_4)_3$ was made possible by ion exchange of Li for Na in $Na_3V_2(PO_4)_3$; this procedure did not remove all the sodium, but cycling was not affected by the presence of the Na^+ ions [59]. No attempt has been made to optimize this cathode material by coating small particles with carbon in order to facilitate electron tunneling to the Li-rich/Li-poor interface.

A high-valent cation in the tetrahedral site of a close-packed oxide-ion array can also be considered to form an $(XO)^{n-}$ polyanion. For example, the spinels $V[LiM]O_4$ contain $(VO_4)^{3-}$ units with Li^+ and M^{2+} ions in the octahedral sites. Electrochemical extraction of Li from these spinels gives the V_{oc}-x curve for the M^{3+}/M^{2+} couple. Fey *et al.* [60] obtained $V°(Co^{3+}/Co^{2+}) \approx 4.2$ V and $V°(Ni^{3+}/Ni^{2+}) \approx 4.8$ V. Orthorhombic $LiV[Mn]O_4$ was transformed to the spinel $V[LiMn]O_4$ under pressure of 55 kbar at 850°C [61]; electrochemical delithiation gave $V°(Mn^{3+}/Mn^{2+}) \approx 3.8$ V all *vs.* Li. These values represent a remarkable stabilization of the redox energies compared to their values with Li in the 8a sites. However, these spinels are not of interest as battery cathodes as the Li^+-ion mobility is reduced by its coexistence with M atoms on the octahedral 16d sites.
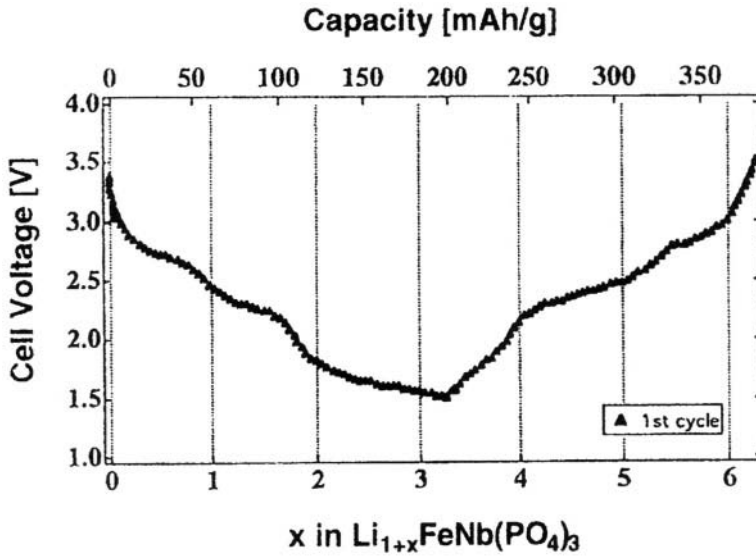
Figure 10. Open-circuit voltage V_{oc} *vs* x for $Li_{1+x}FeNb(PO_4)_3$ taken with a Li anode, after reference 58. Copyright 1998 from Molecular Crystals & Liquid Crystals by John B. Goodenough, Reproduced by permission of Taylor & Francis, Inc., http://www.routledge-ny.com
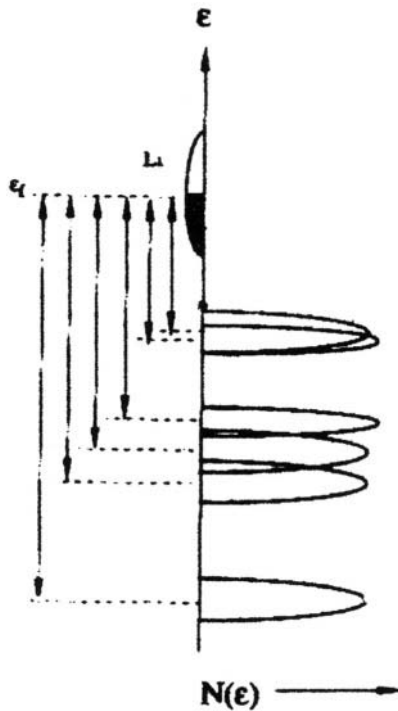

Figure 11. Energies of several redox couples relative to Li for M cations in phosphates with the NASICON structure.
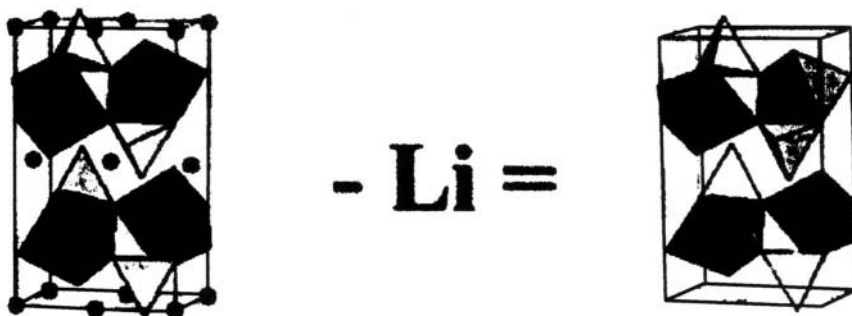
Figure 12. The phospho-olivine structures of triphylite (LiFePO$_4$) and heterosite (FePO$_4$).

LiM(PO$_4$) compounds, on the other hand, form the olivine structure of Figure 12, which has a nearly close-packed-hexagonal oxide-ion array. The Li$^+$ and M^{2+} ions occupy octahedral sites and are ordered into alternate (001) planes, which allows 2D Li$^+$-ion conduction. Electrochemical extraction of Li gave V$^\circ$(Fe^{3+}/Fe^{2+}) $\approx$ 3.5 V *vs.* Li [62]. A small, but first-order displacive structural change of the framework gives a two-phase separation over most of the solid-solution range $0 < x < 1$ of Li$_{1-x}$Fe(PO$_4$) and therefore a flat V-x curve. Figure 13, with a reversible capacity of 150 mAh·g^{-1} provided the cathode particles are coated with carbon [63]. In this structure, V$^\circ$(Mn^{3+}/Mn^{2+}) $\approx$ 4.1 V and V$^\circ$(Co^{3+}/Co^{2+}) $\approx$ 4.8 V *vs.* Li; a V$^\circ$(Ni^{3+}/Ni^{2+}) $\approx$ 5.0 V is smaller than predicted from the relative energies of Figure 11 because the redox couple becomes pinned at the top of the O^{2-}:2p^6 band. In the absence of a carbon coat, the penetration of the Li-rich/Li-poor front into the bulk is restricted by poor electronic conductivity in the two end members, which leads to a considerable reversible capacity loss [62, 64]. The improvement in capacity and current capability by the introduction of the carbon coat is remarkable and promises to provide a strategy for improving the performance of other cathode materials that are poor electronic conductors. Croce *et al* [65], for example, have dispersed lw% Ag or Cu with small particles of LiFePO$_4$ to improve the cathode performance.
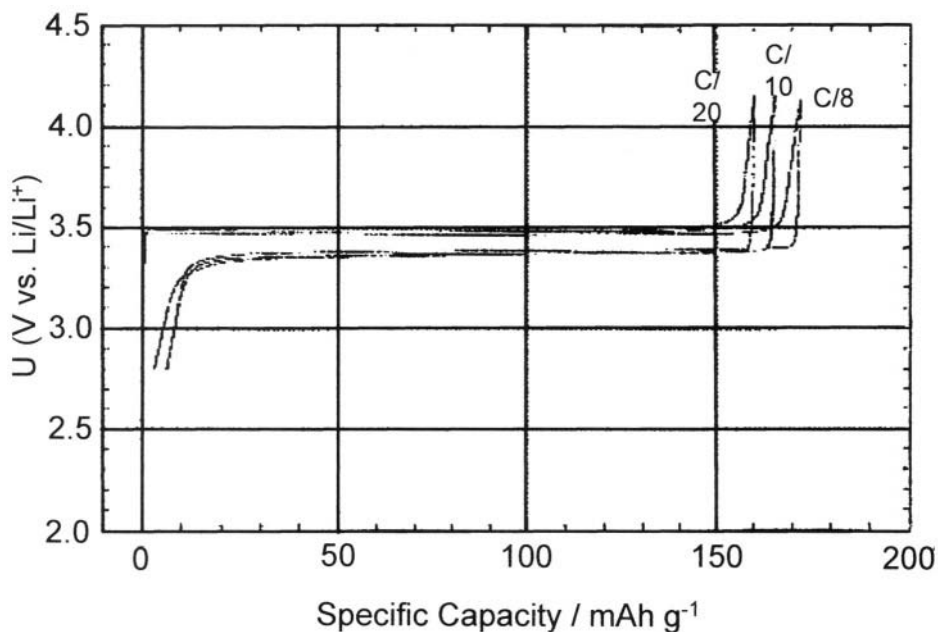
Figure 13. Charge/discharge curves of LiFePO$_4$/1 M LiPF$_6$ in EC/DMC/Li cells cycled at C/8, C/10, and C/20 rates, after reference 66.

3.0   REFERENCES

1.   Y. Yao and J.T. Kummer, *J. Inorg. Nucl. Chem.* **29**, 2453, 1967.
2.   J.T. Kummer and N. Weber, *SAE Transactions* 76, paper 670179, 1967.
3.   M.S. Whittingham and R.A. Huggins, *J. Chem. Phys.* **54**, 414, 1971.
4.   M.S. Whittingham, *Science* **192**, 1126 (1976); *J. Electrochem. Soc.* **123**, 315, 1976.
5.   J. Zaanen, G.A. Sawatzky, and J. W. Allen, *Phys. Rev. Lett.* **55**, 418,1985.
6.   J.B. Goodenough, D.G. Wickham, and W.J. Croft, *J. Phys. Chem. Solids* **5**, 107, 1958.
7.   K. Mizushima, P.C. Jones, P.J. Wiseman, and J.B. Goodenough, *Mater. Res. Bull.* **15**, 783, 1980.
8.   J.B. Goodenough, K. Mizushima, and T. Takada, *Jap. J. Appl. Phys.* **19** SUPPLEMENT **19-3**, 305, 1980.
9.   M.G.S.R. Thomas, P.G. Bruce, and J.B. Goodenough, *Solid State Ionics* **17**, 13, 1985.
10.   R.V. Chebiam, A.M. Kannan, F. Prado, and A. Manthiram, *Electrochem. Commun.* **3**, 642 (2001); *Chem. Mater.* **13**, 2951, 2001.
11.   R.V. Chebiam, F. Prado, and A. Manthiram, *J. Solid State Chem.* **163**, 5, 2002.
12.   H. Arai, M. Tsuda, K. Saito, M. Hayashi, K. Takei, and Y. Sakurai, *ibid* **163**, 340, 2002.

13. M. Ménètrier, I. Saadonne, *S.* Levasseur, and C. Delmas, *J. Mater. Chem.* **9**, 1135, 1999.
14. J.B. Goodenough, *Structure & Bonding* **98***,* 1*,* 2001.
15. D.W. Murphy, P.A. Christian, F.S. Disalvo, and J.N. Cavides, *J. Electrochem. Soc.* **126***,* 497, 1979.
16. K. Ozawa, *Solid State Ionics* **69**, 212, 1994.
17. C. Delmas and I. Saadoune, *Solid State Ionics* **53/56**, 370, 1992.
18. C. Delmas, I. Saadoune, and A. Rougier, *J. Power Sources* **43/44**, 595, 1993.
19. I. Saadoune and C. Delmas, *J. Mater. Chem.* **6**, 193, 1996.
20. E. Zhecheva and R. Stoyanova, *Solid State Ionics* **66**, 149, 1993.
21. A. Rougier, I. Saadoune, P. Gavereau, P. Willmann, and C. Delmas, *Solid State Ionics* **90**, 83, 1996.
22. I. Saadoune and C. Delmas, *J. Solid State Chem.* **136**, 8, 1998.
23. I. Saadoune, M. Ménétrier, and C. Delmas, *J. Mater. Chem.* **7***,* 2505. 1997.
24. J.R. Dahn, W.W. Fuller, M. Obravac, and U. von Sacken, *Solid State Ionics* **69**, 265, 1994.
25. Z. Zhang, D. Fouchard, and J.R. Rea, *J. Power Sources* **70***,* 16, 1998.
26. C. Pouillerie, F. Perton, Ph. Biensan, J.P. Pérès, M. Broussely, and C. Delmas, *J. Power Sources* **96**, 293, 2001.
27. G.T.-K. Fey, V. Subramanian, and C.Z. Lu, *Ionics* **7***,* 210, 2001.
28. H.-J. Kweon and D.G. Park, *Electrochem. and Solid State Letters* **3***,* 128, 2001.
29. A.R. Armstrong and P.G. Bruce, *Nature* **381**, 499, 1996.
30. Seungdon Choi, Ph. D. Thesis, University of Texas at Austin, 2001.
31. T. Ohsuku and Y. Makimura, *Chem. Letters (Japan)* **2001**, 744, 2001.
32. B.L. Cushing and J.B. Goodenough (unpublished)
33. M.M. Thackeray, W.I.F. David, and J.B. Goodenough, *Mater. Res. Bull.* **17**, 785, 1982.
34. M.M. Thackeray, W.I.F. David, P.G. Bruce, and J.B. Goodenough, *Mater. Res. Bull.* **18**, 461, 1983.
35. J.B. Goodenough, *J. de Phys. et le Radium* **20**, 155, 1959.
36. J.M. Tarascon and D. Guyomard, *Electrochim. Acta* **38**, 1221, 1993; *Solid State Ionics* **69**, 222, 1994.
37. M.M. Thackeray, P.J. Johnson, L.A. De Picciotto, P.G. Bruce, and J.B. Goodenough, *Mater. Res. Bull.* **19**, 179, 1984.
38. R. Schöllhorn and A. Payer, *Angew. Chem. (Int. Ed. Engl.)* **24**, 67, 1985.
39. S. Sinha and D.W. Murphy, *Solid State Ionics* **20**, 81, 1986.
40. A.C.W.P. James and J.B. Goodenough, *Solid State Ionics* **27**, 37, 1988.
41. M.M. Thackeray, *J. Electrochem. Soc.* **142**, 2568, 1995.
42. J. Kim and A. Manthiram, *Electrochem. & Solid-State Lett.* **1**, 207, 1998; **2**, 55, 1999; *J. Electrochem. Soc.* **145**, L53, 1998.
43. S.-H. Kang, J.B. Goodenough, and L.K. Rabenberg, *Chem. Mater.* **13**, 1758, 2001.
44. Y. Xia, N. Kumada, and M. Yoshio, *J. Power Sources* **90***,* 135, 2000.
45. R. Thirunakaran, N. Kalaiselvi, P. Periasamy, B. Ramesh Babu, N. G. Renganathan, N. Mumiyandi, and M. Razhaven, *Ionics* **7***,* 187, 2001.
46. G.G. Amatucci, A. DuPasquier, A. Blyr, T. Zheng, and J.M. Tarascon, *Electrochim. Acta* **45**, 255, 1999.
47. G.G. Amatucci, N. Pereira, T. Zheng, and J.M. Tarascon, *J. Electrochem. Soc.* **148**, A171, 2001.

48.   Y.-K. Sun, C.S. Yoon, C.K. Kim, S.G. Youn, Y.-S. Lee, M. Yoshio, and I.-H. Oh, *J. Mater. Chem.* **11**, 2519, 2001.
49.   Y.-K. Sun, G.-S. Park, Y.-S. Lee, M. Yoashio, and K.S. Nahm, *J. Electrochem. Soc.* **148**, A994, 2001.
50.   C. Sigala, D. Guyomard, A. Verbaere, Y. Piffard, and M. Tournoux, *Solid State Ionics* **81**, 167, 1995.
51.   H. Kawai, M. Nagata, M. Tabuchi, H. Tukamoto, and A. R. West, *Chem. Mater.* **1998**, 3266, 1998.
52.   H. Shigemura, H. Sakaebe, H. Kageyama, H. Kobayashi, A. R. West, R. Kanno, S. Morimoto, S. Nasu, and M. Tabuchi, *J. Electrochem. Soc.* **148**, A730, 2001.
53.   H. Kawai, M. Nagata, H. Kageyama, H. Tukamoto, and A. R. West, *Electrochim. Acta* **45**, 315, 1999.
54.   Y. Elin-Eli, W.F. Howard, Jr., S.H. Lu, S. Mukerjee, J. McBreen, J.T. Vaugheg, and M.M. Tackeray, *J. Electrochem. Soc.* **145**, 1238, 1998.
55.   Y.-K. Sun, K.-J. Hong, J. Prakash, and K. Amine, *Electrochem. Commun.* (in press).
56.   J.B. Goodenough, H.Y.-P. Hong, and J.A. Kafalas, *Mater. Res. Bull.* **11**, 203, 1976.
57.   A. Manthiram and J.B. Goodenough, *J. Solid State Chem.* **71**, 349, 1987.
58.   J.B. Goodenough, *Mol. Cryst. Liq. Cryst.* **311**, 1, 1998.
59.   B.L. Gushing and J.B. Goodenough, *J. Solid State Chem.* **162**, 176, 2001.
60.   G.T.K. Fey, W. Li, and J.R. Dahn, *J. Electrochem. Soc.* **141**, 2279, 1994.
61.   A.K. Padhi, W. B. Archibald, K.S. Nanjundaswamy, and J.B. Goodenough, *J. Solid State Chem.* **128**, 267, 1997.
62.   A.K. Padhi, K.S. Nanjundaswamy, and J.B. Goodenough, *J. Electrochem. Soc.* **144**, 1188, 1997.
63.   N. Ravet, J.B. Goodenough, S. Besuer, M. Simoneau, P. Hovington, and M. Armand, **196**[th] Electrochemical Society Meeting, Honolulu, Hawaii (unpublished)
64.   A.S. Andersson and J.O. Thomas, *J. Power Sources* **97-98**, 498, 2001.
65.   E. Croce, A.D. Epifanio, J. Hassoun, A. Deptula, T. Olczae, and B. Scrosati, *Electrochem. & Solid State Lett.* **5**, A47, 2002.

5

Liquid Electrolytes

Jun-ichi Yamaki

Institute of Advanced Material Study
Kyushu University
Kasuga 816-8580
Japan

1.0   INTRODUCTION

Electrolytes based on solvent mixtures of ethylene carbonate (EC) with dimethyl carbonate (DMC) and/or diethyl carbonate (DEC) are commonly used for lithium ion batteries in combination with "4 V" cathodes ($LiCoO_2$, $LiNiO_2$, or $LiMn_2O_4$) because of the high oxidation potential of the solvents. This section reviews the recent (1999-2001) studies on liquid electrolytes for lithium batteries and lithium ion batteries. The studies appearing before 1999 are summarized in other books [1-3]. This chapter focuses on the solvents for electrolytes. Reactivity of salts and solvents are also discussed in Chapters 1, 11, and 13 of this book; ionic liquids are discussed in Chapter 6.

2.0   FUNDAMENTAL PROPERTIES

2.1   *Oxidation Potentials of Electrolytes*

The window of oxidation/reduction stability is a first requirement for electrolyte systems for Li-Ion cells. PC, EC, DMC, DEC, DME, and DEE are well-known solvents for Li cells. Hayashi et al. [4, 5] measured the oxidation potential of 1M $LiClO_4$ or $LiPF_6$ solution of each of those solvents. The measurements were obtained by the potential linear sweep method from 3.0 to 6.0 V vs. Li/Li^+ with a sweep rate of 0.1 $mV \cdot sec^{-1}$. The oxidation potential was determined from the cross point between the potential axis and an asymptote of the potential-current curve. The results are shown in Table 1 and Table 2.

Oxidation potential can be determined electrochemically in two ways. In one approach, the oxidation potential of a given electrolyte is determined as the potential at which an applied current density reaches a given threshold value [6,7]. In the other approach, an extrapolated line is drawn along the potential sweep wave (as shown in Figure 1), and the intersection of this line

and the $i = 0$ line is regarded as the oxidation potential [4,5,8-11]. Although the threshold current is different in each report, the former method appears to be better than the latter for the following reason. When the charge-transfer process dominates the whole Faradaic current, the current-density/potential relationship of the irreversible oxidation processes of electrolytes must be described by the following Butler-Volmer type equation [12],

$$i = (nFC_s k^0)\exp\left[(1-\alpha)nFE/RT\right] \tag{1}$$

where i is the flowing current density (positive on oxidation), n is the number of electrons associated with the reaction, F is the Faraday constant, k^0 is the rate constant of the reaction, C_s is the surface concentration of the reactant, α is the transfer coefficient, R is the gas constant, T is the temperature, and E is the potential. If the obtained current density is very small compared with the limiting current density, C_s can be assumed to be the bulk concentration of the reactant. Thus, the Tafel plot (the log(i–E) relationship) of this measurement is a straight line. In this i–E relationship, the intersection moves following the change in the i range. For instance, while both Figure 1 (a) and (b) show i–E curves for the same equation, the E value of the intersection is quite different (Equation 1 is simplified as $i = A \cdot \exp(BE)$, where $A = nFC_s k^0$ and $B = (1-\alpha)nF/RT$. When i is transformed to i' following the equation $i' = ai$ (a is a constant.), Equation 1 becomes $i' = A \cdot \exp\{B[E+(\ln a)/B]\}$.). Thus, the oxidation potentials obtained by these methods may vary with the experimental apparatus and conditions, and cannot be compared with each other.

Table 1. Oxidation potentials of solvent electrolytes. From reference 4.

| Solvent	Oxidation Potential vs Li/Li⁺	
	1 M LiClO₄	1 M LiPF₆
Propylene Carbonate (PC)	5.8 V	>6.0 V
Ethylene Carbonate (EC)	5.8 V *	>6.0 V
DMC	5.7 V	>6.0 V
DEC	5.5 V	>6.0 V **
1,2-Dimethoxy ethane (DME)	4.9 V *	4.9 V *
1,2-Diethoxy ethane (DEE)	4.7 V *	4.9 V *

* Mixed with PC   ** Mixed with EC

Table 2. Oxidation potentials of 1M LiClO₄ electrolytes. From reference 5.

Solvent	Oxidation Potential vs Li/Li⁺
1,3-Dioxolane (DOL)	4.3 V
Tetrahydrofuran (THF)	4.3 V
2-methyl tetrahydrofuran (2MeTHF)	4.2 V
4-methyl-1,3-dioxolane (4MeDOL)	4.1 V
2,5-dimethyl tetrahydrofuran (diMeTHF)	4.0 V
2-methyl-1,3-dioxolane (2MeDOL)	3.8 V
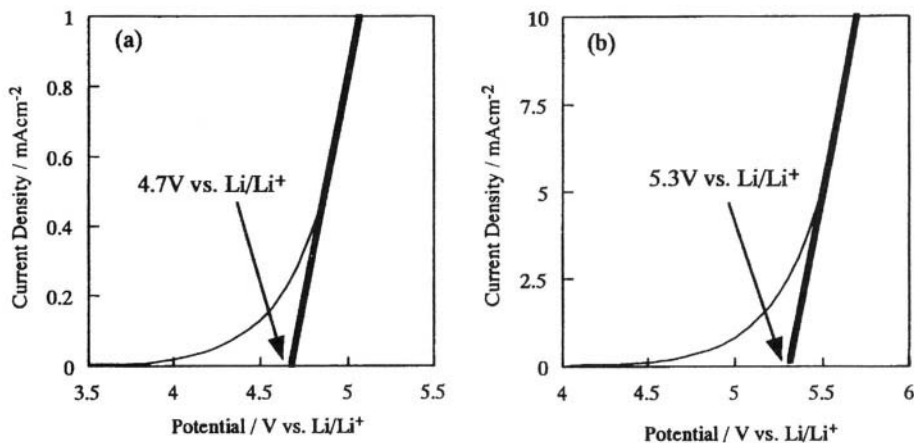
Figure 1. i-E curves of the oxidation of the same organic electrolyte with different i-scales, assuming Equation 1 cam be applied to the oxidation of these electrolytes. From reference 13.
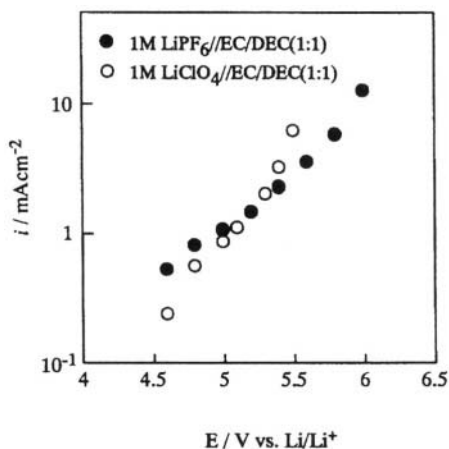
Figure 2. i − E relationship of the anodic oxidation of two organic electrolytes. Electrolytes: 1M LiPF$_6$/(EC+ DEC 1:1) and 1M LiClO$_4$/(EC+ DEC 1:1). Microelectrode: carbon, 10 μm in diameter. From reference 13.

In the author´s research group, Egashira et al. investigated the electrochemical oxidation of organic electrolytes has been investigated using microelectrodes [13]. The electrolytes used were LiClO$_4$/EC/DEC and LiPF$_6$/EC/DEC, widely employed in lithium ion batteries. The oxidation current was measured by the potential step method (where the potential is maintained until the current becomes constant) at potentials ranging from 4.5 V to 5.5 V versus Li/Li$^+$. The current-density/potential relationship of the oxidation of 1M LiClO$_4$/EC/DEC electrolyte on the carbon microelectrode shows good reproducibilily and roughly fits exponential lines. A similar relationship was observed regardless of the material or size of the microelectrodes. Therefore, this method is suitable for comparing the electrochemi-

cal oxidation of organic electrolytes. The different oxidation behaviors of $LiPF_6$ salt and $LiClO_4$ salt electrolytes suggest that the salt anions may initiate the electrolyte oxidation (Figure 2). These properties may include salt decomposition or products or impurities introduced with the salt manufacture.

The oxidation potential of an electrolyte depends on the cathode active material. Imhof et al. [14] found that the starting point of CO_2 gas evolution $(1M\ LiN(SO_2CF_3)_2)$ was 4.2 V at $LiNiO_2$, whereas at $LiCoO_2$ and $LiMn_2O_4$, CO_2 evolution was observed only above 4.8 V.

Kanamura investigated the electrochemical oxidation of a PC electrolyte on an Al electrode using in situ FTIR [15]. The oxidation on Al was strongly influenced by passivation phenomena in the electrolytes. A typical peak showing a decomposition of PC was observed at 5.0 V or 6.2 V for $LiClO_4$/PC or $LiPF_6$/PC, respectively. On the other hand, when $LiN(SO_2CF_3)_2$/PC was used, the same peak was observed at 4.2 V. However, those electrolytes were oxidized even at 4.2 V on the $LiCoO_2$ electrode. Kanamura concluded that this was due to an undesirable catalytic activity of $LiCoO_2$.

2.2   *Reaction Mechanism of Electrolyte Oxidation*

Joho et al. [16] investigated the oxidative decomposition of $LiClO_4$/PC + water, $LiPF_6$/EC, $LiPF_6$/DMC, and $LiPF_6$/EC/DMC using subtractively normalized interfacial Fourier transform infrared spectroscopy (SNIFTIRS). Their experiments, devoted to the electrochemical oxidation of $1M\ LiClO_4$/PC containing various amounts of water $(0<[H_2O]<\ 1000\ ppm)$, revealed that the positions of the infrared bands in the SNIFTIRS spectra were independent of water concentration. They therefore concluded that the same reaction products were formed by oxidative decomposition regardless of the water concentration in the electrolyte. The less water the electrolyte solution contained, the less the electrolyte solution decomposed. The decomposition products of the wet electrolyte solution formed an additional surface layer, which retarded further oxidation. A reaction path involving hydroxyl ions generated due to water dissociation and/or reduction has been proposed by Aurbach et al. [17]:

$$PC + 2OH^- \rightarrow CH_3CH(OH)CH_2OH + CO_3^{2-} \qquad \text{Mechanism I} \qquad (2)$$
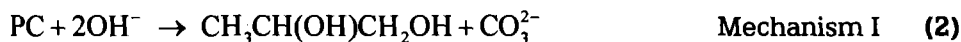
Arakawa et al. [18] used GC-MS to investigate the products of anodic oxidation of PC containing various Li salts, and were able to identify CO_2, propanal, and both the *cis-* and *trans*-2-ethyl-4-methyl-l, 3-dioxolane as decomposition products. They proposed the following reaction path:

$$PC - CO_2 \rightarrow CH_3CHOCH_2 \quad \text{(propylene oxide)} \qquad (3)$$

$$CH_3CHOCH_2 \rightarrow CH_3CH_2CHO \quad \text{(propanal)} \qquad (4)$$

$$2CH_3CHOCH_2 \rightarrow$$

Mechanism II

$$\qquad \text{the cis- and trans-2-ethyl-4-methyl-1,3-dioxolane} \qquad (5)$$

Joho et al. [16] concluded that their SNIFTIRS measurements were compatible with the mechanism shown above in mechanism (II). However, they detected bands that they assigned to the CO_3^{2-} assumed in mechanism (I), even for electrolyte solutions with high water contents. They also investigated the decomposition products of EC and concluded that EC starts to decompose by the same mechanism as PC, and then most of the decomposition products polymerize at the electrode surface. In an electrolyte mixture based on EC/DMC, EC was preferentially oxidized leading to the conclusion that in future attempts to optimize electrolyte of EC/DMC, attention should be focused on the oxidation stability of EC.

Kumai et al. studied gas generation due to electrolyte decomposition in lithium ion cells using GC and GC/MS [19]. The cells (US18650 by Sony) have a carbon anode, a $LiCoO_2$ cathode, and 1M $LiPF_6$/PC/EMC/DEC/DMC (50:25:15:10 in vol.). After a long cycling (2000-3000 cycles) in the normal voltage range (4.2-2.5 V), the composition changed, due mainly to the ester exchange reaction, and the quantities of gaseous products in the cells were small. They posited the following reaction for this electrolyte decomposition.

$$ROCO_2R + Li^+ + ROCO_2Li + R\bullet \tag{6}$$

$$ROCO_2Li + Li^+ + e^- \rightarrow Li_2CO_3 + R\bullet \tag{7}$$

$$R\bullet + \tfrac{1}{2}H_2 \rightarrow Alkyl \uparrow \tag{8}$$

$$R\bullet + R\bullet \rightarrow R\text{-}R \uparrow \tag{9}$$

The equilibrium of the ester exchange reaction $(DEC + DMC \rightleftarrows 2EMC)$ was not established even at the end of cycling. Large amounts of CO_2 and hydrocarbons as well as CO were detected from over-discharged cells. A large amount of CO_2 was detected in the overcharged cells.

2.3 *Oxidation Potentials of Solvents*

Xu et al. [20] examined reliable values of electrochemical stability limits for 1.0 M $Et_3MeN^+PF_6^-$ electrolytes using activated carbon (AC) or glassy carbon (GC) as the working electrode. Their results are shown in Table 3.

Zhang et al. [21] reported the application of density function theory (DFT) to calculate solvent oxidation potentials assuming oxidation occurs via one-electron transfer to form the radical cation. No specific ion-ion, ion-solvent, or ion-electrode interactions were included in their calculations. Those potentials were then compared to the experimental observations (Table 4). Optimized geometries of the radical cations correlate well with the fragmentation patterns observed in mass spectrometry. The oxidation potentials of saturated carbonates were calculated to be approximately 1 V higher than those of the organic ethers, which was consistent with reported literature values.

Table 3. Electrochemical stability of electrolyte[a] comprised of various solvents. From reference 20.

Solvents[b]	Reduction Potential of Solvent (V vs. Li/Li+)		Oxidation Potential of Solvent (V vs. Li/Li+)	
	GC[c]	AC[d]	GC[c]	AC[d]
EC	0.109	1.940	6.702	4.602
PC	0.232	2.253	5.981	4.422
EC/DMC	0.153	2.027	6.686	4.521
PC/DMC	0.184	2.200	5.783	4.101
EC/EMC	0.100	2.055	6.683	4.576
PC/EMC	0.114	2.032	6.201	4.237
AN	0.073	2.201	5.506	4.018
SL/DMC	0.102	1.386	6.563	4.500

a: 1.0 M $Et_3MeN^+PF_6^-$
b: H_2O content for all solvents [with concentrations below 100 ppm]
c: Scan rate 10 mV/s
d: Scan rate 5 mV/s

AN = Acetonitrile
SL = Sulfolane

Table 4. Calculated solvent oxidation potentials compared with experimental values. From reference 21.

Solvent	Solvent Oxidation Potential (V vs Li/Li+)	
	Calculated	Experimental
EC	5.58	6.7[a]
Trans-butylene carbonate (BC)	5.51	-
PC	5.61	5.2 - 5.6[b] 6.0[a]
EMC	5.55	6.2 - 6.7[c]
DEC	5.46	-
DMC	5.62	5.8 – 6.7[d]
DOL	4.17	-
THF	4.35	<4[e]
DME	4.11	4.6[b]
Vinylene carbonate (VC)	4.06	-
Catachol carbonate (CC)	4.23	-

a: Glassy carbon as working electrode and 1.0M $Et_3MeN^+PF_6^-$ in solvent [20].
b: Glassy carbon or Pt as working electrode and $LiClO_4$ as salt.
c: Glassy carbon as working electrode and 1.0M $Et_3MeN^+PF_6^-$ in PC/EMC mixture (lower value) and EC/EMC mixture (higher value) [20].
d: Glassy carbon as working electrode and 1.0M $Et_3MeN^+PF_6^-$ in PC/EMC mixture (lower value) and EC/EMC mixture (higher value) [20].
e: Pt microelectrode and neat solvents without electrolyte.

2.4   *Reduction Potentials of Solvents*

Electrochemical reduction of electrolytes is related to the formation of SEI on the surface of an anode electrode. Therefore, this topic is described in Chapter 1, entitled "The Role of the Solid Electrolyte Interface in Lithium-Ion Batteries." However, I would like to introduce one interesting study here. In further studies, Zhang et al. [22] investigated the reduction potentials of five

organic carbonates—EC, PC, DEC, DMC, and vinylene carbonate (VC)—by cyclic voltammetry using inert (Au or glassy carbon) electrodes in THF/LiClO₄ supporting electrolyte. PC reduction was observed to have a significant kinetic hindrance. The measured reduction potentials for EC, DEC, and PC were consistent with thermodynamic values calculated using density functional theory (DFT) assuming one-electron reduction to the radical anion (Table 5). The experimental values for VC and DMC were, however, much more positive than the calculated values, which was attributed the inconsistency to different reaction pathways [22].

Table 5. Comparison of calculated and experimental potential values of solvent reduction. From reference 22.

Solvent	Potential Values for Solvent Reduction (V vs Li/Li⁺)	
	Calculated	Experimental
EC	1.46	1.36
DEC	1.33	1.32
PC	1.24	1.00 – 1.60
DMC	0.86	1.32
VC	0.25	1.40

2.5   Conductivity

In a very precise study, Brouillette, et al. examined the effects of an electrolyte´s viscosity and density on its specific conductivity [23]. They proposed a simple model for conductivity. Moumouzias et al., measured viscosity and relative permittivities of PC/DEC [24]. They also reported specific conductance of LiBF₄/PC/DEC.

^{7}Li and ^{19}F diffusion coefficients of EC/EMC solvent electrolytes with LiPF₆, LiN(C₂F₅SO₂)₂, or LiBF₄ were measured using NMR by Capiglia et al. [25]. The diffusion coefficients of ^{19}F are always higher than those of ^{7}Li. They considered the Li⁺ ion solvation to be the reason for this. The cationic transport number of 1M LiPF₆, LiN(C₂F₅SO₂)₂, or LiBF₄/EC/EMC (2:8 in vol.) was 0.43, 0.48, or 0.47, respectively.

Geoffroy et al. [26] examined the dependence of viscosity and conductivity on temperature and solvent composition for solutions of LiPF6 and LiClO4 in EC/diglyme (DG). The goal was to identify the organic electrolyte system with the highest conductivity possible at room temperature. A maximum conductivity of EC/DG (50:50) was obtained around 1.1 M for both salts (10 mS/cm for LiClO₄ and 9.5 mS/cm for LiPF₆ at 25°C). A flat maximum of conductivity at about 50% (v/v) in EC was observed when the composition of the mixed solvent was varied. DSC results showed that this electrolyte system is a potential candidate for Li cells working at ambient or higher temperatures, as it is safe and stable to at least 200°C.

Hayashi et al. [4, 27] also measured the specific conductivity of PC-mixed or EC-mixed solvent electrolyte (1:1 in volume) from -20°C to 60°C. The results at 20°C are shown in Table 6. In general, the order of increasing conductivity was for **DME>DEE≈DMC>DEC.**

Table 6. Specific conductivity of each electrolyte at 20°C. From References 4, 27.

Co-solvent	Specific Conductivity (20°C) / mS cm^{-1}			
	PC mixed solvent electrolyte		EC mixed solvent electrolyte	
	1M LiClO$_4$	1M LiPF$_6$	1M LiClO$_4$	1M LiPF$_6$
DME	12	14	14	15
DEE	7.5	9.5	8.5	10
DMC	6.5	10	8	10
DEC	4	7	6	7

Ding et al. [28] measured the conductivity of **LiPF$_6$/EC/EMC** at different salt contents **(0.4-1.8 mole·kg^{-1})**, solvent compositions (0.23 to 0.54 mole fraction of EC), and temperatures (-40 to 60°C) in the ranges of their practical values. They fit these data to a fourth degree trivariate polynomial (conductivity, salt concentration, mole fraction of EC, and temperature), and obtained a close fit.

The improvement of the low-temperature performance of Li ion cells is an important target for their use in cold countries and in space applications. Smart et al. [29] found that 1M **LiPF$_6$//EC/DMC/DEC(1:1:1)** performs well at low temperature (-20°C). [Editor´s note: see chapter #, Temperature Effects on Li-Ion Cell Performance for an extensive discussion on low temperature performance and electrolytes for improved low-temperature performance.]

2.6   Electrolyte Structure

Knowledge of the structure of electrolyte solutions is paramount to an understanding of the reactivity of electrolytes with cell components and the key to designing new electrolytes.

Doucey et al. [30] studied the structure of **LiAsF$_6$/DMC** using infrared and Raman spectroscopies. By splitting bands, they found that a dissociation of the lithium salt into its ionic species, **Li$^+$** and **AsF$_6^-$**, occurs in PC solution. In DMC solutions, there are contact ion pairs, free anions, solvated ion pairs, and polymeric ion pairs.

Li et al. [31] undertook a theoretical study of **LiClO$_4$** in EC, PC, and EC/PC. Ab initio calculations have been used to study pair interactions between lithium ion and **ClO$_4^-$**, **LiClO$_4$.,** and polar aprotic solvents: EC, PC, and EC/PC. Little molecular association is detected in pure EC solutions. In EC/PC mixtures, it is found that the radius of the complex ion solvent is

smaller for the EC/PC mixture than in the case of pure PC, leading to higher ionic conductivities. Solvent-separated species are present in dilute (ca. 0.15M) solutions, whereas ion pairs and solvent-separated complexes are found in concentrated (ca. 0.8M) solutions.

Hayashi et al. [32] investigated the influence of the solvation state of lithium cations on $Li/LiPF_6/EC+DME/LiMn_{1.9}Co_{0.1}O_4$ cells. The relation they found was that, as the amount of non-solvated DME increases in the electrolyte, the cell cycle life becomes shorter. They supposed that non-solvated DME damages the protective film on the lithium anode.

2.7 *Reactions of LiPF$_6$ Electrolytes With Water*

It is believed that electrolytes with $LiPF_6$ react with water by the following mechanism [1]:

$$LiPF_6 \rightleftarrows LiF \downarrow + PF_5 \tag{10}$$

$$PF_5 + H_2O \rightarrow PF_3O + 2HF \tag{11}$$

See also Chapter 1, Table 1, by Aurbach.

Heider et al. [33] studied the reaction of $LiPF_6$ electrolytes with water. With the GC-MS method, they detected PF_3O and other unknown species. They performed an acid-base titration to measure HF content, which may contain other acids besides HF. They compared calculated HF value and measured acid value. Within the error limit of the detection method, the two values were the same. Glycol, an impurity in EC, was calculated at 149 ppm, close to the measured value of 145 ppm. This is a reasonable fit. However, an increase in the amount of methanol or ethanol in the electrolyte leads to a decrease in the HF level.

Kawamura et al. used EC/DEC, EC/DMC, PC/DEC, and PC/DMC (1:1 in vol.) in a study of the decomposition of $LiPF_6$ electrolytes with water (about 5000 ppm) [34]. The reaction rate was in good agreement with the empirical relation

$$\frac{-d[H2O]}{dt} = k[H2O]^2[LiPF_6] \tag{12}$$

where $[H_2O]$ is the concentration of water, t is time, k is the rate constant, $[LiPF_6]$ is the concentration of $LiPF_6$, and $[LiPF_6] = [LiPF_6]_{t=0} - ([H_2O]_{t=0} - [H_2O])$.

The rate constants obtained from this equation by fitting the experiments are shown in Table 7. The rate constant increased in the order of EC/DMC<EC/DEC<PC/DMC<PC/DEC. By the addition of 0.1M LiCl to 1M $LiPF_6/EC/DEC$, the decomposition with water (1%) was inhibited for at least 50 hours [35].

Table 7. The rate constants of the reactions of LiPF$_6$ electrolytes at 10°C and 30°C. From reference 34.

	1M LiPF$_6$ EC/DMC	1M LiPF$_6$ EC/DEC	1M LiPF$_6$ PC/DMC	1M LiPF$_6$ PC/DEC
k at 10°C [(mole/l)$^{-2}$ hour^{-1}]	0.028	0.090	0.095	0.188
k at 30°C [(mole/l)$^{-2}$ hour^{-1}]	0.36	0.53	0.94	1.79

3.0   NEW SOLVENTS

Iinou at al. [36] studied 3-propyl-4-methylsydnone (3-PMSD) as a new solvent. The energy density for a Li/V$_2$O$_5$ (2025) coin-type cell in LiN(SO$_2$CF$_3$)$_2$/3-PMSD/THF (1:9 in mole) was 380 Wh·kg^{-1}, which was almost equal to that in LiPF$_6$/EC/DME (1:1 in mole).

Cyclic ethers (Table 8) were studied with LiN(SO$_2$CF$_3$)$_2$ by Wang et al. [37]. They concluded that THF and THP electrolytes were much more stable than their alkyl- and alkoxy-derivative electrolytes, since the electron donor performance of alkyl and alkoxy substitutes destroys the stable electron cloud structures of five- and six-membered cyclic ethers. This difference in oxidation stability led to good cycling performances of Li/LiCoO$_2$ coin cells with only LiN(SO$_2$CF$_3$)$_2$/THF and THP electrolytes.

Table 8. The properties of LiN(SO$_2$CF$_3$)$_2$/cyclic ether electrolytes. From reference 37.

Cyclic Ether	Abbreviation	Boiling Point °C	Specific Conductivity mS·cm at 25°C	Oxidation Voltage V
Tetrahydrofuran	THF	65	11.4	4.7
	THF/EC (1:1)	-	12.6	4.8
2-Methyltetrahydrofuran	2-MeTHF	78	2.5	4.3
2-Methyltetrahydrofuran	3-MeTHF	-	-	4.3
Methyl-tetrahydrofurfuryl ester	2-MMTHF	140	-	4.3
2,5-Dimethoxytetrahydrofuran	2,5 DMTHF	145	0.7	-
2-Ethoxytetrahydrofuran	2-ETHF	170	-	-
Tetrahydropyran	THP	88	2.4	4.5
	THP/EC (1:1)	-	7.8	4.6
2-Methyltetrahydropyran	2-MeTHP	-	-	4.0
3-Methyltetrahydropyran	3-MeTHP	109	-	4.1
2-Methoxytetrahydropyran	2-MTHP	128	-	4.2
7-Oxabicyclo[2.2.1]heptane	7-OBCH	119	-	-
	7-OBCH/EC (1:1)	-	-	5.1
Hexamethylene oxide	HMO	122	-	-
	HMO/EC (1:1)	-	-	4.5

Wang et al. [38] continued to study other two-oxygen-atom-containing cycloalkane solvents (Table 9). They concluded that, due to the good oxidation stability of the DOL (dioxolane) solvent, only a slight decline in the discharge capacity of a $Li/LiMn_2O_4$ coin cell with 1M $LiN(SO_2CF_3)_2/EC/DOL$ (5:5) electrolyte was observed even after 300 cycles, compared to 4-MeDOX-based and 2, 4-DMDOX-based mixed solvent electrolytes.

Table 9. The properties of $LiN(SO_2CF_3)_2$/cyclic ether electrolytes. From reference 38.

Two-Oxygen-Containing Cycloalkane	Abbreviation	Boiling Point °C	Specific Conductivity mS·cm at 25°C	Oxidation Voltage V
1, 3-dioxolane	DOL	75	-	4.0[b]
2-methyl-1, 3- dioxolane	2-MeDOL	83	-	4.8[a]
4-methyl-1, 3- dioxolane	4-MeDOL	84[c]	-	4.8[a]
2, 2-dimethyl-1, 3- dioxolane	2, 2-DMDOL	93	-	4.8[a]
2-ethyl-2-methyl-1,3- dioxolane	2, 2-EMDOL	116	-	4.5[a]
1, 3-dioxane	DOX	105	6.0	>5.0
4-methyl-1, 3-dioxane	4-MeDOX	114	5.0	4.9
2, 4-dimethyl-1, 3-dioxane	2, 4-DMDOX	118	-	5.0
1, 3-dioxepane	DOXP	119	-	4.2

1M $LiN(SO_2CF_3)_2$ /EC+X(5:5), $Li/LiMn_2O_4$ coin cell
a: 1M $LiN(SO_2CF_3)_2$ /EC+X(5:5)
b: 1M $LiN(SO_2CF_3)_2$ /X
c: 745 mm Hg

2-Methoxyethyl (methyl) carbonate (MOEMC) was investigated by Gu et al. [39]. The ionic conductance processes occurring in MOEMC and other asymmetric alkyl methyl carbonate-based solutions obeyed the Vogel-Tammann-Fulcher (VTF) mechanism. The VTF equation is

$$\sigma = AT^{-0.5}\exp[-B/(T-T_0)] \tag{13}$$

where σ is the conductivity, A and B are constants, and T_0 was considered as the glass-transition temperature. They attributed such behavior in conductivity to the strong interaction between Li ions and carbonate solvent molecules. The Li-ion battery electrolyte formulated in MOEMC and its blend with EC showed a wide voltage window of stability, and both graphite and $LiCoO_2$ were cycled reversibly.

4.0   NONFLAMMABLE TRIMETHYL PHOSPHATE

Trimethyl phosphate (TMP) has widespread industrial uses as a fire retardant in plastics production, thus TMP-based electrolytes might be expected to exhibit good performance with no risk of flame. Wang et al. [40] introduced the mechanism underlying flame retardation as follows:

TMP solvent, heated by an external heat source, evaporates, reaching the flame in gaseous form

$$TMP_{liquid} \rightarrow TMP_{gas} \tag{14}$$

The gaseous TMP breaks down in the flame to small radical species containing phosphorus.

$$TMP_{gas} \rightarrow [P]\bullet \tag{15}$$

These small radical species containing phosphorus scavenge the $H\bullet$ radicals, which are the main active agent of combustion chain branching reactions.

$$[P]\bullet + H\bullet \rightarrow [P]H \tag{16}$$

Accordingly, the following combustion chain branching reactions are hindered due to a deficiency of $H\bullet$ radicals:

$$RH \rightarrow R\bullet + H\bullet \tag{17}$$

$$H\bullet + O_2 \rightarrow HO\bullet + H_2O \tag{18}$$

$$HO\bullet + H_2 \rightarrow H\bullet + H_2O \tag{19}$$

$$O\bullet + H_2 \rightarrow HO\bullet + H\bullet \tag{20}$$

However, since TMP decomposes at the anode, it is not suitable for lithium secondary batteries. In further studies of TMP it was found that the addition of EC or CO_2 gas to TMP electrolyte enables some kinds of anodes to cycle [41]. It was still difficult to cycle graphite anodes. They then investigated 1M LiPF$_6$/TMP/vinylene carbonate (VC) (90:10) and 1M LiPF$_6$/TMP/VC/vinyl benzoate (VB) (80:10:10). The electrolyte of 1M LiPF$_6$/TMP/VC (90:10) showed an improved graphite anode capacity of 280 mAh·g^{-1}. However, the irreversible capacity was very large (ca. 150 mAh·g^{-1}). Using the electrolyte consisting of 1M LiPF$_6$/TMP/VC/VB (80:10:10), the irreversible capacity decreased to less than 12% without harming the cycling capacity. Then they prepared 14500-type cylindrical cells with 0.8M LiN(SO$_2$CF$_3$)$_2$ + 0.1M LiPF$_6$/TMP/VC/VB (84:8:8) electrolyte. In a nail penetration test, heat generation was quite small, and no flame, smoke, or explosion was observed. However, heating cells to 150°C generated a good deal of heat, probably due to the reaction between TMP and the anode. They found an exothermic DSC peak at around 150°C for this electrolyte with the anode.

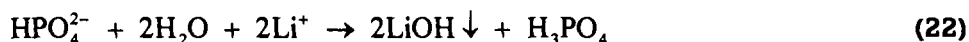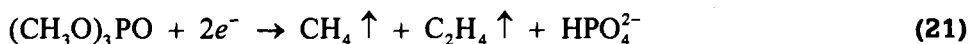Wang, et al. studied electrolytes of 1M LiPF$_6$/EC/PC/TMP (50-x/2:50-x/2:x) [40]. The electrolytes with 15% and 20% TMP were unable to cycle a graphite anode. When the TMP content was reduced to 10%, the graphite anode was effectively cycled. The capacity and coulombic efficiency were 268 mAh·g^{-1}

and 84%. Those for the electrolyte without TMP (x=0) were **342 mAh·g⁻¹** and 88%. At this small (10%) content of TMP, the electrolyte was flammable. The electrolytes with 15% and 20% of TMP were nonflammable. The authors also investigated electrolytes consisting of 1M **LiPF₆/EC/DEC/TMP** (50-x/2:50-x/2:x). The cycling of the graphite anode was improved using this electrolyte. The results are summarized in Table 10.

Table 10. Summary of the fundamental properties of 1M LiPF₆//EC/DEC/TMP (50-x/2:50-x/2:x) electrolytes. From reference 42.

x	Composition EC/DEC/TMP	Nonflammability	Conductivity mS·cm⁻¹ 25°C	Freezing Point °C	Capacity mAh·g⁻¹	Coulomb Efficiency %
0	50/50/0	No	8.3	-23	322	86
20	40/40/20	No	8.5	-15	245	81
25	37.5/37.5/25	No	-	-	224	79
30	35/35/30	No	-	-	115	10

In order to improve the cycling performance of lithium-ion batteries with TMP-based electrolytes, Wang et al. investigated amorphous carbon (AC) [42]. They found that the reduction decomposition of TMP solvent, which occurred without limit on a natural graphite anode and concomitantly generated a large amount of methane and ethylene gas, was considerably suppressed on the AC anode. They attributed this improvement to the disordered structure of AC, which hindered the co-intercalation of TMP solvent. Based on their experiments, they proposed a total reaction formula for TMP reduction decomposition on a natural graphite electrode:

$$(CH_3O)_3PO + 2e^- \rightarrow CH_4 \uparrow + C_2H_4 \uparrow + HPO_4^{2-} \tag{21}$$

$$HPO_4^{2-} + 2H_2O + 2Li^+ \rightarrow 2LiOH \downarrow + H_3PO_4 \tag{22}$$

As a result, an **AC/LiCoO₂** ion cell with 1M **LiPF₆/EC/PC/DEC/TMP** (30:30:20:20) nonflammable electrolyte exhibited promising cycling performance (capacity: **200 mAh·g⁻¹**, 1st cycle coulomb efficiency: 74%).

5.0   FLUORINATED SOLVENTS AND OTHER HALOGENATED SOLVENTS

R. McMillan et al. [43] studied 4-chloro-l,3-dioxolan-2-one (chloro-EC) and 4-fluoro-l,3-dioxolan-2-one (fluoro-EC) to improve the cycling performance of a graphite anode. Chloro-EC mixed solvent electrolyte showed a low current efficiency of ca. 90%. However, fluoro-EC mixed solvent electrolyte showed a high current efficiency of ca. 99.5%.

The solvation states of chloro-EC and 4-trifluoromethyl-1, 3-dioxolan-2-one (**CF₃-EC**) were investigated using ¹³C NMR [44]. The solvation to lithium ions by chloro-EC and **CF₃-EC** was weaker than that by PC due to

the effect of substituted electron attracting halogenated groups. In the system using a CF$_3$-EC 100% solution, the interface impedance between an amorphous carbon anode and the electrolyte was very high. This was attributed to the properties of the surface film on the carbon anode, which contains a trifluoromethyl group.

The decomposition of chloro-EC on a graphite electrode (formation of SEI) was investigated using two in situ techniques: subtractively normalized interfacial Fourier transform infrared spectroscopy (SNIFTIRS) and differential electrochemical mass spectrometry (DEMS) [45]. The applied analytical methods provided conforming information about the onset of CO$_2$ formation (2.2-2.1 V vs. Li/Li$^+$). Hydrogen is evolved below ca. 0.6 V Li/Li$^+$.

Naji et al. [46] investigated new halogenated additives such as α-bromo-γ-butyrolactone, methyl chloroformate, etc., to PC-based electrolytes to improve cycling performance.

N, N-dimethyl trifluoroacetamide was investigated as a co-solvent of PC by Moller et al. [47]. The electrolyte of 1M Li(CF$_3$SO$_2$)$_2$N//PC/*N,N*-dimethyl trifluoroacetamide (90:10, by volume) showed a good performance at a graphite anode (1st cycle efficiency: 87.1%, 2nd cycle efficiency: 98.6, 1st cycle discharge capacity: 353.7 mAh·g^{-1}).

Direct fluorination of γ-butyrolactone (γ-BL) was investigated by Sasaki et al. [48]. α-fluoro-γ-butyrolactone (α-F-γ-BL), β-fluoro-γ-butyrolactone (β-F-γ-BL), and γ-fluoro-γ-butyrolactone (γ-F-γ-BL) were synthesized by this method. The electrolyte of 1M LiPF$_6$/α-F-γ-BL/β-F-γ-BL/γ-F-γ-BL (1:4:5) and 1M LiPF$_6$/α-F-γ-BL/β-F-γ-BL (3:7) showed a better Li electrode cycling efficiency than 1M LiPF$_6$/γ-BL electrolyte [49].

The electrochemical behavior of a graphite electrode in a 1M LiClO$_4$/EC/DEC/fluoroester solution at low temperature was investigated to evaluate the effect of the addition of fluoroesters [50]. Each fluoroester (2.5 ml) shown in Table 11 was dissolved in 50 ml of 1M LiClO$_4$/EC/DEC (1:1) to prepare the electrolyte. Those authors then evaluated the electrochemical behavior of graphite electrode by cyclic voltammetry at 0°C. The peak intensities in the first reduction currents were larger in the order of 1>2>3≈4>5>EC/DEC. The CHF$_2$COOCH$_3$-mixed EC/DEC provided larger capacities than EC/DEC itself and other fluoroester-mixed solvents at 0°C and -4°C. They attributed this to the low molecular weight and small number of fluorine atoms of CHF$_2$COOCH$_3$; these characteristics would offer several advantages, including lower reduction potential as well as higher chemical interaction and miscibility with lithium salt and EC/DEC than other fluoroesters.

Table 11. Electrochemical behavior of 1M LiClO$_4$//EC/DEC/fluoroester. From reference 50.

No.	Fluoroester	The 1st reduction peak potential at 0°C (V vs. Li/Li$^+$)	Capacity at the 6th cycle (mAh/g)		Coulombic efficiency at the 1st cycle (%) ( ) = at the 6th cycle	
			25°C	0°C	25°C	0°C
1	CHF$_2$COOCH$_3$	0.87	355	330	63.5 (95.8)	73.7 (98.5)
2	CF$_3$CF$_2$COOCH$_3$	1.06	300	70	64.7 (95.4)	58.9 (92.3)
3	(CF$_3$)$_2$CHCOOCH$_3$	1.41	310	40	55.5 (95.9)	19.3 (91.8)
4	F(CF$_2$)$_3$COOCH$_3$	1.09	342	70	63.4 (96.7)	50.4 (95.0)
5	H(CF$_2$)$_4$COOCH$_2$CH$_3$	1.10	333	100	69.9 (96.2)	66.1 (95.7)
	None	0.60	358	75	81.9 (98.4)	72.5 (96.1)

Next, Nakajima et al. [51] investigated the effects of the addition of fluoroethers to **1M LiClO$_4$/EC/DEC**. The electrolyte solution was prepared by adding 5 ml of a fluoroether to 50 ml of 1M LiClO$_4$/EC/DEC (1:1 in volume). The results are summarized in Table 12.

Table 12. Electrochemical behavior of 1M LiClO$_4$//EC/DEC/fluoroether. From Reference 50.

No.	Fluoroether	The 1st reduction peak potential at 0°C (V vs. Li/Li$^+$)	Capacity at the 20th cycle (mAh/g)		Coulombic efficiency at the 1st cycle (%) ( ): at the 6th cycle*	
			25°C	0°C	25°C	0°C
a	CF$_3$CF$_2$CH$_2$OCH$_3$	0.59	357	283	61.0 (94)	69.7
b	(CF$_3$)$_2$CHCF$_2$OCH$_3$	0.67	347	285	52.2 (92)	70.0
c	HCF$_2$CF$_2$CH$_2$OCHF$_2$	0.57	352	247	70.1 (94)	81.2
d	CF$_3$CHFCF$_2$OCH$_2$CH$_3$	0.81	347	311	53.9 (86)	81.1
e	CHClFCF$_2$OCH$_2$CF$_3$	0.66	361	292	76.6 (96)	78.9
	None	0.60	364	271	84.9 (99)	79.8

*Coulombic efficiency at the 6th cycle at 0°C is 96% to 98%.

In Yamaki et al. [52], we investigated the thermal stability of fluorinated esters. In that study, we used partially fluorinated carboxylic acid esters (Table 13) as the electrolyte solvent and **LiPF$_6$** as the salt. **LiPF$_6$** salt was dissolved in esters 1´(MFA: methyl difluoroacetate) and 2´ (EFA: ethyl difluoroacetate) to a salt concentration of 1 molar. In the other fluorinated esters, however, **LiPF$_6$** salt could be dissolved to a salt concentration of less than 0.2 molar. Therefore, we used the solutions of 1´ and 2´ fluorinated esters with 0.2 M of **LiPF$_6$,** and the other fluorinated esters were saturated with **LiPF$_6$**. For the sake of comparison, we prepared the solutions of corresponding esters with 0.2 M of **LiPF$_6$**. We also performed similar measurements employing the conventional electrolyte solution used in lithium batteries, **1M LiPF$_6$/ EC+DMC 1:1** in volume.

Table 13. Solvents used in the studies in Reference 52.

Non-fluorinated Solvent		Fluorinated Solvent	
Sample Number	Solvent	Sample Number	Solvent
1	CH_3COOCH_3 (MA)	1'	CHF_2COOCH_3 (MFA)
2	$CH_3COOCH_2CH_3$ (EA)	2'	$CHF_2COOCH_2CH_3$ (EFA)
3	$CH_3CH_2COOCH_3$	3'	$CF_3CF_2COOCH_3$
4	$CH_3CH_2COO\ CH_2CH_3$	4'	$CF_3CF_2COO\ CH_2CH_3$
5	$H(CH_3)_2CCOOCH_3$	5'	$F(CF_3)_2CCOOCH_3$
6	$H(CH_2)_3COOCH_3$	6'	$F(CF_2)_3COOCH_3$
7	$H(CH_2)_3COOCH_2CH_3$	7'	$F(CF_2)_3COOCH_2CH_3$
8	$H(CH_2)_4COOCH_2CH_3$	8'	$H(CF_2)_4COOCH_2CH_3$
9	$H(CH_2)_7COOCH_2CH_3$	9'	$F(CF_2)_7COOCH_2CH_3$

We monitored the thermal stability of fluorinated esters (Table 14) using a TG-DSC. Each sample (5 μl for liquid) for TG-DSC measurement was packed in a stainless steel case, which was then crimp-sealed in an argon-filled glove box. In some cases, a piece (weighing several milligrams) of lithium metal or a charged $LiCoO_2$ pellet was packed and sealed along with a sample in the stainless steel case. Confirmation that the case did not leak was obtained from TG data, which we measured at the same time as the DSC measurement. A $LiCoO_2$ pellet was prepared by mixing $LiCoO_2$, acetylene black, and a polytetrafluoroethylene binder, packed in a coin cell with lithium metal anode and 1M $LiPF_6/EC+DMC$ electrolyte, and then charged to $Li_{0.5}CoO_2$ in a constant-current mode.

Table 14. Initial exothermic peak temperatures from thermogravimentric analyses of solvents in Table 13. From reference 52.

Solvent	Non-fluorinated Solvent Initial Peak Temperature (°C)			Solvent	Fluorinated Solvent Initial Peak Temperature (°C)		
	Electrolyte	Electrolyte + Li metal	Electrolyte + $Li_{0.5}CoO_2$		Electrolyte	Electrolyte + Li metal	Electrolyte + $Li_{0.5}CoO_2$
1	280	220	230	1'	290	290	310
2	210	110	240	2'	210	180	210
3	260	90	200	3'	280	330	210
4	210	90	200	4'	250	180	240
5	250	70	250	5'	270	290	180
6	260	90	170	6'	260	300	230
7	210	90	180	7'	260	170	220
8	240	120	170	8'	250	300	230
9	250	120	170	9'	230	160	220

It seems that the thermal stability of the $LiPF_6$/fluorinated esters was similar to those of the $LiPF_6$/corresponding esters except for esters 3, 4, 5, and 7 (Table 14). It should be noted that the fluorinated esters contained

smaller amounts of $LiPF_6$ than the corresponding esters, except for 1 and 2. In $LiPF_6$ electrolytes, ionic dissociation is not high, and associated $LiPF_6$ is in equilibrium with LiF and PF_5. PF_5 is a strong Lewis acid, which reacts with a small amount of water in electrolytes following the reaction $PF_5 + H_2O \rightarrow PF_3O + 2HF$. Assuming an analogy with this reaction, organic solvents may have reacted with PF_5 at a high temperature.

Many of the fluorinated ester systems coexisting with Li metal provide an exothermic peak temperature higher than the melting point of lithium metal, while the corresponding ester systems generate an exothermic reduction below the melting point of lithium metal (Table 14). This indicates that non-fluorinated esters may react with lithium metal at low temperature because of their enol form, and that fluorinated esters may help to produce a thick and effective protection layer (SEI) on Li metal to prevent further reduction of $LiPF_6$ solution even above the melting point of lithium metal.

The cycling efficiency of the lithium metal electrode was estimated by a cycle test using a coin cell. The cycling efficiency of the lithium metal electrode with 1M $LiPF_6$ / MA, MFA, EA, or EFA is 30%, 84%, 0%, or 50%, respectively.

The positions of the exothermic peaks of the $LiPF_6$ / various fluorinated esters and corresponding esters / $Li_{0.5}CoO_2$ systems are also summarized in Table 14. With the exception of esters 2´ and 5´, all fluorinated esters tended to inhibit the reaction with $Li_{0.5}CoO_2$.

The cycling performance of Li/LiCoO$_2$ cells with 1M $LiPF_6$ / MA, MFA, EA, or EFA was investigated. The MFA and EFA electrolytes showed very good performances. However, the cell with the MA or EA electrolyte could not be cycled because of the low oxidation potentials of the solvents.

Unfortunately, many fluorinated carboxylic acid esters did not dissolve 0.2 M $LiPF_8$, and we used saturated solutions for the experiments. However, ca. 1 M $LiPF_6$/EC/DMC/ fluorinated carboxylic acid esters (1:1:2 in vol.) can be prepared for all the fluorinated carboxylic acid esters listed in Table 13. Using the mixed solvent electrolyte, we investigated the thermal stability of the electrolyte system coexisting with Li metal [53]. The results are shown in Table 15. The onset temperature became higher by the addition of CHF_2COOCH_3. The addition of CHF_2COOCH_3, $CF_3CF_2COOCH_2CH_3$, or $F(CF_2)_3COOCH_3$ decreased the exothermic energy. These results indicate that CHF_2COOCH_3 was the most effective additive in this study.

A precise thermal study was undertaken [53] for 1M $LiPF_6$-CHF_2COOCH_3 and 1M $LiPF_6$/EC+DMC or PC, (ca. 1M $LiPF_6$-CHF_2COOCH_3/EC/DMC (x:50-x/2:50-x/2) and ca. 1M $LiPF_6$/CHF_2CO-OCH_3-PC (x:100-x)) changing the mixing ratio with the coexistence of lithium metal. The survived lithium metal content was estimated using DSC by the endothermic vs. exothermic heat ratio at lithium melting and freezing from 300 °C. The electrolyte volume for

DSC is $5\mu l$, the lithium weight is 1.3 mg, the heating rate is 5°C/min., and the temperature range is from room temperature to 300°C. As the volume ratio of CHF_2COOCH_3 increased from 0% to 100%, the amount of survived lithium metal increased from 0% to 95%.

Table 15. Onset temperatures of ca. 1 M LiPF$_6$/EC/DMC/fluorinated carboxylic acid esters (1:1:2 in vol.) with the coexistence of lithium metal, and the exothermic energy of electrolytes from 180 to 220°C. From reference 53.

Fluorinated Solvent	Onset Temperature (°C)	Exothermic Energy (J/g)
No addition (1 M EC+DMC)	180	2900
CHF_2COOCH_3	210	700
$CHF_2COOCH_2CH_3$	175	> 3500
$CF_3CF_2COOCH_3$	168	2100
$CF_3CF_2COOCH_2CH_3$	172	> 3500
$F(CF_3)_2CCOOCH_3$	173	3400
$F(CF_2)_3COOCH_3$	167	1900
$F(CF_2)_3COOCH_2CH_3$	169	3000
$F(CF_2)_4COOCH_2CH_3$	168	3000

The Li cycling efficiencies of 1M $LiPF_6$/EC/DMC, 1M $LiPF_6$/CH-F_2CO-OCH$_3$-mixed EC+DMC (50 w.%), 1M $LiPF_6$/PC, 1M $LiPF_6$ /CHF$_2$COOCH$_3$-mixed PC (50w.%), and 1M $LiPF_6$ /CHF$_2$COOCH$_3$ were 70%, 75%, 71%, 71%, and 85%, respectively. These results indicate that the single solvent electrolyte of CHF_2COOCH_3 showed the highest cycling efficiency and that the addition of CHF_2COOCH_3 to EC+DMC can improve cycling efficiency. However, the addition to PC cannot improve cycling efficiency.

The conductivities of 1M $LiPF_6$/EC/DMC, 1M $LiPF_6$/CHF$_2$COOCH$_3$-mixed EC+DMC, 1M $LiPF_6$/PC, 1M $LiPF_6$/CHF$_2$COOCH$_3$-mixed PC, and 1M $LiPF_6$/CHF$_2$COOCH$_3$ were 12 mS/cm, 14 mS/cm, 7 mS/cm, 13 mS/cm, and 12 mS/cm, respectively. The conductivity increased by the addition of CHF_2COOCH_3 to EC+DMC (50 w.%) or PC (50 w.%). We attributed these results to the lower viscosity of CHF_2COOCH_3 as compared to the viscosity of EC+DMC or PC.

6.0   ELECTROLYTE ADDITIVES

The effects of organic additives (2-methylfuran, 2-methyltetrahydrofuran, 2-methylthiophene, or polyethylene oxide (PEO)) in 1M $LiPF_6$/EC/DMC or 1M $LiPF_6$/EC/DEC were investigated on lithium electrodes [54]. Each of the additives decreased the interfacial resistance between the negative electrode and the electrolyte solution. Among the three additives, PEO was excellent.

Since PEO showed excellent properties, Matsuda et al. [55] then investigated additional properties of polymer materials, polyvinylpyr-rolidone (PVP), polyacrylonitrile, or PEO in the electrolyte solutions, EC/PC

(1:1 in vol.)//0.25M $LiBF_4$ or $Li(CF_3SO_2)_2N$. In the electrolyte solutions containing PVP, the charge-discharge current efficiency of lithium on the Ni electrode was the highest, and the interface resistance between a lithium metal electrode and the electrolyte solution was small during the charge-discharge cycle.

Wrodnigg et al. [56] proposed a new electrolyte with advantageous low-temperature performance. [Editor´s note: See Chapter 11, by Salomon, et al., for a comprehensive treatment of low temperature performance and electrolytes.] This electrolyte contained ethylene sulfite (ES) and PC. They studied 1M $LiClO_4/PC/ES$ (95:5 by volume). At the low temperatures tested, the PC-based electrolytes showed better performance than the EC-based electrolytes. The problem was that PC-based electrolytes could not cycle at the graphite anode. By adding ES, the PC-based electrolytes showed a good ability to cycle at a graphite anode because of improved SEI formation. Those authors also studied Propylene sulfite (PS) [57]. They extended their study to other sulfur-containing organic compounds, such as the linear sulfites, dimethylsulfite (DMS) and diethyl sulfite (DES), and others [58]. Comparing the electrochemical performance of the cyclic sulfites with that of the linear sulfites, they found that the filming strength (SEI) decreases in the order: ES>PS>>DMS>DES. The linear sulfites DMS and DES are not suitable as electrolyte additives in PC-based electrolytes. What about the use of DMS and DES as electrolyte additives in EC-based electrolytes? Judging from the constant current charge/discharge cycling data, DMS and DES together form an inferior electrolyte co-solvent for EC, compared with the co-solvent formed by DMC and DEC. However, electrolyte mixtures of DMS or DES with EC exhibit much better electrolyte conductivities [59].

7.0 OVERCHARGE PROTECTION BY REDOX SHUTTLE ADDITIVES

As research on the Li ion cell proceeds and the cell´s capacity increases, safety problems due to abuses such as overcharging become a greater concern. In addition to control by the charger, other safety mechanisms presently used are a control integrated circuit, a pressure-activated current breaker, and a positive temperature coefficient (PTC) device. There have been several reports on chemical prevention of overcharging [60-62]. The redox shuttle additives are oxidized on cathodes at potentials slightly higher than the potential at full charge. The oxidized additives move to anode and are reduced to their original forms. Some derivatives of ferrocene have been studied [60-62]. The overcharge protection potentials by the ferrocene derivatives are from 3 to 3.5 V, which is too low for the application to Li ion cells.

Recently, dihydrophenazine derivatives (N,N'-bis-(2-hydroxypropyl) dihydrophenazine, and N,N'-diethyldihydrophenazine) have been studied as redox shuttle additives by Tran-Van et al. [63]. N,N'-bis-(2-hydroxypropyl) dihydrophenazine in 1M LiClO4/PC/DME (1:1) showed a short first plateau at around 3 V followed by a much longer one at 3.8 V. However, N,N'-diethyldihydrophenazine did not work as a redox shuttle additive.

Adachi et al. [64] studied metal complexes of Fe, Ru, Ir, or Ce with ligands of phenanthroline or bipyridine. These complexes showed redox potentials at around 4 V. However, they did not work well in preventing overcharging, probably due to their low solubility and mobility. Those authors also studied aromatic compounds with two methoxy groups and a halogen compound directly substituted on the benzene. These compounds were stable up to about 4 V (vs. Li/Li^+), and oxidized above this potential. These compounds provided redox shuttle overcharge protection when added to the electrolyte of a $Li/LiCoO_2$ coin-type cell with 1M $LiPF_6/PC/DMC$. 4-bromo-l, 2-dimethoxybenzene showed the best performance (Table 16), and also showed no problem with a nongraphitizable carbon anode.

Table 16. Shuttle voltage of $Li/LiCoO_2$ coin-type cells with benzene derivatives. Reprinted from reference 64 with permission of The ElectroChemical Society, Inc.

Benzene Derivative	Shuttle Voltage (V)	Discharge Capacity (mAh/g)	Calculated Capacity (mAh/g)
4-bromo-1, 2-dimethoxybenzene	4.27	146	147
4-fluoro-1, 2-dimethoxybenzene	3.93	92	-
2-bromo-1, 4-dimethoxybenzene	4.17	126	131
2-fluoro-1, 4-dimethoxybenzene	4.04	92	106

8.0   THERMAL STABILITY

Recently, the study of the utilization of the high-performance Li-ion cells as power sources of electric vehicles (EV) and other applications requiring large cells has been undertaken by a number corporations and laboratories. Spotnitz discusses issues pertaining to the scale-up of lithium-ion cells and batteries in Chapter 14. However large-sized Li-ion cells have not been commercially realized as their performance and safety are still being characterized and improvements are engineered. Organic compounds are used as electrolytes of Li-ion cells, and these compounds decompose at elevated temperatures with heat generation. Therefore the generation of heat by chemical decomposition and the chemical reactions in the cells are an important factor in to be considered. In the past 10 years, the thermal stability or the thermal behavior of Li-ion cells has been investigated energetically using DSC or Accelerating Rate Calorimetry (ARC).

8.1　　Thermal Stability of Cells

Biensan et al. examined the thermal behavior of materials in lithium-ion cells using DSC (Table 17). They concluded that non-active materials, like binders, should also be optimized if one wants to improve the thermal stability of the electrochemistry.

Table 17. Thermal behavior of materials in Li ion cells. Reprinted from reference 65 with permission of Elsevier Science.

Temperature Range (°C)	Reaction	Energy (J/g)	Comment
110-150	Li_xC_6 + electrolyte	350	Rupture of passivation layer
130-180	Fusion separator P. E.	-190	Endothermic
130-220	Solvents + $LiPF_6$	250	Low energy
160-190	Fusion separator P. P	-90	Endothermic
150-300	Decomposition of $Li_{0.1}Mn_2O_4$ + Electrolyte	450	Oxygen emission T= ca. 300°C
180-500	Decomposition of $Li_{0.3}NiO_2$ + Electrolyte	600	Oxygen emission peak T= ca. 200°C
220-500	Decomposition of $Li_{0.45}CoO_2$ + Electrolyte	450	Oxygen emission peak T= ca. 230°C
240-350	Li_xC_6 + PVdF binder (rinsed)	1500	Violent-propagation
660	Fusion of aluminum	-395	Endothermic

Electrolyte: 1M $LiPF_6$/PC/EC/DMC (1:1:3)

8.2　　Thermal Stability of Electrolytes

Botte et al. studied the thermal stability of **$LiPF_6$/EC/EMC** electrolyte using DSC by. [66]. In their work, hermetically sealed and crimped DSC pans (in a dry room) were used during the experiments. 1M **$LiPF_6$/EC** electrolyte showed an exothermic reaction from 250 to 300 °C, and the reaction temperature fell as the concentration of **$LiPF_6$** decreased. 1M **$LiPF_6$/EMC** electrolyte showed an endothermic peak from 220 to 280 °C and a very small exothermic peak. They concluded that the endothermic peak could be related to the decomposition of the salt or cracking of the EMC.

The thermal stability of **$LiPF_6$/carbonate** electrolyte was studied by Kawamura et al. [67]. Figure 3 shows the DSC curves of 1M **$LiPF_6$/EC-DEC** (1:1 in vol.), **1M $LiPF_6$/EC/DMC** (1:1 in vol.), **1M $LiPF_6$/PC/DEC** (1:1 in vol.), and **1M $LiPF_6$/PC/DMC** (1:1 in vol.). Exothermic peaks between 230 and 280°C were observed for the mixed solvents with **$LiPF_6$,** suggesting that **$LiPF_6$** is related to the exothermic decomposition reaction. The peak temperatures of the electrolytes containing DEC were 15-20°C lower than those of the electrolytes containing DMC.
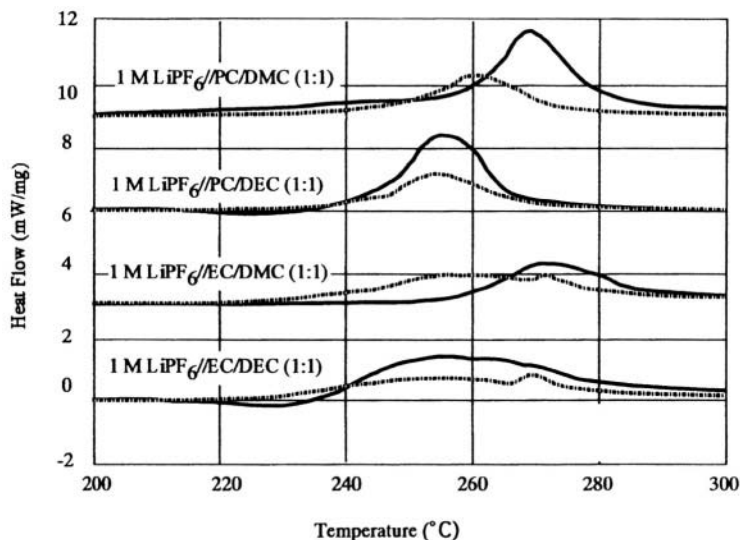
Figure 3. DSC profiles of 1M LiPF₆/EC/DEC (1:1 in vol.), 1M LiPF₆/EC/DMC (1:1 in vol.), 1M LiPF₆/PC/DEC (1:1 in vol.), and 1M LiPF₆/PC/DMC (1:1 in vol.) electrolytes with or without water. Solid Line: without H₂O; Dashed Line: With H₂O. From Reference 67.

$LiPF_6$, which is not dissociated in electrolytes, produces a strong Lewis acid, PF_5. PF_5 attacks the electron lone pair of oxygen in water and decomposes [68]. By analogy, PF_5 may attack the electron lone pair of oxygen in solvent and then decompose. Indeed, Sloop et al. [69] showed experimentally that the reaction products of PF_5 and EC/DMC are the same as the thermal decomposition products of $LiPF_6$/EC/DMC electrolyte. Mori et al. [70] identified the thermal decomposition products of $LiPF_6$/Diisopropyl carbonate as $(CH_3)_2CHF$, $CH_3CH=CH_2$, $(CH_3)_2CHOH$, CO_2, and $(CH_3)_2CHO(CHCH_3)_2$.

DSC curves of the $LiPF_6$ electrolytes with water are also shown in Figure 3. Smaller exothermic peaks were obtained for the electrolytes with added water than for those without water. The reason for the reductions in these peaks was the decrease in $LiPF_6$ caused by the reaction between $LiPF_6$ and H_2O. Table 18 shows the calorific value of electrolytes and that of electrolytes with water (about 10000 ppm). The heat-generation curves have a tendency to shift to lower temperature with the addition of water, a tendency that is probably caused by the solvents´ reaction with HF (that is, the reaction product of $LiPF_6$ and water).

The thermal stability of 1M $LiClO_4$ electrolytes with or without water (approximately 10000 ppm) was investigated by Kawamura et al. [67]. The peak temperature of electrolytes containing DEC was 10°C lower than that of electrolytes containing DMC. This result is similar to that for electrolytes containing $LiPF_6$. The reason why there is no great difference

in the DSC curves between only electrolytes and electrolytes plus water is that $LiClO_4$ does not react with H_2O. **Table 19** shows the calorific values of electrolytes containing $LiClO_4$ with or without water (approximately 10000 ppm). The heat value of electrolytes containing DEC was larger than that of electrolytes containing DMC. The heat value of $LiClO_4$ electrolytes was two or three times that of the $LiPF_6$ electrolytes.

Table 18. Calorific values of 1M $LiPF_6$/EC/DEC (1:1), 1M $LiPF_6$/EC/DMC (1:1), 1M $LiPF_6$/PC/DEC (1:1), and 1M $LiPF_6$/PC/DMC (1:1) with/without water. From reference 67.

	Calorific Value (J/g)			
	$LiPF_6$/EC/DEC	$LiPF_6$/EC/DMC	$LiPF_6$/PC/DEC	$LiPF_6$/PC/DMC
without water	500	370	530	380
with water	200	230	270	230

Table 19. Calorific values of 1M $LiClO_4$/EC+DEC (1:1), 1M $LiClO_4$/EC+DMC (1:1), 1M $LiClO_4$/PC+DEC (1:1), and 1M $LiClO_4$/PC+DMC (1:1) with/without water. From reference 67.

	Calorific Value (J/g)			
	$LiClO_4$/EC/DEC	$LiClO_4$/EC/DMC	$LiClO_4$/PC/DEC	$LiClO_4$/PC/DMC
without water	1040	820	1250	940
with water	950	830	1030	760

8.3 Thermal Stability of Electrolytes With Carbon Anode

The thermal stability of carbon anodes in an electrolyte is controlled by a solid electrolyte interphase (SEI) formed on the lithiated carbon anode. Edstrom et al. [71, 72] reported that thermal breakdown of the SEI when using $LiBF_4$ electrolytes starts at 58°C (Graphite, $LiBF_4$-EC+DMC), while Richard et al [73] considered from their experiments that the use of $LiPF_6$ shifts the breakdown temperature to 102°C. However, Zhang et al. [74] suggested that the exothermic reaction (MCMB, $LiPF_6$/EC+DMC) at around 130°C is related to the surface passivation of the lithiated carbon materials (not thermal breakdown of the SEI). Von Sacken et al. [75] also proposed a reaction model based on a simple heterogeneous reaction between the electrolyte solvent and the lithiated carbon, where the reaction produces a passivating film on the carbon surface. Richard et al. [73] reported that the initial form of self-heating rate profile at around 100°C (MCMB, $LiPF_6$/EC+DEC) was a result of the conversion of metastable solid electrolyte interphase (SEI) components to stable SEI components. The question thus arises as to what is the real reason for the exothermic reaction at around 100°C.
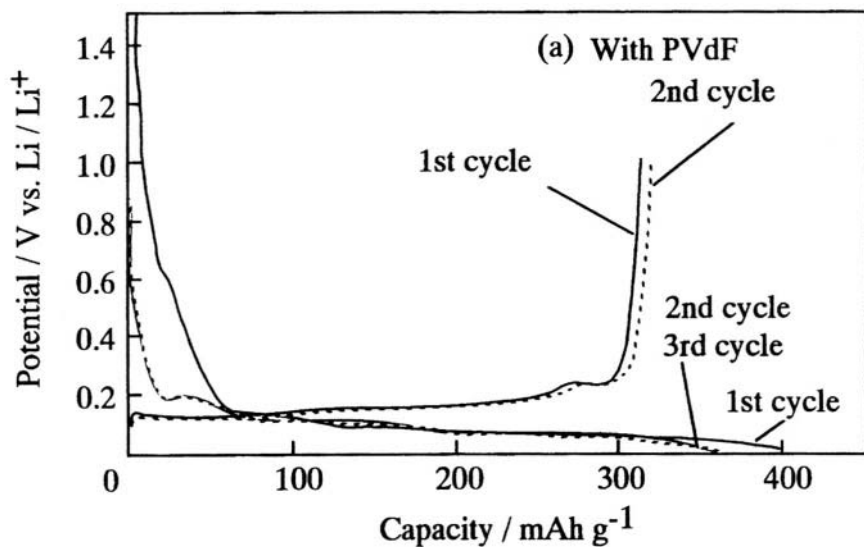
Figure 4a. Cycling profile of a graphite anode *with* PVDF binder versus a lithium foil counter electrode. From reference 76
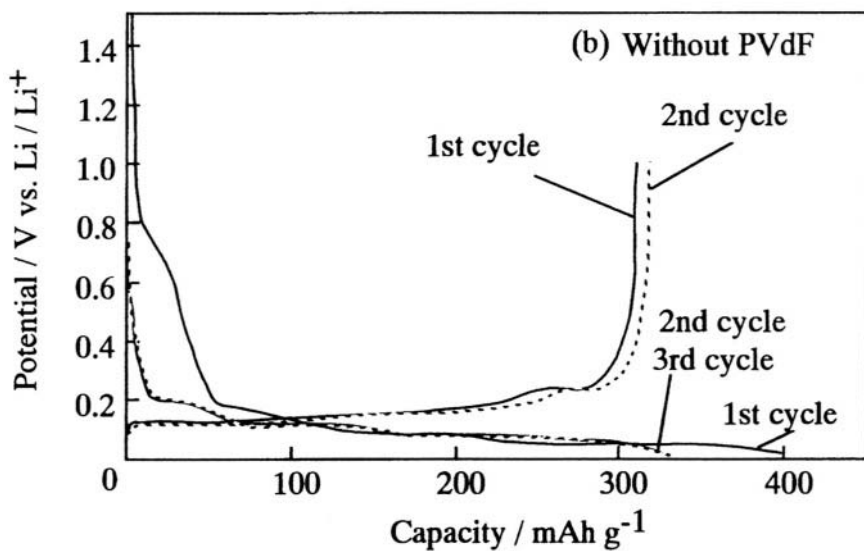

Figure 4b. Cycling profile of a graphite anode *without* PVDF binder versus a lithium foil counter electrode. From reference 76

We investigated the thermal stability of LiPF$_6$/EC/DMC (1:1 in vol.) electrolyte with a lithiated graphite anode in detail [76]. Figure 4 shows the cycling profile of a graphite anode with a lithium foil as a counter electrode. Figure 4(a) presents the profile of a typical graphite anode containing a PVdF-binder. Figure 4(b) shows the profile of a graphite anode without a PVdF-binder; the anode was made using an oil hydraulic press. The third discharge capacity of those samples was nearly 300 mAh·g^{-1}.. Thus, the lithiated PVdF-free anode was used for DSC measurement.

Figure 5 shows DSC curves of (a) the fully lithiated graphite with the electrolyte and PVdF (the usual graphite anode), (b) the fully lithiated graphite with the electrolyte (the anode made using an oil hydraulic press), (c) the fully delithiated graphite with the electrolyte and PVdF (the usual graphite anode), (d) the fully lithiated graphite with PVdF (the usual graphite anode) with a washing/vacuum-drying procedure, and (e) the electrolyte. The washing/vacuum-diying procedure for sample (d) was performed to remove the electrolyte. The precise process is to wash the anode with EC+DMC (1:1 v/v) solvent several times, followed by vacuum drying at 60°C for 3 hr. The heat flow shown is based on the total weight of the sample. Sample (a) shows a mild heat generation starting from 130°C, with a small peak at 140°C. The mild heat generation continued until a sharp exothermic peak appeared at 280°C. The lithiated graphite with the PVdF-binder-free electrolyte (sample (b) did not show the small peak at 140°C. Samples (c) and (d) also did not show small peaks at 140°C. Therefore, three components—the PVdF binder, the lithiated graphite, and the electrolyte—are necessary in order for the small peak to appear at 140°C. From their experiments using an accelerating rate calorimeter (ARC), Richard et al. [73] reported that the peak of the self-heating rate profile vs. temperature at around 100°C (MCMB, LiPF$_6$/EC+DEC) was a result of the conversion of metastable SEI components to stable SEI components. Their experiments were carried out under adiabatic conditions. We believe that the peak of the self-heating rate profile at around 100°C corresponds to the small peak at 140°C in our experiments. Therefore, if the consideration of Richard et al. [73] is correct, the sample (b) should show the small peak at 140°C. From our experiments, the small peak at 140°C seems to be caused by the reaction (SEI formation) of the electrolyte and lithiated graphite, whose surface is covered by the PVdF-binder without SEI formation at a lower temperature. The PVdF-binder covers a portion of the surface area of graphite when an anode is fabricated. After charging, graphite particles are lithiated and SEI is formed on the graphite particle surfaces. However, the areas of the graphite particles coveredby the PVdF-binder do not form SEI because the PVdF-binder prevents contact between the lithiated graphite particles and the electrolyte at room temperature. When the temperature is higher than that, the protective effect of the PVdF-binder becomes insufficient. This is probably caused by swelling of the PVdF-binder by the

electrolyte as the temperature rises. Okamoto et al. [77] reported that the small peak at 140°C disappears after graphite anode (with PVdF) is aged with LiPF$_6$/EC+DMC+diethyl carbonate (DEC) electrolyte.
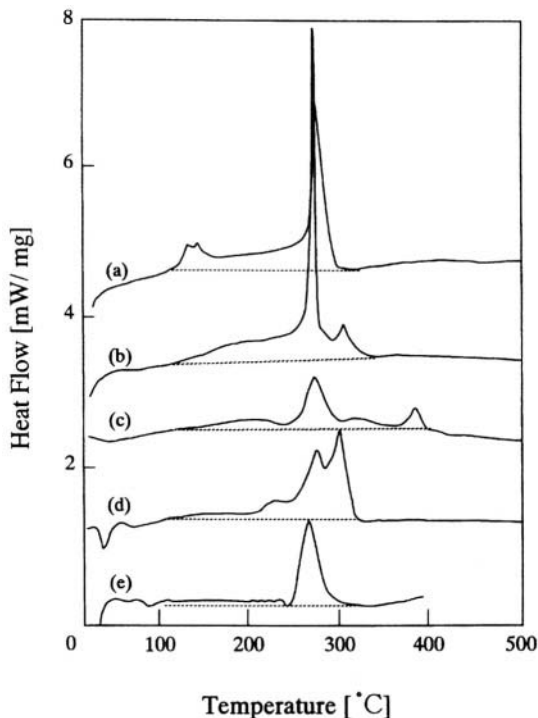
Figure 5. DSC curves of a) the fully lithiated graphite with the electrolyte and PVdF (the usual graphite anode), b) the fully lithiated graphite with the electrolyte (the anode made using an oil hydraulic press), c) the fully delithiated graphite with the electrolyte and PVdF (the usual graphite anode), d) the fully lithiated graphite with PVdF (the usual graphite anode) with washing/vacuum-drying procedure, and e) the electrolyte (1M LiPF$_6$/EC/DMC). From reference 76.

DSC measurements were carried out for PVdF and PVdF with Li metal. PVdF begins to decompose at 400°C. PVdF with Li metal shows an exothermic reaction from 290°C. Therefore, a peak at 390°C in Figure 5(c) is the decomposition of PVdF. A peak at 300°C in Figure 5(d) is the reaction of PVdF with the lithiated graphite.

A mild heat generation continued from 130°C until a sharp exothermic peak appeared at 280°C for the samples (a) and (b) in Figure 5. As considered by von Sacken et al. [75], this mild heat generation is caused by a simple heterogeneous reaction between the electrolyte solvent and the lithiated carbon, where the reaction produces a passivating film on the carbon surface. In other words, the mild heat generation comes from the reaction of lithiated carbon with the electrolyte to form a new SEI. The

lithiated graphite and electrolyte can react if the electrolyte permeates the SEI to reach the lithiated graphite surface. Therefore, the samples (c) (delithiated graphite) and (d) (without the electrolyte) in Figure 5 show very little heat generation in this region compared with the DSC curves of the samples (a) and (b). Those low levels of heat generation may be the result of reactions of components in SEI.

A sharp exothermic peak at 280°C is observed if the lithiated graphite and electrolyte co-exist as shown in Figure 5. Therefore, the exothermic reaction is a direct reaction of the lithiated graphite and electrolyte caused by a breakdown of the SEI. The electrolyte also decomposes at around 280°C. Hence, the electrolyte decomposition may cause the breakdown of SEI.

9.0   REFERENCES

1.   D. Aurbach, G.E. Blomgren, L.A. Dominey, I. Galasiu, R. Galasiu, Y. Gofer, S. Komaba, X. Liu, T. Osaka, D.A. Scherson, J. Thonstad, I. Weissman, and A. Zaban, *"Nonaqueous Electrochemistry",* D. Aurbach, ed., Marcel Dekker, Inc., 1999.
2.   J. Barthel and H.J. Gores, *"Handbook of Battery Materials",* J.O. Besenhard, ed., Chap. 7, Wiley-VCH, 1999.
3.   M. Morita, M. Ishikawa, and Y. Matsuda, *"Lithium Ion Batteries",* M. Wakihara and O. Yamamoto, eds., Chap. 7, Kodansha and Wiley-VCH 1998.
4.   K. Hayashi, Y. Nemoto, S. Tobishima, and Y. Sakurai, *DENKI KAGAKU,* 66, 1307, 1999.
5.   K. Hayashi, Y. Nemoto, S. Tobishima, and J. Yamaki, *Key Engineering Mat.* **157-158,** 273, 1999.
6.   H.H. Horowitz, J.I. Habermann, L.P. Klemann, G.H. Newman, E.L. Strogryn and T.A. Whitney, in *Lithium Batteries,* H.V. Venkatasetty, Editor, p. 131, The Electrochemical Society Proceedings Series, Pennington, NJ, 1981.
7.   M. Ue, M. Takeda, M. Takehara and S. Mori, *J. Electrochem. Soc.,* **144,** 2685, 1997.
8.   K. Hayashi, S. Tobishima, H. Arai and J. Yamaki, in Proceedings of the 35th Battery Symposium in Japan, Nagoya, Japan, p. 151, 1994.
9.   C.W. Walker, Jr., J.D. Cox and M. Salomon, *J. Electrochem. Soc.,* **143,** L80, 1996.
10.   J. Barthel, R. Buestrich, E. Carl and H.J. Gores, *J. Electrochem. Soc.,* **143,** 3572, 1996.
11.   S.S. Zhang and C.A. Angell, *J. Electrochem. Soc.,* **143,** 4047, 1996.
12.   A.J. Bard and L.R. Faulkner, *Electrochemical Methods,* p. 257, John Wiley & Sons, New York, 1980.
13.   M. Egashira, H. Takahashi, S. Okada, and J. Yamaki, *J. Power Sources,* **92,** 267, 2001.
14.   R. Imhof and P. Novak, *J. Electrochem. Soc.,* **146,** 1702, 1999.
15.   K. Kanamura, *J. Power Sources,* **81-82,** 123, 1999.
16.   F. Joho and P. Novak, Electrochim. Acta, **45,** 3589, 2000.
17.   D. Aurbach and H. Gottlieb, Electrochim. Acta, **34,** 141, 1989.
18.   M. Arakawa and J. Yamaki, J. Power Sources, **54,** 250, 1995.

19. K. Kumai, H. Miyashiro, Y. Kobayashi, K. Takei, and R. Ishikawa, *J. Power Sources,* **81-82,** 715, 1999.
20. K. Xu, S. P. Ding, and T. R. Jow, *J. Electrochem. Soc.,* **146,** 4172, 1999.
21. X. Zhang, J. K. Pugh, and P. N. Ross, Jr., *J. Electrochem. Soc.,* **148,** E183, 2001.
22. X. Zhang, R. Kostecki, T.J. Richardson, J.K. Pugh, and P.N. Ross, Jr., *J. Electrochem. Soc.,* **148,** A1341, 2001.
23. D. Brouillette, G. Perron, and J.E. Desnoyers, *Electrochim. Acta,* **44,** 4721, 1999.
24. G. Moumouzias, G. Ritzoulis, V. Komvokis, C. Zovoilis, and D. Siapkas, *J. Power Sources,* **81-82,** 830, 1999.
25. C. Capiglia, Y. Saito, H. Kageyama, P. Mustarelli, T. Iwamoto, T. Tabuchi, and H. Tukamoto, *J. Power Sources,* **81-82,** 859, 1999.
26. I. Geoffroy, P. Willmann, K. Mesfar, B. Carre, and D. Lemordant, *Electrochim. Acta,* **45,** 2019, 2000.
27. K. Hayashi, Y. Nemoto, S. Tobishima, and J. Yamaki, *Electrochimica Acta,* **44,** 2337-2344, 1999.
28. M. S. Ding, K. Xu, S. S. Zhang, K. Amine, G. L. Henriksen, and T. R. Jow, *J. Electrochem. Soc.,* **148,** A1196, 2001.
29. M. C. Smart, B. V. Ratnakumar, and S. Surampudi, *J. Electrochem. Soc.,* **146,** 486, 1999.
30. L. Doucey, M. Revault, A. Lautie, A. Chausse, and R. Messina, *Electrochimica Acta,* **44,** 2371, 1999.
31. T. Li and P.B. Balbuena, *J. Electrochem. Soc.,* **146,** 3613, 1999.
32. K. Hayashi, Y. Nemoto, S. Tobishima, and Y. Sakurai, *J. Power Sources,* **81-82 ,** 782, 1999.
33. U. Heider, R. Oesten, and M. Jungnitz, *J. Power Sources,* **81-82,** 119, 1999.
34. T. Kawamura, A. Kimura, S. Okada, and J. Yamaki, *Extended Abstracts of the 41st Battery Symposium in Japan,* 280. 2000.
35. T. Kawamura, A. Kimura, S. Okada, and J. Yamaki, *Extended Abstracts of the 42nd Battery Symposium in Japan,* 226, 2001.
36. S. Iinou, M. Handa, and Y. Sasaki, *Electrochemistry,* **67,** 22, 1999.
37. X. Wang, E. Yasukawa, and S. Mori, *J. Electrochem. Soc.,* **146,** 3992, 1999.
38. X. Wang, E. Yasukawa, and S. Kasuya, *J. Electrochem. Soc.,* **147,** 2421, 2000.
39. G.Y. Gu, S. Bouvier, C. Wu, R. Laura, M. Rzeznik, K.M. Abraham, *Electrochim. Acta,* **45,** 3127, 2000.
40. X. Wang, E. Yasukawa, and S. Kasuya, *J. Electrochem. Soc.* **148,** A1058, 2001.
41. N. Shinoda, J. Ozaki, F. Kita, and A. Kawakami, Abstract 335, *The Electrochemical Society and The Electrochemical Society of Japan Meeting Abstracts,* Vol. 99-2, Honolulu, HI, Oct 17-22,1999.
42. X. Wang, E. Yasukawa, and S. Kasuya, *J. Electrochem. Soc.* **148,** A1066, 2001.
43. R. McMillan, H. Slegr, Z.X. Shu, and W. Wang, *J. Power Sources,* **81-82,** 20, 1999.
44. H. Katayama, J. Arai, and H. Akahori, *J. Power Sources,* **81-82,** 705, 1999.
45. M. Winter, R. Imhof, F. Joho, and P. Novak, *J. Power Sources,* 81-82, 818, 1999.
46. A. Naji, J. Ghangaja, P. Willmann, and D. Billaud, *Electrochim. Acta,* **45,** 1893, 2000.
47. K.-C. Moller, T. Hodal, W.K. Appel, M. Winter, and J.O. Besenhard, *J. Power Sources,* **97-98,** 595, 2001.
48. Y. Sasaki, R. Ebara, N. Nanbu, M. Takehara, and M. Ue, *J. Fluorine Chem.* **108,** 117, 2001.

49. R. Ebara, N. Nanbu, M. Takehara, M. Ue, and Y. Sasaki, *Extended Abstracts of the 42nd Battery Symposium in Japan,* 228, 2001.
50. T. Nakajima, K. Dan, and M. Koh, *J. Fluorine Chem.,* **87,** 221, 1998.
51. T. Nakajima, K. Dan, M. Koh, T. Ino, and T. Shimizu, *J. Fluorine Chem.,* **111,** 167, 2001.
52. J. Yamaki, I. Yamazaki, M. Egashira, and S. Okada, *J. Power Sources,* **102,** 288, 2001.
53. K. Sato, I. Yamazaki, S. Okada, and J. Yamaki, *Solid State Ionics,* in press.
54. Y. Matsuda and M. Sekiya, *J. Power Sources,* **81-82,** 795, 1999.
55. Y. Matsuda, T. Takemitsu, T. Tanigawa, T. Fukushima, *J. Power Sources,* **97-98,** 589, 2001.
56. G.H. Wrodnigg, J.O. Besenhard, and M. Winter, *J. Electrochem. Soc.,* **146,** 470, 1999.
57. G.H. Wrodnigg, T.M. Wrodnigg, J.O. Besenhard, and M. Winter, *Electrochem. Commun.* **1,** 148, 1999.
58. G.H. Wrodnigg, C. Reisinger, J.O. Besenhard, and M. Winter, *ITE Battery Lett.* **1,** 110, 1999.
59. G.H. Wrodnigg, J.O. Besenhard, and M. Winter, *J. Power Sources,* **97-98,** 592, 2001.
60. K.M. Abraham, D.M. Pasquariello, and E.B. Willstaedt, *J. Electrochem. Soc.,* **137,** 1856, 1990.
61. S.R. Narayama, S. Surampudi, A.I. Attia, and C.P. Bankston, *J. Electrochem. Soc.,* **138,** 2224, 1991.
62. M. N. Golovin, D. P. Wilkinson, J. T. Dudley, D. Holonko, and S. Woo, *J. Electrochem. Soc.,* **139,** 5, 1992
63. F. Tran-Van, M. Provencher, Y. Choquette, and D. Delabouglise, *Electrochim. Acta,* **44,** 2789, 1999.
64. M. Adach, K. Tanaka, and K. Sekai, *J. Electrochem. Soc.,* **146,** 1256, 1999.
65. P. Biensan, B. Simon, J.P. Peres, A. de Guibert, M. Broussely, and J.M. Bodet, *J. Power Sources,* **81-82,** 906, 1999.
66. G. G. Botte, R. E. White, and Z. Zhang, J. Power Sources, **97-98,** 570, 2001.
67. T. Kawamura, A. Kimura, M. Egashira, S. Okada, and J. Yamaki, J. Power Sources, in press.
68. D. Aurbach, A. Zaban, Y. Ein-Eli, I. Weissman, O. Chusid, B. Markovsky, M. Levi, E. Levi, A. Schechechter, E. Granot, *J. Power Sources,* **68,** 91, 1997.
69. S.E. Sloop, J.K. Pugh, S. Wang, J.B. Kerr and K. Kinoshita, Electrochem. *Solid State Lett.,* **4,** A42, 2001.
70. S. Mori, H. Asahina, H. Suzuki, A. Yonei, E. Yasukawa, *8th International Meeting on Lithium Batteries Extended Abstracts,* Nagoya Japan, June 16-21, 40, 1996.
71. K. Edstrom, A.M. Andersson, A. Bishop, L. Fransson, J. Lindgren, A. Hussenius, *J. Power Sources,* **97-98,** 87, 2001.
72. A.M. Andersson, K. Edstrom, J.O. Thomas, *J. Power Sources,* **81-82,** 8, 1999.
73. M.N. Richard, J.R. Dahn, *J. Electrochem. Soc.,* **146,** 2068, 1999.
74. Z. Zhang, D. Fouchard, J.R. Rea, *J. Power Sources,* **70,** 16, 1998.
75. U. von Sacken, E. Nodwell, A. Sundher, J.R. Dahn, *J. Power Sources,* **54,** 240, 1995.
76. J. Yamaki, H. Takatsuji, T. Kawamura, and M. Egashira, *Solid State Ionics,* in press.
77. A. Okamoto, T. Sasaki, S. Komatsu, K. Nakamitsu, H. Tsukamoto, M. Mizutani, *GS News Technical Report,* **56,** 18, 1999.

6

Ionic Liquids for Lithium Ion
And Related Batteries

Andrew Webber
Energizer
25225 Detroit Rd.
P. O. Box 450777
Westlake, OH 44145
USA

George E. Blomgren
Blomgren Consulting Services Ltd.
1554 Clarence Ave.
Lakewood, OH 44107
USA

1.0   INTRODUCTION

This chapter reviews the use of ionic liquids, also known as molten salts, in lithium ion and related battery systems. This topic was not included in previous treatises of lithium-ion technology and its inclusion reflects the significant advances made in this area in recent years. Ionic liquids have experienced a resurgence of interest as electrolytes for ambient temperature batteries and capacitors. In large part, this is because new materials have been found that are less corrosive than $AlCl_3$-based electrolytes, which was the focus of work for many years. Many of these new salts are also hydro-lytically stable. Moreover, these new electrolytes contain the lithium or sodium ions necessary to run lithium or sodium cells. This makes them much more suitable for practical consumer batteries. Much of the work has been done in half-cells or with solid metal anodes, but the findings can often be applied to lithium-ion analogs. Consequently, both metal and carbon-based anodes are included in this review. In general, we have limited the scope to articles published since 1990. Readers are referred to the chapters in Mamantov and Popov´s book for work prior to 1990 [1]. Developments in ionic liquids for capacitors are reviewed elsewhere in this book.

Much of the literature, both before and after 1990 on ionic liquids for batteries, is dominated by work by the United States Air Force (Wilkes, Carlin and Fuller), by Covalent Associates (Carlin and Fuller), and by Koura´s, Riechel´s, Kohl´s and Osteryoung´s groups. The USAF also sponsored much of the work by Riechel and Osteryoung. Recent reviews on this topic are in Mamantov and Popov´s book [1], by Fung in 1998 [2] and Takahashi et al. in 1999 [3]. Carlton and Fuller also presented an overview in 1997 [4]. Note that Symposia on Molten Salts are periodically sponsored as part of the

semiannual Electrochemistry Society Meetings. Ionic liquids continue to be studied as electroplating media as well. Several papers also describe iodide-based ionic liquids as electrolytes for dye-based solar cells, using the I^-/I_3^- couple [5-8].

2.0   WHY USE IONIC LIQUIDS?

Ionic liquids have unique characteristics that potentially have great advantages for use in batteries, namely:

Non-fiammability - This has obvious advantages for any cell system. Studies have shown that while direct application of an external flame can make the organic salt present in these electrolytes burn, the fire is immediately extinguished when the external flame is removed [4]. While technically one might more accurately call this "self-extinguishing" or fire retardant rather than non-flammable, the effect is very dramatic. With the exception of some phosphate esters [9-16], other phosphorus-containing materials [13,17] and a $LiPF_6$/poly-acrylonitrile gelled electrolyte [18,19], we know of no other liquid electrolytes that have this property. (Note that the use of $LiPF_6$ salt is also important in the flame resistance of these organic electrolytes $LiPF_6$) [13,18,19]. While the impact of this property on actual cell safety has yet to be demonstrated, it would seem reasonable to expect that self-extinguishing electrolytes would be much better at avoiding thermal runaway that can occur in cells and would offer an extra degree of safety. This property can also act to overcome variability in mass production of cells. One might be able to reduce the high cost of electronic circuits required to prevent current lithium-ion cells from becoming overcharged, although overcharge protection is necessary for maintaining cell cycle life as well as safety.

Low vapor pressure - This attribute has several important consequences and is of course a contributing reason for the self-extinguishing nature of the liquids. Ionic liquids will not evaporate under normal conditions so that cells do not need to be hermetically sealed to keep the electrolyte in the cell, although preventing moisture ingress will still require good seals. The low vapor pressure also makes manufacture of cells safer and less expensive than when using conventional liquid electrolytes, which usually require engineering controls and industrial hygiene monitoring to ensure employee safety.

In addition, microbatteries and other small batteries benefit from having a non-volatile electrolyte. This facilitates filling the cell, especially in the real world where line stoppages can cause manufacturers to scrap or rework cells due to loss of solvent during any downtime. More importantly, the low vapor pressure means that extra electrolyte is not needed just to maintain a wet cell during storage and that electrolyte permeation through the cell seal and packaging material is not a problem. In some thin cell designs, the packaging

materials required to contain organic electrolytes normally used for lithium and lithium ion batteries constitute a major portion of the cell volume and cost. Ionic liquids may help lower costs and regain some of the space otherwise lost to the cell packaging materials.

The low vapor pressure also allows drying ionic liquids under vacuum [20], sometimes at very high temperatures [21]. Conventional electrolytes are usually made using solvents dried over molecular sieves and salts that are either vacuum dried and/or made under strict anhydrous conditions. The electrolyte is then blended, stored and handled under rigorously controlled conditions to avoid moisture pick-up. This adds significantly to the cost of conventional electrolytes. In addition, there is no easy way to recover a batch of electrolyte if it becomes exposed to moisture in the air. Molecular sieves cannot be used to dry finished electrolytes because of Na-Li ion exchange that occurs since lithium and lithium ion cells are very sensitive to sodium contamination of the electrolyte. Li-based sieves have been used, but these are not readily available and even small traces of sodium left in such sieves generally leave unacceptable levels of sodium in the electrolyte. Methods whereby the electrolyte is refluxed using sieves in a soxhlet-type arrangement avoid the Na-Li ion exchange, but these are seldom used because of the possibility of electrolyte degradation at elevated temperatures. For lithium ion cells in particular, the salts commonly used are hydrolytically unstable and generate HF on exposure to water. Thus, the industry relies upon strict quality control to avoid moisture exposure. By contrast, ionic liquids that use the hydrolytically stable salts described in this review can be dried at any time and their manufacture is consequently more forgiving and potentially less expensive.

High thermal stability - Ionic liquids usually have very high thermal stability. This greatly increases the operating temperature of the system and allows one to make specialized batteries for high-temperature applications such as down-hole drilling, engine sensors, etc.

Good electrochemical stability - This is usually evidenced by the wide electrochemical window that can be achieved with molten salts, especially for neutral melts. Such wide windows allow one to use very strong reducing and oxidizing agents as anode and cathode, yielding high cell voltages (if desired) and high energy density.

Low toxicity - Ionic liquids that do not use $AlCl_3$ are normally benign, making the batteries safer to make and safer for the consumer if the cell is abused.

Materials compatibility - Material issues can be difficult to control and expensive to overcome. Corrosion problems at both anode and cathode have been reported in lithium ion cells. With the exception of ionic liquids based on $AlCl_3$, many of the ionic melts are not aggressive and have excellent stability to most of the metal and plastic materials manufacturers use to make cells.

No solvents present - Electrolyte manufacture is simplified in that fewer components are required. Consumer exposure to organic solvent vapors if the cell were to fail and/or is abused is eliminated. Indeed, the cell may continue to work even if the cell casing or seal are compromised, at least for a period of time.

High melting points - This leads to high viscosity and can be a problem in that low temperature operation may be poor, or even non-existent if the melt freezes. However, it also offers the prospect of excellent shelf life in thermally activated reserve batteries, which are of interest for many military purposes. More importantly, many ionic liquids remain liquid well below the -20°C requirement for normal consumer batteries. Some have temperature ranges from -40 to +200°C [4]; 1-n-butyl-3-methylimidazolium tetrafluoroborate remains liquid down to -82°C [22].

High ion content - As described above, these salts have very good conductivity despite their high viscosity because they have a very high concentration of charge carriers. This high concentration also helps overcome concentration polarization in batteries during high rate discharge, increasing the power that the cell can deliver. (The high ion content is also a major advantage in capacitors where the charge storage is a function of the charge carrier concentration.)

Rechargeability – Ionic liquids have been used to electroplate a wide variety of metals: Ag, Al, Au, Bi, Co, Cr, Cu, Fe, Ga, Hg, In, Li, Na, Nb, Ni, Pb, Pd, Sb, Sn, Ti and Zn [23]. This implies that many of these could function as anodes in a rechargeable cell.

Thus, ionic liquids have many of the attributes of polymer electrolytes. Moreover, being liquids they do not suffer from the problem of delamination at critical interfaces in the battery that can be a major issue with polymer electrolytes.

3.0   CHALLENGES AND OVERVIEW OF
MAIN ADVANCES

Despite all the aforementioned advantages, ionic liquids still have hurdles to overcome before they can be commercialized as battery electrolytes. Much of the earlier work used mixtures of various organic chloride salts with $AlCl_3$. The organic chlorides used varied, but much of the work utilized n-butyl pyridinium chloride (BPC) and 1-ethyl-3-methylimidazolium chloride (EMIC). Note that in the literature the latter is often referred to as methylethylimidazolium chloride [24]. The structures of these and several other commonly used cations are shown in Figure 1. EMIC, which has a wider electrochemical window than BPC, was developed by Wilkes et al. [25]. Subsequently, other cations that are even more stable than EMI have been developed. However, ionic liquids that use $AlCl_3$ suffer from a number of disadvantages. While aluminum and other metals have been successfully plated and stripped for a number of years, the problem

in batteries has always been what cathode to use. In addition, the $AlCl_3$ ionic liquids are corrosive, moisture sensitive and aggressive to other materials, including many polymers [26]. Moreover, the wide voltage window claimed for many of the melts really only applied to the neutral state and "... exact neutrality is difficult to attain and worse to maintain, since any chemical or electrochemical process ... will remove the melt from the neutral composition" [27].

As soon as the composition drifts even slightly away from neutrality the voltage window shrinks, as shown in Figure 2. When the melt becomes acidic, $Al_2Cl_7^-$ reduction moves the cathodic limit up by 2V. In basic melts, Cl^- oxidation moves the anodic limit down by 1.4V. The chemistry involved with the anodic and cathodic voltage limits is outlined in Figure 3.

A major improvement was made with the recognition that one could add an alkali metal halide (usually NaCl or LiCl) and effectively buffer acid melts to give neutral, buffered melts [27-29]. Buffered melts have *a* very wide electrochemical window. They are also stable, since they are insensitive to impurities or small changes in electrolyte composition during charge and discharge and/or storage. Moreover, buffering of this type also introduces lithium and sodium ions into the electrolyte required for a practical primary or secondary lithium/sodium metal or ion battery. Adding protons or other additives, such as $SOCl_2$, have greatly improved lithium and sodium cycling. However, such melts still contain $AlCl_3$, which makes cell manufacture expensive. $AlCl_3$ may also be a safety concern for consumer batteries.
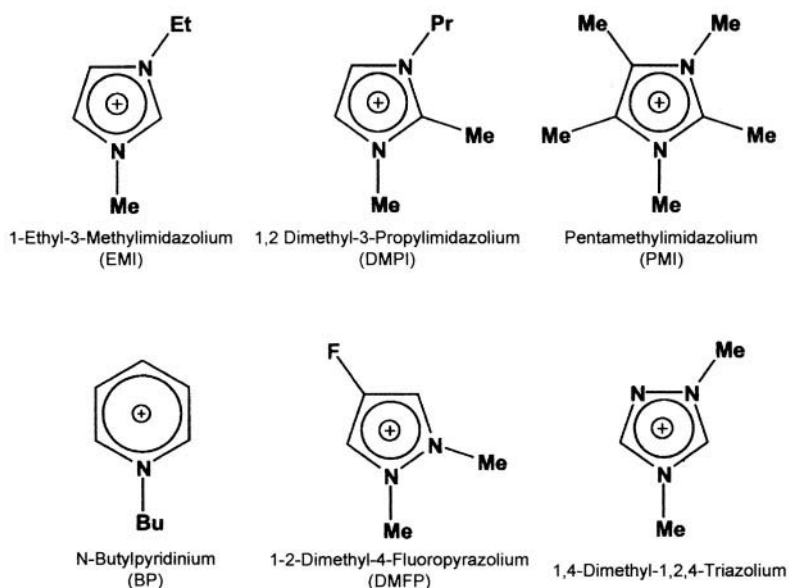
Figure 1. Structures for some of the cations more commonly used for room temperature ionic liquids.
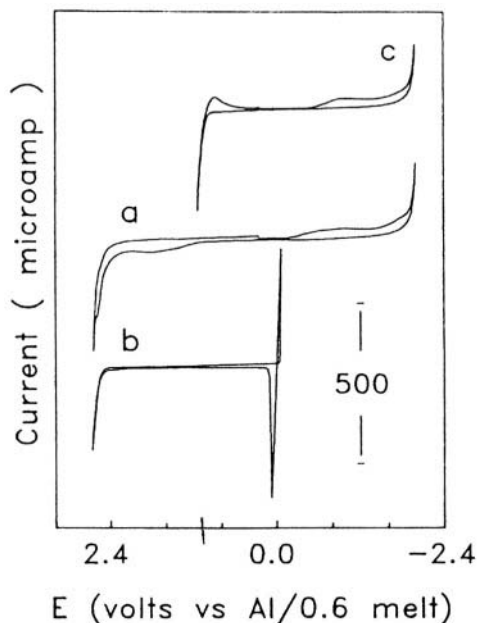
Figure 2. Cyclic voltammetry of unbuffered EMIC/AlCl$_3$ melts on a tungsten electrode at 20 mV/s. Curve (a) is for a neutral melt (50:50 EMIC:AlCl$_3$); curve (b) is for an acidic melt (45:55 EMIC:AlCl$_3$); curve (c) is for a basic melt (53:47 EMIC:AlCl$_3$). These show the drastic changes in voltage window with acidity. (from reference 27, reproduced by permission of The Electrochemical Society, Inc.

Another set of real advances that have opened up the field is that ionic liquids can be made using less aggressive anions such as BF$_4^-$, PF$_6^-$ or the bis(trifluoromethanesulfonyl)imide anion (CF$_3$SO$_2$)$_2$N$^-$, which we shall abbreviate as TFSI$^-$ [4,20,21,30-59]. (Note that there is some discussion in the literature as to whether these and similar anions should be called imide or amide.) Several authors claim that the BF$_4^-$ or PF$_6^-$ salts are stable in air. While these materials are much less reactive to water than those containing AlCl$_3$, LiPF$_6$ and to a lesser extent LiBF$_4$ undergo slow hydrolysis in moist air. Lacking studies demonstrating long term stability of ionic liquids containing BF$_4^-$ or PF$_6^-$ anions to the moisture in ambient air, such claims should be viewed only in a relative sense. More importantly, some of the newer salts use anions such as TFSI$^-$; this renders the ionic liquid completely hydrolytically stable. These melts are much less aggressive than those containing AlCl$_3$ and are far more desirable from a safety viewpoint. These ionic liquids can also dissolve the large amounts of lithium salts required for lithium and sodium cells. Generally, they have excellent electrochemical windows and thermal stability. They have been used to study anion resistance to oxidation without the complicating factors associated with organic solvents [45,60].
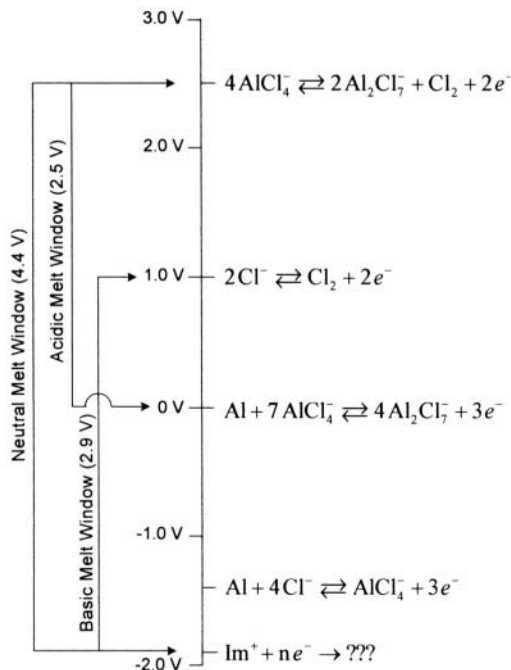
Figure 3. Chemistry controlling the electrochemical windows for EMIC/AlCl$_3$ ionic liquids. From reference 28, reproduced by permission of The Electrochemical Society, Inc.

Various workers have studied electrolytes made by blending ionic liquids with solvents [35,36,43,51,61-63], polymer electrolytes [26,48,50,55,58,64-68], polymers as electrode binders [21,48,53,69] and ionomers whereby elements of the ionic liquids are incorporated into the polymer backbone [70-75]. Such work has opened up new fields for these materials and simultaneously blurred the distinctions among ionic liquids, and rubber, glassy, gel, ionomer and polymer electrolytes. This is exemplified by a complex scheme in a review by Angell [26]. In this chapter, we have included such materials only when the salt forms the major component of the electrolyte, such as polymer-in-a-salt electrolytes or PISE [76,77].

4.0 PHYSICAL PROPERTIES OF ROOM TEMPERATURE IONIC LIQUIDS

4.1 Melting Properties

As mentioned in the Introduction, the melting properties of the ionic liquids of interest are crucial for the application to batteries designed to operate in ambient conditions. Most simple salts have very high melting points, although eutectics in phase diagrams of salt mixtures are quite common. None of these eutectics for simple salts is low enough to allow operation or study at room

temperature. It was only the advent of large organic cations that first allowed the possibility of liquid phase salts at room temperature and below.

Most of the history of room temperature ionic liquids deals with chloroaluminate salts. These solutions are formed from reaction of an organic halide (usually a chloride) with the molecular solid aluminum chloride (Al_2Cl_6). A discussion of the physicochemical properties of the various chloroaluminate ions is given in Reference 3. The molecular nature of aluminum chloride is due to the formation of bridge bonds involving two chlorine atoms between the aluminum centers. The remaining chlorine atoms are bonded as pendant groups on the aluminum atoms. In this arrangement, each aluminum atom is in a tetrahedral environment of chlorine atoms, which is the most stable configuration. However, when the aluminum halide is brought into contact with the organic halide, a spontaneous reaction occurs to form aluminum tetrahalide ions (in the simplest case) and the organic cation, forming a new salt that has a much lower melting point. If the organic cation is sufficiently polarizable and has enough configurations to add substantially to the configuration entropy, the melting point of this new salt is below room temperature. The reaction for chlorides can be written simply as:

$$2MCl + Al_2Cl_6 \rightarrow 2M^+ + 2AlCl_4^- \qquad\qquad \textbf{(1)}$$

If there is insufficient aluminum chloride added to the solution to complete the reaction of Equation 1, the solution is called chloro-basic or just basic. If excess aluminum chloride is added, the solution is called chloro-acid or just acid. If exact stoichiometry prevails (that is no excess chloride ion or excess aluminum chloride) the solution is called neutral. In the case of adding excess aluminum chloride, the following reaction occurs:

$$2AlCl_4^- + Al_2Cl_6 \rightarrow 2Al_2Cl_7^- \qquad\qquad \textbf{(2)}$$

An additional reaction can occur as the solution becomes more acidic as seen in Equation 3:

$$2Al_2Cl_7^- + Al_2Cl_6 \rightarrow 2Al_3Cl_{10}^- \qquad\qquad \textbf{(3)}$$

The large polarizable anions $(AlCl_4^-, Al_2Cl_7^-$ and $Al_3Cl_{10}^-)$ contribute to melting point lowering. The composition of a typical solution, calculated from measured equilibrium constants for Equations 1-3 by Melton et al. [27], is shown in Figure 4. The formation constant for tetrachloroaluminate is considerably larger than that for the dialuminate, which is larger than that for the trialuminate. This accounts for the near 100% of tetrachloro-aluminate at mole fraction $AlCl_3$ of 0.5 and the lower amounts of the other constituents at higher mole fractions.

The lowest eutectic points are generally found in the acidic range and the tetrachloroaluminate may be a congruently or an incongruently melting compound at higher temperature. Typical phase diagrams of chloroaluminate solutions for EMIC and $AlCl_3$ and two other solutions, BPC and trimethylphenyl-ammonium chloride (TMPAC) with $AlCl_3$, are given in Figures 5 and 6. Note in these figures, that the basic solutions, at less than about 35% $AlCl_3$, and acidic solutions, at greater than about 70% $AlCl_3$, melt above room temperature.
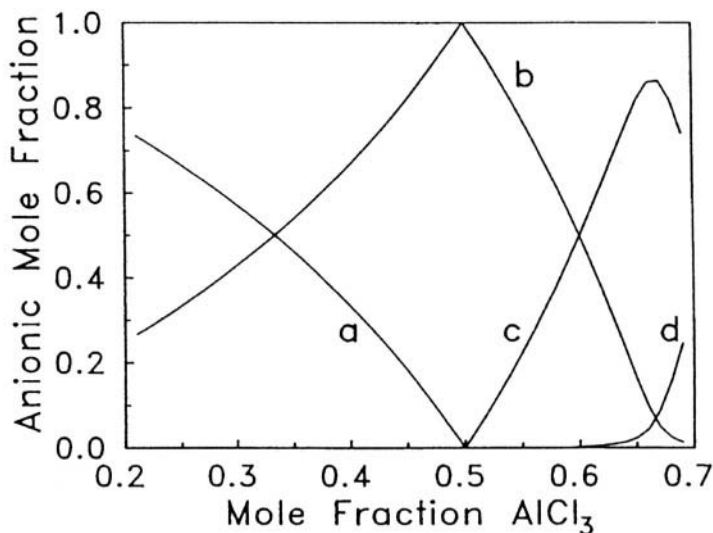
Figure 4. Calculated mole fractions of anionic species in EMIC-$AlCl_3$ melts at 40°C. Curves (a) Cl^-, (b) $AlCl_4^-$, (c) $Al_2Cl_7^-$, (d) $Al_3Cl_{10}^-$. From reference 27, reproduced by permission of The Electrochemical Society, Inc.

Therefore, one must be careful in specifying the solution composition in order to define these as room temperature ionic liquids, especially for the chloroaluminate melts using aluminum anodes. Here, the acidity changes drastically in the vicinity of the negative electrode during deposition and dissolution (charge and discharge). A considerable amount of work has been done on buffering the chloroaluminate melts in order to assure a neutral solution. For example addition of NaCl to an acidic melt causes the reaction:

$$NaCl_{(s)} + Al_2Cl_7^- \rightarrow Na^+ + 2AlCl_4^- \tag{4}$$

Providing excess solid sodium chloride assures that any formation of chloroacidic species, for example, due to electrode reaction, is quickly neutralized by the sodium chloride, and thus the solution is buffered. The solution is considered buffered from the acidic side in this case, because the buffer prevents the formation of excess acid (see Reference 80 for a review of these concepts). This work and additional studies on the use of other species for buffering (such as HCl, LiCl and $MgCl_2$) are discussed later, but it is noted here

that $MgCl_2$ buffers the solution from the basic side because of the formation of $MgCl_4^{2-}$ ion, a reaction that takes up excess chloride ion. The effect of small additions of these agents does not have much effect on the phase diagram, although systematic studies of multicomponent phase diagrams are rare.
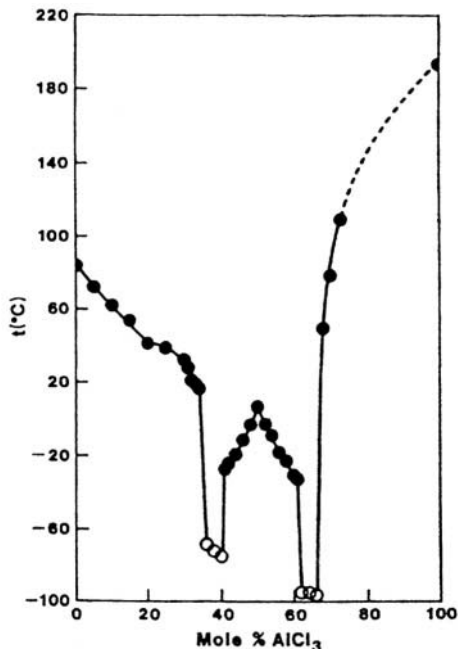
Figure 5. Phase diagram for the EMIC-AlCl₃/molten salt system. From reference 78, reproduced with permission from Elsevier Science.

An important area of new research is on nonhaloaluminate solutions. Cooper and Sullivan [30] found that organic cations, such as the N-substituted imidazolium ions, e.g. l-ethyl-3-methylimidazolium (EMI), formed room temperature ionic liquids with complex anions such as trifluoromethanesulfonate (triflate or $CF_3SO_3^-$) or methanesulfonate (mesylate or $CH_3SO_3^-$). At about the same time, Wilkes and Zaworotko [20] found that EMI cation also formed room temperature ionic liquids with the acetate ($CH_3CO_2^-$) or tetrafluoroborate (BF_4^-) anion. In fact, the melting points of these and similar liquids are difficult to measure because of the frequent occurrence of supercooling and glass formation as the temperature is lowered [38]. Cooper and Sullivan measured the melting points of EMI triflate as -10°C and EMI mesylate as 39°C, while Wilkes et al. measured the melting point of EMI acetate as -45 °C and $EMIBF_4$ as 15°C. These salts tend to be air and water stable. This is in sharp contrast to the chloroaluminate salts, which easily form hydrolysis products on exposure to moisture (generally in the form of complex oxychlorides) that have important effects on the electrochemistry of the melts as well as on the physical

properties. Many of the nonhaloaluminate salts have substantial solubility for lithium or sodium salts of the same or different anions. This leads to solutions of great interest for alkali metal or lithium ion batteries. Since the pioneering work described above, many salts have been investigated and a number of salts are now known to have liquidity at room temperature. Table 1 gives the melting points of several of these salts.
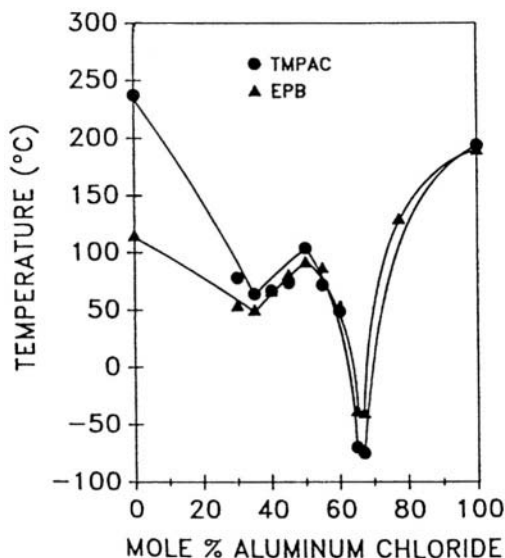
Figure 6. Phase diagram of TMPAC-AlCl₃ (closed circles) and ethyl pyridinium bromide-AlCl₃ (closed triangles). From reference 79, reproduced by permission of The Electrochemical Society, Inc.

Table 1. Physical properties of selected room-temperature ionic liquids.

Salt	Melting Point (°C)	Specific Conductance (mS/cm)	Viscosity (P)	Reference
EMI triflate	-10	9.29	0.427	30
EMI mesylate	39	1.67	1.60	30
EMIBF₄	12	13.8	0.377	38
EMI TFA	-14	9.6 (20°C)	0.35	34
TES TFSI	-35.5	7.1	0.30	81
EMI HCA	-90	13.73	0.160	82
TMPA HCA	-75	3.40	0.362	79
TMS HCA	ca 0	5.5	0.393	83
TMP HCA	ca 0	5.0	0.373	84
EMI TFSI	22	3.9	0.44	34
MPP TFSI	12	1.4	0.63	49

Cations: EMI–1-ethyl-3-methylimidazolium, TMS–trimethylsulfonium, TES–triethylsulfonium, TMP–tetramethylphosphonium, TMPA–trimethylphenylammonium, MPP–n-methyl,n-propylpyrrolidinium.
Anions: triflate–trifluoromethanesulfonate, mesylate-methanesulfonate, TFA–trifluoroacetate, TFSI–bis-(trifluoromethanesulfonyl)imide, HCA–heptachlorodialuminate

4.2   Conductivity and Viscosity Properties

The chloroaluminates are generally highly conductive and may have quite low melting points. In addition, the viscosity can be rather lower than that for other ionic liquids. The salts of other anions often have sufficient conductivity, comparable to solutions of lithium salts in organic solvents typically used in lithium and lithium ion batteries. If either the cation or anion is too large, however, the conductivity drops below a useful level and the viscosity climbs substantially. Other factors that are important for conductivity are the degree of resonance stabilization of the ions (as measured by the number of resonance structures and the degree of aromaticity) and the shape of the ions (spherical is better than linear). Table 1 shows some physical properties of selected solutions. Many more cations and anions have been combined in various works, but we regard the selected solutions as promising directions for lithium battery research. Several workers have indicated that the possible number of ionic liquids at room temperature is an extremely high number – even in the millions! It should be noted in the table that EMI HCA has the highest conductivity, but that most of the others are adequate for lithium battery work. An exception is EMI mesylate, which is included in order to illustrate some points. The anion in this case (methylsulfonate) is considered a hard base and, in organic solvents, readily associates with cations to form ion pairs. We regard this factor as an important reason for the high melting point and low conductivity for this near room temperature ionic liquid. Triflate (trifluoromethanesulfonate), by comparison, is a much softer base due to the presence of electron withdrawing fluorine atoms on the carbon, which cause a smearing of the negative charge over the whole anion. The properties of EMI triflate are consequently much more useful for battery applications. Other anions of interest are PF_6^- and AsF_6^- [60] because of their low basicity and relatively small size. Beti (bis-perfluoroethanesulfonylimide) [45] is larger and more nearly linear, but its very low basicity is a trade-off, and the anion is consequently of considerable interest.

The temperature dependence of conductivity and viscosity are quite important. For systems with porous electrodes, the viscosity may be as important as the conductivity because it is necessary for fluid flow to occur as the internal volume of the electrode changes due to the electrode reaction. For example, a carbon electrode in a lithium ion cell must breathe as lithium is intercalated during charge and removed during discharge. Similarly, the lithiated metal oxide electrode loses volume during charge as lithium is removed while it gains volume during discharge due to lithiation. Both conductivity and viscosity are monotonic functions of temperature, but have opposite behavior. Conductivity increases with a rise in temperature while viscosity decreases, as illustrated in Figure 7.
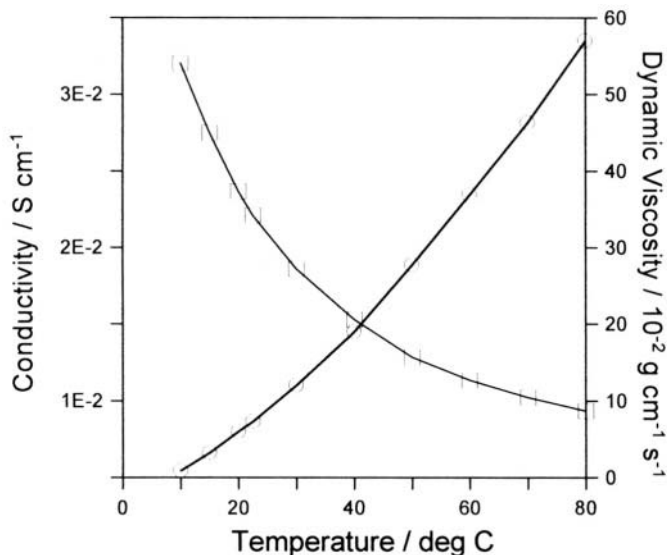
Figure 7. Specific conductivity (S·cm⁻¹) and dynamic viscosity (10⁻² g·cm⁻¹s⁻¹ or cP) of EMI TFSI. From reference 34, reproduced with permission. Copyright 1996, The American Chemical Society.
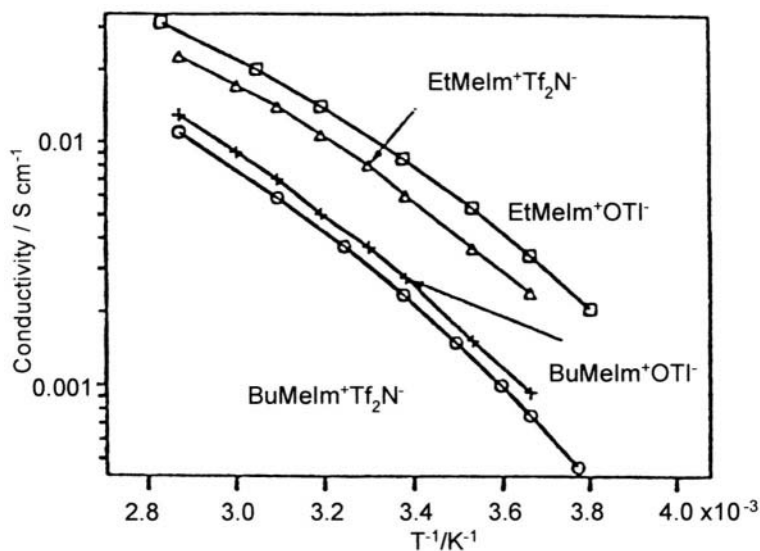
**Figure 8.** Specific conductivity (S cm⁻¹) of some imidazolium salts with TFSI (Tf₂N⁻ in graph) and Triflate (OTf⁻ in graph) as a function of the reciprocal of the absolute temperature in K. From reference 34, reproduced with permission. Copyright 1996, The American Chemical Society.

Figures 8 and 9 show typical log conductivity versus reciprocal absolute temperature curves. Clearly the behavior is not of the Arrhenius type, but has a more complicated relationship. In fact, conductivity data for ionic liquids frequently follow the VTF behavior [85].
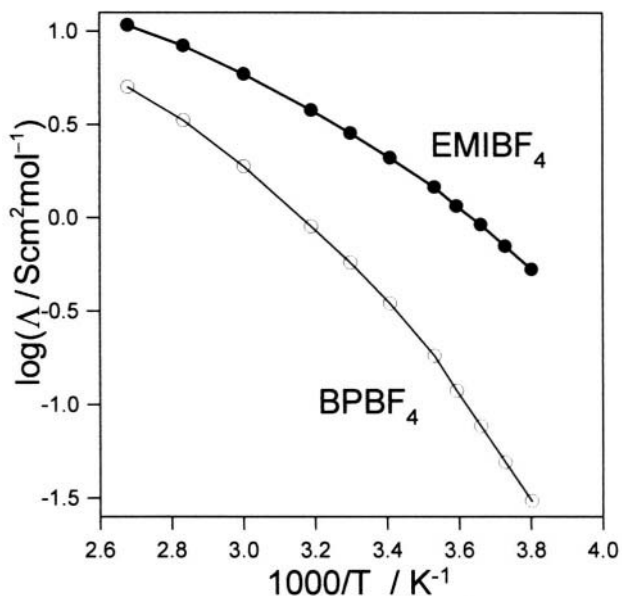
Figure 9. Arrhenius plots of molar conductivity of EMIBF₄ and BPBF₄. From reference 50, reproduced by permission of The Electrochemical Society, Inc.
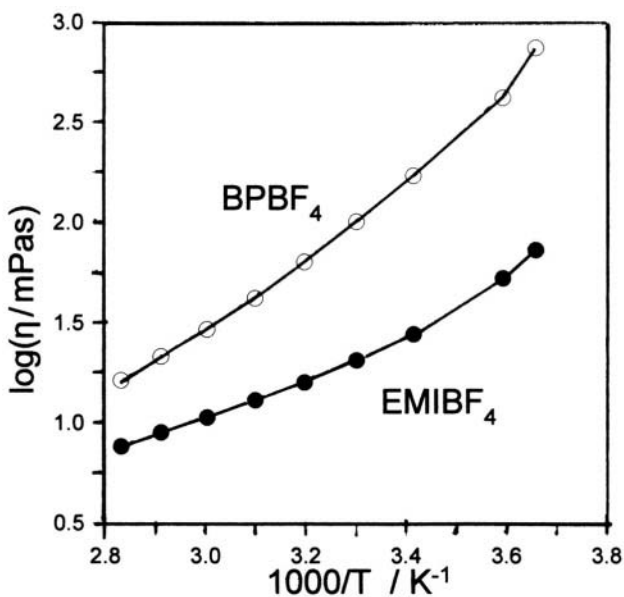
Figure 10. Arrhenius plots of viscosity of EMIBF₄ and BPBF₄. From reference 50, reproduced by permission of The Electrochemical Society, Inc.

Viscosity behavior with temperature can be close to the Arrhenius type [86]. However, the dependence on reciprocal temperature of the logarithm of viscosity usually applies over a limited temperature range. VTF behavior is often observed for viscosity data as well as for conductivity [85]. Figure 10 shows typical behavior. It is clear that low temperature can be a problem for ionic liquids when the sensitivity to temperature is too great. This problem is usually observed by studies of battery behavior. For example, an electrolyte may perform quite well in a battery at room temperature, but if the sensitivity to temperature is high, the battery will develop high impedance with a temperature reduction of only a few degrees. Conversely, the impedance may be strongly lowered with a modest increase in temperature in this case. The theory of transport properties of ionic liquids has not been well developed. However, it is certain that concepts such as the Nernst-Einstein, Stokes-Einstein relationships and the Fuoss-Onsager type conductivity relationships do not apply to these materials. Also, the semi-empirical VTF equation is useful in correlating data, but is of little use in drawing structural or mechanistic conclusions. One hopes that theoretical chemists can develop theories to help the experimentalist define important relationships.

4.3 *Electrochemical Properties of Ionic Liquids*

The electrochemical stability of ionic liquids toward both anodic oxidation and cathodic reduction (also called the electrochemical window) is extremely important for the functioning of battery couples. We discuss significant details as they apply to specific battery couples in a later section. However, some general comments are appropriate here. Reactions have been fairly well analyzed for chloro- and bromoaluminate melts [87]. On the anodic side (moving toward positive potentials in a cyclic voltammetry experiment), the accepted reaction for basic, neutral and acidic solutions, is the generation of halogen atoms from various halide containing species. This step is followed by generation of dihalogen and in some cases trihalide ions. The trihalide ions are themselves reducible at more positive potentials. On the cathodic side for acidic melts, a fairly reversible reduction of Al^{3+} ions to aluminum occurs, often complicated by nucleation and passivation phenomena. For neutral and basic melts, an irreversible reduction of the organic cation is observed. Figure 11 shows typical cyclic voltammograms for neutral bromide and chloride melts [87]. For EMI cations, the potential is about -2.0 V vs. the Al/Al^{3+} reference electrode. Some other cations have been found to be more negative than EMI^+. For example, 1,2-dimethyl-3-propylimidazolium (DMPI) cations are reduced at about -2.5 V [88], while tetramethylphosphonium cations are reduced at about -2.7V [84].

These values are all within the nominal window of lithium and sodium ions (see further) and thus the organic cations are expected to be stable. Unfortu-

nately, we do not know the extent of the irreversibility of the organic reaction, since there is no oxidation peak on the reverse sweep (Figure 11). It seems that the organic cation is metastable to reduction, but in the presence of catalytic materials, or strongly reducing alkali metals, some reaction(s) do occur as evidenced by the relatively low efficiency of charge and discharge in half cells. This situation is common in alkali metal batteries as most solvents in conventional lithium and lithium ion batteries are only metastable and are found to react with lithiated carbon or lithium metal. The extent of reaction is determined by the nature of the products formed in the reaction. If the products form a passivation layer (SEI), the reaction is limited and only *a* slow corrosion is evidenced. If the layer is porous, or if the products are soluble, the reaction proceeds until one of the reactants is exhausted. Several workers have tried passivating agents as discussed later, but no completely satisfactory solution has been found to this problem. Certainly, the discovery of truly neutral ionic liquids with stable inorganic or organic anions (non-chloride or bromide containing) has improved the situation substantially vis-à-vis the organic cation stability and further progress is expected.
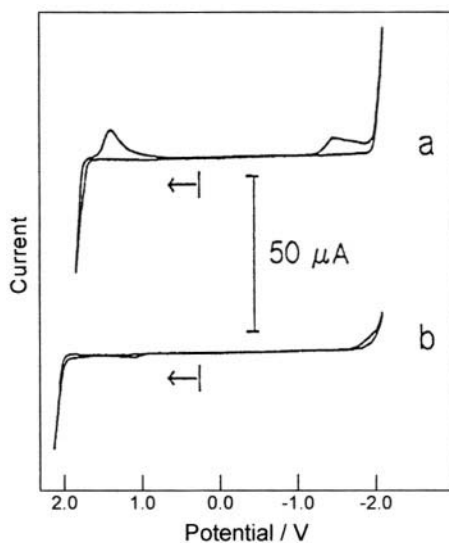
Figure 11. Cyclic voltammograms of neutral a. EMI Br – AlBr$_3$ and b. EMI Cl – AlCl$_3$ melts. From reference 87, reproduced by permission of The Electrochemical Society, Inc.

5.0   PHYSICAL PROPERTIES OF IONIC LIQUID – POLYMER ELECTROLYTES

A careful definition of the various classes of polymer and glassy electrolytes is given by Angell et al. [85]. Utilizing these definitions, it is only the polymer in salt electrolyte (PISE) system that concerns us here. In these systems, an ionic liquid and a polymer are mixed together (the salt in excess

compared to the polymer) with a solvent to form a rubbery conductive material, which does not flow under stress after evaporation of the solvent. Because this work is in the beginning stages, only a few important cases are given here. The EMI triflate and EMI BF_4 ionic liquids have been mixed with PVDF-HFP copolymers to form a rubbery gel [65]. The conductivities of the resulting electrolytes are shown in Table 2 from the work of Fuller et al. [65]. Mixtures with amorphous polyethylene oxide from the same work show order of magnitude lower conductivities than the above.

Table 2. Conductivity of Ionic Liquid Polymer Mixtures at Room Temperature (ca.22°C). Data from reference 65. Reproduced with permission of The Electrochemical Society, Inc.

Ionic liquid	Ionic liquid-to-polymer weight ratio	Specific Conductance (mS/cm)
EMI triflate	1:1	1.8
EMI triflate	2:1	5.6
EMI triflate	5:1	8.0
EMI triflate	10:1	7.3
EMI triflate	No polymer	9.3 (25°C)
EMI BF_4	2:1	5.8
EMI BF_4	7:1	11.0
EMI BF_4	No polymer	13.8 (25°C)

No information is given on the mechanical properties. Angell and coworkers have pointed out that it is not necessary to have a room temperature ionic liquid [26]. Indeed solid electrolytes have many well-known attractive properties for lithium-ion batteries. Several lithium salts have given conductivities comparable with PEO – lithium salt mixtures, which are heavily weighted with polymer. Since these values are not really adequate for most lithium ion battery applications, however, they are not covered further here.

6.0 ELECTROCHEMISTRY AND BATTERIES USING IONIC LIQUIDS

This and the following sections are divided into anode (negative electrode) type and cathode (positive electrode) type, as much of the research and development work has focused on one or the other. Full cell studies are incorporated into the cathode sections. Carbon, which has been used as both anode and cathode is given its own section. The ionic liquids are also subdivided into those based on $AlCl_4^-$ and those using less aggressive anions such as BF_4^- and $TFSI^-$. Much of the work reports current efficiencies for relatively short term cycling experiments using chrono-potentiometry or cyclic voltammetry. Very little work on long term cycling has been reported. Current

efficiency data must be interpreted with care. Even ignoring the difference in time-scales, the cycle life or cycling efficiency in a full cell depends on the efficiencies at both electrodes (usually on the limiting electrode) and, in addition, on maintaining the balance of charge in the cell. Ideally, the inefficiencies at anode and cathode would be matched in some way.

The formal reduction potentials (Table 3) in **EMIC/AlCl₃** melt show that of the alkali metals ions only sodium and lithium are stable in these melts [28]. (Here and elsewhere in this chapter, potentials are given vs. an Al/Al (III) electrode unless otherwise stated.) Thus, most of the anode work has centered on Al, Li and Na electrodes. However, as pointed out in the section on Physical Properties, the stability is not thermodynamic and passivation of the active metal surface is generally required to obtain high efficiency. Reduction of organic cations on less active metals such as aluminum or zinc does not seem to occur.

Table 3. Formal Potentials in a EMIC/AlCl₃ melt (V vs. Al/Al(III)) Data from reference 28. Reproduced with permission of The Electrochemical Society, Inc.

Li^+	-2.14 V
Na^+	-2.15 V
K^+	-2.71 V
Rb^+	-2.77 V
Cs^+	-2.87 V
EMI^+	-2.3 V

7.0   ALUMINUM ANODES –   AlCl₃ TYPE MELTS

Aluminum can be readily plated and stripped in acid **EMIC/AlCl₃** melts, containing $Al_2Cl_7^-$ ions, and forms a fairly reversible anode [4], although complicated to some extent by nucleation phenomena. The aluminum deposition reaction is shown in Equation 5:

$$4Al_2Cl_7^- + 3e^- \leftrightarrow Al + 7AlCl_4^- \tag{5}$$
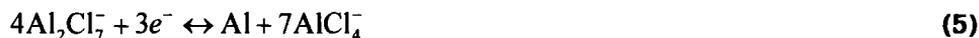
However, in basic or neutral melts that lack $Al_2Cl_7^-$ ions, the organic cation (EMI) is reduced at a higher potential than $AlCl_4^-$. Consequently, the $AlCl_4^-$ ions in such melts cannot be reduced to yield aluminum [61]. In principle, **AlCl₃-free** ionic liquids or even basic melts could be used for primary aluminum cells, but in practice it is difficult to see how to match this with a cathode process and still keep the melt composition uniform during charge and discharge. Aluminum plating can suffer from nucleation polarization [89,90]. Acetonitrile, benzene, tetrahydrofuran, diethyl ether, 1,2-dichlorobenzene, and toluene have been reported as additives or co-solvents to improve the kinetics and/or boost conductivity by lowering the melt viscosity [61,91-94]. Boon et al. found that bromine analogs of **EMIC/AlCl₃** solutions also worked, but that they offered no advantage over the chloride melts [87].

Most work has been done using aluminum foil, wire, or aluminum plated from the melt. Cycle testing in an **BPC/AlCl₃** melt showed that anodes made using aluminum powder slurries (ca. **180** μm particles) could also give high efficiency, even at high rates **(5-10 mA·cm⁻²)** [95]. Capacity was **140 mAh·g⁻¹** and cycle life was 85 cycles. Adding graphite to aluminum powders improved efficiency, as did pretreating the aluminum (in wire or powder form) with phosphoric acid, especially at high rates [96]. Unfortunately, graphite:Al ratios greater than 1 on a weight basis were required for good cycling. Factoring in the relative densities, this would result in a very low energy density anode.

Just as **EMIC/AlCl₃** was developed as a more stable ionic liquid than **BPC/AlCl₃**, Gifford and Palmisano [88] demonstrated that blocking the acidic 2-position on the imidazolium ring inhibits the reduction of the imidazolium cation (see Figure 1 for structures). This is the basis for l,2-dimethyl-3-alkyl imidazolium salts, especially the l,2-dimethyl-3-propylimidazolium chloride **(DMPIC)/AlCl₃** melts that have lower melting points and a wider electro-chemical window (4.8 V*)* than their l,2-dimethyl-3-ethylimidazolium counter-part (4.4 V). The substrate metal is very important in determining the window; platinum, for example, catalyzes reduction of the imidazolium cation, narrowing the electrochemical window. Tungsten and glassy carbon are much better substrates as they are less catalytic for **EMI⁺** reduction. Cathodic stability with DMPIC was enhanced relative to EMIC by 0.3 V on W and 0.5 V on Pt [88]. In the **DMPIC/AlCl₃** melt, even when basic, aluminum remains shiny and stable. Gifford and Palmisano cycled aluminum with 96 and 100% current efficiency on tungsten using current reversal chronopotentiometry at 1 and **5 mA·cm⁻²**, respectively. The lower efficiency at **1 mA·cm⁻²** is presumed to be due to slow chemical reaction of the plated aluminum during the long times associated with low currents [88]. Ionic liquids based on DMPI salts, both with and without **AlCl₃**, have subsequently been used by many groups to boost stability and plating efficiency of their systems [2,4,21,32,42,52,53,55,60,72,88,97-104]. Figure 12 shows a selection of generic cation structures that have been reported as candidates for room temperature ionic liquids.

Vestergaard et al. developed a triazolium-based ionic liquid, 1,4-dimethyl-1,2,4-triazolium chloride/AlCl₃ that could cycle aluminum on an aluminum collector [105]. On tungsten, cation absorption blocked the surface preventing aluminum deposition. This work is one of many examples highlighting the importance of the substrate for stripping and plating studies. Other imida-zolium salts with alkyl groups at the 2-position have been reported; for example, l,2-dimethyl-3-hexylimidazolium iodide has been used in solar cells [5,8]. More recently, pentamethylimidazolium (PMI) [46] and l,2-dimethyl-4-fluoropyrazolium (DMFP) salts have been developed that are even more stable [54,106], although the PMI melts are solid at room temperature. (The structures for these specific cations are given in Figure 1.)
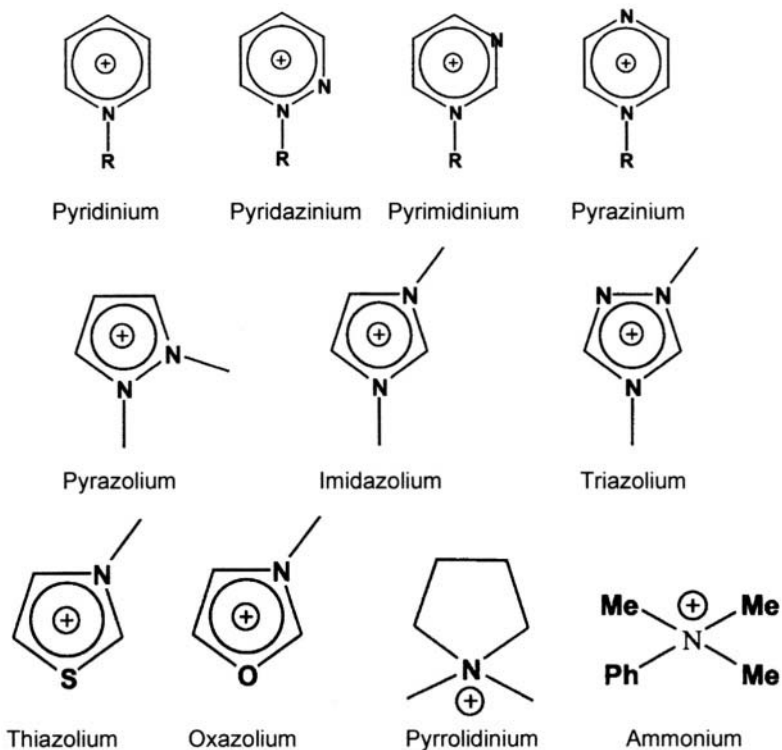
Figure 12. Base structures for some cations used for room temperature ionic liquids.

Blomgren and Jones showed that room temperature ionic liquids can be made using simple onium salts [79,83,84,107-109]. Specifically, they studied **Me₃PhNCl/AlCl₃** [79,107], **Me₃SCl/AlCl₃** [83,108], and **Me₄PCl/AlCl₃** [84,109]. The ammonium and sulfonium salts were reduced at similar potentials to EMI cations. **Me₄PCl/AlCl₃** melts gave a very wide electrochemical range that extended 0.5V more negative than EMI-containing melts [84]. Note that extending the window this far should allow one to plate and strip lithium efficiently, although this was not reported. The neutral and basic **Me₃PhNCl/AlCl** melts are solid at ambient temperature, but the 1:2 **Me₃PhNCl/AlCl₃** mixture melts at -70°C. The 1:2 **Me₃SCl/AlCl₃** melts remain fluid down to -50°C, and the **Me₄PCl/AlCl₃** acid melt freezes around -5°C. Aluminum plating and stripping was demonstrated in all three liquids at **0.5mA·cm⁻²**. Zhao and VanderNoot have reported 85-90% efficiency in **Me₃PhNCl/AlCl₃** melts [90] and describe various onium salts for use in aluminum cells, including **Me₃PhNCl, Me₃SCl,** tetraalkyl/aryl ammonium salts, phosphonium and trialkyl/aryl sulfonium salts (such as **Ph₂EtSBF₄, PhCH₂Me₃NCl**) [110]. Specific examples given used a 1:2 acidic **Me₃PhNCl/AlCl₃** melt for secondary **Al-SnCl₂** and **Al-FeCl₂** cells. Papageorgiou and Emmenegger

reported improved aluminum deposition kinetics in this melt if 1,2-dichloro-benzene, diethylether or possibly anisole were used as co-solvents [93].

Adding organic bases such as acetonitrile or benzonitrile facilitates aluminum oxidation in acidic melts [91,110]. However, these bases tie up the $Al_2Cl_7^-$ ions in acid and block aluminum deposition, rendering them unsuitable for secondary cells. Nevertheless, current densities were increased almost tenfold with no sign of passivation effects. Consequently, they may be useful additives for primary aluminum cells. Aluminum can be used in basic melts as an anode for primary cells (cf. work with chlorine, bromine and WCl_6 cathodes referred to in Reference 92). Cathode selection remains a challenge for aluminum cells, although $Me_3PhNCl/AlCl_3$ has been used to run $Li-MnO_2$ cells [107]. Difficulties of using conventional transition metal oxides have been overcome by using polymers, but this reduces energy density (see cathode section). Moreover, the moisture sensitivity and corrosiveness of $AlCl_3$-based ionic liquids make them undesirable for consumer batteries.

8.0   SODIUM ANODES – $AlCl_3$ TYPE MELTS

High temperature sodium cells using ionic liquids as electrolytes have been developed for a number of years. However, these have several well-known drawbacks. If the operating temperature could be lowered to at least below the melting point of sodium (98°C), the system would be much safer. Also, the need for the β″-alumina separator used in the high temperature cells, which is expensive, brittle and very resistive below 175°C [111,112], would be obviated. Unfortunately, despite claims about the extremely wide electrochemical window of conventional $EMIC/AlCl_3$ melts, three factors limited their utility for sodium cells. The wide window only really applies at neutrality and it is hard to make and even harder to keep a melt balanced at the neutral point, as discussed above. Secondly, the $EMIC/AlCl_3$ electrolyte lacks sodium ions and thus could not operate a sodium-based cell. Thirdly, the *location* of the window is as important as the width (see Figure 2). Unfortunately, sodium reduction occurs more negative of EMI reduction in such melts, despite the formal potentials given in Table 3. Consequently, sodium cannot be plated from $EMIC/AlCl_3$ melts; the EMI cation is reduced before the sodium ions.

The first two problems were overcome by Melton et al. who found that adding an alkali metal halide, usually LiCl or NaCl, to an acidic $EMIC/AlCl_3$ melt effectively **buffers** the melt to the neutral point [27]. Subsequently, halide-buffered melts have been used by many groups to enhance sodium and lithium plating [2,24,28,29,41,86,93,113-118]. Equation 6 shows the reaction used to make a buffered solution:

$$MCl + Al_2Cl_7^- \rightarrow M^+ + 2AlCl_4^- \tag{6}$$
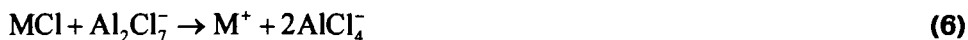
Riechel and Wilkes showed that these melts are buffered very slightly on the acidic side so that they do contain traces of $Al_2Cl_7^-$ ions, as evidenced by small aluminum plating and stripping peaks around 0.1V [24]. However, these are small enough that they do not interfere with lithium and sodium cycling. This is especially so with sodium; the higher solubility of NaCl than LiCl helps keep the $Al_2Cl_7^-$ content very low [116]. The act of adding alkali metal halides also provides the electrolyte with the alkali metal ions that are need to run lithium or sodium batteries. However, in addition to this, one needs to prevent reduction of the imidazolium cation. This is especially challenging when trying to cycle sodium; lithium reduction lies at a more positive and hence accessible potential. Sodium deposition is not observed in NaCl-buffered **EMIC/AlCl₃** melts [113] and two approaches have been taken to overcome this: adding protons and other additives to suppress the **EMI⁺** reduction and using a more stable cation, such as **DMPI⁺**.

Adding HCl or **EMI·HCl₂** [112-115,119-122], triethanolamine [116, 123] (TEOA) and triethanolamine hydrochloride [113,116,123-125] **(TEOA·HCl)** moves the EMI cation reduction so that it lies more negative than sodium reduction (Figure 13). Riechel and Wilkes showed that the EMI reduction could be shifted by about 0.2 V to -2.4 V by adding HCl [113]. This was confirmed by Gray et al. [112]. Riechel et al. examined the effect of adding 0 to 0.4% HC1 to a NaCl-buffered **AlCl₃-EMIC** melt and saw a 10-fold reduction in the EMI cation reduction current at -2.1 V and a 0.3 V voltage shift [115]. However, in the absence of NaCl, the EMI reduction position was *not* affected by HCl. This suggests that HCl changes the **EMI⁺** reduction peak on the sodium surface, presumably by modifying the surface. The result is that plating/stripping efficiencies of both sodium and lithium were significantly increased by HCl addition [113,126]. Sodium plating and stripping on tungsten and platinum yielded efficiencies of up to 89% [113]. The plated sodium was readily stripped and gave a stable potential during many hours of storage. However, voltage stability in itself does not indicate that the plated sodium is sufficiently stable.

Gray found that sodium plating efficiency on a tungsten collector was essentially zero for such cells unless the partial pressure of HCl was at least 6 mmHg [112,126]. Cyclic voltammetry showed that, if this level is maintained, sodium plating efficiencies on tungsten of 65-75% can be attained, as long as the potential does not go too negative. Moreover, the efficiency increases with the plate thickness because of a lower (plating) overpotential on sodium than on tungsten. This overpotential may cause preferential reduction of the **EMI⁺** cation on tungsten electrodes. Recall that the 0.2 V shift in **EMI⁺** reduction is not large so that there is often some overlap with sodium ion reduction. Chronopotentiometry has given some very high efficiency values for sodium plating in acidified melts, up to 94% efficiency at high current density with little or no time spent at open circuit [112]. However, current densities of at

least $5 \ \text{mA}\cdot\text{cm}^{-2}$ were required to attain such high efficiencies and these experiments are generally on the time-scale of a few minutes only. Efficiency dropped as the time between the pulses was increased or the current density was reduced. Both of these effects suggest that chemical degradation of the plated sodium is the main cause for lower efficiencies in experiments with longer and more practical timescales.
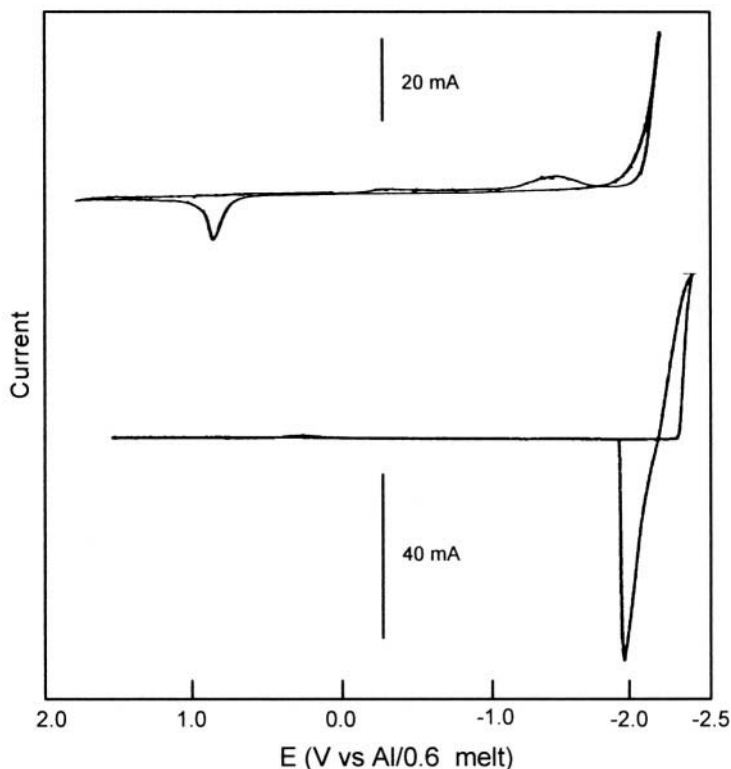
Figure 13. Cathodic scan cyclic voltammograms of a NaCl-buffered neutral EMIC/AlCl₃ melt at a Pt working electrode. Scan rate 100 mV/s. Top scan without EMI·HCl₂. Bottom scan with added EMI·HCl₂. From reference 113, reproduced by permission of The Electrochemical Society, Inc.

From a practical viewpoint, ionic liquids containing the substantial amounts of HCl required to keep the vapor pressure above 6 mmHg are undesirable [116]. HCl volatilizes quite readily and it is not easy to control the HCl content; one has to periodically add HCl, use a large excess to begin with and/or control the partial pressure of HCl above the melt. These methods are especially challenging if one wants to take advantage of the thermal stability of these liquids to run the cell over a wide temperature range. Piersma et al. [116,123,124] showed that certain ethanolamines, specifically TEOA and **TEOA·HCl**, stabilized **EMIC/AlCl₃** melts in much the same way as HCl. Both lithium and sodium could be cycled using these

additives. Trialkylamines, LiH and **LiAlH₄** were all ineffective. TEOA performed almost as well as did **TEOA·HCl**. Consequently, the improvement was attributed to proton transfer from the ethanol groups, not from the HCl in **TEOA·HCl**. Sodium plating in these solutions still suffered from the co-reduction of **EMI⁺** cations, but the sodium deposits were more stable, probably due to a co-deposited organic film.

Thionylchloride **(SOCl₂)** has also been used to overcome the sodium-melt reactivity. Carlin, Fuller and Osteryoung [127,128] reported that adding small amounts (ca. 0.02 to 0.1M) of **SOCl₂** is very effective in stabilizing deposited lithium and sodium and significantly better than HCl. *In situ* optical microscopy showed uniform, stable sodium deposits, although lithium deposits were dendritic [128-130]. Sodium films plated in the presence of **SOCl₂** are much more stable on open circuit and charge/discharge efficiencies of 85% were attained; moreover, repeated cycling, at **1-3 mA·cm⁻²,** maintained this efficiency. Short-term shelf studies (15 mins) found virtually no loss in efficiency (86-91%) when **SOCl₂** was added, compared to a sharp drop in efficiency when only HCl was added (21% efficiency vs. 77% before the 15-minute storage) [127].

The general idea behind this approach is to add a very *reactive* material that rapidly coats the plated lithium with a film that blocks further solvent-lithium reaction. Such films must have high lithium ion transport, which usually requires that they be very thin. This approach is similar to the widespread use of ethylene carbonate (EC) in organic electrolytes for lithium ion cells. Studies have shown that the surface of the anode and even the cathode is controlled by the reaction of the electrode with EC. Thus, adding what is in reality an unstable material effectively stabilizes the cell. The stabilization effect of **SOCl₂** was attributed to the formation of a protective thin film of LiCl on the sodium surface. The relative high boiling point of **SOCl₂** rendered the melts stable even after some time in the open. However, longer-term storage (for several hours) again demonstrated that the sodium deposits were somewhat unstable; stripping efficiency after 17 hours of storage dropped to 71%. EQCM studies of NaCl-buffered **DMPIC/AlCl₃** melts with added **SOCl₂** also suggested co-reduction of the electrolyte when plating sodium; the electrode gains more weight than it should if only sodium reduction were occurring [131]. Some, but not all, of this additional weight is removed during the stripping process.

Care must be taken not to plate at too high an overpotential as EMI cations and sodium ions will then be reduced together, lowering efficiency [113,115,126]. This has the effect of limiting the rate at which the sodium can be plated and may require precise (i.e. costly) charging circuitry, with control of individual cells in a battery pack. Xie and Riechel [132] find that the products of the EMI reduction are electroinactive and stated that cells

should be able to tolerate small amounts of such degradation. However, while any cell system that consumes substantial amounts of the electrolyte is obviously not viable, even minor anode inefficiencies can cause a cell to become unbalanced during cycling unless there exists a balancing inefficiency at the cathode side.

Gifford and Palmisano´s studies [88] on NaCl- and LiCl-buffered melts of EMIC or DMPIC with $AlCl_3$ have shown that blocking the acidic 2H position of the EMI cation helps stabilize the cation and improved aluminum plating and stripping in the melt. Others have used this feature to improve the cycling efficiency of alkali metals with carbon [98,99], sodium [117] and lithium anodes [21,32,42,52,53,60,120]. DMPI moves the cathodic potential limit more negative to expose the sodium reduction. This improves the stability of the melts and sodium can be plated directly from buffered-DMPIC melts, even without added HCl, $SOCl_2$ or other additives.

Methanesulfonyl chloride (MSC)/$AlCl_3$ melts buffered with NaCl have also been shown to give very high current efficiencies for sodium of 80-90% [117]. Up to 97% efficiency was reported for some chronoamperometry experiments using 100s cycles between -0.75 and -2.6 V vs. Al/Al (III), even without any additives such as HCl, TEOA·HCl or $SOCl_2$ [131,133]. EQCM data in the same study indicates that the MSC electrolyte is co-reduced with the sodium. However, in the case of MSC, the mass lost on stripping matches almost exactly that for the sodium reoxidation. The by-products formed during the plating step appear to remain on the electrode. Noteworthy was the finding that the plated sodium had low self-discharge rates in this electrolyte [131].

Almost all of the non-$AlCl_3$ melts have been developed and tested for lithium cells. Consequently, they are described in that section. Nevertheless, many of the same approaches and materials described therein could also be applied to sodium analogs.

9.0   LITHIUM ANODES

9.1 $AlCl_3$ Type Melts

Lithium reduction occurs at more positive potentials than sodium [28] and so co-reduction of the EMI^+ cation is less of a problem than for sodium cells. However, in addition to efficient plating and stripping, secondary cells require chemical stability of the plated anode in the electrolyte for extended periods. Unfortunately, freshly plated lithium metal appears to be more reactive than sodium to the EMIC/$AlCl_3$ melt. *In situ* optical microscopy in LiCl-buffered EMIC/$AlCl_3$ melts show that the lithium forms gray, granular type deposits that rapidly react with the electrolyte to form a brown film, eventually turning a cream color [114,120-122]. Notwithstanding the above, Fung and Chau report [86] that in cyclic chronopotentiometric studies at 3-10 mA·cm^{-2} Li-Al

anodes gave 70-90% efficiency in this melt. Using aluminum current collectors and cycling LiAl instead of lithium metal raises the potential of the anode, more clearly separating it from the melt´s cathodic limit. However, LiAl is not without detriments. The capacity and cell voltage will be lower than if lithium metal could be used and the integrity of the anode, especially at the high lithium content required for high energy density, becomes poor. Nevertheless, the alloy can significantly improve stability and cycle life. For example, anodes were cycled for over 300 cycles with good efficiency, albeit accompanied by significant capacity fade. Koura and Ui [134] found that pretreating the electrolyte with lithium metal gave reversible plating and stripping, but only on aluminum. Like Fung and Chau, they were actually cycling lithium using a LiAl anode. XRD measurements confirmed the identity of their Li_2Al electrode that gave 280 mAh·g^{-1} at -1.5 V vs. Al.

Similarly to the case for sodium, adding HCl to the LiCl-buffered melt improves reversibility [114,121,122], but the effect is clearer for lithium than for sodium (compare Figures 13 and 14). Current efficiencies on short times scales of voltammetry were high (>90%). Furthermore, the lithium deposits were gray/blue and were stable on open circuit for at least 15 minutes.
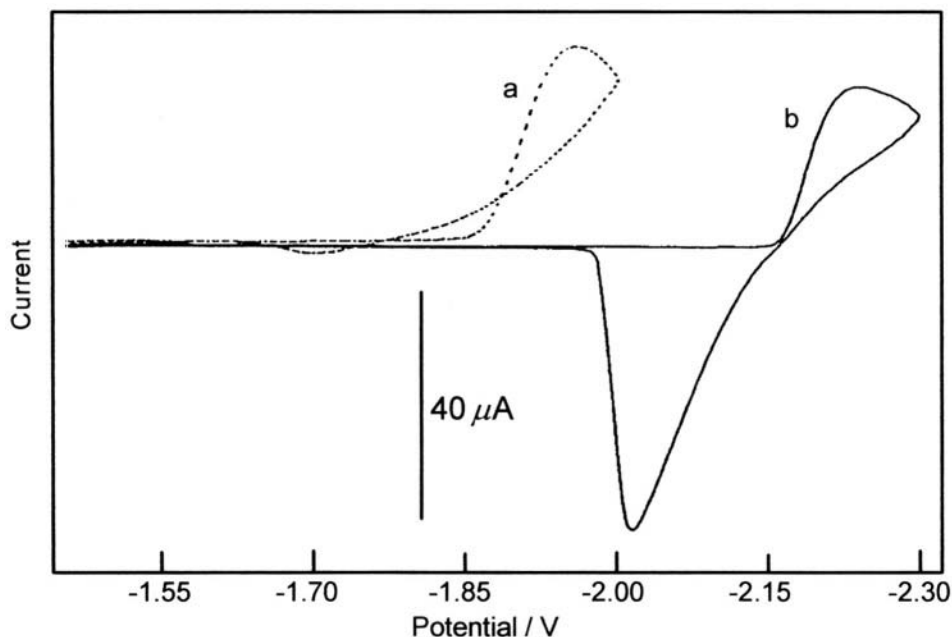
Figure 14. Lithium plating and stripping in a LiCl-buffered neutral melt comprising 1.1:1.0:0.1 $AlCl_3$:EMIC:LiCl at a 250µm tungsten electrode (a) without HCl_2^- and (b) with added HCl_2^-. Scan rate was 500 mV/s. From reference 114, reproduced by permission of The Electrochemical Society, Inc.

However, with longer exposure the deposited lithium reacted with the electrolyte to form a brown film. Moreover, charge efficiency dropped to 75% in chronopotentiometry experiments (2-minute plate and strip at **0.5-3 mA·cm^{-2}**, no rest period), although overpotentials were low. When rest times were increased to 1 and 15 minutes, this efficiency dropped even further to 77 and 21%, respectively. Thus, while HCl helps stabilize the plated lithium, shelf life is still woefully inadequate. Studies with lithium disk electrodes demonstrated that, with or without HCl, anode polarization was very large – discharging at **0.6 mA·cm^{-2}** gave a 0.6V polarization [121,122]. The dissolution rate was controlled by chloride diffusion reflecting the following:

$$Li + 2Cl^- \rightarrow LiCl_2^- + e^- \tag{7}$$

Optical studies also show that a brown film is formed at nucleation sites and that if HCl is present it reacts spontaneously to form bubbles of hydrogen [121,122]. However, if *excess* LiCl is added to an HCl-free melt, lithium anodes remain bright and stable in the now basic melt.

Additives that have been used to enhance lithium cycling are TEOA and **TEOA·HCl** [116,124], thionyl chloride [118,127,128] and **PhSOCl$_2$** [135]. Benzene and other organic solvents have been added to such melts to lower nucleation polarization and improve the morphology of the plated lithium [94]. Cyclic voltammetry on LiCl-buffered **EMIC/AlCl$_3$** melts containing TEOA and **TEOA·HCl** gave higher efficiency with the additives and the process was "nearly reversible;" coulombic efficiencies were 74% [116]. However, the deposited lithium was still not stable with time.

Koura reported [118] a ten-fold increase in the lithium limiting current when **SOCl$_2$** was added to a **EMI/AlCl$_3$** electrolyte. On a voltammetric timescale, the process was found to be reversible. Adding **SOCl$_2$** was much better than their previous approach of adding lithium metal to the melt to scavenge acidic impurities [118,134]. Carlin, Fuller and Osteryoung´s work with **SOCl$_2$** was less promising with lithium anodes than for sodium. The plated anodes were stable on open circuit and plating/stripping efficiencies above 90% could be achieved. Figure 15 shows how well **SOCl$_2$** addition suppresses the EMI cation reduction at -1.6 V to permit lithium plating at -2.3V. However, dendrites form on cycling and charge/discharge efficiency rapidly dropped from 86 to 69% in only 4 cycles [4,127,128,130]. Also, storage for several hours showed that the Li deposits were unstable, stripping efficiency being only 35% after 10.6 hours [127]. Fung and Zhou report similar advantages for adding **PhSOCl$_2$,** and were able to cycle a **Li-Al/LiCoO$_2$** cell [135]. After 6 cycles, charge efficiency was stable but, as the cell was cathode-limited, the performance of the anode is not clear.

Overall, **SOCl$_2$** is far more effective than HCl in boosting lithium cycleability and stability, but shelf stability is still inadequate. Additional or better additives

are needed to stabilize the plated lithium. Unfortunately, the technical approach to find such additives is unclear. In view of the considerable effort expended in generally unsuccessful attempts to find "magic additives" for lithium in organic electrolytes, the likelihood for success would seem rather low. In particular, additives that alter the lithium SEI layer would likely tend to interact or dominate each other such that combinations of additives would not be significantly more effective than the best single additive. On balance, sodium stability with $SOCl_2$ seems more achievable.

Angell, Xu and Zhang demonstrated lithium deposition and stripping in a "quasi-ionic liquid or ionic oil" of $Li[AlCl_3-SO_3Cl)$ formed by reacting $LiClSO_3$ with $LiAlCl_4$ [117,136]. Analogous ionic liquids are formed by mixing the following with $LiAlCl_4$: $Cl_3P=N-CH_3$, $Cl_3P=N-P(O)Cl_2$, CH_3SO_2Cl and especially $Cl_3P=N-SO_2Cl$ [67,117,136-138]. In addition to lithium, sodium was cycled in the analogous ionic liquid, $NaAlCl_4/Cl_3P=N-SO_2Cl/AlCl_3$ [117]. This material had a 6V electrochemical window (ignoring what was attributed to a slow aluminum deposition at -1 V). While CH_3SO_2Cl is highly corrosive and extremely aggressive to the skin, "ionic rubbers" have been made using $LiAlCl_4/CH_3SO_2Cl$ with polymethylmethacrylate [26,67,137]. This immobilizes the CH_3SO_2Cl to reduce the hazard associated with it. Note that some of these ionic liquids, such as $Cl_3P=N-SO_2Cl$ and $Li[AlCl_3-SO_3Cl)$, contain no carbon atoms and thus are more likely to be truly non-flammable, although toxicity would be problem if cells were to vent.
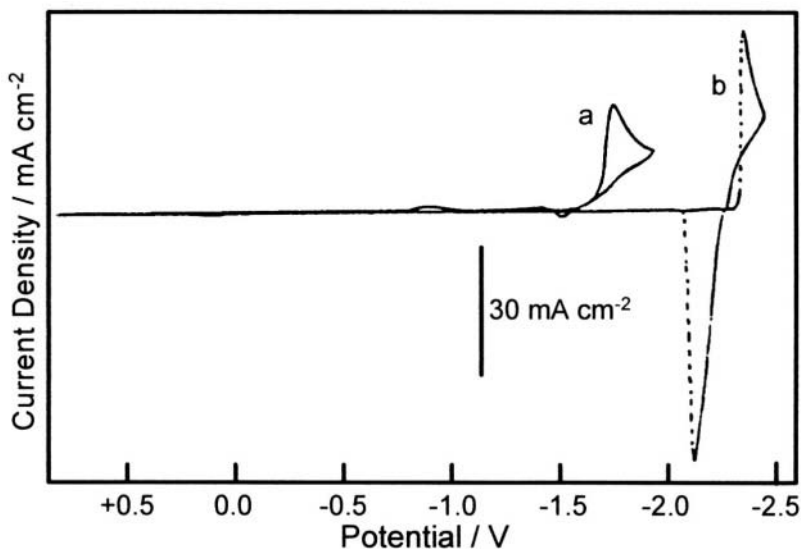
Figure 15.   Lithium plating and stripping in a LiCl-buffered neutral melt comprising 1.1:1.0:0.1 $AlCl_3$:EMIC:LiCl at a 250μm tungsten electrode without $SOCl_2$ and with the addition of 23mM $SOCl_2$. Scan rate was 100 mV·s⁻¹. From reference 128, reproduced by permission of The Electrochemical Society, Inc.

1,2 -dimethyl-4-fluoropyrazolium (DMFP) chloride/AlCl$_3$ melts have also been described for use in rechargeable Li/SCl$_3$AlCl$_4$ cells [106]. (The authors use SCl$_3^+$ as a probe for stability to oxidants.) The DMFP electrolytes are more stable to high potential cathodes than EMI$^+$ salts; EMI$^+$ reacts spontaneously with S(IV) species. Thus, DMFP and the DMPI cations offer ways to significantly improve the stability of ionic liquids.

9.2 *Nonhaloaluminate Melts or Hydrolytically Stable Melts*

Cooper and Sullivan [30] replaced the AlCl$_4^-$ of an EMIC/AlCl$_3$ melt with the hydrolytically stable CF$_3$SO$_3^-$ (triflate) anion. The resultant EMI triflate melts are air and moisture stable. Similarly, Wilkes and Zaworotko made EMIBF$_4$ as well as the corresponding acetate salt [20]; Carlin and Fuller also made and tested EMIBF$_4$ melt [33,139]. Substituted pyridimium, imidazolium and many other analogs have also been made [42,50]. Moreover, large amounts of the corresponding lithium salt can be dissolved in these melts, making them suitable for lithium and lithium ion battery electrolytes [42]. In essence, the organic cation salt acts like the "solvent" and the added lithium salt the charge carrier for the battery. Carlin, Fuller and Osteryoung [33,38,139] found that the cathodic limit of EMIBF$_4$ is extended by ca. 0.2 V to -2.2 V on a Pt electrode when 0.2M LiBF$_4$ is added, although no such benefit was noted on glassy carbon. While this is not enough to see lithium deposition, addition of small amounts of water extends the cathodic limit by another 0.8 V to -3 V. Since the anodic limit is +2 V, this electrolyte has a large voltage window of 5 V. Chronopotentiometry at 0.5 mA·cm^{-2} on platinum gave efficiencies that were still modest, 60%. The water was thought necessary to passivate the platinum current collector for EMI reduction. Efficiencies of over 90% were consistently attained when the platinum electrode was replaced with aluminum, forming a β-LiAl anode that is reduced about 0.35V more positive than lithium metal. Thus, a combination of moving the cathodic limit of the melt lower by adding LiBF$_4$ and water and moving the plating process to higher potentials with β-LiAl has, on the chronopotentiometric time-scale at least, produced a stable melt with high lithium efficiency. It is particularly impressive that this electrolyte was cycled, albeit on a short time-scale, in ambient air. In fact, small amounts of water, HCl or lithium oxide may even improve cycling in these melts, at least in the short term [140]. This electrolyte was also used to successfully cycle LiCoO$_2$ (see below) to form, at least in principle, a 4 V rechargeable cell [139].

Koch et al. disclose a wide variety of ionic liquids that are based on nitrogen-containing heterocyclic cations and large, polyatomic anions such as ▮▮▮▮▮▮▮▮▮▮▮▮ and (CF$_3$)$_x$PF$_{6-x}^-$ where x = 2 to 6 [42]. Pyridinium, pyridazinium, pyrimidinium, pyrazinium, imidazolium, pyrazolium, thia-

zolium, oxazolium and triazolium cations are mentioned (see Figure 12 for some of these structures). Examples given were EMI, BP, DMPI and perfluorinated EMI cations. These melts are hydrophobic and can dissolve the large amounts of lithium salts required for use in primary and secondary lithium cells. Focusing on the more stable DMPI cation, developed by Gifford and Palmisano [88], Koch et al showed [42] that melts using PF_6^-, AsF_6^-, TFSI$^-$ and Me$^-$ anions are stable to around 5 V vs. Li on platinum, tungsten and glassy carbon electrode; DMPIMe being stable to 5.35 V on platinum and having a very wide electrochemical window (Figure 16). No specific battery data was given but good stability in capacitors was demonstrated. Impedance studies of DMPITFSI and DMPIMe melts containing 0.25M of the corresponding lithium salt in Li/Li cells demonstrated that these melts gave stable conductivities and also stable interfacial resistances for 16 weeks [32]. This is one of the few studies that investigates the stability of lithium in ionic liquids over realistic timeframes.
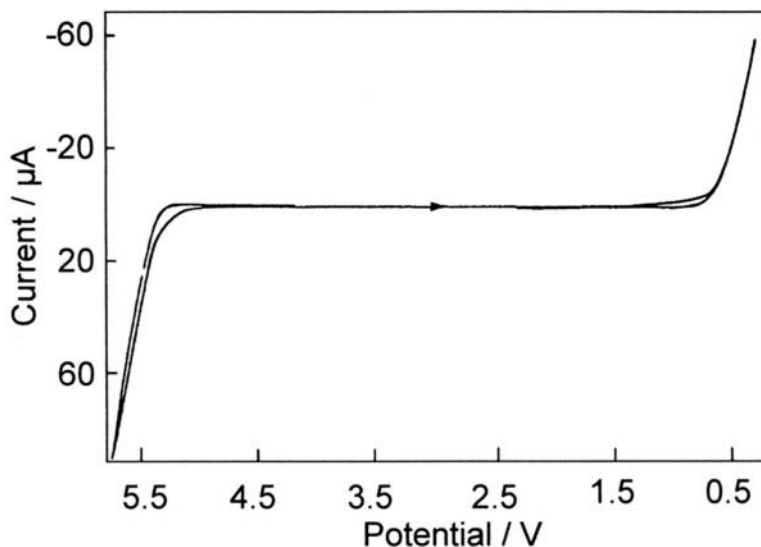
Figure 16. Cyclic voltammogram of DMPIMe on a glassy carbon electrode at 22 ºC showing a 4.5 V window for an air-stable ionic liquid. Scan rate was 20 mV·s^{-1}. Electrode area was 0.07 cm^2. From reference 60, reproduced with permission of The Electrochemical Society, Inc.

MacFarlane et al. developed a new family of ionic liquids based on pyrrolidinium [49] and tetraalkylammonium cations [39,43,44] with the TFSI$^-$ anion; the TFSI$^-$ anion is known to be an excellent "plasticizing species" for polymer electrolytes. Matsumoto et al attained 81% efficiency for lithium plating and stripping in one of these melts, Me$_3$PrNTFSI [56]. Ngo and McEwen studied pentamethylimidazolium salts using TFSI$^-$, I$^-$ or PF_6^- anions [46]. This cation is extremely stable. Unfortunately, the large size of the cations results in high viscosity, low conductivity and melting points above
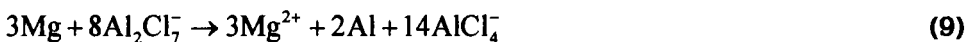
ambient. Building on their work with **AlCl₃-containing** ionic liquids [106], Caja et al. used l,2-dimethyl-4-fluoropyrazolium tetrafluoroborate with added **LiAsF₆** (or $LiBF_4$) to cycle **Li-Li$_x$Mn$_2$O$_4$** cells [54]. The cells were cathode limited and thus did not shed much light on anode performance. However, their stability experiments did show great promise for using this with lithium anodes. In one of the few studies on stability for extended periods, they found that the melts seemed stable to lithium for 14 days at 60°C with no change in the Raman spectrum of the melt. One impressive finding was that lithium metal heated to 170°C (close to the 181°C melting point of lithium) in this electrolyte does not attack the electrolyte and even remains shiny. This completely overshadows the instability of lithium at high temperatures in regular organic solvent electrolytes.

These ionic liquids can also be mixed with conventional organic solvents, further blurring the distinction between ionic liquids and strong electrolytes [62,42]. For example, adding 2M DMPITFSI to a propylene carbonate/dimethyl carbonate blend gave a 26-fold increase in conductivity over that of the ionic liquid alone; the organic solvents keep the viscosity low while the ionic liquids provide the high charge carrier concentration [42].

Patents covering a wide range of other hydrolytically stable ionic liquids for secondary batteries have appeared [42,56]. Matsumoto et al. describe ammonium salts (alkyl, aryl, arylalkyl and heterocyclic) of various anions, including **TFSI⁻**, **Triflate⁻**, **BF₄⁻**, **AlCl₄⁻**, **PF₆⁻**, **Al₂Cl₇⁻** and **Al₃Cl₈⁻** [7]. For example, cyclic voltammetry showed that **Me₃HxNTFSI** with added LiTFSI gave a melt that had a 6 V window and within which lithium could be cycled. Ammonium hydrogen maleates, mixed with a lithium salt, have been described for use in lithium cells, capacitors and electrochromic displays [141].

10.0 MAGNESIUM AND OTHER ANODES

Buffered **MEIC/AlCl₃** melts can be made using **MgCl₂** although they are not completely buffered [142]. Magnesium metal displaces aluminum from acid melts [103,143]. While this precludes using such a melt for a magnesium battery, the reaction has been used to make buffered neutral melts from acid melts [179]. This method could also be applied for lithium and sodium buffered melts.

$$MgCl_2 + 2Al_2Cl_7^- \rightarrow Mg^{2+} + 4AlCl_4^- \tag{8}$$

$$3Mg + 8Al_2Cl_7^- \rightarrow 3Mg^{2+} + 2Al + 14AlCl_4^- \tag{9}$$

In basic **EMIC/AlCl₃** melts, magnesium spontaneously reacts with the EMI cation, forming a yellow solution and generating bubbles. This was overcome by using basic **DMPIC/AlCl₃** melts in which magnesium stays

shiny for at least 3 months [102,103]. Unfortunately, magnesium, like aluminum, cannot be plated in basic melts, even in the presence of $SOCl_2$. However, unlike aluminum and lithium, magnesium can be anodically dissolved into the melt (as in a primary battery) without forming a passivating layer of the metal chloride. Instead, the $MgCl_2$ complexes with chloride ions to form soluble $MgCl_4^{2-}$ [102,103,143]. The oxidation rate is limited by chloride diffusion to the magnesium. Magnesium buffered melts have been studied for use with V_2O_5 aerogel/xerogels, hydrated vanadium bronzes, MoO_3, $NiCl_2$ and $CdCl_2$ cathodes (see cathode section below). However, new approaches are needed before a rechargeable magnesium cell could be developed, possibly using the hydrolytically stable ionic liquids developed for lithium and sodium batteries.

Tin has been plated from $BPC-SnCl_2$ melts and this process is reversible on the voltammetric time-scale [41]. While no battery work was disclosed, this could form the basis for a tin-based battery. Cadmium was found to be reversible in a substituted ammonium chloride melt, $(EtOCH_2)(Et)(Me)_2NCl/AlCl_3$. The cathodic limit of this melt was lower that for $EMIC/AlCl_3$ melts. However, Al, Li and Zn were inactive and work with this melt was suspended [144]. Calcium and $CaCl_2$ buffered melts have also been studied [143].

Nakagawa et al. [145] used a $Li_4Ti_5O_{12}$ intercalation anode with a $LiBF_4/EMIBF_4$ electrolyte to cycle a $LiCoO_2$ cell. Like using LiAl anodes, this approach uses a less energetic anode than lithium metal and trades off energy density for better stability and cycle life. Since this cell was cathode limited, its performance is detailed in the cathode section.

11.0   CATHODES

11.1   Oxides

Chronopotentiometry by Carlin and Fuller [139] showed that their $EMIBF_4/LiBF_4$ melt could cycle both a β-LiAl anode (between -2.81 and -2.52 V) and a commercial $LiCoO_2$ cathode (between 1.05 and 1.46 V) at $0.5mA \cdot cm^{-2}$ for at least short cycles (5 minutes). While the electrodes were tested separately, not in a full cell, the comparable charge and discharge voltage expected for a full cell would be 4.27/3.57 V. Using $PhSOCl_2$ to stabilize the anode deposits in a LiCl buffered $EMIC/AlCl_3$ melt, Fung and Zhou [135] cycled $LiCoO_2$ in both a half cell and cathode-limited full cell configuration, the latter employing a lithium anode with an aluminum collector, essentially a LiAl anode. The results in Figure 17 and Table 4 describe a well-behaved cathode with very little fade for such a non-optimized system. The cumulative capacity fade was only 3% over the first 20 cycles. While initial charge efficiency was low, this was essentially overcome by cycle 6 in both half and full cells. Separate tests on the carbons alone established that some of the excess charge capacity in

the first few cycles could be attributed to intercalation of anions into the carbons. Cycling the full cell between 2.9 and 4.2 V gave a stable discharge capacity of **112 mAh·g⁻¹** after the cell had completed the formation cycles.

Table 4. Half-Cell cycling of LiCoO₂ in a LiCl buffered EMIC/AlCl₃ containing added PhSOCl₂: Cathode performance with various carbon conductors. Data taken from reference 135 and reproduced with permission from Elsevier Science.

	Graphite	Coke	Acetylene Black
Charge efficiency on cycle 1	58.8%	39.1%	25.8%
Charge efficiency on cycle 20	91%	84%	80%
Discharge capacity on cycle 1 (mAh/g)	141	131	116
Discharge capacity on cycle 20 (mAh/g)	138	127	113
Capacity fade over 20 cycles (mAh/g)	3	4	3
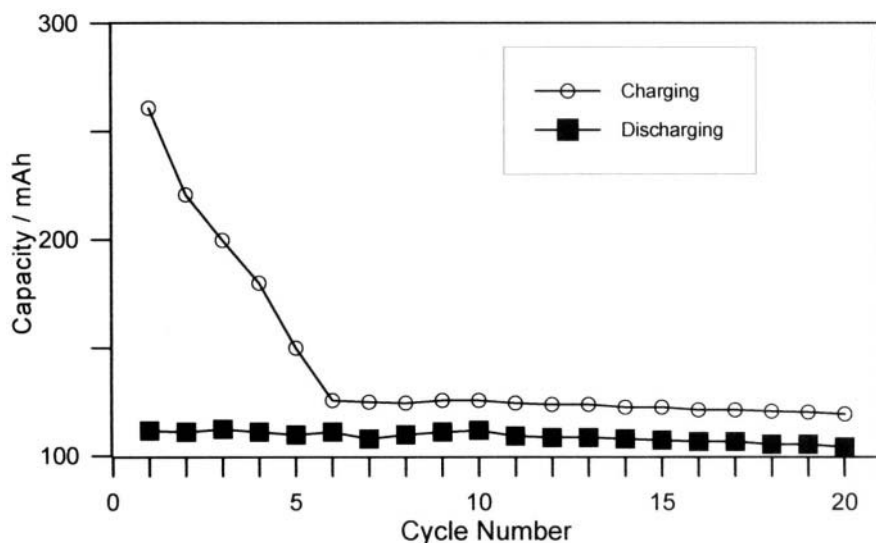
Figure 17. Charge and discharge capacity of a LiAl/LiCoO₂ battery using 1:1.2:0.15 EMIC/AlCl₃/LiCl mixture with 0.05 mol/Kg added PhSO₂Cl. Cathode was 85:10:5 LiCoO₂:graphite:Teflon by weight. Current density was 1mA·cm⁻². From reference 135, reproduced with permission from Elsevier Science.

Nakagawa et al [145] demonstrated a $Li_4Ti_5O_{12}/LiBF_4$-$EMIBF_4/LiCoO_2$ cell that delivered **140-145 mAh·g⁻¹** $LiCoO_2$ over 150 cycles with almost no fade. The charge/discharge rate was 0.1C and the system did not do well at higher rates, discharge capacity being less than **40 mAh·g⁻¹** at 0.5C. Nevertheless, this performance is impressive for a non-optimized system. While the lower energy density of the anode may detract from the overall cell capacity, trading energy density for improvements in stability, and possibly safety, is the essence behind lithium ion batteries.

Koura et al [146,147] used LiCl buffered **EMIC/AlCl₃** melts to cycle cells with lithium anodes (plated onto aluminum) paired with $LiCoO_2$, $LiNiO_2$,

$LiMn_2O_4$ and crystalline-V_2O_5 cathodes. Discharge capacity and efficiency were: $LiCoO_2$ – 124 mAh·g^{-1} and 91.9%; $LiNiO_2$ – 100 mAh·g^{-1} and 74.0%; $LiMn_2O_4$ – 92 mAh·g^{-1} and 65.7%; and c-V_2O_5 – 146 mAh·g^{-1} and 100%. Solubility measurements showed less than 0.1% solubility in the melt for all of these cathodes. The crystalline-V_2O_5 cathodes were cycled for more than 100 cycles between 3.2 and 2 V [146]. Xu, Angell and Zhang [26,67,117,137,138] have developed completely carbon-free molten salts such as trichlorophosphazo-sulfuryllium chloride, $Cl_3P{=}NSO_2Cl$. This was mixed with $LiAlCl_4$ and used to cycle a $Li/Li_xMn_2O_4$ cell at 0.1 mAh·g^{-1} for 60 cycles, between 4.2 and 2 V (Figure 18). After the initial 20 cycles, additional capacity fade was minimal [117]. 15:85 $LiAlCl_4$:CH_3SO_2Cl was also cycled in this cell. Cathode polarization was high with operating voltages being only 2.5 V instead of the 3 V normally expected from this couple. Nevertheless, capacity was ca. 100-130 mAh·g^{-1} (corresponding to x=0.7 to 0.9). Li-MnO_2 cells using $Me_3PhNCl/AlCl_3$ melts are described by Jones and Blomgren [107]. However, details on efficiency were not given.
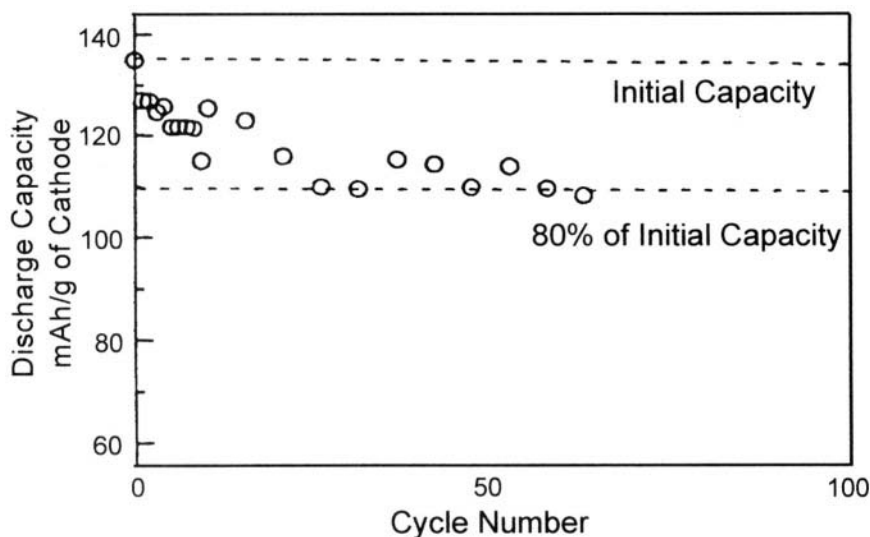
Figure 18. Discharge capacity for a $Li/Li_{1+x}Mn_2O_4$ cell using a "quasi-ionic liquid" electrolyte comprising a $LiAlCl_4/Cl_3P{=}N{-}SO_2Cl/AlCl_3$ mixture. The cell was cycled at 0.1 mA·cm^{-2} between 3.75 and 2V. From reference 117, reproduced by permission of The Electrochemical Society, Inc.

$Li/Li_xMn_2O_4$ cells using $LiAsF_6$ in $DMFPBF_4$ gave almost 100% efficiency over 25 cycles, although charging capacity decreased with cycling and was generally very low, starting out at about 27% of the theoretical value of 148 mAh·g^{-1} [54]. These authors used SCl_3^+ as a stability probe in developing this electrolyte. Combined with the impressive stability to lithium metal described previously, this electrolyte seems to be a very promising candidate for lithium batteries. Fung and Zhou [180] report reversible behavior for spinel $Li_xMn_2O_4$ in

EMIC/AlCl$_3$/LiAlCl$_4$ melt, somewhat complicated by irreversible intercalation of AlCl$_4^-$ into the graphite used in the cathode. Cathode efficiency was high for both the x=0.6→1 and x=1→2 stages. If the cathode was further charged so that x<0.6, cyclability degraded rapidly. The second step (x=1→2) from 4.3 to 3.5V gave 120 mAh·g^{-1} (86% of theoretical) and 98% efficiency after 20 cycles, by which point capacity had dropped to 103 mAh·g^{-1}.

Vanadium oxides have been studied as cathodes for Li, Na and Mg cells using buffered EMIC/AlCl$_3$ melts. Na$_{0.7}$K$_{0.3}$V$_3$O$_8$ has been reported to cycle reversible in such melts [135]. Novák et al [149] found that magnesium ions could be intercalated into hydrated V$_2$O$_5$ xerogels from a MgCl$_2$/EMIC/AlCl$_3$ melt. The xerogels showed reversible intercalation of magnesium and initially 170 mAh·g^{-1}. However, capacity dropped rapidly with cycling, possibly due to V$_2$O$_5$ solubility reported previously [150]. The same group also investigated the intercalation of magnesium into hydrated vanadium bronzes – M(V$_3$O$_8$)(H$_2$O)$_y$ where M = Li, Na, K, Mg$_{0.5}$ and Ca$_{0.5}$ [149]. Mg(V$_3$O$_8$)$_2$ gave about 150 mAh·g^{-1} for the first cycle and more than 80 mAh·g^{-1} (0.6 e$^-$/V) after 60 deep cycles (Figure 19). Unfortunately, the water present in these cathodes is necessary for efficient discharge; dried samples give much lower capacity. Moreover, the water is lost from the structure during cycling (although not during storage), leading to high fade rates. Notwithstanding the above, the materials gave more stable performance in the ionic liquids than in a conventional Mg(ClO$_4$)$_2$/acetonitrile electrolyte.

Ryan, Riechel and Xie (125,132) performed voltammetric, controlled potential electrolysis and UV/vis measurements on V$_2$O$_5$, NaVO$_3$, Na$_3$VO$_4$, V$_2$O$_4$ and V$_2$O$_3$ in acid, basic and buffered neutral EMIC/AlCl$_3$ melts. V$_2$O$_4$ and V$_2$O$_3$ were found to be insoluble in these melts at ambient temperature, despite an earlier report of V$_2$O$_4$ being soluble in LiCl-buffered BPC/AlCl$_3$ melts at 60°C (150). While desirable properties for most lithium batteries, Ryan, Riechel and Xie emphasized soluble cathodes that are better suited for redox batteries being considered for load leveling applications. V$_2$O$_5$ xerogel dissolves in acidic melts but was evaluated in buffered melts. Scans in NaCl-buffered melts suggest 2 reversible couples, attributed to V(V)→V(IV) and V(IV)→V(III) reductions. In LiCl-buffered melts, very broad pseudo-reversible peaks were observed. Voltammetry showed that NaVO$_3$, Na$_3$VO$_4$ and V$_2$O$_5$ discharged similarly, probably going from V(V) to V(IV). However, the reaction products were not identified in this work. Rechargeability was poor for all three and the higher solubility of NaVO$_3$ is a disadvantage for conventional cells (non-redox). The authors concluded that these materials were not suitable for secondary cells, but that Na$_3$VO$_4$ and V$_2$O$_5$ may be useful as a primary cell cathode.

Lithium, sodium and especially magnesium intercalation into MoO$_3$ were studied in both organic electrolytes and in MgCl$_2$/EMIC/AlCl$_3$ melts [151]. With the magnesium-containing melt, 150 mAh·g^{-1} (0.76 e$^-$/MoO$_3$) was achieved at

80°C, although by cycle 4 this dropped to **100 mAh·g⁻¹**. While there are severe limitations with magnesium-based anodes, this work does demonstrate that cathodes for cells using ionic liquids need not be limited to lithium and sodium.
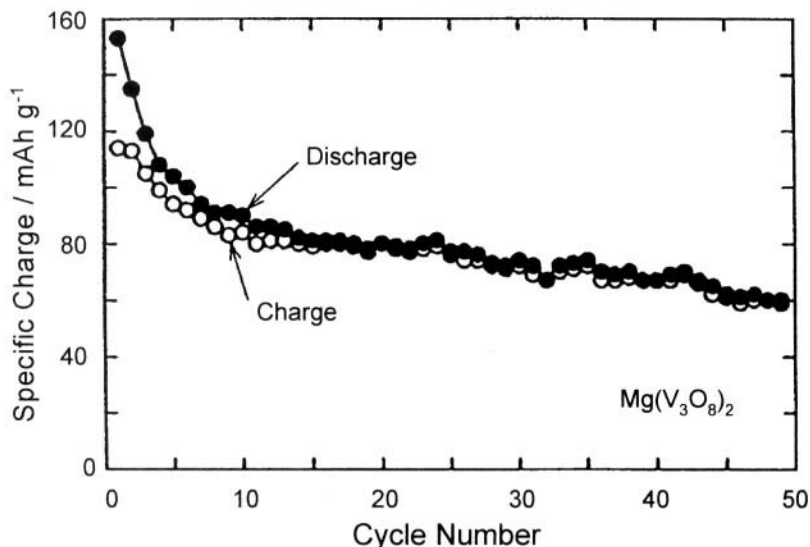
Figure 19. Voltammetric cycling data for $Mg(V_3O_8)_2$ in a $MgCl_2/EMIC/AlCl_3$ electrolyte. The cathode was cycled at 0.05mV/s between 0.5 and 1.7V vs. Al/Al^{3+}. From reference 149, reproduced with permission of The Electrochemical Society, Inc.

11.2   Chlorides

Many metal chlorides can also give respectable energy density [92]. Lipsztain and Osteryoung [152] reported that $FeCl_2$ is insoluble in neutral melts of both **BPC/AlCl₃** and **EMIC/AlCl₃** while being soluble in the acidic melts. $FeCl_3$, $FeCl_2$ and $NiCl_2$ exist as $FeCl_4^-$, $FeCl_4^{2-}$ and $NiCl_4^{2-}$ complexes in basic melts [92,153-156]. $NiCl_2$ and $CdCl_2$ cathodes were studied in buffered and magnesium-buffered neutral **DMPIC/AlCl₃** melts [103]. They form $NiCl_4^{2-}$ and $CdCl_4^{2-}$ in non-buffered melts. In the **MgCl₂-buffered** melts, $NiCl_4^{2-}$ reacts to form $NiCl_2$, at least some of which appears to precipitate out according to reaction (10). By contrast, the $CdCl_4^{2-}$ remains in solutions as $CdCl_4^{2-}$.

$$NiCl_4^{2-} + MgCl_2 \rightarrow MgCl_4^{2-} + NiCl_2 \downarrow \qquad\qquad \textbf{(10)}$$

Pye et al [101,156] evaluated iron, copper and nickel chlorides as possible cathodes in NaCl-buffered, neutral **EMIC/AlCl₃** melts for room temperature sodium batteries. Both the **Fe(II)→Fe(III)** and **Fe(II)→Fe(0)** processes were studied, confirming and adding to the earlier work by Lipsztain and Osteryoung. Oxidation of Fe(II) to Fe(III) occurs at +0.4V. In basic melts,

$FeCl_2$ is soluble and gives slow reduction kinetics. Iron could be deposited from both acid and buffered neutral melts at about -0.8 V, but reversibility was only high in the acid melts. Moreover, the chloride ions released when elemental iron is formed actually make the melt more basic. Overall, $FeCl_2$ is not promising due to its low voltage [152,156]. $CuCl_2$ reduces about 1V above $FeCl_2$ but in neutral [156] and basic [92] melts the oxidized from is soluble. $NiCl_2$ is insoluble in both the oxidized and neutral forms, has given ca. 100% efficiencies and gives 2.5V vs. sodium [101]. This makes it the most promising of these chlorides [156]. However, passivating layers appear to limit the charge density and so high surface area current collectors would likely be required, lowering energy density and increasing cost [101,156]. Al-$FeCl_3$ cells where the cathode was deposited on an RVC matrix could cycle at high current densities (ca. 10 $mAh \cdot g^{-1}$) in acid melts [92,155]. The discharge was controlled by the RVC matrix. Shorting and dendrites were problems, although not necessarily related to each other. Cyclic voltammograms of vanadium and niobium chlorides show V(III)→V(II) and Nb(V)→Nb(IV) redox behavior in EMIC/$AlCl_3$ melts, although the kinetics are slow [157]. Hanz and Riechel [158] found that while VCl_3 was insoluble in acidic and neutral MEIC/$AlCl_3$ melts, it was soluble in basic melts, forming VCl_4^-, VCl_5^{2-} and VCl_6^{3-} species. Each of these could be oxidized to their corresponding V(IV) species at 1.33, 1.23 and 1.00 V, respectively (as depicted in Figure 20).

$$VCl_{3(s)} \underset{}{\overset{+Cl^-}{\rightleftarrows}} VCl_4^- \underset{}{\overset{+Cl^-}{\rightleftarrows}} VCl_5^{2-} \underset{}{\overset{+Cl^-}{\rightleftarrows}} VCl_6^{3-}$$

$$\qquad 1.33V \updownarrow -e^- \qquad 1.23V \updownarrow -e^- \qquad 1.00V \updownarrow -e^-$$

$$VCl_{4(liq)} \underset{}{\overset{+Cl^-}{\rightleftarrows}} VCl_5^- \underset{}{\overset{+Cl^-}{\rightleftarrows}} VCl_6^{2-}$$

Figure 20. Redox scheme for the oxidation of VCl_3 to various V(IV) species in basic EMIC/$AlCl_3$ melts. Adapted from reference 158 used with permission of the American Chemical Society.

One of the major drawbacks of using a chloride cathode is that the electrode can inject or remove chloride ions from the electrolyte during charge and discharge. This has the effect of changing the melt acidity in the region of the cathode, affecting cell stability and possibly low temperature operation of the melt. For example, consider the reaction for an Al/$FeCl_3$ cell

$$Al + 3FeCl_3 + AlCl_4^- \rightarrow Al_2Cl_7^- + 3FeCl_2 \qquad\qquad (11)$$

Secondary Al-$SnCl_2$ and Al-$FeCl_2$ cells were made using a 1:2 acidic $Me_3PhNCl/AlCl_3$ melt in the anode compartment and the same electrolyte with the soluble cathode in a cathode compartment separated from the anolyte by a

glass frit [110]. Long term stability and feasibility of such cells, **Al/AlCl₃-PhMe₃NCl ‖AlCl₃-PhMe₃NCl-FeCl₂/graphite,** really requires a separator that blocks the catholyte from reaching the anode. Even if such a separator could be found, it would likely be very resistive.

SCl₃⁺ is a very strong oxidant that can give cells with a voltage above 4.2V, but EMI and BPC cations react with **SCl₃⁺**. **Li/SCl₃AlCl₄** cells can be made using LiCl-buffered l,2-dimethyl-4-fluoropyrazolium **chloride/AlCl₃** melts [106]. Raman studies show no sign of **SCl₃⁺** degradation in such melts. **SCl₃AlCl₄** can be added or made *in situ* by the reaction of sulfur with the molten salt. The cells did exhibit high internal resistance, attributed to the **β-alumina** separator, and efficiencies were low (ca. 30%). A sodium-sulfur cell was cycled using **LiAlCl₄:Cl₃P=N-SO₂Cl** in a polymethylmethacrylate matrix [67].

11.3   *FeS₂ and TiS₂*

High temperature **Li-FeS₂** cells have been under development for many years. These use purely inorganic molten salts and usually have to be operated at 170-250°C. Takami and Koura [159] were able to cycle a **Li-FeS₂** using an acidic **LiCl/BPC/AlCl₃** melt at 90°C and above with 90-100% efficiency. Below 90°C, the capacity dropped and efficiency was also very poor. Preliminary reports by You et al. [148] show that the first two-electron reduction of **FeS₂** to **Li₂FeS₂** can be cycled at 20°C in LiCl-buffered **EMIC/AlCl₃** melt. **TiS₂** has also been tested as a cathode in a LiCl-buffered **BPC/AlCl₃** melt [150].

11.4   *Halogens*

Chlorine and bromine cathodes have been considered for use with Al, Zn, Mg and Cd anodes but these are very unattractive cathodes to work with for safety reasons. Chlorine attacks the **EMI⁺** cation, although once halogenated, the cation and melt seemed to be stable [160]. In addition, halogen solubility in the melts makes them act like liquid cathodes with accompanying problems in terms of anode stability and separator requirements [92].

11.5   *Polymers*

Polymeric cathodes have been studied as cathodes in molten salt systems, mainly by Koura and Osteryoung; specifically polypyrrole [161-163], polythiophene [164], polyfluorene [165,166], polyaniline [167-172] and polyaniline polystyrene sulfonate [173] were evaluated. In many cases, the cathodes have been synthesized in the ionic liquids as well. These cathodes can be used with several anodes, even aluminum. Such systems have low to moderate specific

energies $(<100 \text{ mWh·g}^{-1})$ [4,100] and very low volumetric energy densities due to the low density of the polymers compared to conventional oxide cathodes (the density difference often being a factor of five).

Polypyrrole can be charged and discharged much faster in $EMIC/AlCl_3$ melt than conventional organic electrolytes [162], although rates begin to drop if the films are much thicker than l00nm [163]. Tang and Osteryoung [170,171] found that PAN is electroactive in basic, neutral and acidic melts, but that the redox couple is more stable and facile in basic melts. Koura et al. [168,172] confirmed this. The oxidizing form is conductive while the reduced form is insulating [170]. This raises one other drawback with polymeric electrodes in that the electrode conductivity is often a strong function of the state of charge, being at some point a very poor conductor. Aluminum´s requirement for an acidic melt containing $Al_2Cl_7^-$ ions causes problems for the PAN cathode because $Al_2Cl_7^-$ ions are too large to smoothly intercalate into the PAN structure. PAN cathodes cycle much more easily and reversibly in basic or neutral melts that contain the smaller Cl^- or $AlCl_4^-$ anions instead of $Al_2Cl_7^-$ ions. PAN differs by about 1 V in acid compared to basic melts. Koura [172] used this to make a PAN-PAN cell with an acid $EMIC/AlCl_3$ anolyte and basic catholyte. Charge/discharge efficiencies of 90% could be achieved, using a polymer for both electrodes. However, the low density and low voltage lead to a low energy density. This and the need for a separator are serious drawbacks. Koura et al. [167,169,174] also report 95% efficiencies and 80 mAh·g^{-1} PAN for Al-PAN cells using acidic $BPC/AlCl_3$ melt. Similarly, a Li/Al-PAN cell was cycled using acidic $BPC/AlCl_3$ or $EMIC/AlCl_3$ melts [175]. Efficiency actually climbed from 39 to 80% during the first four cycles. A PAN/polystyrene sulfonate copolymer gave 95-100% efficiency with an aluminum anode in a LiCl-buffered $BPC/AlCl_3$ melt $(60:33:6.7 \text{ AlCl}_3:BPC:LiCl)$. It also gave better rate capability than a comparable Al/PAN cell, although the maximum rate tested was 0.2 mA·cm^{-2} [173].

Carlin and Osteryoung report [100] a cathode based on the oxidation of Ph_3SiCl to form a polymeric species with EMI^+. Subsequent discharge of this material gave $32\text{-}57 \text{ mA·cm}^{-2}$ at 1.65 V. The precise nature of this cathode remains unclear, but the system showed good reversibility and extremely high rate capability, cycling at 100 mA·cm^{-2} [4].

12.0 CARBON

Like polymeric electrodes, carbon can form a positive or negative electrode by virtue of doping the material with anions or cations. The ions intercalate into the structure of the carbon and can often be deintercalated reversibly. In addition, work on carbons for lithium-ion type cells where essentially metallic lithium intercalates into graphitic carbons has been studied. Preliminary reports of lithium intercalation in carbon [97,176] were

later shown by the same authors, using XRD and XPS, to be due to $LiAlCl_4$ reduction to give a somewhat passivating film of LiCl and LiAl [4,177]. Thus, in essence they were cycling Li_xAl on a carbon surface and not C_xLi. The blocking nature of this film renders this process irreversible and impractical for a lithium battery.

$$AlCl_4^- + (4+x)Li^+ + (3+x)e^- \rightarrow 4LiCl + Li_xAl \qquad (12)$$
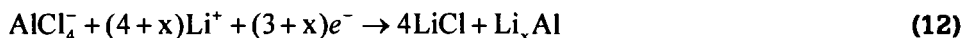
Carlin et al [4,98,99] established that high voltage batteries can be made by using ionic liquids lacking lithium or sodium salts where the ionic liquid anion and cation intercalate into carbon electrodes. This is somewhat similar to the doping of carbons in organic electrolytes. However, solvent cointercalation can lead to graphite exfoliation in such cases. In addition, the voltage window can be restricted by the solvent, thus lowering the energy density. Ionic liquids simplify the possible chemistry and side-reactions as the battery only uses two components, the ionic liquid and graphite. The wide voltage window of these electrolytes also helps avoid side reactions. These batteries are called DIME batteries for Dual Intercalating Molten Electrolyte batteries [99]. Figure 21 shows the effect of substituting graphite, into which the ions can intercalate, for glassy carbon, where no intercalation is observed. Instead of intercalation, the glassy carbon electrode merely shows the degradation of the EMI^+ and $AlCl_4^-$ ions at the limits of the voltage window for this melt.
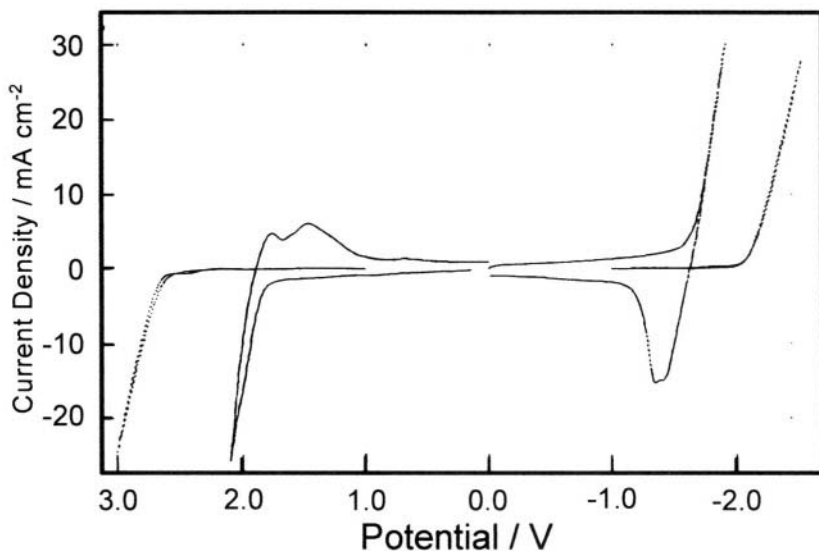
Figure 21. Staircase cyclic voltammograms in $EMIC/AlCl_3$ on glassy carbon and graphite. Scan rate is 50 mV/s. Scans B and D were run on glassy carbon and show irreversible reduction of EMI^+ and irreversible oxidation of $AlCl_4^-$, respectively. Scans A and C were run on graphite and show intercalation and subsequent deintercalation of EMI^+ and $AlCl_4^-$ ions into the graphite structure, respectively. From reference 99, reproduced by permission of The Electrochemical Society, Inc.

DIME batteries using **EMIC/AlCl₃** electrolyte give low efficiency for the EMI/C electrode, due to the instability of EMI. Blocking the 2-position of EMI by using 1-ethyl-2,3 -dimethyl imidazolium **chloride/AlCl₃** gave much better anode efficiencies, but this melt is solid below 72°C [98]. Switching to the more stable **DMPIC/AlCl₃** melts gave far better efficiency and an electrolyte that was liquid at room temperature [98,99]. Depending on the technique, **AlCl₄⁻** intercalation into the cathode was about 80% efficient, **EMI⁺** intercalation into the anode 60% and **DMPI⁺** 80-94%. Moreover, the high efficiency for DMPI was obtained at reasonable rates (charged at **1 mA·cm⁻²** and discharged at **0.25 mA·cm⁻²**). The instability of the EMIC intercalate was demonstrated by using a 10 hour hold time between charge and discharge; efficiency plummeted to only 2%. This work also explored the use of less aggressive ions than **AlCl₄⁻**, specifically, **PF₆⁻**, **BF₄⁻**, **Triflate⁻** and **PhCO₂⁻**, albeit using the less stable EMI cation. Note that the latter two anions result in electrolytes that are hydrolytically stable; even those using **PF₆⁻** or **BF₄⁻** are likely to react much more slowly with water than **AlCl₃–based** ionic liquids. **AlCl₄⁻** gave the best anion efficiency, but work using different carbons and/or more stable cations may well help to improve the performance of all the salts. More recent studies comparing **EMIBF₄** with **DMPIBF₄** for DIME batteries gave 65-71% efficiency for intercalation of the **BF₄⁻** anion into graphite/PVDF-HFP electrodes and 91% for DMPI cation vs. 78% for the EMI cation [53]. The DMPI melts were again better in terms of efficiency and charge retention. Note that both cations can exfoliate graphite at high rates. Related studies on a **graphite/PVDF-HFP/DMPIBF₄** composite electrode show that incorporating ionic liquids into the electrode can improve electrode performance [21].

In addition to intercalating anions into graphite, Sutto et al [52] find that **TiS₂** and **TaS₂** can also accept **BF₄⁻** anions from these same melts (efficiencies were 79% for **TiS₂** and 48% for **TaS₂**). **TaS₂** would exfoliate, but **TiS₂** actually gave better charge retention for **BF₄⁻** than did graphite. Iron has also been intercalated into graphite to form Fe-GIC´s in acidic **EMIC/AlCl₃** melts containing **FeCl₂** [178].

Despite these interesting advances, one must recognize that DIME batteries have inherently low energy density. Fully charged cells are thought to require 24 carbons per intercalated ion; the process goes by a similar staging process as occurs in lithium ion anodes [4]. Consequently, theoretical energy densities are less than **100 mWh·Kg⁻¹** and lie between that for capacitors and conventional batteries. Using carbon as an anode for a lithium-ion type of cell also reduces the energy density of the cell. This approach does not seem feasible with **AlCl₃-containing** melts due to the formation of LiAl instead of Li$_x$C. However, using carbon in **AlCl₃–free** melts with added lithium salts should work in analogous fashion as Nakagawa et al.´s **Li₄Ti₅O₁₂** intercalation anode, at least in principle.

13.0   FUTURE

The field could benefit from a closer cooperation between those developing the new materials and battery scientists. The former have the expertise to make and study these materials but are often ill-equipped to do the testing that is required to see how these materials perform in actual batteries. To become viable electrolytes, several important attributes need to be tested that are rarely reported. For example, long-term stability (as opposed to tests lasting minutes or a few hours) is obviously a basic requirement for these materials. In addition, much of the testing is done at rather low rates ($0.1 \ mA \cdot cm^{-2}$), whereas many consumer applications require much higher current densities ($1\text{-}10 \ mA \cdot cm^{-2}$), especially for rechargeable cells. Cycle life and balancing capacities and the inefficiencies at each electrode need to be considered more. Overcharge protection needs to be given attention, although the self-extinguishing nature of ionic liquids may limit the consequences of uncontrolled overcharging to reduced cycle life as opposed to thermal runaway.

Notwithstanding the above, the use of buffered $AlCl_3$ melts, especially with additives such as HCl, TEOA·HCl and $SOCl_2$ to enhance cycling efficiencies, has opened up new possibilities for ionic liquids as electrolytes for room temperature batteries. More stable cations such as DMPI and DMFP have also advanced the field considerably. Of special interest are the $AlCl_3$-free molten salts, such as DMPITFSI and DMFPTFSI. These liquids overcome safety and environmental problems associated with $AlCl_3$ and can readily accept the corresponding lithium and sodium salts, so that conventional cathodes can be used. Work has shown that anodes, (metal and carbon) can cycle in ionic liquids and several cathodes have been found. Most importantly, lithium cells can be made using either the $AlCl_3$-based or the $AlCl_3$-free ionic liquids. This opens the possibility of using the extensive range of cathodes known to intercalate lithium ions in such cells. LiAl alloy anodes have given some impressive cycle life. While such anodes cannot match the energy density of a lithium anode for the first cycle, over the lifetime of a rechargeable cell their lower fade rate may well overcome the voltage and capacity penalties of using the alloy. Similarly, while carbon anodes cannot be used to cycle lithium in $AlCl_3$-containing melts, this could prove feasible in $AlCl_3$-free melts, much in the same way as Nakagawa et al.´s $Li_4Ti_5O_{12}$ intercalation anode [145]. Just as conventional lithium and lithium ion cells cannot operate without acceptable passivation agents, more thought and experimentation need to be given to passivation of active metals in ionic liquids (or quasi ionic liquids).

Extensive studies on hybrid materials are also changing the ways we think about these materials and have blurred the distinctions between solution electrolytes, polymer electrolytes and ionic liquids.

The advantages of ionic liquids for batteries are very significant, if they can be realized. In particular, the non-flammability and tremendous thermal stability of many of the electrolytes are very impressive with some being stable to lithium metal at 170°C [54]. While much remains to be worked out, the pieces are in place to develop lithium and sodium batteries using ionic liquids. Many of the essential elements for constructing viable batteries have been addressed and it would seem timely to emphasize full cell work more. The low vapor pressure of ionic liquids would seem to be especially advantageous for thin and microbatteries, aiding in both filling the cell, maintaining wetted interfaces and enabling thinner, less expensive packaging materials and processes.

14.0   REFERENCES

1.   *Chemistry of Nonaqueous Solutions, Current Progress,* G. Mamantov and A.I. Popov, ed., VCH Publ., New York, 1994.
2.   Y.S. Fung, Trends Inorg. Chem., **5,** 117, 1998 and references therein.
3.   S. Takahashi, N. Koura, S. Kohara, M-L. Saboungi and L.A. Curtiss, *Plasmas Ions,* **2,** 99, 1999 and references therein.
4.   R.T. Carlin and J. Fuller, **12**[th] Ann. Battery Conf. Appl. Adv., 261, 1997 and references therein.
5.   N. Papageorgiou, Y. Athanassov, M. Armand, P. Bonhôte, H. Petterson, A. Azam and B. Grätzel, *J. Electrochem. Soc.,* **143,** 3099, 1996.
6.   P. Bonhote, A.-P. Dias, *U.S. Patent 5,638,832,* 1997.
7.   H. Matsumoto, Y. Miyazaki and H, Ishikawa, *Jap. Pat., 2,981,545,* 1999.
8.   H. Matsumoto, T. Matsuda, T. Tsuda, R. Hagiwara, Y. Ito and Y. Miyazaki, *Chem. Letters,* 26, 2001.
9.   K. Yokoyama, S. Fujita, A. Hiwara, Y. Naruse, M. Toriida and A. Omaru, *U.S. Patent 5,580,684,* 1996.
10.   K. Yokoyama; S. Fujita, A. Hiwara, Y. Naruse, M. Toriida and A. Omaru, *U.S. Patent 5,580,684,* 1998.
11.   X. Wang, E. Yasukawa and S. Kasuya, *196*[th] *Electrochem. Soc. Meeting,* Abstract #321, 1999.
12.   N. Shinoda, J. Ozaki, F. Kita and A. Kawakami, *Electrochem. Soc. Proc. Vol.,* **99-25,** 440, 2000.
13.   D. Peramunage, J.M. Ziegelbauer and G.L. Holleck, *198*[th] *Electrochem. Soc. Meeting,* Abstract #144, 2000.
14.   X. Wang, E. Yasukawa and S. Kasuya, *J. Electrochem. Soc.,* **148,** A1058, 2001.
15.   X. Wang, E. Yasukawa and S. Kasuya, *J. Electrochem. Soc.,* **148,** A1066, 2001.
16.   E.-H. Song, W.-I. Jung, D.-C. Hwang and H.-G. Noh, *U.S. Patent 6,232,020,* 2001.
17.   S.C. Narang, S.C. Ventura, B.J. Dougherty, M. Zhao, S. Smedley and G. Koolpe, *U.S. Patent 5,830,600,* 1998.
18.   H. Akashi, *U.S. Patent 5,658,686,* 1997.
19.   H. Akashi, K. Sekai and K.-I. Tanaka, *Electrochim. Acta,* **43,** 1193, 1998.
20.   J.S. Wilkes and M.J. Zaworotko, *Chem. Commun.,* 965, 1992.

21. T.E. Sutto, H.C. De Long and P.C. Trulove, *Electrochem. Soc. Proc. Vol.,* **99-41,** 32,1999.
22. P.A.Z. Suarez, S. Einloft, J.E. Dullius, R.F. de Souza and J. Dupont, *Polyhedron,* **15,** 1217, 1996.
23. See for example, J.S.-Y. Liu and I-W. Sun, *J. Electrochem. Soc.,* **144,** 140, 1997 and references therein.
24. T.L. Riechel and J.S. Wilkes, *J. Electrochem. Soc.,* **140,** 3104, 1993.
25. J.S. Wilkes et al, *Govt. Rept. FJSRL-TR-81-011/OrderAD-A107,989,* Oct. 1981.
26. C.A. Angell, K. Xu, S-S. Zhang and M. Videa, *Solid State Ionics,* **86-88,** 17, 1996.
27. T.J. Melton, J. Joyce, J.T. Maloy, J.A. Boon and J.S. Wilkes, *J. Electrochem. Soc.,* **137,** 3865, 1990.
28. C. Scordilis-Kelley, J. Fuller, R.T. Carlin and J.S. Wilkes, *J. Electrochem. Soc.,* **139,** 694, 1992.
29. T.J. Melton and J.S. Wilkes, *U.S. Patent 5,096,789,* 1992.
30. E.I. Cooper and E.J.M. Sullivan, *Electrochem. Soc. Proc. Vol.,* **92-16,** 386, 1992.
31. J. Fuller, R.T. Carlin, H. De Long and D. Haworth, *J. Chem. Soc. Chem. Commun.,* 299, 1994.
32. V.R. Koch, C. Nanjundiah, G. Battista Appetecchi and B. Scrosati, *J. Electrochem. Soc.,* **142,** L116, 1995.
33. R.T. Carlin and J. Fuller, *U.S. Patent 5,552,238,* 1996.
34. P. Bonhôte, A.-P. Dias, N. Papageorgiou, K. Kalyanasundaram and M. Grätzel, *Inorg. Chem.,* **35,** 1168, 1996.
35. A.B. McEwen, R. Chadha, T. Blakley and V.R. Koch, *Electrochem. Soc. Proc. Vol.,* **96-25,** 313, 1996.
36. A.B. McEwen, S.F. McDevitt and V.R. Koch, *J. Electrochem. Soc.,* **144,** L84, 1997.
37. C. Nanjundiah, S.F. McDevitt and V.R. Koch, *J. Electrochem. Soc.,* **144,** 3392, 1997.
38. J. Fuller, R.T. Carlin and R.A. Osteryoung, *J. Electrochem. Soc.,* **144,** 3881,1997.
39. J. Sun, D.R. MacFarlane and M. Forsyth, *Ionics,* **3,** 356, 1997.
40. P.A.Z. Suarez, V.M. Selbach, J.E.L. Dullius, S. Einloft, C.M.S. Piatnicki, D.S. Azambuja, R.F. de Souza and J. Dupont, *Electrochim. Acta,* **42,** 2533, 1997.
41. G. Ling and N. Koura, *Denki Kagaku,* **65,** 149, 1997.
42. V.R. Koch, C. Nanjundiah and R.T. Carlin, *U.S. Patent 5,827,602,* 1998.
43. J. Sun, M. Forsyth and D.R. MacFarlane, *J. Phys. Chem. B,* **102,** 8858, 1998.
44. J. Sun, M. Forsyth and D.R. MacFarlane, *Molten Salt Forum,* **4-5,** 585, 1998.
45. J.L. Goldman and A.B. McEwen, *Electrochem. Soc. Proc. Vol.,* **98-15,** 507, 1998.
46. H.L. Ngo and A.B. McEwen, ***194**[th] Meeting Electrochem. Soc.,* Abstract #954, 1998.
47. J.L. Goldman, H.L. Ngo and A.B. McEwen, ***194**[th] Meeting Electrochem. Soc.,* Abstract #312, 1998.
48. J. Fuller, A.C. Breda and R.T. Carlin, *J. Electroanal. Chem.,* **459,** 29, 1998.
49. D.R. MacFarlane, P. Meakin, J. Sun, N. Amini and M. Forsyth, *J. Phys. Chem. B,* **103,** 4164, 1999.
50. A. Noda and M. Watanabe, *Electrochem. Soc. Proc. Vol.,* **99-41,** 202, 1999.
51. J.L. Goldman and A.B. McEwen, *Electrochem. Solid-State Lett.,* **2,** 501 (1999).
52. T.E. Sutto, H.C. De Long and P.C. Trulove, *Electrochem. Soc. Proc. Vol.,* **99-41,** 43, 1999.
53. T.E. Sutto, C. Sienerth, H.C. De Long and P.C. Trulove, *Electrochem. Soc. Proc. Vol.,* **99-41,** 54, 1999.

54. J. Caja, T.D.J. Dunstan, D.M. Ryan and V. Katovic, *Electrochem. Soc. Proc. Vol.,* **99-41,** 150, 1999.
55. R.A. Mantz, H.C. De Long, R.A. Osteryoung and P.C. Trulove, *Electrochem. Soc. Proc. Vol.,* **99-41,** 169, 1999.
56. H. Matsumoto, M. Yanagida, K. Tanimoto, T. Kojima, Y. Tamiya and Y. Miyazaki, *Electrochem. Soc. Proc. Vol.,* **99-41,** 186, 1999.
57. A.B. McEwen, J.L. Goldman, D. Wasel and L. Hargens, *Electrochem. Soc. Proc. Vol.,* **99-41,** 222, 1999.
58. M. Forsyth, S. Jiazeng and D.R. MacFarlane, *Electrochim. Acta,* **45,** 1249, 2000.
59. H. Liang, H.Li, Z. Wang, F. Wu, L. Chen and X. Huang, *J. Phys. Chem. B,* **105,** 9966, 2001.
60. V.R. Koch, L.A. Dominey, C. Nanjundiah and M.J. Ondrechen, *J. Electrochem. Soc.,* **143,** 798, 1996.
61. J. Robinson and R.A. Osteryoung, *J. Electrochem. Soc.,* **127,** 122, 1980.
62. N. Takami and T. Osaki, *Jap. Pat. Appl., 11-260,400,* 1999.
63. A.B. McEwen and E.-E. Yair, *U.S. Patent 5,965,054,* 1999.
64. C. Liu and C.A. Angell, *Solid State Ionics,* **86-88,** 467, 1996.
65. J. Fuller, A.C. Breda and R.T. Carlin, *J. Electrochem. Soc.,* **144,** L67, 1997.
66. J. Fuller, A.C. Breda and R.T. Carlin, *Molten Salt Forum,* **4-5,** 605, 1998.
67. C.A. Angell, S.-S. Zhang and K. Xu, *U.S. Patent 5,824,433,* 1998.
68. A. Lewandowski and A. Swiderska, *200th Electrochem. Soc. Meeting,* Abstract #127, 2001.
69. R.T. Carlin, J. Fuller and Y. Ein-Eli, *190th Electrochem. Soc. Meeting,* Abstract #847, 1996.
70. M. Watanabe, S.-I. Yamada and N. Ogata, *Electrochim. Acta,* **40,** 2285, 1995.
71. R. Pyati and R.W. Murray, *J. Electrochem. Soc.,* **143,** 401, 1996.
72. Y. Nakai, K. Ito and H. Ohno, *Solid State Ionics,* **113-115,** 199, 1998.
73. H. Ono and K. Ito, *Jap. Unex. Pat. Appl.,* 10-083821 (1998).
74. H. Ohno, *Electrochim. Acta,* **46,** 1407, 2001.
75. M. Yoshizawa and H. Ohno, *Electrochim. Acta,* **46,** 1723, 2001.
76. J. Fan, R.F. Marzke, E. Sanchez and C.A. Angell, *J. Non-Cryst. Solids,* **172-174,** 1178, 1994.
77. C.A. Angell, J. Fan, C. Liu, Q. Lu, E. Sanchez and K. Xu, *Solid State Ionics,* **69,** 343, 1994.
78. Y. Ito and T. Nohira, *Electrochim. Acta,* **45,** 2611 (2000).
79. S.D. Jones and G.E. Blomgren, *J. Electrochem. Soc.,* **136,** 424, 1989.
80. R.A. Osteryoung, *Electrochem. Soc. Proc. Vol.,* **99-41,** 12, 1999.
81. H. Matsumoto, T. Matsuda and Y. Miyazaki, *Chem. Letters,* **12,** 1430, 2000.
82. A.A. Fannin, D.A. Floreani, L.A. King, J.S. Landers, B.J. Piersma, D.J. Stech, R.L. Vaughn, J.S. Wilkes and J.L. Williams, *J. Phys. Chem.,* **88,** 2614 (1984), Supplementary Material.
83. G.E. Blomgren and S.D. Jones, *Electrochem. Soc. Proc. Vol.,* **90-17,** 273, 1990.
84. G.E. Blomgren and S.D. Jones, *Electrochem. Soc. Proc. Vol.,* **92-16,** 379, 1992.
85. K. Xu and C.A. Angell, *Symp. Mat. Res Soc.,* **369,** 505, 1995.
86. Y.S. Fung and S.M. Chau, *J. Appl. Electrochem.,* **23,** 346, 1993.
87. J.A. Boon, J.S. Wilkes and J.A. Lanning, *J. Electrochem. Soc.,* **138,** 465, 1991.
88. P.R. Gifford and J.B. Palmisano, *J. Electrochem. Soc.,* **134,** 610, 1987.
89. R.T. Carlin, W. Crawford and M. Bersch, *J. Electrochem. Soc.,* **139,** 2720, 1992.

90.   Y. Zhao and T.J. VanderNoot, *Electrochim. Acta,* **42,** 1639, 1997.
91.   F.M. Donahue, L.R. Simonsen and R.L. Moy, *U.S. Patent 4,882,244,* 1989.
92.   F.M. Donahue, S.E. Mancini and L. Simonsen, *J. Appl. Electrochem.,* **22,** 230, 1992 and references therein.
93.   N. Papageorgiou and F.-P. Emmenegger, *Electrochim. Acta,* **38,** 245, 1993.
94.   Q. Liao, W.R. Pitner, G. Stewart, C.L. Hussey and G.R. Stafford, *J. Electrochem. Soc.,* **144,** 936, 1997 and references therein.
95.   N. Koura, H. Tsuda and K. Ui, *Denki Kagaku,* **64,** 1195, 1996.
96.   N. Koura, C. Yazawa and S. Ito, *Denki Kagaku,* **63,** 613, 1995.
97.   M.J. Lysaght, M. Hedenskoog, R.T. Carlin and J. Fuller, *Electrochem. Soc. Proc. Vol.,* **94-13,** 392, 1994.
98.   H.C. De Long and R.T. Carlin, *Electrochem. Soc. Proc. Vol.,* **94-13,** 736, 1994.
99.   R.T. Carlin, H.C. De Long, J. Fuller and P.C. Truelove, *J. Electrochem. Soc.,* **141,** L73, 1994.
100. R.T. Carlin and R.A. Osteryoung, *J. Electrochem. Soc.,* **141,** 1709, 1994.
101. S.L. Pye, G.E. Gray, J. Winnick and P.A. Kohl, *189th Meeting Electrochem. Soc.,* Abstract #10, p.10, 1996.
102. J. Fuller and R.T. Carlin, *Proc. Symp. Electrode Mater. Processes Energy Cone. Storage IV,* 218, 1997.
103. J. Fuller, R.T. Carlin, R.A. Osteryoung, P. Koranaios and R. Mantz, *J. Electrochem. Soc.,* **145,** 24, 1998.
104. A.B. McEwen, H.L. Ngo, K. LeCompte and J.L. Goldman, *J. Electrochem. Soc.,* **146,** 1687, 1999.
105. B. Vestergaard, N.J. Bjerrum, I. Petrushina, H.A. Hjuler, R.W. Berg and M. Begtrup, *J. Electrochem. Soc.,* **140,** 3108, 1993.
106. G. Mamantov, J. Caja, T.D.J. Dunstan, *U.S. Patent 5, 552, 241,* 1996.
107. S.D. Jones and G.E. Blomgren, *U.S. Patent 4,764,440,* 1988.
108. S.D. Jones and G.E. Blomgren, *U.S. Patent 4,839,249,* 1989.
109. G.E. Blomgren and S.D. Jones, *U.S. Patent 5, 188, 914,* 1993.
110. T.J. Vandernoot and Y. Zhao, *World Patent Application, WO 00/16415* 2000.
111. C.-L. Yu, J. Winnick and P.A. Kohl, *J. Electrochem. Soc.,* **138,** 339, 1991.
112. G.E. Gray, P.A. Kohl and J. Winnick, *J. Electrochem. Soc.,* **142,** 3636, 1995.
113. T.L. Riechel and J.S. Wilkes, *J. Electrochem. Soc.,* **139,** 977, 1992.
114. C. Scordilis-Kelley and R.T. Carlin, *J. Electrochem. Soc.,* **140,** 1606, 1993.
115. T.L. Riechel, M.J. Miedler and E.R. Schumacher, *Electrochem. Soc. Proc. Vol.,* **94-13,** 491, 1994.
116. B. J. Piersma, D.M. Ryan, E.R. Schumacher and T.L. Riechel, *J. Electrochem. Soc.,* **143,** 908, 1996.
117. K. Xu, S. Zhang and C.A. Angell, *J. Electrochem. Soc.,* **143,** 3548, 1996.
118. N. Koura, K. Hzuka, Y. Idemoto and K. Ui, *Electrochem.,* **67,** 706, 1999.
119. T.A. Zawodzinski and R.A. Osteryoung, *Inorg. Chem.,* **27,** 383, 1988.
120. R.T. Carlin and C. Scordilis-Kelley, *Electrochem. Soc. Proc. Vol.,* **92-16,** 364, 1992.
121. R.T. Carlin and C. Scordilis-Kelley, *Electrochem. Soc. Proc. Vol.,* **93-9,** 350, 1993.
122. C. Scordilis-Kelley and R.T. Carlin, *J. Electrochem. Soc.,* **141,** 873, 1994.
123. B.J. Piersma, *Electrochem. Soc. Proc. Vol.,* **94-13,** 415, 1994.
124. B.J. Piersma, *185th Meeting Electrochem. Soc.,* Abstract #954, p.1460, 1994.
125. D.M. Ryan and T.L. Riechel, *Electrochem. Soc. Proc. Vol.,* **96-7,** 381, 1996.
126. G.E. Gray, J.Winnick and P.A. Kohl, *Proc. 28th IECEC,* **1,** 1139, 1993.

127.   J. Fuller, R.A. Osteryoung and R.T. Carlin, *J. Electrochem. Soc.,* **142,** 3632, 1995.
128.   J. Fuller, R.T. Carlin and R.A. Osteryoung, *J. Electrochem. Soc.,* **143,** L145, 1996.
129.   J. Fuller and R.T. Carlin, *189ᵗʰ Meeting Electrochem. Soc.,* Abstract #1175, 1996.
130.   J. Fuller and R.T. Carlin, *Electrochem. Soc. Proc. Vol.,* **96-7,** 372, 1996.
131.   S.H. Park, J. Winnick and P.A. Kohl, *J. Electrochem. Soc.,* **148,** A346, 2001.
132.   J. Xie and T.L. Riechel, *14ᵗʰ Ann. Battery Conf. Appl. Adv.,* 135, 1999.
133.   S. Park, J. Winnick and P. Kohl, *200ᵗʰ Electrochem. Soc. Meeting,* Abstract #160, 2001.
134.   N. Koura and K. Ui, *J. Jpn. Inst. Light Met.,* **47,** 267, 1997.
135.   Y.S. Fung and R.Q. Zhou, *J. Power Sources,* **81-82,** 891, 1999, and references therein.
136.   K. Xu and C.A. Angell, *Electrochim. Acta,* **40,** 2401, 1995.
137.   K. Xu, N.D. Day and C.A. Angell, *J. Electrochem. Soc.,* **143,** L209, 1996.
138.   C.A. Angell, S.-S. Zhang and K. Xu, *U.S. Patent 5,855,809,* 1999.
139.   R.T. Carlin and J. Fuller, *Electrochem. Soc. Proc. Vol.,* **96-7,** 362, 1996.
140.   J. Fuller, R.A. Osteryoung and R.T. Carlin, *187ᵗʰ Electrochem. Soc. Meeting.* Abstract #15, 1995.
141.   M. Watanabe, K. Ida and M. Ue, *Jap. Pat. Appl., 10-168,028,* 1998.
142.   P. Koronais and R.A. Osteryoung, *J. Electrochem. Soc.,* **146,** 2995, 1999.
143.   P. Koronaios and R.A. Osteryoung, *Electrochem. Soc. Proc. Vol.,* **98-11,** 244, 1998.
144.   J.R. Stuff, S.W. Lander, Jr., J.W. Rovang and J.S. Wilkes, *J. Electrochem. Soc.,* **137,** 492, 1990.
145.   H. Nakagawa, S. Izuchi, S. Sano, K.-I. Takeuchi, K. Yamamoto and H. Arai, *Yuasa-Jiho,* **91,** 31,2001.
146.   N. Koura, K. Ui and K. Takeishi, *J. Jpn. Inst. Light Met.,* **47,** 273, 1997.
147.   K. Ui, N. Koura, Y. Idemoto and K. Itzuka, *Denki Kagaku.* **65,** 161, 1997.
148.   J.K. You, Z.G. Lin, Y.S. Fung and R.Q. Zhou, *Electrochem. Soc. Proc. Vol.,* **97-18,** 539, 1997.
149.   P. Novák, W. Scheifele, F. Joho and O. Haas, *J. Electrochem. Soc.,* **142,** 2544, 1995.
150.   J.-P. Pereira-Ramos, R. Messina, C. Piolet and J. Devynck, *J. Power Sources,* **20,** 221, 1987.
151.   M.E. Spahr, P. Novák, O. Haas and R. Nesper, *J. Power Sources,* **54,** 346, 1995.
152.   M. Lipsztajn and R.A. Osteryoung, *Inorg. Chem.,* **24,** 716, 1985.
153.   T.M. Laher and C.L. Hussey, *Inorg. Chem.,* **21,** 4079, 1982.
154.   C. Nanjundiah, K. Shimizu and R.A. Osteryoung, *J. Electrochem. Soc.,* **129,** 2474, 1982.
155.   S.E. Mancini and F.M. Donahue, *Electrochem. Soc. Proc. Vol.,* **90-17,** 389, 1990.
156.   S. Pye, J. Winnick and P.A. Kohl, *J. Electrochem. Soc.,* **144,** 1933, 1997.
157.   Y. Katayama, I. Konishiike, K. Shinozaki, T. Miura and T. Kishi, *Electrochem. Soc. Proc. Vol.,* **99-41,** 122, 1999.
158.   K.R. Hanz and T. Riechel, Inorg. Chem., **36,** 4024, 1997.
159.   N. Takami and N. Koura, *J. Electrochem. Soc.,* **136,** 730, 1989.
160.   F.M. Donahue, J.A. Levisky, F.G. Reynolds and J.S. Wilkes, *Electrochem. Soc. Proc. Vol.,* **86-1,** 332, 1986.
161.   R.W. Berg, N.J. Bjerrum, H.A. Hjuler, I.M. Petrushina and B. Vestergaard, *Danish Patent 170,626,* 1995.

162. P.G. Pickup and R.A. Osteryoung, *J. Electroanal. Chem.,* **195,** 271, 1985.
163. P.G. Pickup and R.A. Osteryoung, *J. Am. Chem. Soc.,* **106,** 2294, 1984.
164. L. Janiszewska and R.A. Osteryoung, *J. Electrochem. Soc.,* **134,** 2787, 1987.
165. L. Janiszewska and R.A. Osteryoung, *J. Electrochem. Soc.,* **135,** 116, 1988.
166. J.F. Oudard, R.D. Allendoerfer and R.A. Osteryoung, *Synth. Met.,* **22,** 407, 1988.
167. N. Koura and H. Ejiri, *Electrochem. Soc. Proc. Vol.,* **90-17,** 85, 1990.
168. N. Koura and H. Ejiri, *Denki Kagaku,* **58,** 923, 1990.
169. N. Koura, H. Ejiri and K. Takeishi, *Denki Kagaku,* **59,** 74, 1991.
170. J. Tang and R.A. Osteryoung, *Synth. Met.,* **44,** 307, 1991.
171. J. Tang and R.A. Osteryoung, *Synth. Met.,* **45,** 1, 1991 and references therein.
172. N. Koura, H. Ejiri and K. Takeishi, *J. Electrochem. Soc.,* **140,** 602, 1993.
173. K. Takeishi, N. Koura and S. Ito, *Denki Kagaku,* **63,** 629, 1995.
174. K. Takeishi and N. Koura, *Denki Kagaku,* **63,** 947, 1995.
175. K. Takeishi, N. Koura and S. Ito, *Electrochem. Soc. Proc. Vol.,* **93-9,** 541, 1993.
176. R.T. Carlin, J. Fuller and M. Hedenskoog, *J. Electrochem. Soc.,* **141,** L21, 1994.
177. R.T. Carlin, J. Fuller, W.K. Kuhn, M.J. Lysaght and P.C. Trulove, *J. Appl. Electrochem.,* **26,** 1147, 1996.
178. Y. Katayama, S.-I. Jige, T. Miura and T. Kishi, *Electrochem. Soc. Proc. Vol.,* **98-11,** 199, 1998.
179. J. Xie and T.L. Riechel, *J. Electrochem. Soc.,* **147,** 4247, 2000.
180. Y.S. Fung and R. Zhou, *Electrochemistry,* **67,** 713, 1999.

7

Lithium-Ion Secondary Batteries with Gelled Polymer Electrolytes

Yoshio Nishi

Sony Corporation
1-11-1 Osaki, Shinagawa-ku
141-0032 Tokyo
Japan

1.0   INTRODUCTION

Lithium ion secondary batteries (LIBs) with non-aqueous electrolytes were successfully developed and introduced into the market for the first time in 1991 by Sony Corporation.

They have outstanding properties in comparison with conventional secondary batteries with aqueous acidic or alkaline electrolytes including nickel / cadmium, nickel / metal hydride and lead-acid secondary cells. The features of LIBs are as follows.

1. High operating voltage (3.7 V on the average),
2. High gravimetric and volumetric energy densities,
3. No memory effect.
4. Low self-discharge rate (less than 10% per month),
5. Operation over a wide temperature range.

These features have given a huge boost to LIB*s* and the number of cells produced has increased from year to year. In Japan, as far as the production amount is concerned, LIB*s* surpass the other small-sized rechargeable batteries for consumer use. LIB*s* are now indispensable for mobile gears such as cellular phones, notebook personal computers, personal digital assistants (PDAs) and portable audio-visual equipment.

One of the most undesirable problems in batteries for domestic use has been the leakage of electrolyte solutions. The sources of this trouble are mainly abuses like the reverse connection between more than one cell, and caustic alkaline or strong acidic electrolyte solutions could cause chemical burns or worse. In the case of LIB*s*, they contain flammable constituents including organic electrolyte solutions and lithiated carbon, and the electrolyte leakage might lead to an accidental fire in the worst possible case.

The conversion of electrolytes in electrochemical cells from aqueous solutions to polymer, especially in lithium cells including LIB*s*, could realize the cells without electrolyte leakage, and thus polymer electrolytes have been investigated intensively by many researchers.

The ionic conductivity of polymer electrolytes, however, is by far lower than that of liquid phase electrolytes. Gelled polymer electrolytes (GPE*s*), which are composed of polymer matrices and solvents or plasticizers, have been developed in place of genuine polymer electrolytes to improve ionic conductivity. And in the end of 1990*s*, LIB*s* with GPE*s*, which will be called lithium polymer batteries (LPB*s*) hereafter for convenience´s sake, were put on the market.

2.0   GELLED POLYMER ELECTROLYTES

Various kinds of polymer materials have been investigated as matrices for GPE*s* including poly(methyl methacrylate) (PMMA), poly(vinylidene fluoride) (PVDF), poly(ethylene oxide) (PEO) and poly(acrylonitrile) (PAN).

GPE*s* can be classified into two categories according to their structures as follows: One is a homogeneous GPE in which a polymer matrix and solvent or plasticizer are uniformly mixed to form a single phasecomposite. The other is a GPE with phase separation in which a solvent is maintained in a porous polymer matrix.

Typical GPE*s* will be reviewed briefly below before touching upon Sony´s technologies on GPE*s* and LPB*s*.

2.1   PEO Based GPE

While PEO has been investigated as a matrix of a genuine polymer electrolyte, it is also promising as a matrix of a GPE. The addition of an organic solvent to PEO is able to improve ionic conductivity of the resulting GPE up to 10^{-3} $S \cdot cm^{-1}$.

PEO based GPE*s* are used in LPB*s* by several Japanese battery manufacturers including Sanyo Electric Co. Ltd., Yuasa Corporation, Hitachi Maxell Ltd. and Mitsubishi Chemical Corporation.

Figure 1 shows the LPB preparation procedure adopted by Sanyo [1]. A positive electrode coated with $LiCoO_2$, a negative electrode coated with graphite and polyethylene micro-porous separator are wound together to form an elliptical cell element. The element is inserted in a plastic bag followed by the injection of the mixture of an electrolyte solution and a precursor of PEO. The electrolyte solution consists of the solvent mixture of ethylene carbonate (EC) and diethyl carbonate (DEC), and $LiN(SO_2 C_2F_5)_2$ as a sustaining salt. Then the cell is heated to polymerize the PEO precursor.
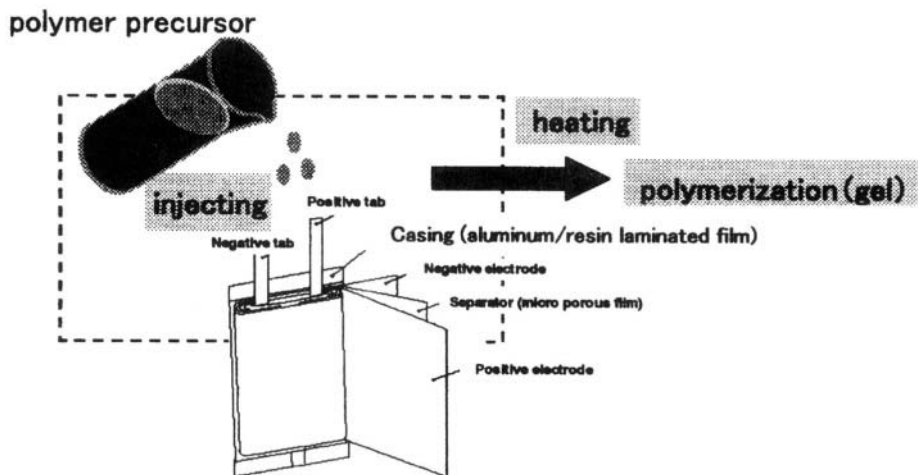
Figure 1. Polymerization process of Sanyo's LiPB

One of the crucial issues in this procedure would be the difficulty in completely polymerizing all of the PEO precursor because even a small amount of residual monomer might cause poor performance in cells. Thorough polymerization can be achieved by heating the precursor up to high temperature, and the higher the temperature, shorter the polymerization time. Heat-treatment at high temperature, however, is harmful to separator, a cell envelope made of plastic film and active electrode materials. Compromise between these factors might be industrially important.

Sanyo claims that the weight ratio of the PEO precursor to the electrolyte solution is very important to uniform impregnation of the mixture within the coated layer of the electrode active materials and too much precursor causes the increase of viscosity of the mixture and results in poor impregnation. The favorable weight ratio of the precursor to the electrolyte solution is between 1:12 and 1:8 according to Sanyo.

Typical drain capability data of Sanyo cell are shown in Figure 2. The cell dimension is 3.6 mm (thickness), 35.0 mm (width) and 62.0 mm (height) and the nominal capacity is 570 mAh.

2.2   *PAN Based GPE*

A PAN based GPE has been investigated by Akashi and coworkers [2]. They use the solvent mixture of EC/PC (propylene carbonate) as plasticizers and $LiPF_6$ as a sustaining salt, and the suitable combination ratio of PAN / solvent / salt

brings about good ionic conductivity as high as 3×10^{-3} S·cm^{-1}. The adoption of LiPF$_6$ as a sustaining salt also enables the resulting GPE to have flame retardant or self-extinguishing properties.
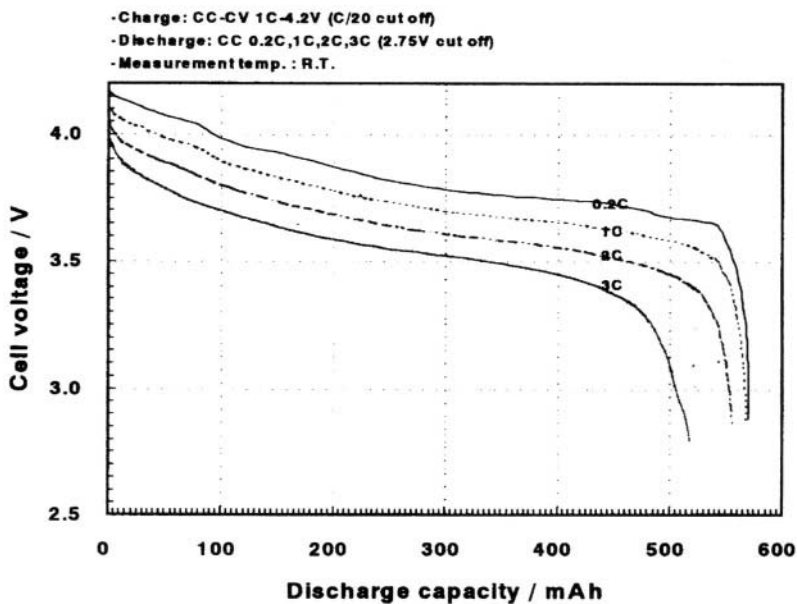
Figure 2. High-rate characteristics of Sanyo's LPB

2.3   PVDF/HFP Based GPE

Technologies on PVDF based GPE*s* have been disclosed by Bellcore [3,4]. A polymer matrix is a copolymer of vinylidene fluoride (VDF) and hexafluoropropylene (HFP) and the LiPF$_6$ solution in EC/DMC (dimethyl carbonate) (2:1) is added to the matrix to make up a GPE of the phase separation type. HFP plays an important role in the reduction of the crystallinity of the resulting copolymer, increasing its capacity to hold the electrolyte solution. It is claimed that ionic conductivity of their GPE is almost 10^{-3} S·cm^{-1}.

In Bellcore´s LPB, LiMn$_2$O$_4$ is used as an active material for a positive electrode and carbon for a negative electrode. Figure 3 shows the manufacturing scheme of their LPB*s*. Perforated copper and aluminum foil are used as current collectors for the negative and positive electrodes respectively. The film of the plasticized polymer (PVDF / HFP) matrix is sandwiched between two electrodes followed by fusion using a hot roll to form an electrode element. Then, the plasticizer in the film is removed by immersion of the element in an organic solvent and the element is enveloped in a bag of aluminum-laminated plastic film. The solvent is eliminated by heating the bag, preferably under reduced pressure. The electrolyte solution of a suitable Li salt is injected into the bag to make up a GPE.
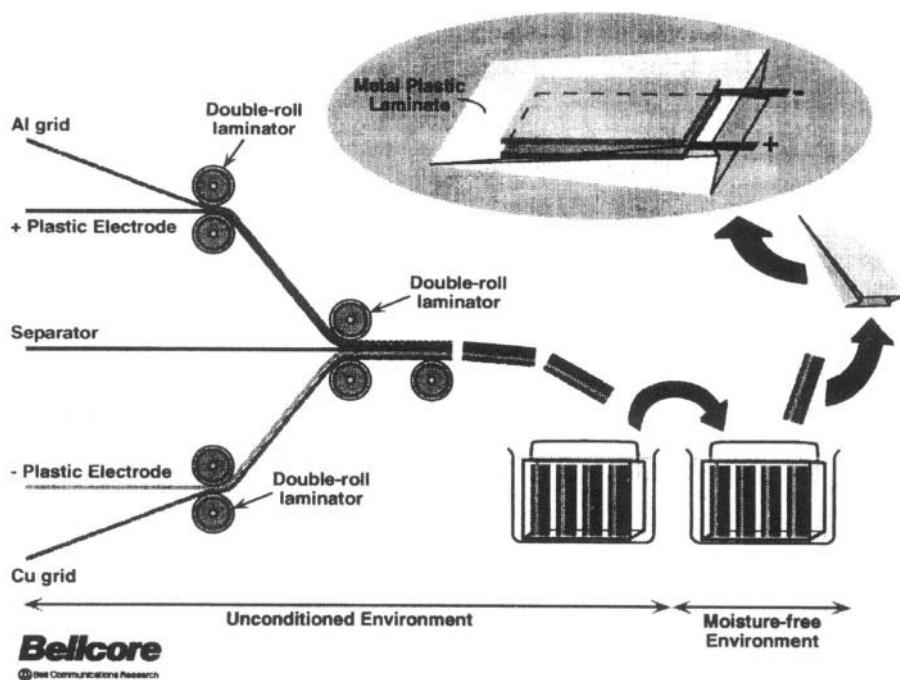
Figure 3. Schematic of dry lithium-ion battery processing (Courtesy of Bellcore).

From the mass production point of view, however, Bellcore's technology might be said to be rather complicated. The elimination process of the plasticizer is essential so far as cell performance concerned because the plasticizer residue is apt to cause poor cyclability in the resulting cells.

3.0   SONY'S LPB TECHNOLOGY

Sony started to develop LIBs with GPEs at the end of the 1980s even when LIBs had not make a name for themselves yet, because it was considered that LPBs were promising and technologies on polymer electrolytes would become indispensable before long.

3.1   *Development Concept*

Sony's concepts of development of LPBs have been as follows.

1. Vapor pressure of organic solvents in GPEs is as low as possible.
2. GPEs have good adhesiveness to active electrode materials.
3. All the solvents are confined within polymer matrices and no free organic solvents is present, which enables no electrolyte leakage.
4. GPEs have high ionic conductivity in the wide temperature range, especially in low temperatures.

5. Plastic film used as an envelope for the electrode element constitutes an insuperable barrier against solvent vapor permeation and moisture infiltration.
6. Manufacturing process is simple and favorable for mass production.

Sony examined several polymer matrices including PEO, PAN [2], and PVDF / HFP, and found that GPE*s* derived from block copolymer of VDF and HFP with selected molecular weight distribution [5,6] could yield high ionic conductivity, excellent adhesiveness to electrode active materials and sufficient mechanical strength.

3.2   PVDF/HFP Block Copolymer

When Sony prepared random copolymer of VDF and HFP which had molecular weight equivalent to that of PVDF having a melting point of 175 °C, properties of this copolymer were intermediate between the crystalline nature of PVDF and the pliant nature of PHFP and thus its melting point was around 130~140 °C, considerably lower than that of PVDF.

On the other hand, in the case of block copolymer with the same molecular weight as random copolymer mentioned above, properties of each monomer reflected independently on the resulting copolymer and, for example, PVDF portions in the copolymer hardly lost its crystalline nature and PHFP portions maintained their pliancy. A melting point of block copolymer is observed between those of PVDF and PHFP, about 150 °C, higher than that of random copolymer.

Holding capacity of electrolyte solutions by random copolymer increased as PHFP contents increased, because PHFP enhanced amorphous nature of the copolymer. An increase of PHFP ratio up to 80% (by weight) enabled the copolymer to hold enough electrolyte solution, which, however, resulted in severe decline of mechanical strength in GPE membrane.

The block copolymer kept high mechanical strength which was brought about by crystalline parts (PVDF), maintaining the high electrolyte-absorbing capacity even if the PHFP portion in the copolymer was not so large. It was demonstrated that 3~7.5% (in weight) of PHFP was adequate for the copolymer to have the sufficient electrolyte-absorbing capacity as well as mechanical strength. In addition to this, it was found that desirable weight-average molecular weight (Mw) of the copolymer was greater than 550,000 because smaller molecular weight caused poor adhesiveness.

A mixture of two types of copolymer, namely one with larger molecular weight (Mw>550,000) and the other with smaller molecular weight (550,000> Mw>300,000), could be used to reduce viscosity of resulting GPE*s*, which was beneficial to the process of applying them to electrodes. In this case, the favorable ratio of copolymer with larger molecular weight was greater than 30% (in weight) to realize good adhesiveness.

3.3   *Organic Electrolyte Solution*

It is well recognized that PC is spontaneously decomposes during lithium insertion into graphite anodes. Thus EC based electrolytes are generally used in the LIB system with graphite anodes. GPE*s,* in general, have lower ionic conductivity than the liquid electrolyte system due to their solid nature and adoption of EC as GPE plasticizer causes further deterioration of ionic conductivity because EC is solid at room temperature. It is desirable that PC based electrolyte solutions are used as plasticizer to enhance ionic conductivity of resulting GPE*s*. Thus preparation of graphite anodes that are compatible with PC is very beneficial to improve ionic conductivity of GPE*s*.

Surfaces of graphite particles were modified with amorphous carbonaceous materials, and this particular graphite could adapt itself for PC. Sony compounded PVDF / HFP, PC, EC and $LiPF_6$ into a GPE and found that the charge / discharge efficiency in the first cycle of the novel graphite anode in this GPE system reached greater than 90% in spite of utilization of PC.

An above-mentioned GPE was self-standing and could be handled as a solid matter as shown in Figure 4. The GPE of the first generation had ionic conductivity with a range of **3~4 mS·cm⁻¹** in the room temperature (Figure 5, the lower line) and it has been improved by the optimization of the salt concentration, PC/EC ratio, VDF/HFP ratio and Mw of polymer matrix. As a consequence of this improvement, ionic conductivity has reached to **9 mS·cm⁻¹** (Figure 5, the upper line).
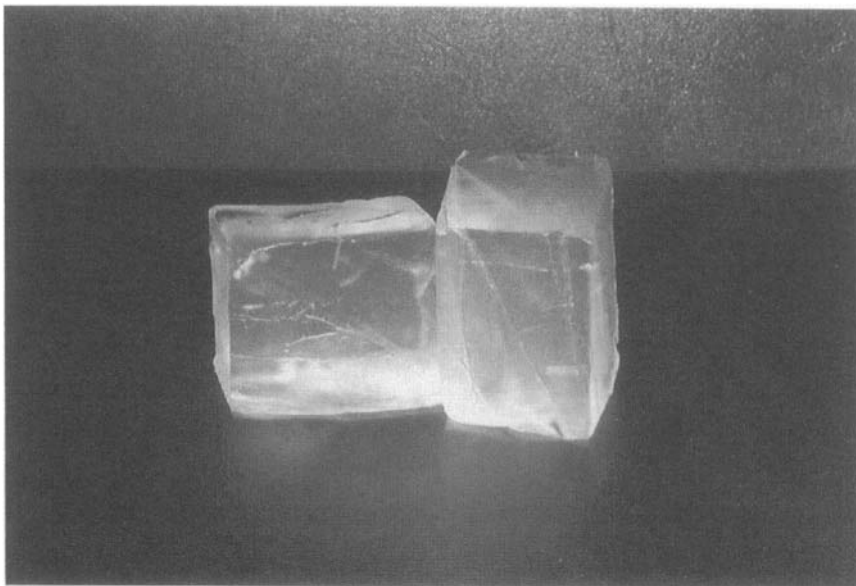
Figure 4. A block of Sony's GPE
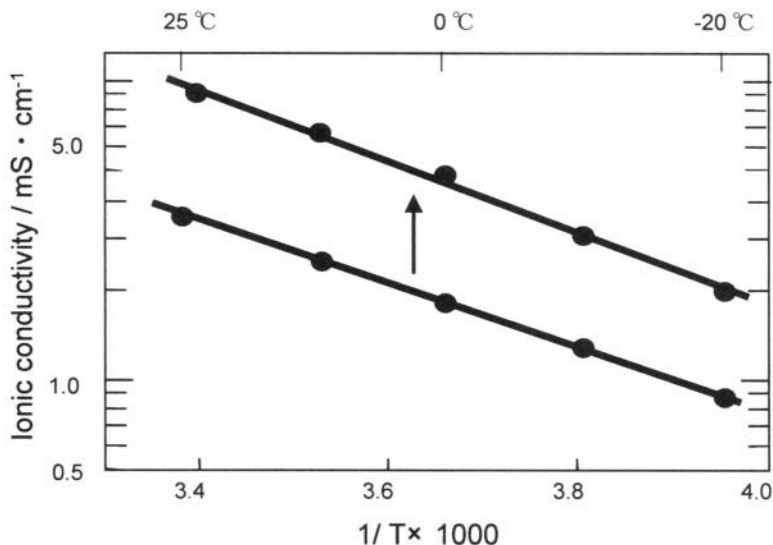
Figure 5. Ionic conductivity of Sony GPE

3.4   *Vapor Pressure of Solvent in GPE*

GPE*s* contain organic solvents as plasticizer and the reduction of vapor pressure is crucial. Amount of vaporized solvents from our GPE was measured to estimate the vapor pressure of solvents retained in GPE*s*.

Microporous polyethylene separator and the matrix polymer were soaked in the electrolyte solution and they were heated at various temperatures for 60 minutes. The vapor amounts from both samples were measured and compared. The result is shown in Figure 6 and it is clearly seen in this figure that vapor pressure of solvents in Sony GPE is significantly low even at high temperature like 100 °C, while microporous separator can hold the solution at low temperature probably due to large surface tension in the micropores but vaporization of solvents increase steeply as temperature rises.

3.5   *Summary of Sony GPE*

Summary of the Sony GPE is as follows:

1. Block copolymer of VDF and HFP with the selected blend ratio and optimum molecular weight is favorably adaptable to matrix polymer of GPE*s*.
2. The resulting GPE is self-standing and has sufficient mechanical strength.
3. PC is used as a constituent of plasticizer to enhance ionic conductivity, and in order to realize this, specially modified graphite which is compatible with PC is developed as an active material for a negative electrode.

4. The GPE has high ionic conductivity which is applicable to an electrolyte of electrochemical cells.
5. The vapor pressure of our GPE is kept very low even at high temperatures.
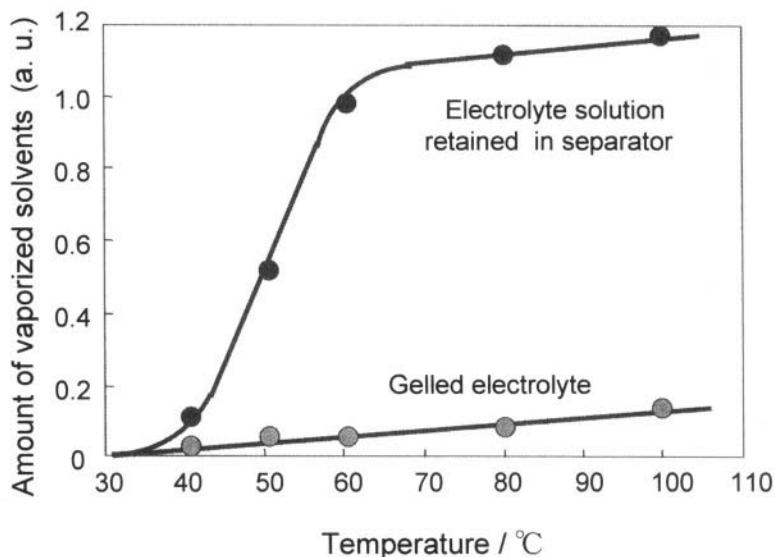
Figure 6. Extent of solvent vaporization.
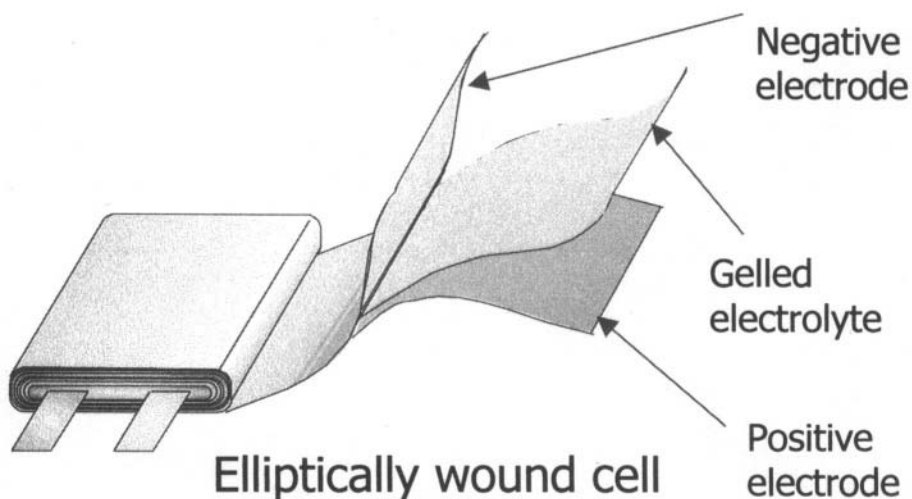
Figure 7. Structure of Lithium Polymer Battery element

3.6   *Outline of Lithium Polymer Battery*

The novel GPE mentioned above was adopted as an electrolyte for Sony´s LPB. A schematic drawing of the Sony LPB is illustrated in Figure 7. $LiCoO_2$ and a small amount of carbon were coated on aluminum foil to prepare a positive electrode. Graphite for a negative electrode material was designed elaborately to be compatible with PC and was coated on copper foil. In addition to GPE membrane, very thin separator, micro-porous polyethylene film with thickness around 10 μm, was used to prevent mechanical short circuits between positive and negative electrodes.

The positive electrode, GPE membrane, separator and the negative electrode were wound together to form an elliptical electrode element and the element was enveloped in a bag of plastic film. The envelope for the electrode element is required to prevent solvents permeation from the inside of a cell and also to stop moisture penetration from ambient into a cell. Aluminum-laminated film is generally utilized for this purpose.

It was found, however, that an envelope of aluminum-laminated polymer film could not sufficiently stop moisture infiltration. A significant amount of moisture penetrated through adhesive for a margin of the envelope rather than through the aluminum-laminated film (Figure 8). To make this adhesive layer moisture-tight, new adhesive and a special gluing process were developed. A gluing margin of 5 mm wide was necessary to suppress moisture infiltration at first, but introduction of the new adhesive and process enabled the width of this margin to be reduced to almost 2 mm (Figure 9). This is undoubtedly beneficial to improvement of energy density of LPB*s*.

3.7   *Cell Performance*

The generally accepted opinion on LPB*s* has been that rate capability, low temperature performance, and cyclability compare unfavorably with those of conventional LIB*s* due to poor ionic conductivity of GPE*s*. Most of these drawbacks have been overcome by the introduction of block copolymer of PVDF / HFP and PC based plasticizer described above. Principal performance data will be presented below.

Rate capability: A LPB cell 35 mm wide, 54 mm high and 3.8 mm thick was constructed as shown in Figure 10 and the nominal capacity was 760 mAh. Discharge curve profiles under several load conditions are illustrated in Figure 11 and it can be seen from this figure that voltage drop is not so large even at high discharge currents like the 3 C mA rate and a cell is able to be discharged with sufficient capacity above the voltage range of 3.0 V. Discharge capacity retention (capacity at 0.2 C = 100%) is plotted against discharges rate in Figure 12. Even at the 3 C mAh discharge rate, capacity retention is almost 90% at the cut-off voltage of 3.0 V and is no less inferior to that of LIB*s*.
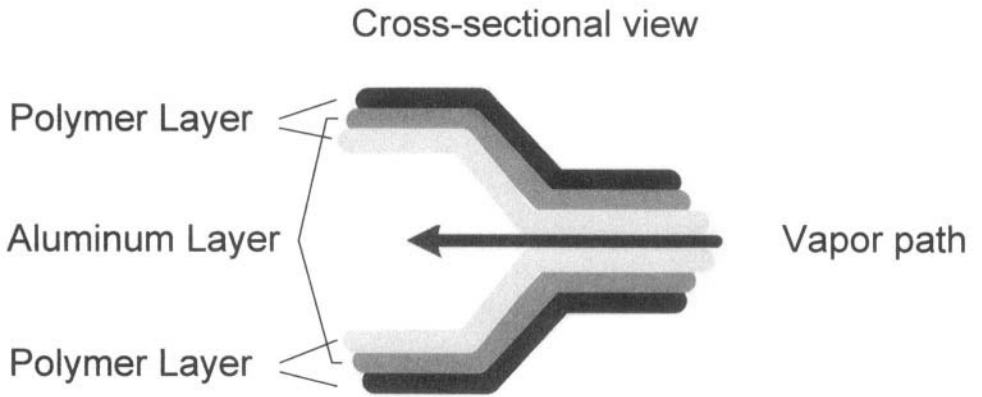
Figure 8. Schematic drawing of LPB envelope and path of ambient moisture infiltration
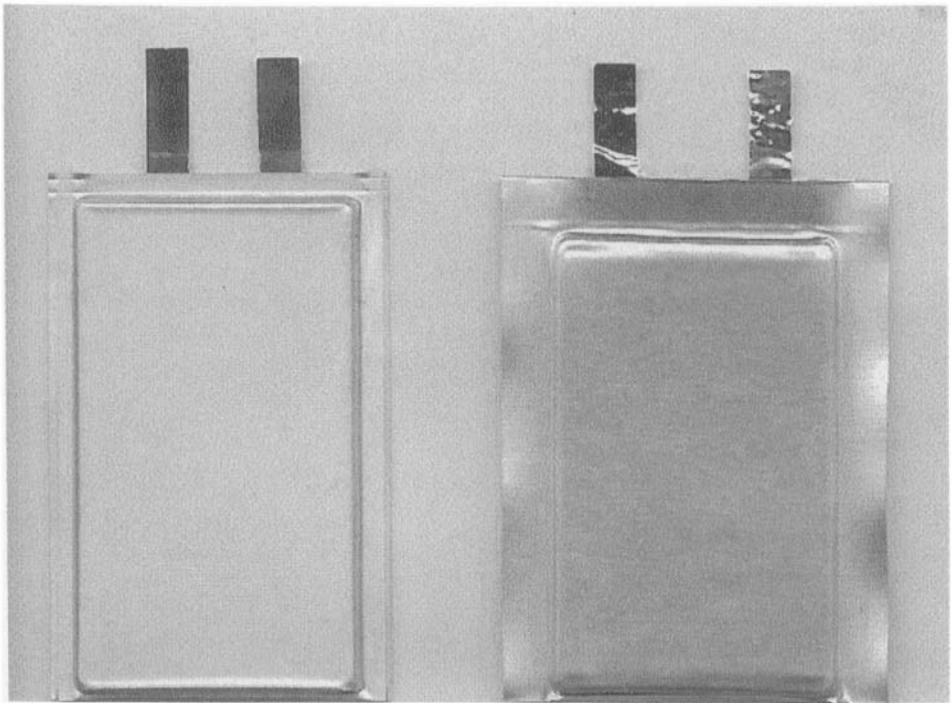
Figure 9. Reduction of margin width for gluing

Figure 10. Commercial Lithium-Ion Polymer Battery
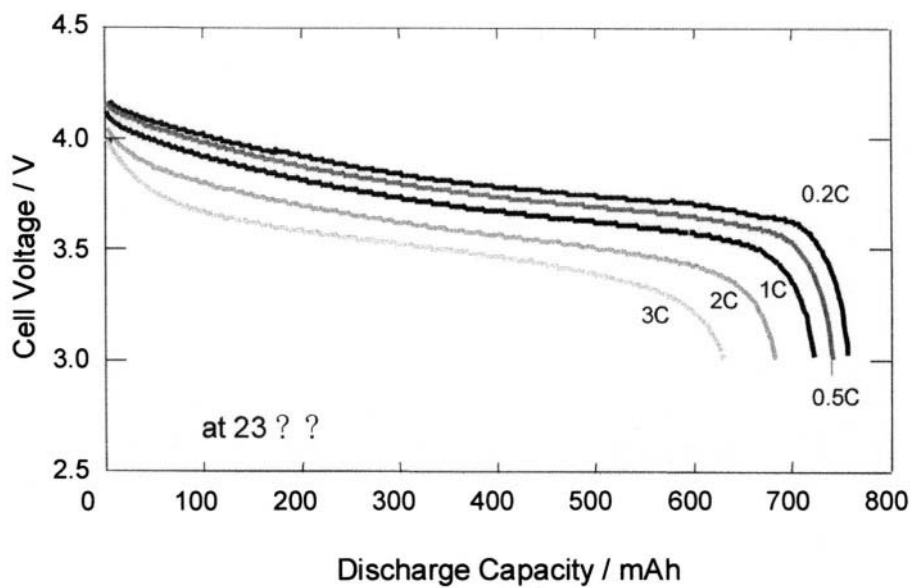
Figure 11. Discharge performance at various rates
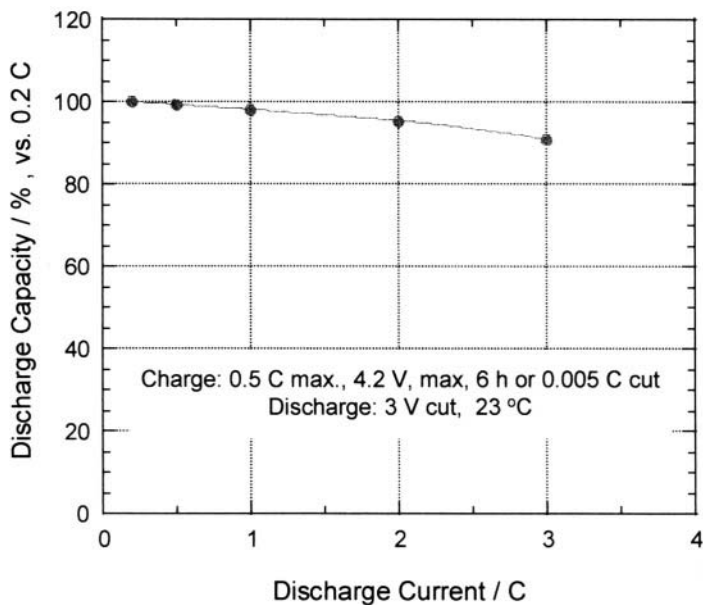
Figure 12. Rate capability
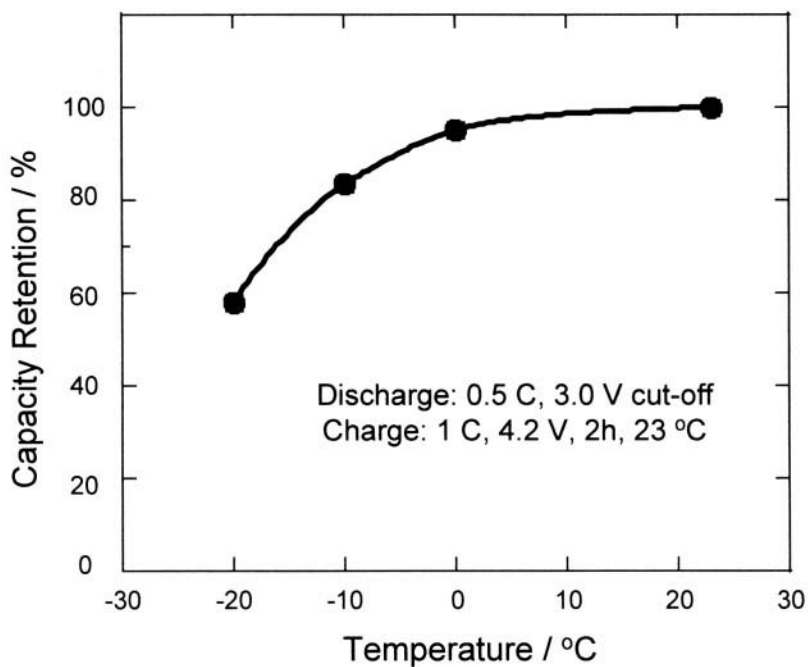
Figure 13. Temperature dependence of capacity retention

Low temperature characteristics: Dependence of discharge capacity on the ambient temperature is shown in Figure 13. Charge and discharge conditions are given in the figure. The capacity retention of 60% is achieved at –20 °C at the moderate discharge rate of 0.5 C.

So-called GSM pulse discharge mode in cellular phones requires excellent drain capability to batteries even at low temperatures. The GSM pulse discharge mode (2 A for 6 ms / 0.15 A for 4 ms) was applied to cells at various temperatures and capacity retention was determined. The result is given in Figure 14 and the cell performance is satisfactory again. The capacity retention is over 40% at –20 °C.

Cycle performances: Cells were charged with the constant current-constant voltage method (1 C mA and 4.2 V) and then they were discharged at constant current of 1 C mA to the cut-off voltage of 3.0 V. The capacity retention during this cycling course in the room temperature is shown in Figure 15. The performance is excellent and the capacity retention at 1,000th cycle is about 85%.

Charge characteristics: Changes of cell voltage, charge current and cell capacity are illustrated in Figure 16 under the constant current (0.5 C) / constant voltage (4.2 V) charging method. The behavior during the time course of charge is exactly similar to that of conventional LIBs.
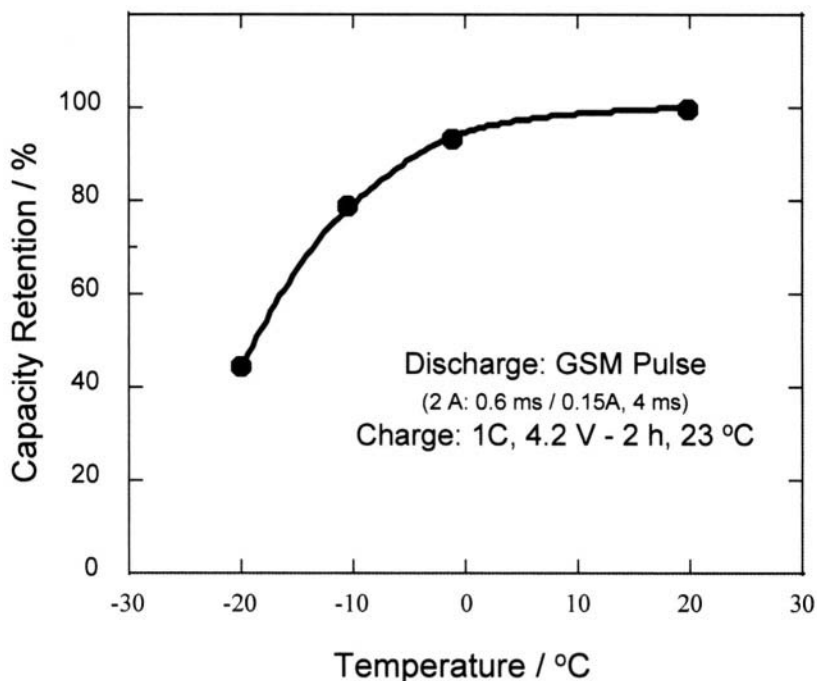
Figure 14. Temperature dependence of capacity retention at GSM pulse discharge.
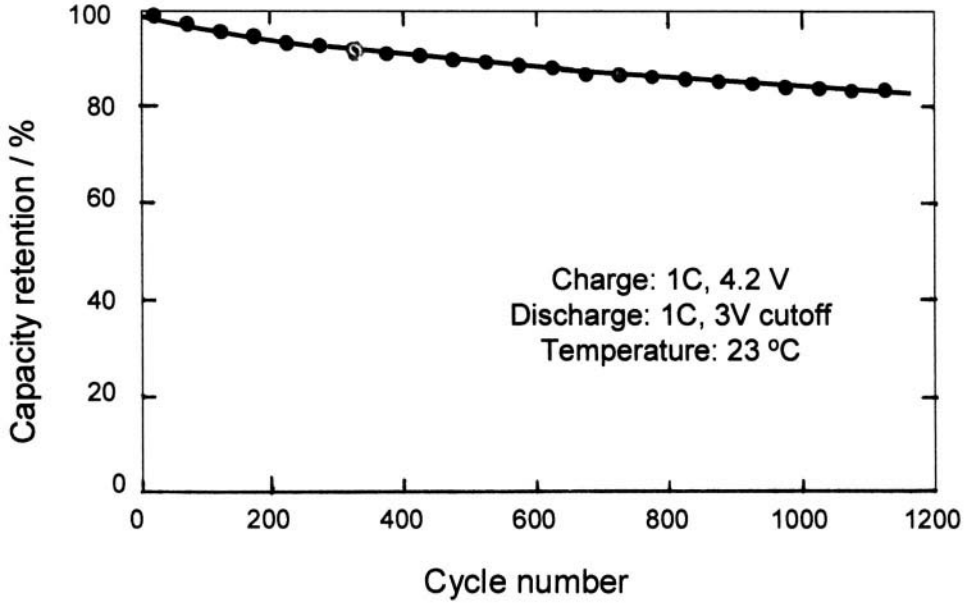
Figure 15. Cycle characteristics
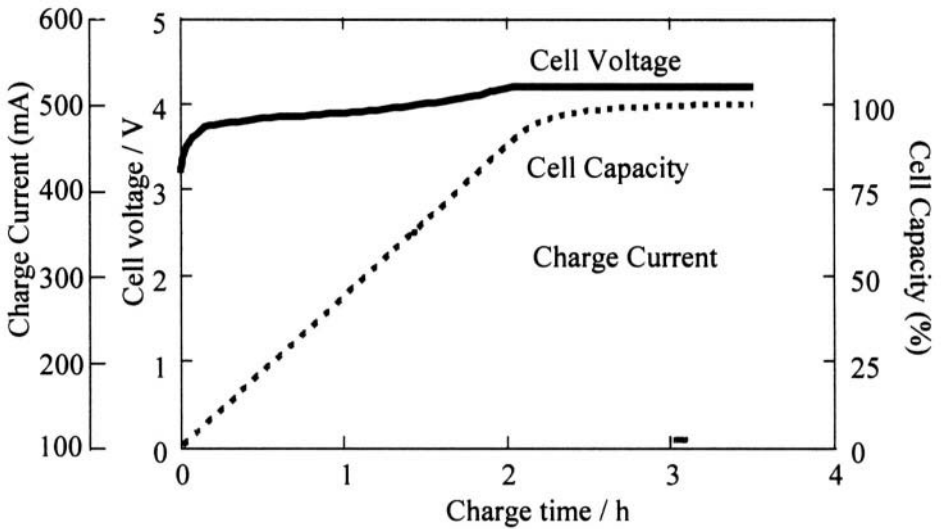
Figure 16. Charge characteristics

4.0   CONCLUSIONS

GPB*s* with the comparable properties to conventional LIB*s* were developed in which block copolymer between VDF and HFP was used. The ratio of PHFP to PVDF in the copolymer was 3~7.5% and Mw is greater than 550,000.

The PC based electrolyte solution was mixed in the copolymer matrix to enhance ionic conductivity of resulting GPE*s* and modified carbon which was compatible with PC was developed to enable this GPE to be applied to LPB*s*. Developed GPE*s* had ionic conductivity as high as **9 mS·cm^{-1}**.

Table 1. Specifications for Sony Lithium Polymer Battery

Size (D x W x H)	3.8 x 35 x 62 mm
Weight	15 g
Nominal Capacity	760 mAh
Nominal Voltage	3.7 V
Charge Voltage	4.2 V
Charge Time	150 min.
Energy Density (Volumetric)	375 Wh·dm^{-3}
Energy Density (Gravimetric)	190 Wh·kg^{-1}
Cycle Performance	85% at 1000th cycle
Temperature Range	-20 °C ~ 60 °C
Cathode	LiCoO$_2$
Anode	Graphite

Principal properties of prepared LPB*s* are summarized in Table 1 and it can be justly said that they can easily stand comparison with conventional LIB*s*. Gravimetric energy density deserves special mention. It is much higher than LIB*s* because an aluminum-laminated film bag is used in place of a metal can as a housing material.

These LPB*s* are attractive as power sources for mobile gear including cellular phones, PDA*s*, notebook personal computers and portable audio-visual equipment.

5.0   REFERENCES

1. S. Narukawa, I. Nakane and H. Watanabe, presented at The Committee of Battery Technology, The Electrochemical Society of Japan (29th Sep., 2000)
2. H. Akashi, K. Tanaka and K. Sekai, 5th International Symposium on Polymer Electrolytes, poster P-10. Sweden: Uppsala (Aug. 1996)
3. F.K. Shokoohi, J.M. Tarascon, A.S. Gozdz, P.C. Warren and G.G. Amatucci, presented at The 13th International Seminar on Primary and Secondary Battery Technologies and Applications, Boca Raton, Florida, USA (March 1996)

4. J.M. Tarascon, A.S. Gozdz, C. Schmutz, F.K. Shokoohi and P.C. Warren, *Solid State Ionics.* **86-88,** 49, 1996.
5. T. Hatazawa, T. Kondo and Y. Iijima, Japanese Patent Kokai 11-312536 (in Japanese), 1999.
6. T. Hatazawa, K. Kezuka and Y. Iijima, Japanese Patent Kokai 11-312535 (in Japanese), 1999.

ABBREVATIONS

DEC	diethyl carbonate
DMC	dimethyl carbonate
EC	ethylene carbonate
GPE	gelled polymer electrolyte
HFP	hexafluoropropylene
LIB	lithium ion secondary battery
LPB	lithium ion secondary polymer battery
Mw	weight-average molecular weight
PAN	poly(acrylonitrile)
PC	propylene carbonate
PDA	personal digital assistant
PEO	poly(ethylene oxide)
PHFP	poly(hexafluoropropylene)
PMMA	poly(methamethylacrylate)
PVDF	poly(vinylidenefluoride)
VDF	vinylidene fluoride

8

Lithium Polymer Electrolytes

Bruno Scrosati
Department of Chemistry
University of Rome "La Sapienza "
00185 Rome
Italy

1.0   INTRODUCTION

The present development trend in lithium ion batteries is focused on the replacement of the common liquid electrolyte with a lithium ion conducting polymer electrolyte membrane to finally achieve the fabrication of batteries having a full plastic structure. Such plastic lithium ion batteries are expected to be less expensive and more easily scaled up than their liquid counterparts. In addition, the absence of free liquid allows packaging in light-weight plastic containers unlike conventional batteries which require metallic casing. Finally, since the electrolyte membrane and the associated plasticized electrodes can be formed as laminates, the plastic battery can be fabricated in any desired shape or size, a target difficult to be achieved with liquid electrolyte cells [1,2]. All these features make the plastic lithium battery a very appealing product and indeed, the concept is presently pursued by many battery manufacturing companies. A relevant example of these industrial efforts is reported and described in Chapter 9 by Brodd.

The key component of the plastic battery is the polymer electrolyte membrane that has to fulfill a series of stringent requirements, including among others: i) good mechanical properties (to assure easy battery fabrication), ii) high ionic conductivity (to assure low internal resistance), iii) high lithium ion transport (to avoid concentration polarization), iv) wide electrochemical stability (to be compatible with high voltage electrodes), v) low cost (in order to fill a large market) and vi) benign chemical composition (to be environmentally compatible).

The identification of membranes capable of combining all the above stressed features is not an easy task. And indeed, intensive research and development work has been devoted in recent years to achieve this goal.

Historically, the first type of ionically conducting membranes to be considered for battery applications were those formed by blending high molecular weight poly(ethylene oxide) PEO with a lithium salt, LiX where X is preferably a large soft anion. These solvent-free membranes

have been widely described in the literature, e.g. [3]. Their structure may be broadly described as a sequence of polymer chains coiled around lithium ions while the anions are more loosely coordinated. Because of their particular structural position, the Li^+ ions can be released to transport the current only during unfolding of the coordinating PEO chains. Thus, fast Li^+ ions transport and high conductivity are available only when the PEO component is in an amorphous state, which occurs, on average, at temperatures above 70 °C.

Obviously this constraint limits the applicability of the PEO-based electrolytes and alternative structures have to be considered for obtaining high ionic mobility in a wider temperature range. The most promising results have been obtained by the characterization of electrolytes formed a polymer matrix swollen by a lithium ion conducting liquid solution. Two types of these membranes have been developed to the point of practical application in lithium ion plastic batteries. One is the porous membrane originally developed at the Bellcore (now Telecordia Technologies) Laboratories in the United States [4,5]. This membrane is based on a copolymer of vinylidene difluoride with hexafluoropropylene, PVdF-HFP, which is first preconditioned by the addition of an extractable plasticizer and a finely dispersed ceramic filler [6]. This so-formed highly porous membrane is then swollen by a typical lithium ion solution, e.g. a solution of lithium hexafluorophosphate, $LiPF_6$ in a ethylene carbonate-dimethyl carbonate, EC-DMC solvent mixture. The fabrication procedure has been further modified by substituting the extraction step by a phase-inversion process [7].

The Bellcore membrane is a well known product currently used in various academic and industrial projects aimed to the production of lithium ion plastic batteries. Therefore, this chapter will be mainly focused on the second type of polymer electrolytes, namely on those electrolytes prepared by a direct trapping of liquid solutions in a polymer matrix. Particularly interesting in this category are the electrolyte membranes obtained by the gelification of organic liquid solutions (e.g. the cited $LiPF_6$ in EC-DMC solution) in polymer (e.g., poly(acrylonitrile), PAN or poly(methylmetacrylate) PMMA or poly(vinylidene fluoride) FVdF) network. The following part of this chapter is addressed to the description of these commonly called " gel-type membranes", with particular concern to their latest developments.

2.0   GEL-TYPE MEMBRANES

Historically, gel membranes were first reported by Feullade and Perche [8]. However, the relevance of these membranes in the battery field has been fully recognized only recently [1]. Generally, the laboratory synthesis of gel-type membranes involves the dissolution of the lithium salt and of the selected polymer host in an appropriate liquid solvent or liquid solvent mixture. The resulting solutions are homogenized, heated to 90-100 °C and finally cooled to room temperature between glass plates to

promote cross linking of the membrane in the desired shape and thickness [9]. This simple laboratory method, which can be easily scaled up to the industrial level by the use of suitable lamination machines, produces mechanically stable, self-sustaining membranes. A typical, laboratory prepared example is shown in Figure 1.
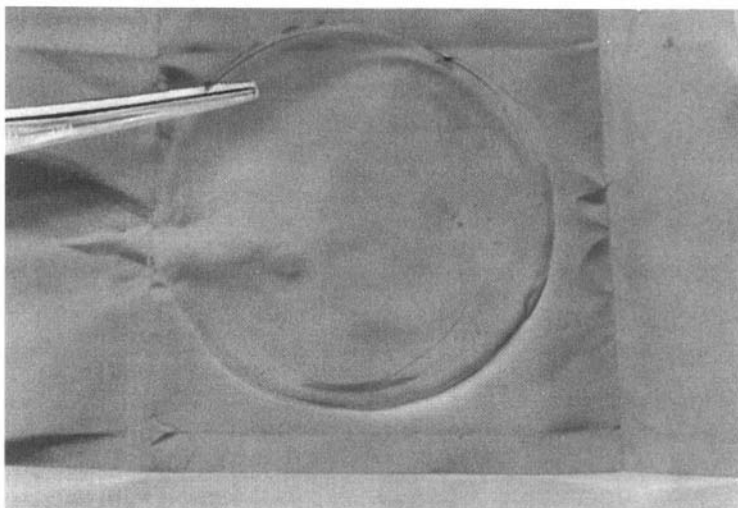
Figure 1. Typical appearance of a laboratory prepared, gel-type, lithium conducting, membrane.

For simplicity' s sake all the membranes are hereafter addressed by writing in sequence the selected lithium salt, the liquid solvent (or solvent mixture) and the hosting polymer. For instance, the notation **LiPF$_6$-EC-DMC-PAN** refers to a membrane formed by a solution of lithium hexafluorophosphate in a ethylene carbonate-dimethyl carbonate solvent mixture immobilized in a poly(acrylonitrile) matrix.

2.1   *Ionic Conductivity*

The value of the ionic conductivity of the membranes can be measured effectively by impedance spectroscopy on cells formed by sandwiching the given membrane sample between two lithium-ion-blocking (e.g., stainless-steel, SS) electrodes. A typical result, referring to the **LiPF$_6$/EC/DMC/PAN** membrane is shown in Figure 2.

The impedance response is basically a capacitive line whose intercept with the real Z' axis gives the value of the membrane's resistance. The value of the conductivity is then obtained by knowing the cell constant.

Two important conclusions can be drawn from this impedance behavior. First, the full linearity in the high frequency region is convincing evidence of the integrity of the membrane. In fact, should phase separation and/or crystallization had be present, these would have been

evidenced by the appearance of semicircles or, more generally, by deviation from linearity in the high frequency region of the impedance spectra. The second key feature of the impedance study of Figure 2 is the low ohmic value of the intercept that leads to a room temperature ionic conductivity of **0.6x10^{-2} S·cm^{-1}** for the **LiPF$_6$/EC/DMC/PAN** membrane. The conductivity remains high for a wide temperature range, extending from room temperature to 70-80 °C, as shown by Figure 3.
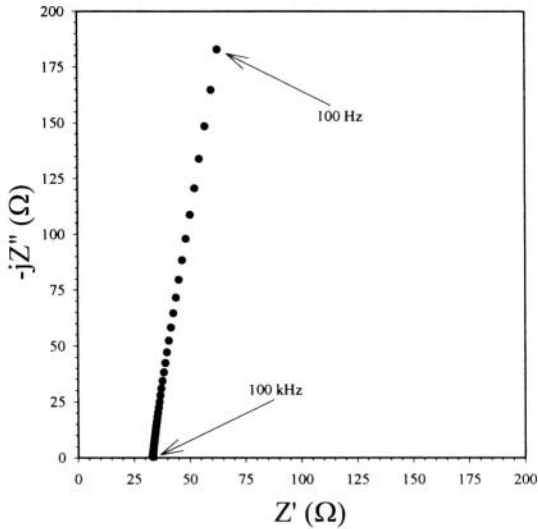
Figure 2. Impedance spectrum of a SS / LiPF$_6$ -EC-DMC-PAN/ SS (SS=stainless steel) cell at room temperature. Frequency range : 100 kHz-1Hz. Derived from reference 9 and reproduced with permission from Elsevier Science.
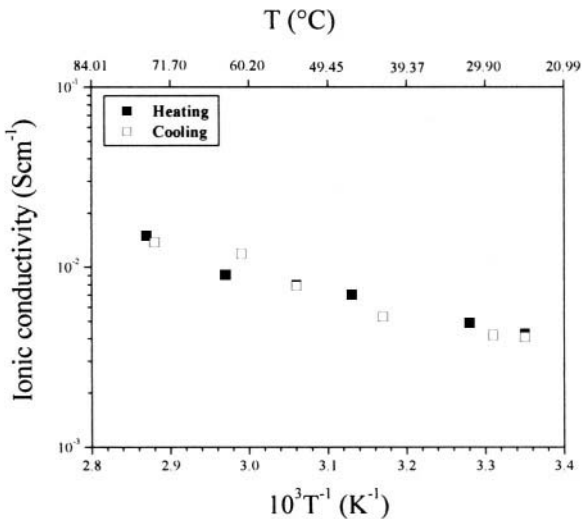
Figure 3. Conductivity Arrhenius plot for the LiPF$_6$/EC/DMC/PAN gel-electrolyte membrane. Data obtained from impedance spectroscopy. Derived from reference 9 and reproduced with permission from Elsevier Science.

Similar values of conductivity have been found for other types of membranes, either varying from the type of the liquid solution [10,11] or for the type of polymer matrix [12,13], see Table 1. This Table demonstrates the availability of a large selection of gel membranes, which although mechanically stable (see Figure 1), have in general a conductivity approaching that of their liquid counterpart.

The mechanism of ionic transport in these high-conducting gel electrolytes has been investigated by dynamic light scattering using $LiClO_4/EC/PC/PMMA$ as a sample membrane [14,15]. The results have provided strong evidence of three relaxation processes, i.e. i) and ii) a fast and a slow diffusive motion of the low molar mass solvent components and iii) a segmental motion of the polymer matrix. The temperature dependence for the diffusion process followed an Arrhenius behavior while the segmental motion was well described by a Vogel-Tamman-Fulcher (VFT) trend. By comparing the temperature dependencies of the relaxation times with that of the impedance data, a close relation between the conductivity and the fast diffusion process was found, this showing that the ionic transport is related to the diffusive motion of the solvent within the gel. This motion is strongly decoupled from the segmental motion of the polymer backbone, this finally demonstrating that the ionic transport in the gel membranes occurs mainly within the liquid solvent. The mechanism of conductivity in the gel electrolytes is thus completely different from the mechanism that controls the ionic transport in the solvent-free, PEO-based polymer electrolytes.

All these results suggest that in the strictest definition, gel membranes cannot be classified as "true" polymer electrolytes, but rather as hybrid systems where excess of liquid phases are contained within a polymer matrix [16]. In this respect, the key questions are: i) whether this definition totally applies for the entire category and ii) whether all these electrolytes are effectively two-phase systems where the polymer is a passive component acting as a rigid framework for regions of liquid solutions, or whether they are integrated systems, where the polymer provides the stability of the gel network down to areas near the Li^+ ions [17]. Investigation by NMR [18,19] and Raman [20,21] spectroscopy has shown that some interactions do occur between the polymer backbone and the electrolyte solution. The extent of the interaction depends upon the characteristic of the gel membrane's components. For example, for electrolytes based on the PAN matrix, coordination between the polymer backbone and both the solvent molecules and the solvated ions have been evidenced, while this interaction is weaker for electrolytes with the PMMA matrix. Therefore, the latter can be primarily regarded as simple hybrid systems while the former are systems characterized by interactions at the microscopic level between the polymer and the solution.

Table 1. Electrochemical properties at 25 °C of some selected examples of gel-type polymer electrolytes (average thickness: 100 μm). Reproduced from reference 28 with permission from Elsevier Science.

Electrolyte Membrane	Molar Composition	Conductivity [S·cm⁻¹]	Anodic Break-down Voltage vs. Li⁺/Li⁰ [V]
LiClO₄-EC-PC-PAN	8.0 -38.0 - 33.0 - 21.0*	1.1×10^{-3}	5.0
LiClO₄-EC-PC-PAN	4.5 - 56.5 - 23.0 - 16.0*	1.1×10^{-3}	4.9
LiClO₄-EC-DMC -PAN	4.5 -56.5 - 23.0 - 16.0*	3.9×10^{-3}	5.1
LiClO₄-EC-DEC-PAN	4.5 - 53.5 - 19.0 - 23.0*	4.0×10^{-3}	4.8
LiClO₄-γBL-PAN	4.5 - 79.5 - 16.0*	2.8×10^{-3}	5.0
LiAsF₆-EC-PC-PAN	4.5 - 56.5 - 23.0 - 16.0*	0.9×10^{-3}	4.3
LiAsF₆-γBL-PAN	4.5 - 79.5 - 16.0*	4.1×10^{-3}	4.6
LiPF₆-γBL-PAN	4.5 - 79.5 - 16.0*	4.4×10^{-3}	5.1
LiPF₆-EC-γBL-PAN	4.5 - 56.5 - 23.0 - 16.0*	5.5×10^{-3}	4.6
LiPF₆-EC-DMC-PAN	4.0 - 20.0 - 62.0 - 14.0*	4.2×10^{-3}	4.4
LiN(SO₂CF₃)₂-EC-PC-PAN	4.5 - 56.5 - 23.0 - 16.0*	1.0×10^{-3}	4.6
LiN(SO₂CF₃)₂-EC-□BL-PAN	4.5 - 56.5 - 23.0 - 16.0*	2.6×10^{-3}	4.7
LiClO₄-EC-PC-PMMA	4.5 - 46.5 - 19.0 - 30.0*	0.7×10^{-3}	4.6
LiAsF₆-EC-PC-PMMA	4.5 - 46.5 - 19.0 - 30.0*	0.8×10^{-3}	4.8
LiN(SO₂CF₃)₂-EC-PC-PMMA	4.5 - 46.5 - 19.0 - 30.0*	0.7×10^{-3}	4.9
LiN(SO₂CF₃)₂-EC-DMC-PMMA	5.0 - 50.0 - 20.0 - 25.0*	1.1×10^{-3}	4.8
LiC(CF₃SO₂)₃-EC-DBF-PVdF	3.5 - 36.5 - 30.0 - 30.0*	0.017×10^{-3}	————
LiC(CF₃SO₂)₃-EC-DBF-PVdF(C₃F₆)	3.5 - 36.5 - 30.0 - 30.0*	0.035×10^{-3}	4.8
LiC(CF₃SO₂)₃-EC-PC-PVdF(CTFE)	1.2 - 42.0 - 16.8 - 40.0*	0.1×10^{-3}	4.6

(* = this value is referred to monomer)

These structural differences may be important selection criteria in view of battery applications. In general, PAN-based membranes, having characteristics somewhat approaching those of a "true" polymer electrolyte entity, are be expected to be more stable than PMMA-based membranes or, generally, than membranes having characteristics of purely hybrid systems.

In general, the main feature of these gel-type membranes is their unique configuration which, due to the polymer entangling component, gives them an overall plastic self-standing appearance (see Figure 1) combined, thanks to the loosely-bound liquid component, with a high ionic conductivity (see Figure 3). The drawback is that the liquid component may eventually leak out from the membrane, this being detrimental in term of conductivity and probably to battery reliability and safety. This may obviously be a serious issue and thus, various approaches are considered to improve the membrane integrity under various operating conditions. One of these approaches involves the dispersion of selected ceramic powders in the polymer mass in order to form new types of composite membranes [22]. Figure 4 shows the impedance responses of one example of these composite membranes formed by dispersing 6 weight percent (w/o) of nano-particle size Al_2O_3 in the **LiPF₆/EC/DMC/PAN** system. The measurements were taken at different temperatures and at various storage times for each testing temperature.
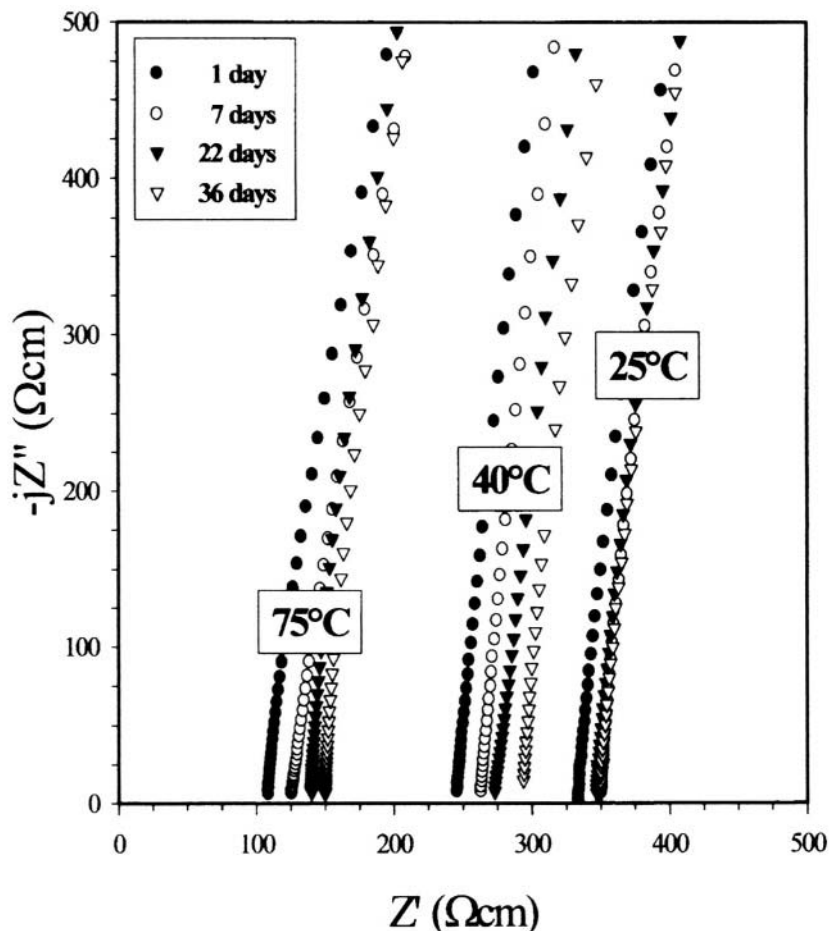
Figure 4. Impedance response at various temperatures of the LiPF$_6$/EC/DMC/PAN + 6 w/o Al$_2$O$_3$ composite gel electrolyte membrane. Measurements carried out at various progressive storage times of stainless steel, blocking electrode cells. Frequency range: 100 kHz-1Hz. The spectra are normalized for thickness and active area of the cells. Derived from reference 22 and reproduced with permission from Elsevier Science.

The value of the conductivity, derived from the intercept on the real Z' axis, is quite high, i.e. of the order of 3×10^{-3} S·cm^{-1} at room temperature. In addition, the intercepts exhibit only minor shifts even after long storage times and show no evidence of deviation from linearity. These features concur to demonstrate that the addition of the ceramic filler considerably contributes to enhancing the stability of the PAN-based electrolyte membrane without affecting its conductivity. The test was extended to temperature higher than ambient (i.e. 40 °C and 75 °C, see Figure 4) in order to approach critical conditions where liquid release is more easily expected to occur. Again, no shifts or semicircles are detected in the high frequency intercepts, thus demonstrating that the ceramic-induced stabilizing effect is maintained above

ambient and, especially at temperatures as high as 75 °C. Figure 5 compares the time evolution at this temperature of the conductivity of the composite membrane with that of a analogous, ceramic-free membrane. The superior behavior of the former is demonstrated by the fact that its conductivity does not appreciably change upon long storage times while in the same testing period that of the ceramic-free membrane decays by about two orders of magnitude.
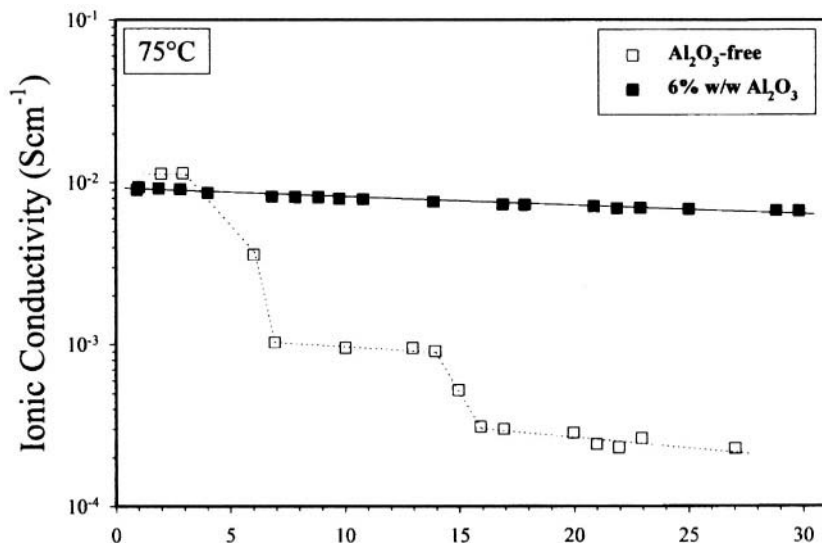
Figure 5. Time evolution at 75 °C of the conductivity of a LiPF$_6$/EC/DMC/PAN + 6 w/o Al$_2$O$_3$ composite gel electrolyte membrane and of an analogous, ceramic-free membrane. Data obtained by impedance spectroscopy.

Obviously, is the dispersed ceramic filler which makes the difference, although is effective action in preventing liquid leakage is not yet totally clear. It has been shown that ceramic filler, when properly selected in terms of their nature and particle size, may greatly influence the characteristics and the properties of polymer electrolytes of different types [23-26]. In the case of the gel membranes here discussed, it may be assumed that the improvement in integrity may be associated to: i) an enhancement in mechanical properties due to the ability of the polymer chains in entangling with the ceramic particles and ii) to the liquid-phylic tendency of the ceramic particles which may help in holding the liquid component within the membrane structure [27].

2.2   *Electrochemical Properties*

As shown above, the conductivity of the gel membranes is in average sufficiently high to in principle assure battery operation in terms of controlled IR drops. However, full evaluation of the membrane's practical value, requires also the establishment of other electrochemical properties, such as the stability window and the compatibility with the electrode materials.
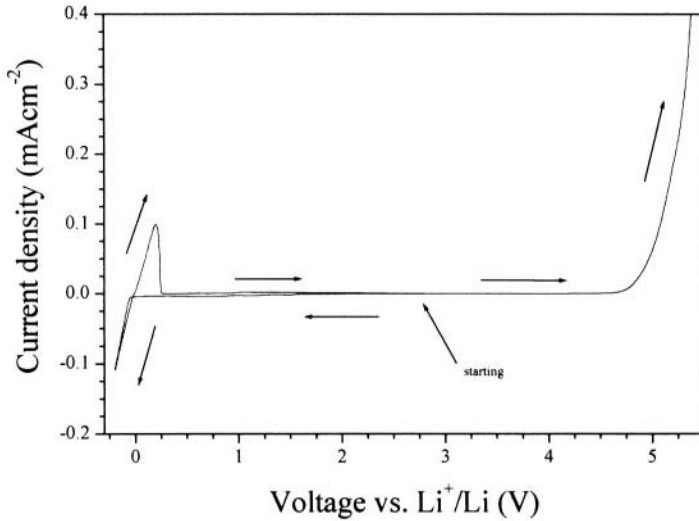
Figure 6. Current-voltage curve of a Ni blocking electrode in a $LiPF_6$/EC/PC/PAN electrolyte cell. Room temperature. Scan rate: $0.1 mV \cdot s^{-1}$. Counter electrode: Li metal.

In general, the electrochemical stability of an electrolyte is established by determining its breakdown voltage. This test can be carried out by performing sweep voltammetry on cells using the given membrane as the electrolyte, a "blocking" (i.e. not reversible to the membrane's mobile ion) working electrode and a third reference electrode. Under these conditions, the voltage at which the current starts to flow-through the cell may be assumed as the decomposition of the electrolyte. In the case of the gel-type membranes here under discussion, the test may be run by using a Ni blocking electrode and a Li reference electrode. Results obtained for the **$LiPF_6$-EC-PC-PAN** electrolyte are shown in Figure 6. The current onset is detected around 4.3 V vs. Li and similar values are obtained for the generality of the gel-type membranes, see Table 1 [28]. These values are high enough to allow the safe use of the membranes as electrolyte separators for the most common lithium-ion electrode couples.

As pointed out above, it is also desirable to extend the electrochemical characterization of the gel electrolyte membranes also requires the establishment of their compatibility with electrode materials. This may be achieved by determining the charactereristics of the lithium intercalation-deintercalation processes of these materials in cells based on the given membrane as the electrolyte and lithium metal as the counter electrode.

As an example, Figure 7 shows the result obtained in the case of a typical lithium ion cathode, i.e. a chromium-stabilized lithium manganese spinel [29], cycled in a **$LiClO_4$/EC/DMC/PAN** electrolyte cell [30], to promote and evaluate the process:

$$LiCr_yMn_{2-y}O_4 \Leftrightarrow Li_{1-x}Cr_yMn_{2-y}O_4 + Li \tag{1}$$
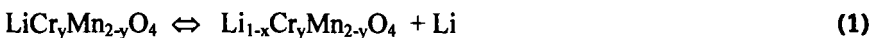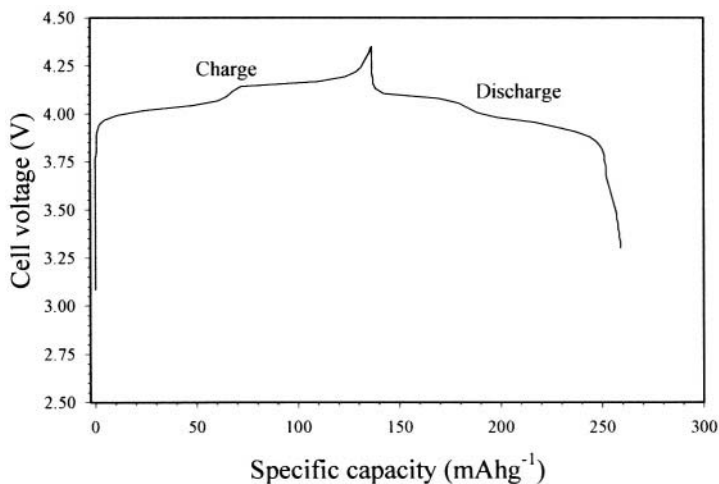
Figure 7. Voltage profiles of the lithium deintercalation-intercalation cycle of the chromium-stabilized manganese spinel cycled in a LiClO$_4$/EC/DMC/PAN electrolyte cell at room temperature and at 0.1 mA·cm^{-2} rate. Lithium counter electrode. Charge: lithium deintercalation; discharge: lithium intercalation Derived from data in reference 30.

The trend of Figure 7 demonstrates that the voltage profile and the cycling capacity (about **130 mAh·g^{-1}**) match those expected for this cathode material in liquid electrolyte cells. Furthermore, the electrode can be extensively cycled with a contained capacity loss (see Figure 8). Similar results have been obtained with other lithium metal oxides, e.g. , **LiNi$_y$Co$_{(1-y)}$O$_2$** [29] this finally demonstrating the compatibility of the gel membranes with the most common lithium ion cathode materials.
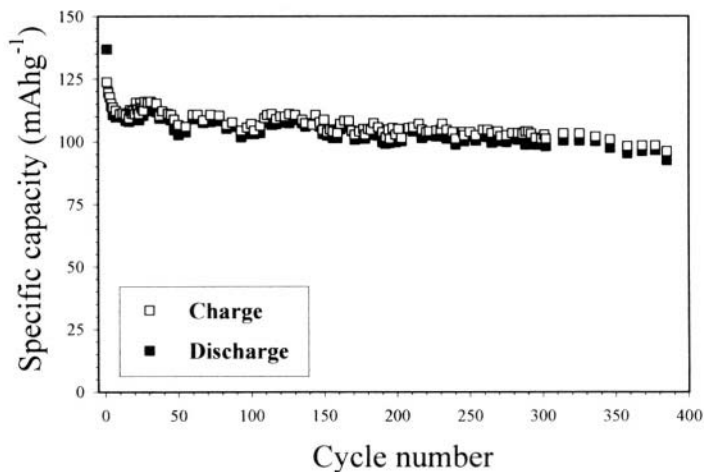
Figure 8. Capacity delivery versus number of cycles of a chromium-stabilized manganese spinel cycled in a LiClO$_4$/EC/DMC/PAN electrolyte cell at room temperature and at 0.1 mA·cm^{-2} rate. Lithium counter electrode. Charge: lithium deintercalation; discharge: lithium intercalation. Derived from data in reference 30.

As in the case of the cathodes, also the electrochemical response of the anodes, can be evaluated by following their lithium intercalation-deintercalation processes, again in cells using the gel membrane as the electrolyte and Li metal as the counter electrode. Figure 9 shows the voltage response of a graphite electrode cycled in a **LiClO₄/EC/DMC/PAN** electrolyte cell. Also in this case, the response, which is associated with the process:

$$xLi + 6C \Leftrightarrow Li_xC_6 \qquad\qquad (2)$$

approaches that observed in liquid electrolyte cells, namely a voltage profile which during the intercalation process decreases along a series of distinguishable plateaus which correspond to the occurrence of the progressive staging graphite phases. A similar trend is reproduced upon the reverse, lithium deintercalation process, although with an apparent loss in capacity. As well demonstrated in the case of liquid electrolyte cells, this formal excess of capacity during the initial cycles may be associated with side reactions involving the decomposition of the electrolyte with the formation of a passivation layer on the graphite electrode surface.
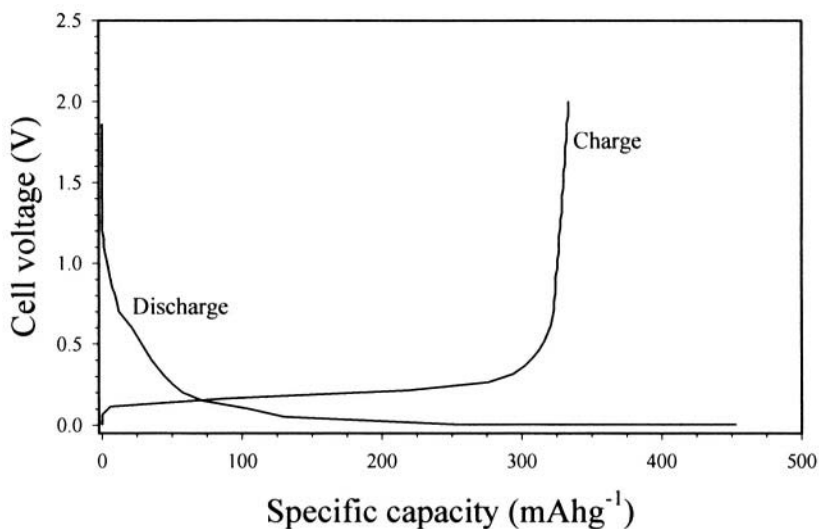
Figure 9. Typical voltage response of the Li intercalation – deintercalation process of a graphite electrode in a LiClO₄/EC/DMC/PAN electrolyte cell. Temperature: 25°C. Lithium counter electrode. Cycling rate: C/4.

However, in contrast with the response observed in liquid electrolytes, in gel electrolyte cells the graphite electrode appears to suffer by a certain capacity decay under prolonged cycling. This may be ascribed to a progressive loss of active material sites due to the difficulty in exchanging a suitable amount of the liquid component from the membrane to the bulk of the electrode.

3.0   SWELLED MEMBRANE ELECTROLYTES

The partially unsatisfactory response of the anode in the gel membrane cells may be solved in two ways, i.e. :i) by replacing the liquid-phobic carbonaceous electrodes with more liquid-compatible oxide compounds and ii) by replacing the standard gel electrolytes with membranes containing excess of liquid. The fist approach is discussed in another chapter of this book. The second approach may be pursued by considering membranes capable of being swelled by large quantity of liquids still retaining their mechanical integrity.
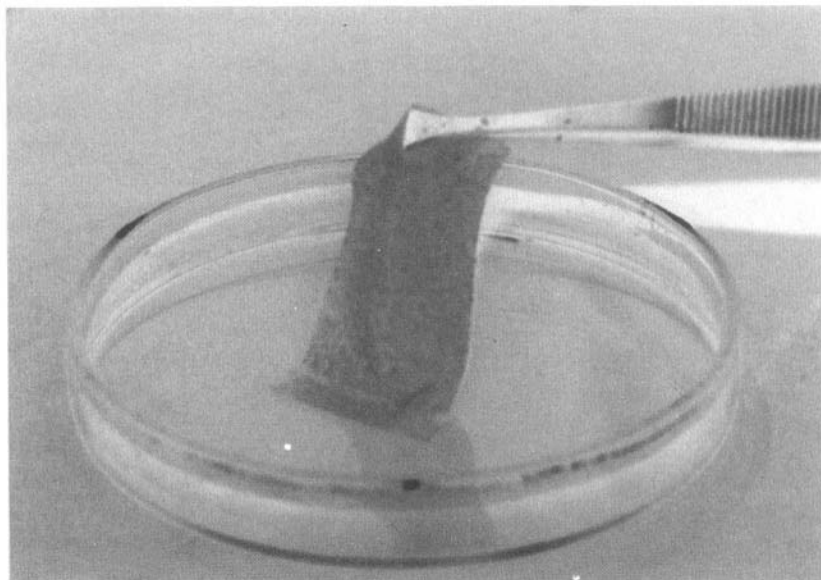
Figure 10. The process of liquid swelling in a PEO-based, composite membrane.

An example is provided by a membrane formed by combining linear PEO with a lithium salt and with a nano-particle size particle SiO_2 filler (31). This dry, composite membrane is then activated by dipping it in a non-aqueous diethylcarbonate (DEC)-ethylcarbonate (EC) solvent mixture, see Figure 10. The membrane can be swelled by a large amount of liquid in a very short time, as shown by Figure 11 that reports the swelling fraction versus dipping time. The result confirms the fast swelling rate that leads to a 300 weight percent of the membrane after only few minutes of dipping in the liquid.

Figure 12 compares the Arrhenius plot of the ionic conductivity of a $LiClO_4$ (1M), EC-DEC liquid electrolyte in comparison with that of a $P(EO)_{10}LiClO_4 + 10$ wt% nano-particle SiO_2 composite membrane swelled (300 wt%) in an EC(25 % molar)-DEC solvent mixture. The conductivity of the two systems are comparable, reaching at 20 °C the values of 2.5×10^{-3} $S \cdot cm^{-1}$ for the liquid electrolyte and 2.1×10^{-3} $S \cdot cm^{-1}$ for the swelled membrane [31].
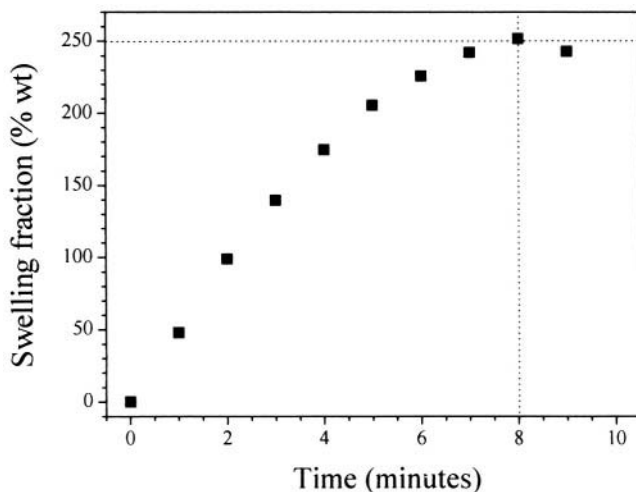
Figure 11. Swelling fraction versus time for a $P(EO)_{10}LiClO_4+10wt\%$ nano-particle SiO_2 composite membrane after dipping in an EC(25% molar)-DEC solvent mixture at room temperature. *From reference 31 reproduced by permission of The Electrochemical Society, Inc.*
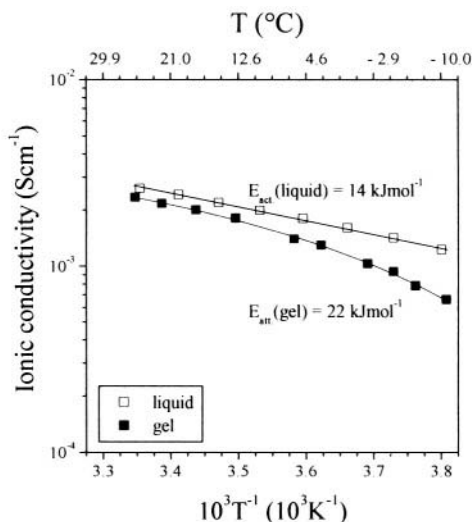
Figure 12. Arrhenius plot of the ionic conductivity of $LiClO_4$ (1M), EC-DEC liquid electrolyte in comparison with that of the $P(EO)_{10}LiClO_4+10wt\%$ nano-particle SiO_2 composite membrane swelled (300%) in an EC(25 % molar)-DEC solvent mixture. *From reference 31 reproduced by permission of The Electrochemical Society, Inc.*

In addition to providing high conductivity, the large amount of swelled liquid is expected to favor interfacial contacts, especially in the case of carbonaceous electrodes. This is somewhat confirmed by Figure 13 that reports the initial cycles of a graphite electrode in a cell using the swelled PEO-based electrolyte. The electrode cycles with a capacity delivery approaching the theoretical value, i.e. **370 mAh·g⁻¹**, i.e., with a trend similar to that observed in liquid electrolytes. In addition, this high capacity appears to be retained also in the following cycles (31).
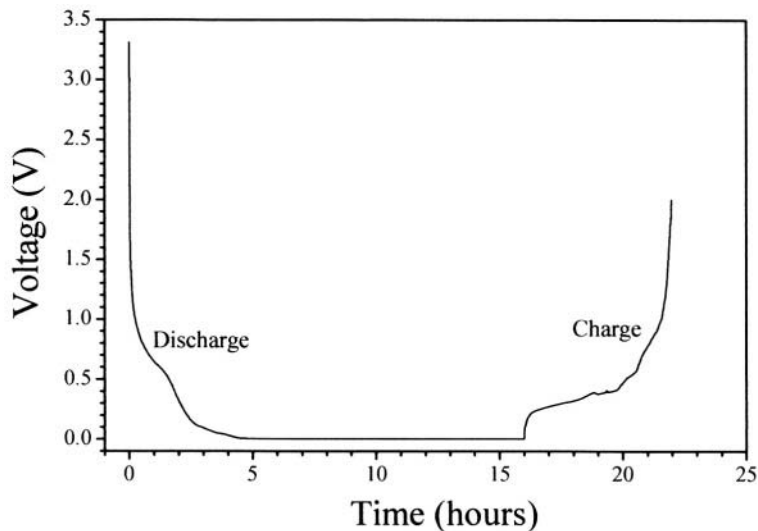
Figure 13. Typical voltage response of the Li intercalation – deintercalation process of a graphite electrode in a P(EO)$_{10}$LiClO$_4$+10wt% nano-particle SiO$_2$ composite membrane swelled (300%) in an EC(25 % molar)-DEC solvent mixture cell   Temperature:25°C. Lithium counter electrode. Cycling rate: C/4. From reference 31 reproduced by permission of The Electrochemical Society, Inc.
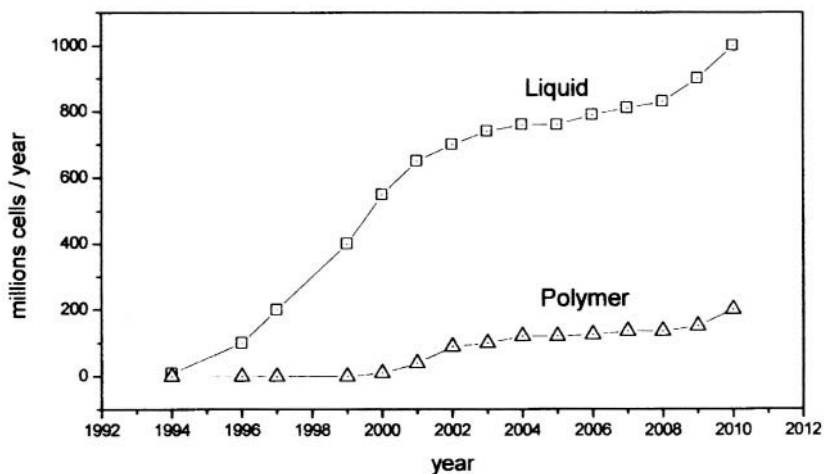
Figure 14. Expected trend of the lithium ion battery in the consumer electronic market. Derived from data in reference 32.

4.0   CONCLUSIONS

In recent years substantial progress has been achieved in the area of polymer electrolytes developed and designed to act as separators in plastic lithium ion batteries. Some of this progress, and particularly those related to gel-type and to liquid-swelled membranes are reported and discussed in this chapter. Another chapter of this book demonstrates the feasibility

of a particular polymer electrolyte for the fabrication of commercial lithium ion plastic batteries.

All these facts confirm that the passage from liquid to plastic systems is not just an academic concept, but rather a practical reality. Indeed, many battery manufacturers in Japan, in the US and in Europe have production lines in operation for the fabrication of lithium ion plastic batteries of various size and capacity.

On the basis of these facts it is possible to foresee that lithium ion plastic batteries will soon achieve a well-established role in the consumer market, see Figure 14 [32].

5.0   ACKNOWLEDGEMENTS

6.0   REFERENCES

1.   B. Scrosati, in " Lithium Ion Batteries. Fundamental and performances", M.Wakihara and O. Yamamoto Eds, Kodansha, Wiley-VCH, Tokyo, Weinheim, pp. 218, 1998.
2.   J.M. Tarascon and M. Armand, *Nature,* **414**, 359, 2001.
3.   F.M. Gray, "Polymer Electrolytes" Royal Society of Chemistry Monographs, Cambridge, 1997.
4.   J.M. Tarascon, A.S. Gozdz, C.Schmutz, F.K. Shokoohi, P.C. Warren, *Solid State Ionics,* **86-88**, 49, 1996.
5.   T.Gozdz, C.Schmutz and J-M. Tarascon, US Patent 5,296,318.
6.   J.M. Tarascon, G.C. Amatucci, C.N. Schmutz, A.S. Gozdz, P.C. Warren and F.K. Shokoohi, IMLB-8, Nagoya, Japan, June 1996, abstr. I-C-I.
7.   A. Du Pasquier, P.C.Warren, D,Culver, A.S. Gozdz, G.G. Amatucci and J.M. Tarascon, **196**[th] Meeting of the Electrochem. Soc., Hawaii, October 17-2, 1999, Abstr. No. 116.
8.   G.Feullade and Ph. Perche, *J.Appl.Electrochem.,* **5**, 63, 1975.
9.   G.B.Appetecchi, F.Croce, P.Romagnoli, B.Scrosati, U.Heider, R.Oesten, *Electrochem. Comm.,* **1**, 83, 1999.
10.   G.B.Appetecchi, F.Croce, B.Scrosati, **J.Power Sources**, 66, 77, 1997.
11.   G.B.Appetecchi, F.Croce, G.Dautzenberg, F.Gerace, S.Panero, E.Spila, B.Scrosati, *Gazz. Chim.It.,* **126**, 405, 1996.
12.   G.B.Appetecchi, F.Croce, A. De Paolis, B. Scrosati, *J.Electroanal. Chem.,* **463**, 248, 1999.
13.   T.Osaka, T.Momma, H.Ito, B.Scrosati, *J.Power Sources,* **68**, 392, 1997.
14.   C.Svamberg, J.Adebahr, H.Ericson, L.Borjesson, L.M.Torell and B. Scrosati, *J.Chem.Phys.,* **111**, 11216, 1999.
15.   C.Svamberg, J.Adebahr, R.Bergnan, B.Scrosati, P.Jacobsson, *Solid State Ionics,* **136**, 1147, 2000.
16.   P.E. Stallworth, J.J. Fontanella, M.C. Wintersgill, C.D. Scheider, J.J. Immel, S.G. Greenbaum and A.S. Gozd, *J.Power Sources* **81**, 739, 1999.
17.   B.Scrosati, *The Chemical Record,* **1**, 173, 2001.

18.   P.E. Stallworth, S.G.Li. S.G. Greenbaum. F. Croce, S. Slane, M.Salomon, *Solid State Ionics,* **73**, 119, 1994.
19.   C.A. Edmondson, M.G. Wintersgill, J.L.Fontanella, F. Gerace, B. Scrosati, S.G. Greenbaum, *Solid State Ionics,* **85**, 173, 1996.
20.   D. Ostrovskii, L. Torell, G.B. Appetecchi, B. Scrosati, *Solid State Ionics,* 106, 19, 1998.
21.   D. Ostrovskii, A. Brodin, L. Torell, G.B. Appetecchi, B. Scrosati, *J. Phys. Chem,* **109**, 7618, 1998.
22.   G.B. Appetecchi, P.Romagnoli and B. Scrosati, *Electrochem.Comm.,* **3**, 281, 2001.
23.   F. Croce, G.B. Appetecchi, L. Persi and B. Scrosati, *Nature,* 394, 456, 1998.
24.   F. Croce, R. Curini, A. Martinelli, L. Persi, F. Ronci and B. Scrosati, *J.Phys. Chem., B,* 103, 10632, 1999.
25.   E. Quartarone, P. Muscarelli and A. Magistris, *Solid State Ionics,* **110**, 1, 1998.
26.   A.S. Best, A.Ferry, D.R. MacFarlane and M.Forsyth, *Solid State Ionics,* **126**, 269, 1999.
27.   F. Gray and M. Armand, in "Energy Storage Systems for Electronics", "T.Osaka and M. Datta Eds, Gordon and Breach, the Netherlands, 2000, pp. 351.
28.   G.B. Appetecchi, F.Croce, R.Marassi, L.Persi, P.Romagnoli, B. Scrosati, *Electrochim. Acta,* **45**, 23, 1999.
29.   L.Guoha, H.Ikuta, T.Uchida and M.Wakihara, J.Electrochem. Soc., **143**, 178, 1996.
30.   G.B. Appetecchi and B. Scrosati, *J.Electrochem. Soc.,* **144**, L138, 1997.
31.   Y.Aihara, G.B. Appetecchi and B. Scrosati, *J.Electrochem. Soc.,* in press
32.   H.Takeshita, **18**th Intl.Seminar & Exhibit on Primary & Secondary Cells, Fort Lauderdale, Fla, March 2001.

9

Lithium-Ion Cell Production Processes

Ralph J. Brodd

Broddarp of Nevada, Inc.
2161 Fountain Springs Drive
Henderson, NV 89074
USA

Kazuo Tagawa

Hoshen Corporation
10-4-601 Minami Senba 4-chome
Chuo-ku, Osaka 542-0081
Japan

1.0   INTRODUCTION

The strong market drive for a safe, room temperature, and high-energy rechargeable battery has fueled the development of the lithium-ion (Li-Ion) technology. The Li-Ion cell has the highest energy density of any rechargeable cell and the improvement in performance has been spectacular. Sony made the first commercial introduction in 1991 after an intense technology development as described by Nagaura and Tozawa [1]. They established the basic chemistry, construction and process for the manufacture of the Li-Ion system. Today, there are over 30 manufacturers, worldwide with production ranging from approximately 4,000 cells per day to 100,000 cells per day. Although there is a 25-fold difference in the number of cells fabricated, the basic operations are the same for all. The manufacturing of Li-Ion batteries is a complex and unforgiving process. Each step of the process has its own characteristics and potential problem areas.

This chapter is intended to provide the reader with a basic knowledge of the over-all Li-Ion manufacturing processes. The implementation and details may differ for each manufacturer all of whom hold the details as proprietary. Intense competition between cell manufacturers and the drive for higher capacity cells to power portable electronic devices, such as notebook and cellular telephone applications, has resulted in exceptional performance improvements. Figure 1 depicts the increase in capacity of the typical ICR18650 cell over the past 10 years. The driving force behind the expansion in performance and production volume has been the advent of portable electronics, notebook computers, cellular telephones, camcorders and the like. The spectacular growth in production volume of Li-Ion cells is given in Figure 2 for all types of Li-Ion cells, prismatic, cylindrical and polymer.
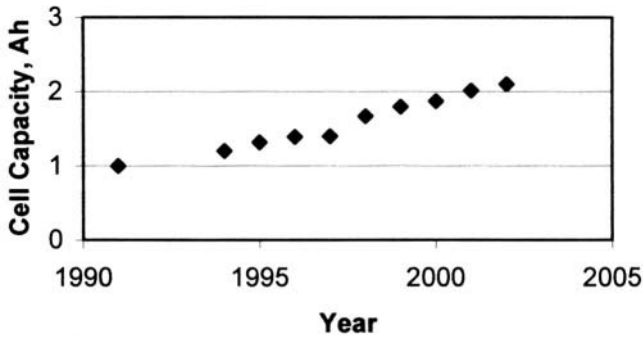
Figure 1. Historical improvement in capacity of an 18650 Li-Ion Cell. Data derived from reference 2.
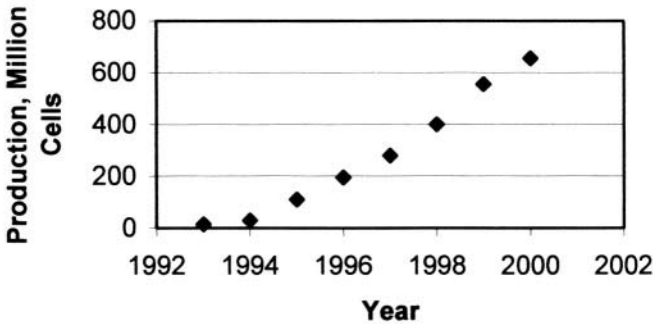
Figure 2. Production growth for Li-Ion cylindrical and prismatic cells. Data derived from reference 3.

The International Electrotechnic Commission has established a common designation to describe the chemistry and size of Li-Ion cells [4]. The letters designate the chemistry and form factor while the numbers specify the physical dimensions of the cell. The first letter describes the general chemistry, the second letter designates the specific cathode chemistry and the third letter designates the shape.

First letter:	I – Li-Ion chemistry
Second letter:	C- cobalt, N- nickel, M-manganese
Third letter:	C- cylindrical, P-prismatic

The first two numbers that follow designate the diameter in mm and the last three designate the height in tenths of mm. Thus a cell designated ICP18650 is a Li-Ion cell with a cobalt cathode that has a diameter of 18 mm and a length of 65.0 mm.

For rectangular (prismatic) cells the initial letters have the same meaning but the first two numbers designate width in mm, the next two numbers are the height in mm and the last two numbers are the length in mm. Thus, a cell designation IMP360965 describes a prismatic Li-Ion cell with a manganese cathode cell that measures 36 mm in width, 9 mm in height and is 65 mm long.

2.0   CELL DESIGN

Some general comments are necessary. The lithium battery is a high-energy system and must be treated with care. Electrical, mechanical and thermal abuse can initiate thermal runaway conditions that can cause the cell to self-destruct. Careful attention to every detail in cell design and in production is required. A quality assurance program designed to establish and produce the product with zero defects; six 9's reliability and ISO 9000 level must be practiced. A final comment, inspection of the product at the end of the fabrication process is not an acceptable method of assuring high quality and safe operation. Quality and reliability cannot be inspected into a product after the fact. As in any commercial process, it is difficult to say that one step is more important than another. Figure 3 depicts a generalized flow chart for the assembly process. Comments for each of the steps will follow in this and the next section.

The internal designs for the Li-Ion cell must result in uniform current density across, and through, the electrode structures. Large surface area electrodes are employed to give the cells high rate performance. The pore structure and the combination of conductive carbons give good contact to all the particles of the active material. Good contact is essential between the active materials, the conductive carbon and the current collector, for full utilization of the active materials and for good efficiency during high rate performance. A binder, usually a polymer such as polyvinylenedifluoride (PVdF), is used to hold the electrode structure together and bond it to the current collector. The binder needs some flexibility to accommodate the volume changes that occur in the active materials during charge and discharge. Additives to the coating slurry may improve contact of the active mass to the current collectors. The collector foils may be coated with a conductive carbon paint to protect surfaces from corrosion and to improve the contact of the active mass to the current collector. The steel cans should be clean and nickel plated to provide a stable surface and minimize can corrosion before cell assembly.

The capacity of a given cell size constitutes a trade-off in geometric surface area, coating thickness (loading), thickness of the current collector and thickness of the separator so that the electrodes fit snugly into the can. The capacity is determined by the amount of active material coated onto the current collector. The active material loading $(\text{mg} \cdot \text{cm}^{-2})$ is determined by the

cell design and by the total surface area of the electrode. Larger geometric electrode areas for reaction reduce the polarization (voltage loss) due to the kinetics of the electrode reactions and lower the voltage drop across the separator. Porous electrode structures are employed to further increase the reaction surface by extending the reaction zone away from the surface and into the bulk of the anode and cathode. Since all of the electrodes are porous structures, the reader may wish to review the principles of porous electrode operations [5,6]. It is possible to use this modeling approach to determine the best materials for a particular application. Shi and Brodd [7] demonstrated that modeling of the carbon and graphite could differentiate between graphite and hard carbons in cell performance.

The electrolyte must have a wide voltage range of stability with little or no reactivity up to 5 volts vs. lithium. This is a safety measure in case the voltage control circuitry malfunctions. Cells in multiple cell packs could then be exposed to significantly greater voltages than recommended. Good cell operation requires a minimum conductivity of 10^{-3} S·cm^{-1} to permit high current discharge with a minimum of resistive heating and voltage loss. A thin, large geometric electrode area separator also reduces the ohmic loss.

Cell designs that are tolerant to abuse conditions without venting or self-destruction are imperative. Safe operation demands that no lithium metal be formed in the cell during any cell use or abuse condition. The deposition of lithium metal forms dendrites that internally short the cell. The primary control of lithium deposition is the ratio of the negative to the positive capacity of the individual electrodes in the cell. The voltage control in the charging methodology and cell balance are the main determinates to prevent lithium deposition. The negative electrode has about 10% higher usable capacity than the positive as noted in Figure 4. This prevents lithium metal deposition onto the anode on charge, as the cathode determines the capacity of the cell. If lithium metal deposits on the electrode surface, it reacts with the electrolyte and could initiate thermal runaway. The actual capacity ratio is a trade-off between the desire for higher capacity cells and the need for a safety factor to resist abuse conditions.

Thermal runaway is the term used to describe the situation when a cell spontaneously self-destructs. It occurs during uncontrolled charging or from electrical or physical abuse of the cell. Often, the cause is an internal short that heats the cell by releasing the total cell energy into the cell. If a cell is shorted, the cell reactants are capable of heating the cell to very high temperatures (450°C, or more, for an ICC18650). As long as the cell temperature remains below about 120°C, the cell is stable. However, at temperatures above about 120°C, the electrolyte solvents react vigorously with the cathode active material and generate additional heat. Above 250°C oxygen from decomposition of the cathode oxide can react with the organic solvents of the electrolyte. These reactions are autocatalytic and cannot be stopped once they begin.

POSITIVE ACTIVE MATERIAL	CONDUCTIVE DILUENT	BINDER	NEGATIVE ACTIVE MATERIAL	CONDUCTIVE DILUENT	BINDER
$LiCoO_2$ $LiNi_xCo_{1-x}O_2$ $LiMn_2O_4$ PVdF	Acetylene Black Graphite Carbon	PVdF NMP DMF	Carbon Graphite PVdF	Acetylene Black Graphite Carbon	PVdF NMP DMF

Paste Mixing   Paste Mixing

Aluminum Foil ———→ Coating   Coating ←——— Copper Foil

Drying   Drying

Calendaring   Calendaring

Slit to Width   Slit to Width

Reeled Stock   Reeled Stock

Winding Core

Separator ———————→ Insert Wound Elements in Can

Can, Case ———————→ Spot Weld Bottom Contact

Vacuum & Heat Drying

Electrolyte ———————→ Vacuum Addition of Electrolyte

PTC, CID Top Insulator Plate, Cap ———————→ Insert Top Parts

Close and Seal

Top Cap Welding

Wash

Formation 1 to 3 Cycles ———→ Storage, Aging 2 Weeks to 1 Month ———→ Acceptance Testing ———→ Shipping

Figure 3. Process outline for Li-Ion cell fabrication
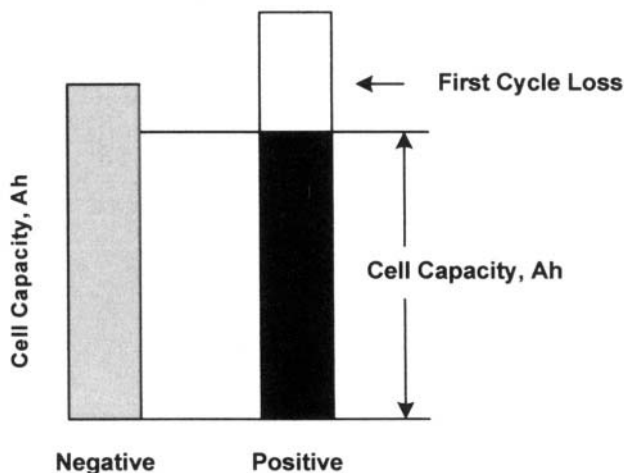
Figure 4. Depiction of Electrode Capacity Relationship in a Li-Ion Cell

Another safety measure is the use of a "shut-down" separator. This is generally a microporous polyethylene that undergoes a phase transformation at about 110°C. The phase change closes the pores and increases the internal resistance of the cell. This effectively stops cell operation. In general, thin electrodes are used to obtain high rate discharge and charge capability. Once the internal design is set, the dimensions, materials and electrode compositions can be determined for all manufacturing processes. Safety features included in the cell design are the PTC and CID devices usually incorporated into the cell top plate and seal. The PTC is a positive temperature coefficient device that changes resistance at a set temperature or current flow and stops a thermal runaway condition from developing. The CID is a current interrupt device that is incorporated into the cell cap. It serves a similar purpose to the PTC as it interrupts the electrical connection between the cathode tab and the positive terminal when the internal pressure in the cell reaches a given pressure. This device is activated from the vapor pressure of the electrolyte solvent when it reaches a set value. Finally, the cell vent activates at pressures just higher than the CID to release the volatile solvent and stop cell action.

3.0   COATING ELECTRODE STOCK OR FOILS

The manufacturing/assembly processes for a Li-Ion battery require precision and accuracy when coating the positive and negative electrode stock coated with the active material. The coating process is a critical element in ensuring a high capacity, high reliability product. If the coatings are of poor quality, only low performance batteries will be produced. The initial steps in

the preparation of the active mass determine the outcome. A schematic for electrode coating operations is shown in Figure 5.

Cohen and Gutoff [8] describe a methodology to arrive at the best coating technique for a particular application, based on the rheology of the coating slurry, required precision and speed of coating. Common types of coaters include extrusion, reverse roll coating and knife over roll or doctor blade. Typical coating heads used in production are shown in Figures 6 and 7. The slot die and reverse roll coating processes, with interrupted coating, are preferred over the doctor blade (not shown). Both the slot and reverse roll coating can easily handle the viscosity and coating speeds for the anode and cathode coating slurries. Both have sophisticated electromechanical technology for control of the coating thickness across and down web. Regardless of the choice of coating head, the coated foil passes through an oven to evaporate the solvent and leave a precise amount of active mass $(mg \cdot cm^{-2})$ on the foil. Many coating solvents are classed as hazardous and cannot be released to the atmosphere. As a cost saving measure, the solvent is generally recovered for reuse in the process. To avoid any contamination of the environment the solvent may be incinerated.
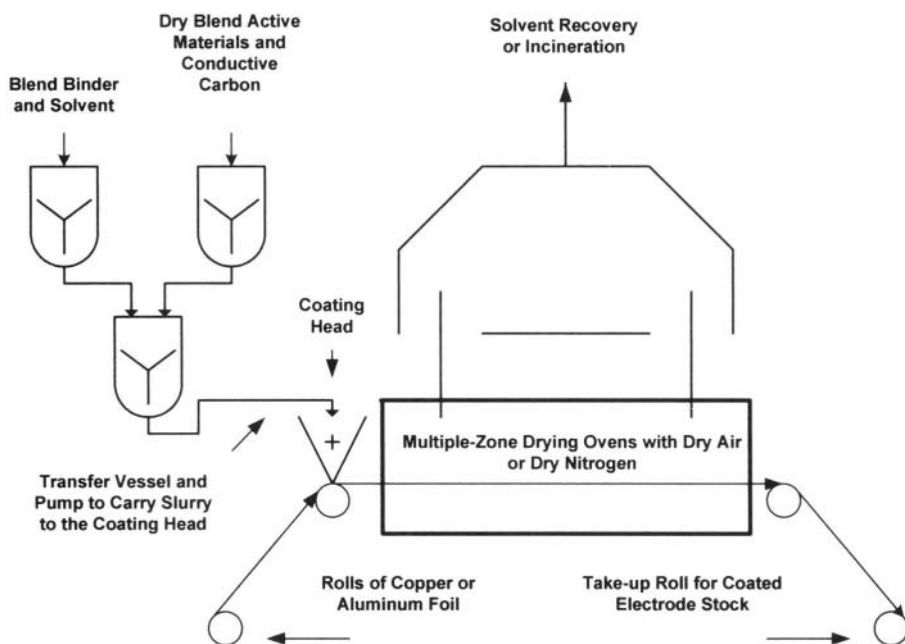
Figure 5. Coating process for anode and cathode electrodes (not to scale)
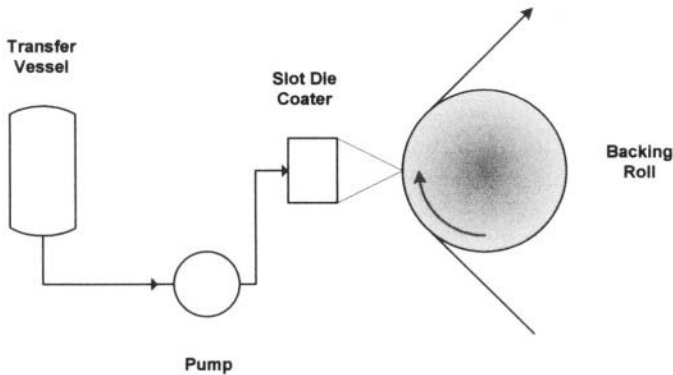
Figure 6a. Slot Die with Interrupted Coating by Movement of the Die and Stripe Coating.
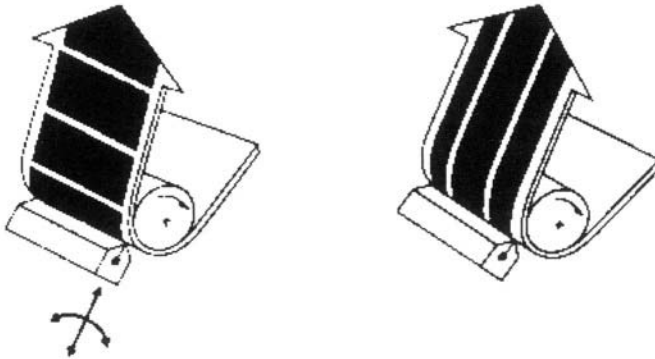
Figure 6b. The slot die can produce interrupted coating by movement of the die or strips by shims in the die orifice. (Courtesy of Toray Engineering Co.)

A common process is the reverse roll coating. In this process, the reverse rolls are raised and coating is interrupted while the foil continues to move. The slot die can perform the same operations with equal precision. The automated manufacturing process requires interrupted coating with precision lengths of coating area. Both the slot die and reverse roll coating heads can handle the anode and cathode coating slurries. Each has sophisticated electromechanical technology for excellent control of the coating thickness across and down web. Regardless of the choice of coating method, the coated foil passes through an oven to evaporate the solvent and leave a precise amount of active mass on the foil.

The coating operations begin by mixing the active materials, polymer binder and conductive diluent. The objective of the dry blend is to coat the nonconductive particles of the active material with a thin film of the conductive carbon. This coating provides electrical contact to the current collector for full utilization of all the particles in the mix. The polymer is

dissolved in the coating solvent in a separate container. The dry mix blend and the solvent solution are then combined to form a slurry as depicted in Figure 5. Care must be exercised to have good control and detailed specifications of the basic raw materials, such as chemical composition, particle size distribution, impurity level, etc. The properties of the materials and the rheology coating slurry should not vary from lot to lot. Slight changes in particle size distribution of the cathode active material can change the rheology of the coating mixture and influence the performance of the cathode. The ratio and amounts of the materials are determined by the cell design and the size of the mixer. An intensive mixing procedure is used to dry blend the non-conducting active material and the carbon before adding the coating solvent and binder. When mixing the cathode, it is essential to coat the non-conductive active material with the conductive diluent, usually a carbon black. This ensures that each particle in the porous structure is coated and can connect through the conductive matrix to the current collector. The solvent additions are used to adjust the viscosity of the slurry (or paint) for the coating operation. Polyvinylenedifluoride (PVdF) is the binder of choice and the solvent is N-methylpyrollidinone (NMP).
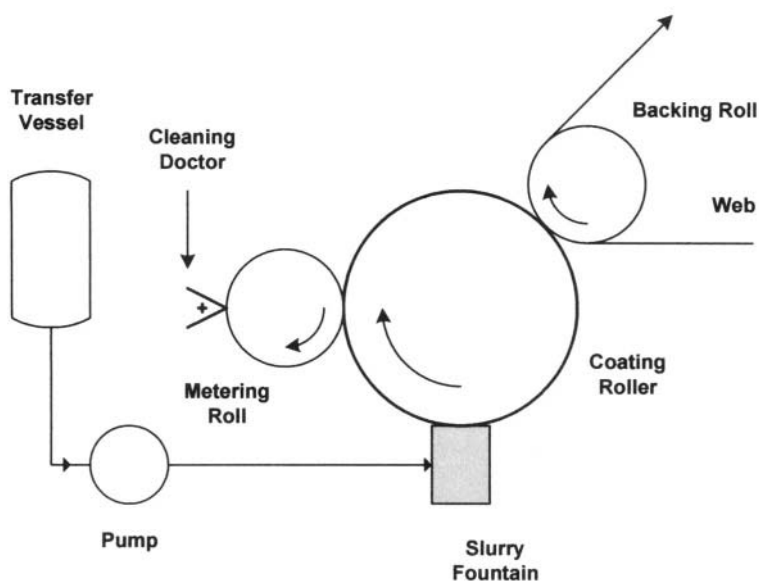
Figure 7. Setup for reverse roll coating operations. Movement of the coating roller away from the web produces interrupted coatings

The slurry from the mixing operation is placed in sealed containers, which serve as the reservoir and transfer medium for the coating operations. Precise amounts of coating slurry are pumped from the storage container with a gear pump, or similar precision pump, to avoid any entrainment of air in the fluid going to the coating head.

After coating, the rolls are calendared to produce a precision thickness, and then slit to width for the specific cell design. Two or three passes through the calendar may be required to arrive at the desired thickness. If the coating is very porous and thick, compacting in one pass can produce foils with uneven porosity. The final thickness control is essential for the winding step in the assembly process so that the electrode coil has the proper dimensions to fit snugly into the can.

The uniformity of the coating thickness and composition is critical to good performance as well as in the subsequent cell assembly processes. Many installations measure the coating thickness on a continuous basis using a beta gauge whose operation is based on absorption of the beta emissions by the coated materials. The gauge can be mounted and swept across the coating to provide a continuous measure control of the amount of material in the coating. This allows continuous feedback to the control panel for on-line correction of the amount of material being coated. It is also possible to measure the amounts and thickness of the roll after coating by punching out a sample at the start and end of the roll and measuring its thickness. This method does not allow on-line correction and may result in rejection of the full roll by QA.

It is possible to coat both sides simultaneously, but this is seldom done in practice, as it requires exceptionally good process control. Usually, the electrode stock is passed through the coating operation twice to coat each side of the current collector foil. The coated foils are then calendared to compact the coated layer. Calendaring usually takes two passes to compress the final coating into a uniform thickness. Two passes provide better control of pore size and thickness in the final product. The electrode foils are then slit to size for cell assembly.

4.0   CELL ASSEMBLY

Most Li-Ion cells, both cylindrical and prismatic, use the wound core construction. The strips have the required loading of active material ($mg \cdot cm^{-2}$), length, width and thickness to match the cell designs. The coating operation produces interrupted coating to match the length of the coil. The winding machines are designed to operate automatically using strips of anode, cathode and separator fed from separate reels. The operations start by welding the tabs onto the uncoated section of the foils. The winding machine then cuts the strip to the proper length and winds the combination anode-cathode-separator into a tight coil or bobbin in jellyroll fashion. As the wound core increases in diameter, the winding machine automatically compensates to maintain constant tension as the coil increases in diameter for close tolerance on the diameter. The elliptical wind for prismatic cells is a more complex and slower process. Any irregularity leads to a gap between the separator and electrode, which may

cause a malfunction, shortened cycle life or safety issue. The winding operations are complex and require a high level of precision and automatic control. It is also possible to hand wind cells but that requires a significant degree of manual dexterity and the ability to control tension through practice. A good technician can wind 300 cells of reasonable quality per day. However, the repeatability of hand wound cells varies with the individual. It is difficult to get mandatory precision day after day using the hand wound techniques.

Figure 10 depicts a typical production process for cylindrical cells. The winding operation uses reels of anode and cathode from the coating, calendaring and slitting operations. The size of the reels is determined largely by the ability of the operator to lift and position them on the winding machine and the desire for continuous operation. The process for fabricating prismatic cells is very similar to that for cylindrical cells and is shown in Figure 11. Each manufacturer has proprietary methodology to implement each of the cell fabrication steps.

After winding, the coil is checked for internal shorts before being inserted into the can. Early rejection of potential cell faults is an economy and prevents investing more work on bad cells. The bobbin is inserted into the can so that the can provides constant pressure to hold the anode and cathode close together, and eliminate any voids between them. Some manufacturers may insert a mandrel to stabilize the center of the coil. Unless all operations are carried out in a dry room or dry box, the absorbed water in the active materials must be removed by heat and vacuum before the electrolyte filling process.
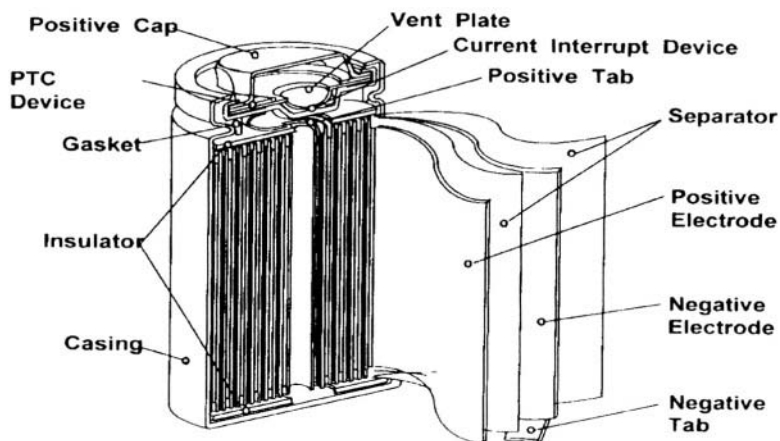
Figure 8. Expanded view of the internal construction of a cylindrical cell (Courtesy of Sanyo)
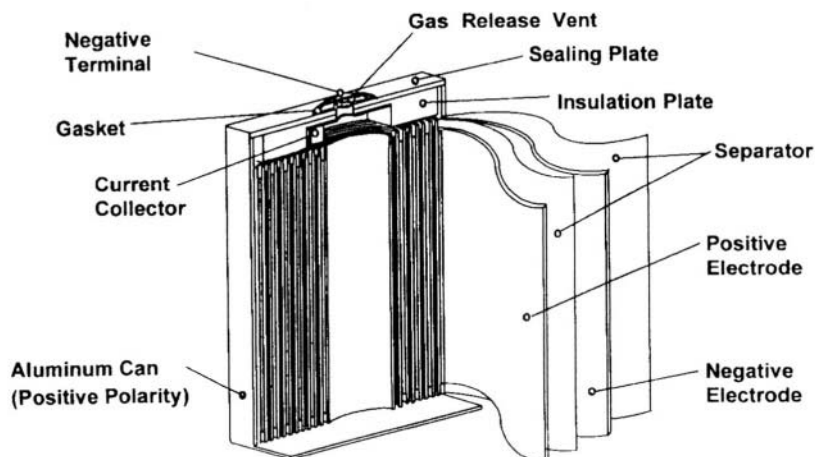
Figure 9. Expanded view of the internal construction of a prismatic cell (Courtesy of Sanyo)

Electrolyte is metered into the cell by a precision pump and vacuum filled to ensure that the electrolyte permeates and completely fills the available porosity in the separator and electrode structures. Precision pumps meter the exact amount of electrolyte needed for good cell operation. The amount of electrolyte is generally arrived at by trial and error, based on the performance of the cells. The electrolyte is invariant (same number of Li^+ ions enter as leave the electrolyte during charge and discharge). The electrolyte salt is usually $LiPF_6$ dissolved in organic carbonate solvents (see the chapter on Liquid Electrolytes by J. Yamaki). Each manufacturer has a different combination of solvents with ethylene carbonate (EC) being a common denominator for most.

After filling the cell with electrolyte, the cell is sealed by controlled compression of a polymer gasket or grommet placed between the cell can and the top plate. The pressure on the polymer gasket seal is controlled to keep it within the elastic limit of the polymer. If the elastic limits are exceeded, the polymer cold flows and compromises the seal. Each manufacturer uses a somewhat different mechanical construction to seal the cells but the final results are essentially identical. Typically, a shoulder or ledge is formed near the top of the cell. This serves as the base for the seal and to hold the jellyroll in place and prevent telescoping or changing position of the wound bobbin under the influence of vibration and shock. Any shift in position causes a change in the current distribution and results in poor cycle life or lithium plating in high performance cells. The cell top plate seal contains a vent, PTC and CID safety devices. Both the

CID and PTC are safety devices designed to activate and prevent dangerous temperatures and pressures from developing internal to the cell. Each lot of devices is checked for proper operation before incorporation into the top assembly.

After the seal is applied the cells can be washed, jacketed and labeled. They are given a serial number to trace the day of manufacture and to identity all cell components (electrode materials, electrolyte, separator and the like). The information on capacity and voltage is stored with the cell number and used later to match cells for pack assembly.

While the processes, above, are depicted for small sealed cells used in portable electronics, the process for larger batteries for space and automotive applications follow the same general outline. The cells can be laser welded with glass to metal seals to provide long lasting hermetic seals. With the larger cells, greater care must be exercised to insure safe operation, even under abuse conditions.

5.0   FORMATION AND AGING

After washing and jacketing, but before the start of the formation process, the voltage and impedance of all cells is measured to sort out any shorted cells. The cells are then charged for the first time (formation). The conditions of the first charge are important for at least two reasons: 1) the SEI layer forms on the anode to protect it from reacting spontaneously with the electrolyte during normal cell operation, and 2) it establishes the good electrical contact between the active materials and the electrolyte. The first charge follows the manufacturer's recommended procedure for charging the cells but often starts at a lower current and then increases to the normal charging current at about one-third of the way into the charge period. Cells may continue cycling within the voltage limits for charge and discharge for one or two more cycles after formation. After formation or cycling, cell voltage and capacity are measured and stored for later use in the cell selection process. The aging period varies between two weeks and one month, depending on the manufacturer. The voltage of the cells is measured again after storage. Differences in voltage at the start and end of the storage period are used to sort-out cells with "soft-" or "micro-" shorts. Cells with internal shorts will have a lower voltage after storage and separate themselves from the normal voltage and capacity distribution. It may be necessary to evacuate the larger cells after formation to remove the formation gases.
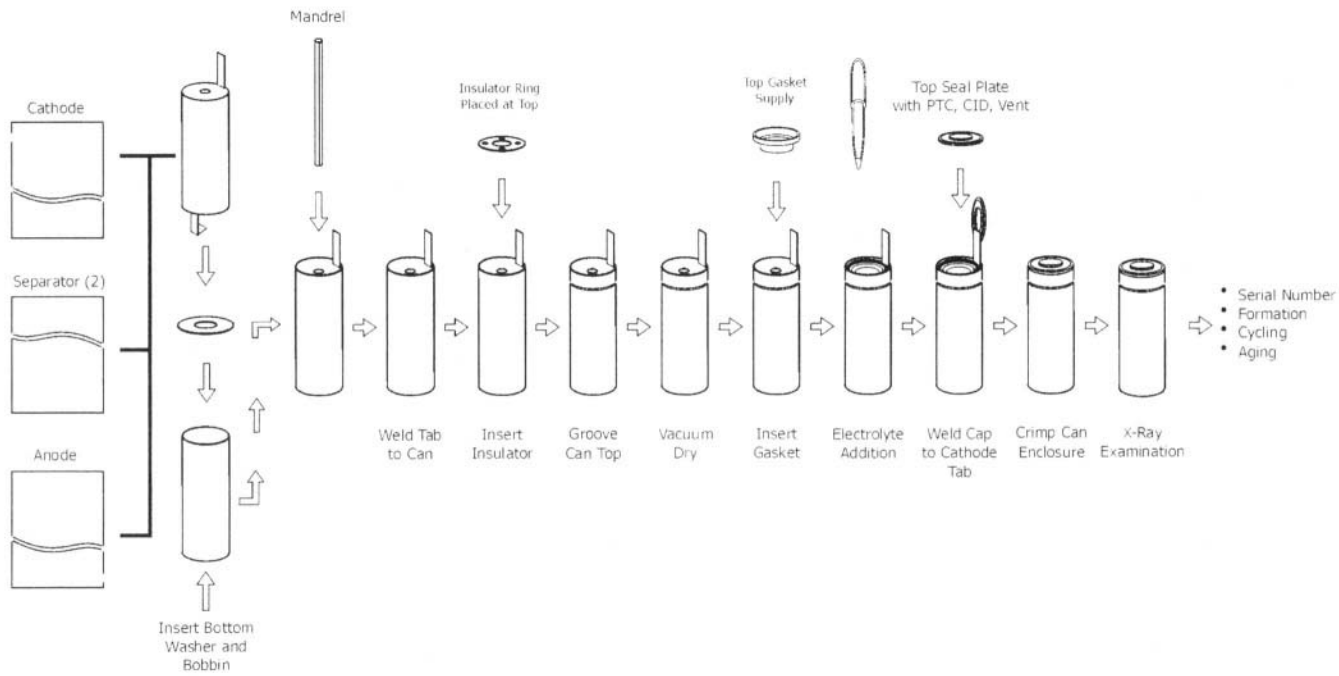
Figure 10. Stylized depiction of the assembly process for cylindrical Li-Ion cells. (Courtesy of Hohsen Corp.)

Cathode

Separator (2)

Anode

Insert Bobbin and Bottom Washer into Can

Can

Weld Tab to Can

Position Top Washer in Can

Twist Tab

Top Assembly PTC, CID, etc.

Weld Top Assembly To Tab

Position Cap in Cell

- Serial Number
- Formation
- Cycling
- Aging

X-Ray Examination

Seal Fill Tube

Electrolyte Addition

Vacuum Dry

Laser Weld Top Cap
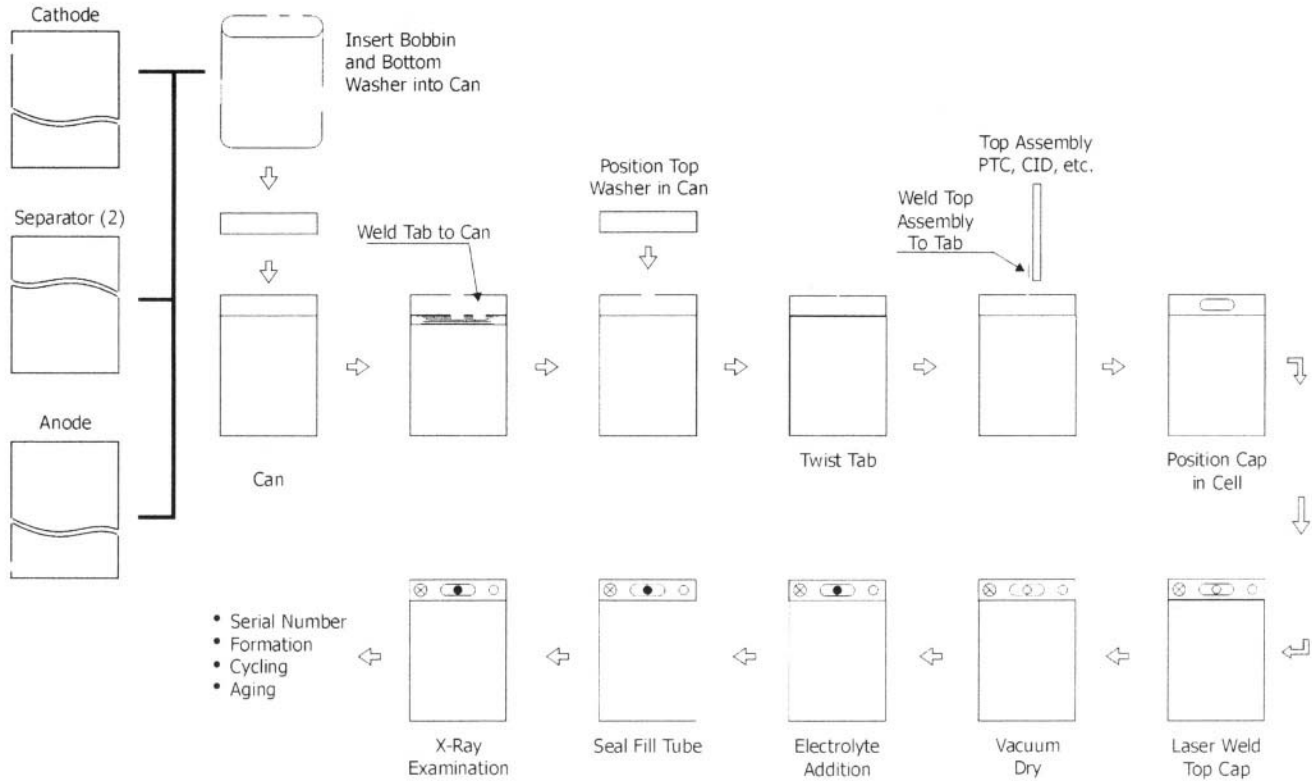
Figure 11. Stylized depiction of the assembly process for a prismatic Li-Ion cell (Courtesy of Hohsen)

6. LI-ION POLYMER BATTERIES (LIPB)

A depiction of the three types of cell construction, cylindrical and prismatic wound cells and the prismatic polymer cells in Figure 12 shows that polymer cells can use the full rectangular cavity for active materials. Recent activities in polymer battery technology have been reviewed recently [9–11]. All current Li-Ion polymer (LiPB) cells use "plasticized" or "gel" electrolytes for good room temperature conductivity. The organic liquid electrolyte is held by a polymer such as PVdF or acrylate. These polymer electrolyte films are dry to the touch but can contain 30% to 50% liquid solvent. Huang and Akridge [12] demonstrated that the Li-Ion and LiPB cells gave the same performance. This is expected as both have the same chemistry and theoretical energy storage capability with polymer and liquid electrolyte. This is to be expected as they both have the same chemistry. While present commercial LiPB cells have lower capacity, they are very early on the engineering improvement curve so that continued engineering improvements can be expected to produce equivalent performance in two or three years.

There is no generally accepted production process for LiPB cells. The first volume production of LiPB cells used a "hybrid" construction in which conventional Li-Ion processes for prismatic cells were employed with one minor modification. The polymer precursors and polymerization initiators were incorporated into the organic electrolyte and inserted into the cell during the normal electrolyte filling operation. After closing, a new step was added to heat the cell in the range of 60°C to 80°C. The heat activates the polymerization, which forms a plasticized polymer electrolyte *in situ.* As a result, the present production equipment could be used with a minimum of new investment. The normal "shut-down" separator is a part of the construction and gives this approach a greater safety factor in operation.

| Cylindrical | Prismatic | Prismatic |
| (liquid electrolyte) | (liquid electrolyte) | (polymer electrolyte) |
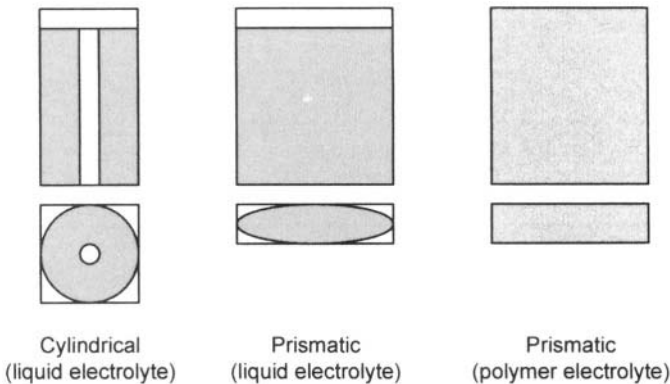
Figure 12. The effect of form factor on the volume utilization for the three common cell constructions. The LiPB soft packaging allows more efficient use of the available volume in the cell.

Brodd, et al [13] described the first production concept for manufacturing lithium polymer cells depicted in Figure 13. Although the facilities and processes were implemented, no significant production resulted. The light-weight metalized-polymer-film packaging concept shown in Figure 14 has been incorporated in polymer cell production. This gives LiPB cells a weight advantage over the conventional liquid electrolyte cells with heavy metal cases, as it is considerably lighter than the steel or aluminum cans used in regular cell constructions. Polymer constructions also permit thin format, large footprint batteries such as would fit in the bottom of a laptop computer, or a curved form to give a cellular phone an ergonomic fit. This soft packaging (as opposed to a metal can) is a key advantage for polymer cells. It results in lower cost, lower weight and freedom of footprint in cell designs. It also facilitates shorter design cycles in new product development. After heat-sealing, the sides are trimmed and folded to the required specification.

The first attempt to commercialize LiPB polymer cells were based on the technology developed by Bellcore Laboratories (now Telcordia) and referred to as the Bellcore process [14,15]. It has proven to be an elegant laboratory process but is difficult to implement in large-scale production. The basic element of polymer cell construction is the unit cell (bicell), shown in Figure 15. The real advantage of this type of cell fabrication is that the individual electrodes are internally bonded together to form an integral unit. No outside pressure from the cell container is required to maintain intimate contact between the electrodes. The internal bonding of the anode-separator-cathode eliminates the need to maintain stack pressure and strong metal cans as for the wound constructions of the liquid electrolyte cells. This gives the polymer cells less sensitivity to shock and vibration. Overall, the capital investment costs for LiPB cell production are lower than that for the liquid electrolyte counterpart.

Polymer cell manufacturing, depicted in Figure 16, starts with casting of the electrode stock, as described in the Coating section. The electrode films are cast onto a slip-sheet instead of the current collector foils as for the regular cylindrical and prismatic cell. The cast strips are calendared, slit to width, coiled onto a reel and fed to the bicell machine as for the wound construction. Cutting the electrode strips to length and automatically stacking after lamination forms the bicells. The bicell stack is laminated (heat-bonded) together with the expanded metal current collectors as depicted in Figure 15. This Bellcore process incorporates a plasticizer, such as dibutylphthalate (DBP), into the casting of the electrode stock for flexibility in handling. DPB must be removed before the first charge (formation) as DBP is electrochemically active and produces compounds that interfere with good cell operations. Expanded metal foil current collectors are used to facilitate the extraction process, rather than the solid foil used for the regular Li-Ion production.
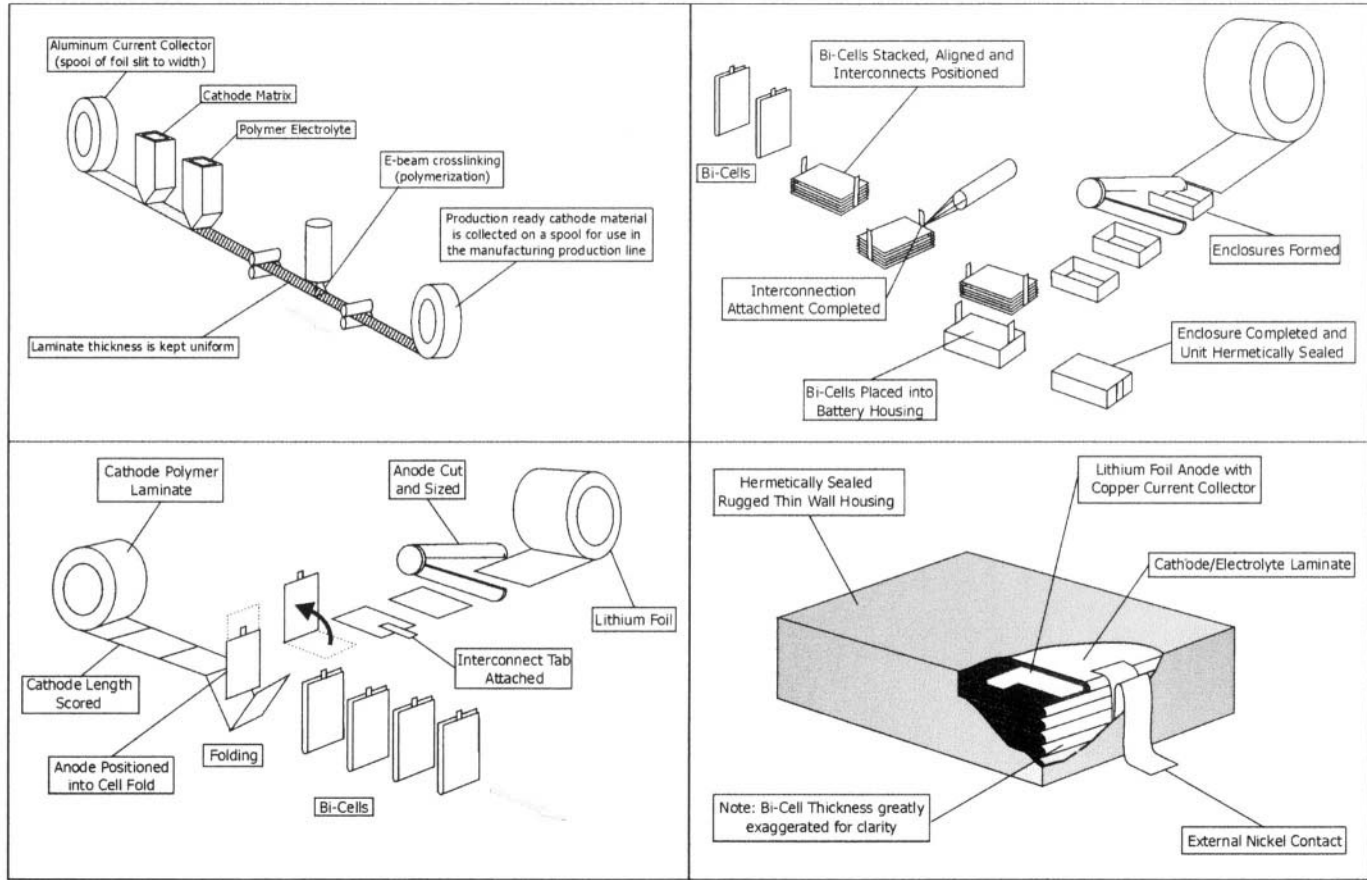
Figure 13. Production Process for Lithium Polymer Cells. (a) Coating Cathode onto Current collector, (b) Automated Bicell Assembly, (c) Stacking Bicells, Apply current collectors and Seal Cell, (d) Soft Packaging Cutaway.
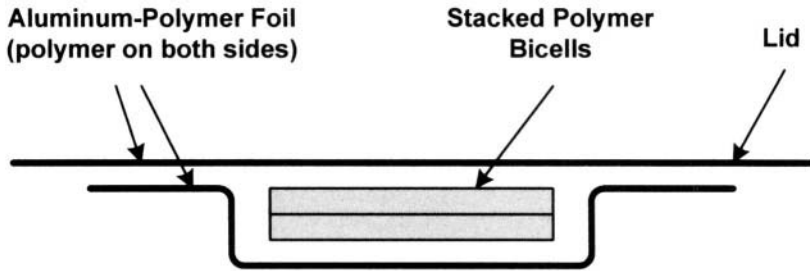
Figure14. Depiction of cold-formed soft polymer packaging with stacked bicell construction

After cell assembly and formation, the polymer cells undergo the same storage, voltage and impedance measurements, labeling, serial number application and selection criteria as all other Li-Ion cells. The soft-sided cell cases are more susceptible to internal gas generation and can "puff-up." As a result, polymer cells with the soft packaging may be re-evacuated after formation to remove the gases generated on formation and then resealed.
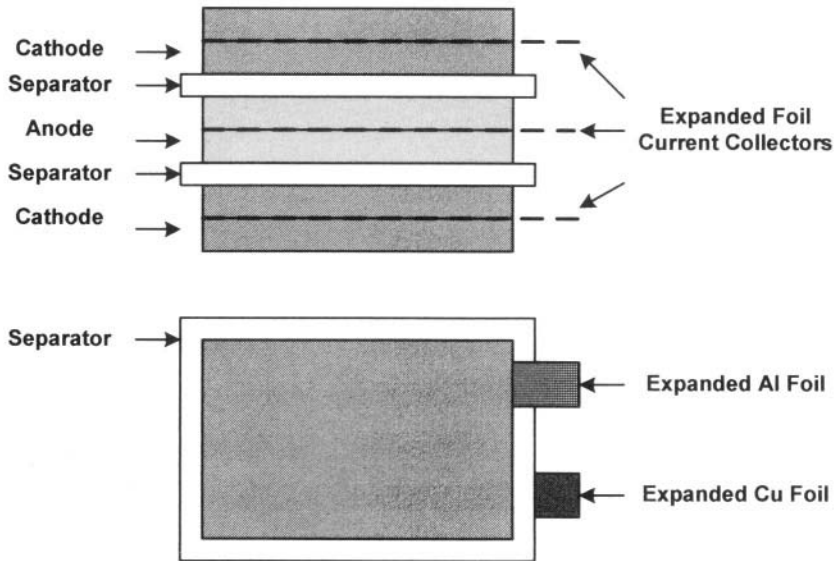
Figure 15. Bicell construction for polymer cells

Motorola, Polystor, Danionics, Philips and Sony have developed several other polymer-based LiPB systems. These are in various stages of commercial development but little is known about the production details. PolyStor [17,18] has initiated commercial production under a license for the Motorola technology. It uses a PVdF binder but eliminates the extraction step of the Bellcore process. This process can be adapted for the wound constructions as well as for the stacked flat plate constructions. Another technology has

been developed by Philips **Lithylene™,** in which polymer rivets replace the mechanical function of the metal can to hold the electrodes together [19]. The layers are assembled and holes cut through the bicell with a laser. The holes are filled with an inert polymer to bond the unit bicell construction together.
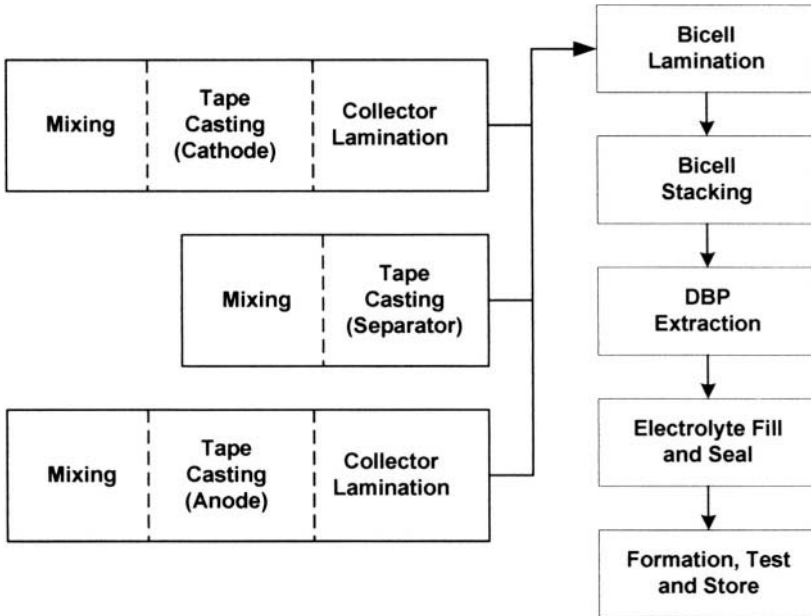
Figure 16. Schematic of Bellcore Process

7.0   SAFETY

The U.S. Department of Transportation classifies all Li-Ion and LiPB batteries as hazardous materials for shipping in the same category as lithium metal primary batteries [20]. It grants exceptions based on the amount of lithium intercalated into the anode (cell capacity) and the ability of the cells to pass specified tests. In the 1998 annual report of the DOE ad-hoc Working Group, two groups reported experimental evidence that Li-Ion anodes have significantly lowered reactivity against water compared to lithium metal [21]. Both groups independently reported essentially equiva-lent results regarding the lowered reactivity of the lithiated carbon anode materials with water. Compared to lithium metal, the reaction rates were ten to twenty times slower and only one half of the total intercalated lithium reacted with water.

There are several groups that regulate, or provide testing, to verify safe operation of Li-Ion cells under abuse conditions. In addition, the UL

Laboratories [22,23], the International Electrotechnic Commission [4] and the United Nations [24] have developed standardized safety testing procedures. These tests are designed to assure that cells are safe to ship and are resistant to typical abuse conditions such as internal shorting, overcharge, overdischarge, vibration, shock and temperature variations that may be encountered in normal transportation environments. Other organizations, International Maritime Organization (IMO), International Air Transport Association (IATA), International Civil Air Organization (ICOA) all follow the DOT and UN recommendation on the transport of Li-Ion batteries. The various safety tests must be carried out on a regular basis for all changes in cell design and for new cell constructions to establish an envelope for safe operation. Any serious accidents involving Li-Ion cells will impact all manufacturers, not just the one whose cell self-destructed.

8.0   REFERENCES

1. T. Nagaura and T. Tozawa, *Progress in Batteries and Solar Cells,* **10**, 218, 1991.
2. N. Miyazaki, *Update on Li-Ion Development,* Presentation at the **118**th International Seminar on Primary and Secondary Batteries, Ft. Lauderdale FL, March 5 -8, 2001.
3. H. Takeshita, *Global Battery Market Trend,* Presentation at the **17**th International Seminar on Primary and Secondary Batteries, Ft. Lauderdale FL, March 6 - 9, 2000.
4. *Secondary lithium cells and batteries for portable applications,* International Electrotechnic Commission, IEC 61960-1 and IEC 61960-2.
5. J. Newman, *Electrochemical Systems,* Prentice Hall, Englewood Cliffs, N.J., 1973.
6. M. Doyle and J. Newman, *J. Electrochem. Soc.* **143**, 1890, 1996.
7. H. Shi and R. J. Brodd, in *Progress in Batteries and Battery Materials,* JEC Press, Nagoya, Vol. 15, p21.
8. E. Cohen and E. Gutoff, *Modern Coating and Drying Technology,* Wiley-VCH, New York, 1992.
9. R. J. Brodd, W. Huang and J. R. Akridge, Macromolecular Symposium, T. Kajiyama, Ed. Wiley-VCH, New York, 2000, p229.
10. R. J. Brodd, in *Interfaces, Phenomena and Nanostructures in Lithium Batteries,* The Electrochemical Society, Pennington, NJ, PV 2000-36, pp 533.
11. R. J. Brodd, *Polymer Battery R&D in the U.S., 2001, J. Power Sources China,* in press.
12. W. Huang and J. Akridge, *ITE Letters,* **1**, 1999.
13. R. J. Brodd, J. T. Lundquist, J. L. Morris and D. R. Shackle, *New Rechargeable Polymer Battery System, Proc. Ninth Annual Battery Conference on Applications and Advances,* IEEE, Piscataway, NJ, 1994, p135.
14. A. S. Gozdz, J-M. Tarascon, O. S. Gebizlioglu, C. N. Schmutz, P. C. Warren and F. K. Shokooyi, in *Rechargeable Lithium and Lithium-Ion Batteries,* S. Megahed, B. M. Barnett and X. Xie, Eds. The Electrochemical Society, Pennington, NJ, PV94-28, p. 400, 1994

15. S. Gozdz, C. N. Schmutz, J. M. Tarascon and P. C. Warren, U.S. Patent 5,456,000, 1995
16. B. Lee, C. Yi, J. S. Kim and J. T. Kim, Presentation at the Korean Electrochemical Society Meeting, Seoul, Korea, October, 1999.
17. J. Kaschmitter, *Advanced Li-Ion Development,* Presentation at the 17th International Seminar on Primary and Secondary Batteries, Ft. Lauderdale FL, March 6-9, 2000.
18. R. Ochoa, *Li-Polymer Development at Motorola Energy systems Group,* Presentation at the 17th International Seminar on Primary and Secondary Batteries, Ft. Lauderdale FL, March 6-9, 2000.
19. H. Feil, *Philips **Lithylene™** Thin Battery Technology,* Presentation at the 18th International Seminar on Primary and Secondary Batteries, Ft. Lauderdale FL, March 5 - 8, 2000.
20. *Hazardous Materials Regulations,* Code of Federal Regulations, CFR173.185.
21. Meeting Summary, ad hoc Advanced Battery Readiness Working Group, March 4 - 5, 1998, National Renewable Energy Laboratory, Task AS015502, contract DE-AC36-83CH10093.
22. UL1640, *Lithium Batteries,* Underwriters Laboratories, Inc.
23. UL2054, *Household and Commercial Batteries,* Underwriters Laboratories, Inc.
24. *Recommendations on the Transport of Dangerous Goods,* Manual of Tests and Criteria, United Nations, New York, 1999

10

Low Voltage Lithium-Ion Cells

Bruno Scrosati

Department of Chemistry
University of Rome "La Sapienza"
00185 Rome
Italy

1.0   INTRODUCTION

Lithium ion batteries, based on a carbonaceous anode and a lithium metal oxide cathode, are high-energy power sources that are well established in the consumer electronics market. The lithium ion concept, however, can be extended to any electrode combination that assures a cyclic transfer of lithium ions across the cell. In general, a lithium ion cell can be considered as based on a lithium-rich $Li_yM_nY_m$ electrode and a lithium-accepting A_zB_w electrode. The electrochemical process is:

$$Li_yM_nY_m + A_zB_w \quad \Leftrightarrow \quad Li_{(y-x)}M_nY_m + Li_xA_zB_w \tag{1}$$

where x is the number of lithium equivalents that reversibly pass from the lithium-rich to the lithium-accepting electrode.

The feasibility of this concept dates back to the early 1980s, when it was first proposed by Armand [1] and Murphy [2] and then experimentally demonstrated by Lazzari and Scrosati [3]. In these first types of lithium ion, or as initially called, rocking chair batteries [1], the lithium rich negative electrode was $LiWO_2$ [3] or $Li_6Fe_2O_3$ [5] while the non-intercalated pristine, positive electrode was TiS_2 [3], WO_3 [5], NbS_2 [5] or V_2O_5 [5], respectively. The electrolyte used was a solution of a lithium salt, e.g., 1M $LiClO_4$, in an organic solvent, e.g., propylene carbonate, PC. The values of the open circuit voltage, OCV, of these early cells:

$LiWO_2$ / $LiClO_4$-PC/ TiS_2 OCV= 2.1V   **(2)**

$LiWO_2$ / $LiClO_4$-PC/ WO_3 OCV= 2.5V   **(3)**

$LiWO_2$ / $LiClO_4$-PC/ NbS_2 OCV= 2.0V   **(4)**

$Li_6Fe_2O_3$ / $LiClO_4$-PC/ TiS_2 OCV= 2.2V   **(5)**

$Li_6Fe_2O_3$ / $LiClO_4$-PC/ V_2O_5 OCV= 3.0V   **(6)**

fell between 2.0 and 3.0 V. These values are about 1V lower than that offered by "standard" lithium ion batteries, e.g., the 4V of the common $C/LiCoO_2$ electrode combination, this being attributed to the lower potential difference of the selected electrode couples. Figure 1 compares the potential ranges of various lithium intercalation electrodes. The potential are relative to the lithium metal and their range is reported in terms of x equivalents of intercalated lithium per mole, see [1]. The potential difference of the various electrode combinations depends on their relative position in the diagram. Clearly, the choice of graphite as anode appears appropriate, since its potential approaches that of the Li metal in its fully intercalated state, LiC_6. The replacement of graphite with any other A_zB_w lithium-accepting anode is a penalty in the cell potential, its value increasing as much as the given anode´s potential diverges from that of graphite.

Therefore, an obvious drawback of non-graphite lithium ion cells is their relatively low voltage. However, this is counterbalanced by various specific favorable aspects, including:

i) an operating voltage range within the stability window of the electrolyte (see Figure 1), thus preventing any decomposition phenomena with associated irreversible capacity losses, as those typically associated with graphite [7]; this advantage has important reflections in the reliability and safety of the cell;

ii) a wide choice of electrode materials, extending to compounds that are naturally abundant and non-toxic, with advantages in cost and environ-mental compatibility.
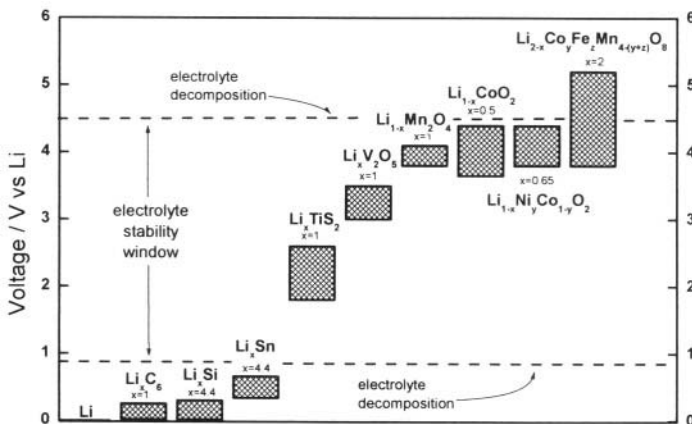
Figure 1. Potential ranges vs. Li of various $Li_{(1-x)}M_nY_m$ or $Li_xA_zB_w$ compounds reported in terms of x equivalents of intercalated lithium per mole. Derived from reference 6. Reproduced by permission of the Electrochemical Society, Inc.

This concept assumes further interest when passing form liquid electrolyte to polymer electrolyte lithium ion cells, i.e. on cells using a lithium ion conducting membrane as the electrolyte separator. These membranes, that are generally formed by trapping liquid solutions in a polymer matrix, are discussed in another chapter of this book. Common examples include the gelification in a polymer matrix (e.g., poly(acrylonitrile) PAN or poly(vinylidene fluoride) PVdF) of solutions of a lithium salt (e.g., $LiClO_4$ or $LiPF_6$) in an organic solvent mixture (e.g., ethylene carbonate-dimethyl carbonate, EC-DMC or ethylene carbonate-propylene carbonate, EC-PC). These gel-type membranes have a high conductivity, approaching that of the trapped liquid solutions and accordingly, they are presently exploited for the development of lithium ion polymer cells of practical interest [8], most of them based on the "conventional" graphite-lithium cobalt oxide electrode combination. However, these membranes are also suitable separators for new types of low-voltage, plastic-like batteries.

2.0   POLYMER CELLS

The first example of low-voltage, polymer batteries was reported in 1994 by Croce et. al. [9] who described a cell of the type:

$$TiS_2 / LiClO_4\text{-EC-PC-PAN} / LiCoO_2 \tag{7}$$

The cell uses a membrane formed by the gelification in a PAN matrix of a solution of $LiClO_4$ in the EC-PC mixture. This polymer electrolyte is simply noted as $LiClO_4$-EC-PC-PAN. The TiS_2 anode accepts Li^+ ions from the $LiCoO_2$ cathode during the charge process and releases them during the discharge process:

$$TiS_2 + LiCoO_2 \Leftrightarrow Li_xTiS_2 + Li_{(1-x)}CoO_2 \tag{8}$$
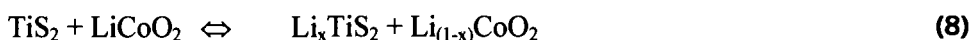
where x is the amount of lithium exchanged in the process.

The cell was assembled by contacting a thin film anode formed by chemical vapor deposition of TiS_2 on an aluminum foil substrate (thickness of *ca.* 5 μm) with a thin layer of the electrolyte (average thickness of *ca.* 50-100 μm) and finally, a cathode membrane formed by casting a slurry of $LiCoO_2$, acetylene black and PVC on a metal substrate (average thickness of *ca.* 50 μm). In the charged state, the cell assumes a voltage of 2.1V and can be repeatedly cycled with an exchange of x= ~1 per TiS_2 mole with the voltage profile shown in Figure 2.

The same type of electrode combination was extended by the authors to a cell using a polymer electrolyte based on the combination of a lithium perchlorate salt and a poly(ethylene oxide), PEO polymer [10]. The voltage response was similar to that above described. However, the cell suffered by the constraint of a high temperature operation due to the limits of the conductivity of the electrolyte.
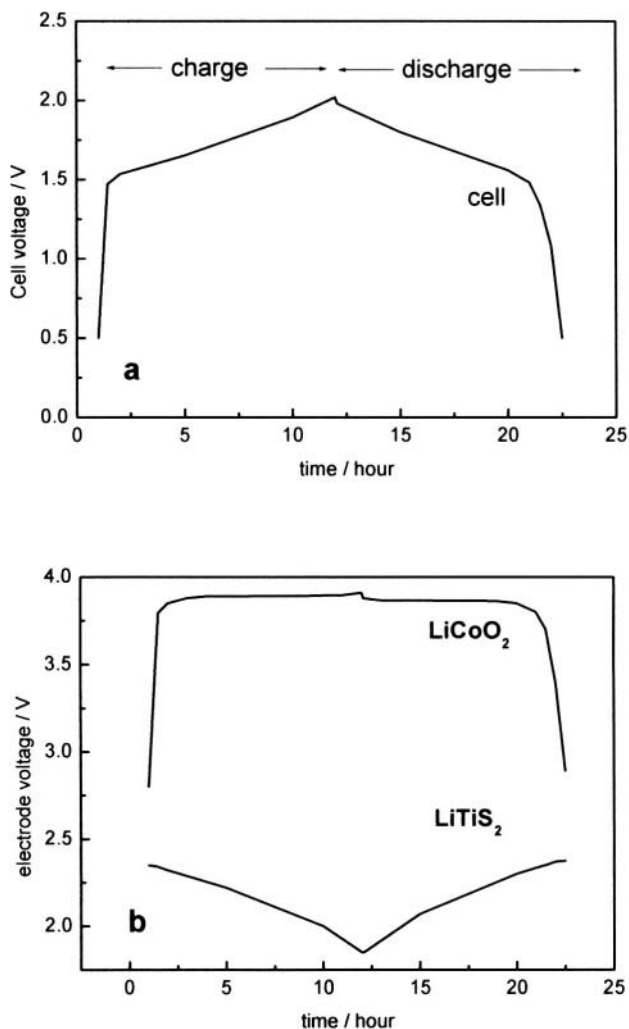
Figure 2. Typical charge-discharge cycle (a) and single-electrode polarization curves (b) of the Li$_x$TiS$_2$ /LiClO4-EC-PC-PAN/Li$_{(1-x)}$CoO$_2$ thin film cell at room temperature and at a 0.02 mA·cm^{-2} current density. Derived from reference 9. Reproduced by permission of the Electrochemical Society, Inc.

A more versatile, new type lithium ion polymer cell, proposed by Spila et. al [11], involved the combination of a polymer electrode, i.e. polypyrrole, pPy, a graphite, C electrode and a poly(methyl methacrylate) PMMA-based gel electrolyte:

This battery concept is interesting because it is based on an unusual electrode operation. The graphite electrode operates on the well known lithium intercalation-deintercalation process:

$$6C + x\ Li^+ + xe^- \Leftrightarrow Li_xC_6 \tag{10}$$

while at the same time, the pPy, $(C_4H_3N)_y$ electrode undergoes a doping-undoping process accompanied by the insertion–deinsertion of the electrolyte anion [12], i.e., the perchlorate ClO_4^- anion:

$$(C_4H_3N)_y + xClO_4^- \Leftrightarrow (C_4H_3N)_y\ (ClO_4^-)_x + xe^- \tag{11}$$
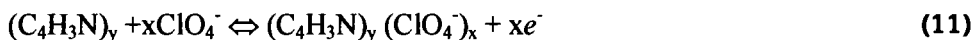
Accordingly, the overall process of the cell is:

$$6C + (C_4H_3N)_y + x\ Li^+ + xClO_4^- \Leftrightarrow (C_4H_3N)_y\ (ClO_4^-)_x + Li_xC_6 \tag{12}$$

involving the cycling transfer of both the lithium cation and the perchlorate anion. Accordingly, this new type of cell has been termed "dion" battery.

It should be noted that the electrochemical process of polypyrrole can be modified by pre-doping it with a large anion, such as the dodecylsulphate anion. In such a case, the large anions are somewhat immobilized in the polymer matrix, so that it is mainly the lithium ion that participates in the electrodic process [13]. Therefore, under these conditions the cell may operate on the cyclic transfer of lithium from the graphite electrode to the polypyrrole electrode, according to:

$$(C_4H_3N)_y\ (DS)_z + LiC_6 \Leftrightarrow (C_4H_3N)_y(DS)_z(Li)_x + Li_{(1-x)}C_6 \tag{13}$$
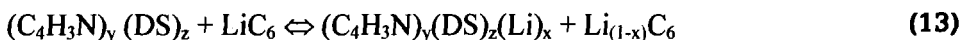
where DS = dodecylsulphate and z is its doping level. The polypyrrole cathode and the graphite anode operate in potential ranges of 2.5-3.3 V vs. Li and 0.17-0.02 V vs. Li, respectively, see Figure 3.

The C-pPy cell can be repeatedly cycled at high rates. Figure 4 illustrates a cycle response at 0.75 C rate and Figure 5 shows the Ragone plot of the cell. Considering the thin film, high surface area of the electrodes, the cell can be regarded as a combination between a "classical" battery and an "advanced" supercapacitor [14]. This property gives to the cells the unique capability of being used in the consumer electronic market as a plastic, low-cost disposable power source and in prospect, in the hybrid electric vehicle to provide the peak power requested for starting, acceleration and so on.

A similar concept was recently proposed by Amatucci et. al. [15] who reported on a nonaqueous asymmetric cell, i.e. on a new type of device having a high rate capability as a supercapacitor, as well as a reasonably high energy density as a battery. This was accomplished by combining a positive electrode capable of storing charge via a reversible, non faradaic or pseudocapacitive reactions of the electrolyte anions, with a negative electrode capable of sustaining a fast and reversible intercalation of the electrolyte lithium ions. A high surface area, synthetic PAN-based activated carbon was selected as the positive electrode. The choice of the negative electrode was dictated by the identification of the proper

Li intercalation compound, i.e. of a compound having electrochemical performance comparable with those of the positive electrode, such as a high rate capability and a long cycle-life. These features apply to $Li_4Ti_5O_{12}$, a compound exhibiting a two-phase lithium insertion-deinsertion process evolving around a flat 1.5V vs. Li plateau [16] with practically no changes in its crystal lattice [16,17]. This unique, high structural stability assures the required high-rate and long cycle-life requirements, especially when the $Li_4Ti_5O_{12}$ is prepared in a nanostructured form.
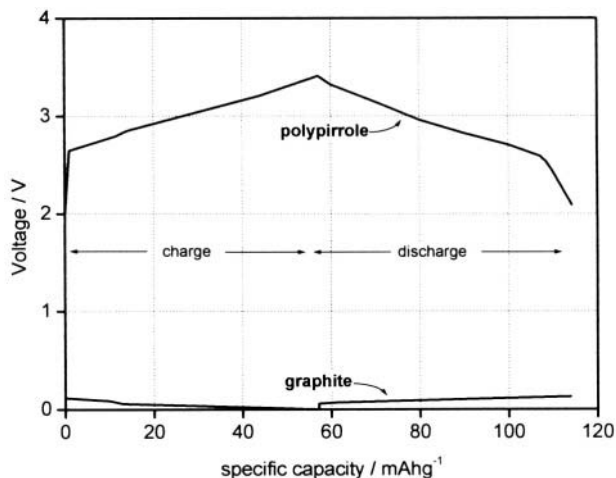
Figure 3. Typical charge–discharge cycle of the polypyrrole cathode and the graphite anode in a plastic C-pPy cell. Room temperature and 0.75 rate. Derived from reference 11. Reproduced by permission of Elsevier Science Ltd.

The asymmetric cell proposed by Amatucci et. al. (15) can be schematized as follows:

$Li_4Ti_5O_{12}$ / 1M LiPF$_6$ in EC-DMC (2:1 vol ratio)/ activated carbon   **(14)**
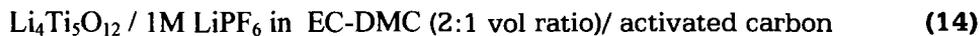
The electrochemical process of this cell involves the double layer charge-discharge (by PF_6^- ions) at the carbon positive electrode and the complementing Li^+ intercalation-deintercalation at the $Li_4Ti_5O_{12}$ negative electrode. Figure 6 shows the cycling response of the cell under 10C high cycling rate [15].

The authors also illustrated an overall plastic fabrication of the cell. For this purpose the electrodes were acetone cast as composite (PVdF-HFP binder, PC plasticizer, carbon black) thin film on an aluminum grid. The electrodes and the separator (a thin Celgard felt) were heat-laminated into a bicell configuration essentially consisting in two asymmetric cells sharing a common current collector. After removing the PC plasticizer by extraction in ether, the cell were activated by a 1.5M LiPF$_6$ acetonitrile electrolyte. Figure 7, shows

charge-discharge cycles of this plastic hybrid battery at various high rates. Under these conditions the energy density of the battery was reported to be of the order of **25 Wh·kg⁻¹** (15), i.e. a value considerably higher than that of nonaqueous supercapacitors.
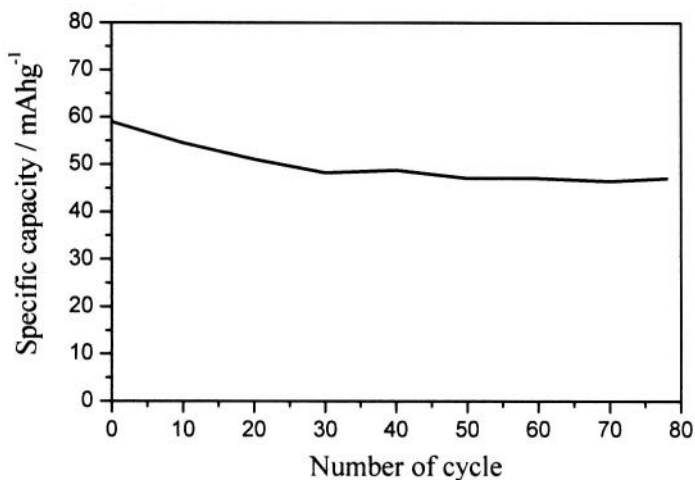
Figure 4. Cycling behavior of a plastic C-pPy cell. Room temperature and 0.75 rate. Derived from reference (11). Reproduced by permission of Elsevier Science Ltd.
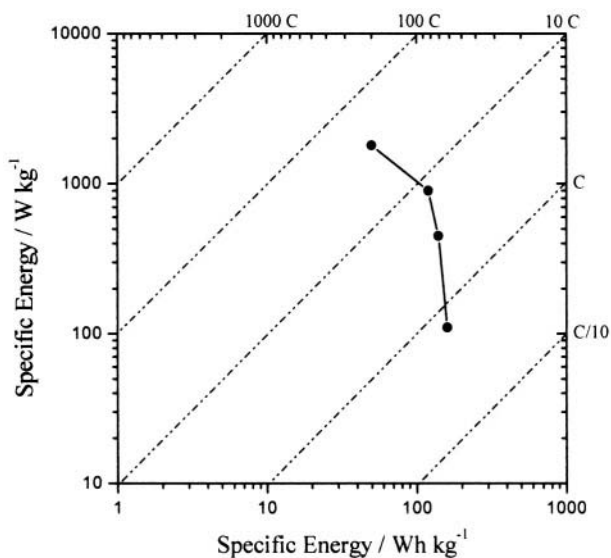
Figure 5. Ragone plot of a plastic C-pPy cell. Derived from reference (11). Reproduced by permission of Elsevier Science Ltd.
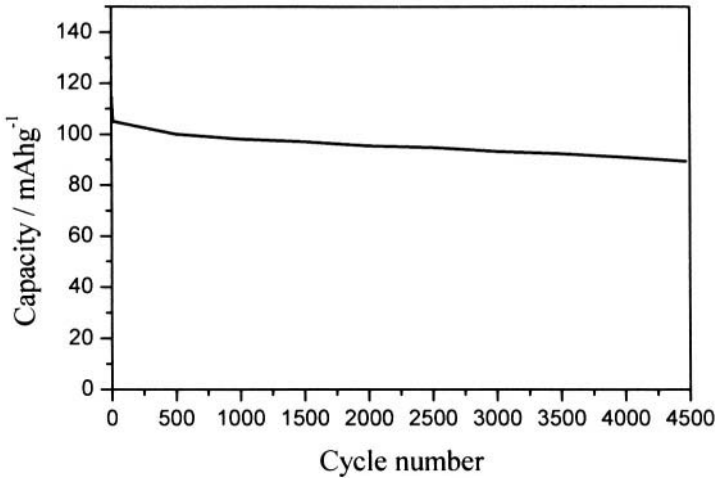
Figure 6. Cycling behavior of an activated carbon/Li₄Ti₅O₁₂ cell at 10C charge-discharge rates. Derived from reference (15). Reproduced by permission of the Electrochemical Society, Inc.
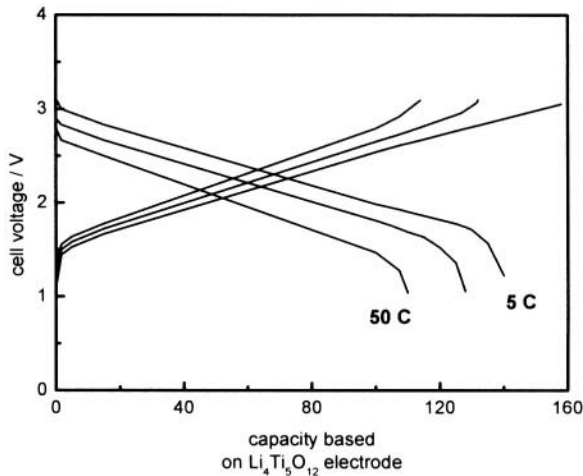
Figure 7. Charge-discharge profiles at various rates for the plastic activated carbon/ Li₄Ti₅O₁₂ battery. Derived from reference 15. Reproduced by permission of the Electrochemical Society, Inc.

3.0   CELLS WITH HIGH-VOLTAGE CATHODES

The structurally stable $Li_4Ti_5O_{12}$ has also been used as preferred anode material for other types of innovative lithium ion cells. An example is the cell based on the combination of $Li_4Ti_5O_{12}$ with a high voltage mixed spinel $Li_2Co_{0.4}Fe_{0.4}Mn_{3.2}O_8$ cathode [18]. In this case, the $Li_4Ti_5O_{12}$ anode was prepared

by dispersing stoichiometric amount of TiO_2 and $LiOH \cdot H_2O$ in hexane. After removing the solvent, the resulting powder was ground and calcinated at 800 °C for 24h under oxygen flux. [19] The synthesis of $Li_2Co_{0.4}Fe_{0.4}Mn_{3.2}O_8$ involved the mixing of water-acetic acid solutions of the precursors, i.e. lithium hydroxide, manganese acetate, cobalt and iron nitrate, followed by the evaporation to dryness and the annealing of the resulting powders [20].

For their use in the lithium ion cell, the two compounds were formed as film electrodes by blending them in mixture with a polyvynilidene fluoride (PVdF) binder (about 5 weight per cent) and a carbon (Super P) electronic conductor (about 5 weight per cent). The slurry was then cast onto an Al foil (in the cathode case) or onto a Cu foil (in the anode case) to form the desired electrode films. The complete Li-ion cell was assembled in a coin cell configuration by contacting in sequence the $Li_4Ti_5O_{12}$-based anode film, a felt separator disk soaked with the $LiPF_6$-PC solution and the $Li_2Co_{0.4}Fe_{0.4}Mn_{3.2}O_8$ - based cathode film.

Figure 8 shows the cyclic voltammmetry of the $Li_4Ti_5O_{12}$ single electrode. The current-voltage trend reflects the previously outlined fast kinetics associated with the 1.5V electrochemical process, which involves the highly reversible Li intercalation-deintercalation process into and out the stable host structure.
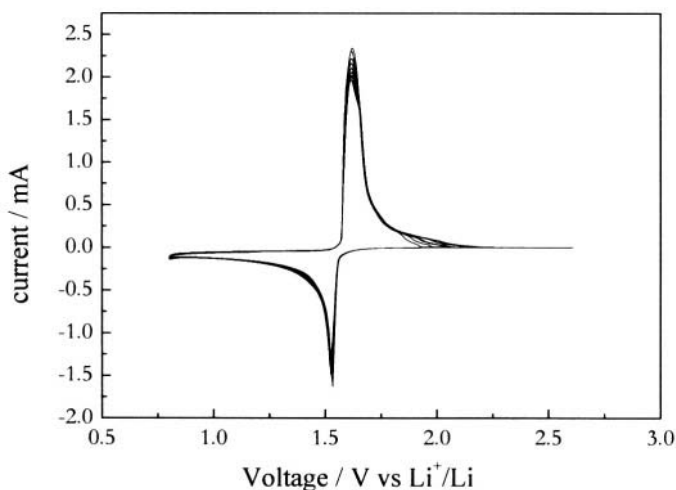
Figure 8. Cyclic voltammetry of the $Li_4Ti_5O_{12}$ electrode in a $LiPF_6$-PC cell. Counter and reference electrode:Li. Room temperature.Scan rate: 0.1 mV·s^{-1}

Figure 9 shows the cyclic voltammmetry of the $Li_2Co_{0.4}Fe_{0.4}Mn_{3.2}O_8$ electrode. The current-voltage trend demonstrates the two-step electrochemical process. As originally reported by West and co-workers [21] the first peak (probably associated to Mn redox) evolves around 4V and the

second around 5V vs Li. The peaks are highly reversible, suggesting fast kinetics for both processes. In addition, a good capacity, associated with the high potential region starting with cycle number 2, is clearly shown.

Figure 10 shows a typical constant current charge-discharge cycle of the complete $Li_4Ti_5O_{12}/LiPF_6$-$PC/Li_2Co_{0.4}Fe_{0.4}Mn_{3.2}O_8$ cell at the C/5 rate. The two well defined plateaus shown in Figure 9, which correspond to the two-step Li intercalation in the mixed spinel cathode, are clearly reproduced in this figure. The results of Figure 10 also confirm the promising operational features of this cell which cycles with a high reversibility and good capacity delivery around an average 3.5 V level.
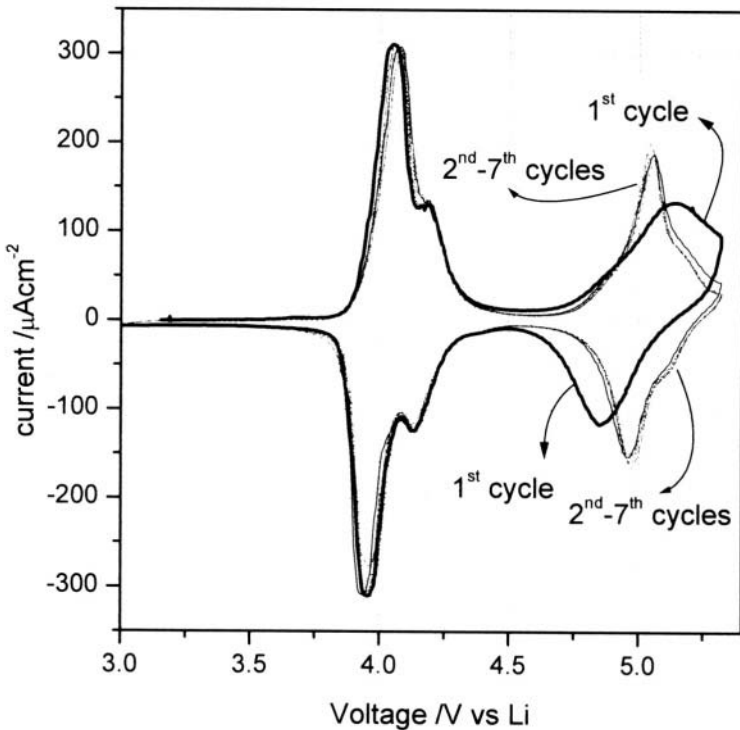
Figure 9. Cyclic voltammetry of the $Li_2Co_{0.4}Fe_{0.4}Mn_{3.2}O_8$ electrode in the $LiPF_6$-PC cell. Counter and reference electrode: Li. Scan rate: 0.1 $mV \cdot s^{-1}$ Room temperature. Derived from reference 18. Reproduced by permission of Elsevier Science.

This particular cell, in addition to novelty, presents some interesting aspects when compared with common lithium ion systems, i.e. cells based on the graphite/lithium cobalt oxide combination. For instance, there are various and relevant merits of replacing graphite anodes with $Li_4Ti_5O_{12}$. One is certainly is the already stressed, high structural stability during Li-intercalation-dintercalation, which helps assure long cell cycle-life. Another

advantage of $Li_4Ti_5O_{12}$ as anode material is, paradoxically, its relatively high operating voltage, which in fact allows its use within the stability window of the most common liquid electrolytes. This avoids any decomposition phenomena and/or the need of a protective passivation layer, as it is the case of graphite anodes. This "clean", electrochemical operation may have important reflections in cell reliability and safety.
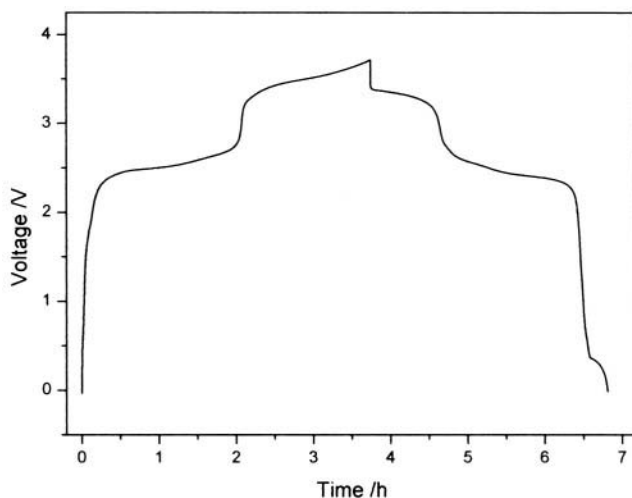
Figure 10. Typical charge-discharge cycle of a $Li_4Ti_5O_{12}$/$LiPF_6$-PC/$Li_2Co_{0.4}Fe_{0.4}Mn_{3.2}O_8$ cell at C/5 rate. Room temperature. Derived from reference 18. Reproduced by permission of Elsevier Science.

Drawbacks with respect to graphite are the lower specific capacity and the lower overall cell voltage. However, the latter may be overcome by compensating the 1.5 V $Li_4Ti_5O_{12}$ with a high voltage cathode, such as the $Li_2Co_{0.4}Fe_{0.4}Mn_{3.2}O_8$ cathode. Clearly, this combination requires the availability of an electrolyte solution having a stability window large enough to allow 5 V electrode operation.

The search for electrolytes having a high oxidation stability is a general goal in lithium battery technology. The reader should refer to Chapter 5, by Yamaki for a discussion of electrolyte solvents, Chapter 1, by Aurbach for a discussion of electrolyte reactivity with electrode materials, chapter 6, by Blomgren and Webber for an introduction of the use of ionic liquids in Li-ion batteries, Chapters 7 and 8, by Nishi and Scrosati, respectively for polymer electrolytes, and Chapters 11 by Salomon, et al. and Chapter 12, by Broussely for discussion of low and high temperature stability, respectively. A possible approach is that of selecting the salts and the solvents which are expected to be the most stable candidates among the known lithium cell electrolyte materials Presently, the choice is restricted to few cases and even these are not always completely satisfactory. An example is

the electrolyte solution prepared by dissolving $LiPF_6$ in propylene carbonate, PC.

Figure 11 shows a sweep voltammetry of a Super P carbon working electrode in a cell using the $LiPF_6$-PC electrolyte and metallic lithium as the reference and the counter electrode. The figure shows that the onset of the current, which is representative of the electrolyte decomposition, occurs over 5 V vs Li. Although somewhat influenced by the type of the working electrode, this value is high enough to allow to place the $LiPF_6$ -PC solution among reasonably stable electrolytes.

Even though it is more stable than other common lithium ion solutions, this electrolyte is still not totally suitable for use as a safe separator in the $Li_4Ti_5O_{12}/Li_2Co_{0.4}Fe_{0.4}Mn_{3.2}O_8$ cell. In fact, an examination of the profile of the charging cycle reveals that, starting at around 3.6 V, the cell voltage begins to slowly increase (see Figure 10). This can be attributed to a partial oxidation of either the solvent, the electrolyte salt or both [18]. Indeed for a cell voltage of 3.6 V, the potential at the $Li_2Co_{0.4}Fe_{0.4}Mn_{3.2}O_8$ electrode reaches values of the order 5.2 V vs. Li, i.e. beyond the stability of the electrolyte. Therefore, the characterization of electrolytes of increased stability towards oxidation remains one of the key research areas in this new types of Li-ion cells.
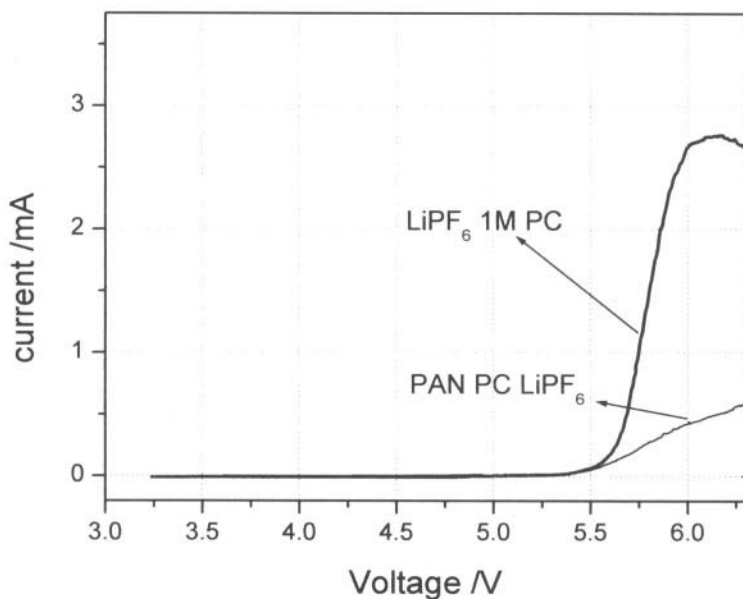
Figure 11. Sweep voltammetry of the Super P carbon electrode in a $LiPF_6$ -PC cell. Counter and reference electrode: Li. Scan rate: 0.1 $mV \cdot s^{-1}$. Room temperature. Derived from reference 18. Reproduced by permission of Elsevier Science.

4.0   CELLS WITH PHOSPHO-OLIVINE CATHODES

One way of improving the stability of a given liquid electrolyte is that of immobilizing it in a polymer matrix in order to form a gel-type membrane. Indeed, it is expected that interactions with the polymer backbone may somewhat modify the properties of the salt-solvent solution, including its electrochemical stability [22]. This is confirmed by Figure 12, which compares the sweep voltammetry of Super P carbon electrode in a $LiPF_6$-PC electrolyte and a $LiPF_6$-PC-PAN gel electrolyte. The higher stability of the latter is clearly shown.

A similarly high stability is also obtained with other types of gel electrolytes. Figure 13 shows the current-voltage curve of a working stainless-steel electrode swept in a cell using a $LiClO_4$-EC-PC-PVdF gel electrolyte membrane and a lithium metal counter electrode. The onset of the current, representative of the anodic breakdown voltage of the electrolyte, is of the order of 5.0 V vs. Li.

This stability value makes the $LiClO_4$-EC-PC-PVdF gel electrolyte a valid separator for the development of lithium ion polymer batteries of practical interest. An example has been provided by describing a new cell based on the combination of a $LiTi_2O_4$ anode and a $LiFePO_4$ cathode [23].
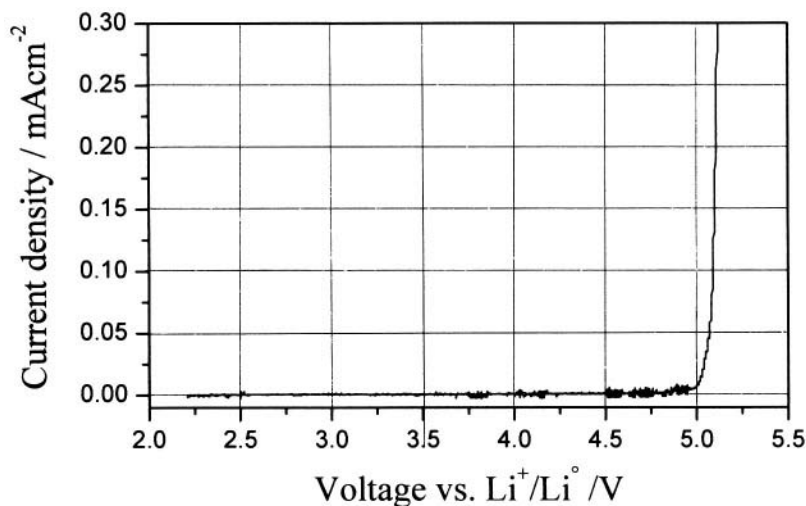
Figure 12. Sweep voltammetry of a stainless-steel electrode in a $LiClO_4$-EC-PC-PVdF gel polymer electrolyte cell. Room temperature. Counter electrode: Li. Scan rate: 0.1 mV·s^{-1}. Derived from reference 23. Reproduced by permission of Elsevier Science.
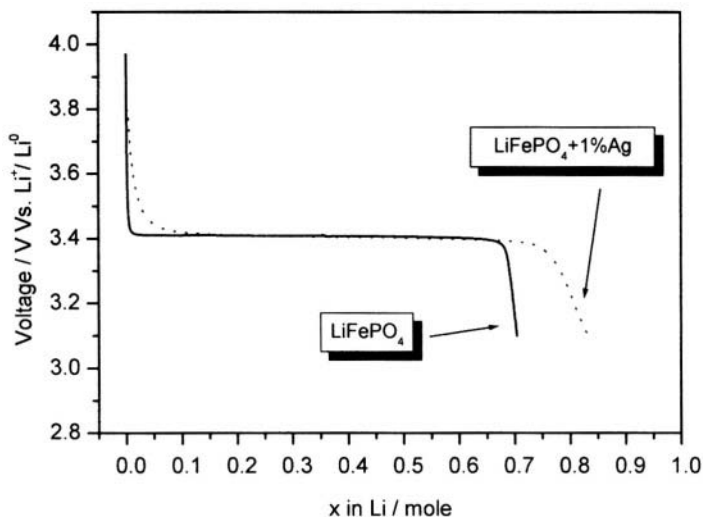
Figure 13. Discharge curves of a "standard" LiFePO₄ electrode and of a modified, Ag-added LiFePO₄ electrode at room temperature and at a C/10 rate. Li counter electrode. LiClO₄ EC-DEC(1:1) electrolyte.

The electrochemical and structural characteristics of one electrode, i.e. $Li_4Ti_5O_{12}$ and of its analogues, such as $LiTi_2O_4$, have been already discussed. The other electrode is the $LiFePO_4$ compound recently introduced Goodenough and co-workers [24]. This compound is attracting considerable attention as a new type of lithium ion cathode material due to the low cost and the environmental compatibility of its basic constituents. $LiFePO_4$ adopts the ordered olivine structure and is characterized by the following lithium extraction – insertion process:

$$LiFePO_4 \Leftrightarrow Li_{1-x}FePO_4 + xLi^+ + xe^- \tag{15}$$

where the maximum exchange of 1 mole of Li for formula unit (x=1) corresponds to a theoretical specific capacity of **170 mAh·g⁻¹**. Due to the occurrence of the above two-phase redox reaction, $LiFePO_4$ is characterized by flat discharge-charge curves evolving around 3.5V vs. Li.

An issue of this electrode is the increasing loss of capacity as the cycling rate increases, this being associated with the diffusion-controlled kinetics of the electrochemical process. These poor kinetics are due to the fact that the electrochemical reaction involves a first order transition from $LiFePO_4$ (tryphylite) to $FePO_4$ (heterosite), these two phases coexisting in single material particles. The associated lithium extraction process is accompanied by the movement of the interface between the two phases and a limit may be reached where the process becomes controlled by the diffusion of lithium across the relatively small free volume in the tryphylite framework [24]. In

addition, the electronic conductivity of $Li_{1-x}FePO_4$ progressively decreases as the value of x increases and this also contributes to limit the extent and the rate of the overall electrochemical process.

Ways to by-pass the above-mentioned kinetic limitations are to enhance its ionic/electronic conductivity by suitable preparation procedures. This strategy was first suggested by Armand and co-workers [25] who reported improvements in electrochemical kinetics by properly modifying the morphology of the $LiFePO_4$ powders, i.e. by the addition of an electronically conductive substance, e.g. low particle-size carbon, during the course of the synthesis. This approach has been followed by other authors [26,27]. Yamada et.al. [28] have shown that the control of the annealing temperature and thus, ultimately of the particle size, of $LiFePO_4$ is a crucial condition for assuring good electrochemical performance of this cathode material. Recently, it has been shown that the electrochemical kinetics of the $LiFePO_4$ electrode may also be improved by specifically designed preparation procedures that involve the dispersion of low particle size metal (copper or silver, respectively) powders during the sol-gel formation of the $LiFePO_4$ particles [29]. The basic idea is that these metal powders may act as nucleation sites for the growth of the $LiFePO_4$ particles, this helping in obtaining samples with low and uniform size, as well as in enhancing their overall electronic conductivity. Figure 14 compares the low rate discharge of a common $LiFePO_4$ electrode with that of a Ag-added $LiFePO_4$ electrode. The increase in capacity when passing from the standard to the modified electrode is clearly shown.
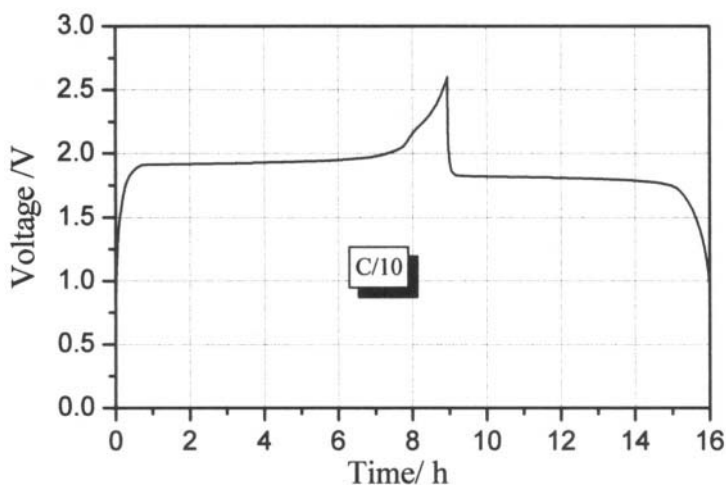
Figure 14. Galvanostatic charge-discharge cycle of the polymer $LiTi_2O_4/LiClO_4$-EC-PC-PVdF gel/ $LiFePO_4$ lithium-ion cell at room temperature and at C/10 rate. Derived from reference 23. Reproduced by permission of Elsevier Science.

The electrochemical process involves the exchange of lithium ions between the two electrodes, i.e.:

$$LiTi_2O_4 + x\ LiFePO_4 \Leftrightarrow Li_{1+x}Ti_2O_4 + x\ FePO_4 \quad \text{with } 0<x>1. \tag{16}$$

figure 15 shows a low-rate, charge-discharge cycle of the $LiTi_2O_4$/gel/ $LiFePO_4$ polymer cell at room temperature. The cycle evolves around 2 V as expected on the basis of the single electrode potentials, i.e. 1.5 V vs. Li for the $LiTi_2O_4$ anode and 3.5 V vs. Li for the $LiFePO_4$ cathode (24). To be noticed the very flat voltage profile resulting from the two-phase electrochemical reactions of both electrodes. Indeed, the cell operates with a very stable 2V voltage over the entire cycle with a capacity delivery of about $140\ mAh \cdot g^{-1}$ referred to the cathode.

Figure 16 shows the capacity delivered upon cycling under different cycling rates, i.e. C/10 for the first cycle and C/5 for the following cycles. The good cycling performance is associated to the special structural features of the two electrodes in the course of the lithium insertion-extraction process. The very small changes in the $LiTiO_2$ lattice have been already outlined. The $LiFePO_4$ olivine structure is quite robust and thus, not particularly affected by the evolving of the electrochemical process [24].

5.0   OTHER TYPES OF CELLS

Another interesting example of alternative lithium-ion cells is that associated with the combination of a tin oxide, SnO_2 anode with a $LiNi_{0.8}Co_{0.2}O_2$ cathode [30]. Considerable interest is presently devoted to crystalline and/or amorphous metal oxides [31], such as tin oxides, SnO_y [32,33], as alternative to graphite in lithium-ion batteries. These oxides operate via the formation and dissolution of a lithium alloy rather than by the lithium intercalation-deintercalation reaction which is characteristic of most carbonaceous anodes. In principle, the alloy-forming decomposition reaction offers a much higher specific capacity than that of carbon intercalation, i.e., $710\ Ah \cdot g^{-1}$ versus $370\ Ah \cdot g^{-1}$ in the case of $Li_{4.4}Sn$ versus LiC_6. However, metal electrodes such as Sn, cannot be repeatedly cycled due to the large volume changes which accompany alloy formation [34]. These changes, which may extend up to 300%, cause progressive cracking of the metal particles and thereby induce losses of contact between them. Therefore, although greatly appealing in terms of storage capacity, lithium alloy electrodes are difficult to use in practice. The replacement of the corresponding oxides as starting electrode materials has in part solved this problem. In fact, when an oxide, e.g. SnO_2, is negatively polarized in a lithium cell, it undergoes a first irreversible reaction:

$$SnO_2 + 4Li \Rightarrow Sn + 2Li_2O \tag{17}$$

which leads to metal Sn particles that remain finely dispersed in the Li_2O matrix. This produces a favorable morphology which facilitates the subsequent reversible lithium alloy formation process, e.g:

$$Sn + 4.4Li \Leftrightarrow Li_{4.4}Sn \qquad (18)$$

Apparently, the lithium oxide, by surrounding the tin particles, creates a sufficient amount of free volume to accommodate the mechanical stresses experienced by the metal during the alloy formation-decomposition process. This greatly improves the cycling performance albeit some capacity fade, due to the occurrence of tin particle aggregation, may still be observed over prolonged cycle tests. [31].

This "optimized" convertible oxide has been prepared in the form of a composite thin anode and assembled in a PAN-based gel electrolyte lithium-ion cell using a $LiNi_{0.8}Co_{0.2}O_2$ composite film cathode [30]. The overall process of this battery is expected to be articulated in two steps, i.e.:

$$SnO_2 + y\ LiNi_{0.8}Co_{0.2}O_2 \Rightarrow 2Li_2O + Sn + yLi_{(y-4)}Ni_{0.8}Co_{0.2}O_2 \qquad (19)$$

Followed by:

$$Sn + yLi_{(y-4)}\ Ni_{0.8}Co_{0.2}O_2 \Leftrightarrow Li_xSn + yLi_{y-(4+x)}\ Ni_{0.8}Co_{0.2}O_2 \qquad (20)$$
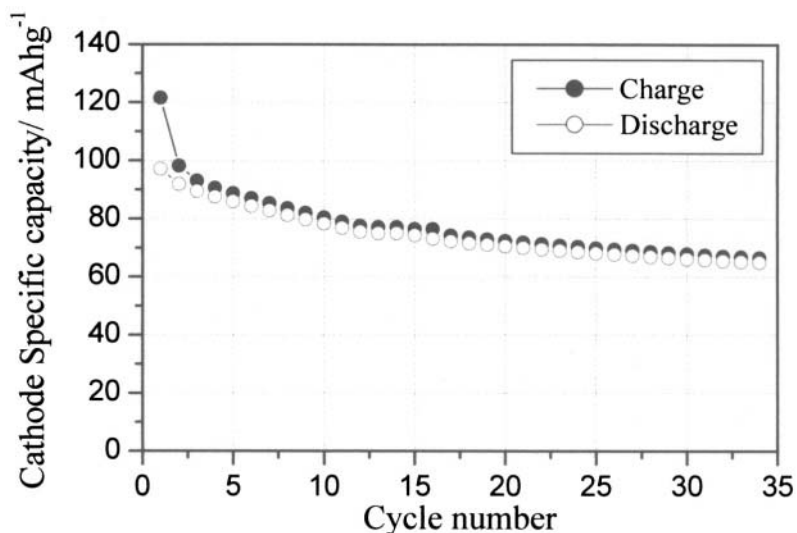
Figure 15. Capacity upon cycle number for the polymer $LiTi_2O_4/LiClO_4$-EC-PC-PVdF-gel/$LiFePO_4$ lithium-ion cell at room temperature. Rate: first cycle C/10; following cyclesC/5. Voltage limits: charge 2.5V; discharge 1.1 V. Derived from reference 23. Reproduced by permission of Elsevier Science.
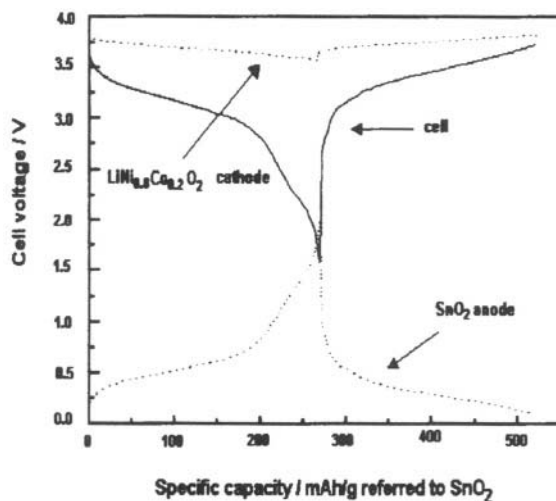
Figure 16. Typical voltage profile of a discharge-charge cycle of a SnO_2/ $LiClO_4$-EC-DMC-PAN/$LiNi_{0.8}Co_{0.2}O_2$ lithium-ion cell. The single anode and cathode voltage profiles are also shown. Room temperature, cycling rate: 0.25 mAcm^{-2}, lithium reference. The capacity is referred to the SnO_2 anode. Derived from reference 30. Reproduced by permission of the Electrochemical Society.

The SnO_2 electrode was firstly activated into Li_xSn by a single discharge-charge cycle in a cell with a Li anode, then removed and used as anode in combination with the $LiNi_{0.8}Co_{0.2}O_2$ cathode in a $LiClO_4$-EC-DMC-PAN gel electrolyte cell [30]. The latter cell was not optimized in terms of anode-to-cathode balance, but contained excess cathode capacity (y in equation [20]) in order to assure full cycling operation of the Li_xSn electrode.

Figure 16 shows the voltage profile of a typical discharge-charge cycle of this cell, along with anode and cathode voltage excursions [30,34] Clearly, the Li_xSn anode cycles with a trend comparable to that usually obtained in more-conventional liquid electrolyte cells (32, 34), delivering a reversible capacity of ~ 450 mAh·g^{-1}. This capacity level is retained upon further cycling albeit with a slightly progressive fade, this again being in similarity to the trend typically experienced in the parent liquid-electrolyte cells.

Finally, a new type of low-voltage lithium ion cell was recently reported by Baba and co-workers [36]. The cell used a thin film V_2O_5 negative electrode, a layer of lithium phosphorous oxynitride electrolyte (Lipon) and a thin film $LiMn_2O_4$ positive electrode. This solid state cell is light and compact and exhibits charge-discharge cycles characterized by sloping voltage profiles ranging between 0.3V and 3.5V.

6.0   CONCLUSION

This chapter has described various types of lithium ion batteries exploiting a variety of electrodes different from the established graphite anode and lithium cobalt oxide cathode. An apparent drawback of these batteries is their relatively low voltage. However, this is counterbalanced by various specific favorable aspects, including:

i)   the operating voltage range within the stability window of the electrolyte, thus preventing any decomposition phenomena with associated irreversible capacity losses, thus assuring high reliability and safety to the cell;

ii) the choice of electrode materials based on components that are naturally abundant and non-toxic, thus resulting in a low cost and environmentally compatible cell;

iii) the polymeric configuration of the cell that allows fabrication in the form of a very thin laminate that can be housed in a plastic container, thus allowing diversified, low-volume sizes.

iv) the availability of various cell structures including asymmetrical configurations, thus widening the applicability range into the high rate, capacitor-type market.

All these features concur to suggest that these cells can eventually find a profitable niche in the market, possibly as a thin-layer, plastic-like, disposable power source for 1.5V operating common consumer electronics.

7.0   ACKNOWLEDGEMENTS

8.0   REFERENCES

1.   M.Armand, in "Materials for Advanced Batteries", D.W. Murphy, J. Broadhead and B.C.H. Steele Eds, Plenum Press, New York, 145 1979.
2.   D.W. Murphy, F.J. Di Salvo, J. N. Carides and J.V. Waszczak, Mat. Res. Bull., **13,** 1395, 1978.
3.   M.Lazzari and B.Scrosati, *J.Electrochem. Soc.,* **127,** 773, 1980.
4.   M.Lazzari and B.Scrosati, U.S. Patent 4,464,447, Aug 7, 1984.
5.   B.Di Pietro, M.Patriarca and B.Scrosati, *J.Power Sources,* **8**, 289, 1982.
6.   B.Scrosati, *J.Electrochem. Soc.***139**, 2776, 1992
7.   S.Megahed and B.Scrosati, *J.Power Sources,* **51**, 79, 1994
8.   S.Panero and B.Scrosati, *J.Power Sources,* **90**, 13, 2000
9.   F. Croce, S.Passerini and B.Scrosati, *J.Electrochem. Soc.,* **141**, 1405, 1994.

10. F. Croce, S.Passerini, B.Scrosati, E.Plichta, W. Behl, M.Salomon, D. Schleich, *J.Power Sources,* **43-44**, 481, 1993.
11. E.Spila, S.Panero, B.Scrosati, *Electrochim. Acta,* **43**, 1651, 1998
12. B. Scrosati; in *Polymer electrodes " in "Solid State Electrochemistry"* P. G. Bruce Ed.,Cambridge University Press, 1995, pp. 229 – 263.
13. S.Panero, P.Prosperi and B.Scrosati, *Electrochim. Acta,* **37**, 419, 1992.
14. S.Panero, A.Clemente and E. Spila, *Solid State Ionics,* **86** , 1285,1996
15. G.C. Amatucci, F.Badway, A.Du Pasquier, T.Zheng, *J.Electrochem.Soc.,* **148**, A930, 2001
16. T.Ohzuku, A.Ueda, and N.Yamamoto, *J.Electrochem.Soc.,* **142**, 1431, 1995.
17. S.Panero, P.Reale, F.Ronci, B.Scrosati, V.Rossi Albertini and P.Perfetti, Phys.Chem. Chem. Phys., **3**, 845, 2001.
18. S.Panero, D.Satolli, M.Salomon and B.Scrosati, *Electrochem. Comm.,* **2**, 810, 2001.
19. S.Panero, P.Reale, F.Ronci, V.Rossi Albertini and B.Scrosati, *Ionics,* **6**, 461, 2000
20. F. Bonino, S.Panero, D.Satolli and B.Scrosati, *J.Power Sources,* **97-98**, 389, 2001
21. H.Kawai, M.Nagata, H.Tukamoto, A.R. West, J. *Power Sources* **81**, 67, 1999
22. D.Ostrovskii, A.Brodin, L.Torell, G.B.Appetecchi, B.Scrosati, *J.Chem.Phys,* **109**, 7618, 1999.
23. L.Persi, F.Croce and B.Scrosati, *Electrochem.Comm.,* in press
24. A.K.Padhi, K.S.Nanjundaswamy and J.B.Goodenough, *J.Electrochem.Soc.,* **144**, 1188, 1997.
25. N.Ravet, Y.Chouinard, J.F. Magnan, S.Besner, M.Gauthier and M. Armand, *J.Power Sources,* **97-98**, 503, 2001
26. P.P.Prosini, D.Zane, M.Pasquali, *Electrochim. Acta,* **46**, 3517, 2001
27. H.Huang, S-C.Yin andL.F.Nazar, **200**[th] ECS Meeting, S.Francisco, Sept. 2-7, 2001, Abstr. N.202
28. A.Yamada, S.C.Chung and K.Hinokuma, *J.Electrochem.Soc,* **148** , A224 2001.
29. F. Croce, A. D´Epifanio, J.Hassoun, A. Deptula, T.Olczac and B. Scrosati, *Electrochem and Solid State Lett,* in press
30. S.Panero, G.Savo, B. Scrosati, *Electrochemical and Solid State Letters,* **2**, 365, 1999.
31. LA. Courtney and J.R. Dahn, *J.Electrochem. Soc.,* **144**, 2045, 1997.
32. Y.Idota, T.Kubota, A. Matsufuji, Y. Maekawa, T. Miyasaka, *Science,* **276**, 1395, 1997.
33. T.Brousse,S.M.Lee, L. Pasquerau, D.Defives and D.M.Schleich, *Solid State Ionics,* **113-115**, 51, 1998.
34. R.A. Huggins , *Solid State Ionics,* **113-115**, 57, 1998.
35. G.B.Appetecchi, F.Croce, R.Marassi, S,.Panero,F.Ronci, G.Savo and B. Scrosati, *Solid State Ionics,* **143**, 73, 2001.
36. M.Baba, N.Kumagai, N.Fujita, K. Ohta, K.Nishidate, S. Komaba, H.Groult, D. Devilliers, B.Kaplin, *J. Power Sources,* **97-98**, 798, 2001.

11

Temperature Effects on Li-Ion Cell Performance

Mark Salomon
Hsiu-ping Lin
MaxPower, Inc.
220 Stahl Road
Harleysville, PA 19438
USA

Edward J. Plichta
Mary Hendrickson
US Army CECOM RDEC
Army Power Division
AMSEL-R2-AP-BA
Ft. Monmouth, NJ 07703-5601
USA

1.0   INTRODUCTION

This chapter constitutes a review on the effects of temperature on the performance of Li-ion cells. Since Li-ion cells is the overall theme of this chapter, by definition one is dealing only with rechargeable systems. The chapter is divided into several sections that address the general properties of electrolyte solutions for low to high temperatures $(-40 \leq t/°C \leq 80)$, the formulation of electrolyte solutions specifically designed for low to high temperature operation, the effect of temperature upon charging and discharging Li-ion cells including storage properties and the effects of additives. In addition, we recognize and briefly discuss the historical importance of studies involving metallic Li anodes leading to important developments in Li-ion cells. Many properties such as solvent effects on passivation, high and low temperature performance including storage, and additive effects on cycle life and delivered capacity were discovered during research on rechargeable Li metal-anode-based $(Li(m))$ cells.

The most important questions addressed in this chapter can be summarized as follows:

1. What are the factors involved in developing chemically and electro-chemically stable electrolyte solutions capable of high conductivities over a large temperature range $(e.g.\ for\ -40 \leq t/°C \leq 80)$?
2. Why do Li-ion cells sustain permanent capacity loss, in addition to the usual self-discharge, upon storage at high $(t/°C \geq 50)$ temperatures?

3. Why do Li-ion cells sustain permanent capacity loss, in addition to the usual self-discharge, upon cycling and storage at low temperatures (e.g. for $t/°C \leq -20$)?

While we do not have all the answers to these questions, we emphasize the nature and properties of electrolyte solutions, which directly effect electrochemical properties of Li-ion cells at all, temperatures. Limited background information on room temperature properties of non-aqueous electrolyte solution is covered in this chapter since many early studies, particularly on systems with metallic Li anodes, have played a major role in the development of Li-ion cells up to the present. More detailed reviews on the general properties of liquid and polymer-based electrolyte systems are given in separate chapters in this book. The literature on primary, secondary and tertiary *data* covering the effects of temperature on the behavior of Li-ion cells is enormous, and within the scope of this review, we focused on (*a*) the history of rechargeable Li-based based batteries leading to the present day *state-of-the-art,* and (*b*) using this historical background, where the current problems are and how present researches are addressing these problems. We are aware that many original and important studies are not cited in this review, and we apologize to our colleagues for this necessary oversight.

2.0   GENERAL BACKGROUND REVIEW

2.1   *Background on Performance Requirements*

Depending on the application, there are widely differing requirements for storage, performance and safety of Li-ion cells. For most commercial applications such as portable electronics, the temperature requirements are modest: operational temperature range between -0°C and 45°C, and capacity retention of not less than 85 % upon storage at around 50°C. For more advanced applications (military, electric vehicles and aerospace), the requirements for Li-ion cells are much more severe as summarized in Tables 1-3.

A survey of these problems and recent advances are covered in Sections 3.1 to 3.3 below. The key problems to be addressed in meeting and exceeding these various requirements are identification of the limiting cell components: the electrolyte, anode and/or cathode.

Table 1. Comparisons of performance objectives for military and commercial applications.

	Military (Portable Electronics)	Commercial (Electric Vehicles)
Energy Density: Wh/kg	120	180
Energy Density: Wh/L	229	360
Power Density: W/kg	175	≥ 50
Cycle Life	> 224	> 500
Temperature range	- 40 to +71 °C	Ambient to ~ 65°C

Table 2. Performance goals for space applications

	GEO	LEO	Terrestrial Missions
Capacity (Ah)	25 to 50	25 to 50	20
Operational Temperature Range ($t/°C$)	-5 to +30	-5 to +30	-100 to +65
Discharge Rate (for −5 °C to +30 °C) (for −40 °C to +65 °C) (for −100 °C to +65 °C)	C to C/20	C to C/2	C/5 to C C/? to ?
Cycle Life	≥ 1,500	≥ 30,000	≥ 500
DOD (depth of discharge) in %	80 (max)	≥ 40	100
Gravimetric Energy Density (Wh/kg)	> 100	> 100	> 100
Volumetric Energy Density (Wh/L)	≥ 250	≥ 250	≥ 250

Table 3. US Army MIL-PRF-49471B Specifications for Li-Ion Battery Storage (abridged)*

*After 300 cumulative hours, the battery must retain at least 85% of initial capacity

Cumulative Storage Time	Storage Temperature $t/°C$
36	36 to 40
42	44 to 63
93	69 to 71
60	41 to 55
69	35 to 39

2.2   *Properties of Pure and Mixed Electrolyte Solutions Relating to Conductivity*

Over the years, many interesting reviews have been published on the conductivities and properties relating to conductivities of non-aqueous electrolyte solutions [e.g. 1-4]. While a majority of studies have focused on low temperature behavior, a few report conductivity data up to temperatures up to around 80 °C [e.g. see 2-5]. As shown below, it is now common knowledge that electrolyte solutions with acceptable low temperature conductivities (10^{-4} to 10^{-3} S·cm^{-1}) can be formulated, but high conductivities do not translate into redox stability at the anode and cathode materials of Li-ion cells. A list of selected aprotic solvents found useful in Li-ion cell development is given in Table 4. The important properties of dielectric constant and viscosity are often used as guides to formulate highly conductive solutions, but the relationship between these two properties is often complex and not subject to "theoretical" prediction, but more often are optimized by "trial and error" investigations. For example, a solvent with a high dielectric constant such as PC is, on this basis,

predicted to exhibit high solubilities towards Li salts, and minimum or negligible ion association, and as a consequence, high conductivities. On the other hand, solvents such as MF, MA, 2MeTHF that have very low dielectric constants (see Table 4) would lead one to expect that ion-association is very high and consequently ionic conductivities would be very low. For example, Table 5 lists the ion association constants for $LiAsF_6$, $LiPF_6$ and $LiN(SO_2CF_3)_2$ in MF, MA, PC and 2MeTHF. In spite of the high association constants of salts in MF and MA, conductivities of their solutions are significantly higher than corresponding conductivities in PC solutions as shown in Figure 1.
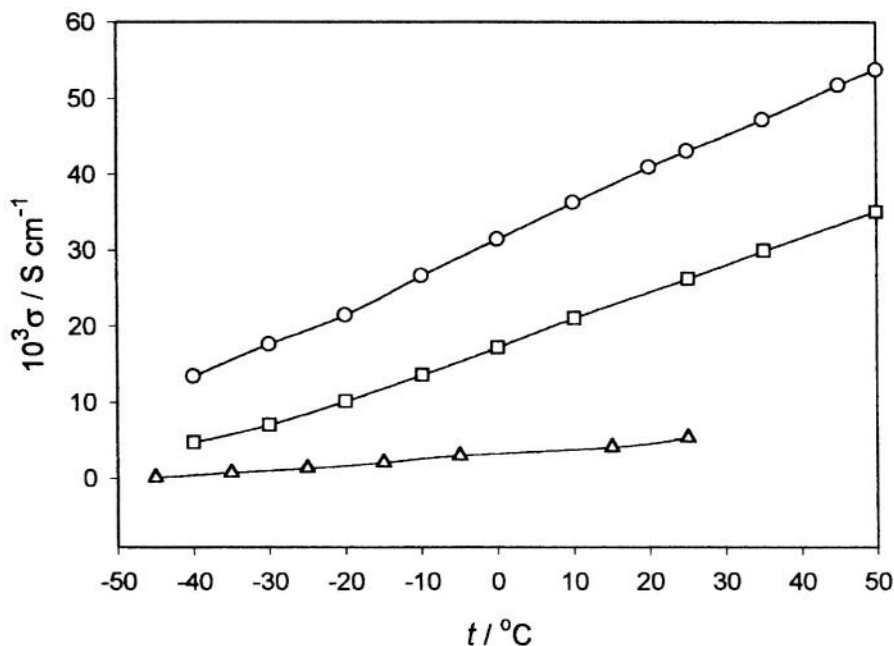
Figure 1. Temperature dependence of selected electrolytes in MF, MA and PC.

O- 2.0 mole dm^{-3} $LiAsF_6$ + 0.4 mol dm^{-3} $LiBF_4$ in MF [15].[a]
□- 2.0 mol dm^{-3} $LiAsF_6$ in MA [12].[a]
Δ- 0.891 mol kg^{-1} $LiPF_6$ in PC [9].[b]
[a]Mol dm^{-3} units based on solutions prepared at 25°C.
[b]Data for 1 mol dm^{-3} $LiClO_4$-PC solutions from -40°C to 60°C [15] overlap the curve for $LiPF_6$.

It is therefore clear that the dielectric constant of a solvent is not the best criteria to be used in formulating an electrolyte capable of high conductivities over a large temperature range. It is also clear that, to a point (e.g. solutions in 2MeTHF are extremely low in conductivity due to extraordinary ion association as seen in Table 5), viscosity also plays a major role in governing solution conductivities. As an example, Figure 2 compares the viscosities of $LiAsF_6$ in MF and PC as a function of temperature at 25°C. In PC solutions where the concentration of $LiAsF_6$ is 1.5 mol·dm^{-3}, the viscosity is already high at 20.7 cP and

subsequently increases rapidly reaching a value of 412 cP at 3.0 mol·dm^{-3}. For LiAsF$_6$ in MF, the viscosity at 1.5 mol·dm^{-3} is 0.978 cP, and at 3.0 mol·dm^{-3}, the viscosity is 3.27 cP. At -50 °C, the viscosity of a 2.0 mol·dm^{-3} LiAsF$_6$ + 0.4 mol·dm^{-3} LiBF$_4$ solution in MF is 7.42 cP at which point the solution conductivity is 0.00978 S·cm^{-1} [16]. In view of the known reactivity of solvents such as MF and THF, the accepted solution to the development of stable and conductive electrolyte solutions is the use of solvent mixtures and the introduction of stable electrolytes and small amounts of either inorganic or organic additives to improve the redox stability of the solutions as well as to improve the stability of the active electrode materials themselves. Both approaches are discussed below.

A number of early studies on binary mixtures of solvents such as γ-BL, PC, DME, and THF have demonstrated that the conductivities of LiClO$_4$, LiAsF$_6$ and LiPF$_6$ exhibit maxima greatly exceeding the conductivities in the pure solvents [e.g. 10, 17-20]. Again, it is the viscosity effect that plays a major role in this effect. These studies show that the value of the dielectric constant approximately follows ideal mixing rules, but that the effect of solvent composition upon viscosity typically exhibits significant negative deviations from ideality. An example of this latter effect is shown in Figure 3 for PC-DME mixtures as a function of temperature from [1].
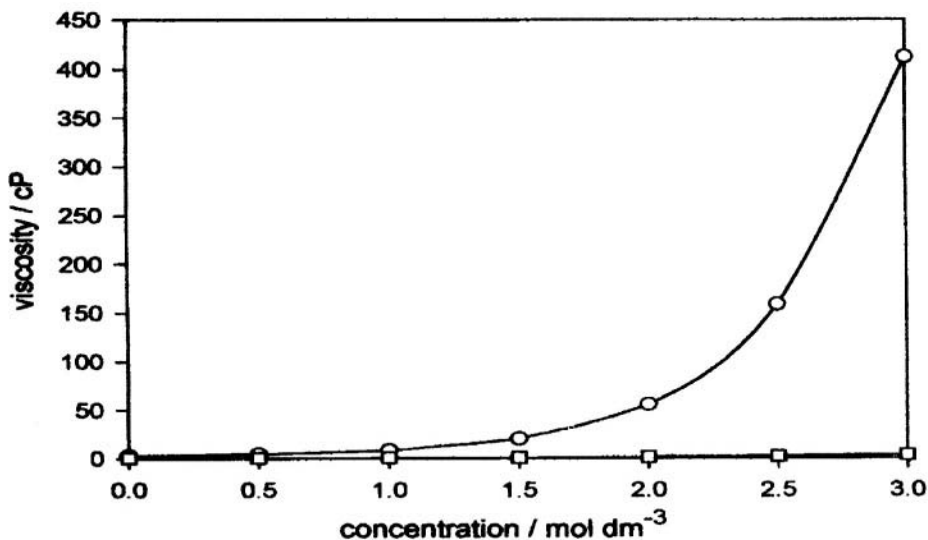
Figure 2. Comparisons of viscosities of LiAsF$_6$ solutions in MF and PC at 25°C. Derived from data in Reference 5.

O – PC [] - MF

Table 4. Physical Properties of Selected Organic Liquids in Order of Increasing Dielectric Constant

(All data refer to 25°C unless noted otherwise)

Solvent	Formula	ε	η/cP	FP/°C	BP/°C
Toluene (tol)	C_7H_8	2.379	0.552	-95	110.6
Ethylmethyl carbonate (EMC)	$CH_3OC(O)OCH_2CH_3$	2.4	0.65	-55	107
Propylmethyl carbonate (PMC)	$CH_3OC(O)0CH_2CH_2CH_3$	2.8	~0.75	-43	131
Diethyl carbonate (DEC)	$(CH_3CH_2O)_2C=O$	2.82	0.748	-43.0	126.8
Dimethyl carbonate (DMC)	$(CH_3O)_2C=O$	3.12	0.585	0.5	90
Methyl butyrate (MB, 20°C)	$CH_3CH_2CH_2COOCH_3$	5.5	0.64	-84	103
n-Propyl acetate (PA)	$CH_3C(O)OCH_2CH_2CH_3$	6.002	0.551	-95.0	101.5
Ethyl acetate (EA)	$CH_3C(O)OCH_2CH_3$	6.02	0.426	-83.6	77.1
Methyl propionate (MP)	$CH_3CH_2C(O)OCH_3$	6.2	0.43	-88	79
Methyl acetate (MA)	$CH_3C(O)OCH_3$	6.67	0.364	-98.05	56.9
4-Methyl-1,3-dioxolane (4MeDOL) ($C_4H_8O_2$)		6.8	0.6	-125	85
2-Methyltetrahydrofuran (2MeTHF) ($C_5H_{10}O$)		6.97	0.47	-137.2	79.9
1,2 Dimethoxyethane (DME)	$CH_3CH_2CH_2OCH_3$	7.07	.407	-58	84.5
Methyl formate (MF) ($C_2H_4O_2$)		8.90	0.328	-99.0	31.75
Dichloromethane (DCM)	CH_2Cl_2	8.93	0.410	-94.9	39.6
γ-Butyrolactone (γ-BL) ($C_4H_6O_2$)		41.77	1.727	-43.4	202
Propylene carbonate (PC) ($C_4H_6O_3$)		64.92	2.53	-49	241
Ethylene carbonate (EC, 40°C) ($C_3H_4O_3$)		89.6	1.85	36.4	248
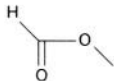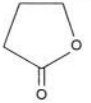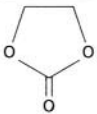
Table 5. Ion association constants, K_a, of selected salts in MF, MA, PC and 2MeTHF at 25°C

Solvent	Salt	$K_a/mol^{-1} dm^3$	Reference
MF	LiAsF$_6$	$4.8 \cdot 10^4$	6
MF	LiN(SO$_2$CF$_3$)$_2$	$2.3 \cdot 10^4$	12
MA	LiAsF$_6$	$1 \cdot 10^6$	7, 8
PC	LiAsF$_6$	~0 to 1	9-11
PC	LiPF$_6$	~0 to 2	11
PC	LiN(SO$_2$CF$_3$)$_2$	~0	12
2MeTHF	LiAsF$_6$	$2.5 \cdot 10^7$	13
2MeTHF	LiPF$_6$	$3.3 \cdot 10^7$	14
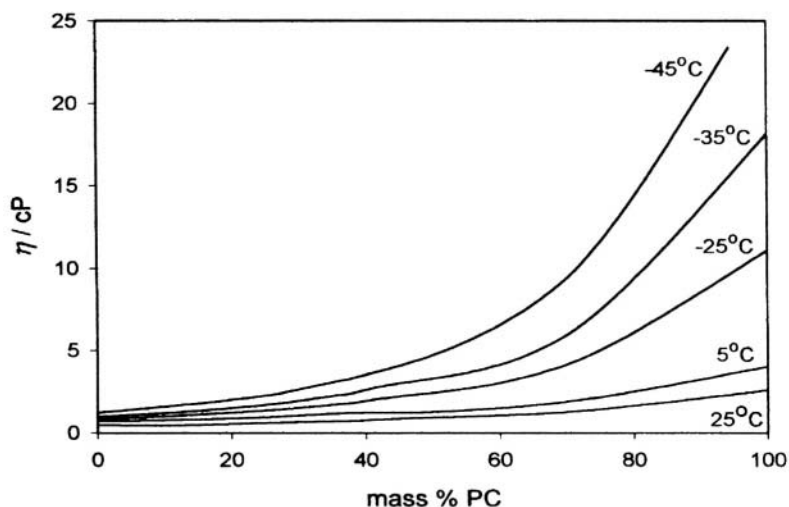
Figure 3. Viscosities in binary mixtures of PC and DME as a function of temperature. Derived from data in reference 1.

As will be discussed below, alkyl and cyclic carbonate solvents are the most important components in present day formulations of electrolyte solutions for Li-ion batteries. Thus a brief discussion on their basic properties relating to dielectric and viscosity properties, particularly when used as a major component in mixed solvents, is of interest. Dramatic differences in dielectric properties of alkyl carbonates arise from structural differences. The donor number of DMC (structure I) = 15.1, $\varepsilon = 3.12$, and its dipole moment $\mu = 0.9$. DEC has a similar structure (II) and donor number, and dielectric and viscosity properties similar to DMC (see Table 4).

I   II

Now consider both PC and EC (structures III and IV, respectively)

III   IV
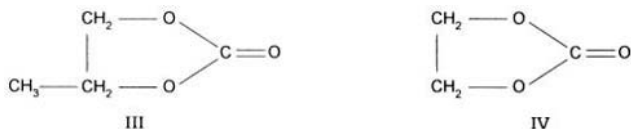
that have similar donor numbers of 15.1 for PC and 16.4 for EC, but have much higher relative dielectric constants and dipole moments. The reason why DMC and DEC have such low dielectric constants and dipole moments is due to a *trans* configuration of the O-R alkoxy groups with respect to the carbonyl group which results in partial nullification of the dipole vectors: in fact ultrasonic relaxation spectra have identified the *trans-to-cis* equilibrium in these solvents [21]. The cyclic nature of PC and EC **preclude** a *trans* structure, which results in their highly polar character and hence high *relative* dielectric constants. When solvents are mixed, the result can influence the aggregation properties of *trans-cis* molar ratios resulting in a departure of the mixed solvent from those properties based on ideal mixing rules. For the binary mixtures discussed above, the low frequency dielectric properties (i.e. the static permittivity or relative dielectric constant) appears to be approximately additive. On the other hand, the viscosities of binary mixtures of aprotic solvents almost universally exhibit large negative deviations from ideality as, for example, shown in Figure 3. Qualitatively, the adherence of ε and departure of η from ideal mixing can be attributed to the breakdown of solvent structure combined with aggregation of one component. For example, Barthel and Feuerlein [19] found that in the binary PC/DME system, relaxation times for both components follow the Debye equation relating the relaxation time, τ, to η only for short relaxation times and at low PC concentrations. At long relaxation times, and as PC is added to the mixture, the $\tau - \eta$ relation for PC becomes non-linear indicating aggregation of PC molecules (i.e. the "structure breaking" effect). The overall effect of large negative deviations of η from ideality is to contribute to the "synergistic" effect of conductivities of lithium salts in solvents mixtures. These concepts originally discovered for binary solvent mixtures are of course applicable to ternary and quaternary mixed solvents and constitute one of the bases for successful development of more stable electrolyte solutions as discussed below.   That is, the careful formulation of mixed solvents optimizing both the viscosity and dielectric constant of the mixture in combination with a stable electrolyte has indeed resulted in complex electrolyte solutions capable of exhibiting conductivities of 10^{-4} to 10^{-2} S/cm over the temperature range of -40°C to 80°C.

2.3   *Electrolytes*

The search for a stable and environmentally friendly lithium electrolyte has been the focus of much research in recent years as reviewed by Dominey [3] and, more recently, by Heider, Blomgren and Webber in this book, and thus our discussions here will be brief. Due to solubility limitations with salts with such as CH_3COOLi, LiF, and LiCl, initial studies largely focused on $LiClO_4$, $LiAsF_6$, $LiBF_4$ and $LiSO_3CF_3$ (lithium triflate), but due to safety and environmental concerns ($LiClO_4$ and $LiAsF_6$) and low conductivities ($LiBF_4$ and $LiSO_3CF_3$), there is continuing extensive research on developing new electrolytes. Electrolytes presently finding increased use in various Li-ion cells are $LiPF_6$ and lithium imide (lithium bis(trifluorosulfonyl)imide) first prepared by Armand [22]. The methide salt LiMe, $LiC(SO_2CF_3)_3$ (lithium tris(trifluorosulfonyl)methide), introduced by Dominey [23] has important properties (high thermal and electrochemical stability) but has found limited application due to its unavailability on a commercial basis. When it is made available to the electrochemical R&D community, this salt will undoubtedly undergo extensive studies for use in Li-ion cells over a very wide temperature range. The present standard electrolyte for Li-ion cells is $LiPF_6$, but this salt suffers from many problems. It is well know that the solid decomposes at around 30°C [24], and that in solution, $LiPF_6$ decomposes at around 80 - 85°C [25] (or lower) which is problematic when Li-ion batteries are discharged at high rates or stored at high temperatures. Figure 4 compares the results of thermogravimetric analyses for selected salts based on the data of Sasaki et al. [26]. These results clearly show that the most thermally stable salts are the imide, triflate and perchlorate (the methide salt was shown to be thermally stable to around 350°C [23]).

In addition to the poor thermal stability of $LiPF_6$, this salt is known to react with trace quantities of water according to [27]

$$LiPF_6 + H_2O \rightarrow LiF + POF_3 + 2HF \tag{1}$$

The existence of HF in solution raises the possibility of the reduction of H^+ forming H_2, and indeed H_2 has been found to be the main gaseous product during the first few cycles in Li-ion cells [38]. $LiPF_6$ is also known to be in equilibrium with PF_5 according to [25]

$$LiPF_6 \rightleftharpoons LiF + PF_5 \tag{2}$$

Sloop et al. also demonstrated that PF_5 is the active reagent in the reaction with the solvent (a EC/DM mixture in their study), and that PF_5 preferentially reacts with EC. They cite the literature [39] in proposing that EC reacts through a ring opening polymerization with CO_2 formation:

$$EC \rightarrow [(CH_2CH_2O)_nCOO]_m + CO_2 \tag{3}$$
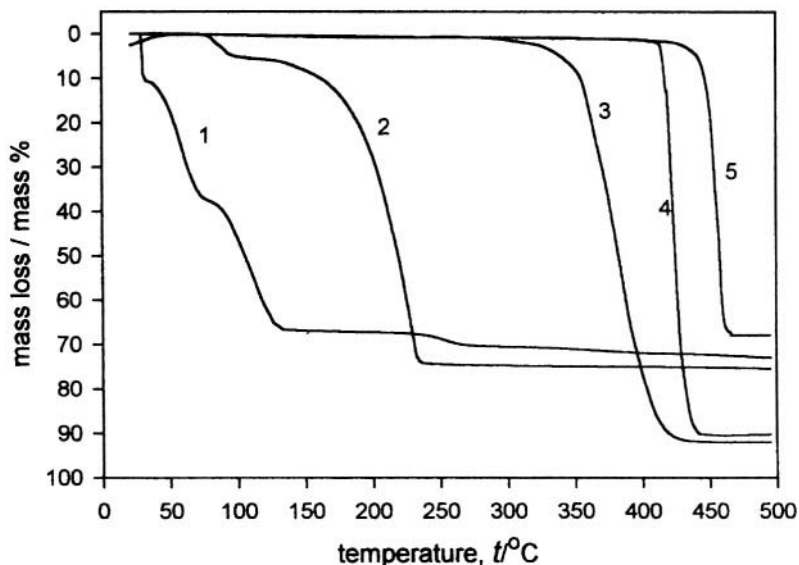
Figure 4. TG curves for Li salts at a heating rate of 1°C min⁻¹ in air. From data in reference 26.

1. LiPF₆   2. LiBF₄   3. LiN(SO₂CF₃)   4. LiSO₃CF₃   5. LiClO₄

The reaction proceeds at room temperature and is greatly accelerated at higher temperatures (e.g. 85°C). Additional problems with HF are its effects in dissolving cathode materials, especially $LiMn_2O_4$ [28, 29], and its reaction with SiO_2 (an important component of several polymer-based membranes and electrolytes) to produce SiF_4 according to

$$12HF + 3SiO_2 \quad \rightarrow \quad 6H_2O + 3SiF_4 \tag{4}$$

It is well recognized that any electrolyte must be electrochemically stable in addition to possessing high thermal stability and high conductivity over a wide temperature range. Most electrolytes discussed above do indeed exhibit high electrochemical stability, but the imide salt appears to be reactive at aluminum current collectors required for high voltage cathodes such as $LiCoO_2$ and $LiMn_2O_4$. The reactivity of the imide salt with Al (commonly used as a current collector) at high potentials has been reported by Krause et al. [30] and by Behl and Plichta [31]. Breakdown of the protective Al_2O_3 film and subsequent corrosion of Al becomes a serious problem at potentials above 3.5 V *vs*. Li/Li^+. The breakdown of the passive film on Al can be prevented by the addition of a fluoride salt such as $LiPF_6$, $LiBF_4$ or $LiAsF_6$ which, by virtue of their tendency to form radicals such as PF_5 or AsF_5 which form highly insoluble films on Al such as AlF_3, serve to stabilize the Al substrate. Figure 5 shows the current-time relation at constant potential for 1 mol·dm⁻³ LiIm in an EC/PC/DMC (20/20/60 v/o) solution with and without 0.5 mol·dm⁻³ $LiBF_4$. With $LiBF_4$ addition, the corrosion of Al is significantly repressed. On the other

hand, electrolyte solutions containing LiMe (Figure 6) does not show any indications of Al corrosion.

Our conclusions here are that at Al, LiIm without added salts such as $LiAsF_6$ or $LiBF_4$ is perfectly acceptable for Li-ion cells with low voltage cathodes (under 4 V *vs.* Li/Li^+) such as $LiFePO_4$ and, probably, $Li_xV_2O_5$, and for use with high voltage cathodes such as $LiCoO_2$, the addition of a second electrolyte such as $LiBF_4$ is required.

To resolve the problems associated with safety, thermal and electro-chemical stability and conductivity, new syntheses of new electrolytes are the subject of new and important studies. Not withstanding the importance of the methide salt for which commercial availability is expected shortly, a number of important new developments are worth highlighting. Lithium bis(perfluoro-ethyl-sulfonyl)imide, $LiN(SO_2C_2F_5)_2$ or LiBETI, is very similar to that for the imide salt as it is stable up to 330°C [26]. In addition to its high thermal stability, the LiBETI salt was also shown to be unreactive towards water [27]. The studies by Barthel et al. on chelatoborates [32] such as bis[2,3-pyridinediolato(2-)-O,O´]borate are of special interest as are studies on new methide salts such as $Li[C_2(SO_2CF_3)_4(S_2O_4C_3F_6)]$ [32].

2.4   Solubilities

Since the early days of R&D on rechargeable Li batteries (mainly metallic Li anodes), it has been recognized that essentially all solvents and electrolytes are thermodynamically unstable in the presence of a clean Li surface, i.e. the observed stability of the Li(m) anode is due to the formation of an inert and insoluble passive film on the surface of Li(m). The model of this passive film was elegantly developed by Peled in several publications, [34,35] in what is now known as the *solid electrolyte interphase,* or *SEI*. The SEI is basically an electronic insulator and simultaneously an ionic conductor, and the stability of the anode is due to the compactness and low solubility of the passive film. In 1988 and 1989, Plichta et al. [15, 36] reported the unique ability of DMC and DEC to significantly improve the cycling efficiency of Li(m) anodes, and based on earlier work by Aurbach et al. [37], assumed this was due to the formation of insoluble carbonate films on the surface of Li(m). Subsequent studies by Aurbach et al. on the reaction products of carbonate-based solvents have identi-fied a number of components of the SEI that include Li_2O, Li_2CO_3 and $ROCO_2Li$ species [40-43]. As an example of the corrosion reaction of EMC (solvent reduction) proceeding *via* radical formation, Aurbach proposed the following:

$$EMC + Li^+ + e^- \quad \rightarrow \quad CH_3CH_2OLi + CH_3OCO^\bullet \tag{5}$$

followed by

$$Li^+ + CH_3COO^\bullet + e^- \quad \rightarrow \quad CH_3OLi + CO \tag{6}$$

For EC reduction, Aurbach et al. [40] proposed the following mechanism:

$$2EC + 2e^- + 2Li^+ \quad \rightarrow \quad LiOCO_2CH_2CH_2OCO_2Li \tag{7}$$
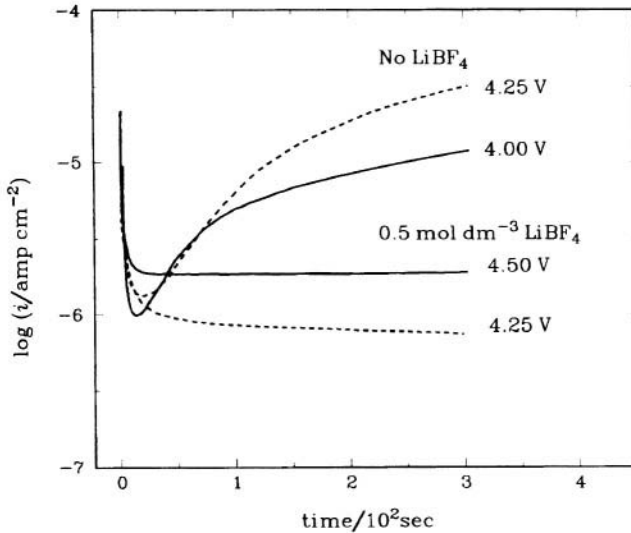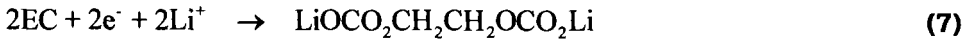
Figure 5. Current density vs. time plots at various potentials for 1 mol dm^{-3} LiIm in EC/PC/DMC (20:20:60 by volume) without and with 0.5 mol dm^{-3} LiBF$_4$. Reprinted from reference 31 with permission from Elsevier Science.
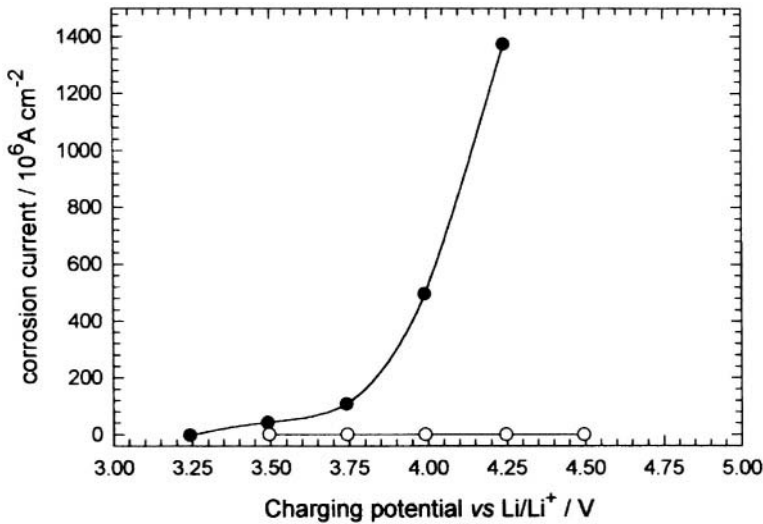
Figure 6. Current density vs. potential plots at Al in EC/PC/DMC solutions containing 1 mol dm^{-3} LiIm (solid circles) and 1 mol dm^{-3} LiIm with 0.5 mol dm^{-3} LiBF$_4$ (open circles) which overlaps with a 1 mol dm^{-3} LiMe solution.

Similar mechanisms were proposed by Yoshida et al. [43], who also reported that in addition to the formation of insoluble oxides, carbonates and alkoxides, methane, ethyne, CO and H_2 are formed. According to the studies of Aurbach [40-42] and Ein-Eli [44-46], the SEI in these carbonate solvents is composed largely of Li_2CO_3, $ROCO_2Li$ and ROLi where R is mainly CH_3 rather than CH_3CH_2, and the least soluble species is Li_2CO_3. For the four solvents, EC, DMC, EMC and DEC, the stability of the passive film follows the order EC > DMC > EMC >> DEC, and that of the reduction products of these solvents, EMC produces the most Li_2CO_3 [44-46]. Based on these findings, almost all present day electrolyte formulations for rechargeable Li-ion cells contain one or more of these carbonate solvents, particularly EC, DMC and the asymmetric solvent EMC. The use of these solvents in combination with low viscosity solvents for low temperature applications is discussed in Section 3 below.

Compared to aqueous solutions, the solubilities of electrolytes in these organic solvents [Table 4] are exceedingly high often approaching 4 $mol\cdot kg^{-1}$. These highly concentrated solutions can have very little *free* solvent available therefore resulting in highly viscous solutions. For example, 1 kg of PC contains 9.8 moles of solvent compared to 55.5 moles of water in 1 kg of H_2O. If we *assume* that in PC the total solvation number of a LiX salt is 4 (3 cation + 1 anion solvent coordination) compared to 5 for water, a 2 *m* solution of LiX in PC will have a free solvent (mole fraction) concentration of 0.19. For the corresponding 2 m aqueous solution, the remaining (uncoordinated) solvent concentration is 0.82 mol fraction. To avoid high viscosities, particularly at low temperatures, it is common practice to employ solutions where the LiX concentration ≤ 1.5 $mol\cdot dm^{-3}$, preferably ≤ 1.0 $mol\cdot dm^{-3}$. Quantitative determination of solubilities is often very difficult due to high viscosities creating a problem of equilibrating the system, and the tendency of these highly concentrated solutions to form metastable solutions. Thus solubilities of lithium salts in these organic solvents are often, by necessity, qualitative, particularly when studying solutions over a wide temperature range: it is very common to see only tabulated qualitative data in the literature [e.g. 47, 48]. As an example, Table 6 below is reproduced from [48], and a similar table can be found in [47].

Table 6. Electrolyte phases at low temperatures (solvent composition based on volume units).

Composition	-30°C	-35°C	-40°C	-42.5°C
EC:DEC:DMC (1:1:1) 1 $mol\cdot dm^{-3}$ $LiPF_6$	liq	liq + solid	liq + solid	solid
EC:DEC:DMC:PC (3:3:3:1) 0.9 $mol\cdot dm^{-3}$ $LiPF_6$	liq	liq + solid	Solid	Solid
EC:DEC:DMC:EMC (3:5:4:1) 0.8 $mol\cdot dm^{-3}$ $LiPF_6$	liq	liq	Liq	Liq
EC:DEC:DMC:EMC (3:5:4:2) 0.8 $mol\cdot dm^{-3}$ $LiPF_6$	liq	liq	liq + solid	liq + solid

A new approach opening the door for expanded research on salts that have extremely small solubilities, e.g. CF_3COOLi and LiF, has been the focus of several publications by McBreen et al. [49–51]. These authors synthesized a number of cyclic aza-ether compounds with electron withdrawing CF_3SO_2 groups attached to the aza-nitrogens to produce anion receptors capable of strongly coordinating anions thereby increasing solubilities [49]. More recent work [50,51] on boron-based anion receptors has been more fruitful. A series of fluorinated alkyl and aryl borate and borane compounds have been synthesized [50], and demonstrated to strongly coordinate anions thus permitting high concentrations (~ 1 mol·dm^{-3}) of salts such as CF_3COOLi and LiF to be utilized in Li-ion cells. These new boron-based anion receptors are thermally stable, insensitive to moisture, and highly conductive as seen in Table 7 reproduced from [51]. Note the enhanced stability of solutions based on LiF and CF_3COOLi with equimolar concentrations of the anion receptor TPFPB (tris(pentafluorophenyl)borane). $(C_6F_6)_3B$. The solvent employed is a 1:1 mixture (by volume) of EC:DMC.

Employing the cell $Li(m)/LiMn_2O_4$, the authors demonstrated extended cycling at 55°C at very near 100 % efficiency [51]. Information on the solubilities of these boron-based anion receptors at low temperatures has not yet been reported.

Table 7. 25°C conductivities of EC/DMC solutions with TPFPB and 1 mol dm^{-3} Li salts.

Electrolyte	Before storage 10^{3}σ/S cm^{-1}	7 days storage at 55°C 10^{3}σ/S cm^{-1}	14 days storage at 55°C 10^{3}σ/S cm^{-1}
LiPF$_6$ (no additive)	10.2	9.26	8.87
LiF + TPFPB	1.62	2.81	2.81
CF$_3$COOLi + TPFPB	3.21	3.23	3.23

Table 8. Mass uptake of representative PVDF polymers[a]

Polymer T/°C	Kynar 741			Kynar 2081			S-1010 PC
	PC	DMC	EC	PC	DMC	EC	
23							7.3%
30	14%	14%	7%	39%	60%	21%	
40	15%	15%	7%	52%	148%	26%	
50	16%	17%	8%	101%	Soluble	32%	32.2%
60	21%	24%	10%	Soluble	Soluble	45%	

For liquid-based systems, the present state-of-the-art for commercial Li-ion batteries almost universally employs either PVDF homopolymers or PVDF-HFP copolymers for electrode binders and, in some cases, for the electrolyte separator-matrix [52]. These polymers are most effective for commercial processing of composite electrodes on current collector metal foils such as Cu and Al, and

appear to be very inert, at least to temperatures up to 120°C [53]. These polymers are known to swell upon introduction of the liquid electrolyte solution, and, in addition, their solubility properties may be a source of cell failure during operation and storage at elevated temperatures. Table 8, based on manufacturer´s literature, shows the potential problem with the solubility of various PVDF polymers as a function of temperature. This potential problem with PVDF-based polymer binders and electrolyte matrixes certainly, in our opinion, warrants further studies into the selection of binders and their effects on behavior of and storage of Li-ion cells at elevated temperatures. EPDM (eththylene-propylene-diene) binder materials introduced by NASA´s JPL laboratory in 1983 [54] was compared to PVDF for stability at high temperature (70°C), [55] but the results comparing stabilities of these binders were inconclusive.

2.5 *Additives*

Inorganic and organic additives have historically played an important role in stabilizing the SEI as well as improving the solution properties of lithium salts. Considering the former, one early study of interest is that of Rauh and Brummer [56] who reported significant improvement in the cycling efficiency of lithium on Ni substrates by the addition of nitromethane and SO_2. Shortly after this study, Goldman et al. [57] reported similar improvements in lithium cycling in 1 mol·dm^{-3} $LiAsF_6$ solutions in 2MeTHF. Subsequently, the improved stability of 2MeTHF solutions was found to be due to trace impurities of 2-methyl furan, 2MeF [58]. The use of 2MeF as an additive appears to work well with cyclic ether based solvents in Li(*m*) cells with low voltage cathodes such as TiS_2 [3], but not with high voltage Li-ion cells. Early work on the use of CO_2 additions to metallic Li anodes has shown this to be very effective in increasing the cycling efficiency of Li [15,59], but interest in this approach for Li-ion cells is minimal, presumably due to the reluctance to pressurize these cells. An alternate approach for stabilization of graphitic anodes suggested by several investigators is to use additives such as chloroethylene carbonate [60, 61] or alkyl pyrocarbonates such as dimethyl and diethyl pyrocarbonate [62] that result in the liberation of CO_2 *in situ*. Basically, the mechanism for the improved stability of graphitic anode materials involves the formation of a thin, highly insoluble passive film *before* the typical electrolyte solutions based on mixtures of carbonates and esters react to form a less stable SEI. Normally, in the absence of additives, the SEI at the anode is formed during the initial cell charging (Li$^+$ intercalation) at around 0.8 V *vs.* Li/Li$^+$; as an example we cite some of our recent work, Figure 7, on MCMB 2528 in 1 mol·dm^{-3} $LiPF_6$ in a 1:3 mixture (by mass) of EC:EMC [63].

From Figure 7, the SEI is observed to form starting at potentials around 0.8 – 0.7 V *vs.* Li/Li$^+$ and is followed by Li$^+$ intercalation in several stages between around 0.2 to 0.08 V [64,65]. The SEI produced by reduction of alkyl and cyclic

carbonates, with the exception of PC, which cointercalates causing exfoliation of graphitic anodes [e.g. 66], is very effective at room temperature, but is problematic at low and high temperatures. CO_2 additions to the solvent either as a dissolved gas or *via in situ* production from chloroethylene carbonate or pyrocarbonates discussed above was shown to reduce at around 1.4V *vs.* Li/Li^+, i.e. *prior* to the reduction of the base carbonate solvent [e.g. 61]. This concept has been advanced by the introduction of new film-forming additives such as ethylene sulfite, ES, [67] and unsaturated compounds such as vinylene carbonate, VC, [68-70]. Figure 8 shows the dramatic effect of addition of ES to a PC solution containing $1 \ mol \cdot dm^{-3}$ $LiClO_4$. In the absence of ES, the reactivity of PC is clearly seen starting at around 0.8 V. In the presence of 5 vol.% ES, Figure 8 shows the reduction of ES at around 1.8 V and inhibition of PC reduction. This effect of ES was confirmed by Cassel et al. [71] who also found that ES additions to solvents containing EC, PC and trimethyl phosphate (TMP) were very effective in inhibiting the reduction of the aggressive solvent TMP, but their findings suggest that ES may be oxidized at the high voltage cathode $LiCoO_2$. On the other hand, SAFT´s studies [68-70] with VC (which also has a high reduction potential of 1.2 V *vs.* Li/Li^+) additions to carbonate solvent mixtures are extremely promising as VC appears also to be resistant to oxidation at the cathode as shown in Figure 9 (taken from [68]). This figure shows SAFT´s data for the capacity retention after high temperature storage of a graphite-$LiCoO_2$ cell in a solution containing $1 \ mol \cdot dm^{-3}$ $LiPF_6$ in a 1:1:1 (by mass) mixture of EC:DMC:DEC compared to a fresh MCMB/$LiCoO_2$ cell with $1 \ mol \cdot dm^{-3}$ $LiPF_6$ in EC:EMC (1:3 by mass) [72].
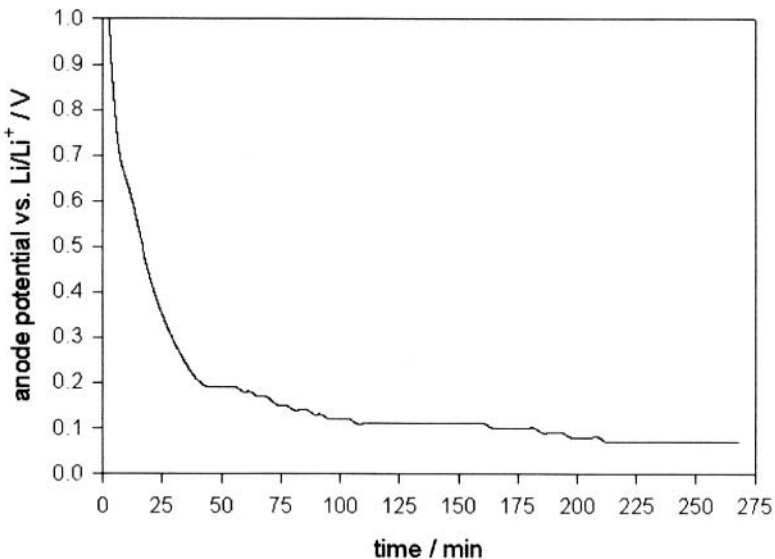
Figure 7. Potential – time profile for the first cycle charge of an MCMB 2528 graphite anode in a C/$LiCoO_2$ cell at 25°C.
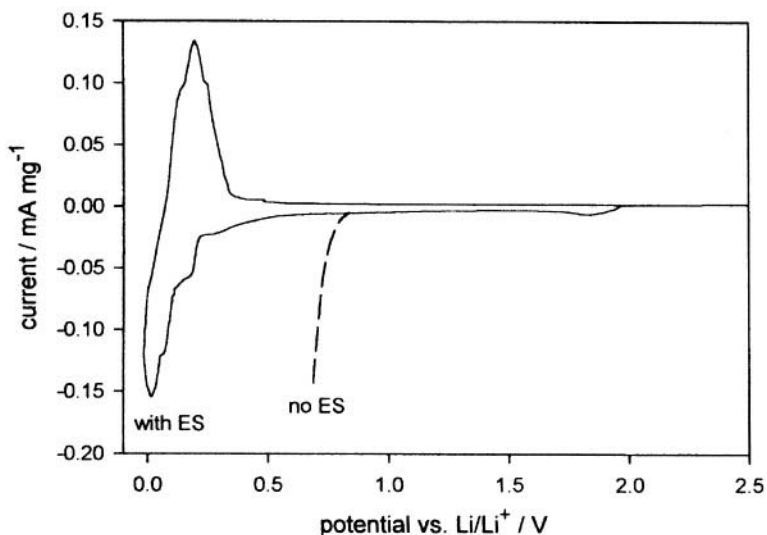
Figure 8. Voltammograms of TIMREX KS6 graphite in 1 mol dm^{-3} LiClO$_4$ in PC solutions with 5 vol. % ES (solid line) and without ES (dashed line).
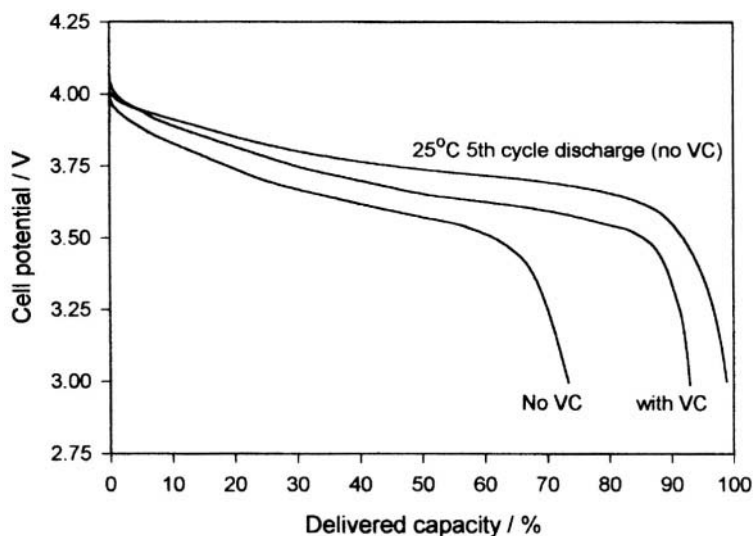
Figure 9. Capacity retention of graphite/LiCoO$_2$ cells after 6 months of storage at 60°C with and without VC [68] compared to the room temperature fifth discharge of a fresh cell. From data in reference 72.

Other effective derivatives of VC are cited in [70] such as propylidene carbonate, ethylidene ethylene carbonate, and isopropyl-idene ethylene carbonate.

Additional improvement in the electrochemistry of Li-ion cells relate to solution properties such as ion solvation and conductivity. For example, it has been established that addition of cyclic ethers such as 12-crown-4 (12C4) to PC-

based solutions prevents co-intercalation of PC into graphitic materials due to the preferential coordination of Li^+ by the crown ether [e.g. 73-75]. The enhancement of conductivities by addition of TPFPB to electrolyte solutions by McBreen et al. has been mentioned above. This effect is also observed for Li salts in solvents containing cation coordinating ligands such as ethylenediamine and N,N,N´,N´-tetramethyl-EDA [76] as well as in solutions containing crown ethers [77-81], cryptand 222 [78] and calyx[4]arene-bis-crown-6 [82]. A striking feature of these studies in solutions containing EDA and TEDA crowns and crypts is the increase in the lithium ion transference number. This is strictly the effect of the preferential coordination of Li^+ by the macrocyclic ligand: even though the ligand is a large species, Li^+ solvated by organic solvents have large solvation spheres as it is normally 3-4 coordinated by solvent molecules. We know that addition of these macrocyclic ligands to organic solvents and their mixtures will improve the cycling efficiency of graphitic anodes (see above), but continued studies along these lines have not been pursued. The reasons for this are probably the lack of solubility and temperature data on these systems, the possible toxic effects of crown ethers, and the possible reaction (oxidation) of crown ethers at high voltage cathodes. On the other hand, the increase in the Li^+ transference number in solutions containing fluorinated alkyl and aryl borate and borane compounds such as TPFPB is strictly due to the large size of the anion + anion-receptor complex. In addition, McBreen et al. [50,51] have demonstrated the unique properties such as thermal and electrochemical stability of these anion-receptors, and at this time, this approach appears to have advantages over the use of cation coordinating ligands.

3.1   *Liquid Electrolytes for Low to High Temperature Applications*

Based on the concepts discussed in Section 2.3 above, it is clear that to optimize the electrolyte solution for chemical and electrochemical stability, and for conductivity, a mixed solvent approach is required. For chemical and electrochemical stability, clearly solvents containing EC, EMC, DMC and, to a lesser extent, DEC are required: other useful asymmetric carbonate-based solvents have also been studied, e.g. ethylpropyl and isopropylmethyl carbonates [45], methylpropyl carbonate [83] and 2-methoxyethyl (methyl) carbonate [84], but the key solvents for electrochemical stability are EC, EMC and DMC. The superiority of a 1:1:1 (by volume) mixture of EC:EMC:DMC with 1 mol dm^{-3} $LiPF_6$ was reported in [85], and 1:1:1 (by volume) of EC:EMC:DEC with 1 mol·dm^{-3} $LiPF_6$ was reported in [86]. Figure 10 summarizes the conductivities of various electrolytes in 1:1:1 mixtures of EC:EMC:DMC and EC:DEC:DMC. At -40°C, the conductivities of 1 mol·dm^{-3} $LiPF_6$ solutions are $\geq 1 \cdot 10^{-3} \text{ S·cm}^{-1}$ while those for LiMe and LiBETI are all $\leq 0.5 \cdot 10^{-3} \text{ S·cm}^{-1}$. The low temperature cycling behavior of Li-ion cells in $LiPF_6$ solutions is superior in the EC:EMC:DMC electrolyte (e.g., compare Figures 11 and 12).
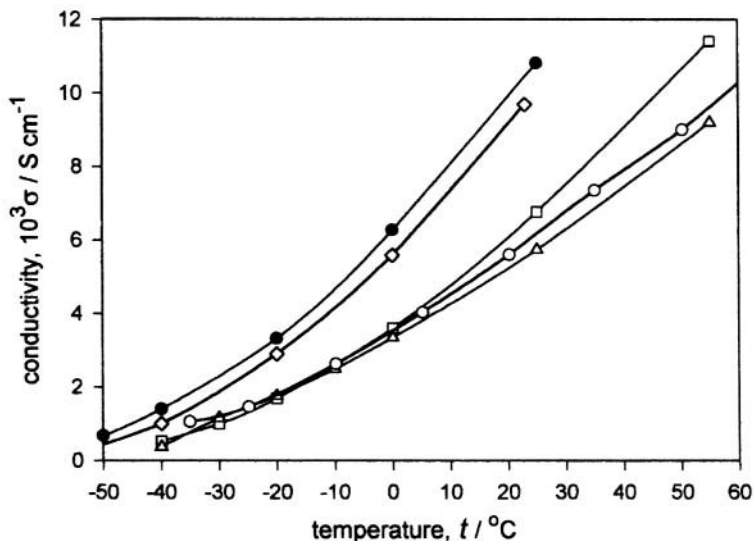
Figure 10. Conductivities of various electrolytes in ternary carbonate mixtures as a function of temperature.

• LiPF$_6$/EC:EMC:DMC [85]   ◊ LiPF$_6$/EC:DEC:DMC [87]   □ LiMe/EC:EMC:DMC [88]
o LiBETI/EC:DEC:DMC [89]   Δ LiBETI/ EC:EMC:DMC [88]

From the conductivity data shown in Figure 10 which shows little difference between EC:EMC:DMC and EC:DEC:DMC solutions, the poor delivered capacity observed at -40°C for the latter mixed solvent system may be due, in part, to the increased reactivity of DEC as discussed in Section 2.2 above. High temperature storage in DEC-containing solutions is inferior to carbonate-based solutions without DEC additions, but even the promising mixture of EC:EMC:DMC has its problems. From Figure 9, it is seen that when stored at 60°C for 6 months, the **MCMB-LiCoO$_2$** cell experiences a 30 % loss in capacity [72]. However, Au et al. [91] report that similar cells stored at 50°C for 7 days only experiences a 2 % permanent loss in capacity. This difference can be attributed to several factors: Au et al. charged their cells to 4.0 V vs. 4.1 V to the cells reported in [72], and they stored their cells at a lower temperature for less time. While charging to 4.0 V results in a decrease in available capacity, it offers a solution to the high temperature storage problem. On the other hand, the use of small additions of VC to the electrolyte solution results in remarkable capacity retention over prolonged storage at higher temperatures. The detailed reasons for these problems associated with carbonate-based solvents appear to be complex and not fully understood, but clearly the use of additives is a promising solution to these problems.
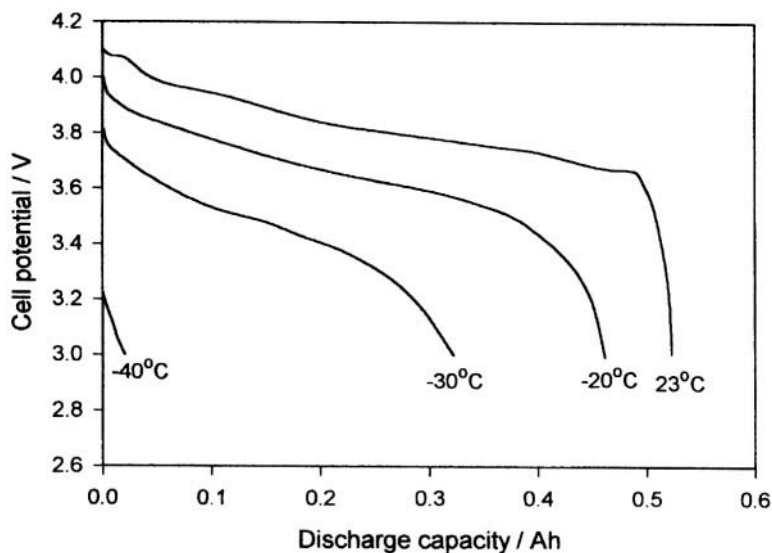
Figure 11. Discharge of MCMB-LiCoO₂ 500 mAh (approx) cells in EC:DEC:DMC as a function of temperature. Cells charged at room temperature to 4.1 V and discharged 3.0 V at 25 mA (C/20 rate). Derived from data in reference 90.

Recent improvements in developing electrolyte solutions with conductivities of the order of 10^{-3} $S \cdot cm^{-1}$ at temperatures $\leq -50°C$ involve the use of an ester [88,92] or hydrocarbon [3, 93] as a solvent component in a carbonate-based solvent mixture. Figure 13 summarizes the recent literature data on these systems. The use of esters such as MA, EA, MB generally have very low freezing points and low viscosities which make them ideal components in a carbonate-based solvent mixture, but they are known to be "aggressive" solvents as they are highly reactive at potentials below 1 V *vs.* Li/Li⁺. However, the use of additives such as VC in these solutions greatly improves cycle life performance [92]. The use of toluene (tol) as a solvent component has a number of desirable properties that include its large liquidus range (see Table 4) and its stability towards lithium. In addition, the solubilities of lithium oxides, carbonates, fluoride compounds and alkoxides which are the basic compounds found in the passivating anode films are highly insoluble in these solvents. This property is expected to increase the stability of the passive anodic film by both significantly decreasing its solubility and by producing a thinner and more compact passive film. In addition, hydrocarbon solvents such as toluene do not generally solubilize or excessively swell polymers such as PVDF that is an important material in Li-ion cells as binders or as an electrolyte host matrix. An electrolyte of 1 $mol \cdot dm^{-3}$ LiPF₆ in a 1:1:1:1 mixture of EC:EMC:MA:tol appears to cycle well at 25°C [93], but cycling performance data at low and high temperatures are not available.
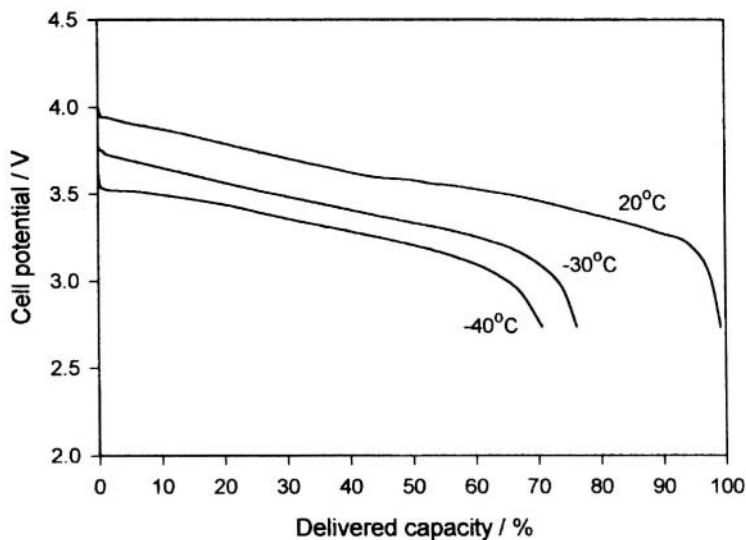
Figure 12. Discharge of MCMB-1028/LiNi$_{0.8}$Co$_{0.2}$O$_2$ 40 Ah cells in EC:EMC:DMC as a function of temperature. Cells charged at room temperature to 4.0 V with charge terminated at 0.05 A, and discharged at 3 A to 2.75 V. For low temperatures, cells were thermostated for 24 h prior to discharge. Data interpolated from reference 91.
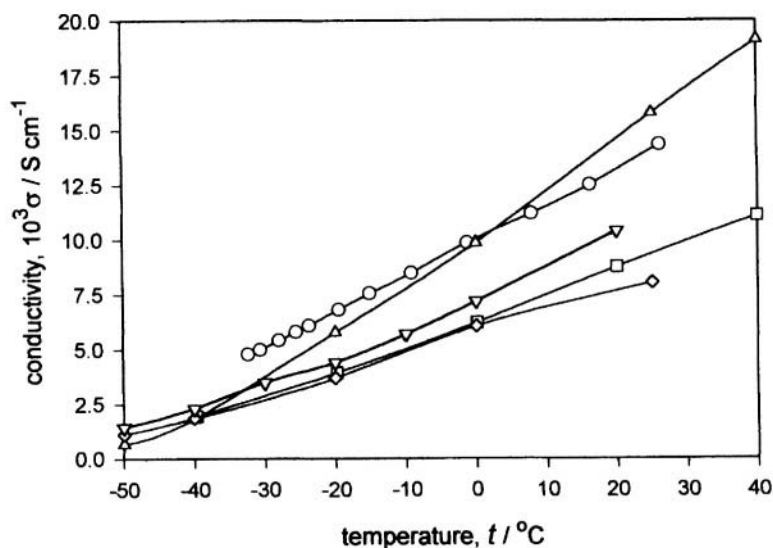
Figure 13. Conductivities of 1 mol dm^{-3} electrolytes in carbonate-based solvents as a function of temperature.*

△ LiPF$_6$ in EC:DMC:MA [93]   o LiPF$_6$ in EC:DMC:EA [92]   ▽ LiAsF$_6$ in EC:PC:DCM [2]
▢ LiPF$_6$ in EC:DMC:MB [92]   ◇ LiPF$_6$ in EC:DMC:MA:tol [93]

*Solvent compositions: EC-DMC with EA or MB not specified, but probably high in EA and MB contents in view of their high conductivities; EC:DMC:MA 1:1:1 by volume; EC:PC:DCM 25:25:50 v/o: EC:DMC:MA:tol 1:1:1:1 by volume.

Low temperature performance relating to storage and performance constitutes an important problem with Li-ion cells. However, as discussed above, careful formulation of mixed solvents is now known to produce electrolyte solutions with conductivities $\geq 1 \cdot 10^{-3}$ S·cm^{-1} at temperatures down to at least -40°C, and our conclusion is that while decreased solution conductivity certainly decreases available capacity at low temperatures, it is not the major problem for long term cycling and storage of Li-ion cells [e.g. see 48,63,94]. Irreversible capacity losses at low and high temperatures during charging and discharging, and upon storage, are due in large part to physical and chemical changes of the SEI at both anode and cathode, and to enhanced electrolyte oxidation and reduction: a general review of these phenomena is discussed below. While losses in capacity under these conditions are generally described as "irreversible," it is noted that in many cases the original capacities are "recoverable." For example, with carbon-based anodes, loss in capacity is usually due to a number of factors described below which result in growth of the SEI. The lithium involved in this continual growth comes from the cathode, and the net result is that there is a continual loss of lithium from the cathode with the consequence that this increasing lithium loss from the cathode results in "irreversible" capacity loss **in a balanced cell.** Similar phenomena exist in the case where a SEI layer is formed at the cathode and there is insufficient lithium in the anode to restore the cathode to full capacity upon charging.

3.2   *Temperature Effects on Carbon-Based Anodes*

The nature of the SEI, which is dependent upon the nature of the electrolyte and the nature and composition of the solvent components is a crucial issue governing the performance of both hard and soft carbon anode materials as discussed above. The determination of individual processes which limit the low temperature capabilities of carbon-based anodes is complex, but experiments have been designed to identify, at least qualitatively, individual mechanisms relating to dissolution or growth of the SEI, Li(m) deposition, or to slow electrode kinetics and/or slow solid-state Li$^+$ diffusion. In "half-cells" of the type

Li(m)	Electrolyte Solution	Coke or Graphite	(8)
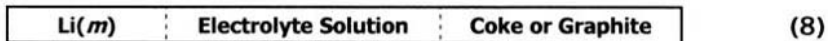
with or without a third (reference) electrode, the potential of the carbon-based electrode can usually be controlled to prevent deposition of metallic Li; such half-cells are normally cycled between 1.5V (charge cutoff voltage for Li removal) and 0.0 V (discharge cutoff voltage for Li intercalation) *vs.* Li/Li$^+$. On the other hand, typical "full" Li-ion cells of the type

Carbon-Based Anode on Cu Current Collector	Electrolyte Solution	LiCoO$_2$ Cathode on Al Current Collector	(9)
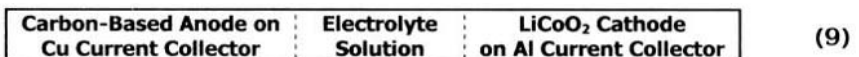
are normally charged to a *cell voltage* between 4.0 and 4.2 V, and discharged to a *cell cutoff voltage* of around 3.0 V at room temperature or 2.5 V at low

temperatures. Thus, given that the anode is usually rate-limiting in cells of the type given in Equation 9, resistance polarization due to the thickness and compactness of the SEI, polarization due to slow Li^+ solid-state diffusion, and activation polarization can result in deposition of metallic Li. In the event of deposition of metallic Li, the consequence is a continual growth of the thickness and increase in resistance of the SEI, and of course the loss of available lithium from the cathode thus resulting in irreversible capacity loss of the cell. Deposition of metallic Li has been confirmed in [63,95], and slow solid-state Li^+ limiting diffusion has been found in [48]. Huang et al. found that at -40°C, the extraction and intercalation of lithium from coke and graphite widely differed which is not expected *if* the SEI acts to control low temperature behavior. Using half-cells (Equation 8) and very low discharge current densities (0.00095 $mA·cm^{-2}$) corresponding to lithium intercalation, Huang et al. [48] found that at -40°C, a discharge capacity of 216 $mAh·g^{-1}$ was obtained for MCMB 1028 graphite compared to its capacity of 282 $mAh·g^{-1}$ at room temperature. At a higher discharge rate of 0.0095 $mA·cm^{-2}$, this same graphite had a discharge capacity of only 12 $mAh·g^{-1}$ at -40°C. At -40°C, these half-cells could be charged (corresponding to lithium extraction) at 0.285 $mA·cm^{-2}$ to 87% of their room temperature capacity.

In a recent study, Lin et al. [63] have found that low temperature cycling of the cell given in Equation 10 leads to an irreversible loss in capacity. At modest rates of charge and discharge (C/5) at -20°C, the loss in capacity is around 15% after only 15 cycles.

MCMB 2528Cu CurrentCollector	1 mol dm^{-3} LiPF$_6$ / EC:DMC (1:3 by mass) in PVDF matrix	LiCoO$_2$ Al Current Collector	(10)

To determine which electrode was limiting cycle life, a Li reference electrode was placed in the above cell, and the cell cycled at various temperatures between the voltage limits of 2.5 to 4.15 V. The room temperature (~25°C) first charge-discharge potential is given in Figure 14, and the first thing to notice is that polarization at the anode is more severe than at the cathode. Starting at -20°C, cycling of cell (10) at C/5 resulted in deposition of metallic lithium. At -40°C, the deposition of Li(m) upon charging at C/10 is severe as shown in Figure 15. Prior to charging and after a 30 minute rest period from the previous discharge at -40°C, the potential of the anode stabilizes at around 0.3 V *vs.* Li/Li^+ which suggests that a significant amount of Li was not deintercalated from the most dilute stage of Li_xC_6 [see references 64 and 65 for discussion of the staging phenomena]. As soon as charging is begun, the anode potential immediately drops to potentials negative to the reversible Li/Li^+ potential. At the end of the tenth cycle charge at -40°C, the OCV of the anode stabilizes at the reversible Li/Li^+ potential, and subsequent discharge reveals a large *IR*

drop before both metallic Li and intercalated Li are oxidized with extremely low efficiency. The large *IR* drop observed during the tenth cycle discharge is attributed to significant growth of the SEI due to the reaction (reduction) of the electrolyte solution with the freshly plated Li(*m*).

The stability of the SEI at carbon and graphite anode materials is also affected by high temperature storage. Cells (Equation 9) stored at high temperatures (above 40°C) appear to suffer irreversible capacity loss due to several factors, which are not fully understood. Using cells of the type given in Equation 8, a detailed analysis of this problem was studied by Zheng et al. [55] for various MCMB materials, and a summary of their experimental results is given in Table 9. Cells were stored in the fully charged and fully discharged state for four days at 70°C, and the capacity loss for the carbon electrodes stored in the discharged state were always greater than in the charged state. The capacity loss was attributed to breakdown of the SEI thus allowing intercalated lithium atoms to continuously diffuse from the interior of the carbon particles through the damaged SEI and react with the electrolyte solution to reform the damaged SEI layer. Zheng et al. conclude that increasing the stability of the SEI by use of additives is an important area for future studies.
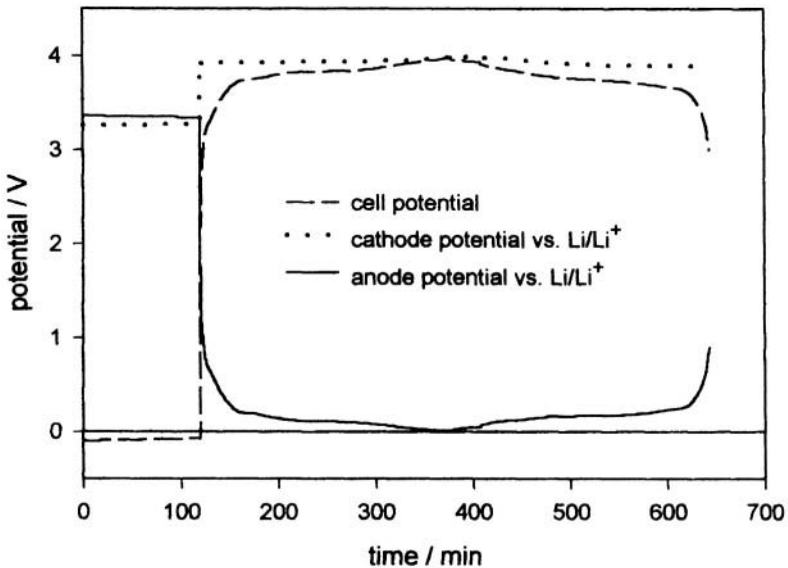
Figure 14. First cycle charge and discharge for cell (10) at room temperature. Rates are C/5 for both charge and discharge.
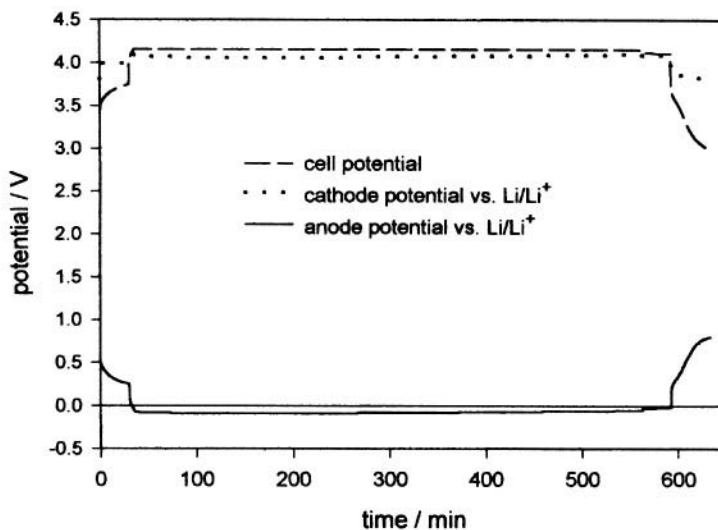
Figure 15. Tenth cycle charge and discharge for cell (10) at -40°C. Rates are C/10 for charge and C/5 for discharge.

Table 9
Capacity data for Cell (**8**) before and after storage at 70°C for 4 days [from Reference 55].

MCMB Type	BET surface area/$m^2 g^{-1}$	1st cycle discharge capacity/mAh/g	First cycle charge loss	Capacity loss after storage[a]	Capacity loss after storage[b]
2528	1.5	368	8 %	6.4 %	12.8 %
1028	2.5	364	10 %	7.6 %	18.5 %
628	3.3	440	30 %	10.4 %	28.2 %
2510	1.5	333	26 %	10.7 %	23.3 %
[a]For storage of fully charged cell ($x \approx 0$ in Li_xC_6, and cell potential ~1.5 V)					
[b]For storage of fully discharged cell ($x \approx 1$ in Li_xC_6, and cell potential ~0.01 V)					

3.3 Temperature Effects on Metal Oxide Cathode Materials

In this section, we emphasize the temperature effects on capacity retention and rate capabilities of the two most important cathode materials, namely Li_xCoO_2 (for x ~0.5 to 1.0), $LiNi_xCo_{1-x}O_2$ (for x ~0.8 to 0) and the spinel $LiMn_2O_4$. Although we limit our review on other materials such as $LiNiO_2$, we point out that there is an interesting publication on this material published in 1994 by Ebner et al. [96]. A recent review by Erlich [103] compliments much of the discussions given below, and extensive discussion relating to temperature effects on commercial Li-ion cells are found in this excellent review.

It is well established that efficient and long term cycling of Li-ion cells is largely dependent upon the stability of the SEI formed at the anode. It is certain that an SEI also forms at metal oxide cathode materials. An initial study by Aurbach et al. [97] reported spectroscopic results of traces of Li_2CO_3 on metal oxide surfaces (attributed to reaction with atmospheric CO_2), and in a subsequent study of $LiNiO_2$ and $LiMn_2O_4$ surfaces using spectroscopic techniques (XPS, EDAX, FTIR), Aurbach et al. [104] found Li_2CO_3 on pristine surfaces and upon storage and cycling, a variety of other species such as ROLi, $ROCO_2Li$ and LiF form. Imhof and Novak [98] used a mass spectroscopic method to detect the formation of CO_2 at these metal oxides which, for $LiNiO_2$, $LiMn_2O_4$ and carbon starts at around 4.2 V *vs.* Li/Li^+: the composition of the film was not identified. Amine et al. [99] studied the effect of elevated storage temperature on high power 18650 cells based on $graphite/LiNi_{0.8}Co_{0.2}O_2$ with 1 mol dm^{-3} $LiPF_6$ in EC:DEC(1:1) Cells were stored at temperatures from 40°C to 70°C for one month (two weeks for storage at 70°C) in various states of charge, and all experienced very significant impedance increase and loss in power. Interfacial resistance at the cathode was found to be a major reason for the decrease in power capability after storage. Initial high-resolution transmission electron microscopy on a cross-sectioned particle of the cathode material indicated the presence of a thick amorphous film on the surface of the particles. Wang et al. [100] employed a ^7Li NMR technique to study the effect of high temperature storage of similar $graphite/LiNi_{0.8}Co_{0.2}O_2$ cells. Cells having a 60% state of charge were stored at 50°C for eight weeks and at 70°C for two weeks. Analyses of the NMR spectra for the cathodes confirmed the existence of stoichiometric $LiNi_{0.8}Co_{0.2}O_2$ in addition to a Li-containing SEI. The analyses showed that storage at 70°C yields a Li-containing SEI about 10% greater than the SEI formed at 50°C. A recent study by Balasubramanian et al. [127] reported the formation of thick deposits of LiF on $LiNi_{0.85}Co_{0.15}O_2$ cathodes cycled in 18650 Li-ion cells at 40°C and 70°C. The electrolyte solution used in this study was 1 $mol \cdot dm^{-3}$ $LiPF_6$ in EC:DEC (1:1). The authors concluded that the source of LiF is due to the decomposition of $LiPF_6$ according to Equation 2 above. This again confirms the problem with $LiPF_6$ and the need to replace this salt in Li-ion cells and batteries.

Most studies on the loss in capacity and power associated with $LiNi_xCo_{1-x}O_2$ address high temperature properties. Information on low temperature properties associated with cycling and storage are noticeably absent from the literature. Some of these factors are discussed below. In most studies dealing with high temperature storage, the causes of irreversible capacity loss or power loss in $LiNi_xCo_{1-x}O_2$ materials deal mainly with electrolyte solution oxidation and the resulting formation of a cathodic SEI. However, there are other areas of potential problems, which,

while not confirmed, are mentioned simply for suggested possible areas of future exploration. It is however known that $Li_{0.5}CoO_2$ is subject to thermal instability forming $LiCoO_2$ and Co_3O_4 at temperatures above 80°C [101,102]. While temperatures exceeding 80°C are quite rare for Li-ion cells, in large battery stacks under high current drain, and during storage in confined areas in hot climates, temperatures reaching 80°C are not totally unexpected. Long-term storage data should be of interest here. In addition, the possibility of cathode degradation in charged cells (e.g. for $x \approx 0.5$ in Li_xCoO_2) upon long-term storage at high temperatures due to phase instability is an area, which may have relevance for future research.

The large capacity losses upon high temperature storage of Li-ion cells based on the spinel $LiMn_2O_4$ is well established and are due to a number of factors which include a disproportionation of the spinel, $2Mn^{3+}(s) \rightarrow Mn^{4+}(s) + Mn^{2+}(sln)$, electrolyte decomposition [105, 106], and the Jahn-Teller lattice distortion which occurs at temperatures above 7°C [107] or 20°C [108]. The presence of HF due to water impurities in $LiPF_6$-containing solutions (see Equation 1 above) is particularly detrimental leading to increasing dissolution of the spinel upon storage according to [e.g. see 109, 110]

$$2LiMn_2O_4 + 4H^+ \rightarrow 3\lambda\text{-}MnO_2 + Mn^{2+} + 2Li^+ + 2H_2O \qquad (11)$$
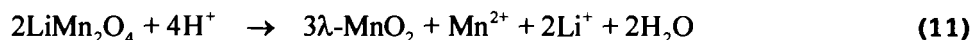
which regenerates water thus leading to rapid capacity fade, particularly at high temperatures. By replacing the problematic electrolyte $LiPF_6$ with a more stable salt, the dissolution of the spinel can be significantly reduced and, in some cases, practically eliminated [e.g. 51, 111]. Du Pasquier et al. [111] have shown that replacing $LiPF_6$ with $LiClO_4$, $LiBF_4$ or $LiAsF_6$ does in fact significantly reduce Mn dissolution, but the penalties here are reduced conductivities for $LiClO_4$ and $LiBF_4$, and environmental concern with $LiAsF_6$. A unique approach to this problem was reported by Sun et al. [51] by using an anion coordinating ligand such as tris(pentafluorophenyl)borane (TPFPB) which produces highly conductive solutions, even with salts such as LiF (see Table 7 above). Solutions of LiF and TPFPB are thermally stable, insensitive to moisture and do not produce acidic species (e.g. see Equations 1 and 2). The coulombic efficiency at 55°C of the cell (12) reported by Sun et al. is significantly improved by replacing $LiPF_6$ with the composite LiF + TPFPB electrolyte as seen in Figure 16.

Li (*m*)	1 mol dm^{-3} LiF + TPFPB in EC/DMC (1:1 vol ratio)	LiMn$_2$O$_4$	(12)
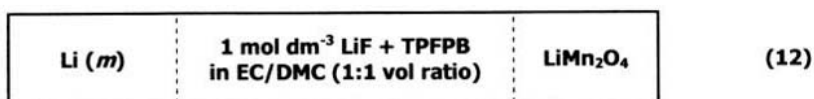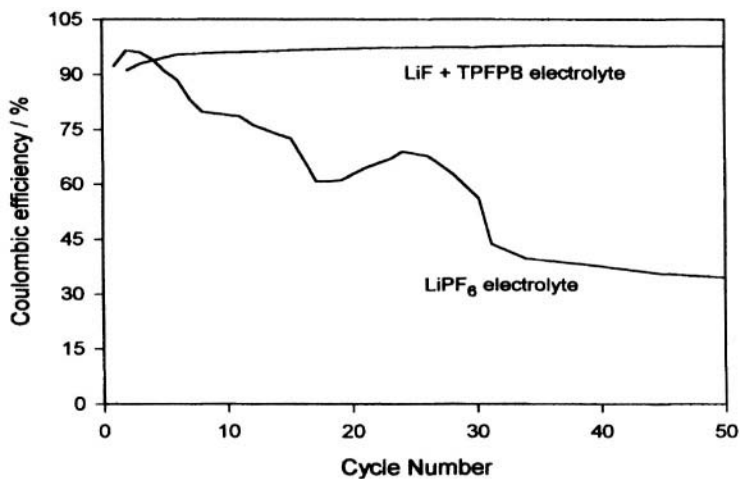
Figure 16. Coulombic efficiency for Li/LiMn$_2$O$_4$ cells cycled at 55°C between 3.5-4.5 V at C/3 (based on data from reference 51 and averaged by the present authors).

The rate capabilities and deliverable capacities of various cathode materials at very low temperatures is a complex subject. For example, at room temperature and at low rates (e.g. C/10), Li-ion cells utilizing LiMn$_2$O$_4$ cathodes are stated to have slightly higher or close to equal capacities to Li-ion cells utilizing LiCoO$_2$ cathodes (12) but at higher rates (e.g. C/10 to 4C), Li-ion cells utilizing LiCoO$_2$ cathodes are clearly superior. There are however other studies suggesting that at room temperature, Li-ion cells with LiMn$_2$O$_4$ materials have better rate capabilities [113]. At low temperatures, LiCoO$_2$ based Li-ion cells can deliver useful capacities at temperatures down to -40°C whereas the capacity of LiMn$_2$O$_4$ – based Li-ion cells at -30°C and below are very poor. Comparing LiCoO$_2$ and LiMn$_2$O$_4$ low temperature capabilities in Li-ion cells, part, and probably a large part of the poor low temperature performance of LiMn$_2$O$_4$ can be attributed to its intrinsic (solid-state) conductivities that is much smaller for LiMn$_2$O$_4$ than for LiCoO$_2$ as seen in Figure 17. Tukamoto and West [114] and Juan and Liu [115] both used pressed pellets sintered at 800°C in these studies, and measured the conductivities by either the 4-point probe method or by impedance spectroscopy. The LiCoO$_2$ material used by Tukamoto and West was prepared by the ceramic method, and the LiMn$_2$O$_4$ prepared by Guan and Liu was a sol-gel derived material. The near metallic conductivity of LiCoO$_2$ exists over a small composition range (x $<\sim$0.9 in Li$_x$CoO$_2$) and is associated with the Co^{4+} valence state, and for lower values of x, the material appears to be a p-type semiconductor [114,126]. LiNi$_x$Co$_{1-x}$O$_2$ materials have electronic conductivities intermediate to those shown in Figure 17 [e.g. see 116], and details on the electronic structures of these materials can be found in (117).
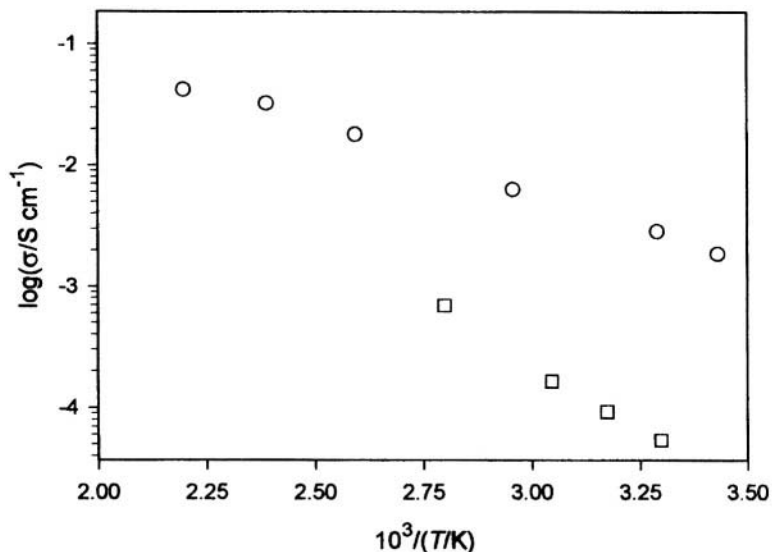
**Figure 17.** Comparison of electronic conductivity of $LiCoO_2$ and $LiMn_2O_4$.

o – $LiCoO_2$ (ref. 114).   □ - $LiMn_2O_4$ (ref. 115).

The question of which electrode is rate limiting as a function of temperature is complex and not fully resolved. Many factors influence the rate capabilities of both anode and cathode including nature of the SEI, particle sizes, surface areas, solution conductivities, Li^+ transference numbers, diffusion coefficients, and electronic properties of all cell components. The chemical diffusion coefficient, D, of Li^+ in graphite is generally thought to be greater than that for any of the common cathode materials. In the non-aqueous electrolyte solutions of interest to Li-ion cells, D is generally assumed to follow the order of graphite > $LiCoO_2$ > $LiNi_xCo_{1-x}O_2$ > $LiMn_2O_4$. However, the reported results for D are based on different experimental techniques and different diffusion models, and the results are often inconsistent. For example, for Li^+ intercalation into graphite at room temperature, values of D from 10^{-6} $cm^2 \cdot s^{-1}$ to 10^{-7} $cm^2 \cdot s^{-1}$ (dilute stage 1 to stage 4) were reported by Funabiki et al. [118], values of 10^{-9} to 10^{-11} $cm^2 \cdot s^{-1}$ were reported by Nishizawa et al. [119] for MCMB 2528, and upon deintercalation, values of 10^{-8} to 10^{-12} $cm^2 \cdot s^{-1}$ were reported by Piao et al. [120]. The value of D at -20°C was also reported by Barsoukov et al. [121] to be 8 times lower than the room temperature value. These D values are comparable to those for $LiCo_{0.65}O_2$ ($5 \cdot 10^{-8}$ to $5 \cdot 10^{-9}$ $cm^2 \cdot s^{-1}$ [122,123]), but generally D values for $LiMn_2O_4$ are consistently lower ranging from 10^{-11} $cm^2 \cdot s^{-1}$ [124] to $2 \cdot 10^{-12}$ $cm^2 \cdot s^{-1}$ [125]. Based on these chemical diffusion coefficients, one would predict that $LiCoO_2$ materials should have greater rate capabilities than $LiMn_2O_4$ materials, which is experimentally what is found. However, for graphitic materials compared to $LiCoO_2$, and based on

which values of D one wishes to compare, one would predict that the rate capabilities are either almost equal or greater for graphite, which, in our view, is not the case. Based on the results for cell [10] from [63] (see Figures. 14, 15), it appears that the anode is the rate-limiting electrode, particularly at low temperatures. The cells employed in Reference [63] were very closely balanced (after allowance is made for the irreversible capacity loss due to the initial SEI formation at the anode). Another related approach was used by Plichta and Behl [85] who studied the following cells:

Li(m)	1 mol dm^{-3} LiPF$_6$ in EC/EMC/DMC (1:1:1 vol ratio)	LiCoO$_2$

(13)

SFG-44 graphite Cu current collector	1 mol dm^{-3} LiPF$_6$ in EC/EMC/DMC (1:1:1 vol ratio)	LiCoO$_2$ Al current collector

(14)
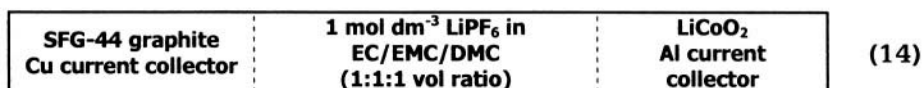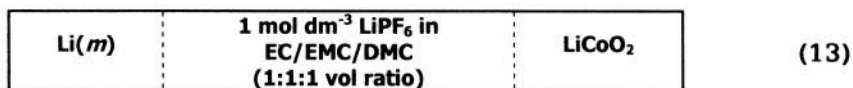
The SFG-44 composite graphite electrodes had a theoretical capacity of 24 mAh, and the composite LiCoO$_2$ electrodes had a theoretical capacity of 42 mAh, i.e. almost twice the capacity of the graphite electrodes to insure a large Li excess for intercalation into the graphite after the initial formation of the SEI. The results of successive cycling of these cells from 25°C to -40°C are shown in Figures 18 and 19 from which it is clearly seen that the graphite electrode is severely limiting at temperatures below -20°C.
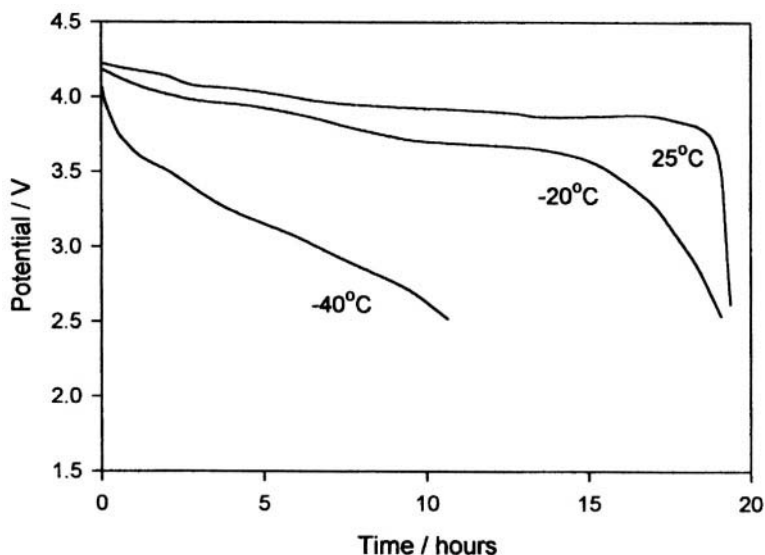
Figure 18. Typical discharge curves for cell (13) at a constant current of 1 mA as a function of temperature. The LiCoO$_2$ electrode was 0.51 mm thick and 15.7 mm in diameter. Data interpolated from reference 85
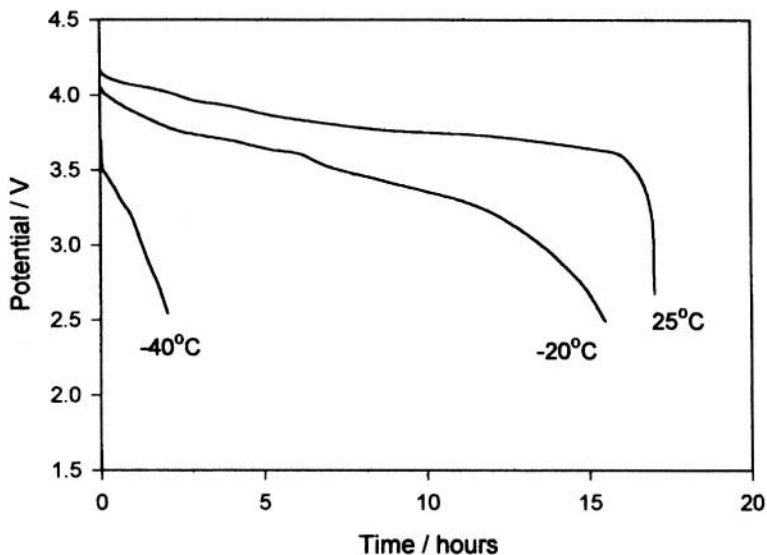
Figure 19. Typical discharge curves for cell (14) at a constant current of 1 mA as a function of temperature. The LiCoO$_2$ electrode was 0.51 mm thick and 15.7 mm in diameter. Data interpolated from reference 85.

4.0   SUMMARY AND CONCLUSIONS

Much progress has been made in improving the performance of Li-ion cells at temperature extremes since the last major review in 1994 [128]. The chemistry of liquid electrolytes and their interaction with anode and cathode materials is complex, and methods of improving stabilities over a wide temperature range is a delicate balance of various properties. For example, to insure high conductivities down to -40°C, a low viscosity solvent is almost always required. However, most low viscosity solvents such as esters and ethers are classified as "aggressive" solvents as they readily react with anode materials (esters and ethers) or high voltage cathode materials (ethers). The most successful approaches to improving the chemical and electrochemical stability of electrolyte solutions are now based on the use of mixed solvents, preferably ternary and quaternary mixtures of cyclic and alkyl carbonates with low viscosity components. One major conclusion reached by the scientific community regarding the electrolyte solution is the need to replace **LiPF$_6$** with more stable and highly conductive electrolytes.

The stability of anode and cathode materials is also complex. In addition to their interaction with the electrolyte solution, the problems of thermal stability, Lithium ion diffusion, irreversible phase changes, and intrinsic electronic

resistivities all contribute to limitations in cell performance over the wide temperature range of -40°C to ~71°C. Associated with these limitations is the nature of the SEI, which forms at **both** the anode and cathode. The use of additives to eliminate, or at least minimize the problems associated with SEI formation has been partly achieved by the use of additives. This is also an important area for future exploration.

5.0   ACKNOWLEDGEMENTS

6.0   REFERENCES

1.   J. Barthel, H-J. Gores, G. Schmeer and R. Wachter, *Topics in Current Chemistry,* Vol. 111, Springer, Berlin, pages 33-144, 1982
2.   J.T. Dudley, D.P. Wilkinson, G. Thomas, R. LeVae, S. Woo, H. Blom, C. Horvath, M.W. Juzkow, B. Denis, P. Juric, P. Aghakian and J.R. Dahn, *J. Power Sources,* **35**, 59,1991.
3.   L. Dominey in *Lithium Batteries: New Materials, Developments and Perspectives.* G. Pistoia, ed., Elsevier, Amsterdam, 1994.
4.   H.-J. Gores and J. Barthel, *Pure & Appl. Chem.,* **67**, 919,1995.
5.   W.B.Ebner,*Proc. 29ᵗʰ Power Sources Symposium,* p. 69,1980.
6.   E. Plichta, M. Salomon, S. Slane and M. Uchiyama, *J. Solution Chem.,* **16**, 225, 1987.
7.   M. Salomon, S. Slane, E. Plichta and M. Uchiyama, *J. Solution Chem.* **18**, 977, 1989.
8.   M. Salomon, M. Uchiyama, M. Xu and S. Petrucci, *J. Phys. Chem.,* **93**, 4374, 1989.
9.   J. Barthel, H-J. Gores and G. Schmeer, *Ber. Bunsenges. Phys. Chem.,* **83**, 911, 1979.
10.   M. Salomon and E. Plichta, *Electrochim. Acta,* **28**, 1681, 1983.
11.   M. Ue, *J. Electrochem. Soc.,* **141**, 3336 (1994): **143**, L270, 1996.
12.   M. Salomon, *J. Solution Chem.,* **22**, 715, 1993.
13.   N. Inoue, M. Xu and S. Petrucci, *J. Phys. Chem.,* **91**, 4628, 1987.
14.   M. Delsignore, H.E. Maaser and S. Petrucci, *J. Phys. Chem.,* **88**, 2405, 1984.
15.   E. Plichta, S. Slane, M. Uchiyama, M. Salomon, D. Chua, W.B. Ebner and H.-p. Lin, *J. Electrochem. Soc.,* **136**, 1865, 1989.
16.   W.B. Ebner, H.-. Lin and J.A. Simmons, *Sixth Quarterly Report,* U.S. Army Laboratory Command, Contract N°. SLCET-TR-86-0004-6.
17.   H-J. Gores and J. Barthel, *J. Solution Chem.,* **9**, 939, 1980.
18.   N. Margalit and H.J. Canning, *J. Electrochem. Soc.* **127**, 344C, 1980.
19.   J. Barthel and F. Feuerlein, *Z. Physik. Chem., N.F.,* **148**, 157, 1986.
20.   Y. Matsuda, M. Morita and F. Tachihara,*Bull. Chem. Soc. Jpn.,* **59**, 1967, 1989.
21.   D. Saar, J. Brauner, H. Faber and S. Petrucci, *J. Phys. Chem.,* **82**, 2531, 1978.
22.   M. Armand and F. Moursli, *U.S.* Patent 4,505,997, March, 1985.

23. L.A. Dominey, V.R. Koch and T.J. Blakley, *Electrochim. Acta,* **37,** 1551 (1992): U.S. Patent 5,273,840, December, 1993.
24. T.C. Ehlert and M.M. Hsia, *J. Chem. Eng. Data,* **17,** 1699, 1972.
25. S.E. Sloop, J.K. Pugh, S. Wang, J.B. Kerr and K. Kinoshita, *Electrochem. Solid-State Lett.,* **4,** A42, 2001.
26. Y. Sasaki, M. Handa, K. Kurashima, T. Tonuma and K. Usami, *J. Electrochem. Soc.,* **148,** A999, 2001.
27. C.G. Barlow, *Electrochem. Solid-State Lett.,* **2,** 362, 1999.
28. S. Lu, W.F. Averill, A.D. Robertson and W.F. Howard in *Proc. 13th Intern. Seminar on Primary and Secondary Battery Technology and Application.* Florida Educational Seminars, Boca Raton, FL., 1996.
29. D.H. Jang, Y.J. Shin and S.M. Oh, *J. Electrochem. Soc.,* **143,** 2204, 1996.
30. L.J. Krause, W. Lamanna, J. Summerfield, M. Engle, G. Korba, R. Och and R. Atanasoski, *J. Power Sources,* **68,** 320, 1997.
31. W.K. Behl and E.J. Plichta, *J. Power Sources.* **72,** 132, 1998.
32. J. Barthel, A. Schmid and H.-J. Gores, *J. Electrochem. Soc.,* **147,** 21 (2000) and references cited therein.
33. R. Jüschke, M. Köckerling and P. Sartori, *Z. Naturforsch,* **53b,** 135, 1998.
34. E. Peled in *Li Batteries,* J.P. Gabano, Ed., Academic Press, NY, 1983.
35. E. Peled in *Proc. Symp. Li and Li-ion Batteries,* S. Megahed, Ed., The Electrochemical Society, Pennington, NJ, 1995.
36. E. Plichta, M. Salomon, S. Slane and M. Uchiyama, U.S. Patent 4,786,499, November 1988.
37. D. Aurbach, M. Daroux, P. Faguy and E. Yeager, *J. Electrochem. Soc.,* **134,** 1611, 1987.
38. M.M. Thackeray, M.F. Mansuetto, D.W. Dees and D.R. Vissers, *Mater. Res. Bull.,* **31,** 133, 1996.
39. L. Vogdanis, B. Martens, U. Uchtmann, F. Hensel and W. Heitz, *Makromol. Chem.,* **191,** 465, 1990.
40. D. Aurbach, Y. Ein-Elim, B. Markovsky, A. Zaban, S. Luski, Y. Carmeli and H. Yamin, *J. Electrochem. Soc.,* **142,** 2882, 1995.
41. D. Aurbach, A. Zaban, Y. Gofer, O. Abramson and M. Ben-Zion, *J. Electrochem. Soc.,* **142,** 687, 1995.
42. D. Aurbach, I. Weissman, H. Yamin and E. Elster, *J. Electrochem. Soc.,* **145,** 1421, 1998.
43. H. Yoshida, T. Fukunaga, T. Hazama, M. Terasaki, M. Mizutani and M. Yamachi, *J. Power Sources,* **68,** 311, 1997.
44. Y. Ein-Eli, S.R. Thomas and V. Koch, *J. Electrochem. Soc.,* **143,** L273, 1996.
45. Y. Ein-Eli, S.F. McDevitt and R. Laura, *J. Electrochem. Soc.,* **145,** L1, 1998.
46. Y. Ein-Eli, *Electrochem. Solid-State Lett.,* **2**, 212, 1999.
47. M. Salomon, *Pure & Appl. Chem.,* **70,** 1905, 1998.
48. C.-K. Huang, J.S. Sakamoto, J. Wolfenstine and S. Surampudi, *J. Electrochem. Soc,* **147,** 2893, 2000.
49. H.S. Lee, X.Q. Yang, J. McBreen, L.S. Choi and Y. Okamoto, *J. Electrochem. Soc.,* **143,** 3825, 1996.
50. H.S. Lee, X.Q. Yang, C.L. Xiang and J. McBreen, *J. Electrochem. Soc.,* **145,** 2813, 1998.
51. X. Sun, H.S. Lee, X.Q. Yang and J. McBreen, *Electrochem. Solid-State Lett.,* **4,** A184, 2001.

52.   Bellcore US Patent N°. 5,296,318, March 22, 1994: see also F.K. Shokoohi, P.C. Warren, S.J. Greaney, M.-M. Tarascon, A.S. Gozdz, and G.C. Amatucci, *Proc. 35th Power Sources Conference,* Cherry Hill, NJ, 8-11 June 1996.
53.   A. Du Pasquier, F. Disma, T. Bowmer, A.S. Gozdz, G. Amatucci and J-M. Tarascon, *J. Electrochem. Soc.,* **145,** 472, 1998.
54.   S.P.S. Yen, D.H. Shen and R.B. Somoano, *J. Electrochem. Soc.,* **120,** 1107, 1983.
55.   T. Zheng, A.S. Gozdz and G.G. Amatucci, *J. Electrochem. Soc.,* **146,** 4014, 1999.
56.   R.D. Rauh and S.B. Brummer, *Electrochim. Acta,* **22**, 85, 1977.
57.   J.L. Goldman, R.M. Mank, J.H. Young and V.R. Koch, *J. Electrochem. Soc.,* **127,** 1461, 1980.
58.   K.M. Abraham, J.S. Foos and J.L. Goldman, *J. Electrochem. Soc.,* **131,** 2197, 1984.
59.   J.O. Besenhard, P. Castella and M.W. Wagner, *Mater. Sci. Forum,* **91-93,** 647, 1992.
60.   Z.X. Shu, R.S. McMillan and J.J. Murry, *J. Electrochem. Soc.,* **142,** L161, 1995.
61.   M. Winter and P. Novák, *J. Electrochem. Soc.,* **145**, L27, 1988.
62.   M.C. Smart, B.V. Ratnakumar and S. Surampudi in *Proc.* **196**[th] *Meeting of the Electrochemical Society,* Honolulu, HI, 17-22 October, 1999.
63.   H.-p. Lin, D. Chua, M. Salomon, H-C. Shiao, M. Hendrickson, E. Plichta and S. Slane, *Electrochem. Solid-State Lett.,* **4,** A71, 2001.
64.   J.R. Dahn, *Phys. Rev. B: Condens. Matter,* **44,** 9170, 1991.
65.   T. Ohzuku, Y. Iwakoshi and K. Sawai, *J. Electrochem. Soc.,* **140,** 2490, 1993.
66.   Z.X. Shu,, R.S. McMillan and J.J. Murray, *J. Electrochem. Soc.,* **140,** 922, 1993.
67.   G.H. Wrodnigg, J.O. Besenhard and M. Winter, *J. Electrochem. Soc.,* **146,** 470, 1999.
68.   Ph. Biesan, J.M. Bodet, F. Perton, M. Broussely, C. Jehoulet, S. Barusseau, S. Herreye and B. Simon. Paper Presented at the **10**[th] *International Meeting on Lithium Batteries.* Como, Italy, 28 May to 2 June, 2000.
69.   *French Patent* Fr 94 04889, April, 1994.
70.   B. Simon and J-P. Boeuve, *U.S. Patent* 5,626,981, May, 1997.
71.   F. Cassel, D. Chua, H.-p. Lin and M. Salomon, *Monthly Report to The U.S. Army CECOM Laboratory* under Contract No. DAABO7-99-C-D278, September, 2000.
72.   A. Choblet, D. Chua, H.-p. Lin and M. Salomon, *Monthly Report to The U.S. Army Research Laboratory* under Contract No. DAAD17-99-C-0004, August, 1999.
73.   J.R. Dahn, R. Fong and M.J. Spoon, *Phys. Rev. B,* **24,** 6424, 1990.
74.   O. Chusid, Y. Ein-Eli, D. Aurbach, M. Babai and Y. Carmeli, *J. Power Sources,* **43-44,** 47, 1993.
75.   Z.X. Shu, R.S. McMillan and J.J. Murray, *J. Electrochem. Soc.,* **140,** L101, 1993.
76.   S-I. Tobishima and A. Yamaji, *J. Power Sources,* **12,** 53, 1984.
77.   M. Salomon, *J. Solution Chem.,* **19,** 1225, 1990.
78.   M. Salomon, *J. Electroanalyt. Chem.,* **355,** 265,1993.
79.   M. Salomon and G.T. Hefter, *Pure & Appl. Chem.,* **65,** 1533, 1993.
80.   A.F. Danil de Namor, M.A. Llosa Tanco, M. Salomon and J.C.Y. Ng, *J. Phys. Chem.,* **98,** 11796, 1994.
81.   A.F. Danil de Namor, J.C.Y. Ng, M.A. Llosa Tanco and M. Salomon, *J. Phys. Chem.,* **100,** 14485, 1996.
82.   A. D´Aprano, J. Vicens, Z. Asfari, M. Salomon and M. Iammarino, *J. Solution Chem.,* **25,** 955, 1996.

83. M. Hendrickson, E.J. Plichta, W.K. Behl, G. Au and L. Locke, *Proc. 39th Power Sources Conference.* Cherry Hill, NJ, 12-15 June (2000), page 96.

84. G.Y. Gu, R. Laura, and K.M. Abraham, *Electrochem. Solid-State Lett.,* **2,** 486, 1999.

85. E.J. Plichta and W.K. Behl, *Proc. 38th Power Sources Conference,* Cherry Hill, NJ, 8-11 June 1998, page 444.

86. E.J. Plichta, M. Hendrickson, R. Thompson, G. Au, W.K. Behl, M.C. Smart, B.V. Ratnakumar and S. Surampudi, *J. Power Sources,* **94,** 160, 2001.

87. M.C. Smart, B.V. Ratnakumar, C.-K. Huang and S. Surampudi, *Proc. Electrochem. Soc.,* San Diego, CA, 2-8 May 1998, abstr. 53.

88. M. Hendrickson and E.J. Plichta, unpublished results (in course of publication).

89. B. Ravdel, K.M. Abraham, R. Gitzendanner and C. Marsh, *Proc. Electrochem. Soc.,* San Francisco, CA, 2-7 September 2001, abstr. 97.

90. M.C. Smart, B.V. Ratnakumar, C.-K. Huang and S. Surampudi, *Aerospace Power Systems Workshop,* Williamsburg, VA, 21-23 April 1998.

91. G. Au, L. Locke and J. Rafferty, *Proc. 16th Annual Battery Conference on Applications and Advances,* Long Beach, CA, 9-12 January 2001, pp. 17-22.

92. S. Herreyre, O. Huchet, S. Barusseau, F. Perton, J.M. Bodet and Ph. Biensan, *J. Power Sources,* **97-98,** 576, 2001.

93. H.-C. Shiao, D. Chua, H-p. Lin, S. Slane and M. Salomon, *J. Power Sources,* **87**, 167, 2000.

94. J. Fan, G. Nagarajan, R.M. Spotnitz and M. Anderman, *Proc. Symp. on Lithium Batteries,* S. Surampudi and R. Marsh, eds. The Electrochemical Society, **98-16,** 512, 1999.

95. M.C. Smart, B.V. Ratnukumar, S. Surampudi, Y. Wang, X. Zhang, S.G. Greenbaum, A. Hightower, C.C. Ahn and B. Fultz, *J. Electrochem. Soc.,* **146,** 3963, 1999.

96. W. Ebner, D. Fouchard and L. Xie, *Solid State Ionics,* **69,** 238, 1994.

97. D. Aurbach, M.D. Levi, E. Levi, B. Markovsky, G. Salitra, H. Teller, U. Heider and V. Hilarius in *Batteries for Portable Applications for Electric Vehicles,* C.F. Holmes and A.R. Landgrebe, eds., *Proc. Electrochem. Soc.,* **97-18,** 941, 1997.

98. R. Imhof and P. Novák, *J. Electrochem. Soc.,* **146,** 1702, 1999.

99. K. Amine, C.H. Chen, J. Liu, M. Hammond, A. Jansen, D. Dees, I. Bloom, D. Vissers and G. Henriksen, *J. Power Sources,* **97-98**, 684, 2001.

100. Y. Wang, X. Guo, S. Greenbaum, J. Liu and K. Amine, *Electrochem. Solid-State Lett.,* **4,** A68, 2001.

101. A. Honders, M.M. der Kinderen, A.H. van Heeren, J.H.W. de Wit and G.H.J. Broers, *Solid State Ionics,* **14,** 205, 1984.

102. D.D. MacNeil and J.R. Dahn, *J. Electrochem. Soc.* **148,** A1205, 2001.

103. G.M. Ehrlich, *Lithium-Ion Batteries,* in *Handbook of Batteries, third edition,* D. Linden and T.B. Reddy, eds. McGraw-Hill, NY, 2001.

104. D. Aurbach, K. Gamolsky, B. Markovsky, G. Salitra, Y. Gofer, U. Heider, R. Oesten and M. Schmidt, *J. Electrochem. Soc.,* **147,** 1322, 2000.

105. R.J. Gummow, A. de Kock and M.M. Thackeray, *Solid State Ionics,* **69**, 59, 1994.

106. J-M. Tarascon, W.R. McKinnon, F. Coowar, T.N. Bowner, G. Amatucci and D. Guyomard, *J. Electrochem. Soc.,* **141,** 1421, 1994.

107. A. Yamada and M. Tanaka, *Mat. Res. Bull.,* **30,** 715, 1995.

108. H. Abiko, M. Hibino and T. Kudo, *Electrochem. Solid-State Lett.,* **1,** 114, 1998.

109.   A. Blyr, C. Sigala, G. Amatucci, D. Guyomard, Y. Chabre and J-M. Tarascon, *J. Electrochem. Soc.,* **145,** 194, 1998.

110.   E. Wang, D. Ofer, W. Bowden, N. Iltchev, R. Moses and K. Brandt, *J. Electrochem. Soc.,* **147,** 4023, 2000.

111.   A. Du Pasquier, A. Blyr, P. Courjal, D. Larcher, G. Amatucci, B. Gérand and J-M. Tarascon, *J. Electrochem. Soc.,* **146,** 428, 1999.

112.   G.M. Ehrlich and C. Marsh, *Proc. Workshop for Battery Exploratory Development,* Burlington, Vermont, June 30 - July 3, 1997, pp. 247-251.

113.   L. Xie, D. Fouchard and S. Megahed, *Proc. Mat. Res. Soc. Symp.,* **393,** 285, 1995.

114.   H. Tukamoto and A.R. West, *J. Electrochem. Soc.,* **144,** 3164, 1997.

115.   J. Guan and M. Liu, *Meeting Abstracts, 190th Meeting of The Electrochemical Society,* San Antonio, Texas, October 6-11, 1996: abstract 865 (page 1066).

116.   J. Cho, H Jung, Y. Park, G. Kim and H-S. Lim, *J. Electrochem. Soc.,* **147,** 15, 2000.

117.   P.G. Bruce, *Chem. Commun.* 1817, 1997.

118.   A. Funabiki, M. Inaba, Z. Ogumi, S. Yuasa, J. Otsuji and A. Tasaka, *J. Electrochem. Soc.,* **145,** 172, 1998.

119.   M. Nishizawa, R. Hashitani, T. Itoh, T. Matsue and I. Uchida, *Electrochem. Solid-State Lett.,* **1,** 10, 1998.

120.   T. Piao, S-M. Park, C-H. Doh and S-I. Moon, *J. Electrochem. Soc.,* **146,** 2794, 1999.

121.   E. Barsoukov, J. Hyun Kim, J. Hun Kim, C.O. Yoon and H. Lee, *J. Electrochem. Soc.,* **145,** 2711, 1998.

122.   M.G.S.R. Thomas, P.B. Bruce and J.B. Goodenough, *Solid State Ionics,* **17** 13, 1985.

123.   K. Mizushima, P.C. Jones, P.J. Weisman and J.B. Goodenough, *Solid State Ionics,* **3/4,** 171, 1981.

124.   P.G. Dickens and G.F. Reynolds, *Solid State Ionics,* **5,** 52, 1981.

125.   M. Lanz, C. Kormann, H. Steininger, G. Heil, O. Haas and P. Novák, *J. Electrochem. Soc.,* **147,** 3997, 2000.

126.   M. Carewska, S. Scaccia, F. Croce, S. Arumugam, Y. Wang and S. Greenbaum, *Solid State Ionics,* **93,** 227, 1997.

127.   M. Balasubramanian, H.S. Lee, X. Sun, X.Q. Yang, A.R. Moodenbaugh, J. McBreen, D.A. Fischer and Z. Fu, *Electrochem. Solid-State Lett.,* **5,** A22, 2002.

128.   G. Pistoia, Editor. *Lithium Batteries: New Materials, Developments and Perspectives.* Elsevier, Amsterdam, 1994.

12

Mathematical Modeling of Lithium Batteries

Karen E. Thomas
John Newman
Department of Chemical Engineering
University of California at Berkeley
& Lawrence Berkeley National Labs
Berkeley, California
USA

Robert M. Darling
International Fuel Cells
South Windsor, Connecticut
USA

1.0   INTRODUCTION

Previous reviews of the equations, numerical methods, and uses of models of lithium batteries are given in references [1,2,3,4]. We refer the reader to these reviews for references regarding early works, and focus in this paper on work published since these reviews. However, we acknowledge that much of the theory used in modeling lithium batteries was developed previously for other battery systems, such as lead acid, alkaline zinc-MnO_2, molten salt LiAl-FeS, and nickel-metal hydride. When citing the development of some model formulations, we cite these original works even though they do not specifically apply to lithium batteries.

Early work on modeling lithium batteries, performed prior to the ready availability of high-speed digital computers, used simplified models neglecting kinetic or concentration effects, assuming constant properties, or neglecting the separator, in order to obtain a close approximation to battery behavior within the limits of computational power available at the time. Today´s computers can easily simulate the entire cell sandwich, obviating the need for the simplifying assumptions used previously. We therefore see no need to review the history of the development of the full-cell-sandwich model, and simply present the model in the best form developed to date in Section 3, followed by considerations of special situations which are not essential to the basic modeling framework. Simplifying cases which have contributed to our understanding of the lithium battery are presented in Section 5. Finally, we discuss applications of modeling, such as interpreting experimental data and optimizing geometric parameters.

2.0   FEATURES OF THE LITHIUM BATTERY

Figure 1 shows a schematic of a lithium battery. Lithium battery electrodes are usually made by coating a slurry of the active material, conductive filler, and binder onto a foil current collector. This porous configuration provides a high surface area for reaction and reduces the distance between reactants and the surfaces where reactions occur. In these porous electrodes, the electrochemical reaction is distributed over the surface of the particles of active material, and will vary across the depth of the electrode due to the interaction of potential drop and concentration changes in both the solution and solid phases. Porous electrode theory is used to understand these interactions.

Most electrodes used in lithium batteries are insertion compounds. In an insertion reaction, lithium ions from solution combine with an electron in the electrode to reside in an interstitial site in the host lattice. Such materials exhibit long cycle lives because the electrochemical reaction causes relatively little disturbance to the active material. They are also rather convenient to model, because volume changes can usually be neglected, and there is little change in the morphology of the electrode during cycling. In contrast to phase-change electrodes, such as the $Cd\,|\,Cd(OH)_2$ electrode, the potential of the solid material in insertion electrodes varies with state of charge *(i.e.,* lithium concentration). The combination of lithium diffusion in the solid phase and the nonlinear dependence of the chemical potential on lithium concentration lead to interesting situations in these materials.
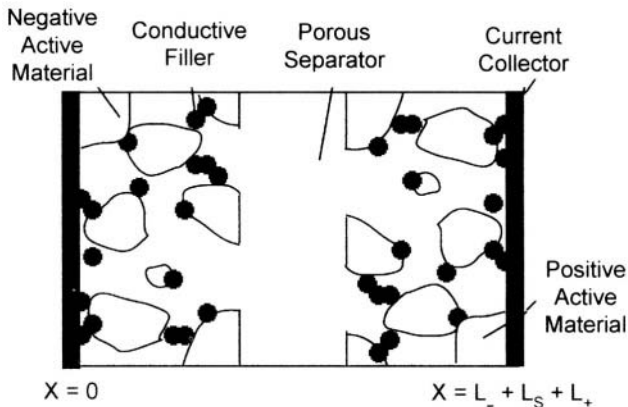
Figure 1. Diagram of a lithium-ion cell.

The organic electrolytes used in lithium batteries generally exhibit nonideal behavior, and usually concentrated solutions of 1 to 1.5 M are used. Moreover, mass transport in the nonaqueous electrolytes used in lithium batteries often has a large impact on battery performance at moderate to high current densities, and cannot be assumed to be negligible. Fortunately, the electrolyte in most cases consists of a single salt in a homogeneous solvent, a case which is

easily treated rigorously by concentrated solution theory. The solvent may be a single liquid, a mixture of liquids, a gel, or a polymer. Technically in solvent mixtures, ions will interact differently with the different solvent components, causing gradients in solvent composition as ions drag solvent molecules along with them during passage of current. However, for realistic battery electrolyte conditions, the assumption that a solvent mixture behaves as a single solvent does not appear to introduce significant error [5]. Electrolytes with multiple salts and solvents can be treated using concentrated solution theory [6,7,8], although experimental determination of the complete set of transport properties is difficult. For an electrolyte of n ions and solvent species, $n(n–1)/2$ transport properties are required to describe mass transport completely.

A battery consists of three regions: positive electrode, negative electrode, and separator. The importance of considering interactions among mass transport and potential in the electrolyte in all three regions when considering solution-phase limitations in one of the regions has been demonstrated [9].

3.0   BASIC EQUATIONS

In this section we describe the equations required to simulate the electrochemical performance of porous electrodes with concentrated electrolytes. Extensions to this basic model are presented in Section 4. The basis of porous electrode theory and concentrated solution theory has been reviewed by Newman and Tiedemann [1]. In porous electrode theory, the exact positions and shapes of all the particles and pores in the electrode are not specified. Instead, properties are averaged over a volume small with respect to the overall dimensions of the electrode but large with respect to the pore structure. The electrode is viewed as a superposition of active material, filler, and electrolyte, and these phases coexist at every point in the model. Particles of the active material generally can be treated as spheres. The electrode phase is coupled to the electrolyte phase via mass balances and via the reaction rate, which depends on the potential difference between the phases. All phases are considered to be electrically neutral, which assumes that the volume of the double layer is small relative to the pore volume. Where applicable, we also indicate boundary conditions that would be used if a lithium foil electrode were used in place of a negative insertion electrode.

3.1   *Potential in the Electrolyte*

We define the potential in the binary electrolyte to be measured by a reference electrode that undergoes the reversible half-cell reaction

$$s_- M_-^{z_-} + s_+ M_+^{z_+} + s_o M_o \rightleftharpoons n e^- \tag{1}$$

The gradient of the potential in the solution, as measured by such a reference electrode with respect to another reference electrode of the same kind at a fixed position, is then determined by [10]

$$\nabla\Phi_2 = -\frac{i_2}{\kappa} - \frac{\nu RT}{F}\left(\frac{s_+}{n\nu_+} + \frac{t_+^o}{z_+\nu_+} - \frac{s_o c}{n c_o}\right)\left(1 + \frac{d\ln f_\pm}{d\ln c}\right)\nabla\ln c \qquad (2)$$

In lithium batteries, one usually selects the reference electrode to be lithium metal, and a 1:1 binary electrolyte is generally used. Then $s_o = s_{--} = 0, s_+ = -1, \nu_+ = n = 1$, and $\nu = 2$, and the above equation reduces to

$$\nabla\Phi_2 = -\frac{i_2}{\kappa} + \frac{2RT}{F}\left(1 - t_+^o\right)\left(1 + \frac{d\ln f_\pm}{d\ln c}\right)\nabla\ln c \qquad (3)$$

The second term on the right side accounts for concentration overpotential. In porous media, the conductivity is corrected by the Bruggeman relation, $\kappa = \varepsilon^{1.5}\kappa_\infty$, where κ_∞ is the conductivity of the bulk electrolyte.

Since only potential differences, and not absolute potentials, are measurable, Φ_2 has an arbitrary datum as a boundary condition. Reference 11 sets $\Phi_2 = 0$ at the positive electrode-current collector interface.

3.2   *Potential in the Solid*

The potential in the porous solid (electrode) phase is determined from Ohm´s Law:

$$I - i_2 = -\sigma\nabla\Phi_1 \qquad (4)$$

where $I - i_2 = i_1$ is the current in the electrode phase and the electronic conductivity of the bulk solid is corrected for the volume fraction of the electrode by the Bruggeman relation, $\sigma = \sigma_\infty (1-\varepsilon)^{1.5}$. σ_∞ is the conductivity of the nonporous composite (active + conductive filler + binder) electrode.

This equation has one boundary condition in each electrode region. For galvanostatic operation, the boundary condition in the negative electrode is $i_2 = I$ at the negative electrode-separator interface, and in the positive electrode it is $i_2 = 0$ at the positive electrode-current collector interface. When all six governing equations are solved simultaneously, these boundary conditions enforce the requirement that the potential in the solid phase be adjusted so that the total amount of reaction across the electrode is equal to the applied current. For potentiostatic operation, $\Phi_1\big|_{x=L_-+L_s+L_+} - \Phi_1\big|_{x=0} = V$.

3.3   Transport in the Electrolyte

3.3.1   Dilute Solution Theory

Dilute solution theory is not often used in the treatment of lithium batteries, because most electrolytic solutions used in lithium batteries exhibit concentrated behavior. However, dilute solution theory becomes useful for cases such as the examination of side reactions such as redox shuttles for overcharge protection, because concentrated solution theory becomes more complicated when there are more than three species (anion, cation, and solvent) in solution.

The basic flux equation for dilute solution theory is

$$\frac{N_i}{\varepsilon} = -D_i \nabla c_i - z_i u_i F c_i \nabla \Phi + \frac{c_i \mathbf{v}_o}{\varepsilon} \tag{5}$$

where N_i is the flux of species i across the apparent area of the electrode, N_i/ε is the flux through the region occupied by the solution phase, and the mobility is usually related to the diffusivity by the Nernst-Einstein equation, $D_i = RT u_i$. Dispersion can be included in this equation if solvent velocity in the electrodes is significant [1], but this is rarely the case in the thin cell configurations commonly used in lithium batteries. The effective diffusivity used in this equation includes effects of tortuosity.

The electrostatic potential in solution is then obtained by recognizing that the current density in solution is due to the net flux of ions:

$$\nabla \Phi_2 = -\frac{i_2}{\kappa} - \frac{\varepsilon F}{\kappa} \sum_i z_i D_i \nabla c_i \tag{6}$$

In dilute solution theory, this equation is used instead of Equation 3.

3.3.2   Concentrated Solution Theory

Concentrated solution theory includes interactions among all species present in solution whereas dilute solution theory assumes that ions interact only with the solvent and not with other ions. In addition, dilute solution theory assumes that all activity coefficients are unity. There is substantial evidence that both liquid and especially polymer electrolytes used in lithium batteries exhibit concentrated behavior [12,13,14,15].

The foundation of concentrated solution theory is the Stefan-Maxwell multicomponent diffusion equation [16,17],

$$c_i \nabla \mu_i = RT \sum_i \frac{c_i c_j}{c_T \mathcal{D}_{ij}} \left(\mathbf{v}_j - \mathbf{v}_i \right) \tag{7}$$

where $\mathbf{v}_i$ is the velocity of species i in the interstitial solution phase with respect to a reference velocity and $\mathcal{D}_{ij}$ express the pairwise frictional interactions among species. This expression relates the driving force for species motion to all of the pairwise interactions among the components.

With the selection of a reference velocity, the Stefan-Maxwell equations can be inverted to yield flux equations. We choose the reference velocity to be that of the solvent and consider the case of a binary electrolyte, for which flux equations can be obtained for both the cation and anion. Since usually only the cation reacts in lithium batteries, the equations are made simpler later on if we focus only on a mass balance for the anion. By electroneutrality, the mass balance for the anion must be identical to that for the cation. The flux equation for the anion obtained from inverting the Stefan-Maxwell equations is

$$N_- = -\frac{v_-\mathcal{D}}{vRT}\frac{c_T}{c_o}\varepsilon c\nabla\mu_e + \frac{i_2 t_-^o}{z_- F} + c_-\mathbf{v}_o \tag{8}$$

where the diffusion coefficient of the electrolyte, $\mathcal{D}$, and the transference number t_-^o with respect to the solvent are related to the diffusion coefficients $\mathcal{D}_{ij}$ by

$$\mathcal{D} = \frac{\mathcal{D}_{o+}\mathcal{D}_{o-}(z_+ - z_-)}{z_+\mathcal{D}_{o+} - z_-\mathcal{D}_{o-}} \tag{9}$$

$$t_-^o = 1 - t_+^o = \frac{-z_-\mathcal{D}_{o-}}{z_+\mathcal{D}_{o+} - z_-\mathcal{D}_{o-}} \tag{10}$$

From porous electrode theory, the mass balance for the anion is

$$\varepsilon\frac{\partial c_-}{\partial t} = -\nabla \cdot N_- + aj_- \tag{11}$$

where aj_- is the reaction rate of the anion per unit volume. This equation involves averaging over a region small with respect to the overall dimensions but large compared to the pore structure [1,18]. The idea is to capture the essential behavior of a composite medium without having to specify the shape and position of every pore in the porous electrode. Because porous electrode theory treats the electrode as a superposition of solid and solution phases, the electrochemical reaction enters the equation as a homogeneous term rather than as a boundary condition. Substituting in the flux equation, one obtains

$$\varepsilon\frac{\partial c}{\partial t} = \nabla \cdot \varepsilon D\left(1 - \frac{d\ln c_o}{d\ln c}\right)\nabla c + \frac{t_-^o\nabla \cdot i_2 + i_2 \cdot \nabla t_-^o}{z_+ v_+ F} - \nabla \cdot c\mathbf{v}_o + aj_- \tag{12}$$

which was obtained using the relations $c = c_-/v_-$, $\mu_e = v_+\mu_+ + v_-\mu_- = \mu_e^{\Theta} + vRT \ln \gamma_{\pm} m$ (definition of chemical potential for the salt in the electrolyte), $m = c/(c_o M_o)$ (conversion between molality and concentration), and $z_+ v_+ = -z_- v_-$ (charge balance for a binary electrolyte). The chemical diffusion coefficient, D, is the property commonly measured for a binary electrolyte, and is related to the diffusion coefficient of the electrolyte, $\mathcal{D}$, by

$$D = \mathcal{D}\frac{c_T}{c_o}\left(1 + \frac{d \ln \gamma_{\pm}}{d \ln m}\right) \tag{13}$$

Convection in the electrolyte is usually negligible [19]; then the term involving v_o can be neglected. $z_+ v_+$ is 1 for most salts used in lithium batteries, and j_- is zero in the absence of side reactions. If there is no change in volume in the electrode (*i.e.,* the active material does not change in volume as it reacts, and there is no side reaction that changes the electrode porosity), then no mass balance for the solvent is needed. We discuss volume changes in Section 4.8. In the separator, $\nabla \cdot i_2 = 0$, and ε is the volume fraction of electrolyte in the separator (equal to 1 if no inert separator material, such as glass felt or porous polyethylene, is used).

The form of the mass balance presented in Equation 12 is the most convenient for treating multiple reaction pathways, such as arise when treating side reactions, double-layer capacitance, or particle-size distributions (see Section 4). In these situations, $\nabla \cdot i_2$ may have a complicated relationship to the local reaction rates, but the mass balance in the form of Equation 12 remains unchanged. A current balance for calculating $\nabla \cdot i_2$ is discussed in Section 3.6.

The boundary condition at a lithium foil electrode is that the flux of the anion is zero. Then diffusion of the anion is balanced by migration:

$$\varepsilon \frac{\partial c}{\partial x}\bigg|_{x=0} = -\frac{I(1 - t_+^o)}{FD}, \quad \text{foil electrode} \tag{14}$$

The flux of the salt is zero at the current collectors of porous electrodes, where all of the current is in the matrix phase:

$$\frac{\partial c}{\partial x} = 0 \quad \text{at} \quad x = L_- + L_s + L_+ \quad \text{and} \quad x = 0, \quad \text{porous electrodes} \tag{15}$$

The concentration and flux are continuous at the interface between the separator and a porous electrode.

When ion-exchange polymers (ionomers), for which $t_+^o = 1$, are used for the electrolyte, no mass balance equation is needed, because the concentration of cations is fixed by the concentration of immobile anions. In this case, only one transport property, the conductivity, is needed, as opposed to the three trans-

port properties (κ, D, and t_+^o) needed to characterize concentrated solutions and the two transport properties (D_+ and D_-) used for dilute solutions.

The averaging inherent to porous electrode theory introduces some (usually very small) degree of error in calculating the actual potential and concentration at the pore wall. Mass-transfer coefficients can be introduced to try and compensate, such as using an effective mass-transfer equation, $j_n = -k_m(c-c_{wall})$, to solve to solve for the electrolyte concentration at the pore wall [31]. Tsaur and Pollard [8] report that mass transfer within pores has a significant effect on cell performance only for species present in small concentrations.

3.4   *Transport in the Solid*

The porous solid phase in most lithium batteries contains particles which can be modeled as spheres. The active material of the insertion electrodes used in most lithium-ion batteries consists of mobile cations, mobile electrons, and immobile host matrix. If one neglects the effects of stress and anisotropic diffusion, then transport of lithium ions can be described as above, yielding

$$\frac{\partial c_s}{\partial t} = \nabla \cdot D_s \left(1 - \frac{d\ln c_o}{d\ln c_s}\right) \nabla c_s + \frac{i_1 \cdot \nabla t_-^o}{z_+ v_+ F} - \nabla \cdot c_s \mathbf{v}_o \tag{16}$$

Since the active material is generally a good electronic conductor, $t_-^o \approx 1$ and the second term can be neglected. If volume changes in the solid are negligible, then $\mathbf{v}_o$ and $d\ln c_o / d\ln c_s$ are zero, and the mass balance reduces to

$$\frac{\partial c_s}{\partial t} = \frac{1}{r^2} \frac{\partial}{\partial r}\left(D_s r^2 \frac{\partial c_s}{\partial r}\right) \tag{17}$$

with the boundary conditions

$$\left.\frac{\partial c_s}{\partial r}\right|_{r=0} = 0 \quad \text{and} \quad -D_s \left.\frac{\partial c_s}{\partial r}\right|_{r=R} = j_{Li^+,f} \tag{18}$$

and initial condition $c_s(t=0, r) = c_s^o$.

From the boundary condition at the edge of the particle, one sees that any changes to calculations of the reaction rate will be coupled to the mass balance in the solid.

Under this framework, diffusion within a solid particle is considered, but diffusion between adjacent solid particles is neglected. Since the length scale between particles is much larger than the length scale within a particle, this simplification should not introduce much error.

3.5   Reaction Rate

A rate equation is needed to determine the dependence of the local electro-chemical reaction rate on concentration and potential. Usually, the Butler-Volmer rate equation is used

$$i_n = i_0 \left[\exp\left(\frac{\alpha_a F (\Phi_1 - \Phi_2 - U)}{RT} \right) - \exp\left(\frac{\alpha_c F (\Phi_1 - \Phi_2 - U)}{RT} \right) \right] \tag{19}$$

The surface overpotential, $\Phi_1 - \Phi_2 - U$, is the deviation from the thermo-dynamic potential difference between the solid and solution at the existing surface concentrations. U is the open-circuit potential of the solid material evaluated at the surface concentration of the solid with respect to a hypothetical lithium reference electrode in solution just outside the diffuse part of the double layer, at the same local electrolyte concentration, and is a function of solid concentration in insertion electrodes. Thus, U must be specified as a function of intercalant concentration but not as a function of electrolyte concentration. This equation is coupled to Equations 3 and 4 for potential in the solid and electrolyte, and sets the surface overpotential with respect to the local potential in solution and in the solid required to force the reaction.

The magnitude and dependence of U on solid concentration vary considerably among different insertion materials. The shape of the open-circuit-potential profile has a large effect upon the simulation results, and accurate data for this property measured with respect to a lithium reference electrode are very important, especially when one is comparing full-cell-sandwich simula-tions with experimental data. Verbrugge and Koch [20] fit the open-circuit potential of carbon fiber by using a polynomial expansion for the excess Gibbs free energy (Wohl expansion), and this expansion matches the measured U well for the disordered carbon. For cases in which such an expansion does not capture the effects of ordering in the active material, we recommend that a careful empirical fit to measurements of the open-circuit potential be used in the simulations.

The anodic and cathodic transfer coefficients, α_a and α_c, correspond to the fractions of the applied potential which favor the anodic and cathodic directions of the overall reaction, respectively. The dependence of exchange current density on concentration is given by

$$i_0 = i_{0,ref} \prod_i \left(\frac{c_i}{c_{i,ref}} \right)^{\gamma_i} \tag{20}$$

where $i_{0,ref}$ is the exchange current density measured at the reference concentrations $c_{i,ref}$. For an elementary step, $\gamma_i = \beta s_i$ if species i is a reactant in the anodic direction and $\gamma_i = (\beta - 1) s_i$ if species i is a reactant in

the cathodic direction, where s_i is the stoichiometric coefficient (positive for anodic reactants) and β is the symmetry factor representing the fraction of the applied potential that favors the cathodic direction of the elementary step [10]. For complex reactions involving multiple elementary steps, γ_i, α_a, and α_c may be complicated functions of the symmetry factors for each elementary step, and γ_i may differ from α_a and α_c [10]. Presently, reaction mechanisms at electrode interfaces, particularly in the presence of the solid-electrolyte interphase, are not understood in great detail. Fortunately, the rapid kinetics of electrodes used in lithium batteries reduces the importance of the exact reaction mechanism in the battery model. In the absence of more detailed information about reaction mechanisms, the reaction can be assumed to be first order in lithium-ion concentration in the electrolyte and lithium concentration in the insertion electrode, which means that α_a, α_c, γ_{Li_s}, and γ_{Li^+} are equal to 0.5. While the assumption that $\gamma_{Li^+} = \alpha_a$ is not necessarily true for a complex reaction mechanism, such an assumption is commonly used in the literature and will be used in the following equations.

At a lithium foil electrode or at a phase-change electrode, the solid concentration is constant. At an insertion electrode involving the reaction

$$\text{Li}\Theta_s \rightleftharpoons \text{Li}^+ + \Theta_s + e^- \tag{21}$$

the exchange current density is given by

$$i_0 = F(k_a)^{\alpha_c}(k_c)^{\alpha_a}(c_{s,\max} - c_s)^{\alpha_c}(c_s)^{\alpha_a}(c)^{\alpha_a} \tag{22}$$

where $(c_{s,\max} - c_s)$ is the concentration of unoccupied sites in the insertion material. Thus, the exchange-current density tends to zero as the solid concentration approaches either 0 or $c_{s,\max}$.

Some models [2] of polymer electrolytes have treated the polymer as having a fixed number of sites $c_{\max}$ for lithium ions on the polymer lattice. The reaction, *e.g.,* at the lithium foil electrode, was then expressed as

$$\text{Li} + \Theta_p \rightleftharpoons \text{Li}^+\Theta_p + e^- \tag{23}$$

leading to the following expression for the exchange current density:

$$i_0 = F(k_a)^{\alpha_c}(k_c)^{\alpha_a}(c_{\max} - c)^{\alpha_c}(c)^{\alpha_a} \tag{24}$$

There is not much experimental evidence for or against this hypothesis, given the uncertainties in the nature of the polymer-solid interface. However, because exchange-current densities for most electrodes used in lithium batteries tend to be high, the precise nature of the kinetic rate constants is not of large importance.

Since the reaction-rate equation is algebraic, it requires no boundary condition.

3.6   Current Balance

The rate of production of species i per unit volume is aj_i. In the most general case, a species can be produced by heterogeneous electrochemical reactions or homogeneous chemical reactions:

$$aj_i = aj_{i,n} + \sum_k s_{i,k} r_k \tag{25}$$

where $aj_{i,n}$ is the net flux of species i due to electrochemical reaction normal to the active material surface and r_k is the rate of the kth chemical reaction. For an electrochemical reaction expressed by

$$\sum_i s_i M_i^{z_i} \rightarrow ne^- \tag{26}$$

the faradaic reaction of species i is related to the rate of electrochemical reaction by

$$aj_{i,n} = -\frac{as_i}{nF} i_n \tag{27}$$

and i_n is determined by a kinetic relationship as described in the previous section.

By electroneutrality, a current balance relates the divergence of the current to the net pore-wall flux due to reaction:

$$\nabla \cdot i_2 = ai_n \tag{28}$$

For the case of multiple electrochemical reactions,

$$\nabla \cdot i_2 = \sum_l a_l i_{n,l} \tag{29}$$

and

$$aj_{i,n} = -\sum_l \frac{a_l s_{i,l}}{nF} i_{n,l} \tag{30}$$

The boundary condition on this equation is that the divergence of the current is zero in the separator.

3.7   Energy Balance

An energy balance is required to calculate the heat generated by the cell and the temperature changes in a cell or stack of cells. In this section, we discuss the equations needed to calculate the heat generated by the cell. Since most lithium cells are very thin (less than 300 μm thick), temperature gradients perpendicular to the electrodes are neglegible, allowing Peltier heats of individ-

ual electrodes, transport entropy, and thermal diffusion to be neglected. The heat generation therefore need not be calculated as a function of position across an individual cell. Once known, this heat generation can be inserted into a standard heat transfer equation, including conduction, convection, and radiation as appropriate for the battery geometry, to calculate temperature changes across a tall cell or battery stack. Such models are generally concerned with temperature gradients in two- or three-dimensions. We review multidimensional modeling in Section 4.10. Newman [21] discusses issues that arise when the temperature varies perpendicular to the electrodes.

A general energy balance for electrochemical systems is [24]

$$\dot{Q} = I\left(V - U^{\mathrm{avg}} + T\frac{\partial U^{\mathrm{avg}}}{\partial T}\right) + \int \sum_i \left(\bar{H}_i - \bar{H}_i^{\mathrm{avg}}\right)\frac{\partial c_i}{\partial t}\,dx + \sum_k \Delta H_k^{\mathrm{avg}} r_k + C_p \frac{dT}{dt} \quad \textbf{(31)}$$

where $\dot{Q}$ is the rate of heat transferred to the system from its surroundings, and avg indicates that the properties are evaluated at the volume-averaged concentration. This equation states that heat is generated due to resistance to the passage of current *I(V-U)*, reversible entropic heat *I(T∂U/∂T),* and any chemical reactions that may be occuring, such as phase change. In addition, heat may be generated or absorbed by heat of mixing, cause by the formation of concentration gradients, across the electrolyte, across the porous electrode, radially within pores, and radially within particles of insertion material [26]. The heat released upon relaxation of concentration gradients after the current is turned off will be equal and opposite in magnitude to the heat evolved in formation of those gradients. If the second derivative of the enthalpy of the electrolyte with respect to the mole fraction of one component of the electrolyte is positive, then the heat released during relaxation is exothermic. At low currents or in systems with good transport properties and small variation of partial molar enthalpy with concentration, the heat-of-mixing term is negligible.

Bernardi et al. [24] present a detailed derivation of the energy balance, and use it to describe the heat generation in a LiAl | molten LiCl,KC1 | eS cell, include the effects of two reaction steps in the FeS electrode, precipitation of LiCl, and heat of mixing in the molten salt electrolyte. Several authors have compared heat-generation predictions for a single cell to experiment [22,23].

Rao and Newman [25] present a form of Bernardi et al.´s energy balance which is convenient for examining effects of multiple reactions and heat-of-mixing effects across insertion compounds, in which the open-circuit potential varies with state-of-charge:

$$\dot{Q} = IV + \int \sum_l ai_{n,l}(x)\left(U_l(c_s(x)) - T\frac{\partial U_l(c_s(x))}{\partial T}\right)dx + C_p \frac{dT}{dt} \quad \textbf{(32)}$$

where c_s is the local lithium concentration in the solid averaged over the cross-sectional area of the electrode, the integral is over the entire cell, and the reaction rate, i_n, is positive for an anodic reaction. This equation reduces to Equation 31 (without the heat of mixing term) only for the cases of a uniform reaction rate or constant U_H, where the enthalpy potential is given by $U_H = U - T(\partial U/\partial T)$. Because it involves the local reaction rate, rather than the overall applied current, it can be used to treat heat effects of self-discharge and the formation and relaxation of concentration gradients across the insertion electrode. However, it does not include heat of mixing within the electrolyte or within individual particles of active material [26], which in some cases are of equal or greater magnitude to heat of mixing across the electrode.

One of the characteristic features of lithium-ion batteries is the use of insertion compounds as active materials. Ordering effects of lithium on the insertion lattice cause the entropy of reaction, $\partial U/\partial T$, to be of significant magnitude and to vary strongly, even changing sign, with state of charge [27]. Knowledge of the entropy of reaction as a function of state of charge therefore is required for accurate prediction of heat generation from batteries containing insertion electrodes.

Physical properties such as κ, i_0, and D generally display an Arrhenius dependence on temperature. Therefore, as the temperature of the battery increases, these properties increase, the resistance of the cell decreases, and the rate of heat generation decreases. These effects tend to even out temperature distributions across a stack compared to what would be predicted using constant physical properties [28]. In opposition to this trend, the rate of heat generation from side reactions may increase with increasing temperature [29].

3.8   *Solving the Governing Equations*

The previous sections describe the six equations (Equations 3, 4, 12, 17, 19, and 28) necessary to describe the electrochemical performance of the cell. Solving these equations yields the dependent variables c, c_s, Φ_1, Φ_2, i_2, and j. The governing equations involve three ordinary differential equations, two partial differential equations, and one algebraic equation. If explicit calculation of both Φ_1 and Φ_2 is not needed, they may be combined into one variable, $\eta = \Phi_1 - \Phi_2$. If explicit calculation of both j and i_2 is not required, then Equations 19 and 28 may be combined into one equation.

In all but the most simplified cases, the coupled governing equations must be solved numerically. Use of variable physical properties and/or Butler-Volmer or Tafel kinetics makes the governing equations nonlinear. Several different numerical techniques have been used in the literature, including finite difference with control volume formulations for the mass

and charge balances [2,3,30], finite elements [6,31], and the method of lines [32,33]. Time derivatives are handled using Crank-Nicholson formulations or higher-order variations of implicit methods.

For this type of model based upon the fundamental laws of transport, kinetics, and thermodyanmics, a large number of physical properties is required, as listed in Table 1. These properties may all be functions of composition and temperature, in particular, U, κ, D, t_+° and D_s. A summary of the experiments required to measure the parameters needed for the model is given by Doyle and Newman [34]. A full-cell-sandwich model of a lithium battery using the above equations was first presented by Doyle, Fuller, and Newman [2,11]. This model has been validated several times by comparison with experimental discharge and charge data over a wide range of current densities for various lithium and lithium-ion cell chemistries [35,36].

Table 1. Parameters required for the model. Values must be specified for both electrodes. All material properties can be functions of composition and temperature.

Thermodynamic	Kinetic	Transport	Geometric
U	i_0	D	a
ρ (of all components)	α_a, α_c	D_s	L_+, L_s, L_-
$c_{s,\,max}$	R_{film}	t_+°	ε (of electrolyte,
$f_\pm$		κ	active, and filler)
initial c and c_s		σ	
C_p			
$\partial U/\partial T$			

4.0   SPECIAL SITUATIONS

4.1   *Transport in Insertion Electrodes*

Transport in insertion compounds is perhaps one of the easiest solid transport situations to model, because there is no phase change or generation of new product compounds, and volume changes are generally negligible. Therefore, the morphology of the electrodes is relatively constant, and only diffusion need be considered.

4.1.1   *Constant Diffusion Coefficient*

If the solid diffusion coefficient can be approximated as a constant, then Equation 17 is a linear partial differential equation. Then the concentration in the particle resulting from a time-varying rate of reaction at the surface can be obtained by superposing the concentration changes resulting from simple step changes in concentration at the surface. Each step change is initiated at a different time t_n, and the effect of that step at future times is damped as the response decays. In the limit as the time step goes to zero, the flux into the particle can be expressed by Duhamel´s superposition integral [37, 38]

$$\frac{\partial c_s}{\partial r}(R,t) = \int_0^t \frac{\partial c_s}{\partial t}(R,\delta) \frac{\partial \overline{c}_s}{\partial r}(R, t-\delta) d\delta \tag{33}$$

where $\overline{c}_s(r, t)$ is the dimensionless concentration resulting from a unit step change in concentration at the surface of the particle at time t. We see that calculation of the flux into the particle requires only knowledge of the history of the surface concentration of the particle, and we do not need to keep track of the concentration within the particle. This simplification saves computer memory and computation time.

This initial-value type integral equation can be calculated numerically using the method presented by Wagner [39] and Acrivos and Chambré [40]. The time-derivative of c_s can be approximated numerically by $\partial c_s/\partial t = (c_{s,j+1} - c_j)/\Delta t$. Substituting into Equation 33 and discretizing time into time steps t_n yields:

$$\frac{\partial c_s}{\partial r}(R,t_n) = \frac{(c_{s,n}-c_{s,n-1})}{\Delta t} A_1 + \sum_{j=0}^{n-2} \frac{(c_{s,j+1}-c_{s,j})}{\Delta t} A_{n-j} \tag{34}$$

where

$$\frac{D_s}{R} A_n = a(t_n) - a(t_{n-1}) = \frac{D_s}{R} \int_0^{t_n} \frac{\partial c_s}{\partial r}(R,\delta)d\delta - \frac{D_s}{R} \int_0^{t_{n-1}} \frac{\partial c_s}{\partial r}(R,\delta)d\delta \tag{35}$$

The summation in Equation 34 is divided to illustrate that the summation can be stored and updated at each time step [Note: Equation 34 often has been presented in dimensionless form [2, 41]. To avoid confusion, we present it here in dimensional form.] The Laplace transform can be used to obtain series expansions for $a(t)$. At long times,

$$a(\tau) = \frac{2}{\pi^2} \sum_{n=1}^{\infty} \frac{1}{n^2} \left[1 - \exp\left(-n^2\pi^2\tau\right)\right] \tag{36}$$

At short times,

$$a(\tau) = -\tau + 2\left(\frac{\tau}{\pi}\right)^{0.5} \left\{1 + 2\sum_{n=1}^{\infty}\left[\exp\left(-\frac{n^2}{\tau}\right) - n\sqrt{\frac{\pi}{\tau}} \, \text{erfc}\left(\frac{n}{\sqrt{\tau}}\right)\right]\right\} \tag{37}$$

where τ is dimensionless time defined as $\tau = tD_s/R^2$. Doyle [41] states that evaluating three terms of the short-time solution or five terms of the long-time solution provides sufficient accuracy. The long-time solution is used when τ is greater than 0.06. The above equations were derived for spherical particles. Doyle also provides series solutions for $a(t)$ for other shapes of particles such as planar slabs and cylindrical rods (neglecting edge effects and considering only 1-D transport in each geometry).

4.1.2   *Variable Diffusion Coefficient*

If the variation of the solid diffusion coefficient with lithium concentration is significant, then the diffusion equation is nonlinear and the above simplification does not apply. For an electrode composed of spherical particles, a pseudo-two dimensional approach is required, in which the radial diffusion equation (Equation 17) is solved at each mesh point across the porous electrode. A set of radial nodes is then required to compute the radial solid concentration profile at each linear position in the electrode. Note that Equation 17 is derived using the gradient in chemical potential, and assumes only that volume changes are negligible and that all current is carried by electrons in the solid phase. The chemical diffusion coefficient, D_s, used in Equation 17 is related to the binary diffusion coefficient derived from the Stefan-Maxwell equations, $\mathcal{D}$, (also called the binary interaction parameter), by the relationship presented earlier (Equation 13) for concentrated solutions:

$$D_s = \mathcal{D}\frac{c_T}{c_o}\left(1+\frac{d\ln\tilde{\gamma}_{\pm}}{d\ln\Theta}\right) \tag{38}$$

Following convention in the literature, we have changed here from a molal scale to a fractional occupancy scale, defined by $\mu_s = \mu_s^* + \nu RT\ln\tilde{\gamma}_{\pm}\Theta$, where $\Theta = c_s/c_{s,max}$ is the fraction of lithium sites in the lattice which are occupied. Then in Equation 16, the term $1-(d\ln c_0/d\ln c_s)$ should be replaced by $1-(d\ln c_{s,max}/d\ln c_s)$. For insertion compounds, the thermodynamic factor is related to the open-circuit potential by

$$1+\frac{d\ln\tilde{\gamma}_{\pm}}{d\ln\Theta} = -\Theta(1-\Theta)\frac{F}{RT}\frac{\partial U}{\partial\Theta} \tag{39}$$

[Note: Some authors define the thermodynamic factor as $1+(\partial\ln\tilde{\gamma}_{\pm}/\partial\ln\Theta) = -\Theta(F/RT)\cdot(\partial U/\partial\Theta)$ and then combine the $(1-\Theta)$ term with the binary interaction parameter.]

While $\mathcal{D}$ may vary less with concentration than does the chemical diffusion coefficient, McKinnon and Haering [42] provide a theoretical basis for how $\mathcal{D}$ varies with concentration, depending on attractive and repulsive interactions in the lattice. There is a vast experience with materials for which $\mathcal{D}$ varies with concentration [43,44,45]. The assumption that $\mathcal{D}$ is independent of lithium concentration may be valid for some electrode materials, such as carbon fiber [46]. However, since this assumption has no theoretical basis, it should be used only with caution and verified with measurements of the diffusion coefficient as a function of concentration.

While use of a variable diffusion coefficient increases simulation accuracy, it also increases simulation time by up to an order of magnitude, depending on the number of radial nodes used. Therefore, in some cases it is desirable to use a constant diffusion coefficient. This constant should be some average value of the true variable diffusion coefficient. The question arises, what average value of the diffusion coefficient to use for a material that exhibits a diffusion coefficient that varies with state of charge? Paxton and Newman [47] present one method for selecting an average diffusion coefficient which introduces the least error in simulating the behavior of a material whose diffusivity varies in reality.

Verbrugge and Koch [20] describe how to scale the radial dimension when formulating the radial diffusion equation to improve numerical simulations over a wide range of time scales. Mao and White [48] present a method for arranging the matrix when solving pseudo-two dimensional problems that reduces computation time.

4.2 Transport and Volume Change in Phase-Change Electrodes

Several phase-change electrodes are currently being researched for use in lithium-ion batteries, such as lithium-tin and other binary and intermetallic lithium alloys for negative electrodes, and $LiFePO_4$ and variants thereof for positive electrodes. In these materials, the reaction occurs as a moving front through the particle of active material rather than as diffusion down a continuous concentration gradient as in insertion compounds. The new phase must be nucleated at the surface of grains before the phase can propagate through a grain, resulting in a nucleation overpotential. The nucleation over-potential is observed as a sharp dip and then rise in the cell potential at the beginning of discharge. The phase-propagation process can be treated with a shrinking-core model, as described in Appendix C of reference [49] and as applied in the case of LiAl [19].

This type of phase-change reaction is distinct from the dissolution-precipitation reaction which occurs in the Pb, PbO_2, Ag, and Cd electrodes. In a dissolution-precipitation reaction, one solid phase (*e.g.* Pb) dissolves electrochemically (*e.g.* to form Pb^{2+}), combines with an ion in solution, and the product precipitates (*e.g.* $PbSO_4$). Methods for modeling mass transfer and nucleation kinetics in dissolution-precipitation reactions have been described [18,50,51,52,53,8].

Some of the materials recently being considered for use as positive electrodes, such as $LiFePO_4$, are actually insulators rather than electronic conductors. In this case, the assumption that the transference number of electrons is unity is not valid, and semiconducting effects may need to be

considered. Treatment of semiconducting effects in electrodes has been reviewed in the case of the nickel hydroxide electrode [54, 55] and photo-voltaic electrodes [56,57].

4.3   *Nonporous Insertion Electrodes*

Nonporous electrodes are of interest for thin-film microbatteries, especially all-solid-state batteries, and for measurements of the solid diffusion coefficient and exchange-current density, since these measurements require knowledge of the surface area. In the nonporous geometry, no electrolyte, binder, or filler is present in the electrode. Then only two governing equations apply. The electrode has a planar geometry. Let $x = 0$ be the electrode-current collector interface, and $x = L$ be the position of the electrode-separator interface. The first governing equation is Ohm's law in the solid,

$$I = -\sigma \nabla \Phi_1 \tag{40}$$

with the boundary condition

$$I = i_0 \left[\exp\left(\frac{\alpha_a F(\Phi_1 - \Phi_2 - U)}{RT} \right) - \exp\left(\frac{-\alpha_c F(\Phi_1 - \Phi_2 - U)}{RT} \right) \right] \tag{41}$$

If σ is a constant, then Equation 40 can be integrated directly to yield $\Phi_1(L) - \Phi_1(0) = -IL/\sigma$.

The second governing equation is the planar diffusion equation for lithium transport in the solid film

$$\frac{\partial c_s}{\partial t} = \frac{\partial}{\partial x}\left(D_s \frac{\partial c_s}{\partial x} \right) \tag{42}$$

with boundary conditions

$$\left. \frac{\partial c_s}{\partial x} \right|_{x=L} = -\frac{I}{FD_s} \quad \text{and} \quad \left. \frac{\partial c_s}{\partial x} \right|_{x=0} = 0 \tag{43}$$

and initial condition $c_s(x,t=0) = c_s^o$.

For a constant diffusion coefficient and boundary conditions of constant current (galvanostatic operation) or constant surface concentration (*e.g.,* for a potential step experiment), this equation can be integrated directly [58]. For nonconstant boundary conditions but constant diffusion coefficient, the equation can be solved using Duhamel's superposition integral [59]. With an arbitrarily variable diffusion coefficient, the equation must be solved numerically.

4.4   *Particle Size Distribution*

The battery model described above assumes that the active material in the porous electrodes exists in small spherical particles of uniform size. In a real battery, the particles may be of various sizes. A particle-size distribution is modeled numerically by categorizing the particles into size bins, and then treating each bin as a separate phase in the electrode. While each particle size has the same material properties, the particles may experience different diffusion and reaction rates and thus solid-phase concentrations. The reaction rate Equation 19 is computed separately for each particle size bin. The current balance then becomes

$$\nabla \cdot i_2 = \sum_l a_l i_{n,l} \tag{44}$$

where the summation is over the bins of particle sizes. Different particle size bins may have different specific interfacial areas, calculated from $a_l = 3\varepsilon_l / R_l$ for spherical particles. A separate solid material balance of the form of Equation 17 is written for each particle-size bin. The equations for the potential in the electrolyte and solid remain unchanged, and the mass balance in the electrolyte is unaffected if the form of Equation 12 is used. The equation for the potential in the solid is unchanged because the averaging employed in porous electrode theory is over regions that include several particles. Therefore, the solid-phase potential is the same in particles of all sizes at a given position. This analysis neglects any effect of radius of curvature on surface energy and therefore on chemical potential; this assumption is valid for particle radii of order nanometers or larger.

Darling and Newman [60] examine the effects of a particle-size distribution by considering the simplified case of binary distributions in which the volume fractions of the two particle sizes are chosen in such a way that the active-material volume fraction (and thus mass), surface area, and average particle size are the same among all the distributions examined. Thus, the only physical parameter changed in Darling and Newman´s simulations is the presence of two particles sizes, thereby isolating the effect of a particle size distribution. The authors show that an electrode with a particle-size distribution, all else held constant, exhibits larger solid-phase resistance and longer relaxation times than an electrode with uniform particle size. The effect is most pronounced under conditions of nonuniform current distribution across the electrode, such as at high currents or flat dependence of the open-circuit potential on solid concentration.

Figure 2 shows *U* evaluated at the surface concentration of the particles as a function of time during a charge and discharge of a $Li|LiMn_2O_4$. The concentration in the two particle sizes is identical as long as semi-infinite diffusion exists. Once the solid concentration gradients extend to the middle of

the particle, restricted diffusion behavior takes over, and the concentration in the smaller particle will change faster than the concentration in the larger particle. The solid concentration overpotential (difference between actual cell potential and surface potential) is therefore larger in the larger particles. Therefore, for electrodes with the same average particle size, surface area, and volume fraction of active material, the electrode with the most nonuniform particle-size distribution will have the largest overpotential and slowest relaxation times. Another way to think of this is that, in any particle-size distribution, there must always be particles of size larger than the average, and these larger particles will always have larger resistances and time constants for diffusion. For a particle-size distribution with different surface areas, the kinetic overpotential will be larger on the particle size of smaller surface area a_l.
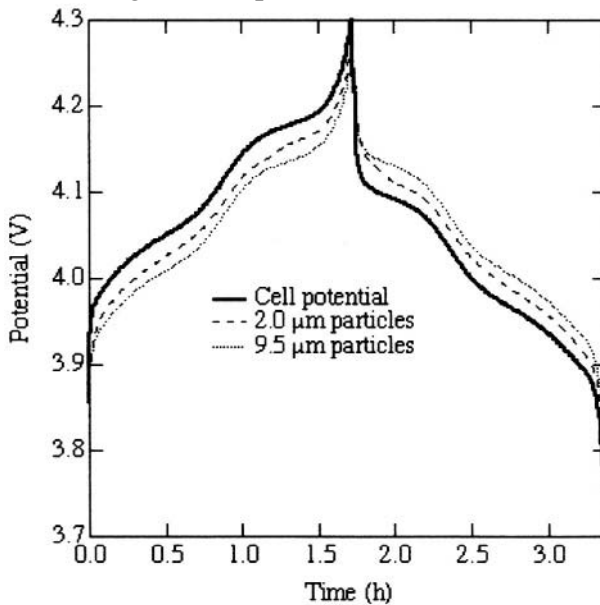
Figure 2. Equilibrium potentials at the surface of particles of two sizes during a charge and discharge. The larger particle has a larger concentration overpotential. From reference 60, reprinted with permission of The Electrochemical Society, Inc.

Particles of different sizes will pack differently than particles of a uniform particle size, and the packing density will affect the porosity of the electrode. Nagarajan et al. [61] addressed the question of how to optimize the particle-size distribution to increase electrode utilization for a 1C-rate discharge, given a correlation between packing density and particle size determined by Yu et al. [62] (neglecting effects of the conductive filler and binder on packing). In essence, this paper tries to optimize the electrode porosity by changing the packing density in the electrode. Nagarajan et al. also demonstrate how a higher fraction of smaller particles can improve electrode response to a high-current pulse discharge.

4.5   *Double-Layer Capacitance*

Double-layer capacitance is of interest when modeling ac-impedance behavior and also when simulating response to rapid current pulses. Small modifications to the current balance are required to account for charging of the double layer [63]. These modifications also appear in the mass balance equation for the electrolyte, since it includes the divergence of the current as a homogeneous consumption term. In many cases, the magnitude of the concentration change due to double-layer adsorption may be negligible, and then only the modified current balance is needed. The current balance is

$$\nabla \cdot i_2 = aF \sum_i z_i j_{i,n} \tag{45}$$

where $j_{i,n}$ is the molar flux of species i away from the electrode surface due to heterogeneous electrochemical reaction. If we are to include double-layer charging, then this flux has both faradaic and capacitive components:

$$a j_{i,n} = a j_{i,f} + a_{dl} j_{i,dl} \tag{46}$$

where here we have accounted for the possibility that the interfacial area for double layer charging may include the conductive filler and therefore be different from the interfacial area for faradaic reaction. The flux into the double layer is related to the capacitance by

$$F \sum_i z_i j_{i,dl} = C \frac{\partial(\Phi_1 - \Phi_2)}{\partial t} \tag{47}$$

For lithium batteries with binary electrolytes, the faradaic flux of the anion is zero. Then the current balance is

$$\nabla \cdot i_2 = aF j_{+,f} + a_{dl} C \frac{\partial(\Phi_1 - \Phi_2)}{\partial t} \tag{48}$$

One can show that [64]

$$j_{i,dl} = -\frac{C}{z_i F} \frac{dq_i}{dq} \frac{\partial(\Phi_1 - \Phi_2)}{\partial t} \tag{49}$$

where the dependence of double-layer adsorption on electrolyte concentration and temperature have been neglected. To get a mass balance for the electrolyte that includes double-layer capacitance, we substitute Equations 46 and 49 into the mass balance (Equation 12) to obtain

$$\varepsilon \frac{\partial c}{\partial t} = \nabla \cdot \varepsilon D \left(1 - \frac{d \ln c_o}{d \ln c}\right) \nabla c - \frac{i_2}{F} \cdot \nabla t_+^o + a\left(1 - t_+^o\right) j_{+,f}$$

$$-a_{dl} \frac{C}{F} \left(t_-^o \frac{dq_+}{dq} + t_+^o \frac{dq_-}{dq}\right) \frac{\partial(\Phi_1 - \Phi_2)}{\partial t} \tag{50}$$

where dq_i/dq indicates the change in surface excess concentration of species i in response to a change in the charge on the electrode. Since information about surface charges is difficult to obtain, we assume that only cations are adsorbed. Then $dq_-/dq = 0$ and $dq_+/dq = -1$. Note that the signs of these terms, Equation 49, and the last term in Equation 50 are reversed if q is defined as the total charge on the solution side of the double layer, rather than on the electrode side as used here. The final mass balance is independent of this definition.

Ong and Newman [65] describe issues of casting these equations into finite-difference form and derive a characteristic time for the decay of capacitive effects upon a step change in galvanostatic current. The time constant is approximately $L^2 a_{dl} C[(1/\kappa) + (1/\sigma)]$, and is on the order of 1 to 100 milliseconds for typical insertion electrodes.

4.6   Film Resistance

It is well known that a passivation layer, called the solid-electrolyte interphase (SEI), forms on the surface of the negative electrode (and likely on the positive electrode to some extent as well) due to reaction with the electrolyte (see Chapter 1). This layer will add a resistance for reaction to occur. The exact nature of the SEI is not well understood. There is evidence that the film on the carbon and lithium electrodes is inhomogeneous, possibly porous, composed of more-reduced species (*e.g.* Li_2CO_3) on the side bordering the active material and less-reduced species (*e.g.* lithium alkyl-carbonates) on the side bordering the electrolyte. A model of transport and reaction in the SEI layer could be based on previous works on passivation layers formed in other systems, *e.g.*, corrosion of iron [66,67], or it could expand upon models of the LiCl layer in lithium-thionyl chloride batteries [68,69].

For the purposes of modeling the overall cell-sandwich behavior, it is not necessary to know the exact details of the SEI layer. Instead, one can assign some overall resistance to the film, and include this resistance in the electrode kinetics. Given that the film is believed to consist of solid lithium salts, it is logical to model transport through the film to a first approximation by migration alone, in which case the film is analogous to a resistor in series with the reaction (no diffusion resistance in the film) [35]. The surface overpotential used in the Butler-Volmer equation should then include the potential drop across this film, so that the modified Butler-Volmer equation has the form

$$i_n = i_o \left[\exp\left(\frac{\alpha_a F(\Phi_1 - \Phi_2 - U - j_n F R_{film})}{RT} \right) - \exp\left(\frac{-\alpha_c F(\Phi_1 - \Phi_2 - U - j_n F R_{film})}{RT} \right) \right]$$

(51)

The film resistance affects the reaction-rate distribution by increasing the kinetic resistance, which makes the reaction rate more uniform. There is evidence that the composition of the film depends on electrode potential, and that the film dissolves and reforms as the cell is cycled. Then it might be appropriate to consider a film resistance which varies with local potential.

In addition to the film resistance around the particles of active material, there may be a contact resistance due to imperfect contact between the electrode and the current collector [70]. This contact resistance is separate from interparticle contact resistance in the bulk of the electrode, which is included in the electrical conductivity σ of the composite electrode material. Contact resistances at the current collector would have a different effect on the current distribution than a film resistance, because this contact resistance would occur only at the boundary of the electrode rather than being distributed throughout the entire surface area of active material like the film resistance. The ohmic potential drop from the contact resistance is treated by simply subtracting $IR_{contact}$ from the cell potential.

4.7   Side Reactions

Side reactions include electrolyte oxidation and reduction, lithium deposition, redox shuttles for overcharge protection, corrosion of current collectors, self-discharge, conversion of active material to inactive phases, and other degradation mechanisms, as reviewed by Reference 4. Side reactions can affect the performance of lithium-ion cells by lowering the coulombic efficiency, creating an imbalance in the state of charge between the positive and negative electrodes, consuming cyclable lithium, increasing cell impedance, or protecting against potentially more deleterious effects of overcharge.

Side reactions can be divided into two categories for the purposes of modeling. The first category includes side reactions which do not involve or produce soluble species other than the electrolyte and solvent, and include lithium deposition and solvent oxidation to form solid products. These types of side reactions are treated with little modification to the framework developed in Section 3 other than the addition of a kinetic equation for the side reaction. The second category includes any side reaction which does involve more than three components in the solution phase, such as redox shuttles. In this case, the governing equations must be modified to add a mass balance for the new component and to include the concentration overpotential of this component.

Darling and Newman [36] describe the methodology for modeling the first category of side reactions, in which the only species in the solution phase are the electrolyte and solvent. The side reaction is modeled by adding a second reaction to the current balance:

$$\nabla \cdot i_2 = a_m i_{n,m} + a_s i_{n,s} \tag{52}$$

where $i_{n,m}$ is the current flux due to the main reaction (lithium insertion) and $i_{n,s}$ is the current flux due to the side reaction. $i_{n,s}$ could be the sum of multiple side reactions. Here Darling and Newman have allowed for the possibility that the surface area upon which the side reaction occurs could be different from that of the main reaction. For example, electrolyte oxidation may occur on the surface of the conductive filler, whereas the main reaction occurs only on the surface of the active material. The effects of the side reaction are coupled to the mass balance in the solid and in the electrolyte, in that $\nabla \cdot i_2$ appears in the electrolyte mass balance, Equation 12, and $i_{n,m}$ determines the flux of lithium into the solid. The total current in the cell is determined by boundary conditions such as galvanostatic or potentiostatic operation. Note that it is possible for $i_{n,m}$ and $i_{n,s}$ to have opposite signs. For example, self-discharge on the positive electrode could occur by coupling a side reaction, *e.g.*, $S \rightarrow S^+ + e^-$, with the main reaction $Li^+ + e^- + \Theta_s \leftrightarrow Li\Theta_s$. The net current could then be zero while the state of charge of the electrode decreased due to self-discharge.

Like the main reaction, the side reaction can be described by the Butler-Volmer equation,

$$i_{n,s} = i_{0,s}\left[\exp\left(\frac{\alpha_{a,s}F}{RT}\eta_{s,s}\right) - \exp\left(\frac{-\alpha_{c,s}F}{RT}\eta_{s,s}\right)\right] \qquad (53)$$

where the surface overpotential for the side reaction is defined as

$$\eta_{s,s} = \Phi_1 - \Phi_2 - U_s - j_n F R_{film} \qquad (54)$$

where U_s is the reversible thermodynamic potential of the side reaction defined with respect to a lithium reference electrode at the same solution composition. U_s can be specified as a function of electrode composition or temperature if such information is available. Computation can be simplified somewhat by assuming that the side reaction is irreversible or the reversible potential of the side reaction is much different from the electrode potential (and therefore the Tafel approximation can be used), or that the rate constant of the side reaction is very large and the overpotential is small (and therefore linear kinetics can be used). Tafel kinetics may be more appropriate for electrolyte degradation reactions, whereas linear kinetics may be appropriate for lithium deposition [4]. For irreversible reactions, a reversible potential is not really defined and does not appear independently in the kinetic expression. For example, if the Tafel approximation is used, then, *e.g.*, for an anodic reaction,

$$i_{n,s} = i_{0,s}\exp\left(\frac{\alpha_{a,s}F(\Phi_1 - \Phi_2 - U_s - j_n F R_{film})}{RT}\right)$$

$$= i_{0,s}\exp\left(\frac{-\alpha_{a,s}F U_s}{RT}\right)\exp\left(\frac{\alpha_{a,s}F(\Phi_1 - \Phi_2 - j_n F R_{film})}{RT}\right) \qquad (55)$$

and we see that U_s can be incorporated into the exchange current density for the side reaction, and is not measured separately.

If the rates of side reactions on the two electrodes are different, then the total flux of lithium into one electrode will not be equal to the total flux of lithium out of the other electrode. An imbalance of the state of charge between the positive and negative electrodes will result. This imbalance effectively leads to a loss of cyclable capacity.

Arora et al. [71] use the equations presented above to simulate lithium metal deposition on carbon negative electrodes during overcharge. Lithium metal deposition will occur wherever the potential of the electrode is driven more negative than the potential of lithium metal, *i.e.*, where $\Phi_1 - \Phi_2 - U_{Li} < 0$. Since all potentials in this work are with respect to a lithium reference electrode, $U_{Li} = 0$. Such a situation might occur when there is excess positive electrode capacity, when large charging currents are used, or when the cell is charged to voltages much larger than its open-circuit potential at full state of charge. A graphical illustration of how potential varies across the carbon electrode is given in Figure 3. We see that the threat of lithium deposition emerges 115 minutes into this C/2-rate charge. The surface of the deposited lithium will react with the electrolyte, causing a resistive material to coat the active material, reducing the amount of cyclable lithium in the system, and clogging pores.
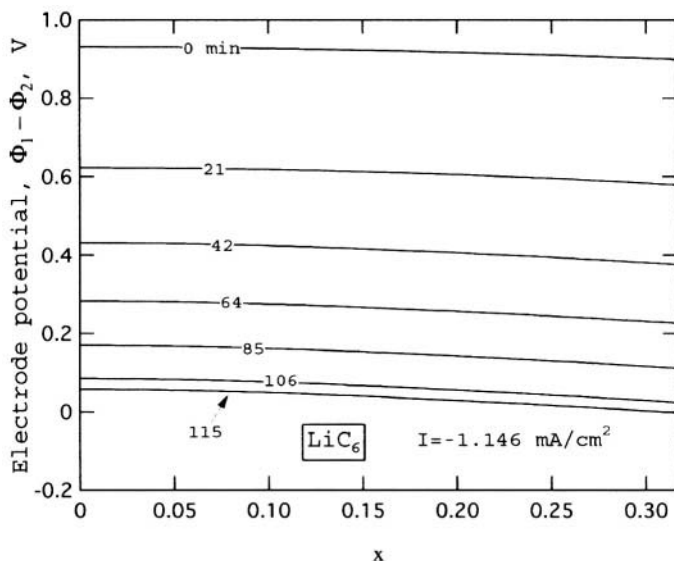
Figure 3. Profiles of Φ_1- Φ_2 across a porous petroleum coke electrode at different times during a C/2-rate (-1.146 mA·cm^{-2}) charge. Time since the beginning of charge is indicated in minutes. After 115 minutes, the potential near the separator interface has dropped below the potential for lithium deposition. From reference 35, reprinted with permission of The Electrochemical Society, Inc.

Arora et al. use the calculated rate of side reaction to explore its effect on film resistance. They estimate the rate of increase of the resistance of the SEI layer from the rate of lithium deposition, assuming that some fraction of the deposited lithium reacts irreversibly to form lithium carbonate. Factors which alleviate driving the potential of the carbon surface to zero will reduce lithium deposition. These factors include increasing the negative:positive active-material mass ratio, reducing the cutoff voltage on charge, reducing the electrode thickness and particle size, and reducing the applied current density. A larger film resistance decreases the potential driving-force for lithium deposition and thus its rate. Therefore, lithium reaction with the electrolyte to form a resistive film will decrease the lithium deposition rate. A more uniform reaction rate, which could be achieved by slower reaction kinetics, higher solution conductivity, or a sloping dependence of open-circuit potential on state of charge, would also reduce the rate of lithium deposition by avoiding driving the potential to zero at the electrode-separator interface before the rest of the electrode is fully charged. Finally, Arora et al. indicate that for a given amount of coulombs of charge reaction, the total amount of lithium deposition is reduced by using taper charging rather than galvanostatic charging.

The second category of side reactions includes those which involve species in solution other than the main electrolyte and solvent. For example, one might be interested in how Mn^{2+} from the dissolution of the positive electrode migrates to the negative electrode and plates out on the surface of the negative electrode, or in examining whether a soluble product of electrolyte reduction at the negative electrode could cause capacity fade by reacting at the positive electrode. In addition to the modification to the current balance given in Equation 56, the governing equations must be modified to include a mass balance for the soluble species and to include the concentration overpotential of this species in its kinetic equation. The modifications can be handled either with full concentrated solution theory, a combination of concentrated solution theory and dilute solution theory, or by dilute solution theory alone.

Treating the system with full concentrated solution theory involves inverting the Stefan-Maxwell equations for all species involved in solution, yielding a flux equation for each species. The flux of each species is coupled to the flux of all other species in these equations, and $n(n–1)/2$ transport properties are required. In addition, the expression for the potential in solution as measured by a reference electrode, Equation 2, is modified to include gradients in chemical potential of all species present. The governing equations for an impurity ion [7,52], impurity solvent [69], and both impurity ion and solvent [8] have been derived. A kinetic expression of the form of Equation 53 for each side reaction completes the set of governing equations. U_s is defined with respect to a lithium reference electrode at the same solution composition, and all concentration overpotential is included in Φ_2.

For impurity species present in dilute concentrations, some may find it more convenient to treat the species using dilute solution theory, which accounts only for interactions of the dilute species with the solvent. Rigorously, Equation 12 was derived for a binary electrolyte with no impurity species in the solution. While it is not completely rigorous to treat one species with dilute solution theory while treating the main electrolyte with equations derived from concentrated solution theory in the absence of the impurity species, the error may be small. The flux of the dilute species is given by Equation 5. The mass balance for the main electrolyte remains unchanged. If Φ_2 is defined by Equation 3, then U_s must be defined as a function of the concentration of the impurity species in order to include the concentration overpotential of the impurity species in the kinetic expression, Equation 53. The Nernst equation, $U_s = U_s^\theta + RT\ln(c_i / c_i^\theta)$, is often used to account for the concentration overpotential of dilute species i. If Φ_2 is defined by Equation 6, then U_s should not be defined as a function of solution composition.

The flux equation, from either concentrated or dilute solution theory, is then inserted into the material balance for the species:

$$\varepsilon \frac{\partial c_i}{\partial t} = -\nabla \cdot N_i + aj_i \tag{56}$$

The reaction term aj_i includes the sum of the main and side electrochemical reactions and also chemical reactions, as indicated in Equations 25 and 30. Possible chemical reactions of interest in lithium batteries include salt precipitation and homogeneous electrolyte decomposition. Once the rate of the side reaction is added to the model, it can be used to calculate various possible effects of the side reaction in addition to consumption of current. For example, one could calculate the change in porosity due to precipitation of products of the side reaction [19]. Precipitation of solid species might also affect the surface area of active material available for reaction [50].

A redox shuttle is an example of a desirable side reaction that prevents overcharge. In this situation, a dissolved species R is selected that can be oxidized to species O at some potential close to the maximum desired potential of the cell. O can diffuse away from the positive electrode to be reduced again at the negative electrode, creating an internal short circuit. One might model a redox shuttle by assuming that initially the shuttle is in its reduced form and that the overpotential for reduction of O is very high at the negative electrode, so that the concentration of O is zero at the negative electrode. Narayanan et al. [72] give an analysis of the effect of potential on redox shuttle current for the case of nonporous electrodes in which the only current is the shuttle current, the diffusivities of the oxidized and reduced species are equal, and migration is neglected.

Side reactions can introduce error into the measurement of physical properties in three ways [73]. Current is consumed by the side reaction, introducing error into calculations of the amount of current that went into the main reaction. Bulk concentrations of salt or solvent may change if the side reaction is substantial, and soluble products of reaction may affect the activity of the electrolyte. Finally, the side reaction causes the potential of the electrode to be a mixed (corrosion) potential. It is commonly assumed that the lithium electrode is covered by the SEI layer. However, there is strong evidence that, in many situations, the protection is not complete and side reactions involving the solvent or anion continuously occur. Such reactions can increase the concentration of lithium ions adjacent to a lithium electrode, introducing error into measurements of the variation in potential with apparent electrolyte concentration, particularly at low electrolyte concentrations. Such concentration-cell measurements are used to obtain activity coefficients and transference numbers via the galvanostatic polarization method. Simulations of the type described in this section can be used to analyze how much error is introduced by the side reaction [73]. It may be preferable to use a less reactive reference electrode, such as $Li_4Ti_5O_{12}$ [74], to reduce this error.

Several works have explored the effects of side reactions in other battery systems in great detail, and their methodologies are applicable to lithium batteries [59,75,76,77,8].

4.8   *Volume Changes and Velocity in the Electrolyte*

Where volume changes and/or solvent velocity are of issue, two equations are needed in addition to the mass balance on the electrolyte. The first is a material balance on the solvent:

$$c_o\left(\frac{\partial \varepsilon}{\partial t}+\nabla \cdot \mathbf{v}_o\right) \;=\; \varepsilon\frac{\partial c_o}{\partial t} - \mathbf{v}_o\cdot\nabla c_o + aj_o \tag{57}$$

The second relates the change in porosity due to volume change in the i solid phases by l electrochemical reactions occuring at rate $i_{n,l}$ and by k chemical reactions occuring at rate r_k

$$\frac{\partial \varepsilon}{\partial t} \;=\; \sum_{solid\ phases}\left(\sum_l \frac{s_{i,l}\bar{V}_i}{nF}ai_{n,l} - \sum_k s_{i,k}\bar{V}_i r_k\right) \tag{58}$$

Changes in porosity cause changes in the velocity of the solvent by pushing the electrolyte out of or into the pores. Changes in porosity would also effect effective properties such as conductivity (see below). For example, a large electrode volume expansion may increase the effective electronic conductivity while decreasing the effective ionic conductivity,

resulting in increased reaction closer to the separator at the expense of reaction within the electrode [78]. Such considerations are generally negligible with insertion electrodes, which achieve high reversibility and thus long cycle life by the very virtue of involving minimal displacement of the active material. However, volume change is of considerable importance in alloy electrodes and systems such as the lithium thionyl-chloride primary battery. In such cases, a reservoir of electrolyte may be incorporated into the battery design to accomodate volume change. Pollard and coworkers [19,8] include an electrolyte reservoir in a one-dimensional model by treating it as a well-mixed region of variable thickness and negligible impact on mass transfer between the separator and positive electrode. While a reservoir of variable volume is an effective method for modeling changes in electrolyte volume, it is an approximation to the true behavior of an electrolyte reservoir, which usually sits on top of the electrodes. Improvements to modeling the effect of the electrolyte reservoir on the distribution of electrolyte concentration within the electrodes require a two-dimensional model [79,80].

Equations 57 and 58 assume that all change in electrode volume is compensated by change in electrolyte volume fraction. This assumption neglects any effects of mechanical stress on changes in electrode area and/or thickness, and may be a poor assumption for alloy or phase-change electrodes [81]. Calculation of such changes in electrode volume would require knowledge of the mechanical properties of the battery container.

4.9   *Effective Properties in Porous Media*

The values of κ, D, and σ used in Equations 3, 12, and 4, respectively, are reduced within the porous electrode relative to their bulk values due to the tortuous path which the ions in solution must make around the solid particles or which the electrons must make around the electrolyte-filled pores. Generally, the effect of volume fraction ε_P and tortuosity of the phase of interest on property P in that phase is accounted for by the Bruggeman relation [82], $P = \varepsilon_P P_\infty/\tau$ where τ is the tortuosity and is usually related to the porosity by $\tau = \varepsilon^{-0.5}$. Because the flux N is defined with respect to superficial area as opposed to electrolyte area, D already gets multiplied once by ε in the mass balance, so $D = D_\infty \varepsilon^{0.5}$.

In gel electrolytes, in which a liquid electrolyte is imbided into a polymer matrix, calculation of the effective diffusivity and ionic conductivity based on the apparent volume fraction of electrolyte in the polymer may be complicated by solvation of the polymer by the solvent, increased tortuosity presented by the polymer, and possible interactions of the ions with solvating groups on the polymer. One way to handle these effects empirically is to treat the tortuosity

as an adjustable parameter which is fit to measurements of diffusivity in actual gels [35]. This empirical tortuosity parameter appears to depends on the nature of the gel´s environment, such as whether the gel is mixed into a porous electrode or free-standing [70]. Such effects may be due to preferential adsorption of the polymer to the solid surface.

Tortuosity also plays a large role in the effective transport properties of polymer electrolytes because obstruction of the sequential motion of polymer chains can block mechanisms of ion transport [83] and because adsorption of the polymer to particles of active material or conductive filler may cause the formation of nanometer-thick glassy polymer films around the solid particles [84]. A better understanding of the effects of tortuosity, polymer-electrode surface forces, and polymer chain length on transport in polymer and gel electrolytes is needed for more accurate treatment of effective transport properties in these systems.

Interparticle contact is of critical importance to the behavior of lithium batteries. Most lithium-ion electrodes contain 2 to 15 wt% conductive filler, such as carbon black, in order to maintain contact among all the particles of active material and in order to reduce ohmic losses in the electrodes. Presently, there are few models available for predicting contact resistance, and the effect of the weight fraction of conductive filler on the overall electronic conductivity of the composite electrode must be determined experimentally. Doyle et al. [35] demonstrate how the full-cell-sandwich model can be used to determine what minimum value of effective electronic conductivity is needed to make solid-phase ohmic resistance negligible. Then, one need only measure the effective conductivity of the composite electrode as a function of filler content, and one need not run separate experiments on complete cells to determine the optimum filler content. Modeling techniques for predicting effective electronic conductivities of composite electrodes are under development, and hold promise to aid in optimizing filler shape and volume fraction [85].

4.10   2- and 3-Dimensional Effects

A one-dimensional model assumes that gradients in potential are negligible in the two directions parallel to the current collectors. Such an assumption is valid for laboratory-scale cells, which are generally small and/or use thick, highly conducting current collectors. When scaling up a cell to a full-scale battery, one may be interested in how potential varies along the current collector due to ohmic drop, and how this potential drop affects the current distribution within the battery. In large batteries, ohmic drop down the current collectors may be significant enough to affect the current distribution, with a higher current closer to the tabs. A two- or three-dimensional model may be desirable then in order to optimize the electrical conductivity (*i.e.,* thickness) of

the current collector, length of electrodes, shape of the current collector, and position of tabs, with respect to overall cost, weight, or volume of the cell [86,87,88,89,90]. They can also be used to understand the potential distribution within the cell and how that distribution affects experimental measurements [91]. The model either can solve the full governing equations treating current and flux as vector quantities, or it can couple the full model for behavior perpendicular to electrode to a simplified resistor-network model for effects parallel to the electrodes[89]. Bernardi et al. [80] review two- and three-dimensional battery models and present results for a lead-acid cell.

In the spiral-wound geometry (also called a jelly roll), the radius of curvature of the electrodes decreases as the radius of the spiral increases, thereby creating a two-dimensional geometry. Spiral-wound geometries have been treated by Evans and White [92] and Podlaha and Cheh [93]. Podlaha and Cheh describe a methodology to simulate a spiral-wound configuration with a one-dimensional model consisting of multiple cell layers connected by "virtual" current collectors. They compare simulations of a spiral-wound alkaline cell to that of a bobbin cell with equivalent total reactant surface area.

The primary focus of two- and three-dimensional models of lithium batteries has been to determine the temperature distribution across a large cell or battery stack [64,95]. The temperature profile across a lithium battery stack is of interest because the rate of cell degradation increases with increasing temperature. As the capacity of the hotter cells in a series-connected stack fades, they will become prone to overcharge and over-discharge, situations which can potentially lead to thermal runaway. Chen and Evans [96] analyze the thermal response of a battery stack to a hot spot created by a short circuit in one cell.

The Biot number is defined as $Bi = hL/k$, where h is the heat-transfer coefficient with the surroundings, L is a characteristic length of the battery, and k is the effective thermal conductivity. If the Biot number is greater than 0.1, then temperature gradients in the battery cannot be neglected. Newman and Tiedemann [97] discuss how thermal aspect ratios (L^2/k) affect the maximum stack temperature for the case of uniform heat generation. Baker and Verbrugge [88] analyze how nonuniformity in the secondary current distribution, caused by ohmic losses along the current collector, can lead to nonuniformity in the temperature profile of a large cell. They assume constant physical properties and linear kinetics. The analysis uses the perturbation technique to extend the one-dimensional secondary current distribution for porous electrodes derived by Euler and Nonnenmacher [98,99] to two dimensions, assuming that all current in the porous electrodes and electrolyte flows perpendicular to the current collectors, and all current in the current collectors flows parallel to the curent collectors. A series solution for the temperature profile in the direction parallel to the current collectors is then derived. They find that their parameter $\bar{L}$, which depends on

the electrical conductivity of the electrodes and current collectors, κ, ε, thicknesses of the cell and current collectors, i_o, and cell height (see their Table II and equation 21), determines the importance of considering two-dimensional variations in the secondary current distribution. For $\tilde{L} \ll 1$, two-dimensional effects can be neglected.

As discussed in Section 3.7, transport and kinetic properties generally exhibit an Arrhenius dependence on temperature, leading to a lower rate of heat generation at higher temperatures. Accurate thermal modeling therefore requires coupling of the electrochemical model to the thermal model through the temperature dependence of the physical properties. Several different techniques for such coupling have been presented. Song and Evans [100] solve the coupled equations directly, and present results for a lithium-polymer bipolar stack under different thermal management conditions. Pals and Newman present two methods for simplifying the computational time. In the first method, an effective heat-transfer coefficient is computed as a function of cell position in a bipolar stack [28]. In the second, an isothermal model for a single cell is used to compute the heat generation of a cell presently at that temperature within a stack [101]. This method introduces some error regarding the effect of the thermal history of a cell. Verbrugge [102] presents a method for reducing the computational power required to simulate the two- or three-dimensional current and temperature distribution (for the case of constant concentration and linear kinetics) for a battery stack composed of many cells. All of these papers show that the improved transport and kinetics at higher temperature lead to a more uniform stack temperature compared to simulations with constant properties.

5.0   ANALYTIC SOLUTIONS FOR SPECIAL CASES

Solutions to simplified forms of the governing equations can prove useful for several reasons. An analytic solution provides a closed-form relationship between independent and dependent variables, which allows calculation of kinetic and transport properties from experiments designed to meet the requirements of the limiting case. They provide dimensionless terms and closed-form relationships that make it easier to identify the effects of different variables and to identify which forces are dominating behavior. Finally, analytic solutions provide a useful starting point for optimization. Many analytic solutions are for "steady-state" operation. Strictly speaking, there is no steady state in the operation of lithium-ion batteries, because the lithium concentration in the active material is continually changing, thereby changing the potential of the active material. The assumption of steady state allows one to examine effects of other parameters in the absence of change in the active material.

An analytic solution for the steady-state current and potential distributions in a porous electrode neglecting any concentration variations was determined early in the development of porous electrode theory [99]. The ratio of ohmic resistance to kinetic resistance determines the uniformity of the secondary current distribution across the porous electrode. For Tafel kinetics, this ratio is $\delta = (\alpha_a FIL/RT)[(1/\kappa) + (1/\sigma)]$, and for linear kinetics it is $v^2 = (\alpha_a + \alpha_c)(FL^2 a i_0/RT)[(1/\kappa) + (1/\sigma)]$ [1]. If either of these dimensionless numbers is large, then ohmic resistance dominates kinetic resistance, and the reaction rate will be higher at the separator-electrode interface than in the middle of the porous electrode. L/v (or L/δ for high currents) is a measure of the penetration depth of the electrode, *i.e.,* how far the reaction penetrates the electrode before concentration gradients in the electrode and electrolyte drive the reaction further. Increasing the thickness of the electrode beyond the penetration depth has little effect on the reaction-rate distribution and thus the overpotential across the electrode. For pure concentration resistance, neglecting all ohmic and kinetic resistance, the penetration depth is L/γ where $\gamma_i = s_i IL/(nF\varepsilon D_i c_{i,\infty})$[1].

The combination of ohmic resistance in the solid and solution phases (neglecting all concentration and kinetic resistance) with transient consumption of active material forms the basis of the reaction-zone model [103,104], which predicts that the reaction-rate distribution will move as a front across the porous electrode, consuming the active material at the separator-electrode interface first, when the electronic conductivity of the solid phase is much higher than the ionic conductivity of the electrolyte phase. Doyle and Newman [105] expanded the reaction-zone model to the case where potential in the active material varies linearly with state of charge. Atlung et al. [106] treated and verified experimentally [107] a similar problem but for ionic and electronic conductivities of equal magnitudes. The reaction-zone model is particularly relevant to studying current distributions and maximum attainable utilization in batteries with ionomer and molten salt electrolytes, in which concentration gradients have a zero or small effect on cell behavior. Full simulations including kinetics and concentration variations showed results similar to the reaction-zone model for cells with molten salt electrolytes [78,19]. The reaction-zone model is less appropriate for electrolytes with lower diffusion coefficients.

Doyle and Newman [108] present the limiting current for the case of uniform current density in a porous electrode. [Note: There has been a misunderstanding in the literature [3] as to how this solution was obtained. Recall that when solving the steady-state form of a transient problem, the initial condition enters in as a constraint that the total mass of electrolyte is constant. Equation 20 of Doyle and Newman´s paper contains a typographical error; the second term on the right side should be positive, not negative. In

addition, the time constant for solution depletion with a current spike given in Equation 42 is not the time constant used in Equations 56 and 57. These equations use the time constant derived when the delta-function reaction rate is left in the differential equation [109], as opposed to being treated as a boundary condition as presented in their Appendix B.] The limiting current across the separator (assumed to have a porosity of 1.0) and porous electrode depends on the porosity ε, separator thickness L_s, and ratio of the thickness of the electrode to that of the separator $r = L_+/L_-$ as given by

$$I_{\lim} = \frac{FDc_\infty}{(1 - t_+^o) L_s f(r, \varepsilon)} \tag{59}$$

where

$$f(r, \varepsilon) = \frac{1}{2(1 + \varepsilon r)} + \frac{(1 + r)^2}{2 r \varepsilon^{3/2}} + \frac{1}{r \varepsilon^{3/2} (1 + \varepsilon r)} \left[\frac{\varepsilon}{3} + \frac{\varepsilon r}{2} - r - \frac{1}{2} - \frac{\varepsilon (1 + r)^3}{3} \right] \tag{60}$$

In addition, the authors compare times for the concentration to become depleted for the case of solution diffusion with uniform current, solution diffusion with a current spike at the separator, and solid diffusion at short and long times. Their figure 8, which plots ratios of these limiting times, allows a qualitative estimate of whether solution-phase diffusion, solid-phase diffusion, or ohmic drop dominates capacity limitations, depending upon the physical parameters of the system. Atlung et al. [110] describe the concentration gradients in the solid for the limiting case of uniform current density at short and long times.

Darling and Newman [111] provide an analytic solution, using Laplace transforms, to the linearized problem at short times after current is turned on, in order to examine the spike in current that forms at the separator-electrode interface when the exchange current density is very large.

Table 2 lists time constants for various physical phenomena that occur in batteries. Perhaps the most important time constant for design of a battery is the characteristic time of discharge, Q/I, where I is the applied current and Q is the coulombic capacity of the electrode as calculated from the volume fraction of active material, electrode thickness, cell area, and specific coulombic capacity of the active material. Ratios of time constants reveal the relative time scales of physical phenomena. For example, if the ratio of diffusion time in a solid particle to discharge time is $\ll 1$, then solid diffusion limitations are negligible in that electrode. For a given electrode, the particle size at which solid diffusion will become limiting is that at which this ratio approaches 1 [11]. If the ratio of diffusion time in the electrolyte to discharge time is $\ll 1$, then a pseudo-steady-state concentration profile is established in the electrolyte early in the discharge process.

Table 2. Time constants of different physical phenomena.

Time Constant	Phenomena
Q/I	Discharge of an electrode with coulombic capacity Q
R^2/D_s	Diffusion in a spherical particle
L^2/D	Diffusion in the electrolyte
$\pi a C L^2 \left(\dfrac{1}{\kappa} + \dfrac{1}{\sigma} \right) \left[\dfrac{\left(2\kappa\sigma / (\kappa^2 + \sigma^2) \right) + \cosh v_s}{2 v_s \sinh v_s} \right]^2$	Double-layer charging of a porous electrode[a]
$nF\overline{V}_{active} L^2 \varepsilon / \left[\kappa \left(\partial U / \partial \Theta \right) \right]$	Relaxation of gradients in utilization across an electrode

[a]v_s is a measure of the current distribution in a porous electrode under linear kinetics with a film resistance [65]: $v_s = aL^2 \left(\dfrac{1}{\kappa} + \dfrac{1}{\sigma} \right) / \left(R_{film} + \dfrac{RT}{Fi_0 (\alpha_a + \alpha_c)} \right)$

6.0   APPLICATIONS FOR MODELS

6.1   *Understanding Limiting Factors*

One of the most useful aspects of computer simulations is that they allow us to ask "What if?": What if we could make the separator infinitely thin, would that remove problems from concentration polarization? What if we increased the transference number at the expense of conductivity, would we gain increased performance? These questions are particularly relevant for the development of polymer electrolytes. Since the three transport properties for a binary electrolyte, κ, D, and t_+^o, all vary substantially with temperature and concentration, and all of these properties are affected by the nature of the polymer and salt, determining which polymer would yield the best performance would require a large number of experiments and would be difficult to analyze. However, simulations can be run easily to compare performance of different polymers in order to evaluate tradeoffs among the transport properties, such as the tradeoff between transference number and conductivity [112] as shown in Figure 4. Thomas et al. [113] show that most of the concentration depletion in polymer electrolytes occurs inside the porous electrode, rather than in the separator, and discuss the limit of gains that can be achieved through thinner separators alone. Figure 5 shows the simulated electrolyte concentration for a Li|polymer electrolyte|V_6O_{13} cell during a C/3-rate discharge, for polymers of two sets of transport properties: those that meet United States Advanced Battery Consortium (USABC) goals ("ideal") and those with the properties of the best polymer available today at $40\,°C$.

Doyle et al. [2] examine the tradeoffs involved with using a higher salt concentration in polymer electrolytes. Conductivity in polymer electrolytes generally displays a maximum at about 1 to 1.5 M salt concentration. One might then choose to use a salt concentration which yields this maximum conductivity.

However, because concentration gradients form upon passage of current, in some operating regimes lower overall resistance might be achieved by using a higher salt concentration. The somewhat lower conductivity in the separator may be more than compensated by the higher conductivity in the porous electrode.
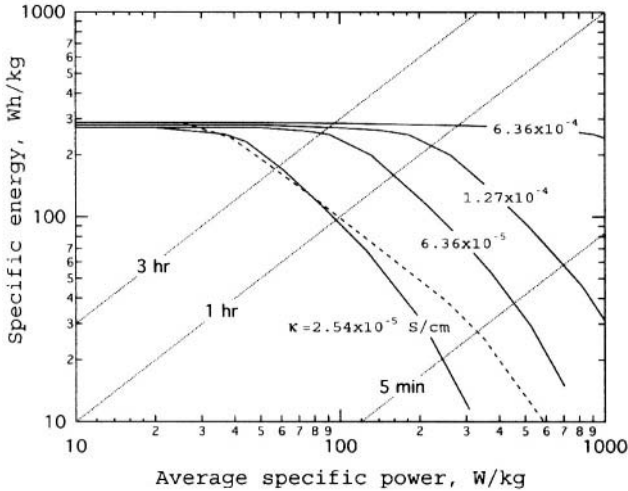
Figure 4. Ragone plot for Li|LiMn₂O₄ cells with different electrolytes. Solid lines: ionomer (unity transference number) with conductivity indicated as parameter. Dashed line: polymer electrolyte with $t_+^0 =$ 0.2, $D = 7.5 \times 10^{-8}$ cm²·s⁻¹, and $\kappa = 2$ to 3.5×10^{-4} S·cm⁻¹ (varying with electrolyte concentration). For this system, the higher transference number of the ionomer outweighs its lower conductivity when the decrease in conductivity is less than a factor of 10. From reference 113, reprinted with permission of Elsevier Science.
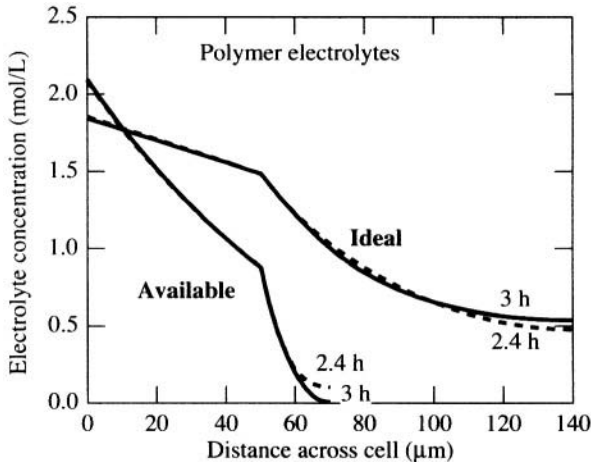
Figure 5. Electrolyte concentration across a Li|polymer|V₆O₁₃ cell during a C/3-rate discharge for a polymer with $t_+^0 = 0.3$, $D = 10^{-7}$ cm²·s⁻¹, and $\kappa = 10^{-3}$ S·cm⁻¹ ("ideal") and a polymer with $t_+^0 = 0.1$, $D = 6 \times 10^{-9}$ cm²/s, and $\kappa = 10^{-4}$ S/cm ("available" at 40°C). The separator is 50 microns thick. The polymer with poorer transport properties develops a large concentration polarization within the positive electrode that severely limits the utilization of the active material. Simply making the separator thinner will not solve this problem. From reference 113, reprinted with permission of Elsevier Science.
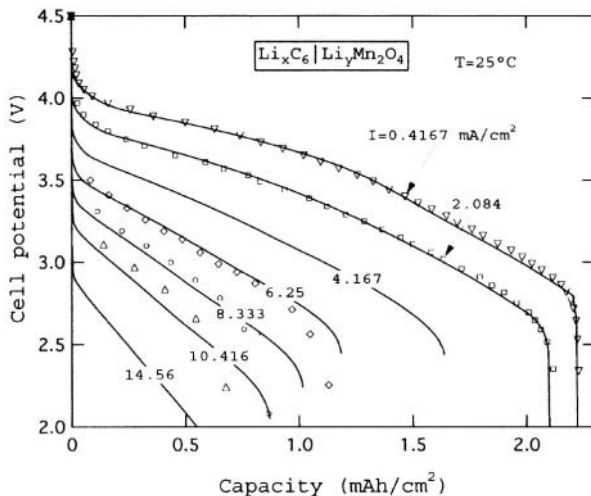
Figure 6. Cell potential during discharge at rates ranging from C/5 (0.4167 mA·cm⁻²) to 7C (14.56 mA·cm⁻²) for a Bellcore-style plastic lithium-ion cell. Markers: experiment. Lines: simulation. From reference 35, reprinted with permission from The Electrochemical Society, Inc.
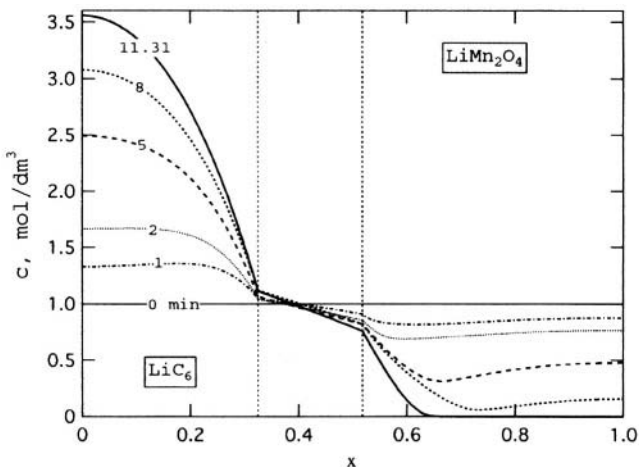
Figure 7. Salt concentration profiles for the same cell as Figure 6 during galvanostatic discharge at 6.25 mA·cm⁻² (3C rate). The separator region is set off by dashed lines. Time since the beginning of discharge is given in minutes. After eleven minutes into the discharge, the electrolyte is depleted in the cathode. From reference 35, reprinted with permission from The Electrochemical Society, Inc.

Doyle et al. [35] show how the full cell-sandwich model can be used to determine maximum and minimum salt concentrations in the cell as a function of time, position, and current density, in order to evaluate the risk of salt precipitation and the effect of salt depletion on accessible capacity. Experiments verified the model´s prediction that salt depletion would limit accessible capacity upon high discharge rates in Bellcore-style plastic lithium-ion batteries. Figure 6 compares model predictions to experimental discharge curves at

currents ranging from the C/5 to 7C rate for a Bellcore cell. Figure 7 shows profiles of electrolyte concentration at different times during one of these discharges, at the 3C rate **(6.25 mA·cm⁻²)**. The time at which the potential drops steeply during discharge corresponds to depletion of salt in the cathode. Most of the concentration polarization is in the porous electrodes, not in the separator. The simulations indicated that increasing the electrolyte volume fraction within the electrodes would reduce concentration polarization and ohmic drop more than would reducing the separator thickness, and this was confirmed by experiments. Reference 11 evaluates how increasing the salt concentration can increase the accessible capacity by delaying the time at which concentration is driven to zero, and describes how the model can be used to evaluate the maximum concentration that can be used at a given current density before salt precipitation becomes a concern.

While most modeling studies concern themselves with the behavior of the system during passage of current, the relaxation of the system after current is interrupted is of interest for measurement of diffusion coefficients and for determination of cell response to sequential charge-discharge cycles. The governing equations remain unchanged. Fuller et al. [114] examine the relaxation of a nonuniform solid concentration, created during passage of current with a nonuniform current distribution. Current flows within the electrode (but with no net current out of the electrode) because of the driving force of the nonuniform state of charge and, to a lesser extent, because of the concentration gradients in the electrolyte. If the open-circuit potential varies steeply with state of charge, then the electrode will rapidly tend towards a uniform concentration. However, if the open-circuit potential varies little with concentration, then there is little driving force for electrochemical equalization in the solid phase. The extreme case of relaxation in a phase-change electrode, in which the open-circuit potential is constant with state of charge, results in little change in the nonuniform distribution of utilization upon relaxation [115]. Fuller et al. show how the presence of a nonuniform solid concentration is actually beneficial when the current is reversed, because reactants are piled up closer to the reacting region (separator-electrode boundary).

Relaxation phenomena affect the accuracy of the "signature-curve" method for obtaining capacity *vs.* discharge rate in a minimum amount of time [116]. The rest time between discharges which yields the most accurate signature curve for cell capacity as a function of discharge rate is slightly less than the characteristic time for relaxation of gradients in the state of charge across the electrode given by

$$\tau = (nF\overline{V}_{active}L^2\varepsilon)\big/\big(\kappa(\partial U/\partial\Theta)\big).$$

6.2   *Optimizing Geometric Parameters*

There are several geometric parameters that can be controlled in the manufacturing and design processes: volume fractions of each phase, especially the electrolyte volume fraction; solid particle diameter; thickness of the

electrodes; and separator area, which determines the current density for a given overall applied current. In addition, the initial salt concentration in the electrolyte and the positive-to-negative capacity ratio are design parameters. Modeling can greatly reduce the amount of experiments needed to optimize these parameters. A full-cell simulation model can be coupled to an optimization algorithm to determine the values of the geometric parameters that yield some optimum objective. The objective must be clearly defined by the designer, and could be maximum energy density or maximum average power density for a given discharge time, maximum peak power density at a specified depth of discharge, or some tradeoff between power and energy, such as the "knee" in a Ragone plot [86]. The optimization procedure tells one the optimum geometric parameters which maximize the performance of materials with given thermodynamic, kinetic, and transport properties. One can then use this information on maximum theoretical performance to compare different materials and to evaluate goals.

Optimizations of lithium-polymer batteries for electric vehicles [113] and lithium-ion batteries for hybrid vehicles [117,11] have been presented. Chiang and Hellweg [118] optimize not just the porosity of the electrode, but how the porosity should vary across an electrode, for maximum power and energy density. The porosity should be higher closer to the separator, where the highest rate of reaction occurs. Newman [104] presents an optimization methodology to achieve maximum energy density for the case of a battery in which the assumptions of facile kinetics, constant concentration, negligible ohmic drop in the electrode phase, and constant open-circuit potential apply. A lithium battery using an ionomer electrolyte might fall under this category. In this case, the optimal values of geometric parameters such as electrode thickness, area, and porosity depend on the dimensionless parameter $T = U\kappa t_d/(QL_s^2)$, where t_d is the design time of discharge and Q is the coulombic capacity of the electrode per unit volume.

Of particular interest in the design of lithium-ion batteries is the optimization of the positive-to-negative capacity ratio [4]. The issue of balancing capacity is of acute importance in nonaqueous batteries because of the absence of a benign overcharge reaction such as the hydrogen and oxygen evolution reactions which occur in aqueous systems. In the absence of side reactions, one would make the capacities of the positive and negative electrodes nearly equal, with the electrode which behaves more favorably at the end of charge and discharge being limiting. However, in the presence of side reactions, particularly the formation reaction to form the SEI layer on the carbon electrode, determining the optimum balance can be more difficult. One must balance the penalties of having excess mass in either electrode against the risks associated with overcharging or overdischarging particular electrodes [119]. Given experimental data for how much cyclable lithium is consumed by a given side reaction, *e.g.,* SEI formation, models can help one assess the likelihood of risks

such as lithium deposition when the negative electrode is undersized or undesirable phase transitions or solvent oxidation when the positive electrode is undersized, in order to find the balance of electrode capacity that maximizes energy density without comprimising safety or cycle life.

6.3   Interpreting Experimental Data

6.3.1   Measuring Transport Properties

As mentioned earlier, electrolytes used in lithium batteries are usually concentrated, binary electrolytes that exhibit nonideal behavior. In addition, polymer and gel electrolytes are opaque, highly resistive, and sticky, and therefore their transference numbers are not easily measurable using traditional techniques such as the Hittorf or moving boundary methods. Recent theoretical studies have described the substantial error involved in measuring transference numbers with techniques that assume ideal behavior [14, 15], and have described how experimental data can be interpreted rigorously using concentrated-solution theory to obtain transference numbers. One method is the galvanostatic polarization technique [120,121,122]:

$$(1-t_+^o) = \frac{mc_\infty F(\pi D)^{1/2}}{4} \frac{d\ln c}{dU} \tag{61}$$

where m is the slope of $\Delta\Phi$ *vs.* $It_i^{1/2}$, where $\Delta\Phi$ is the potential across the electrolyte after galvanostatic polarization at current I for time t_i, and $dU/d\ln c$ is the variation of open-circuit potential with electrolyte concentration.

Pollard and Comte [15] analyzed how to obtain the salt diffusion coefficient and transference number from ac impedance for the case of a binary electrolyte (three species) and for the case of a binary salt in a mixture of two solvents (four species). For the three-species case, the transference number is determined by

$$\frac{1-t_+^o}{z_-v_-} = \frac{s_o c}{nc_o} - \frac{s_-}{nv_-} - F\sqrt{\frac{Z_w(0)\varepsilon A D_c}{vLc_o\bar{V}_o\left(1+\frac{d\ln f_\pm}{d\ln c}\right)}} \tag{62}$$

where $Z_w(0)$ is the width of the arc related to transport resistance on a Nyquist plot and the equation allows for the general case in which any of the three species may be involved in reaction at the electrodes. Note that the quantity t_i^o/z_iv_i is independent of the choice of speciation in the electrolyte (*e.g.*, degree of dissociation), and it is this quantity which appears in Equation 12. Pollard and Comte also present methods to test whether a binary electrolyte obeys the assumptions of dilute solution

theory and whether an electrolyte behaves as a three-component or four-component solution.

Darling [30] has discussed how a distribution of particle sizes in a porous electrode can affect the accuracy of measurements of the solid diffusion coefficient using the galvanostatic intermittent titration (GITT) [123], restricted diffusion [124], and ac impedance [125] methods. At short times, as used in GITT, the particles behave like semi-infinite media, and the response is independent of the particle-size distribution. At long times, as used in restricted diffusion and ac impedance, the response is affected by particle size. Therefore, the GITT technique, in cells properly designed to minimize solution-phase diffusion effects (*i.e.,* thin electrodes and use of a reference electrode or thin separator) is preferred for measuring solid diffusivities. Darling uses an analytic solution to the impedance of a porous electrode, neglecting transport in the electrolyte, to derive the following correction to the ac impedance method:

$$D_s = D_{s,app} \frac{\sum_i \varepsilon_i R_i^2}{\varepsilon_P R_{avg}^2} \tag{63}$$

where ε_P is the volume traction of active material in the electrode, the summation is over all particle sizes and their respective volume fractions in the electrode, D_s is the actual solid diffusion coefficient at a given state of charge, and $D_{s,app}$ is the apparent solid diffusion coefficient one would measure under the assumption that the electrode consisted of uniformly-sized particles of radius R_{avg} with the same volume fraction and surface area as the actual electrode [125]. This equation applies as the exchange-current density tends to infinity. For finite values of the exchange-current density, the difference between the actual and apparent diffusion coefficient varies with $dU/d\Theta$.

Verbrugge and Koch [46] provide an analytic solution for the potential of a cell during a GITT experiment for the case of a variable diffusion coefficient, given by Equations 38 and 39 with a constant binary interaction parameter, and an open-circuit potential which follows a Wohl´s expansion for the excess Gibbs free energy. Zhang et al. [127] compare model simulations to experiments of cyclic voltammetry on a single particle of lithium manganese oxide spinel.

6.3.2   ac Impedance

Meyers et al. [127] present analytic solutions for the impedance of a porous insertion electrode with film resistance, neglecting mass transport in the electrolyte. They present simplified forms of the equation for a single particle and for high-, moderate-, and low-frequency limits, and discuss when solid-phase diffusion overlaps with charge-transfer resistance and also the capacitive effects of the slope of the open-circuit potential. In addition, they demonstrate how to include a distribution of particle sizes in the analytic solution.
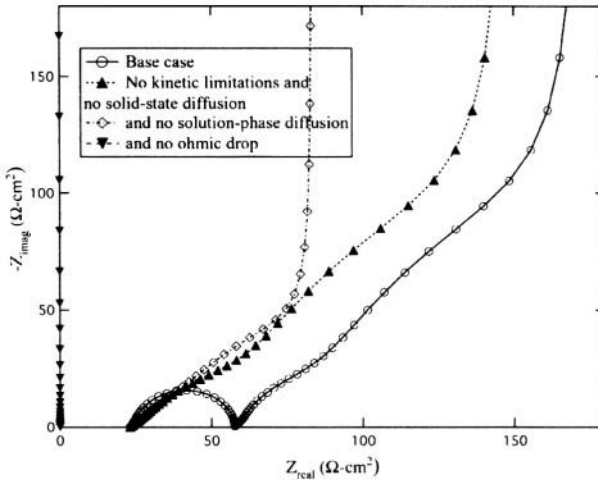
Figure 8. Simulated impedance of a Li|PEO$_{18}$LiCF$_3$SO$_3$|LiTiS$_2$ cell. The base case is the impedance of the full cell. The components of this impedance can be elucidated by progressively setting parameters to have zero impedance. Thus, first we see that the semicircle is due to kinetic impedance and that solid diffusion has little effect, then that solution-phase diffusion within the porous electrode is responsible for much of the shape of the impedance spectrum at low frequencies, and finally that ohmic drop and the capacity of the porous electrode are responsible for a 45° slope at moderate frequencies that shifts to a verticle line at low frequencies. From reference 63, reprinted with permission from The Electrochemical Society, Inc.

When solution-phase mass-transport impedance is also of interest, numerical simulations can be performed. Doyle et al. [63] have demonstrated how numerical simulations of ac impedance can be used to understand the contributions of different aspects of a cell to its measured impedance spectrum. With a model, one can simulate different components (separator, electrodes with and without solid, solution, film, charge transfer, and ohmic resistances) separately by making relevant parameters infinite or zero. These different components can then give insight into the impedance of the full cell (see Figure 8). For example, they demonstrated how effects due to distributed resistances within a porous electrode and due to the slope of the open-circuit potential could be confused with solid diffusion limitations, and show how ignoring these effects could lead to large errors when calculating solid diffusion coefficients from ac impedance data on porous electrodes.

7.0   A BRIEF MENTION OF OTHER KINDS OF MODELING

This review has discussed only continuum-scale models. Other types of models are also used in the study of lithium batteries. Empirical models are used to predict battery life by extrapolating experimental results. Statistical mechanical models help in understanding transport on the molecular level and also in understanding thermodynamic properties of insertion compounds. For example,

molecular dynamic simulations can be used to understand and predict diffusion in multicomponent solutions, and Monte Carlo simulations can illustrate how polymer motion impacts salt transport in polymer electrolytes. Finally, *ab initio* calculations can be used to predict oxidation and reduction potentials and interaction potentials, in order to understand mechanisms of solvent decomposition, to guide discovery of novel electrode materials, and to provide information on interatomic forces needed for statistical mechanical simulations.

List of Symbols

a	surface area of active material per volume of electrode (m^{-1})
c	salt concentration in the electrolyte (mol/m^3 of solution)
c_i	concentration of species i (mol/m^3)
c_s	concentration of lithium in the solid insertion electrode (mol/m^3)
c_T	total concentration of salt and solvent (mol/m^3)
C	double-layer capacitance (F/m^2)
C_P	heat capacity ($J/m^2 \cdot K$)
D_i	diffusion coefficient of species i in dilute solution theory (m^2/s)
D	salt diffusion coefficient (m^2/s)
$\mathcal{D}$	diffusion coefficient based on thermodynamic driving force (m^2/s)
D_s	diffusion coefficient of lithium in an insertion electrode (m^2/s)
$\mathcal{D}_{i,j}$	diffusion coefficient for interaction of species i and j (m^2/s)
$f_\pm$	mean molar activity coefficient of an electrolyte
F	Faraday's constant, 96487 C/equiv
i_n	transfer current normal to the surface of the active material (A/m^2)
i_0	exchange current density (A/m^2)
i_2	current density (A/m^2 superficial area) in the electrolyte
I	total current density in the cell (A/m^2)
j	total fiux due to reaction ($mol/s \cdot m^2$ of active material)
k	thermal conductivity ($W/m^2 \cdot K$)
k_a, k_c	rate constants for the anodic and cathodic directions of a reaction
k_m	mass transfer coefficient (m/s)
L	thickness of an electrode (m)
L_+, L_s, L_-	thickness of positive electrode, separator, or negative electrode (m)
m	molality (mol/kg)
M_i	symbol for the chemical formula of species i or molecular weight (g/mol)
n	number of electrons involved in a half reaction
N_i	flux of species i ($mol/s \cdot m^2$ of apparent area)
q	charge on the electrode side of the double layer (C/m^2)
q_i	surface charge density of species i on the solution side of the double layer (C/m^2)
Q	coulombic capacity of an electrode (C, C/m^2, or C/m^3)
$\dot{Q}$	heat-generation rate (W/m^2)
r	radial position across a spherical particle (m)
r_k	rate of chemical reaction k ($mol/s \cdot m^3$)
R	universal gas constant, 8.3143 J/mol K, or radius of a particle (m)
R_{film}	effective resistance of a solid-electrolyte interphase ($\Omega \cdot m^2$)

s	stoichiometric coefficient, positive for anodic reactants
t	time (s)
t_i^o	transference number of species i with respect to the solvent velocity
T	temperature, K
u	mobility $(m^2 \cdot mol/J \cdot s)$
U	thermodynamic potential measured with respect to a lithium reference electrode (V)
$\mathbf{v}$	velocity (m/s)
V	cell potential (V)
$\bar{V}$	molar volume (m^3/mol)
x	position across cell (m)
y	stoichiometry of lithium in an insertion electrode
z_i	charge of ion i

Greek

α	transfer coefficient
β	symmetry factor for an elementary reaction
ε	volume fraction (of electrolyte unless otherwise specified)
Γ_i	excess concentration of species i in the double layer (mol/m^2)
κ	effective ionic conductivity (S/m)
μ	chemical potential (J/mol)
ν_i	moles of ion i produced when a mole of its salt dissociates
ν	number of moles of ions into which a mole of electrolyte dissociates
ρ	density (kg/m^3)
σ	effective electronic conductivity of a porous electrode (S/m)
Θ	fraction of total lithium insertion sites which are occupied by lithium
Θ_s	site on the lattice of the insertion material which can be occupied by lithium
Θ_P	site on the lattice of a crystalline polymer which can be occupied by lithium salt
Φ	potential
$\gamma_{\pm}$	mean molal activity coefficient
γ_i	exponent for the dependence of i_o on the concentration of species i

Supercripts

o	property is with respect to solvent velocity or initial condition
Θ	secondary reference state of the chemical potential

Subscripts

a	anodic
c	cathodic
dl	double-layer
e	electrolyte
f	faradaic
i	species i
$\lim$	limiting current
m	main reaction
n	electrochemical flux normal to surface of active material
o	solvent in an electrolytic solution
s	side reaction

8.0   REFERENCES

1. J. Newman and W. Tiedemann, *AIChE J.,* **21**, 25, 1975.
2. M. Doyle, T.F. Fuller, and J. Newman, *J. Electrochem. Soc.,* **140**, 1526, 1993.
3. G.G. Botte, V.R. Subramanian, and R.E. White, *Electrochimica Acta,* **45**, 2595, 2000.
4. P. Arora, R.E. White, and M. Doyle, *J. Electrochem. Soc.,* **145**, 3647, 1998.
5. D. Wheeler and J. Newman, in *AIChE Annual Meeting,* paper 126h, Reno, Nevada, November 4-9 2001.
6. K.S. Chen, G.H. Evans, R.S. Larson, M.E. Coltrin, and J. Newman, in *Proceedings of the Electrochemical Society* (G. Halpert, M. L. Gopikanth, K. M. Abraham, et al., eds.) vol. **98-15**, 1998.
7. W.G. Sunu and D.N. Bennion, *J. Electrochem. Soc.,* **127**, 2007, 1980.
8. K.C. Tsaur and R. Pollard, *J. Electrochem. Soc.,* **133**, 2296, 1986.
9. Z. Mao and R.E. White, *J. Power Sources,* **43-44**, 181, 1993.
10. J.S. Newman, *Electrochemical Systems.* Prentice-Hall Inc., Englewood Cliffs, NJ, **2**nded., 1991.
11. T.F. Fuller, M. Doyle, and J. Newman, *J. Electrochem. Soc.,* 141, 1, 1994.
12. M. Ue and S. Mori, in *Proceedings of the Electrochemical Society* (S. Megahed, B.M. Barnett, and L. Xie, eds.), vol. 94-28, p. 440, 1994.
13. G.E. Blomgren, in *Proceedings of the Electrochemical Society* (E.B. Yeager, B. Schlumm, G. Blomgren, D.R. Blakenship, V. Leger, and J. Akridge, eds.), vol. 80-7, p. 35, 1980.
14. M. Doyle and J. Newman, *J. Electrochem. Soc.,* **142**, 3465, 1995.
15. R. Pollard and T. Comte, *J. Electrochem. Soc.,* **136**, 3734, 1989.
16. R.B. Bird, W.E. Stewart, and E.N. Lightfoot, "*Transport Phenomena."* John Wiley and Sons, Inc., New York, 1960.
17. L. Onsager, *Annals New York Acad. Sciences,* **46**, 241, 1945.
18. J.S. Dunning, *Analysis of Porous Electrodes with Sparingly Soluble Reactants.* Ph.D. dissertation, University of California, Los Angeles, 1971.
19. R. Pollard and J. Newman, *J. Electrochem. Soc.,* **128**, 491, 1981.
20. M.W. Verbrugge and B.J. Koch, *J. Electrochem. Soc.,* **143**, 600, 1996.
21. J. Newman, *Ind. Eng. Chem. Res.,* **34**, 3208, 1995.
22. S.A. Hallaj, H. Maleki, J.S. Hong, and J.R. Selman, *J. Power Sources,* **83**, 1, 1999.
23. K. Kanari, K. Takano, Y. Saito, and T. Masuda, in *Proceedings of the International Workshop on Advanced Batteries,* Osaka, Japan, February 22-24, 1995.
24. D. Bernardi, E. Pawlikowski, and J. Newman, *J. Electrochem. Soc.,* **132**, 5, 1985.
25. L. Rao and J. Newman, *J. Electrochem. Soc.,* **144**, 2697, 1997.
26. K.E. Thomas and J. Newman. to be published.
27. K.E. Thomas, C. Bogatu, and J. Newman, *J. Electrochem. Soc.,* **148**, A570, 2001.
28. C.R. Pals and J. Newman, *J. Electrochem. Soc.,* **142**, 3274, 1995.
29. G.G. Botte, B.A. Johnson, and R.E. White, *J. Electrochem. Soc.,* **146**, 914, 1999.
30. R.M. Darling, "*Lithium Manganese Oxide Spinel Electrodes."* Ph.D. Dissertation, University of California, Berkeley, 1998.
31. C.Y. Wang, W.B. Gu, and B.Y. Liaw, *J. Electrochem. Soc.,* **145**, 3407, 1998.
32. B. Wu and R.E. White, *J. Power Sources,* **92**, 177, 2001.
33. Y. Zhang and H.Y. Cheh, *J. Electrochem. Soc.,* **146**, 850, 1999.

34. M. Doyle and J. Newman, *Electrochim. Acta,* **40**, 2191, 1995.
35. M. Doyle, J. Newman, A.S. Gozdz, C.N. Schmutz, and J.M. Tarascon, *J. Electrochem. Soc.,* **143**, 1890, 1996.
36. R. Darling and J. Newman, *J. Electrochem. Soc.,* **145**, 990, 1998.
37. F.B. Hildebrand, "*Advanced Calculus for Applications."* Prentice-Hall Inc., Englewood Cliffs, NJ, **2nd** ed., 1976.
38. M.J. Matlosz, "*Experimental Methods and Software Tools for the Analysis of Electrochemical Systems."* Ph.D. Dissertation, University of California, Berkeley, 1985.
39. C. Wagner, *J. Mathematics and Physics,* **34**, 289, 1954.
40. A. Acrivos and P.L. Chambré, *Ind. Eng. Chem.,* **49**, 1025, 1957.
41. C.M. Doyle, *Design and Simulation of Lithium Rechargeable Batteries,* Ph.D. Dissertation, University of California, Berkeley, 1995.
42. W. McKinnon and R. Haering, "Physical Mechanisms of Intercalation," in *"Modern Aspects of Electrochemistry, "* (R. White, J. Bockris, and B. Conway, eds.), vol. 15, p. 235 Plenum Press, New York, 1983.
43. A. Anani, S. Crouch-Baker, and R.A. Huggins, *J. Electrochem. Soc.,* **134**, 3098, 1987.
44. R. Darling and J. Newman, *J. Electrochem. Soc.,* **146**, 3765, 1999.
45. H. Kanoh, Q. Feng, T. Hirotsu, and K. Ooi, *J. Electrochem. Soc.,* **143**, 2610, 1996.
46. M.W. Verbrugge and B.J. Koch, *J. Electrochem. Soc.,* **146**, 833, 1999.
47. B. Paxton and J. Newman, *J. Electrochem. Soc.,* **143**, 1287, 1996.
48. Z. Mao and R.E. White, *J. Electrochem. Soc.,* **141**, 151, 1994.
49. R. Pollard, "*Mathematical Modeling of the Lithium-Aluminum, Iron Sulfide Battery."* Ph.D. Dissertation, University of California, Berkeley, 1979.
50. J. Dunning, D.N. Bennion, and J. Newman, *J. Electrochem. Soc.,* **120**, 906,1973.
51. M. Abyanch and M. Fleischmann, in *Proceedings of the Electrochemical Society* (R. E. White, M. W. Verbrugge, and J. F. Stockel, eds.), vol. 91-10, p. 96, Penningtion, NJ, 1991.
52. J.S. Chen and H.Y. Cheh, *J. Electrochem. Soc.,* **140**, 1213, 1993.
53. D.M. Bernardi, *J. Electrochem. Soc.,* **137**, 1670, 1990.
54. V. Srinivasan, J.W. Weidner, and R.E. White, J. *Solid State Electrochem.,* **4**, 367, 2000.
55. M. Sinha, *A Mathematical Model for the Porous Nickel Hydroxide Electrode.* Ph.D. Dissertation, University of California, Los Angeles, 1982.
56. M.E. Orazem and J. Newman, "Photoelectrochemical Devices for Solar Energy Conversion" in *Modern Aspects of Electrochemistry,* vol. 18, Plenum Press, New York, 1986.
57. M.E. Orazem and J. Newman, *J. Electrochem. Soc.,* **131**, 2569, 1984.
58. H.S. Carslaw and J.C. Jaeger, " *Operational Methods in Applied Mathematics."* Oxford University Press, London, **2nd** ed., 1948.
59. K.P. Ta and J. Newman, *J. Electrochem. Soc.,* **145**, 3860, 1998.
60. R. Darling and J. Newman, *J. Electrochem. Soc.,* **144**, 4201, 1997.
61. G.S. Nagarajan, J.W. van Zee, and R.M. Spotnitz, *J. Electrochem. Soc.,* **145**, 771,1998.
62. A.B. Yu, R.P. Zou, and N. Standish, *Ind. Eng. Chem. Res.,* **35**, 3730, 1996.
63. M. Doyle, J.P. Meyers, and J. Newman, *J. Electrochem. Soc.,* **147**, 99, 2000.
64. B. Pillay, "*Design of Electrochemical Capacitors for Energy Storage,"* Ph.D. Dissertation, University of California, Berkeley, 1996.

65. I. Ong and J. Newman, *J. Electrochem. Soc.,* **146**, 4360, 1999.
66. V. Battaglia and J. Newman, *J. Electrochem. Soc.,* **142**, 1423, 1995.
67. K.J. Vetter, *"Electrochemical Kinetics, Theoretical and Experimental Aspects."* Academic Press, New York, 1967.
68. K.C. Tsaur and R. Pollard, *J. Electrochem. Soc.,* **131**, 975, 1984.
69. K.C. Tsaur and R. Pollard, *J. Electrochem. Soc.,* **131**, 984, 1984.
70. P. Arora, M. Doyle, A.S. Gozdz, R.E. White, and J. Newman, *J. Power Sources,* **88**, 219, 2000.
71. P. Arora, M. Doyle, and R. E. White, *J. Electrochem. Soc.,* **146**, 3543, 1999.
72. S.R. Narayanan, S. Surampudi, A.I. Attia, and C.P. Bankston, *J. Electrochem. Soc.,* **138**, 2224, 1991.
73. H. Hafezi and J. Newman. to be published.
74. A. Blyr, G. Amatucci, D. Guyomard, Y. Chabre, and J.M. Tarascon, *J. Electrochem. Soc.,* **145**, 194, 1999.
75. Z. Mao and R.E. White, in *Proceedings of the Electrochemical Society* (R.E. White, M.W. Verbrugge, and J.F. Stockel, eds.), vol. 91-10, p. 46, Penningtion, NJ, 1991.
76. E.J. Podlaha and H.Y. Cheh, *J. Electrochem. Soc.,* **141**, 15, 1994.
77. D.M. Bernardi and M.K. Carpenter, *J. Electrochem. Soc.,* **142**, 2631, 1995.
78. D. Bernardi and J. Newman, *J. Electrochem. Soc.,* **134**, 1309, 1987.
79. W.B. Gu, C.Y. Wang, J.W. Weidner, R.G. Jungst, and G. Nagasubramanian, *J. Electrochem. Soc.,* **147**, 427, 2000.
80. D. Bernardi, H. Gu, and A.Y. Schoene, *J. Electrochem. Soc.,* **140**, 2250, 1993.
81. D. Bernardi, E. Pawlikowski, and J. Newman, *J. Electrochem. Soc.,* **135**, 2922, 1988.
82. D.A.G. Bruggeman, *Annalen der Physik,* **24**, 636-679, 1935.
83. D.R. Shriver, R. Dupon, and M. Stainer, *J. Power Sources,* **9**, 383, 1983.
84. G. Tsagaropoulos and A. Eisenberg, *Macromolecules,* **28**, 6067, 1995.
85. X. Cheng, C. Wang, A.M. Sastry, and S.B. Choi, *J. Engineering Materials and Tech..* **121**, 514, 1999.
86. G.G. Trost, V. Edwards, and J.S. Newman, "Electrochemical Reaction Engineering," in *Chemical Reaction and Reactor Engineering,* p. 923, Marcel Dekker, Inc., New York, 1987.
87. M.W. Verbrugge, *J. Electrostatics,* **34**, 61, 1995.
88. D.R. Baker and M.W. Verbrugge, *J. Electrochem. Soc.,* **146**, 2413, 1999.
89. W.H. Tiedemann and J. Newmann, in *Proc. Symp. Battery Design and Opt.* (S. Gross, ed.), vol. 79-1, p. 39, The Electrochemical Society, Princeton, NJ, 1979.
90. W.H. Tiedemann and J. Newman, in *154th Meeting of the Electrochemical Societey,* p. 169, 1979.
91. J. Newman and W. Tiedemann, *J. Electrochem. Soc.,* **140**, 1961, 1993.
92. T.I. Evans and R.E. White, *J. Electrochem. Soc.,* **136**, 2145, 1989.
93. E.J. Podlaha and H.Y. Cheh, *J. Electrochem. Soc.,* **141**, 1751, 1994.
94. J. Lee, K.W. Choi, N.P. Yao, and C.C. Christiansen, *J. Electrochem. Soc.,* **133**, 1286, 1986.
95. Y. Chen and J.W. Evans, *J. Electrochem. Soc.,* **141** 2947, 1994.
96. Y. Chen and J.W. Evans, *J. Electrochem. Soc.,* **143** 2708, 1996.
97. J. Newman and W. Tiedemann, *J. Electrochem. Soc.,* **142**, 1054, 1995.
98. J. Euler and W. Nonnenmacher, *Electrochimica Acta,* **2**, 268, 1960.
99. J. Newman and C.W. Tobias, *J. Electrochem. Soc.,* **109**, 1183, 1962.

100. L. Song and J.W. Evans, *J. Electrochem. Soc.,* **147**, 2086, 2000.
101. C.R. Pals and J. Newman, *J. Electrochem. Soc.,* **142**, 3282, 1995.
102. M.W. Verbrugge, *AIChE J.,* **41**, 1550, 1995.
103. W. Tiedemann and J. Newman, *J. Electrochem. Soc.,* **122**, 1482, 1975.
104. J. Newman, *J. Electrochem. Soc.,* **142**, 97, 1995.
105. M. Doyle and J. Newman, *J. Power Sources,* **54**, 46, 1995.
106. S. Atlung, B. Zachau-Christiansen, K. West, and T. Jacobsen, *J. Electrochem. Soc.,* **131**, 1200, 1984.
107. B.C. Knutz, K. West, B. Zachau-Christiansen, and S. Atlung, *J. Power Sources,* **43-44**, 733, 1993.
108. M. Doyle and J. Newman, *J. Appl. Electrochem.,* **27**, 846, 1997.
109. M. Doyle and J. Newman, *"Analysis of Capacity-Rate Behavior Using Simplified Models for the Discharge Process of Lithium Batteries,"* unpublished, 1997.
110. S. Atlung, K. West, and T. Jacobsen, *J. Electrochem. Soc.,* **126**, 1311, 1979.
111. R. Darling and J. Newman, *J. Electrochem. Soc.,* **144**, 3057, 1997.
112. M. Doyle, T.F. Fuller, and J. Newman, *Electrochim. Acta,* **39**, 2073, 1994.
113. K.E. Thomas, S.E. Sloop, J.B. Kerr, and J. Newman, *J. Power Sources,* **89**, 132, 2000.
114. T.F. Fuller, M. Doyle, and J. Newman, *J. Electrochem. Soc.,* **141**, 982, 1994.
115. R. Pollard and J. Newman, *J. Electrochem. Soc.,* **128**, 503, 1981.
116. M. Doyle, J. Newman, and J. Reimers, *J. Power Sources,* **52**, 211, 1994.
117. C. Fellner and J. Newman, *J. Power Sources,* **85**, 229, 2000.
118. Y.M. Chiang and B. Hellweg, in ***200**th Meeting of the Electrochemical Society,* p. 144, San Francisco, CA, September 3-7 2001.
119. D. Guyomard and J.M. Tarascon, *Solid State Ionics,* **69**, 222, 1994.
120. Y. Ma, M. Doyle, T.F. Fuller, M.M. Doeff, L.C. de Jonghe, and J. Newman, *J. Electrochem. Soc.,* **142**, 1859, 1995.
121. H. Hafezi and J. Newman, *J. Electrochem. Soc.,* **147**, 3036, 2000.
122. P. Georen and G. Lindbergh, *Electrochim. Acta,* **47**, 577, 2001.
123. W. Weppner and R.A. Huggins, *J. Electrochem. Soc.,* **114**, 1569, 1977.
124. J. Newman and T.W. Chapman, *AIChE J.,* **19**, 343, 1973.
125. C. Ho, I.D. Raistrick, and R.A. Huggins, *J. Electrochem. Soc.,* **127**, 343, 1980.
126. D. Zhang, B.N. Popov, and R.E. White, *J. Electrochem. Soc.,* **147**, 831, 2000.
127. J.P. Meyers, M. Doyle, R.M. Darling, and J. Newman, *J. Electrochem. Soc.,* **147**, 2930, 2000.

13

Aging Mechanisms and Calendar-Life Predictions in Lithium-Ion Batteries

Michel Broussely
SAFT
F-86060 Poitiers
France

1.0   INTRODUCTION

With the increasing use of Lithium-ion batteries in many applications other than mobile phones or portable computers, a very long cycle and/or calendar life must be demonstrated. Typical examples are the automotive, space, standby, and other professional applications. Although the cycling characteristics of different active materials has been quite extensively described in the literature, very few has been reported so far on the long-term storage characteristics, as a function of time and temperature, from which an expected battery life could be calculated. The main reason is that the consumer portable applications for which Li-ion has been primarily developed does not require such long-life characteristics while the cycle life is more important. Consequently, fundamental work has been more devoted to study the reversibility of the active materials rather than aging on storage. Another reason might be that this type of study is usually achieved by battery manufacturers and often includes manufacturing process know-how, which is not supposed to be disclosed. Lim et al. [1] made accelerated lifetime studies years ago on a commercial $LiCoO_2$ lithium-ion battery. They concluded that, from the measured capacity loss during storage at different temperatures as well as during cycling, the system would not be able to reach the desired performances for a space application. Since this study many improvements have been implemented in special cell designs to fulfill this high demanding application and, to answer the customer´s demand for a reliable and rational battery life extrapolations, more fundamental work is now being undertaken on this topic to better understand the side reactions mechanisms which impact on the cells´ aging. Many of the papers cited in the references list of this chapter are quite recent, most of them being described in abstracts of recent meetings, for which more detailed will certainly be published in near future.

Taking in account the very large variety of Li-ion systems and technologies, it is difficult to give today an exhaustive and quantitative picture of all the aging reactions likely to occur in any battery design. The aim of this document is to discuss some basic mechanisms, illustrated from chosen examples and data, which should help in the definition of appropriate procedures to predict battery life.

2.0   GENERAL

Aging of a battery can be defined as the modification of its properties with time and use. Essential properties are the available energy and power, and cell mechanical integrity (cell dimensions, leakage, etc.). Basically, energy loss can result from active materials transformation in inactive phases thus reducing the cell capacity at any rate, and/or from increasing of cell impedance, lowering the operating voltage. Power capability loss is directly related impedance growth. Most of the time both effects are jointly observed. Predicting the battery end of life for a specific utilization should consequently address the phenomena having an impact on the relevant characteristics. For example, the life of a high power battery used in pulse discharge is obviously limited by the impedance increase, while high energy used in satellite might be limited by capacity loss.

Two types of aging situations can be distinguished: during use (i.e. on cycling), and on storage. While cycling generally damages the materials reversibility, the interactions between active materials and electrolyte, mostly responsible for aging on storage, would mainly depend on time and temperature. As a general rule, these two aging mechanisms are often considered as additive, but interactions may definitely occur. For example, cycling inducing a volume change of the materials would modify the interface with electrolyte, and favor the reactions at the interface, such as passive film formation. On the other hand, a storage in a fully charge state might be more detrimental to the interface than continuous cycling, as the materials are maintained at the maximum level of reactivity. This is particularly the case of most of the positive materials used in Li ion cells, which OCV is function of state of charge.

3.0   AGING DURING CYCLING

Aging during cycling is often described as the result of reversible degradation of active materials, coming from phase transformations during lithium insertion. This is beyond the scope of this paper to describe these mechanisms, which are extensively studied and published. During the last decade, the fundamental work in solid-state chemistry and crystalline structure analysis has made huge progress in understanding basic mechanisms.

This is extremely helpful to assess the stability of the materials´ electro-chemical properties, and to make a good selection.

Most of the current Li-ion cell technologies have now adopted the positive materials $LiCoO_2$, $LiNi_xCo_yM_zO_2$ (M being a "doping" metallic ion) which has excellent cycling properties can be the material of choice for the large industrial batteries, and $LiMn_2O_4$ which was progressively improved during the last five years, through modifications in initial composition and crystalline structure, and can reach an acceptable level of reversibility at ambient temperature. On the negative electrode side, graphites of different types have been commonly chosen for their voltage and specific capacity properties. Compared to the hard carbon or poorly crystallized structures, the main problem of structure stability was linked to the exfoliation induced by solvent molecule insertion and reduction producing gas. This problem has been largely solved by either the proper choice of solvent mixtures, or selection of graphite type, for example containing a sufficient proportion of the rhombo-hedric versus hexagonal structure [2, 3]. Additives, whose film forming properties prevent the solvent molecule from reaching the carbon layers [4,5] greatly contributes to the excellent stability of the carbon structure even after an extended cycling.

As a first step analysis, cycling tests at the laboratory level can indicate very quickly the potentialities of the compounds. However, for a more precise analysis of a "good candidate", it is often difficult to distinguish between the intrinsic properties of the materials and what is coming from the electrode manufacturing, which may lead to apparent contradictory results. Many published data showing cycle life in lab tests during less than 100 cycles are far worse than can be experimented further in a real cell, with appropriate electrode process. Actually, the type of binder, electronic conductors additives and their processing play a prominent role on the electrode efficiency, and stability during cycling. This is a very important part of the manufacturer´s process know how, which is generally not available.

As an example, Figure 1 illustrates the effect, which can be brought by improper negative electrode processing. This figure represents the evolution of capacity and cell resistance (measured at charged state from a 5 second pulse) of a 6 Ah prismatic spirally wound cell, using $LiCoO_2$ as positive material. From graphite #1 in the regular design, a new graphite (#2) type was used, using the same electrode binder and process.

This new graphite, tested in laboratory cells, exhibited excellent properties, even better than the previous one. Nevertheless, while the initial characteristics were exactly the same as in the regular design, the

tested cell using the new material suffered from a dramatic capacity decrease, associated to a large impedance increase. From cell analysis, this effect was attributed to some lithium plating during charge, resulting from poor electrolyte accessibility to the carbon surface. Lithium is consumed due to the poor cycling efficiency, and the negative electrode pores are clogged by reaction products, thus increasing the problem. It was concluded that the electrode manufacturing process had to be adapted to the new material, whose physical properties are somewhat different.
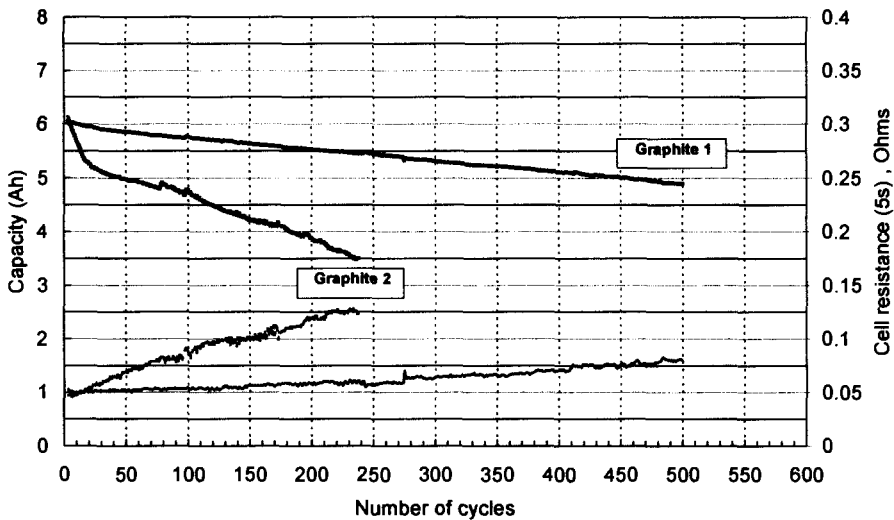
Figure 1. Effect of negative electrode on cycling properties of LiCoO₂ / graphite cell. Charge at C-rate up to 4.1 V until current reaches 80mA; discharge at C/2 rate to 2.7 V.

It is indeed very difficult to answer to the general question "what is the cause of capacity fading of Li-ion cells on cycling?". Some authors ascribe the fading to an interfacial impedance increase at the positive electrode; in some other papers negative electrode and SEI evolution is implicated. In many cases, both electrodes suffer from cycling, as shown for example by Zhang et al. on commercial **LiCoO₂** cells [6, 7]. Electrochemical Impedance Spectroscopy (EIS) is as tool often used to analyze the electrochemical property changes of the electrodes, but clear interpretation is sometimes difficult to assess [8]. In general, the high frequency impedance defining the ohmic resistance of the cell is not affected, contrary to the transfer resistance, which is generally the result of the active surface area degradation [9].

Among all the possible mechanisms for capacity fading on cycling, the following are the most often incriminated:

- Degradation of crystalline structure of positive material (especially for $LiMn_2O_4$)
- Graphite exfoliation
- Metallic lithium plating
- Build-up of passivation film on both electrodes, limiting the active surface area and clogging the electrodes´ small pores (which can also occur on storage)
- Mechanical modification of the composite electrode structure due to volume changes during cycling, leading to active particles de-connection from the conductive network. In Li-ion systems, this effect is limited, because the volume change of insertion material is quite small.

The accelerating cycle-life testing is generally easy to perform by continuous high rate cycling, and real cycle-life can be rather quickly demonstrated. This *accelerated* testing can be considered as a *worst case* for material reversibility, and (usually) rest periods applied during cycling or using lower charge rates result in reducing the capacity and power "fade". To illustrate this fact, the Figure 2 shows an amazing recovery phenomenon that was obtained after a rest period. These high power cells (Ni-based) were submitted to an accelerated high rate, low DOD (about 30%), complicated pulse cycling. A power fade was noted at ambient temperature, and is supposedly irreversible as the duration of experiments was already about six months. These cells where taken out of the equipment. Almost one year later, testing was resumed, and a spectacular power recovery was obtained, followed by a sustained power on further cycling. The cell cycled at 45°C maintained a good power level, which shows that the limitation was actually of kinetic nature, resulting from a cumulative mechanism as the cell cycles. This interesting phenomenon is an exaggerated form of what is generally observed when rest periods are allowed during heavy cycling.

With proper choice of materials and electrode processing, excellent cycling behavior can be obtained from Li ion batteries as illustrated by Figure 3. $LiNi_xCo_yAl_zO_2$ / graphite high energy (HE) cells (150 Wh) made by SAFT have been cycled 1000 times from a complete charge state (4 V) down to 80% depth of discharge (DOD) through a pulse discharge simulating EV utilization (DST cycling), which represents an average of 3 hours rate. The figure represents the specific energy measured every 50 cycles during a C/3 100% DOD discharge to 2.7 V.
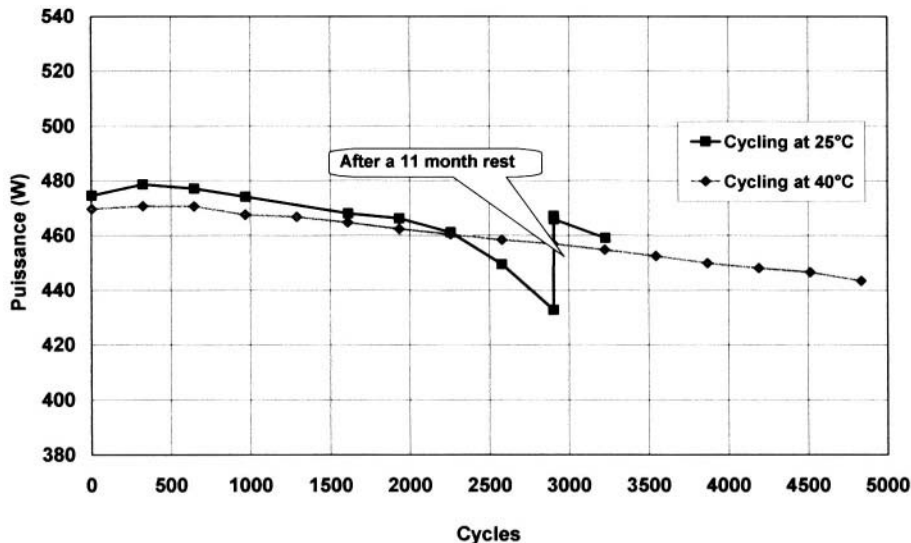
Figure 2. Effect of extended rest period on cell power, cycling continuously at high rate, low average DOD (2500 cycles represent about six months).

From this result, where neither capacity loss nor average voltage drop is experienced, an excellent reversibility of the electrochemical system can be demonstrated at deep DOD cycling.

In general, the cycle life is expected to increase when the DOD of cycling is smaller, because the mechanical stresses induced by the eventual molar volume change as a function of state of charge are reduced. In fact, because of the use of insertion electrodes, there are only small volume changes in the Li-ion systems, which minimizes this effect.

Figure 4 describes 30% DOD cycling, which simulates a Low Earth Orbit (LEO) satellite application. A constant capacity is discharged at each cycle at C/3, from a 3.8 V maximum voltage charge. Every 1000 cycles, a complete charge is made to 4.0 V and discharged to 2.7 V to verify the complete cell energy. Good stability has been recorded so far, and excellent service life may be anticipated to fulfill the application (32000 cycles over 8 years with a minimum of 50% remaining energy).

Increasing the temperature in the 20 to 60°C range should not *a priori* reduce the intrinsic material reversibility, as kinetics of Li^+ insertion should be facilitated, and steric stress effect reduced. However, the general trend is an increase of fading on cycling with temperature. The cause can be attributed to the increasing rate of the side reactions, involving the **interface with the electrolyte.** These reactions are not specially related to cycling, and would also occur during storage.
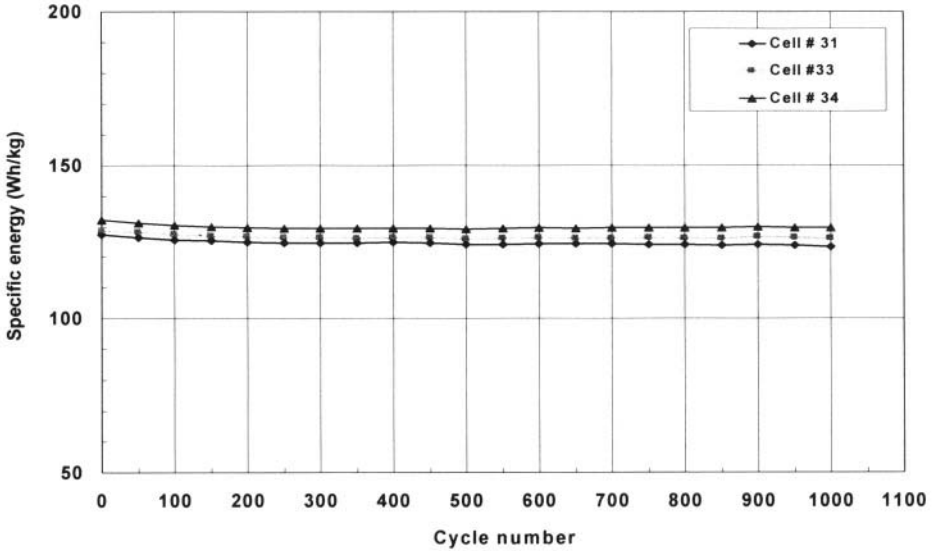
Figure 3. Specific Energy evolution during cycling of a batch of three 150 Wh High Energy LiNi$_x$Co$_y$Al$_z$O$_2$ cells for EV. DST cycling at 80% DOD, diagnostic at C/3 to 2.7 V, charged at 4 V, ambient temperature.
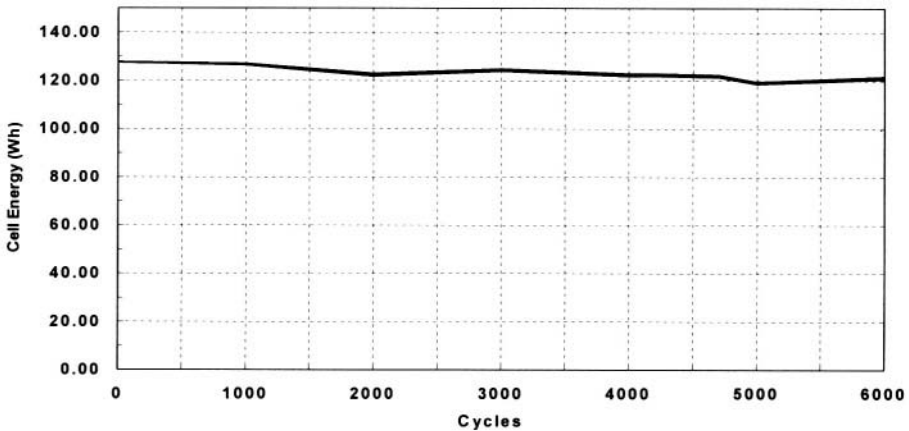
Figure 4. High Energy LiNi$_x$Co$_y$Al$_z$O$_2$ cells designed for satellite application. Energy evolution measured every about 1000 cycles of 30% DOD cycling from 3.8 V. Diagnostic cycle made at C/3 to 2.7 V, from 4.0 V charge.

4.0   AGING DURING STORAGE

Aging on storage will determine the "calendar" life of the cell, mainly depending on the storage conditions, firstly the storage temperature. The cell aging as define previously is due to side chemical reactions involving the different phases in contact between each other.

Assuming that the different inert components (binders, separator, current collector, can, etc.) have been properly selected for their chemical and electrochemical stability with the active materials and electrolyte (which is trivial in any battery design), the main location of side reactions is the ***interface between active materials and electrolyte.*** The interface between the negative material and electrolyte is the most well known and studied. It is the site of a complex chemistry, which may obviously progress with time and temperature, and influence the cell properties.

4.1   The Negative Interface

The excellent shelf life acknowledged for primary lithium batteries is due to the layer resulting from *reduction of the electrolyte by lithium* building on the negative/electrolyte interface of a protective film still conductive to Li^+ ions. Its property is crucial for the battery characteristics: if the reaction products are not passivating enough (i.e. mainly insoluble, and adherent to the surface), the electrolyte molecules will continue to reach the lithium surface, and lead to quick lithium corrosion. On the other hand, if the passivation layer is too thick or too poorly conductive to Li^+, cell internal resistance may increase up to unacceptable value. This is why only a few organic compounds can be used as solvent for electrolyte. This reasoning, which applies to any lithium battery system, has been extensively studied for many years. The most commonly adopted picture is the **SEI**, (Solid Electrolyte Interface) a good ionic and poor electronic conductor, as proposed by E. Peled [10].

Due to the low surface area of the metallic lithium electrode, the amount of lithium lost during the layer formation is quite small. However, this is the reason for failure in trying to make a rechargeable cell with a lithium metal anode with long cycle life: each new metal particle being plated during charge reacts with the electrolyte to protect itself, at "its own expense" (typically about 1 to 2% each cycle).

In Li-ion technology, this layer is also formed at the carbon surface, whose voltage is close to lithium metal and lower than the reduction voltage of the organic solvents of the electrolyte. Due to the larger surface area, the amount of lithium loss is here significant (at the best about 10% of inserted capacity). However, the "miracle" of the Li-ion stability compared to rechargeable lithium metal is that ***this layer is formed essentially once***

during the first charge, and ***remains stable*** as the lithium ions move back and forth through it during cycling. This stability is particularly due to the fact that there is only a *very small molar volume change* of the carbon structure between charged and discharged state. This is a limiting factor for alternative negative Li-alloy electrodes in which volume variation during cycling is too high and destabilizes the layer, which has to be rebuilt at least partly at each cycle, thus consuming lithium. Obviously, long-term stability of this crucial layer should have a prime impact on the capacity retention on aging, therefore on calendar life. A lot of work has been done to attempt to analyze the layer composition; see for example reviews of Aurbach [11], and Yazami [12]. As a simplified view, it is commonly accepted that it is not a homogenous but rather a "multi-layer" organization. While the external part is more or less porous and contains organic compounds like insoluble lithium alkyl carbonates, polyethylene, polypropylene, and lithium carbonate, the "primary" layer, very close to the carbon, would be mainly composed of inorganic species, essentially lithium fluoride LiF (from reaction with $LiPF_6$) and Li_2CO_3. Recently, Peled [13] described different layer compositions on HOPG, thicker and containing $LiPF_6$ on cross section, thinner and containing Li_2CO_3, alkyl carbonates and alkoxides on basal planes. Total average thickness is very small (in the range of tens of nanometers). Depending on the chain length, the alkyl carbonates may be more or less soluble, and act as a "shuttle", responsible for reversible self-discharge, as will be described later in the paragraph discussing negative/positive interactions.

The condition of stability, i.e. stopping the electrolyte molecules´ reduction, *implies that the electrons cannot reach the interface accessible to the electrolyte,* through the "primary" layer. Therefore the layer should be electronically highly resistive, while Li ions must have a high mobility, as they must participate in the main cell reaction.

4.1.1   *Modeling Lithium Corrosion*

A residual electronic conductivity, from electron tunneling through the SEI [14] may therefore induce a continuous reaction at low rate, thus leading to lithium corrosion, and subsequent capacity loss. As this conductivity is expected to increase with temperature following an Arrhenius law, the capacity loss would follow the same profile.

It is reasonable to assume that the rate-determining step for this corrosion is the very low mobility of the electrons (conductivity) through this layer [15]:

$$dx/dt = (k \cdot c \cdot s)/e \tag{1}$$

where *x* is the number of moles of Li being reacted, χ is the specific electronic conductivity of the layer, s is the interface area, e is the layer thickness increase, proportional to the number of moles of Li consumed since t_0: $e = e_0 + A \cdot x$, and e_0 is the initial thickness at t = 0, after cell formation. Thus, the rate equation becomes:

$$dx/dt = B/(e_0 + A \cdot x)$$

where *B* equals **k • χ • s,** and A is a coefficient of proportionality between layer thickness and moles of reacted lithium.

From this equation, the corrosion rate is expected to decrease with time, as the thickness of the layer is increasing. Integration, with *x* = 0, at t = 0 leads to the equation:

$$(A/2) \cdot x^2 + e_0 \cdot x - B \cdot t = 0$$

From that comes the parabolic relation between time t and corrosion *x:*

$$t = A/(2 \cdot B) \cdot x^2 + (e_0/B) \cdot x$$

with *x* equal to the time elapsed after initial formation. Of all the constants, only χ is expected to vary (increase) significantly with temperature.

If we consider that the initial thickness $e_0 = 0$ for t = 0, this equation is similar to the equation proposed by Blomgren [16] to describe the capacity loss of lithium ion cells on cycling $Q = k' \cdot N^{0.5}$, where N the cycle number. This equation is derived from $Q = k \cdot t^{0.5}$, where Q is the capacity loss by lithium corrosion and assumed to be proportional to the time. By extension, the author proposed a similar behavior to be applied to the degradation on shelf life. The initial empirical assumption that the layer growth follows a general law $y^2 = kt$ can be explained by the electronic conductivity of the layer as proposed here. However, the cycling may have a secondary effect, as will be discussed later, because the capacity loss is generally more rapid than during a storage of the same duration.

Figure 5 shows a typical example of capacity degradation during extended storage, at different temperatures, representative of what generally occurs on Li-ion systems. This particular experiment was performed on $LiCoO_2$ / Graphite prototype cells, with a PC/EC/3DMC 1M $LiPF_6$ electrolyte.

The cells are maintained at a constant state of charge by applying a constant voltage (here 3.9 V), and capacity is measured every month at C/5. Within a short time, the capacity loss may be assumed to follow a linear degradation vs. time, i.e. constant loss rate. However, for prolonged testing, especially at high temperature, a clear slope decrease (slower degradation) is noticed.
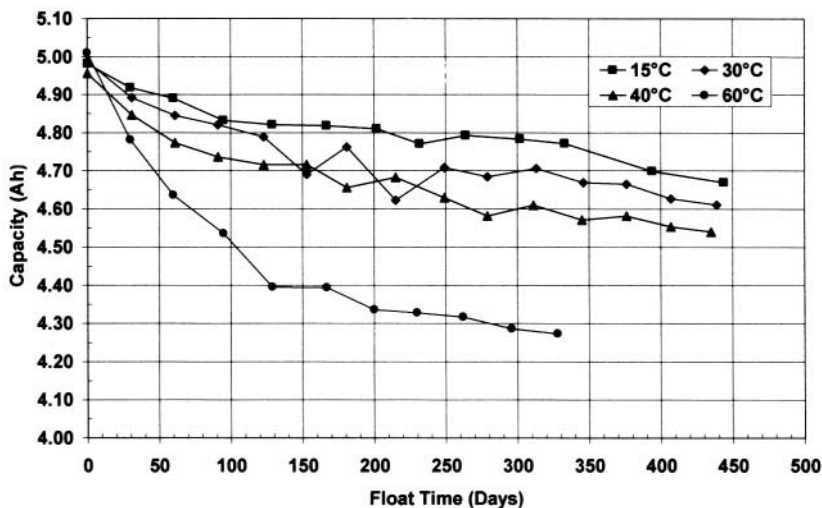
Figure 5. Total capacity degradation of $LiCoO_2$/graphite prototypes Li ion cells (C/5), measured monthly during storage under constant voltage of 3.9 V at different temperatures.

Interestingly, Figure 6 shows that the results do ***not*** depend on voltage applied during storage, between 3.8 and 4.0 V. This important result indicates that in this case, the capacity loss might not be attributed to the positive electrode. Indeed, the oxidation reaction that might occur and reduce the capacity would have been greatly influenced by the positive electrode voltage, as will be described further in other examples, whereas the graphite electrode voltage remains almost constant whatever the state of charge. This is a very useful property of the Li-ion systems in which the positive material potential is function of state of charge. Furthermore, the negative electrode limits the cell capacity since some lithium is lost during the cell first charge to build the SEI layer. Therefore, the capacity loss may be ascribed to the lithium corrosion, following the mechanism described above. Figure 7 compares the t = f(x) curves, with the parabolic model, using data obtained at different temperatures, irrespective of floating voltage, between 3.8 and 3.9 V. Despite the rather low precision on the measured capacity, a fairly good correlation is observed.

Another example is described in Figure 8, with high-energy prototype cells ("A" type, 44 Ah), using a $LiNi_{0.91}Co_{0.09}O_2$ positive material and the same graphite and electrolyte as for the smaller $LiCoO_2$ cells described above. The data fit over a two-year period is excellent because of the better relative accuracy of capacity measurement on this high-capacity cell. As can be seen, the extrapolation made with additional data after a 720-day period is very similar to the one made 300 days before, which validates the model quite well.
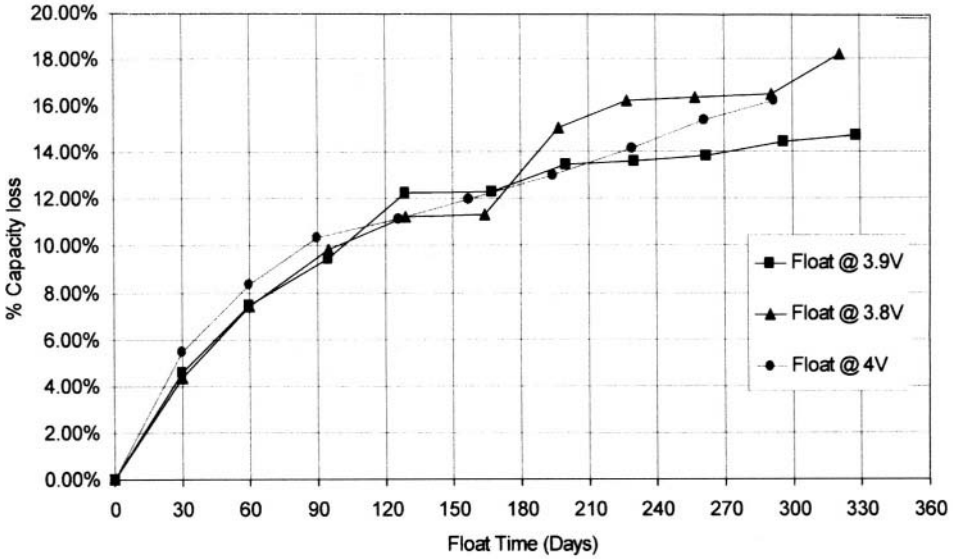
Figure 6. Capacity loss on $LiCoO_2$/graphite prototypes cells, measured at 30°C - C/3, during storage at 60°C at constant voltage from 3.8 to 4.0 V.
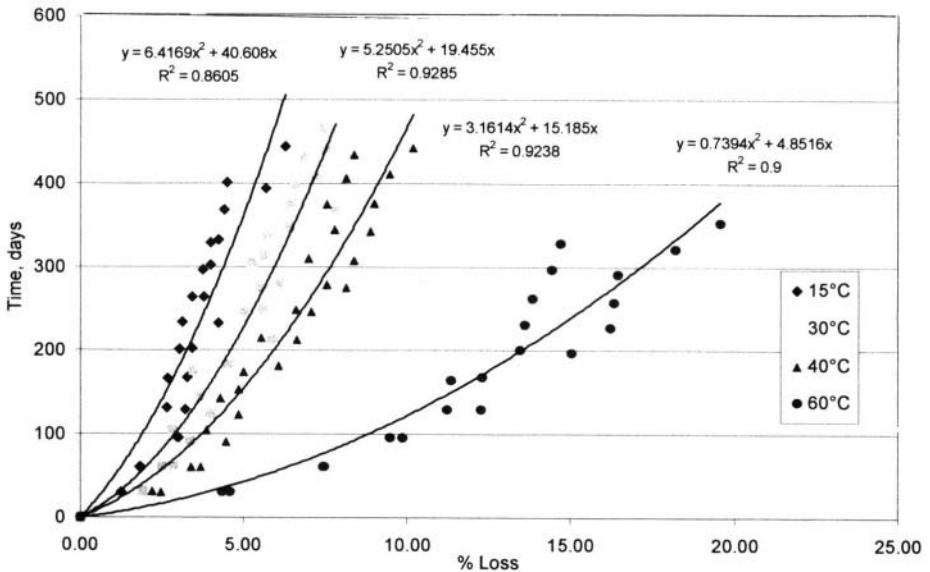
Figure 7. Storage duration as a function of lithium loss, for $LiCoO_2$/graphite prototypes cells on storage at 3.8 V or 3.9 V constant voltage, at several temperatures. Comparison with the parabolic model.
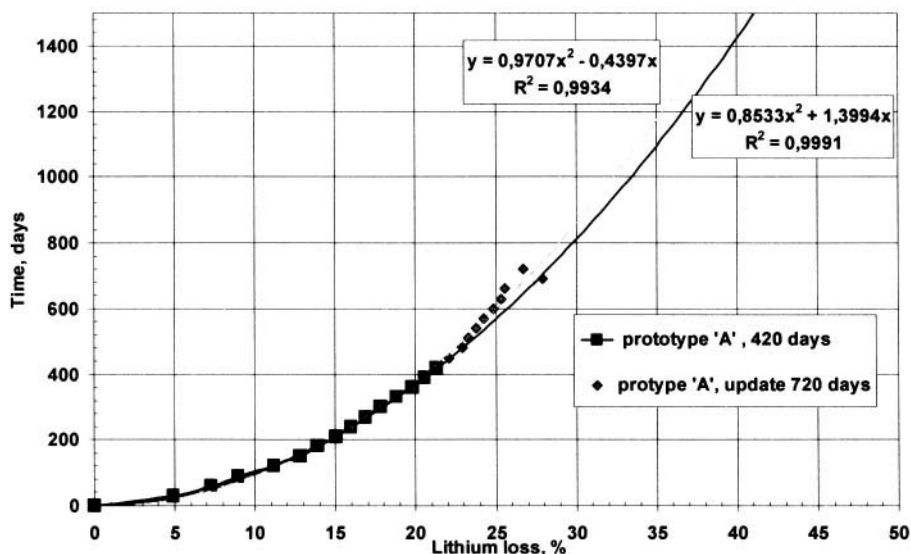
Figure 8. Duration of storage as a function of lithium loss, for $LiNi_{0.91}Co_{0.09}O_2$ /graphite 44 Ah prototypes cells on storage at 3.8 V constant voltage, at 60°C. Capacity is measured at C/10, 60°C. Comparison with the parabolic model.
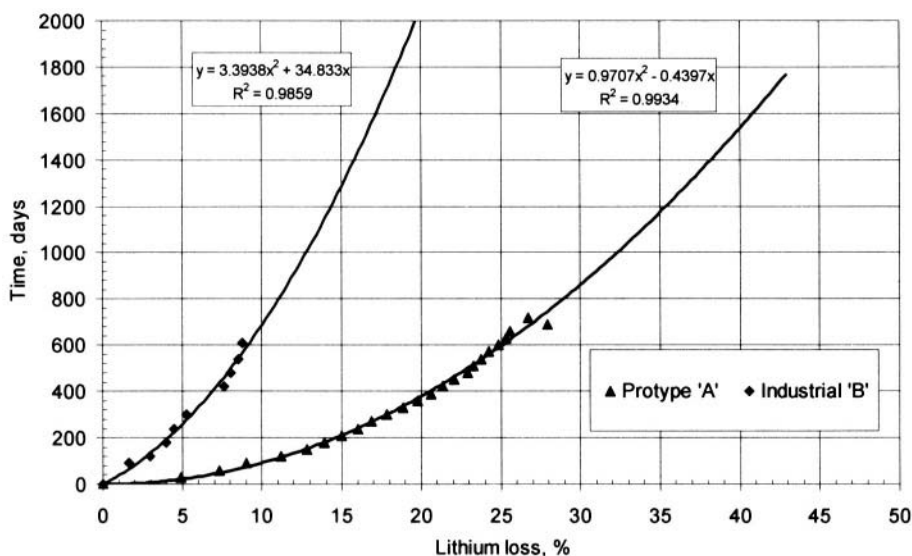
Figure 9. Duration of storage as a function of lithium loss, of high energy (about 40 Ah) prototypes or industrial cells on storage at 60°C. Capacity is measured at C/10, 60°C. Extrapolation is with the parabolic model.

It is interesting to note that the rate of capacity loss observed at 60°C is similar to that of the LiCoO₂ cell, using the same negative and electrolyte. A new cell design made on industrial pilot line was tested under similar conditions (60°C, 3.9 V) and exhibits a great improvement compared to the previous prototype design (stored at 3.8 V) as shown in Figure 9. This improvement may be attributed to the electrolyte modification by addition of few percent of vinylene carbonate (VC), which was discovered to exhibit minimal graphite exfoliation, thus improving cycling behavior [4,5,17,18]. These cells also include a new "doped" nickel oxide LiNi$_x$Co$_y$Al$_z$O$_2$, which may also have some beneficial influence, as will be discussed further.

The lithium loss after 600 days is reduced from 25% to less than 9%, and the extrapolation of the parabolic model predicts an outstanding stability of lithium capacity even at this high temperature, greatly contributing to the expected long cell life. In these experiments with Ni-based cathode materials, the residual capacity is measured at 60°C, a condition in which the cell capacity is limited by the negative electrode. It is actually well known that, unlike LiCoO₂, the nickel-based lithiated oxides exhibit a first cycle efficiency significantly smaller than 100%, typically about 80%. Approximately 0.1 to 0.15 Li/mole cannot be re-introduced during the first discharge, depending on the amount of Ni^{2+} in the crystalline phase [19]. Although part of this lithium is used in the SEI formation, some excess still remains in the carbon. As a result the cell is *positive limited* at the end of discharge, contrary to the other typical positive materials such as manganese or cobalt oxide. However, when the temperature increases to over about 40°C, the positive material is again able to insert all the lithium on discharge. In actuality, the temperature increase allows Li$^+$ to overcome the steric effect that prevents them from reaching the sites close to the Ni^{3+} present in the lithium layers. Therefore the cell exhibits a higher capacity, limited by the amount of lithium in the negative electrode. *To summarize, the positive electrode limits the cell at ambient temperature, while the negative one limits it at high temperature.*

This Li excess of about 15 % of nominal capacity remaining in the carbon at the end of a normal discharge condition shows interesting behavior in this Li-ion system concerning calendar or cycle life. This "free" lithium can be corroded with time or cycling before having any impact on practical cell capacity, thus extending the cell´s useful life.

Figure 10 illustrates the capacity recovered from diagnostic cycles performed periodically during storage at 30°C, at several constant voltages from 3.7 to 4 V. Capacity is checked at C/3 rate at 25°C, then at C/10 at 60°C. The difference in the capacity recovered between 25 and 60°C is not mainly due to a kinetic effect, but to the phenomenon described above.
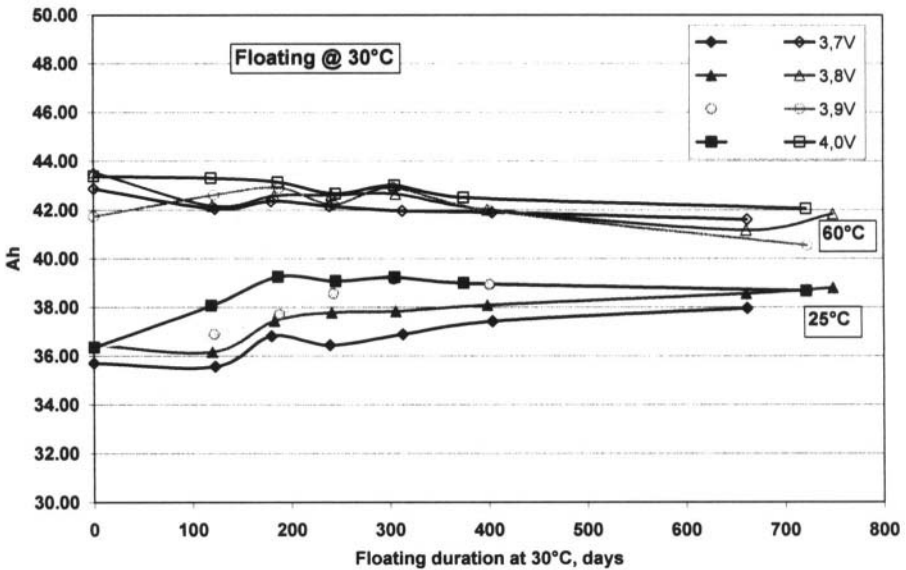
Figure 10. The C/3 capacity degradation during storage of High-Energy cells using LiNi$_x$Co$_y$Al$_z$O$_2$ as positive material. Storage at 30°C, at various float voltages from 3.7 to 4.0 V. Measurements are made at 60°C (C/10) or 25°C (C/3).

It can be concluded from these data that the floating voltage has no effect on capacity under these conditions, and the small loss experienced (average of 3% after about 2 years) can be ascribed to the lithium corrosion through the SEI.

Amazingly, an increase in the capacity recovered at 25°C is noticed during the first period of storage. It is observed during the few first measurements, the discharge made at 60°C permanently improves the positive material capacity. This phenomenon is related to the material crystalline structure as described above, and results from slight modification during discharge at 60°C, permanently releasing some of the sites which where blocked by nickel ions in the lithium layers.

4.1.2 Temperature Effect

The usual way of analyzing the temperature influence is to assume that the side reactions rates follow an Arrhenius law, i.e. increase exponentially with temperature, through a coefficient linked to an "activation energy," E: $k = k_0 \cdot e^{-E/RT}$, or $\log(k) = \ln(k_0) - E/RT$. The difficulty comes from the fact that a global phenomenon (for example, capacity loss, or impedance increase) may result from several reactions, each with their own activation energy and rate constant. Furthermore, the rate of the phenomena observed are often assumed to be constant with time, which can lead to hazardous

extrapolations. The best way, when it is possible, is to determine the rate limiting reaction and, once the equation of variation with time is established, introduce the temperature variation in the identified depending coefficients.

In this particular case of negative interface side reaction, the rate determining step is attributed to the electronic conductivity through electron tunneling, which is analogous to semi-conductivity, known to vary with temperature following the Arrhenius law.

The temperature dependence of the coefficients of the quadratic Equation 2: $t = A/(2 \cdot B) \cdot x^2 + e_0/B \cdot x$ was analyzed from the experiments described in Figure 7. Figure 11 describes the results obtained.
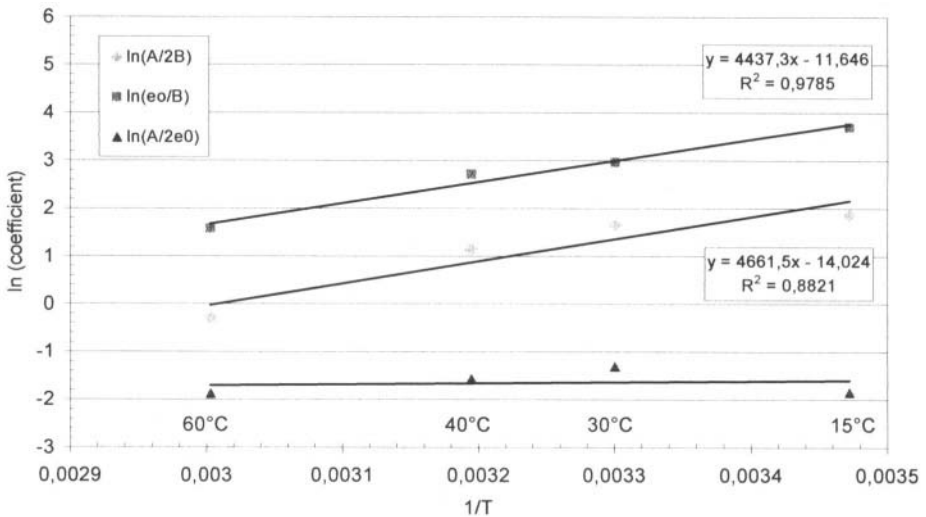
Figure 11. Variation of the logarithm of the coefficients of the parabolic model with temperature, for LiCoO$_2$/graphite prototype cells (from Figure 5).

It can be seen that, over a wide ambient temperature range, the values fit reasonably well linear functions of $\ln[A/(2.B)]$ and $\ln[e_0/B] = f(1/T)$. In addition, the coefficient A, which does not include the electronic conductivity, does not depend on temperature as shown by the ratio $\ln[(A/2)/(e_0/B)] = \ln[A/2e_0]$. That supports the assumption that electronic conductance of the layer is the rate-determining factor.

The activation energy can be deduced from the slopes of the lines, and introduced in Equation 2 to replace the coefficient by their relation to temperature. A general equation can be deduced to calculate the curves at different temperatures and thus calculate the time to a given lithium corrosion at any time and temperature.

$$t = e^{(4661/T - 14)} \cdot x^2 + e^{(4437/T - 11.6)} \cdot x$$

where **t** is expressed in days, and **T** in °K.

Figure 12 gives a representation of the simulation at several temperatures between 10 and 60°C, extrapolating the curves to where large amounts of lithium have corroded.
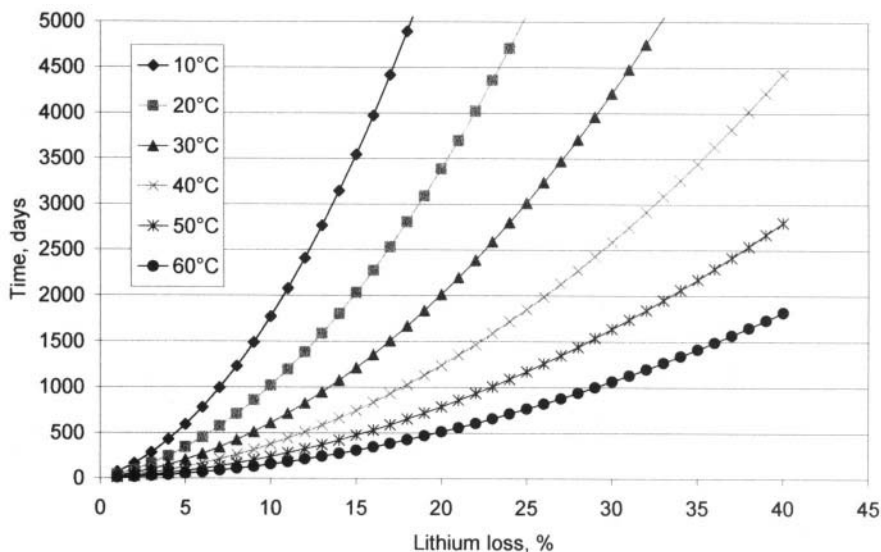
Figure 12. Simulation of Li corrosion (time vs. % Li corroded), as a function of time and temperature, obtained from data on LiCoO$_2$/graphite prototype cells.

The lithium reserve in the nickel-based system as described earlier, allows the time to reach a given nominal capacity loss due to lithium corrosion to be extended. For example, from Figure 12, calculated time to reach 80% of nominal capacity after continuous storage at 40°C would increase from 1200 days (20% loss in **LiCoO$_2$** cells) to 3500 days (35% with Ni-based system), with this cell design.

Comments about this model:

- First, although the model equation is valid for any Li-ion chemistry using a graphite negative electrode, the calculated coefficients and their temperature dependence (activation energy) are applicable to a *specific design and chemistry,* and obtained from storage experimental data. Any other chemistry or design necessitates new storage experiments to deduce the specific rate coefficients (which is also true for any empirical extrapolation method) to determine the calendar life. Figure 9 clearly illustrates that point.

- Second, the passivating layer is assumed to grow homogeneously, independently of temperature except the rate. In some cases, the layer morphology and/or composition may vary with the temperature, modifying accordingly the conductivity and corrosion rate. An important parameter might be the reaction of impurities at the surface, coming from the electrolyte or the positive electrode, also depending on temperature as will be discussed later.

- Finally, this method addresses a specific facet of cell aging, which is the capacity loss under low to moderate rate. It does not take in account a modification in cell power characteristics, which could limit the practical use at high rate. This model is based on the negative interface reaction, and must be combined with possible other identified parameters, which may for example implicate the positive electrode interface.
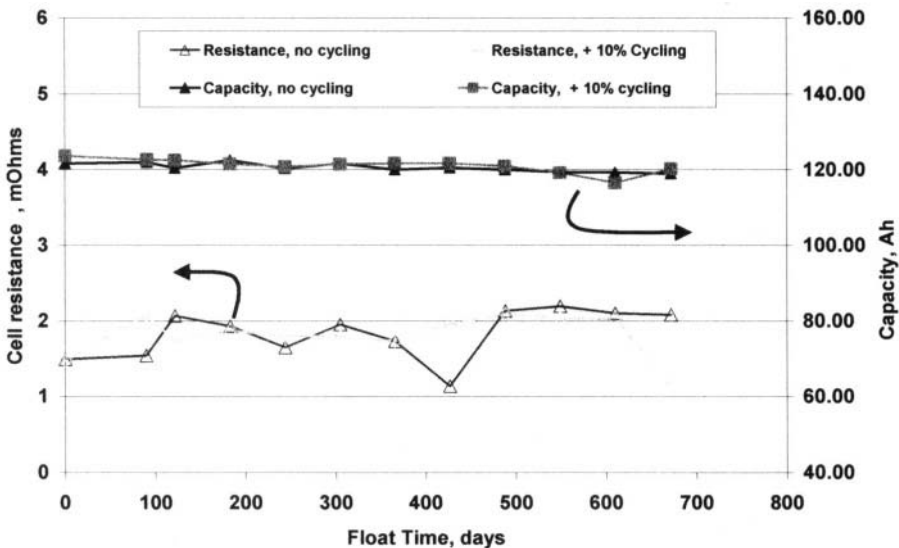
Figure 13. Comparison between pure constant voltage floating and additional 10% DOD daily cycling. Three High-Energy LiNi$_x$Co$_y$Al$_z$O$_2$ cells in parallel. Storage temperature: 40°C, charge/discharge C/5, Resistance measured after a 5 min pulse at 40°C 100% SOC, residual capacity measured at C/8, 40°C.

4.2   Influence of Cycling During Storage

In order to verify whether cycling may significantly modify these conclusions, a special storage condition was applied, consisting of a daily 10 percent DOD cycling in addition to a constant 3.9 V floating voltage.

Figure 13 describes the comparative data between pure floating and floating + 10 percent DOD cycling, during storage at 40°C, 3.9 V. As can be seen, no detrimental effect of the cycling is observed, either on capacity

or resistance. This expected result proves that the SEI is not affected by such cycling, in the same way that no important capacity loss was observed during extended cycling at high DOD, as shown in Figure 2. Furthermore, the resistance measured in the floating condition, i.e. 40°C, does not change significantly.

4.3   *Negative/Positive Interactions*

The direct interaction between the two electrode materials through the electrolyte is known in Li-ion systems, although few studied have been published yet. The *reversible* self-discharge implies that some chemical species, most probably lithium alkyl carbonates, are exchanged between the two interfaces, acting as shuttles to oxidize the lithium from the negative on one side, and reduce the positive electrode on the other side, re-inserting the same amount of lithium. These reactions occur through the interfaces, and, on the negative, should be governed by the same mechanism as described above for the irreversible loss. It is generally seen that the rate of reversible loss decreases with cell aging, which is consistent with a reduction of electronic conductance as described before. In the experiments described above, the reversible self-discharge is not observed, as the cell voltage is maintained.

Strong interaction between positive and negative materials leading to *irreversible* loss has been observed in Li-ion cells using a $LiMn_2O_4$ positive, and many authors have recognized the detrimental effect of the use of this positive material on the negative electrode stability [20, 21]. Indeed, the observed capacity loss during storage or extended cycling is much more pronounced when lithiated carbon is used as negative electrode instead of metallic lithium (whose amount is always in large excess). This clearly demonstrates capacity limitation by the negative electrode, influenced by the positive. From negative electrode analysis Wang et al. [22] found significant growth of the SEI associated with corresponding increase of inactive lithium. In addition to this "thermodynamic" lithium loss, the electrode kinetics is reduced by the layer growth, reducing the discharge ability. They concluded that HF produced by solvent oxidation on $LiMn_2O_4$ is the main responsible for the reversible capacity degradation of graphite electrode, rather than Mn dissolution. Actually, surface treatment of the spinel with Li_2CO_3 to trap the protons improved significantly the cell stability.

Tsunekawa [23] and Tanimoto [24] recently demonstrated that capacity fading of a carbon electrode was strongly enhanced by Mn^{2+} concentration in electrolyte, resulting from manganese spinel dissolution or intentional addition to the solution. Differences in interpretation may come from variation in experimental conditions, as Wang essentially studied the spinel at the

charged state, where little Mn dissolution occurs. The cell stability is lower at about 80% DOD, as described by several authors [25,26]. It is well established that soluble Mn^{2+} ions are produced from dismutation of Mn^{3+} and can therefore undergo reduction on the negative electrode. The reduction of Mn^{2+} on negative interface may proceed down to metallic state, and greatly enhance the electronic conductivity of the layer, subsequently increasing Li corrosion. A similar observation has long been known for the $Li/SOCl_2$ primary system, whose stability relies on the LiCl formation on the lithium surface. A very low level of iron ion impurities in the electrolyte is known to induce significant growth of the layer, with associated increase in self-discharge.

As an example, the Figures 14a and 14b show a comparison of capacity loss observed during storage at high temperature of high-energy cells using manganese spinel or "doped" nickel oxide. The cells have exactly the same size and design, graphite electrode and electrolyte (1M $LiPF_6$ in PC/EC/DMC). They contain $LiMn_2O_4$ (a) or $LiNi_xCo_yAl_zO_2$ (b) materials, both commercially available from industrial manufacturing suppliers. While the capacity of manganese cell drops dramatically, the nickel based cell remains very stable. Associated with the capacity loss, the cell resistance calculated from 30s pulses at the 2C rate increases. It should be noted that the resistance growth is much more pronounced at greater depths of discharge, which indicates that the active interface, probably of the positive electrode, has been considerably reduced, which results in much higher true current density at the interface. The storage was performed at 100% SOC, which might not be the worst case for the spinel cell.

Surface treatment and coating of the positive material can reduce the corrosion rate and improve the cell shelf life and cyclability [22].

4.4   *Aging Reactions Leading to Power Loss*

As a general rule in batteries, power loss resulting from impedance increase is observed during cell aging. There are many reasons why time and temperature could result in internal resistance increase. Electrolyte consumption in aqueous systems (drying effect), separator physical property modifications, binder degradation, electrodes interface passivation, etc.

In Li-ion systems, electrolyte is not involved in the electrochemical reactions and there is no drying effect reported, unless a non-suitable solvent is used which electro-activity domain is not compatible with the active materials potential. The separators, made from microporous polyethylene or polypropylene are remarkably stable in the organic electrolytes, with a very long experience in primary systems. Here again, the side reactions affecting the power capability of the cell should be considered at the *material interface with the electrolyte.*
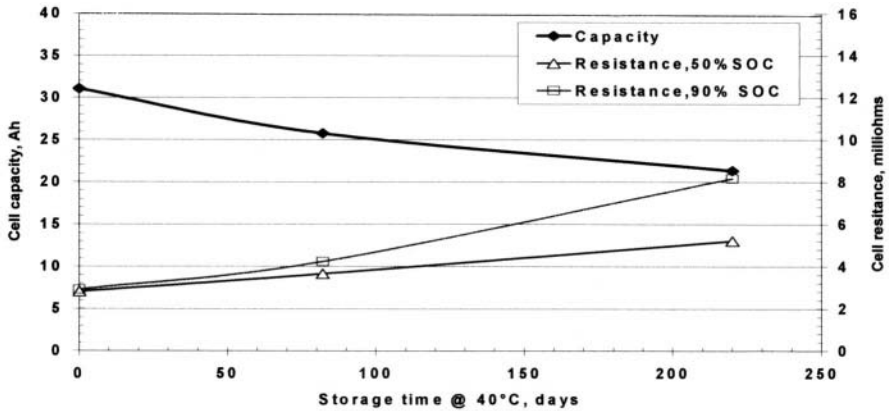
Figure14a. Capacity and resistance changes during storage of a LiMn2O₄ cell at 40°C - 100% SOC, measured at C/3, 20°C
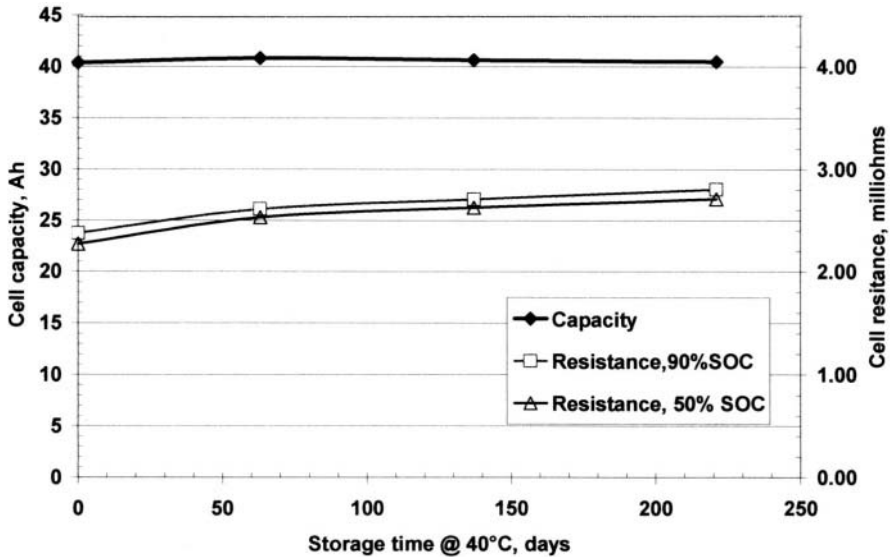
Figure14b. Capacity and resistance changes during storage of a LiNi$_x$Co$_y$Al$_z$O₂ cell at 40°C - 100%SOC, measured at C/3, 20°C

In order to separate the participation of each electrode in the resistance increase, it is customary to introduce a reference electrode inside the cell. What is easy in a laboratory cell becomes much more complicated in an industrial cell, especially without disturbing the properties to be measured. The experimental difficulty is of course amplified when a **long-term storage** at high temperature has to be performed. However, thanks to the electrochemical system properties as discussed earlier, we can interpolate the respective influence of positive and negative side, by testing the cells at different state of charge.

Figure 15 shows the resistance increase in "HE" cells, using the $LiNi_xCo_yAl_zO_2$ previously described, during storage at 30°C, for which capacity retention is described in Figure 10. Several voltage values are applied from 3.8 to 4.0 V. The data represent the resistance of two cells (a, b) stored under the same conditions. The resistance is calculated from cell polarization after 5 minutes, during 25 A pulse at 25°C. An impedance increase is observed under these conditions, which does not vary significantly with the applied voltage. As for the capacity loss, the negative electrode might therefore be designated as responsible for such resistance change.

A second set of experiments was performed, in which the cells are stored at rest, instead of at constant applied voltage. Figure 16 displays the average values of resistance whatever the floating or OCV voltage from 3.7 to 4 V. Each point is the average value for 6 cells. As it can be seen, the behavior is exactly the same, either on float or OCV. In fact, the voltage decreases slightly during the storage periods on OCV due to the reversible self-discharge, but this had no significant effect on the resistance change.

The first observation is a regular increase during about the first year period, followed by stabilization. Interestingly, it was observed that the change in cell polarization is about the same measured either after 1 second or 5 minutes, from which it can be concluded that the polarization increase is **not** due to a diffusion problem.

In an attempt to fit the data with simple equations, the best result is a variation of r or r^2 proportional to the square root of time, as shown of Figure 16 for the global resistance at 5 minutes, including all the data.

If we assume that the increase in negative electrode impedance *dr* is due to the SEI growth and *de* impairs the movement of ionic species, we can expect as a first approach an evolution similar to the layer thickness, expressed as: $dr = K \cdot de$.

The layer thickness *e* is proportional to the lithium consumed by corrosion *x* and is a function of time from Equation 1 as seen previously: $de/dt = A \cdot dx/dt = A \cdot B/e$, i.e. $e \cdot de = A \cdot B \cdot dt$ and $e = 2AB(t+e_0)^{1/2}$.

Cell resistance would therefore follow a general equation $R = Kt^{1/2} + R_0$, which is consistent with one of the model equations. However, while the assumption (Equation 1) that the *electronic* resistance is proportional to the thickness of the "primary" very thin layer in direct contact with the carbon surface, may be considered reasonable, the straight proportionality between the total layer "thickness" increase and overall electrode *ionic* resistance increase is more speculative.

Indeed the total ionic resistance can be expressed as $R = R_{SEI} + R_{liq}$, where R_{SEI} is the ionic resistance of the thin SEI solid phase, and R_{liq} the resistance of the liquid electrolyte filling the pores of the porous "thick" layer. The thickness of the true SEI is in the range of nanometers, while the total thickness is in the range of a tenth of a micron.
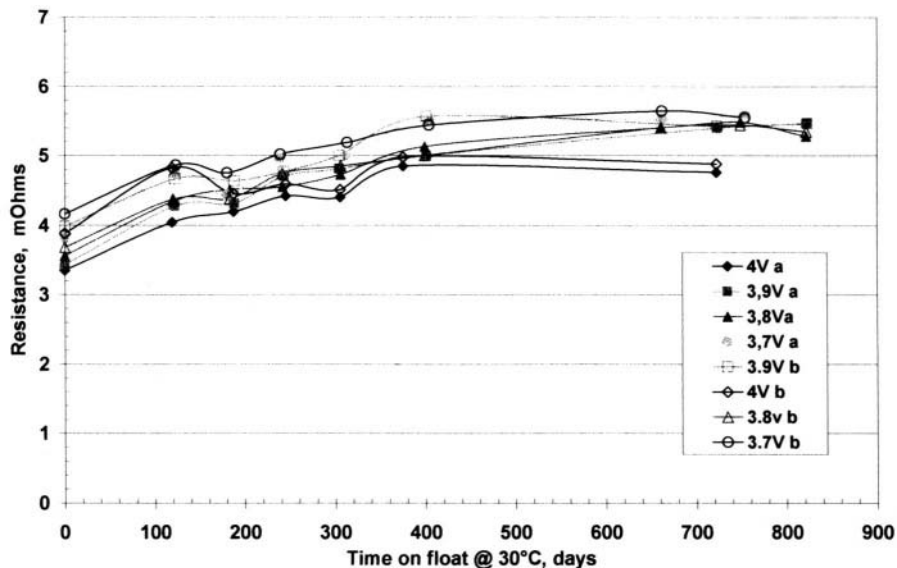
Figure 15. HE "44Ah" cells, "Industrial" type using LiNi$_x$Co$_y$Al$_z$O$_2$ as positive material. Resistance calculated from cell polarization after 5mn, from 25 A pulse at 25°C, after floating at 30°C.
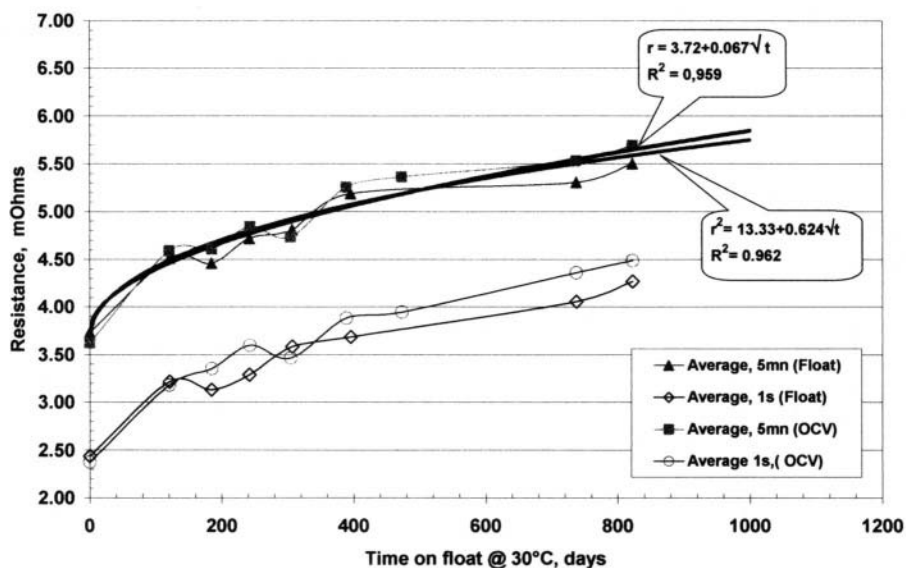
Figure 16. HE "44Ah" cells, "Industrial" type using LiNi$_x$Co$_y$Al$_z$O$_2$ as positive material. Average resistance calculated from cell polarization after 5mn or 1s, from 25 A pulse at 25°C, after storage on OCV or floating at 3.7, 3.8, 3.9, and 4.0 Volts at 30°C.

A simple calculation can be made to assess the order of magnitude of the "thick" layer:

The amount of products initially composing the layer is proportional to the irreversible lithium loss during the first charge. The volume of the materials formed can be deduced from the assumed very simplified theoretical equation: $2nLi + nEC \rightarrow nLi_2CO_3 + (C_2H_2)_n$, which are the main ultimate end products (reduction of other carbonates and VC or LiF formation which actually occurs would not dramatically change the result). Furthermore, the amount of organic gas produced during formation is actually very small compared to the reaction stoichiometry. Although in reality insoluble lithium alkyl carbonates are formed, the proposed simple equation leads therefore to the densest form of the compounds produced, i.e. 2.1 for Li_2CO_3 and 0.9 for the polymer, resulting in a volume of $1.25 cm^3/$ lost Ah.

Assuming 90% charge efficiency, 1 g of graphite will be covered by the equivalent layer volume of about $0.035 Ah = 0.043 cm^3$. From BET measurements, the actual specific surface area of graphite of different types accessible to electrolyte is in the order of 5 to $10 m^2/g$, and the capacity loss due to passivation is actually proportional to this surface area [27]. However, when *processed in electrode* the BET surface falls down to about only $1 m^2/g$. This variation is assumed to be due to the effect of binder addition and calendering. Consequently, the resulting calculated layer (non-porous) average thickness is 43nm. This simple and approximate calculation gives a result, which is quite consistent which has been measured on model electrodes such as HOPG by different techniques [6, 28, 29].

The ionic resistance of the negative passivation layer accounts for only a small part of the total cell resistance. Therefore, increasing the layer thickness/volume by about 33%, which corresponds to 3% more capacity loss as seen in Figure 10, should not be the only reason for the total increase observed, and a direct relation between layer thickness and resistance may not be a valid assumption. The answer should be found in the macroscopic effect of passivation in the negative electrode bulk.

The initial electrode "theoretical" porosity, which is usually in the range of 30 to 40% after electrode manufacturing (calculated value), is significantly reduced by the layer formation, since the *volume of the additional solid phase created is about 10% of the carbon one*. The theoretical porosity after formation (which is only partly accessible to the electrolyte) is then reduced to less than 25 to 35%. This number is probably much lower, as the actual useful initial porosity might be significantly smaller.

Obviously the pores having the smallest diameter, in the range of tenth of microns, will be the most affected, thus impairing the accessibility of the electrolyte to a significant part of the active surface area. During subsequent layer growth on aging, the same phenomenon will continue.

As a conclusion, the impedance increase is more likely due to a *reduction of the active surface area, thus increasing the true current density* during discharge, rather than to a pure ionic conductance drop. This is consistent with the resistance increase is observed from a one-second pulse, which includes the transfer resistance, and is directly proportional to the active surface area. In addition, if the discharge temperature is higher, the observed resistance growth becomes negligible because the polarization decreases, as seen previously in Figure 13 for storage and measurements at 40°C. Stabilization of the resistance observed with time should therefore result from two factors: decreasing of corrosion rate, and initial clogging of the smallest pores, accounting for a significant part of the active surface area. As a consequence, the resistance may stabilize more than expected from the square-root equation.

A larger gradient of electrolyte concentration due to diffusion through the electrode thickness, which would have resulted in much higher voltage drop after five minute pulse, does not seem to occur, because the largest "macroscopic" pores are not affected.

The preliminary conclusions that can be drawn from the above are:

- The effect of impedance increase in these conditions of voltage and temperature is most probably due to the continuation of negative passivation layer building up.
- As observed, and supported by SEI growth theory, the rate of this effect is expected to decrease with time.
- The exact relationship between cell impedance and layer growth is not simple, and would probably depend on the macroscopic properties of electrodes, including pore size distribution.
- The equation model for impedance variation with time and temperature is difficult to establish *à priori,* and presently the best way is to have sufficient long-term data to allow valid empirical extrapolations.

4.5   *The Positive Interface*

4.5.1   *A SEI on the Positive Electrode?*

Often cited to describe any interface reaction, the presence of a "SEI" on the positive interface is still speculative. As described in the preceding paragraph, the Solid Electrolyte Interface concept was proposed to explain the electrochemical behavior (i.e. lithium ion transport) of very reactive but metastable interfaces, such as those formed on lithium metal in the liquid cathode battery systems. Clearly demonstrated on negative interface because all organic solvents are readily reduced at the electrode potential, the presence of a SEI on the positive material is less required because of the

apparent electrochemical stability of the electrolyte towards oxidation. However, the anodic behavior of the organic solvent for electrolytes has been much less investigated than cathodic reactions. The onset potentials depend on the salt, electrode materials and impurities [30]. While the negative SEI can be quantitatively characterized by the very significant amount lithium lost for its formation on the large surface area of the carbon electrode, (negative first charge efficiency, which is now at the best about 90%), nothing similar was observed and reported on positive materials.

From FITR spectra of electrodes during cycling, D. Aurbach et al. [31] identified lithium alkyl carbonates species on $LiNiO_2$, $LiCoO_2$ or $LiMn_2O_4$ similar to those produced on the negative side. Surface film formation can be also observed when metallic electrodes are polarized to high potentials. A possible source of these compounds is the oxidation of the soluble species formed on the anode, responsible for the reversible self-discharge as discussed above. These "soluble" species most likely have a very low solubility and reach saturation in the electrolyte. They are oxidized on the positive interface and diffuse back to the negative, possibly leaving some polymerized residues on the positive interface.

From another detailed spectroscopic study of $LiNiO_2$ or $LiMn_2O_4$ surface in different EC-DMC electrolyte solutions [32], the authors concluded that surface reactions take place on cycling, depending on many factors. The initial active mass particles are usually covered by pristine surface films containing Li_2CO_3 as a major component, which remains essentially stable for a short time in the carbonate solvents. However, when the salt is present in electrolytes ($LiPF_6$, $LiAsF_6$, or $LiCF_3SO_3$) this film is destroyed and replaced upon cycling by a variety of solution-related compounds including ROLi, $ROCO_2Li$, polycarbonates and salt reaction products. Acidic contaminants can catalyze polymerization of the alkyl carbonate solvents to surface polycarbonate species. It has been suggested that the nucleophilic properties of the metal oxides induce surface reactions with alkyl carbonates, which are strong electrophiles. $LiNiO_2$ was found to be more reactive than $LiMn_2O_4$, and higher impedance growth is observed. In $LiPF_6$ solution, contamination with HF plays a very important role, and the impedance strongly increases due to precipitation of LiF at the surface. The large excess of electrolyte volume in the former can explain large differences in impedance magnitude between laboratory cells and actual batteries. A recent study by Ostrovskii et al. [33] demonstrated also a spontaneous reaction between $LiNi_xCo_yO_2$ and $LiMn_2O_4$ uncharged electrodes and carbonates electrolytes, forming new species at the interface.

During aging at high applied-voltage electrolyte components oxidation may induce insulating solid deposits, which may reduce the active surface by impairing Li-ion transport to the insertion material, or by insulating active

particles from the electronically conductive network in the composite electrode matrix. It is expected that this will be enhanced by temperature.

As a consequence, this phenomenon should differ significantly with the nature of the positive and electrolyte materials, and possibly by the nature of the impurities.

4.5.2   Aging Due to the Positive Side Reactions

Working on prismatic **LiCoO₂/graphite** cell, Sasaki et al. [34] suggested that the main cause of deterioration on aging be related to an increase of reaction impedance at the electrode interface, rather than an increase of ohmic resistance. Improvements were obtained through active materials and electrolyte non-disclosed modification.

Data have recently been published by Bloom et al. [35], describing the cell impedance evolution on storage of a small 0.9 Ah (18650 shaped) Li-ion cell designed for high rate. The cell includes a graphite mix negative electrode and $LiNi_{0.8}Co_{0.2}O_2$ positive, in EC/DEC 1M $LiPF_6$ electrolyte. State-of-charge (40 to 80%) and temperature (40 to 70°C) were the parameters explored. In spite that a limited amount of data was collected (about 3 months at the time the paper was published) the impedance increases as expected with temperature but also with increasing state-of-charge. This indicates positive electrode participation in the total cell degradation, which was suggested earlier on the same type of cells by Jungst et al. [36] demonstrating also that the cell impedance at high frequency was not affected.

Based on similar aging experiments on the same type of cells K. Amine et al. [37] ascribed the major power-aging effect to the positive electrode. In this work a more detailed analysis was made from building laboratory cells using micro reference electrode and electrodes from dismantled aged cells. Figure 17 reproduces the results from aging two weeks at 70°C. In this very high temperature condition, the major increase of area specific impedance is due to the positive electrode.

A similar observation has been made in an earlier SAFT design of 18650 cell prototypes using $LiNiO_2$ material [38], as described in Figure 18. Extended charge float was performed at the elevated temperature of 60°C, at different voltages from 3.6 to 4 V, representing states of charge of roughly 40 to 100%.

As can be seen, the cell resistance change during up to 300 days greatly depends on floating voltage, indicating a reaction governed by the positive. The total polarization resistance (5-min pulse) increases dramatically, while the "immediate" voltage drop (10 ms) shows much less variation. This is consistent with a charge transfer resistance increase. After nine months of storage some cells were dismantled, and the electrodes were used to build coin cells with a

lithium counter electrode. Figures 19 and 20 shows the comparative results obtained from cycling such test cells, made with negative and positive electrodes respectively, from cells aged at 60°C/4 V, and 20°C/3.6 V. While the negative carbon electrode remains perfectly stable (Figure 19), the positive electrode from the cell aged under the most severe conditions exhibits a drastic degradation (Figure 20). This effect was also greatly enhanced by increased temperature. It should also be noted that upon dismantling, the composite positive electrode is more stressed than the negative one.

Although the electrode performance was strongly affected, the crystalline structure of the positive material analyzed by X-rays did not show any noticeable modification. An interfacial reaction between electrolyte and positive material is therefore suggested.

The power degradation mechanism of cells using $LiNi_{0.8}Co_{0.2}O_2$ cathodes was also attributed to interfacial processes by Kostecki and McLarnon [39] from recent studies using appropriate microscopic techniques. High temperature storage produces a reduction of surface roughness with temperature measured by AFM, associated with a reduction of electronic conductivity of the surface. This strongly suggests non-conductive surface deposits. Changes in crystal structure and composition of the interface were detected by Raman spectroscopy for selected material particles. Little or no change in bulk electrode structure was detected.

Modification of the positive material, by replacing some Ni with Co and Al ions in $LiNi_xCo_yAl_zO_2$ (x >0.75) dramatically improves its behavior. Improvement of the positive electrode material stability by substitution with aluminum was confirmed by Chen et al. [40]. Area-specific impedance of cells was greatly reduced during one month storage at 50°C, 80% SOC.

Figure 21 shows the resistance (30 s pulse) change for a High-Energy cell using the $LiNi_xCo_yAl_zO_2$ material during a 600-day storage at 40°C, 100% SOC (i.e. 4.0 V). As described earlier, the impedance increases during the first 6 to 9 months, then reach a steady state plateau. In the same time, the capacity loss of the negative electrode is negligible, which results in a very stable specific energy achieved at C/3 rate.

Recent electrolyte and negative electrode optimizations have led to even better stability, as shown in Figure 22, which describes the peak power capability of a High Power cell using the same positive material for HEV application, during the first six months of storage at elevated temperature at 50% SOC. Only small degradation is observed at 60°C, while the 40°C and 25°C exhibits very stable power capability.

More time is therefore needed to enable a calendar life prediction. Large experimental plans have been recently launched in several laboratories on cell prototypes using a similar material in order to develop accurate models [41,42].
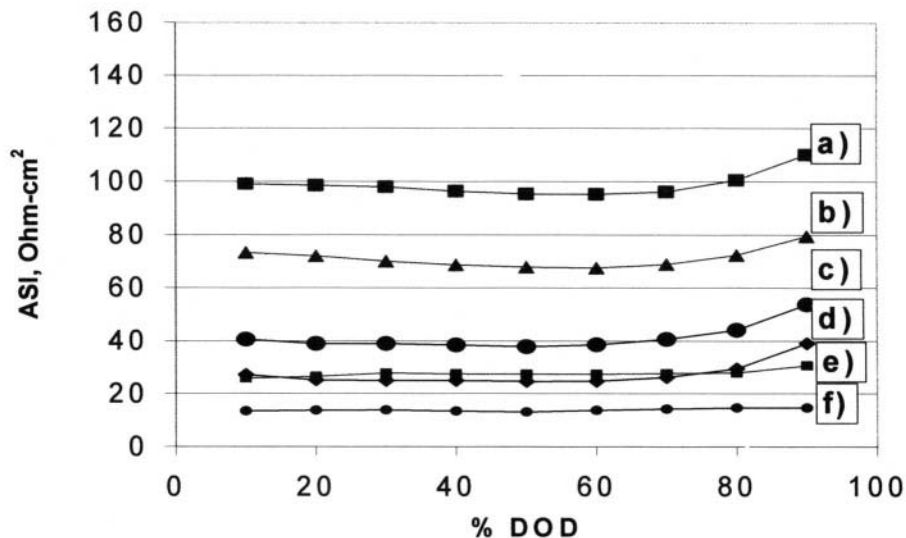
Figure 17. Area specific impedance of: a) aged cell, b) aged positive electrode, c) fresh cell, d) fresh positive electrode, e) aged negative electrode and f) fresh negative electrode. Derived from reference 21. Aged 2 weeks at 70°C.
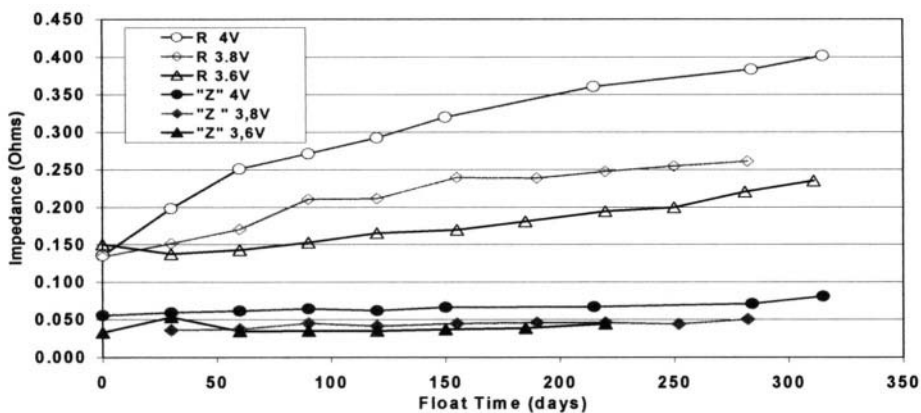
Figure 18. Resistance change (C/5, 15°C) of 18650 prototypes during floating at different voltages, @ 60°C. R is calculated from total relaxation after 5 minute pulse, Z is calculated from 10 ms pulse.
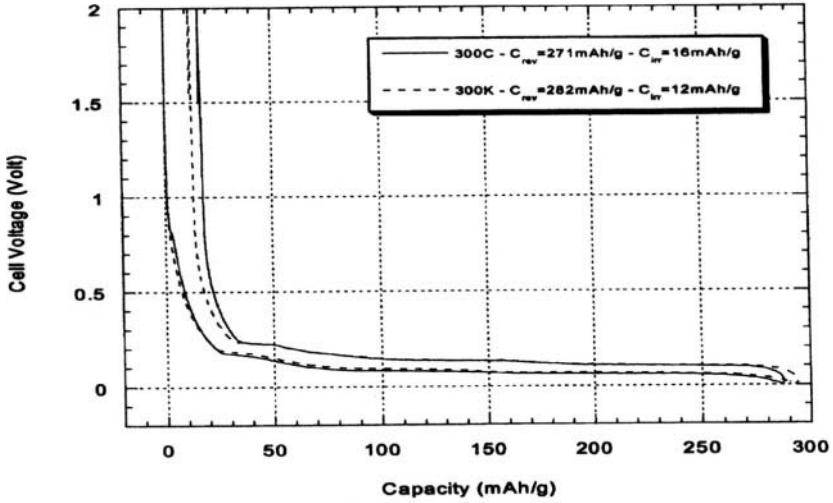
Figure 19. Cycling (C/5) of coin cells made with negative electrode from cells aged at:
- - - - -: 20°C/3.6 V;   —: 60°C, 4 V.
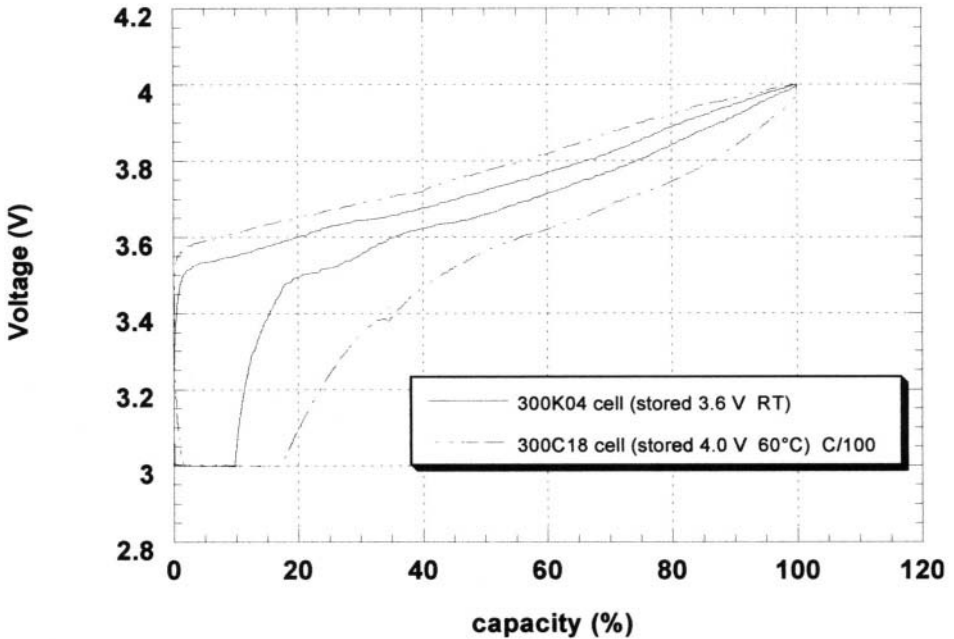
Figure 20. Cycling (C/100) of coin cells made with positive electrode from cells aged at:
— 20°C/3.6 V;   - - -: 60°C, 4 V.

From the present data, it can be concluded that positive electrode aging may have a significant influence on cell power degradation, at high state-of-charge (contrary to the negative mechanism), and depending greatly on temperature. Positive electrode aging due to reaction with electrolyte at the interface can largely be reduced by modification of the material composition, material and electrolyte purity, etc. Excellent power stability can be anticipated from new cell designs using materials such as doped nickel oxide.

4.5.3 Electrolyte Oxidation

Electrochemical oxidation of alkyl carbonates during overcharge is known to produce gas that is used to activate current breakers. At the same time, acidity increases as measured for example by E. Wang et al. [22] for EC/DMC electrolyte on $LiMn_2O_4$, $LiCoO_2$ or carbon electrodes placed at 60°C and polarized at 4.3 V or higher. DMC was found to produce a larger acidity, indicating a higher sensitivity to oxidation than EC.

Tentative initial reactions can be written as:

$$nCH_3OC(O)OCH_3 + nLi^+ + Li_xM_yO_2 \longrightarrow$$

$$nCH_3OC(O)OCH_2 + nH^+ + Li_{x+n}M_yO_2$$

or

$$n\overline{CH_2OC(O)OCH_2} + nLi^+ + Li_xM_yO_2 \longrightarrow$$

$$nCH_3OC(O)O\overline{CH_2} + nH^+ + Li_{x+n}M_yO_2$$
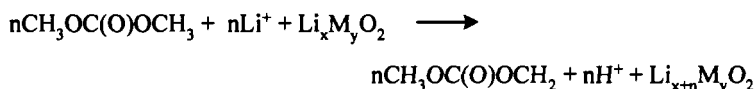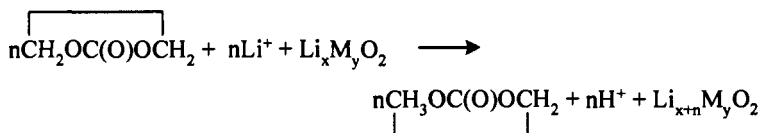
Radicals can then self-decompose or react to form polymers trough chain reactions. These polymers, whose presence was detected by spectroscopic methods, [32] may be responsible for the impedance increase observed. CO_2 can be a side product of radicals self-decomposition and has been actually identified as the major component of the gas produced on overcharge.

The possible formation of CO_2 during high voltage and high temperature storage has been investigated. In their presentation to ECS fall meeting, 1999, Sasaki et al. [34] described $LiCoO_2$ prismatic cells bulging when submitted to an extended two-year storage at 4.1 V, 45°C. Gas pressure increase was attributed to electrolyte decomposition, with pressure increasing at a constant rate and the effect strongly dependent on temperature and cell floating voltage. At 25°C, the variation was about 8 times less, and negligible at 4.0 V at this temperature. High voltage combined with high temperature is therefore the major parameter, clearly pointing to reactivity at the positive interface. Due to their shape, prismatic cells are more sensitive to pressure increase than cylindrical design.
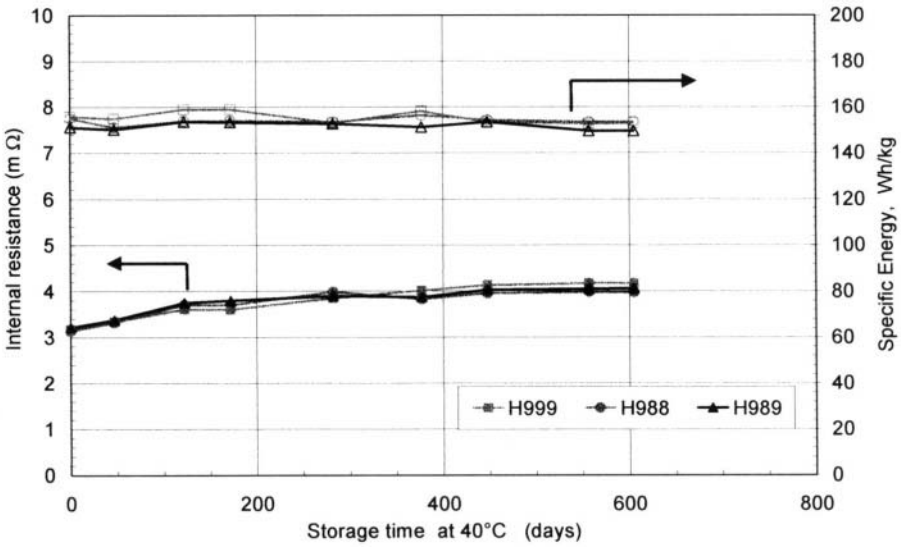
Figure 21. Change Specific Energy and resistance at 80% DOD during storage of a High Energy LiNi$_x$Co$_y$Al$_z$O$_2$ cell at 40°C. Discharge rate: C/3, 20°C, resistance calculated from 30 s pulse. Storage at 100% SOC.
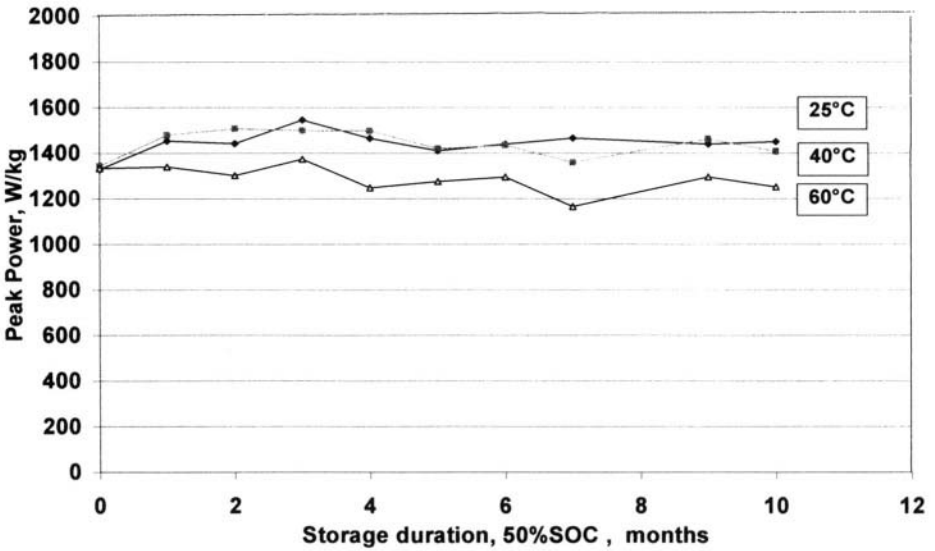
Figure 22. Peak power retention (W/kg, @ 25°C) of latest design HP cells during storage at 50% DOD, 25° to 60°C.

Even without the combined capacity or power loss, the effect of gas generation might then limit the life of cells submitted to long-term high-voltage and high temperature storage, especially if they are equipped for pressure sensitive current breaker or low pressure vent.

Very little has been reported so far on this phenomenon, because it only noticeable in the strong adverse conditions described here. The surface reactivity plays an important role, as does the materials purity.

Figure 23 shows the pressure increase in experimental cells, during storage at 60°C and 4.0 V constant applied voltages. The difference between the curves displayed is the amount and nature of impurities. Therefore, a properly selected material and controlled manufacturing process can overcome this problem, which should not be a limiting factor for most applications, even in severe conditions. For example, less than 10 mL of CO_2 was obtained from analysis of a dismantled 44 Ah cell "A" prototype described earlier after a two-year storage at 70% SOC *and* 60°C. These small quantities of gas can be is easily accommodated in the cell without risk of leakage.

Everywhere possible, slight lowering of the storage or working voltage will considerably reduce this risk, which is an advantage of the Ni-based technology as compared to $LiCoO_2$ or Mn-spinel-based chemistry.
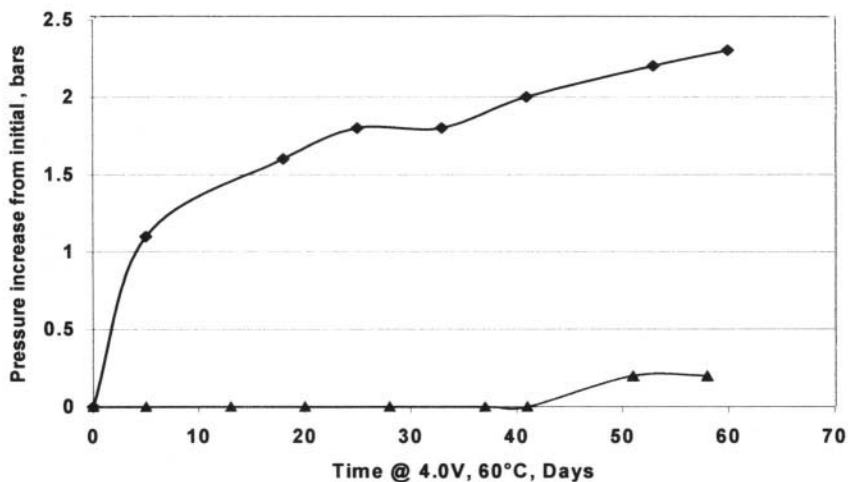
Figure 23. Pressure change in experimental cells during floating at 60°C, 4 V. The different curves are produced with the same positive material, but with different nature and concentration of impurities.

5.0   BATTERY LIFE PREDICTIONS

From all what is described above, it should be difficult to make accurate and reliable cycle-life predictions. In fact, hazardous extrapolations can be avoided providing some basic rules are followed, and good approximations of some of the parameters can be made. The following points are obvious:

1. Unfortunately, there is no unique magic formula for all Li-ion systems; each one has its own chemistry and specific side reactions. Even if the general mechanisms remain the same: i.e. interface reactions between electrolyte and active materials, the rate and activation energy may vary dramatically with the nature of components, additives etc.

2. Life must be calculated using the relevant critical cell characteristics, depending on the application (capacity or energy, power, etc.)

3. Any prediction model, even when temperature is used as an accelerating factor, must be based on a *time scale long enough* to record experimental data. It seems to be a general trend in Li-ion that the side reactions rate decreases with time.

5.1   Examples of Extrapolation for Cycle-Life Predictions

Figure 24 shows energy change during 30% DOD cycling. This is a real time test to simulate LEO (Low Earth Orbit) satellite application. A constant capacity is discharged at each cycle at C/3, from a 3.8 V maximum voltage charge. Every 500 cycles, a complete charge is made to 4 V and discharged to 2.7 V to verify the complete cell energy. Figure 24 shows the best simple fitting equations found after 4000 cycles. In practice, a variation proportional to square root of time shows the best fit with $R^2 = 0.971$, but a linear equation can fit also reasonably with the experimental data, with $R^2 = 0.961$. Both equations may have significant physical meaning. Extrapolations can be made from these empirical fitting equations, as shown in Figure 25 and lead to quite different cycle-life predictions. In this particular case, cycling was pursued to about 15,000 cycles, clearly showing that in fact the linear equation was the most valid, thus demonstrating that the cell is quite able to fulfill the application´s requirement. The new linear fitting equation is fairly identical to the previously established one.
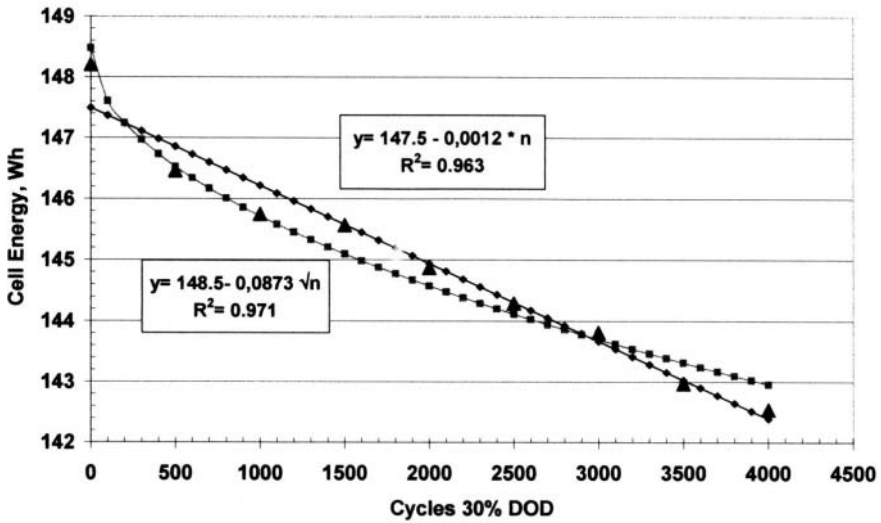
Figure 24. Cell energy change measured every 500 cycles of 30% DOD cycling from 3.8 V. Diagnostic cycle made at C/3 to 2.7 V, from 4.0 V charge. Fitting curves and experimental data during 4000 cycles
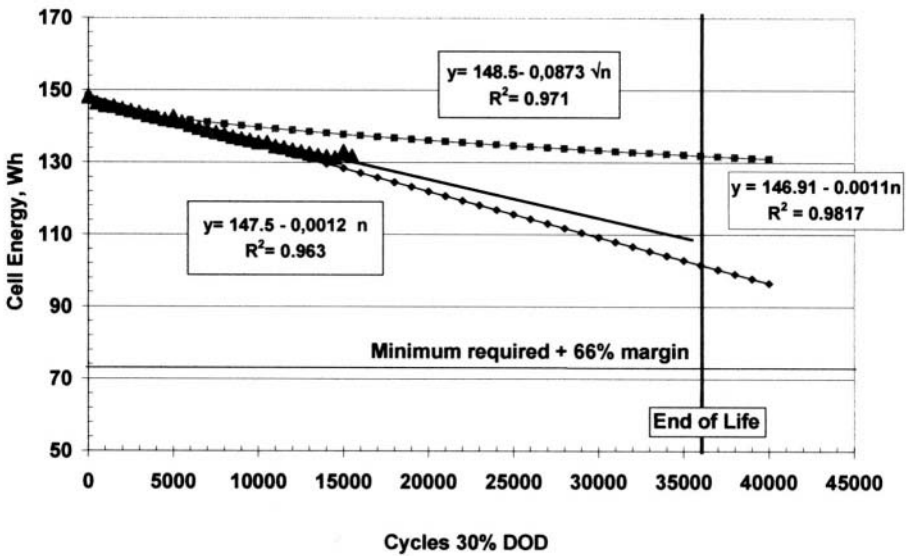
Figure 25. Extrapolation from fitting curves described in Figure 24, and additional data up to 15000 cycles.

5.2   Examples of Extrapolation for Calendar-Life Predictions

From Li corrosion through SEI, a capacity loss versus time can be modeled and predicted. For example, from the results described in Figure 9, a remaining capacity can be calculated for both cell designs, allowing 15% lithium excess in the negative electrode. The results are described in Figure 26. As the lithium corrosion rate is much smaller in the new design, the loss is too small to be significant (at present) at 30°C. Assuming the same temperature coefficient as for the model described in Figure 12 (corrosion rate ratio of 2.15 between 60 and 30°C), a curve can be calculated at 30°C. Due to the lithium excess, no actual capacity loss should be expected from discharge at ambient temperature, as experienced and described in Figure 10. The loss measured at 60°C shown in the same Figure 10 (i.e. measuring the actual amount of lithium) is still small, but the results fits fairly well with the expectation, using the average of all the data (i.e. on 16 cells) reported in Figure 26.

These very positive data address only the lithium capacity, regardless of cell impedance difference. Resistance increase as seen in Figure 16 would reduce the available energy, depending on the drain of application, and limit the available peak power.
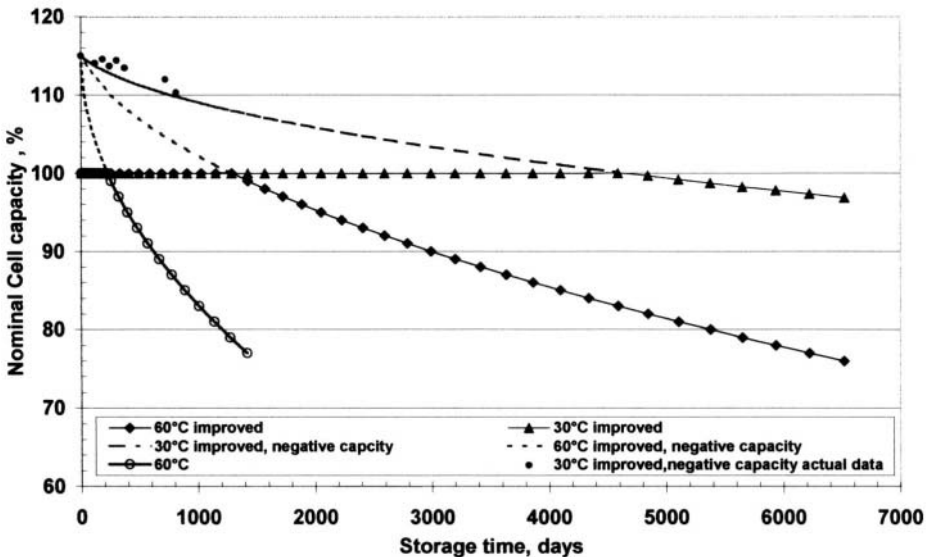
Figure 26. Lithium corrosion model extrapolation for $LiNi_xCo_yAl_zO_2$ cells.
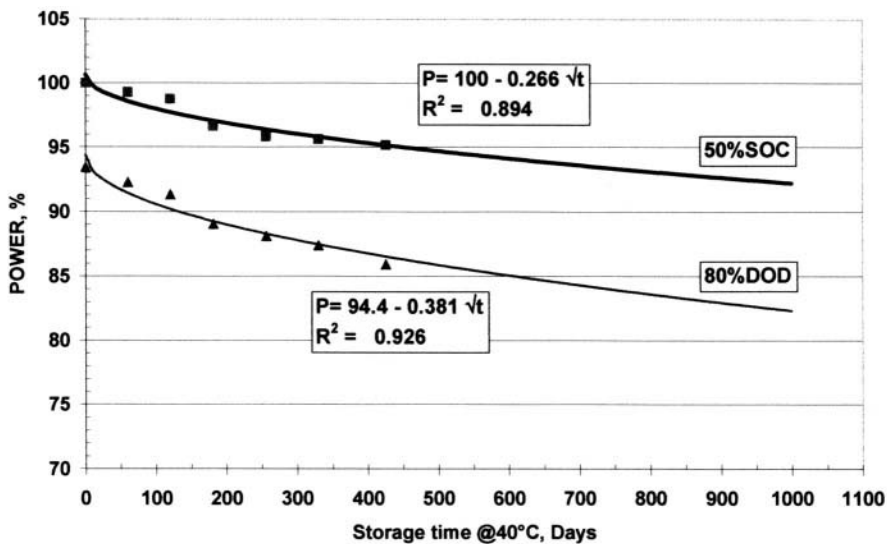
Figure 27. Example of peak power (30 s, 300 A) change during storage at 40°C/100% SOC. Power is expressed as percent of the power available at 50% SOC of the fresh state. 1 KWh Li-ion Module, $LiNi_xCo_yAl_zO_2$ chemistry.

For example, Figure 27 describes the peak power variation for a 1kWh, 12V module for EV application. The power is expressed in percentage of the power obtained at the fresh state (2.7 kW), at 50% DOD, during a 30 second pulse of 300 A (which is not the maximum peak power). As discussed earlier, the impedance, and consequently the peak power, may stabilize better than the model prediction.

Figure 28 shows extrapolation of these curves, from which a calendar-life prediction at 40°C can be made as a function of the application requirements. When sufficient aging has been recorded at ambient (which is in fact still stable), the temperature dependence and extrapolation for other conditions can be made.

Such methods can be also used for cells specially designed for high power application, such as HEV. However, example of Figure 22 cannot lead today to meaningful extrapolations, as the variation is too low even after about one year, regardless of temperature.

6.0   CONCLUSION

Providing a good choice of active materials Li-ion systems can exhibit excellent cycling and calendar life.

The main identified aging parameters include:

1. Negative electrode SEI slow growth, resulting in lithium loss, associated with some impedance increase. Capacity loss can be modeled through a parabolic equation of corrosion in time following an Arrhenius law with temperature, and ***not*** depending on SOC.

2. Electrolyte oxidation on the positive electrode, producing an impedance increase, probably due to carbonate polymerization at the interface. This effect ***depends strongly on SOC,*** temperature, and surface reactivity. The interfacial chemistry, influenced by impurities, plays prominent role.

A very positive point is that the identified aging mechanism follows only monotonous evolution, which minimizes risks of sudden failures, and allows extrapolations with some good probabilities of success.

Although many phenomena still remain to be clarified in more detail, and because the lithium-ion system is still a relatively new electrochemical system, the first experiments over extended period of time are very promising. Many applications, where longevity and reliability are of most importance can now benefit of the high energy and power density of these systems.
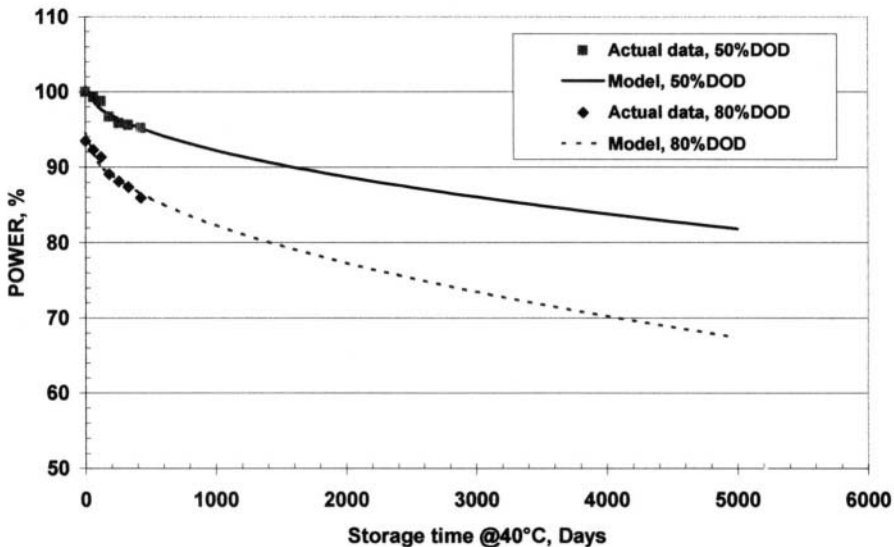
Figure 28. Extrapolation for calendar life at 40°C of peak power from models described in Figure 27

7.0   ACKNOWLEDGEMENTS

8.0   REFERENCES

1.   K.C. Lim, A.M. Lackner, P.O. Braatz, W.H. Smith, J.D. Margerum, H.S. Lim, Electrochem. Soc. Fall Meeting, Paris (1997), abstract n°120

2.   B. Simon, S. Flandrois, K. Guerin, A. Fevrier Bouvier, I. Teulat, P. Biensan, *Journal of Power Sources.* **81-82**, 2-316, 1999.

3.   S. Flandrois, A. Fevrier., P. Biensan, B. Simon, US pat. 5554462

4.   B. Simon, J.P. Boeuve, SAFT patents, FR 94 04889 (1994), EP 0683537 , US 5,626,981

5.   B. Simon, J.P. Boeuve, B. Spigai, M. Broussely, Electrochem. Soc. Fall Meeting, Paris (1997) abstract n°155, vol.97-2, 184.

6.   D. Zhang, B.N. Popov, B.S. Haran, R.E. White, Y.M. Podrazhansky, Proceedings of Li Batteries Symposium, Hawaï ECS /ESJ Joint International Meeting, 645-646, 1999.

7.   D. Zhang, S. Haran, A. Durairajan, R.E. White, Y. Podrazhansky, B. N. Popov, *Journal of Power Sources,* **91**, 2-129, 2000.

8.   J. Li, E. Murphy, J. Winnick, P.A. Kohl, *Journal of Power Sources* **102**, 294-301, 2001

9.   J. Li, E. Murphy, J. Winnick, P.A. Kohl, *Journal of Power Sources* **102**, 302-309, 2001

10. E. Peled , *J. Electrochem. Soc.* **126**, 2047, 1979.

11. D. Aurbach, B. Markowsky, I. Weissman, E. Levi, Y. Ein-Eli, *Electrochimica Acta,* **45**, 67-86, 1999.

12. R. Yazami, *Electrochimica Acta,* 45, 87-97, 1999.

13. E. Peled, D. Bar Tow, A. Merson, A. Gladkich, L. Burstein, D. Glodnitsky, *Journal of Power Sources* **97-98**, 52-57, 2001.

14. E. Peled in Lithium Batteries, J.P. Gabano Editor, Academic Press , New York, 43-72, 1983.

15. M. Broussely, S. Herreyre, P. Biensan, P. Kasztejna, K. Nechev, R.J. Staniewicz, *Journal of Power Sources,* **97-98**,13-22, 2001.

16. G.E. Blomgren, *Journal of Power Sources,* **81-82**, 112-118, 1999.

17. C. Jehoulet, P. Biensan, J.M. Bodet, M. Broussely, C. Moteau, C. Tessier-Lescourret, Electrochem. Soc. Fall Meeting Paris (1997), abstract n°135, vol.97-2,184.

18. Ph. Biensan, J.M. Bodet, F. Perton, M. Broussely, C. Jehoulet, S. Barusseau, S. Herreyre, B. Simon International Meeting on Lithium Batteries, Como, (2000), Abstract n°286.

19. C. Delmas, J.P. Pérès, A. Rougier, A. Demourgues, F. Weill, A. Chadwick, M. Broussely, F. Perton, Ph. Biensan, and P. Willmann, *J. Power Sources,* **54**, 29, 1995.

20. A. Blyr, C. Sigala, G. Amatucci, D. Guyomard, Y. Chabre, J.M. Tarascon, *J. Electrochem.Soc,* **145**,195-209, 1998.

21. T. Aoshima, K. Okahara, C. Kiyohara, K. Shizuka, *Journal of Power Sources* **97-98**, 377-380, 2001.

22. E. Wang, D. Ofer, W. Bowden, N. Iltchev, R. Moses, K. Brandt, *J. Electrochem. Soc,* **147**, 4023-4028, 2000.

23. H. Tsunekawa, S. Tanimoto, M. Sano, K. Kifune, M. Fujita, Meeting Abstracts, 41th Battery Symposium in Japan, Nagoya (2000), 580-581.

24. S. Tanimoto, H. Tsunekawa, M. Sano, K. Kifune, M. Fujita, H. Takeuchi, Meeting Abstracts, 41th Battery Symposium in Japan, Nagoya (2000), 578-579.

25.   T. Saito, M. Machida, Y. Yamamoto, M. Nagamine, Electrochem.Soc Fall meeting, San Fransisco, (2001) abstract 180.
26.   Y. Kogetsu, M. Kohno, T. Hatanaka, T. Saito, J. Yamaura, Electrochem.Soc Fall meeting, San Fransisco, (2001) abstract 181.
27.   F. Joho, B. Rykart, A. Blome, P. Novak, H. Wilhelm, M.E. Spahr, *Journal of Power Sources,* **97-98**, 78-82, 2001.
28.   P. Novak, F. Joho, M. Lanz, B. Ryckart, J-C Panitz, D. Alliata, R. Kötz, O. Haas, *Journal of Power Sources, * **97-98**, 39-46, 2001.
29.   F. Kong, R. Kostecki, G. Nadeau, X. Song, K. Zaghib, K. Kinoshita, F. McLarnon, *Journal of Power Sources, * **97-98**, 58-66, 2001.
30.   D. Aurbach and Y. Gofer, in *Non Aquous Electrochemsitry,* D. Aurbach Editor, Marcel Dekker, Inc., 137-212, 1999.
31.   D. Aurbach, B. Makovsky, M.D. Levi, E. Levi, A Schechter, M. Moshkovich, Y. Cohen, *Journal of Power Sources, * **81-82**, 95-111, 1999.
32.   D. Aurbach, K. Gamolsky, B. Markowsky, G. Salitra, Y. Gofer, U. Heider, R. Oesten, M. Schmidt, *J. Electrochem.Soc, * **147**, 1322-1331, 2000.
33.   D. Ostrovskii, F. Ronci, B. Scrosati,P. Jacobsson, *Journal of Power Sources* **103**, 10-17, 2001.
34.   T. Sasaki, N. Imamura, M. Terasaki, M. Mizutani, M. Yamachi, Meeting Abstracts of Hawaï ECS /ESJ Joint International Meeting (1999), abstract 319.
35.   I. Bloom, B.W. Cole, J.J. Sohn, S.A. Jones, E.G. Polzin, V.S. Battaglia, G.L. Henriksen, C. Moltoch, R. Richardson, T. Unkelhaeuser, D. Ingersoll, H.L. Case, *Journal of Power Sources.* **101**, 238-247, 2001.
36.   R.G. Jungst, G. Nagasubramanian, C.C. Crafts, D. Ingersoll, DD. Doughty, Electrochem.Soc. Fall meeting, Phoenix (2000) abstract 161.
37.   K. Amine, C.H. Chen, J. Liu, M. Hammond, A. Jansen, D. Dees, I. Bloom, D. Vissers, G. Henriksen, *Journal of Power Sources.* **97-98**, 684-687, 2001.
38.   M. Broussely, S. Herreyre, F. Bonhomme, Ph. Biensan, Ph. Blanchard, K. Nechev, G. Chagnon, Electrochem.Soc. Fall meeting, San Francisco (2001). abstract 128.
39.   R. Kostecki and F. McLarnon, Electrochem.Soc. Fall meeting, San Francisco (2001) abstract 168.
40.   C.H. Chen, J. Liu, K. Amine, Electrochem.Soc Fall meeting, San Fransisco, (2001) abstract 176.
41.   R.G. Jungst, G. Nagasubramanian, C.C. Crafts, D. Ingersoll, DD. Doughty, Electrochem.Soc. Fall meeting, San Fransisco, (2001) abstract 132.
42.   C.G. Moltoch, J.P. Christophersen, R.B. Wright, V. Battaglia, Electrochem.Soc. Fall meeting, San Fransisco, (2001) abstract 131.

14

Scale-Up of Lithium-Ion Cells and Batteries

Robert Spotnitz

Battery Design Company
Pleasanton, CA
USA

1.0   INTRODUCTION

Sony´s introduction of the first commercial lithium-ion battery in 1991 [1] revolutionized the battery industry. The outstanding characteristics of lithium-ion batteries (high voltage, high energy density, low self-discharge rate, and good cycle life) make them the preferred choice for many applications. Originally used in portable phones, lithium-ion batteries quickly dominated camcorders, portable computers, then cellular phones, and are now widely used in many consumer electronic devices. Consumer electronics require relatively small lithium-ion batteries (<100 Whr). Much larger batteries are required for aerospace and automotive applications, but have not yet found widespread use due to problems of cost, calendar and cycle life, high temperature stability, low temperature performance, and abuse tolerance. However, lithium-ion technology has made significant progress over the last decade, and large lithium-ion batteries are well poised to penetrate commercial markets. Here, a review is given of the requirements facing large, lithium-ion batteries, the common cell designs including key characteristics, and the design issues for modules and packs.

2.0   APPLICATIONS FOR LARGE LITHIUM-ION BATTERIES

There is significant interest in the use of batteries for satellite, hybrid electric vehicle (HEV) and electric vehicle (EV), and load-leveling applications. Each of these applications has unique requirements that require development of customized batteries.

2.1   *Aerospace Applications [2,3]*

Typically, satellite batteries [4] used for geo-synchronous earth orbit (GEO) must be able to provide 1200-2400 cycles at 60% depth-of-discharge (DOD)

over a 15 year period, or, for a low-earth orbit (LEO), provide 35,000 cycles at 25% DOD over seven years. These performance requirements are easily met with $Ni-H_2$ batteries. $Ni-H_2$ batteries are available with energy densities on a cell level of **40-50 Whr·kg⁻¹** and **50-83 Whr·L⁻¹** [5]. However, lithium-ion batteries for use in satellites have been developed with energy densities on a cell level of **90-140 Whr·kg⁻¹** and **260-310 Whr·L⁻¹**. Besides providing higher energy density, lithium ion provides higher cell voltage (~3.6 V versus 1.25 V for $Ni-H_2$) and that provides greater system reliability because fewer lithium-ion cells are needed to achieve the required system voltage. Isaacson and Teofilo [4] have given $10,000/lb as a rule-of-thumb for launch costs. Using this number, the incentive for using lithium-ion batteries can be quantified by considering that the INTELSAT V $Ni-H_2$ cells alone weighed 24.03 kg; use of lithium-ion cells instead could reduce the cell weight to 12 kg and save over $250,000. A number of companies are currently offering lithium-ion batteries for satellites.

COM DEV, Eagle Picher, GS-Melcotec, Saft, Yardney, Quallion, and MSA are actively developing lithium-ion batteries for aerospace applications. COM DEV´s approach is somewhat unique in that they use small consumer cells (cylindrical containing spirally-wound electrodes) in very large series/parallel strings without charge balancing electronics. The other companies have developed larger cells (>10 Ah) that are connected in series with charge balancing electronics. Eagle Picher, MSA, and Lithion (Yardney) offer prismatic cells that contain stacks of electrodes. GS-Melcotec, Saft, and Quallion offer cells made with spirally-wound electrodes. Saft offers cylindrical cells (40-320 Ah) while GS-Melcotec offers elliptically-shaped cells (50-190 Ah).

Other aerospace applications include aircraft, spacecraft such as NASA´s shuttle and the Mars lander, and unmanned aerial vehicles [6]. Evaluations of lithium-ion batteries for space applications are progressing well and it is widely believed that lithium-ion batteries will supplant $Ni-H_2$ batteries in the future.

2.2   Electric Vehicles

In the early 90´s Sony recognized that lithium-ion technology could be applied to electric vehicles. At the **30th** Tokyo Motor Show in 1995, Nissan demonstrated an electric vehicle powered by Sony lithium-ion batteries. Sony´s prototype battery pack consisted of modules each containing eight cylindrical cells (see Table 1). The cells contained $LiCoO_2$ cathodes and hard carbon anodes.

Development of lithium-ion technology for electric vehicles has been funded by USABC (USA), LIBES (MITI - Japan), and the European Union. The USABC has developed clearly defined goals (see Table 2) as well as test procedures [8].

Table 1. Specification of Sony's prototype lithium-ion cells and modules. Data derived from reference 7.

Specifications	Single cell	Module
Size (mm)	DxL 67x410	WxLxH 440x290x150
Capacity (Ah)	100	100
Weight (kg)	3.3	29
Energy density (Wh/kg)	110	100
Energy density (Wh/l)	250	160
Life (cycles)	>1200	>1200
Self discharge rate (%/month)	<10	<10

Table 2. USABC Battery Goals. [8]

Parameter (units) of fully burdened system	Mid-term goal	Minimum goals for long-term commercialization	Long- term goal
Power Density ($W \cdot L^{-1}$)	250	460	600
Specific Power – Discharge, 80% DOD/30 sec. ($W \cdot kg^{-1}$)	150	300	400
Specific Power – Regen 20% DOD/10 sec. ($W \cdot kg^{-1}$)	75	150	200
Energy Density – C/3 Discharge rate ($Wh \cdot L^{-1}$)	135	230	300
Specific Energy – C/3 Discharge rate ($Wh \cdot kg^{-1}$)	80	150	200
Specific Power/Specific Energy Ratio	2:1	2:1	2:1
Total Pack Size (kWh)	40	40	40
Life (Years)	5	10	10
Cycle Life – 80% DOD (Cycles)	600	1000 to 80% DOD 1600 to 50% DOD 2670 to 30% DOD	1000
Power & Capacity Degradation (% of rated spec)	20	20	20
Ultimate Price – 10,000 units @ 40 kwh ($/kWh)	150	<150 ($75/kWh desired)	100
Operating Environment (°C)	-30 to +65	-40 to +50 20% Performance Loss (10% desired)	-40 to +85
Normal Recharge Time (hours)	6	6 (4 desired)	3 to 6
High Rate Charge	40-80% SOC in 15 min	20-70% SOC in <30 min @ 150 W/kg (<20 min @ 270 Wh/kg desired)	40-80% SOC in 15 min
Continuous discharge in 1 hour – No failure (% of rated capacity)	75	75	75

Currently, Saft (a subsidiary of Alcatel), Japan Storage Battery Co. (JSB), and Shin-Kobe (a member of the Hitachi group) are developing lithium-ion batteries for electric vehicles. Saft and Shin-Kobe use cylindrical cells with spirally-wound electrodes. Shin-Kobe uses a manganese positive and hard carbon negative, while Saft uses **$LiNiCoO_2$-based** positive and a graphite

negative. JSB uses an elliptic cell design and a $LiMn_2O_4$ positive. Nissan´s Altra is powered by lithium-ion batteries, and has significantly greater range than cars powered by Ni/MH batteries. However, only a few Altras were built. Interest in electric vehicles seems to have waned in recent years; an excellent report [9] is available that summarizes the current state of lithium-ion and other advanced batteries for electric vehicles. On the other hand, hybrid electric vehicles are enjoying some success.

2.3   Hybrid Electric Vehicles

Hybrid electric vehicles use both an internal combustion engine (ICE) and an electric motor. The two extreme configurations are (1) a "series" hybrid in which the ICE generates electric power to maintain a charge on the batteries that power the electric motor, and (2) a "parallel" hybrid in which both the ICE and electric motor can independently power the wheels. Parallel hybrids, powered by Ni/MH batteries have met with some success, and some automotive experts believe that, in the long-term, Li-ion batteries will replace Ni/MH batteries. The battery system goals for the Partnership for a New Generation of Vehicles (PNGV) are listed in Table 3.

Table 3. PNGV battery system goals for Hybrid Electric Vehicles. Test procedures are available in reference 10.

Characteristics	Units	Power Assist	Dual Mode
Pulse discharge power	kW	25 (18 s)	45 (12 s)
Peak regenerative pulse power	kW	30 (2 s) (min 50 Wh over 10 s regen total)	35 (10 s) (97 Wh pulse)
Total available energy (over DOD range where power goals are met)	kWh	0.3 (at C/1 rate)	1.5 (at 6 kW constant power)
Minimum round-trip energy efficiency	%	90	88
Cold cranking power at −30°C (three 2-s pulses, 10-s rests between)	kW	5	5
Cycle-life for specified SOC increments	Cycles	300,000 Power Assist cycles (7.5MWh)	3750 Dual Mode cycles (22.5 MWh)
Calendar life	Years	15	15
Maximum weight	Kg	40	100
Maximum volume	L	32	75 (at 165 mm max ht.)
Operating voltage limits (Note: Max. current limited to 217 A at any power level)	Vdc	max≤440 min≥(0.55 x Vmax)	max≤440 min≥(0.5 x Vmax)
Max. allowable self-discharge Rate	Wh/day	50	50
Temperature Range: Equipment Operation Equipment Survival	°C	-30 to +52 -46 to +66	-30 to +52 -46 to +66

As with electric vehicles, Saft, JSB and Shin-Kobe are the leading developers of lithium-ion batteries for HEVs. Properties of JSB cells (Table 4) and Saft cells (Table 5) indicate that the power and energy requirements for HEVs can be easily met with lithium-ion technology. Shin-Kobe´s manganese cell is 40 mm in diameter and 108 mm tall, weighs 300 g, has a capacity of 3.6 Ah, and an output power density at 50% depth-of-discharge of **2000 W·kg⁻¹**.

Table 4. Japan Storage Battery's Lithium-ion cells for hybrid electric vehicles (all 3.6 V nominal).

Cell Type	Nominal Capacity (Ah)	Dimensions (mm)			Mass (kg)	Specific Energy (Wh·kg⁻¹)	Specific Power* (W·kg⁻¹)
		Width	Thickness	Height			
LEV3H	3	85.5	109	19	0.33	33	>1,200
LEC24H	24	133	170	47	21	41	>1,500

* 50% DOD

Table 5. Saft's Lithium-ion cells for hybrid electric vehicles (3.6 V nominal)

Cell Type	C/3 Capacity (Ah)	Dimensions (mm)		Mass (kg)	Specific Energy (Wh·kg⁻¹)	Specific Power* (W·kg⁻¹)
		Diameter	Length			
HP30	31	54	208	1.05	106	1190
HP12	16	47	178	0.68	85	1430
HP6	8	47	104	0.38	75	1420

* 18 second pulse at 50% DOD.

Lithium-ion batteries are used in Nissan´s Tino, a hybrid electric vehicle. The Tino seats five and achieves twice the fuel economy of the corresponding non-HEV car. Only a hundred Tinos will be built and they use Shin-Kobe **LiMn₂O₄** packs. Saft [11] has recently reported good low temperature performance for cold cranking and projects that a 15-year life should be achievable with **LiNiCoO₂-based** cells. Cost and safety appear to be the only issues now limiting use of lithium-ion batteries in hybrid electric vehicles.

2.4 Load Leveling

Electric utility companies must size their plants to meet daytime loads and at night, when demand decreases dramatically, the plants sit idle. If individual homes had storage batteries, then the batteries could charge at night and provide power during the day. Such an approach would reduce the cost of generating electricity and make the grid more stable. This approach has been pursued since 1992 by LIBES (Japan) with some progress (Table 6).

The cycle life requirement for load leveling is still unproven, but, even if successful, the cost may still be problematic.

Table 6. LIBES targets and results for stationary batteries [12].

Property	R&D target	Test Results (FY1998)	
		LiNiCoO$_2$ system	LiMn$_2$O$_4$ system
Capacity (kWh)	2	2.14	2.04
Specific energy (Wh·kg^{-1})	120	116	100
Energy density (Wh·L^{-1})	240	174	213
Energy efficiency (%)	90	96.7	97.1
Cycle life (cycles)	3500	In progress	In progress

3.0   DESIGN OF LARGE LITHIUM-ION CELLS

Lithium-ion cells are available in cylindrical, elliptical, and prismatic shapes (see Figure 1). The cell packages are usually aluminum or steel cans; so-called "soft" packaging (metallized plastic) has not yet proven viable for large lithium-ion cells. Prismatic and elliptic cells can pack together to form more dense modules than cylindrical cells, and prismatic cells can provide greater surface area per unit volume than cylindrical cells (advantageous for heat transfer). However, maintaining compressive force on the electrodes to provide uniform contact is more difficult with prismatic cells. Cylindrical cells contain spirally-wound electrodes (Figure 2). Spiral winding is advantageous because it is amenable to high-speed production and the symmetry provides even distribution of pressure on the electrode stack. By winding the electrodes around a flat mandrel, an elliptical spiral can be created. The elliptical shape provides the advantages of spiral winding and a prismatic shape. A prismatic cell can contain an elliptic wind, but this leaves the corners of cell vacant and uneven pressure on the electrodes; the corners of a prismatic container can be filled or made thick to improve strength of the container. Instead of winding, a cell can be made by stacking electrode plates together, much like traditional battery chemistries. Stacking tends to be more expensive for large-scale production, but can be readily accomplished by hand. Further, the plates can be made with a relatively inexpensive bench-top coating machine. The above discussion applies to small lithium-ion cells as well as large cells. However, large cells require special attention to tabbing, heat transfer, and abuse tolerance.

The chemistries used in large cells mirror those used in small cells. LiCoO$_2$ can be used in aerospace applications where cost is not an overriding concern. Otherwise, LiNiCoO$_2$ (and derivatives such as LiNiCoAlO$_2$) and LiMn$_2$O$_4$ are used. Graphite, hard carbon, mesocarbon microbeads (MCMB), and mixtures of these materials are used for negatives. EC and PC-based solvents with LiPF$_6$ are used as electrolytes. Microporous membranes are used as separators. As mentioned above, Ni-plated steel and aluminum are commonly used to make cell casings.
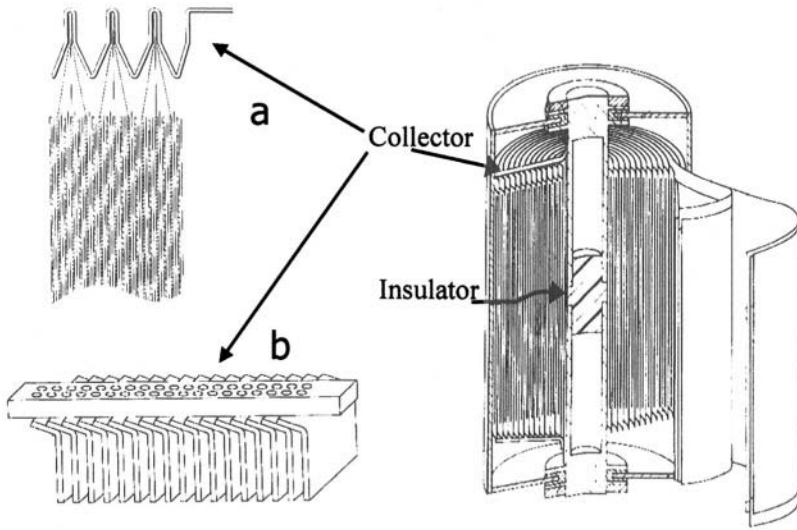
Figure 1. Available shapes of larger-format lithium-ion cells.
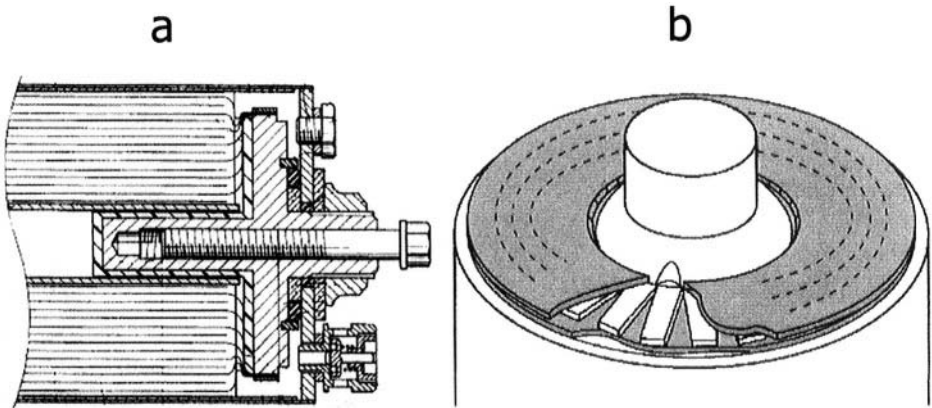
Figure 2. Internal design of spirally-wound elliptic and round cells.

2.1 *Electrode Coatings*

Active materials are usually coated onto metal foils to form electrodes. The coatings consist not only of active material but also binder(s), and, perhaps, conductivity aids. Typical formulations for HEV cells are shown in Table 7. The coating is made by forming a slurry of the components in a solvent (typically N-methyl pyrrolidone). The coating is applied to the foil using reverse roll coating.

Reverse roll coating can produce very thin coatings (~40 microns) useful in high-power cells. After reverse roll coating, the coated electrode is dried to remove solvent, and then calendared to increase density. The properties of the coating largely determine the behavior of the battery.

Table 7. Typical formulations for HEV cells [13].

Positive		Negative	
Material	Weight. %	Material	Weight %
$LiNi_{0.8}Co_{0.2}O_2$	84	MCMB	75
PVDF	8	Graphite	16
Graphite	4	PVDF	9
C Black	4		

The key properties of the coating are loading ($g \cdot cm^{-2}$), apparent and solid density ($g \cdot cm^{-3}$), surface area of active material, adhesion to collector, electrical conductivity, permeability, compressibility, and uniformity. The loading and density of the coating determine the thickness and porosity. The surface area of the active material strongly influences the rate capability of the electrode as well as the abuse tolerance. The electrical conductivity of the coating helps determine the electronic ohmic loss and influences the utilization of the active material. The permeability influences the depth utilization of the electrode. The compressibility, especially the resiliency of the coating, determines how well the cell will cycle; since coatings expand and contract during use, they must be compressible to some extent. Lastly uniformity is critical to obtain balanced cells. If the coating is non-uniform, then local imbalances in the amount of positive and negative material can lead to local overcharge or overdischarge and reduce life. Despite their importance in cell behavior, standardized techniques for measuring electrical conductivity and permeability of coatings have not been developed. Coatings are developed empirically based on experience and trial-and-error testing.

3.2   *Current Collection*

For consumer applications, lithium-ion cells typically use thin metal foils for current collectors (12 μm copper foil for the negative and 20 μm aluminum foil for the positive) that contain a single tab. For spirally-wound cells, the tab is usually located at the end of an electrode on an edge (see Figure 3a). For stacked-plate cells the tab can be integral to the foil (Figure 3b).

As the electrodes get larger, current collection can become more challenging. For prismatic cells made by stacking plates, the dimensions of the individual electrodes usually do not exceed 10 cm x 10 cm and a single tab is adequate. The electrodes are stacked so that the tabs of the electrodes with the same polarity aligned and can be bunched together, and attached to a post that provides external electrical contact. For spirally-wound cells, multiple tabs must

be used. Placing multiple tabs onto the foil collector is a slow process not amenable to high-speed production.
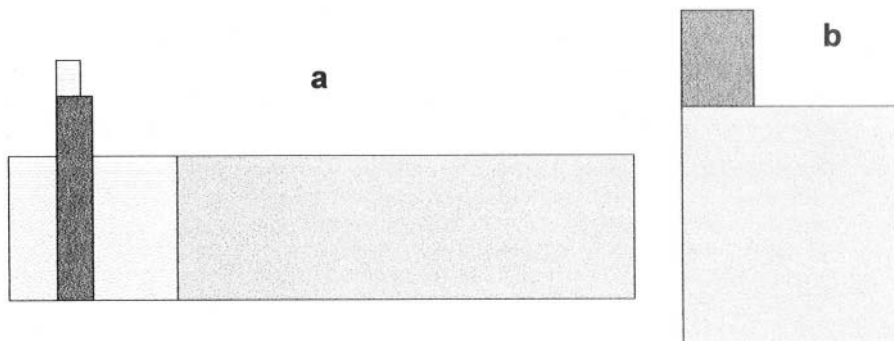
Figure 3. Tabbing for electrodes used in small lithium ion cells. Spirally-wound electrodes (a) and stacked plate (b).

In large batteries with long (>100 cm) electrodes, one edge (either top or bottom) is uncoated throughout the entire length [14]. Sections of the uncoated edge can be cut out to form tabs. The positive and negative electrodes are aligned so that their uncoated edges are on opposite ends. When the electrodes are wound up together, the positive tabs and negative tabs extend out in opposite directions (see Figure 4). This approach can also be used for ellipti-cally-wound cells. The tabs are typically spaced less than a few centimeters apart, so the current collection is effectively continuous along the edge. Since even large lithium-ion cells are less than 50 cm high, the maximum distance current must flow (the distance from the bottom to the top of the electrode) is less than 50 cm. Since current densities for lithium-ion cells are usually below 10 mA·cm^{-2}, the ohmic drop in the metal collector will not significantly influence the current distribution. Calculation methods for collector design can be found in the references [15,16,17].

Edge collection solves the problem of forming multiple tabs, but the prob-lem remains of collecting the tabs and attaching them to a post. Solutions to this problem are described in several patents.

According to an early Sony patent [19], for a cylindrical cell with a center tube, the negative tabs can be welded to the center tube and the positive tabs welded to the can. A more recent Denso patent [20] shows the tabs welded to a collector that is connected to a center tube. The tab connections for the positive and negative electrodes are made in the same way. The electrodes are electrically isolated because the center tube consists of two parts sepa-rated by an insulator (see Figure 5). Also shown in the Figure 5 is a possible collector design taken from Japan Storage Battery [21] and a collector design from Saft [22]; Sanyo has recently described an improved method of making a collector similar to the Saft design [23]. Laser welding is used with a laser

spot size greater than the perforations in the collector plate; the collector plate welds to the tabs, but light reaching the jellyroll is not intense enough to cause damage. Two other current collection schemes are shown in Figure 6. Referring to Figure 6a, the tabs are gathered and pressed against a circular disk; a ring is placed around the tabs to hold them to the disk [18]; this design has the advantage that the jellyroll is stabilized against shock and vibration by the insert that fits in the hollow tube. In another design (Figure 6b) [24] the tabs are collected between two rings.
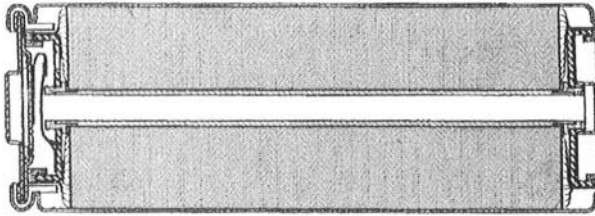
Figure 4. Multi-tabbing arrangement for spirally-wound cell [18].

Figure 5. Current Collection Scheme based on split center tube [20] and possible collector designs from (a) [21] and (b) [22].
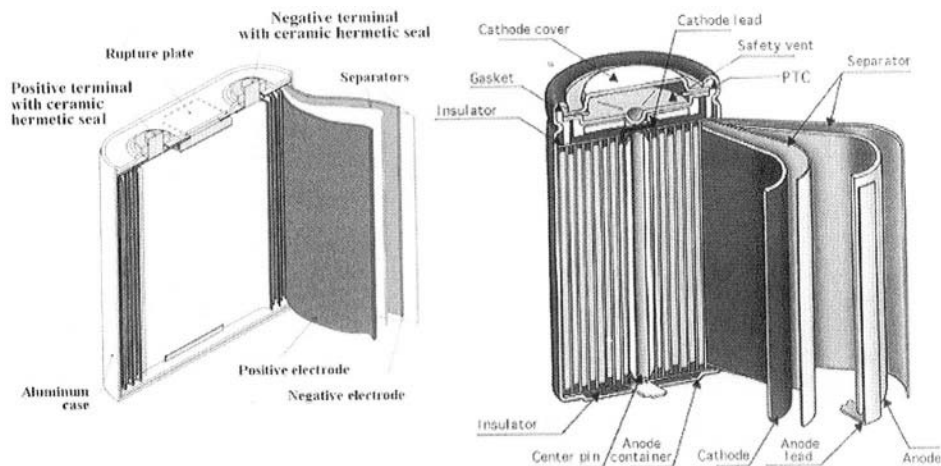
Figure 6. Two approaches for gathering tabs (bussing). (a) tabs welded to the periphery of a circular disk and held in place by a ring [18] (b) tabs sandwiched between two circular disks [24].

The tabbing techniques described above can be applied to prismatically-wound cells; for example see [25]. However, with a prismatic cell, it is convenient to have the positive and negative posts on the top the cell. Since the electrode tabs are gathered at opposite ends of the jellyroll, a conductor must be used to connect the collector at the bottom of the cell to a post at the top of the cell. Even for cylindrical cells, it is not necessary to place the posts at opposite ends. For smaller cells, the can often serves as a terminal. For example, the 3.6 Ah, Shin-Kobe, HEV cell has a negatively charged can (see Figure 7).
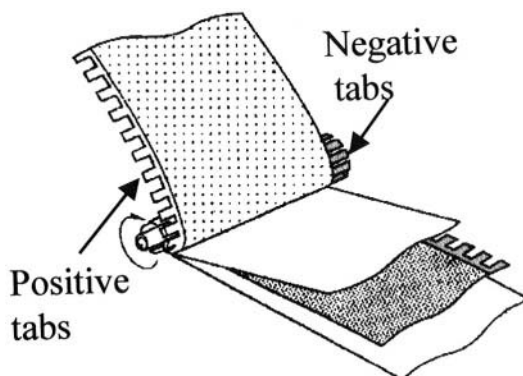
Figure 7. Shin-Kobe cell with negative can [26].

3.3   Seals

Small cells are considerably simpler to seal than larger cells. Small cylindrical lithium-ion cells typically have steel cases that a negative terminal can be directly attached to, and a positive pin in the header. The header is

crimp-sealed to the can with a gasket; the gasket serves as an insulator (see Figure 2) to electrically isolate the negative can from the positive header. The header contains safety devices such as a positive temperature coefficient (PTC) device, a rupture disk, and a current interrupt device. Small prismatic lithium-ion cells are slightly more complex in that the header is welded to (and so in direct electrical contact with) the can. If made of aluminum, the can serves as the positive, or, if made of steel, the can serves as the negative. The header contains the pin of the other electrode and the pin is sealed to the header and electrically isolated by a gasket. Seals for large cells cover larger areas and must withstand greater mechanical forces than seals for small cells. With physically large cells, the cases are normally electrically neutral so both the positive and negative pins must be sealed. Several seal designs for large lithium-ion cells are described in the patent literature.

Figure 8a shows a relatively simple design described in a Nissan patent [18]. A nut is used to compress polymeric seals and electrical isolation is aided by the use of ceramic washers. The header is welded to the tube a the corners, however a crimp seal is also effective for attaching the header to the can [14]. Figure 8b shows a hermetic seal obtained by use of a ceramic spacer brazed onto the header and the pin [27].
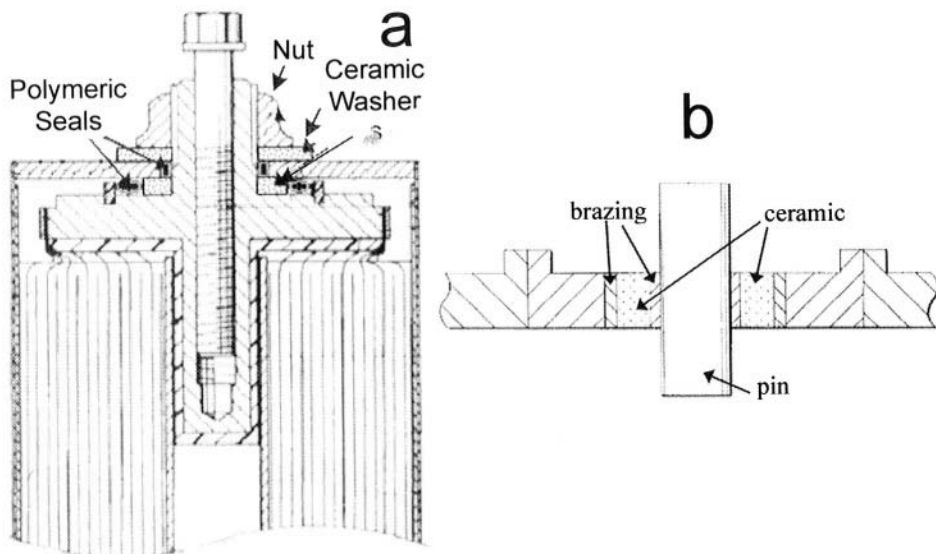
Figure 8. Sealing techniques for large cells. Side views of headers from two patented schemes: (a) compression seal [28], (b) hermetic seal [27].

3.4   *Heat Transfer*

Since cells generate heat, that heat must be dissipated or the cell temperature will rise. Heat generated internally in a cell is transferred by conduc-

tion to the exterior surface of the cell where it is dissipated. Normally cells dissipate heat by conduction and convection to their surroundings, though, during abuse testing, radiation can be an important mode of heat transfer [29]. As cells get larger, the internal distance over which heat must be transferred increases and this greater resistance to heat transfer leads to higher internal cell temperatures. Since high temperatures reduce life and can lead to thermal runaway, the problem of thermal design of large cells has received considerable attention. Engineers and scientists have developed models for estimation of the thermal behavior of large cells, and cell designers have developed cell designs that minimize thermal gradients.

The cell designer faces an interesting compromise when approaching the thermal design of a lithium-ion cell because of the anisotropic thermal properties of the cell components. The metal foils are much more thermally conductive than the active materials and separator, so the thermal diffusivity in the plane of the foil collectors is almost an order of magnitude greater than the thermal diffusivity perpendicular to the plane of the foil collectors (see Table 8). So, for a cylindrical cell with a fixed amount of materials, making the cell tall reduces the diameter and increases the external surface area of the tube, but makes heat conduction in the axial direction more difficult. On the other hand, making the cell short increases the diameter, impeding radial heat transfer while enhancing axial heat transfer. The optimal strategy for setting dimensions will depend on the module design. The module design will determine the effectiveness of heat transfer in the radial and axial directions. For example, batteries designed for space may rely on axial conduction of heat to a central plate, whereas batteries designed for HEVs might depend on radial heat transfer to a cooling fluid.

Table 8. Thermal diffusivity of Sony US-18650 lithium-ion battery components [30].

Material	Thermal Diffusivity (cm$^2 \cdot$s^{-1})	
	Cross-plane	In-plane
Positive Electrode (PE)	0.0133	0.116
Negative Electrode (NE)	0.0119	0.156
PE/Sp/NE	0.0095	0.099
PE/Sp/NE+electrolyte	0.0100	0.079

Of special note, is that large, spirally-wound cells based on a center tube (see Figure 9) can be designed so that the center tube provides conductive heat transfer [31]. Heat fins can be placed at both ends of the tube to further enhance heat transfer.

A significant amount of work has been carried out to develop mathematical models for the thermal design of lithium-ion cells; only a few representative papers will be described here. Chen and Evans [32] considered the problem of heat generation in a prismatic stack of lithium-ion cells using a simple energy balance:
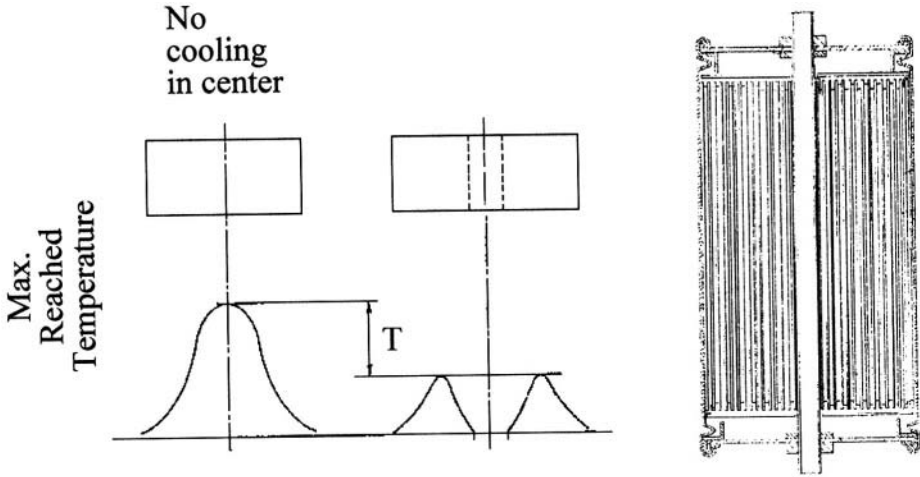
Figure 9. Advantage of center tube for cooling [31]. The center tube conductively transport heat out of the cell.

$$\rho C_p \frac{\partial T}{\partial t} = k_x \frac{\partial^2 T}{\partial x^2} + k_y \frac{\partial^2 T}{\partial y^2} + k_z \frac{\partial^2 T}{\partial z^2} + q \qquad\qquad (1)$$

where T is the temperature, t time, ρ the cell density, Cp the heat capacity, k a thermal conductivity, x, y, and z represent spatial dimensions, and q is the generation rate. The heat generation rate was taken as uniform throughout the cell and determined from experiments with actual cells. The thermal conductivity was computed by averaging reported and estimated properties of the cell components. The calculations indicate, that even for large cells (20x20x20 cm), the cell temperature would not reach extreme values, nor would the temperature gradients be large. Abuse behavior was simulated by setting the internal heat generation rate at the center of the cell to a high value for a short time and following the temperature profile with time; these calculations indicated that thermal runaway could occur in the event of a localized internal short circuit. Kanari et al. [33] used an approach similar to Chen and Evans [32], but considered a cylindrical cell and compared their results to experimental data obtained with a Sony 18650 cell. The heat generation rate (q) was computed based on the following equation,

$$q = -I\left(E_{emf} - V\right) + I\left(T \frac{\partial E_{emf}}{\partial T}\right) \qquad\qquad (2)$$

where I is the cell current, E the cell voltage, and E_{emf} the equilibrium cell voltage. The computed temperatures of the can at both ends and at the mid-point of the tube agreed well with experimental data during discharge and charge (within 2K). Al Hallaj et al. [34] developed a simplified 1-dimensional model that gave good agreement with experimental measurements of the

temperature of a Sony 18650 cell. They used the model to estimate the thermal behavior of larger (10-100 Ah) cells and found that at high discharge rates (1C) the internal temperature increased by ~60°C. Sato [35] compared experimental and model predictions for the temperature rise during discharge of an 80 Ahr Li-ion cell and obtained good agreement. Most recently, Funahashi et al. [36] used a model similar to that of Kanari et al. [33] to compare with actual data for a 250 Wh cell. They found excellent agreement between measured and computed surface temperatures at a 1C discharge up to ~60%DOD (~25°C temperature rise); at higher DOD the model over predicted the temperature rise (model estimated ~36°C increase versus measured ~30°C). The discrepancy is most likely because the I/E data obtained from small cell testing does not accurately represent the large cell I/E behavior. The large cell heats up as it discharges and the small cell I/E data does not reflect this. Since polarization decreases with increasing temperature (as both mass transport and reaction kinetics increase with temperature) the large cell generates less heat than the model predicts. By modeling the polarization due to mass transport and charge transfer, a more accurate estimate of the thermal behavior might be obtained. Models have been developed that include estimates for ohmic and polarization voltage losses and these models have been demonstrated to give good predictions of current-voltage behavior of small lithium-ion cells [37], however, comparisons with thermal behavior have not yet been reported.

The response of batteries to oven heating (an abuse test) has been predicted using a model that accounts for the kinetic behavior of the positive and negative electrodes [38]. Hatchard et al. have gotten reasonable agreement between model calculations and experimental oven tests for 18650 size cells. They have used the model to predict the effect of increasing the radius of a cylindrical cell and of increasing the thickness of a prismatic cell. As expected, in both cases, they found a critical size at which thermal runaway would result.

3.5 *Abuse Tolerance*

Abuse tests for small consumer cells are defined by the International Electrotechnical Committee (IEC), Underwriter´s Laboratories (UL), and the Japan Storage Battery Association (SBA). For electric vehicle batteries, the USABC has developed a test manual that is available from SAE [39]. The USABC manual classifies abuse tests as mechanical, thermal, electrical, and vibration. In Europe, ASTOR is developing standards for advanced automotive batteries [40]. There have been only a few reports on the abuse behavior of large cells.

Saft [41,42] has reported favorable abuse test results for their high power $LiNiCoM_1M_2O_2$/graphite cells. NGK [43] has already reported favorable test results for their 95 Wh (25 Ah) lithium-ion cells $LiMn_2O_4$/hard carbon cells (nail, external short circuit, over-charge, and heating tests). The NGK cell includes

the following safety devices: a shutdown separator, temperature fuse, current fuse and vent. Although the authors report that the NGK cell performed well on the abuse tests, they also note that, during the nail penetration test, large volumes of electrolyte vapor are released; this problem must be solved to make the cells practical. No details of the safety devices were released.

There is little information on the effectiveness of safety devices in the scientific and technical literature, though a number of devices have proven their effectiveness in small lithium-ion cells. Shutdown separators contain a polyethylene layer that melts at ~135°C and stops ionic current flow between the electrodes; shutdown separators protect against internal short-circuit and overcharge in small cells. However, the effectiveness of shutdown separators in large cells has not been published and there is some reason to question how effective a shutdown separator would be in a large cell. The "shutdown" effect of the separator is functional over a limited temperature/time window, typically starting at 135 and ending at 165-180°C. The shutdown effect ends because the separator loses mechanical integrity, and the positive and negative electrodes come into direct physical contact. With large cells, the temperature overshoot might cause the separator to lose physical integrity and cease to function. Similarly, on overcharging a large cell, the temperature could over-shoot and make the separator non-functional. Vents should be equally effective in large and small cells. Positive temperature coefficient devices limit excessive currents but can introduce significant resistance, so might be unacceptable for use in high-power cells. Current interrupt devices in small cells are usually based on physically breaking an electrical connection (frangible tab) due to pressure build-up in a cell. The use of frangible tabs in large cells is complicated because the electrical connections need to be so robust. Large cells typically use external fuses to protect against excessive currents. However, an internal circuit breaker is desirable from a safety viewpoint. Some current interrupt devices for large lithium-ion cells have been described in the patent literature.

Table 9. Results from Abuse Testing of Saft High Power 6 and 12 Ah Cells. Data from references 41 and 42.

Test	Result
Nail test (70 and 100% SOC)	Smoke (max. temp. 214°C); a few "weld" sparks during penetration.
External short circuit (70 and 100% SOC)	Vent of electrolyte, no smoke
Heat test (ramp to 150°C in 30 min. Event after >45 min)	Smoke
Crush (70% SOC)	Vent (6 Ahr cell), smoke (12 Ahr cell)
Impact drop test (70% SOC)	No event
Overcharge (100 A current)	No event up to 4.6V, flame if overvoltage not limited
Salt water immersion	No event (terminal corrosion)
Fuel Fire (radiant heat 890°C)	Fire/no explosion

Two different internal circuit breaker designs for large lithium-ion cells are shown in Figure 10. The first (Figure 10a) has a low-melting alloy connect the internal current bus to the external post. When a high current is drawn from the cell the alloy melts and electrical contact between the electrodes and external post is lost. Alternatively, by limiting the current carrying capability of the weld between the electric feedthrough and the contact disk (Figure 10b), the weld will give way at high currents and electrically disconnect the cell.
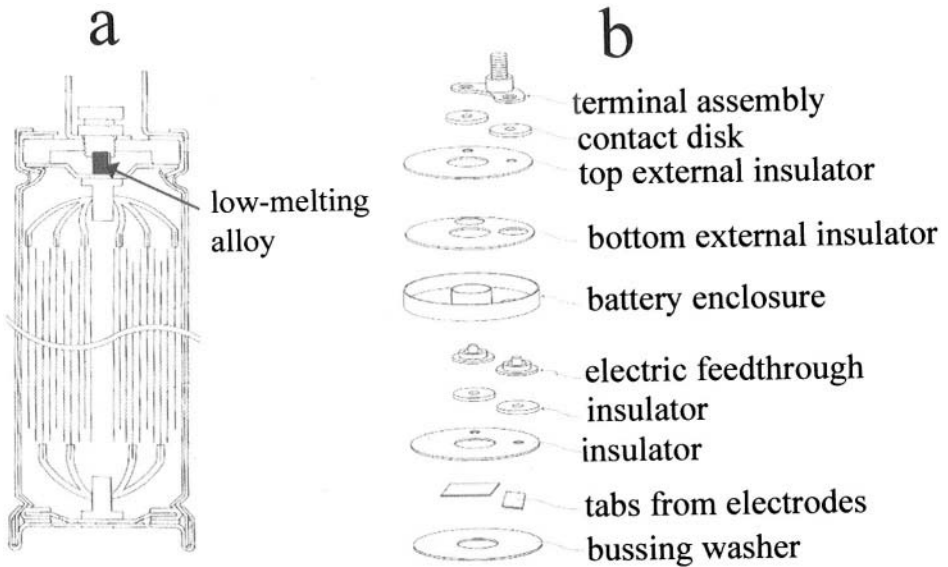
Figure 10. Approaches for current interrupt devices. (a) low melting alloy melts and breaks connection [44] , (b) weld between contact disk and electric feedthrough breaks at high currents[45].

4.0 DESIGN OF LARGE LITHIUM-ION BATTERIES

Large lithium-ion batteries are referred to as packs. Packs consist of modules, and modules consist of cells (Figure 11). Modules include some electronic controls (temperature, voltage, and current sensors, cell balancing) and a thermal management system (air or liquid cooling, conductive). Packs include controllers (thermal, state of charge), module balancing electronics, and electronics to interface with the external system (such as a car). Figure 12 shows a conceptual view of a battery pack.
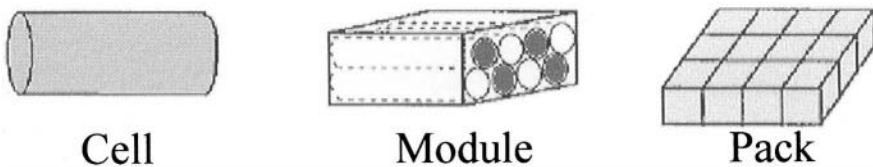
Figure 11. Progression of cell to module to pack [46].

The battery pack consists of modules, module interconnects, electronic controls, and thermal management controls. The modules consist of a housing (structure), cells, cell interconnects, electronic controls, sensors and ducting for thermal management. The electronic controls are normally optically coupled to the sensors to avoid problems with high voltages. The electronics controls are usually linked to a local computer called the Battery Management System (BMS). The BMS protects the pack against abuse and communicates with the external world (perhaps using a standard communication protocol such as Controller Area Network (CAN) [47].
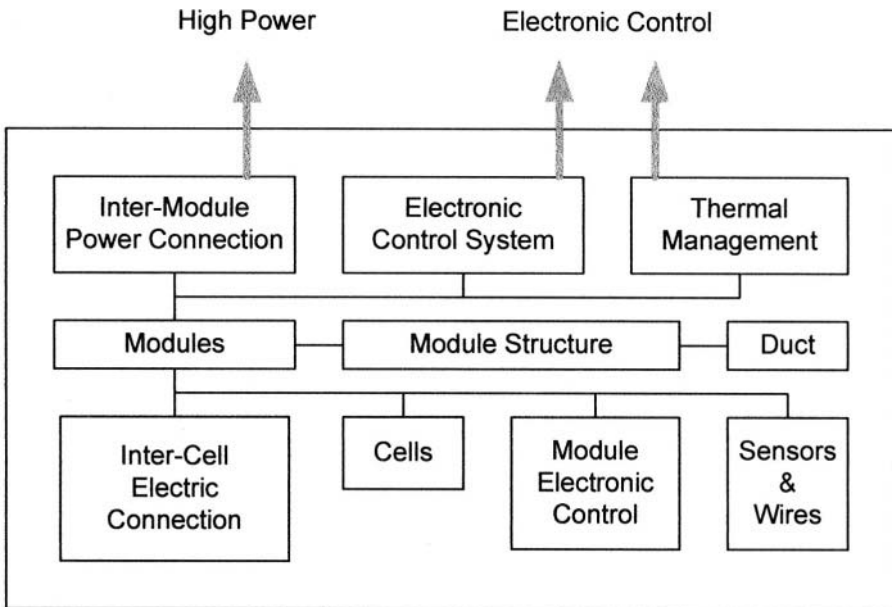
Figure 12. Conceptual scheme for lithium-ion pack [42].

When cells are combined, either in series or in parallel, there is a danger that one or more of the cells will be overdischarged or overcharged. Overcharge is of particular concern with lithium ion cells as they can vent with flame when overcharged. The problem arises because of differences in the capacities and impedances of individual cells. If cells with identical capacity are charged in parallel, the cell with the lowest impedance will receive more current than the other cells. This problem is mitigated in lithium-ion cells (especially those with hard carbon negatives) since the voltage increases significantly with increasing state of charge; the voltage increase due to charging equalizes the SOC among the cells. Still, with large cells, the tendency is to only place cells in series to form modules, and then place modules in parallel to build capacity, or in series to build voltage. Incidentally, modules are typically less than 50 V as the National Electric Code (USA) classifies voltages above 50 as hazardous. When discharging cells in series, the cell

with the lowest capacity might be overdischarged before the cutoff voltage for the string is realized. On charging, the cell with the lowest capacity might be overcharged. The larger the number of cells placed in series, the larger the chance of for overdischarge/overcharge situation to occur. With lithium ion cells, the voltage of each cell (or group of parallel cells) in series is usually monitored.

The use of lithium-ion cells in portable computers has spurred development of techniques for managing cell packs. Off-the-shelf electronic circuits for balancing small lithium-ion cells are now available from several manufacturers. However, small cell manufacturers provide little information about pack behavior. One study [48] of packs consisting of 3 series x 3 parallel, 18650-size lithium-ion cells found that packs lost ~20% discharge capacity after 500 cycles whereas the range for individual cells was 10-20% discharge capacity loss after 500 cycles. Ten packs were cycled by charging to 12.6 V (with each parallel block limited to 4.32 V) and discharging to 8.1 V (with each parallel block limited to 2.5 V). After 300 discharge cycles, the voltage of each cell in each pack was measured and the for each pack the range (min-max value) reported. Similarly, the range at the end of the 300th charge cycle for each pack was determined. The results are shown in Figure 13. The charging protocol involves a constant voltage period which tends to equalize the individual cell voltages. At the end of discharge, the variability in individual cell voltages averages ~35 mV, but can be as large as 70 mV. No such data is available for large cell modules, but one might expect the variability of small cells to be less than that of large cells, since small cells are in high-volume, mass production.
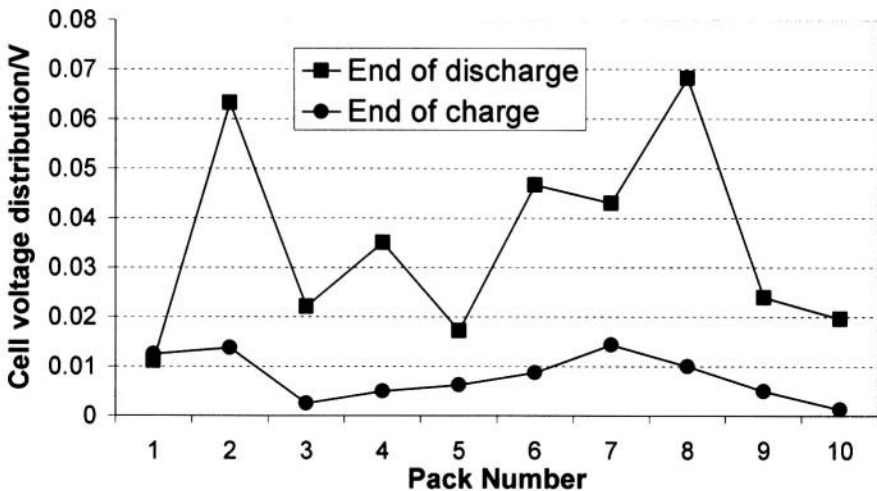
Figure 13. Range of cell voltages within each pack (1 to 10) after 300 cycles at end of discharge and at end of charge [48]. Pack consist of 3Sx3P, 18650 cells (1.2 Ah). Charge at 2.5 A to 12.6 V for 3 h, discharge to 8.1 V at 2 A.

Keeping the number of cells in a module to a minimum increases reliability. The performance of a module is limited by the weakest cell in a series connection. Typically, if one cell fails, the module must be replaced. The probability of a module failing can be reduced by minimizing the number of cells it contains. As mentioned above, the maximum number of cells is usually selected so that the module voltage is less than 50 V.

When forming modules, cylindrical cells cannot pack as densely as prismatic cells. However, packing prismatic cells can be hampered because of the tolerances on the dimensions. The individual cells must be connected using busbars and it is convenient to place the busbars on a panel; see Figure 14 for examples of cylindrical and prismatic modules. For packing cylindrical cells, the terminal posts are easily aligned to fit in the panels. For prismatic cells, the posts might not mate with the panels because of the tolerances of the cell thickness ("A" is Figure 14b). Panels can be designed with flexible gaps (for example, see [49]), or oversized holes in the busbars.
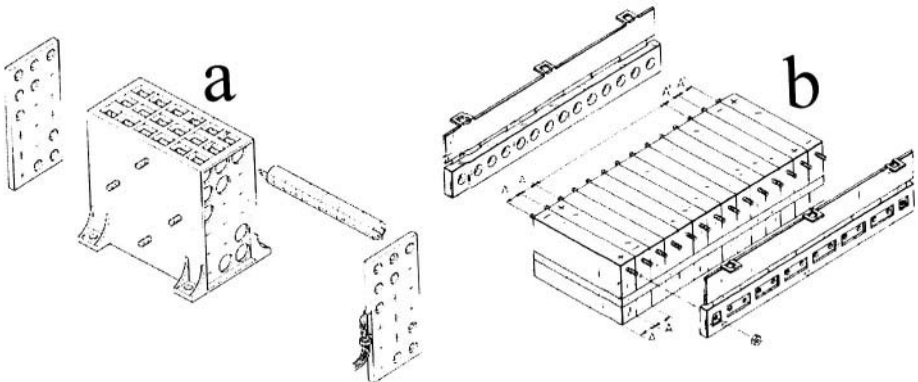
Figure 14. Packing of cylindrical [50] (a) and prismatic [49] (b) cells.

4.1   Electronics and Charge Balancing

Temperature, cell voltages and module currents are usually monitored and can be controlled. Temperatures are measured using a thermistor. Currents are determined by measuring the voltage across a shunt. Voltages can be determined using an A/D convertor. The state of charge (SOC) for the battery can be determined by coulomb counting with some periodic calibration scheme. The strong interest in hybrid electric vehicles with their need to control SOC is fueling development of techniques for SOC determination as evidenced by dozens of patents in this area. For lithium-ion cells, the voltage can often be used to indicate state of charge. Cell balancing is usually required for lithium-ion cells and can be carried out using a number of methods [51], though resistive equalization is the commonly used.

Resistive equalization involves using resistors to bypass cells. For example, the charging current to the cell can be bypassed through a resistor when the cell reaches a maximum charge voltage (see Figure 15). In practice, the cells would be multiplexed to reduce costs. Non-dissipative techniques involving capacitors and/or inductors have been developed, but are considerably more complex and costly to implement.

Electronic systems for battery pack control are commercially available from companies such as Powersmart, AC Propulsion, and Aerovironment.

4.2   Thermal Management

Temperature control is usually required for large lithium-ion battery packs. Cooling is used to prevent overheating that would reduce life and heating is used to improve low temperature performance. In space applications, conductive cooling or heat pipes are used to transfer energy between the battery and a panel. For automotive applications, convective cooling is used, and extensive advice on the design of these thermal management systems is available from the National Renewable Energy Lab [52].

Convective cooling can be carried using air or liquid cooling. Both the Toyota Prius and the Honda Insight (Ni/MH packs) and Nissan Tino (Li-ion pack) hybrid electric vehicles use passenger air to cool their batteries. Air cooling cannot transfer heat at the high rates achievable with liquid cooling, but air systems are considerable simpler to design, operate, and maintain. Air systems may be more voluminous than liquid systems, because larger manifolds are required for air distribution. However, air systems tend to be lower weight and lower cost than liquid systems.
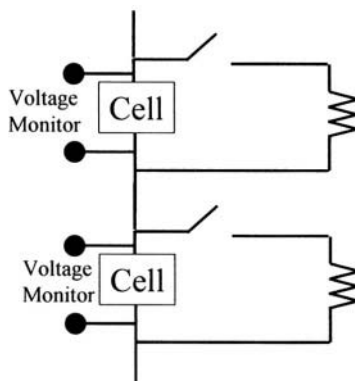
Figure 15. Resistive equalization of cells. When the cell voltage reaches a cutoff value, the switch is thrown, bypassing the charging current around the cell.

4.3   Economics

Little information is available on the costs of large lithium-ion cells and the information that has been published refers to automotive applications. A thorough assessment of the materials availability of materials for use in battery-powered electric vehicles has been published [53]. For lithium-ion batteries based on Mn_2O_4 positives to power all vehicles over the next century, the availability of lithium is the only concern, and only for a pessimistic scenario. However, use of cobalt-based positives would be more problematic, and interestingly, even use of $LiNi_{0.8}Co_{0.2}O_2$ could be difficult.

Anderman et al. [55] have published some cost information for electric vehicle applications based on their survey of battery producers. Figure 16 shows cost estimates from three manufacturers based on volume.

The cost of ~$270/kWh at production volumes of 100,000 packs per year is comparable to that for Ni/MH battery packs, however, it is still significantly above the USABC target (<$150/kWh).

Gaines et al. [46] prepared a report on the cost of lithium-ion batteries for electric and hybrid electric vehicles. They obtained price estimates for materials (see Table 10), and estimated manufacturing costs. They estimate, for an optimistic scenario, a cost of $250/kWh for lithium-ion packs in good agreement with the cost estimates reported in the study by Anderman et al. [55]. For HEV packs, Gaines et al. estimate an optimistic price of $1,095/pack, which is substantially higher than the PNGV goal ($300). Reducing costs is a major challenge facing lithium-ion battery producers.

The material prices provided by Gaines et al. (Table 10 [46]) illustrate the high cost of raw materials for lithium-ion cells. Competitive chemistries, such as Pb-acid and Ni/MH, enjoy substantially lower costs for separators (~10X less) and electrolytes (~100X less). In addition, lithium-ion cells must be assembled in dry rooms to exacting tolerances. However, the dramatic reductions in the price of lithium-ion cells for consumer use is encouraging, as is the recent entry of Chinese producers to the large Li-ion market.

Table 10. Materials costs for Lithium-Ion cells [46]. Separator price varies, $2.50/m^2 is a reasonable value.

Material	Price, $US/kg
Cathode active (LiNiCoO2)	44
Electrolyte	60
Graphite active	30
Binder	45
Copper foil	15
Aluminum foil	20
Carbon conductive additive	20
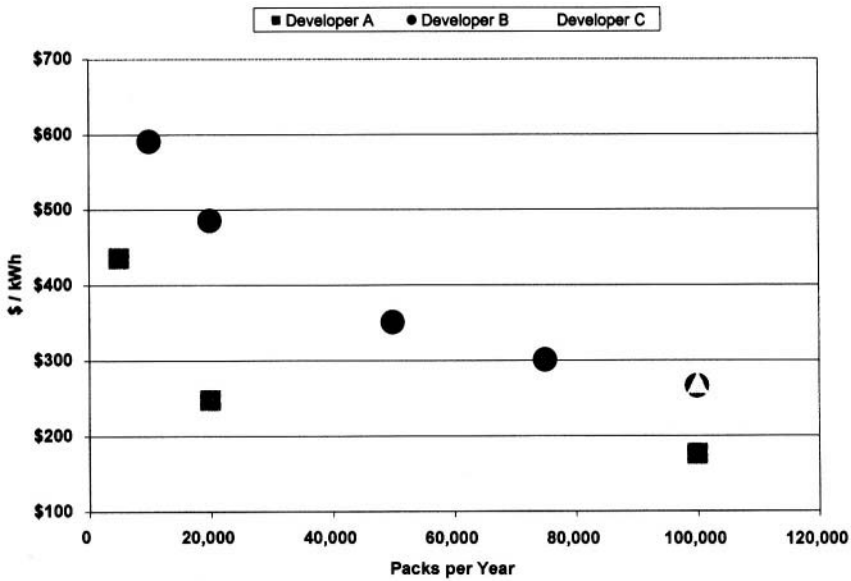
Figure 16. Cost Estimates for Li Ion EV Modules [55].

5.0   CONCLUSIONS

Large lithium-ion cells are finding use in aerospace applications. To find widespread use in other, more cost sensitive applications, both costs and abuse tolerance of lithium-ion cells will need improvement. Electrolyte flammability is of particular concern, since cells can be rupture and vent electrolyte. This issue of electrolyte flammability is being actively studied, and either non-flammable electrolytes or engineering solutions will probably be developed. New materials, such as iron phosphate, may provide significant safety benefits and cost reduction. Reducing the cost of large lithium-ion cells is challenging. The consumer market for lithium-ion batteries is already several billions of dollars annually, so raw material producers should already enjoy low costs through economy-of-scale. To reduce materials costs further will require new and substantial markets for lithium-ion batteries. A substantial market for large lithium-ion batteries will be necessary to drive down the cost of the electronics needed monitor and control cells. The hybrid electric vehicle application holds the best hope for pulling large lithium-ion technology into widespread use. Automakers are well known for driving down costs and have already initiated measures to reduce the costs of separators used in lithium-ion batteries. Thus, there are good reasons to be optimistic about the future for large lithium-ion batteries.

6.0   REFERENCES

1.   Y. Nishi, *J. Power Sources* **100,** 101-106, 2001.
2.   2001 NASA Aerospace Battery Workshop, Huntsville, Alabama Nov. 2001.
3.   19th Annual Space Power Workshop, The Aerospace Corporation, Long
        Beach, California Apr. 2001.
4.   M. J. Isaacson and V. L. Teofilo, The **17th** Annual Battery Conference on
        Applications and Devices, IEEE 02TH8576, Long Beach, CA 2002.
5.   http://www.epi-tech.com/index.htm
6.   R. A. Marsh, S. Vukson, S. Surampudi, B. V. Ratnakumar, M. C. Smart, M.
        Manzo, P.J. Dalton, *J. Power Sources* **97-98,** 25-27, 2001.
7.   Y. Nishi, K. Katayama, J. Shigetomi, H. Horie,13th Annual Battery Conf. on
        Applications and Advances, Long Beach, CA pp. 31-36 1998.
8.   Electric Vehicle Battery Test Procedures Manual, Rev. 2 January 1996.
        http://www.uscar.org/consortia/con-usabc.htm
9.   M. Anderman, F. R. Kalhammer, D. MacArthur, "Advanced Batteries for
        Electric Vehicles: An Assessment of Performance, Cost, and Availability",
        California Air Resources Board, June 2000.
        http://www.arb. ca.gov/msprog/zevprog/2000review/btareport.pdf.
10.   PNGV Battery Test Manual. DOE/ID-10597 Rev. 3 February 2001.
11.   K. Nechev, M. Saft, G. Chagnon, A. Romero, Proc. 2nd Intl. Adv. Automotive
        Battery Conf., Las Vegas, NV, Feb 2002.
12.   T. Tanaka, K. Ohta, N. Arai, *J. Power Sources* **97-98,** 2-6, 2001
13.   R. Sutula, Progress Report for the Advanced Technology Development
        Program, US Dept. of Energy, March 2000.
14.   U.S. Patent 5,736,270 "Battery Device", Apr. 7, 1998. Inventor: H.
        Suzuki, N. Fujiwara. Assigned to Sony Corp.
15.   P. M. Robertson, *Electrochimica Acta,* **22,** 411-419, 1977.
16.   W. G. Sunu, B. W. Burrows, *J. Electrochem. Soc.,* **129,** 688-695, 1982.
17.   W. G. Sunu, B. W. Burrows, *J. Electrochem. Soc.,* **131,** 1-6, 1984.
18.   U.S. Patent 5,693,430; Dec. 2, 1997. Inventors: S. Iwatsu, T. Shimizu, H.
        Takahashi, Y. Kita, K. Katayama, E. Ogami. Assigned to Nissan Motor Co.
19.   U.S. Patent 5,571,632; Nov. 5, 1996. Inventors: K. Teramoto. Assigned to Sony Corp.
20.   U.S. Patent 6,335,114; Jan. 1, 2002. Inventors: H. Ueshima, K. Kami, T.
        Amano, N. Hosokawa, R. Shinkai, M. Yamada. Assigned to Denso Corp.
21.   U.S. Patent 6,040,086; Mar. 21, 2000. Inventors: H. Yoshida, Z. Hagiwara,
        M. Terasaki. Assigned to Japan Storage Battery Col., Ltd.
22.   U.S. Patent 5,972,532; Oct. 26, 1999. Inventors: S. Oweis, G. Chagnon, P.
        Alunans, A. Romero. Assigned to Saft America Inc.
23.   N. Terada, T. Yanagi, S. Arai, M. Yoshikawa, K. Ohta, N. Nakajima, A. Yanai,
        N. Arai, *J. Power Sources* 100 (2001) 80-92.
24.   U.S. Patent 6,245,457; Jun. 12, 2001. Inventor: A. L. Romero. Assigned to Alcatel.
25.   K. Amine, *1st Annual Advanced Automotive Battery Conference,* Las Vegas, 2001.
26.   US Patent Application US 2001/0031291k; 18Oct2001, Inventors: K. Hironaka,
        K. Nakai, Y. Koishikawa, Y. Takatsuka, K. Hara, T. Iguchi, K. Suzuki, K.
        Higashimoto, T. Nakano, Assigned to Shin-Kobe Electric Machinery Co. Ltd.
27.   U.S. Patent 6,335,117; Jan. 1, 2002. Inventors: H. Yoshida, S. Kitano, T.
        Inoue. Assigned to Japan Storage Battery Col., Ltd.

28. U.S. Patent 5,693,430; Dec. 2, 1997. Inventors: S. Iwatsu, T. Shimizu, H. Takahashi, Y. Kita, K. Katayama, E. Ogami. Assigned to Nissan Motor Co.

29. T. D. Hatchard, D.D. MacNeil, D. A. Stevens, L. Christensen, J. R. Dahn, *Electrochemical and Solid-State Letters,* **3** 305-308, 2000.

30. H. Maleki, S. Al Hallaj, J.R. Selman, R. B. Dinwiddie, H. Wang, *J. Electrochem. Soc.,* **146,** 947-954, 1999.

31. U.S. Patent 5,501,916; Mar. 26, 1996. Inventors: K. Teramoto, N. Sugeno. Assigned to Sony Corp.

32. Y. Chen, J. W. Evans, *J. Electrochem. Soc..* **143,** 2708-2712, 1996.

33. Y. Chen, J. W. Evans, *Bulletin of the Electrotechnical Laboratory,,* **60,** 65-75, 1996.

34. S. Al Hallaj, H. Maleki, J.S. Hong, J.R. Selman, *J. Power Sources,* **83,** 1-8, 1999.

35. N. Sato, *J. Power Sources,* **99,** 70-77, 2001.

36. A. Funahashi, Y. Kida, K. Yanagida, T. Nohma, I. Yonezu, *J. Power Sources,* **104,** 248-252, 2002.

37. T. F. Fuller, M. Doyle, and J. Newman, *J. Electrochem. Soc.,* **141,** 962-990, 1994.

38. T. D. Hatchard, D. D. MacNeil, A. Basu, J. R. Dahn, *J. Electrochem. Soc.,* **148,** A755-A761, 2001.

39. SAE Standard J2464, March 1999 "Electric Vehicle Battery Abuse Testing".

40. W. Josefowitz, H. Kranz, D. Macerata, A. Schmolz, H. Mettlach, A. Opel, D. Porcellato, F. Orsini, J. Hansson, Proc. 2nd Intl. Adv. Automotive Battery Conf., Las Vegas, NV, Feb 2002.

41. M. Saft, G. Chagnon, T. Faugeras, G. Sarre, P. Morhet, *J. Power Sources,* **80,** 180-189, 1999.

42. G. Chagnon, P. Allen, K. Hensley, K. Nechev, S. Oweis, R. Reynolds, A. Romero, T. Sack, M. Saft, *1st Annual Advanced Automotive Battery Conference,* Las Vegas, 2001.

43. K. Kitoh, H. Nemoto, *J. Power Sources* **81-82,** 887-890, 1999.

44. U.S. Patent 6,139,986; Oct. 31, 2000. Inventors: T. Kurokawa, H. Nemoto. Assigned to NGK Insulators, Ltd.

45. U.S. Patent 6,218,040; Apr. 17, 2001. Inventor: A. L. Romero. Assigned to Alcatel.

46. L. Gaines and R. Cuenca, Costs of Lithium-Ion Batteries for Vehicles, ANL/ESD-42, US Dept of Energy, May 2000. http://www.doe.gov/bridge

47. ISO 11519-2:1994 "Road vehicles -- Low-speed serial data communication -- Part 2: Low-speed controller area network (CAN)" (1999).

48. K. Ozawa, T. Aita, The 11th Int. Seminor on Primary and Secondary Battery Technology and Application. Deerfield Beach, Fl (1994).

49. U.S. Patent 6,261,719; Inventors: T. Ikeda, S. Saito, Assigned to Yazaki Corp., Toyota Jidosha Kabushiki Kaisha, 17Jul2001.

50. U.S. Patent 6,152,776; Inventors: T. Ikeda, Y. Fukao, Assigned to Yazaki Corp., 28Nov2000.

51. M. Isaacson, R. Hollandsworth, P. Giampaoli, F. Linkowsky, A. Salim, V. Teofilo, The 15th Annaul Battery Conf. On Applic. & Advances, IEEE 00TH8490, ll-14Jan2000.

52. http://www.ctts.nrel.gov/BTM/

53. I. Rade, Requirement and Availability of Scarce Metals for Fuel-Cell and Battery Electric Vehicles, PhD Thesis, Chalmers Univ. of Technology and Goteborg Univ. (2001).

15

Charging, Monitoring, and Control

Walter A. van Schalkwijk
SelfCHARGE, Inc.
Redmond, Washington
Department of Chemical Engineering
University of Washington
Seattle, Washington
USA

1.0   INTRODUCTION

Traditionally, battery chargers are the lowest priority item for portable power systems, especially for cost-sensitive consumer products. To the battery user, the charger is simply a black box supplying electrons. Conversely, designers of battery chargers usually view the battery as a black box that should accept electrons. In recent years, the increased power of integrated circuits has greatly enhanced the sophistication of battery-powered equipment. Portable appliances, whether simple consumer items such as cellular telephones or more sophisticated medical appliances or electronic test equipment have greater and more dynamic power requirements and must operate under an increasingly wide range of environmental conditions, the most notable of which is a wide temperature range. The increased power of integrated circuits (ICs) is also an enabler for advanced charging, monitoring, and control of batteries.

Batteries combined with any monitoring and control electronics are referred to as "smart batteries". Smart battery technology produces accurate information about the state of a battery and enables optimal charge control. An additional factor driving batteries toward electronic control was the need to control individual cells, especially during charge, and to keep strings of cells balanced. This was especially true for early lithium-ion cells and batteries, which often had different operational voltages.

These conditions caused a move toward standardization of smart batteries. Critics objected because they desired to use a unique power management scheme. Manufacturers of battery packs were concerned that the standards would limit them to form factors that would limit their

ability to add value to their products. While there is no standard definition of a smart battery, Duracell defined a smart battery as "a rechargeable battery equipped with a microchip that collects and communicates present, calculated, and predicted battery information to the host system - notebook computer, cellular phone, etc. – under software control" [1]

2.0   SMART BATTERY AND THE SMBus

Smart battery technology is an artifact of engineering, but its impact on lithium-ion battery application deserves mention here. Batteries are dumb: they contain some interesting chemicals, but they contain no information about the energy content of the battery. The perfect battery pack would provide complete information on its history, condition, and imminent abilities under a variety of operational conditions. Portable electronic equipment is increasing in sophistication and in the jobs performed, especially in medical, telecommunications, and test equipment applications. The higher reliability demanded by these applications also demands more sophistication from the battery. These demands, along with the advent of inexpensive, yet sophisticated integrated circuits (ICs) gave birth to the era of the smart battery. Smart batteries are batteries equipped with microchips and often with sensors (temperature, voltage, and current). Early battery-control ICs date back to 1990.

Many batteries claim to be "smart" simply because of the presence of the IC. The IC may only identify the battery chemistry and tell the charger which algorithm to apply. Some batteries claim to be smarter because they control overcharging and over-discharging. Many companies are producing battery control ICs covering a wide cost-performance range. Even though there are some smart battery standards, the definition of a smart battery depends on the context of the application.

The architecture and cost-performance may require a single-wire system or two-wire system and a more sophisticated bus. In the single-wire system, only one wire is needed for data communication. There are wires for the battery positive and negative, and in most cases an extra wire for temperature sensing.

The single-wire system is widely used in cost-sensitive consumer applications where it measures temperature, voltage, and current and computes remaining charge. The system clock is embedded internally. In many cases, the current is not measured, but interpolated algorithmically. More sophisticated battery data, such as state-of-health (SoH) can be obtained if the battery pack is married to its host appliance (e.g., notebook computer). Software/firmware in the host provides further and enhanced analysis of the data over the life of the battery.

2.1 The Smart Battery Specification

A first attempt at standardization of smart batteries took place in 1993 with the introduction of the Smart Battery Specification (SBS) jointly developed by Intel and Duracell. The SBS was an attempt to standardize the communications protocol and data set for power management ICs to communicate with the rest of the system.

The specification defines a System Management Bus (SMBus) interface for Advanced Configuration and Power Interface (ACPI). It defines standard electrical and data interfaces and the smart battery data set (SBData).

The idea behind the SBS was to transfer charge control to the battery, rather than the charger. The battery would identify itself (chemistry, voltage, and size) to the charger and thus dictate the algorithm. The battery controls charge voltage and current levels as well as switching and cutoff levels. This enables a charger to charge more than one battery type.

The SMBus is a two-wire system where one wire handles data and the other handles the clock.

Full SBData implementation is defined as (1) execution of all 34 data value functions, including control and status flags, (2) meeting the accuracy and granularity (precision) requirements of all 34 data value functions, and (3) maintaining the proper SMBus timing and data transfer protocols [2].

The 34 data values can be divided into six categories:

1. Measurements
2. Capacity Information
3. Time Remaining
4. Alarms and Broadcasts
5. Mode, Status, and Errors
6. Historical and Identification

Measurements must take place at a rate that maintains the accuracy of the capacity information. There are other requirements for the timing and use of the data measurements that depend on the application. For example, a battery at rest or charging/discharging at a very low rate does not need measurements at the same rate as a battery charging or discharging at an appreciable rate.

The capacity values are rate-dependent (based initially on C/5 or P/5). Full implementation requires using both types of capacity units: use of power units yields the size of the battery from the data with no additional calculation. Granularity and accuracy also apply to these calculated values.

In the Specification, the granularity of time values is set to 2 minutes, but this may not be fast enough for some applications, especially where the discharge uses very dynamic current.

An SMBus battery contains permanent and temporary data. Permanent data are strings encoded at the time of manufacture. Temporary data is acquired during use.

A full description of the data types and their use can be found in References 2 and 3. The SMBus and specifications are maintained by the SBS Forum [3].

Full compliance with the SMBus Specification can be expensive. The SMBus is divided into three levels. Level 1 has been eliminated because it does not provide for chemistry-independent charging. Level 2 is in-circuit charging where the battery is charged within the appliance or the charging circuit is contained within the pack. Level 3 systems are full-featured external chargers.

Form factor: Many manufacturers have produced nickel-cadmium, nickel-metalhydride and lithium-ion batteries in the "35" and "202" form factors. The former chemistries are dumb batteries; the lithium-ion version has the full SMBus compliance. These packs are designed for use with full-feature chargers, but are sometimes used with chargers that are not in full SMBus compliance. This results in a cost savings, perhaps sacrificing performance and safety.
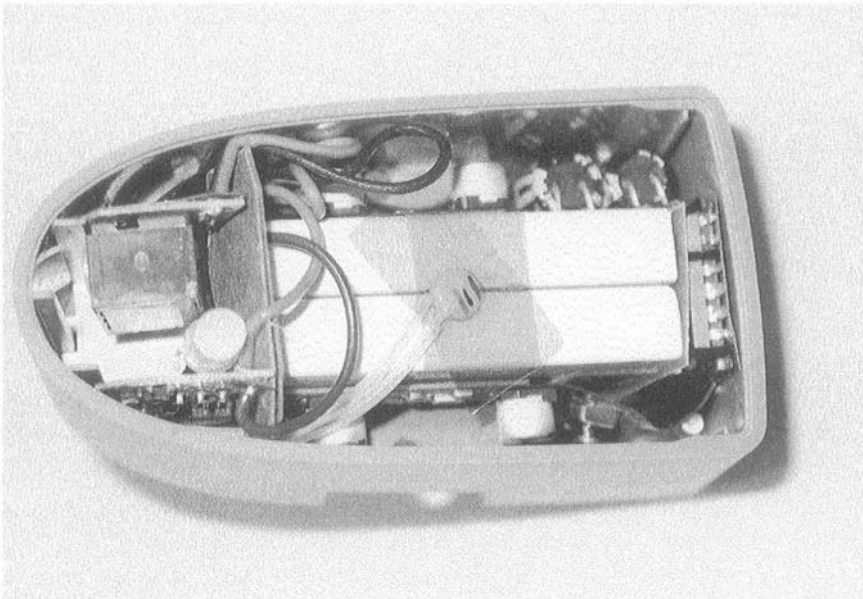
Figure 1. Lithium-ion battery charger with charging circuitry on-board and proprietary charge control. The proprietary architecture is essentially SMBus Level 2 "equivalent." Photo courtesy of SelfCHARGE, Inc.

SMBus batteries and Level 3 chargers are much more expensive than their less intelligent counterparts. In addition, many companies have chosen to implement their own application-specific battery management electronics using only the features they want for any given product. This often results in more components on the circuit board, but often with less cost. In other cases, an SMBus-capable IC is used, but its features are not fully implemented. Packs with on-board chargers can be SMBus Level 2 "compliant" or, if they use proprietary circuitry, they can be SMBus "equivalent" (Figure 1).

The SMBus for smart battery technology has not achieved the acceptance desired by battery manufacturers. Charging technology remains "charger-centric," largely because of economics and the lack of either a dedicated "power-systems" group at electronics manufacturers or a charger manufacturer that has a firm understanding of a battery chemistry´s capabilities.

2.2   Charge Balancing of Lithium-Ion Cells

The need to maintain the safety of lithium-ion cells and packs was one of the factors driving electronic battery management. When cells are combined in series or parallel configurations and operated without electronic protection, it is likely that one or more of the cells can be over-discharged or over-charged. Early versions of lithium-ion cells were not manufactured to the same tight specifications as those of today nor did they have thermal management as efficient as cells manufactured today. Even with the improvements, cells are often grouped in packs or embedded in products where they are exposed to an uneven thermal environment. Small differences in both the manufacture of the cells (capacity and impedance) and operational temperature can lead to cell imbalance.

If cells are connected in series, one cell will always reach full charge before the others. If voltage limits and charge balancing are not used, this can cause severe safety problems. The problem is somewhat less for lithium-ion cells with hard carbon electrodes. Resistive equalization is the most common method of balancing lithium-ion cells, but other methods have been used [4]. With resistive equalization, resistors are used in parallel with cells. The charge current to an individual cell can be bypassed when the cell reaches a maximum voltage.

3.0   CHARGE ALGORITHMS

Typically, the lithium-ion battery is charged by a voltage-limiting device, similar to that used for charging lead-acid or rechargeable alkaline-manganese cells. Voltage control is paramount for lithium-ion batteries and most manufacturers require cells to be controlled to within ± 25 to 50 mV per cell, depending on the cell chemistry, cell size, and manufacturer.

The standard charge algorithm for lithium-ion batteries is to apply a current of 1C to the battery until the cell voltage limit is approached. Here, the circuit switches to voltage control. As the maximum voltage is closely approached, the current drops steadily until charge is terminated at a current somewhere below 0.03 C, depending on the cell´s impedance (Figure 2). This is referred to as a constant-curent / constant-voltage, or CCCV algorithm.

Using the standard charge algorithm with an initial current of 1 C a lithium-ion cell achieves full charge in 2.5 to 3 hours. Increasing the initial current to 1.5 C (permitted by a few cell manufacturers) or 2.0 C (generally not allowed by the manufacturers) does not decrease the charge time appreciably. The cell may achieve a useable state of readiness (60 – 75% state-of-charge) in a shorter amount of time, but the voltage-control section of the algorithm is generally longer and the time to full charge is often about the same as for the 1 C initial charge.

Trickle charge is not applied for lithium-ion batteries because of the risk of overcharge and the accompanying deleterious reactions at anode and cathode. A topping charge is applied periodically to compensate for self-discharge and energy consumed by the battery protection electronics.
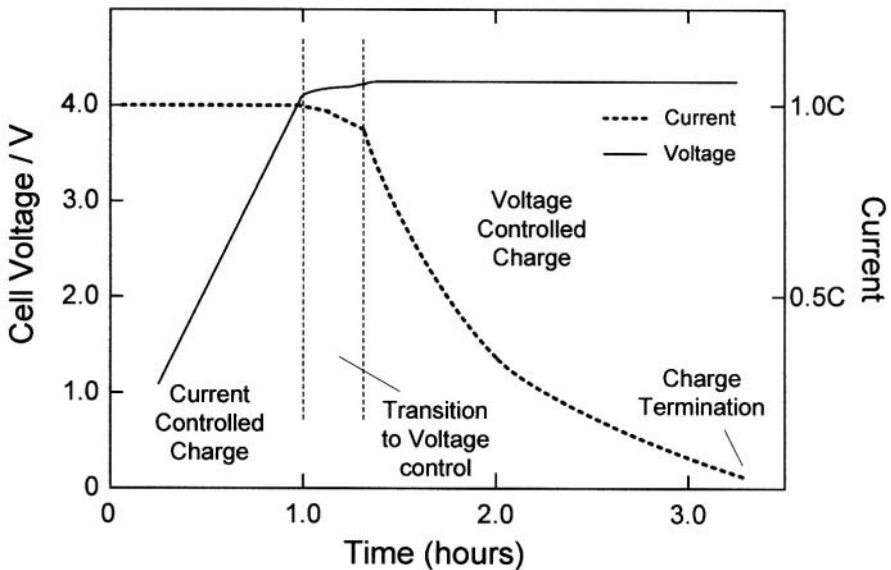
Figure 2. Stages of charge for a standard Lithium-ion charge algorithm.

3.1   *Fast-Charge Algorithms*

It is accepted in many quarters that fast charge methods for lithium-ion batteries either do not significantly decrease the charge time or that they are not safe. Many of the pulse charge techniques used for lead-acid,

nickel-cadmium, and nickel-metalhydride batteries use either an ad-hoc choice of pulses or a waveform designed to manipulate certain chemical and physical processes intrinsic to those battery chemistries. Even those algorithms where consideration has been given to the electrochemical processes, erroneous assumptions have been made which result in pulses that are not efficient: they are not properly tuned to the timescale of the electrochemistry. The electrode processes of the lithium-ion battery are different and do not respond well to the same type of pulse waveforms used for the other chemistries.

Charge algorithms based on ionic relaxation have been developed for lithoim-ion and lithium-polymer batteries but have been slow to be accepted or implemented commercially. This is not due to safety or operational considerations, but to the extra cost associated with a higher power, physically larger and more expensive charger. Some pulse charge algorithms using ionic relaxation are well known and have been developed with different electronic implementations, charge terminations, etc. [5-9].

For insertion anodes used in lithium-ion and lithium-polymer batteries there are several diffusion processes, each with its own time domain. When the battery is charged, each of these processes is occurring simultaneously (described from cathode-to-anode in the cell):

1. Lithium ions diffuse out of the cathode and enter the electrolyte where they are solvated by one or more solvent molecules. They may also form ion-pairs or ion-aggregates in solution, with each type of species having its own temperature-dependent concentration and mobility (diffusivity) in the electrolyte.
2. Driven by the electric current, the lithium-containing species in the electrolyte solution diffuse toward the anode where they form an electrochemical double-layer at the boundary between the electrolyte and the Solid Electrolyte Interphase (SEI). Hereafter this layer will be referred to as the "boundary layer."
3. Lithium ions shed their paired species (anions and solvent molecules) and enter the SEI where they continue to diffuse toward the carbon.
4. Lithium ions move from the SEI into the carbon where they continue to diffuse and occupy available sites in the carbon.

Each of these processes has an associated time constant. Diffusion of the lithium through the solids (carbon, lithiated metal oxide cathode, and SEI) is relatively fast. The processes occurring at and in the boundary layer are the slowest and are rate-limiting.

It is manipulation of the rate-limiting step that will lead to increased rates of charge for a lithium-ion cell (and battery). The processes occurring in a lithium-ion-polymer (a.k.a. lithium-polymer), and a lithium-ion-gel (a.k.a.

lithium-ion-polymer-gel) cell are essentially similar and can be assessed and manipulated by the same methods.

The treatment of the processes in the boundary layer (the boundary layer is that volume of the electrolyte, adjacent to the electrode, where the concentration of lithium ions is in flux and can be manipulated) is not mathematically rigorous nor phenomenologically detailed. The boundary conditions for this treatment are a consideration of the boundary layer with no flux of lithium ions (zero-current condition) and a constant flux (constant-current condition). The intermediate conditions are of interest because they have the ability to manipulate the boundary layer. These intermediate conditions are related to instantaneous current pulses or sinusoidal waveforms.

Most time-dependent diffusion problems in electrochemistry are governed by Fick´s Second Law of diffusion. Fick´s law is in the form of a differential equation, which implies that it describes what is common to all diffusion problems and not just the characteristics of a particular diffusion problem. Fundamentally, the concentration of a species (in this case, ions in solution and near the boundary layer) is a function of position and time

$$c = f(x,t)$$

The objective of pulsing the current into a battery or other electro-chemical device is to maximize the amount of active species, in this case lithium ions, in the boundary layer so they can participate in the battery reaction. In this way, with the concentration of active species (lithium ions) maximized in the boundary layer, the reaction of interest, i.e. charging the battery by inserting these ions into the anode can proceed at its fastest possible rate.

Diffusion toward a planar surface resulting from various waveforms such as a constant flux (constant current), sinusoidal waveforms, sawtooth waveforms and instantaneous pulses are developed mathematically and phenomenologically in chapter 4 of Bockris and Reddy [10].

When the instantaneous current of a square-wave pulse is applied to charging a lithium ion anode, lithium ions enter the carbon and are depleted in the boundary layer. This depletion is illustrated in Figure 3a. When the instantaneous pulse is terminated, there is a *relaxation* of the ions in the boundary layer as they are replenished in the boundary layer and the concentration of lithium-ions increases towards it´s zero-current value, c_o as seen in Figure 3b. If the off-time for the pulse is long enough, the concentration will eventually reach c_o. The problem is that a long off-time for the pulse (short duty cycle) results in a and low average current, so there is no intrinsic advantage to pulsing a lithium-ion battery with a short duty cycle.

A duty cycle (percent on-time for the pulse) must be calculated that will give a maximum time-average concentration of lithium-ions in the boundary layer (Figure 3c) while also producing a time-average current that is effectively fast relative to conventional charging.

The diffusion of lithium ions during the pulse will be determined by the applied current. During the off-time of the pulse the diffusion of Li^+ species in solution will be controlled by the diffusion coefficient of Li^+ in solution.

Thus the square-wave pulse must have a duty cycle that is determined by the flux of lithium ions toward the electrode as driven by the current, J_{on}, and replenishment of Li^+ ions in the boundary layer during the off-time of the pulse which is determined by D_{Li} in the electrolyte. A balance of the time constants associated with these processes will, for a particular applied current and temperature, determine the duty cycle for a square-wave pulse applied to charging lithium-ion batteries. This is duty cycle will maintain the maximum effective amount of lithium ions in the boundary layer for insertion into the anode Figure 4.
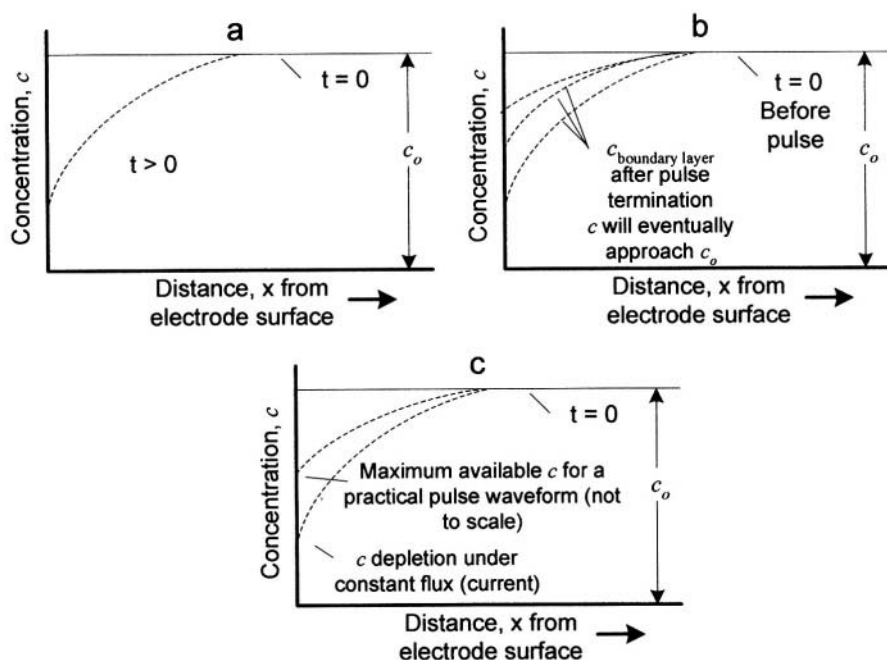
Figure 3. (a) Depletion of the concentration of (lithium) ions near the electrode surface under a constant current, **(b)** replenishment of ions in the boundary layer after termination of a current pulse, and **(c)** depiction of the maximum available concentration of ions in the boundary layer as a result of a current pulse (depletion) and rest (replenishment). The average current must me sufficient to allow a fast charge.
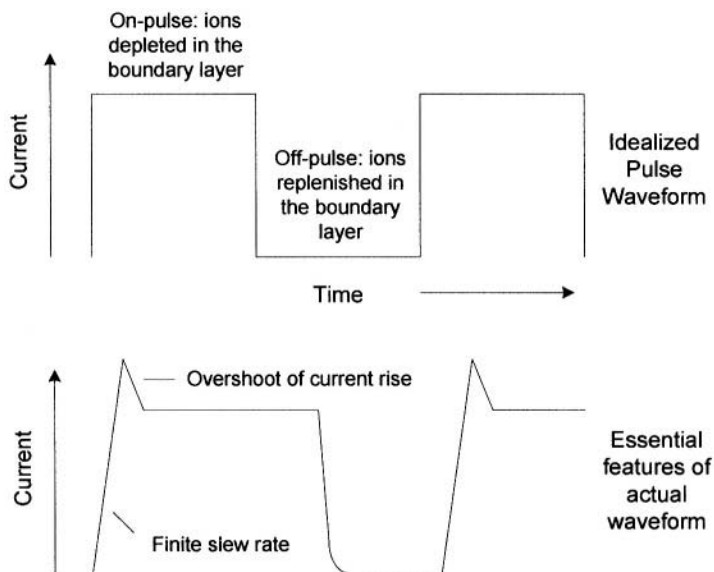
Figure 4. Waveforms for pulse charging of lithium-ion batteries (not to scale). During the on-cycle, lithium ions are depleted in the electrolyte as they are intercalated with movement driven by the current. During the relaxation, solvent can diffuse away from the electrode and ions back into the boundary layer.

3.1.1   *Application of a Pulse Charge Algorithm*

There are several ways to apply and terminate charge algorithms using a pulse algorithm. Two common ways are outlind below:

Charge may be applied as a constant current (constant flux) as is customary for lithium ion batteries. The constant current is applied until the battery reached a pre-determined battery voltage as measured by the charger circuitry, which includes integrated circuits commonly used to supervise battery operation. At the pre-determined battery voltage, the constant current is discontinued and the pulse charge algorithm is applied. When the constant current is removed, the battery voltage as measured by the charge circuitry will decrease slightly due to decreased polarization in the battery. The pulse algorithm is applied until the battery again attains a pre-determined voltage where battery charging is terminated. At no time during any pulse is the battery allowed to go above the voltage specified by the manufacturer. The voltage response to a pulse only becomes critical near the end of charge.

Alternatively, the algorithm can be applied from the start of charge. The amplitude of the charge current pulse can be as large as the 2 C-Rate. The pulse charge is continued until the battery reached a pre-determined voltage (switching voltage). At this pre-determined voltage, the pulse

charge magnitude is reduced and pulse charging is continued until the battery reached a pre-determined termination voltage that is higher than the switching voltage.

In all implementations, the cell voltages are monitored to assure that they remain safely below the maximum allowable cell voltage, V_{max}. Charge is terminated when the voltage response to the pulse charge reaches V_{max}, with the exact termination depending upon the accuracy and precision of the voltage measurement.

In practice, the implementation of a pulse-charge algorithm for lithium-ion batteries is more complex. There are two problems with square wave pulses. First, they are not actually square. There is a finite rise-time (slew rate) and decay upon pulse termination. The rise is often accompanied by an overshoot, which further complicates the waveform. Second, high slew rates will produce electronic noise that generally interferes with most electronic equipment and thus will probable not pass qualification tests by regulatory agencies. The answer is to use finite, but fast slewing rates that (1) approximates an instantaneous flux, (2) has minimal overshoot, and (3) does not cause unacceptable amounts of electronic noise.

This high frequency (low MHz) pulse-charge algorithm, has the perceived disadvantage of only charging the battery to 90 – 95% of full capacity, but reaching that capacity in 20 to 45 minutes. There are several advantages to this: (1) the battery reaches a high degree of operational readiness in a short time, (2) the battery spends little or no time at the high voltages where cell degradation, and (3) after a short time the battery will respond to a topping pulse charge applied with a smaller amplitude. It can be argued that the rest, followed by the topping charge makes pulse charging to 100% take as long as conventional charging, but the point is to safely bring the cells to 90 – 95% in a short time.

4.0   FUZZY LOGIC-BASED MONITORING OF STATE-OF-CHARGE OF LITHIUM BATTERIES

A key element in management of lithium batteries is the accurate and reliable determination of battery state-of-charge (SOC), whether or not the "history" of the battery is known from date of manufacture. Reliable SOC measurements are critical for many devices. Well-known interrogation techniques used to measure battery SOC include coulomb counting [11], voltage recovery [12], and electrochemical impedance spectroscopy (EIS) [13]. Often, these approaches yield data that is highly nonlinear, complex, or intractable, especially for rechargeable battery systems.

An emerging, powerful technique for estimating battery SOC is based on a fuzzy system methodology. Fuzzy systems provide a powerful means of

modeling complex, non-linear systems. In the case of batteries, the fuzzy system approach treats the battery as a black box and simply maps the input characteristics of the battery to its output characteristics without including any physical description of the underlying physico-chemical processes. The fuzzy system approach is a generic method that may be combined with any battery interrogation technique. Furthermore, the fuzzy system methodology can be applied to any battery chemistry, including both primary and rechargeable systems. The fuzzy logic approach may be developed with sparse experimental battery data, which is often insufficient or intractable for conventional analysis methods.

4.1 Fuzzy Logic Background

Measured data may be categorized by bivalent sets, or by fuzzy sets. For example, let us consider a sensor that measures air temperature. The range of possible temperature values can be regarded as a set of all temperatures. A subset of temperatures can be defined as the set of all temperatures between 20 °C and 30 °C. Let us call this subset the set of HOT temperatures. Obviously, a measured temperature value of 25 °C can be categorized as a HOT tempera-ture. Not so obvious is a measured temperature value of 22.5 °C. Is this still a HOT temperature? If so, does it belong to the set of HOT temperatures as much as 25 °C? Bivalent set theory says yes. Not only is 22.5 °C a HOT temperature, but the degree to which it belongs to the set of HOT temperatures, or its "membership value" or "bit" value (*b*inary un*it*), is identical to that of 25 °C, both a value of one. It would have to be according to Aristotle´s "either-or", "1-0", or "black-white" philosophy.

In contrast, a fuzzy set of HOT temperatures can be defined. This fuzzy subset can cover a range of temperatures as did the bivalent set, but now the degree to which a measured data point falls into the fuzzy set of HOT is indicated by a "fit" value (*fuzzy un*it*) *between* zero and one. The fit value is sometimes called the "degree of membership." Figure 5 shows examples of various fuzzy subsets or "membership functions" of the temperature. Depicted is the degree of membership of various temperatures to the fuzzy subsets COLD, WARM, and HOT. The process of assigning membership functions to sets of data is referred to as "fuzzification" of the data.

Fuzzy set theory provides a method to categorize measured data using linguistic variables such as cold, warm, and hot. It accounts for the uncertainty that is inherent in such a linguistic description by using multi-valued sets. Fuzzy systems map measured inputs to desired outputs. They estimate functions by translating the behavior of the system into fuzzy sets and by using rules based on a linguistic representation of expert knowledge to process the fuzzy data. This offers a qualitative rather than a numerical description of a

system. The linguistic representation presents an intuitive, natural description of a system allowing for relatively easy algorithm development compared to numerical systems. The ease of development of fuzzy logic systems should not undermine their powerful capabilities in terms of solving complex <u>control</u> and modeling problems.
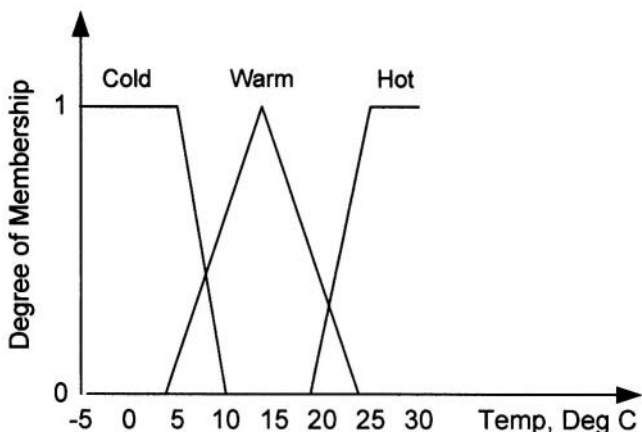
Figure 5. Membership Function for temperature.

A fuzzy system is illustrated in Figure 6 in which both the inputs and outputs are real-valued. The fuzzy system has four conceptual components:

1. a rule base describing the relationship between input and output variables,
2. a database that defines the membership functions for the input and in the case of Mamdani modeling, output variables,
3. a reasoning mechanism that performs the inference procedure,
4. a defuzzification block which transforms the fuzzy output sets to a real-valued output.

The rules relating the input and the output variables are written in an "if...then" linguistic format such as "*if temperature is cold and discharge rate is high **then** SOC is low.*" The "if "terms are referred to as antecedents and the term following the "then" is referred to as the consequent.
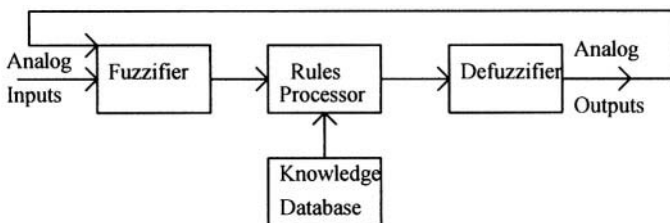
Figure 6. A complete fuzzy inference system.

The membership functions and rule set may be described by an expert or may be generated by use of neural network algorithms. Unsupervised neural networks, such as the subtractive clustering algorithm, can find the initial rules and membership functions using numerical training data that describe the input-output relationship. Supervised neural networks can fine-tune the rules and membership functions generated by the unsupervised neural network. The additive fuzzy system has been proven to be a so-called "universal approximator" that can be used for modeling and control of complex, non-linear systems [14].

An inference system commonly used to develop fuzzy models is the Mamdani fuzzy inference system. The Mamdani approach was developed in the 1970s and was the first inference method applied to control systems [15]. The Mamdani inference procedure describes the output variables as fuzzy sets. The approach uses max-min composition in which the *minimum* of the two antecedents is taken for a particular rule and the *maximum* combination of the rules is determined for aggregating the effects of all the rules. The effect of the max combiner on the output membership functions is to generate an "envelope" of the fired output membership functions. In order to defuzzify this output set, the centroid (weighted average) of the envelope is found by integrating over the 2-dimensional shape. The defuzzification process of the Mamdani approach is computationally intensive.

Another inference system commonly used is the Standard Additive Model (SAM). The SAM inference approach is based on correlation-product inference. This overcomes the loss of information associated with the correlation-min inference in the Mamdani inference method. Also, the additive-combiner in the SAM makes defuzzification simpler than the max-combiner of Mamdani inference. The additive-combiner also accounts for the information in the overlap of the fired output sets that the max-combiner ignores.

A more specific type of SAM is the Sugeno inference. In the Sugeno approach, the output set consists of a piece-wise linear function of the inputs rather than a fuzzy set. This makes the computation of the centroid, to defuzzify the output, much easier than in the Mamdani approach - the calculation simply involves taking the weighted average of a few piece-wise linear functions. In the simplest Sugeno model, in zero-order, the output is a singleton rather than a fuzzy set. For example, a typical fuzzy rule in a zero-order Sugeno model is

if x is A and y is B, then $z = k$

where A and B are fuzzy sets and k is a crisply defined constant. The more general first-order Sugeno model has rules of the form

if x is A and y is B, then $z = p*x + q*y + r$

where A and B are fuzzy sets and p, q and r are all constants.

There are two approaches to optimizing a fuzzy system model, supervised and unsupervised learning. By tuning the input and output membership functions the fuzzy system model may be optimized in a squared error sense. Expert knowledge or a neural network algorithm, such as the back propagation algorithm, may be used to optimize the fuzzy system model in supervised learning. In unsupervised learning, clustering algorithms may be used to find clusters in the input-output space in which initial membership functions and rules can be extracted. The system can then be fine-tuned using a neural network.

The development of fuzzy systems for modeling the discharge characteristics of secondary Li-ion batteries and fuzzy logic-based instrumentation for determining the SOC of Li primary batteries are presented here. The fuzzy systems were designed and simulated using the commercially available, mathematical software package MATLAB$^{®}$ and the Fuzzy Logic Toolbox for MATLAB$^{®}$ [6].

4.2   Fuzzy Logic Modeling of Li-ion Discharge Characteristics

We obtained charge-discharge voltage curves on commercial Sony 18650 Li-ion cells from Sandia National Laboratories. One set of charge-discharge voltage curves was modeled using a fuzzy logic method.
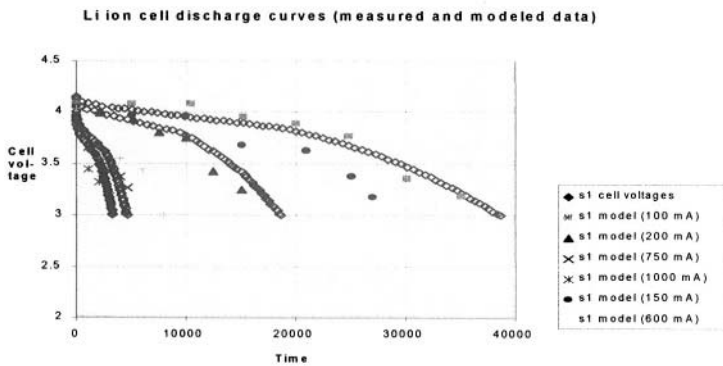
Figure 7. Li-ion cell voltage discharge curves for different discharge rates and fuzzy logic modeled data

Figure 7 shows a set of data on one particular cell taken at different discharge rates. The model is a 2-input 1-output fuzzy system consisting of 4 membership functions for the discharge current (input 1), 7 for time (input 2), and 7 for the cell voltage (model output). These membership functions are shown in Figure 8. The model also comprised 21 rules. The results simulated by the fuzzy model are shown as the symbols in Figure 7 along with the

original data (lines). As can be seen, good agreement is observed between the model-generated data and the original data. Furthermore, Figure 7 also shows some interpolated data generated by the model which was not provided in the original data set (discharge currents of 150 mA and 600 mA) which clearly demonstrate the powerful, accurate, nonlinear interpolation capability of the fuzzy logic methodology. Although this work is preliminary, and the model is not optimized, the results display good accuracy, generalization ability, and nonlinear interpolation capability using a relatively simple model. Thus, this example clearly demonstrates the power and capability of the fuzzy logic methodology as applied to Li-ion cells.
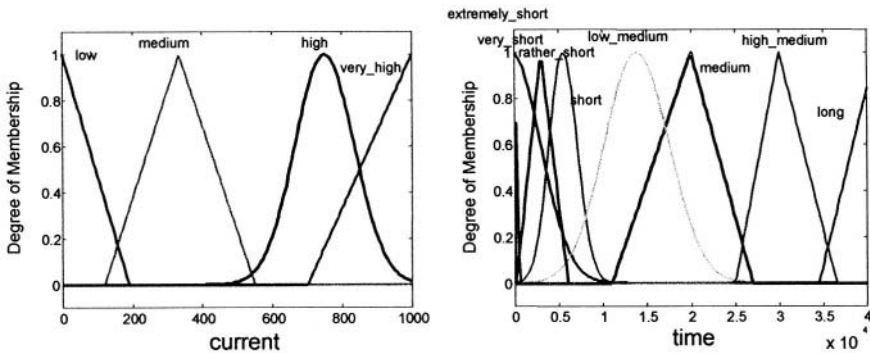
Figure 8a. Input membership functions for the Li-ion cell fuzzy logic model
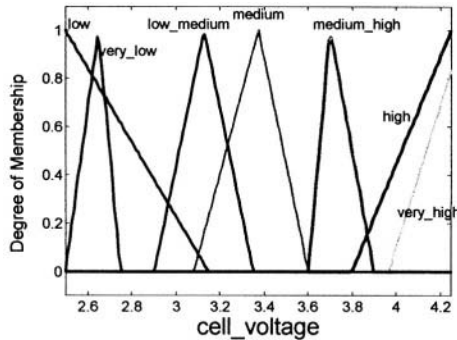
Figure 8b. Output membership function for the Li-ion cell fuzzy logic model.

4.3   *Fuzzy Logic-Based SOC Meters for Primary Li/SO₂ Cells*

4.3.1   *Coulomb Counting-based SOC Meter*

Primary Li/SO₂ cells are important for applications such as the SINCGARS radio. We have developed two fuzzy logic-based approaches to determining the SOC of these cells – one suitable for an internal meter based on Coulomb counting and another suitable for an external meter based on cell impedance measurements.

The internal meter is based on Coulomb counting, which integrates current over time. Since battery capacity is dependent on both the discharge rate and the temperature of the cell, compensation for these factors is required in order to provide accurate SOC determination. We used the data measured by Atwater [1] (summarized in Figure 9), showing battery capacity dependence on rate and temperature, as the basis for compensating available battery capacity in our coulomb counting based meter designs.
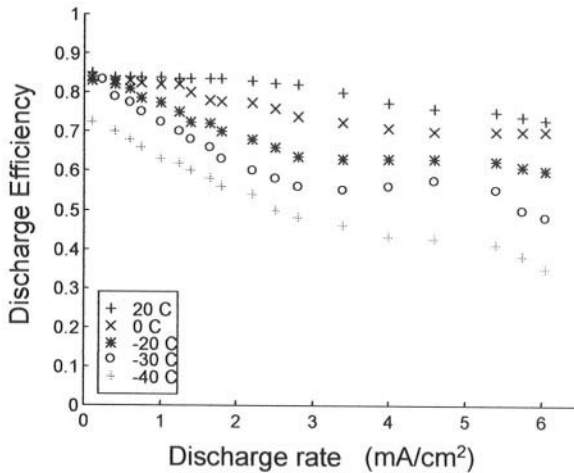
Figure 9. Discharge efficiency curves for Li/SO$_2$ cells
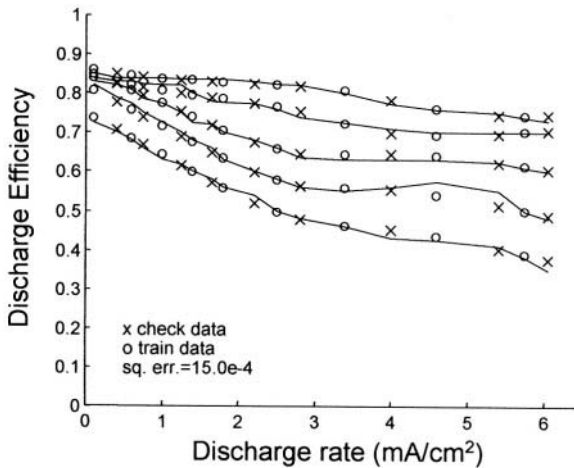
Figure 10. Optimized fuzzy Model Results for Li/SO$_2$ cells

A fuzzy logic model of this system was developed (see reference 17] for details) which took as inputs the cell temperature and the discharge current and output the discharge efficiency. The optimized model was a Sugeno model comprising 4 membership functions for discharge rate, 3 membership functions for temperature, and 5 rules. The accuracy of the

model is shown in Figure 10 where the x´s and o´s are model-generated data and the lines are mathematical curve fits to the original measured data. Furthermore, this model is also seen to have excellent interpolation ability as seen from the model´s response surface shown in Figure 11.
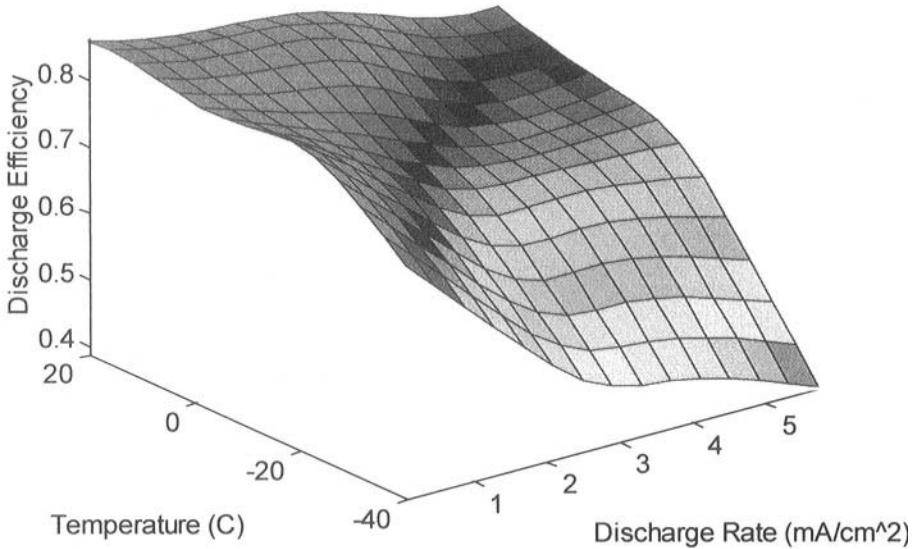
Figure 11. Surface showing interpolation ability of the fuzzy system.

The fuzzy model was used to compensate the available capacity of the battery with variations in temperature and discharge rate. The cell SOC was initially set at 100%. As the battery was being discharged, the available capacity was calculated by integrating the discharge current, subtracting this from the previously determined capacity and dynamically adjusting the available capacity using the discharge efficiency calculated by the fuzzy logic model. The advantage of this approach compared to using a lookup table in this case is that the fuzzy logic model is very code efficient (occupying only about 300 bytes of memory). Additionally, the fuzzy logic model allows for accurate, nonlinear interpolation between measured data points, a difficult task to accomplish analytically in a code efficient manner. Finally, this approach can also be extended to compensate for other factors in a secondary battery (such as cycle number, self-discharge, battery aging, etc.), which would not be easily implemented in lookup tables.

This algorithm has been into hardware using both a Motorola 68HC11 microcontroller and a Motorola 68HC12 microcontroller [18]. An application specific integrated circuit (ASIC) digital fuzzy processor which may be implemented directly into a battery has also been designed [9]. The Motorola 68HC11-based meter has been successfully field tested at the US Army CECOM Labs in Fort Monmouth, NJ.

4.3.2   *Impedance-Based SOC Meter*

Coulomb counting is an excellent means of determining battery SOC as long as the meter is always attached to the battery. However, if the meter cannot be integrated with the battery, an alternative approach must be used to determine the battery´s SOC. We have investigated the measurement of cell impedance in Li/SO_2 cells as a function of battery SOC to see if this can yield a useful means of determining cell SOC. Impedance measurements were made using a Solartron 1250 Frequency Response Analyzer and a PAR 273 Potentiostat /Galvanostat over the frequency range of 0.65 Hz – 65 kHz. An ac voltage signal of 10 mV amplitude was applied to the cell and the ac current response measured. The commercial software programs Zplot and Coreware (Scribner Associates) were used to collect the data. Four commercial 1.2Ah Li/SO_2 cells (PCI series) taken from two different production lots (2 from each lot) were measured. An impediment to obtaining useful impedance data with Li/SO_2 cells is the passivation film that grows on the Li anode in these cells. We found that a 30 sec. discharge at 200 mA was required prior to making the impedance measurements in order to obtain reproducible results. An example of some impedance data as a function of cell discharge rate and cell SOC is shown in Figure 12. Clearly between 90% SOC and 40% SOC there is a steady decline in the impedance independent of the discharge rate and cell production lot. Below 40% SOC, the two 50 mA curves are similar and the two 200 mA curves are similar. More spread in impedance is seen at a frequency of 4 kHz. By combining this data with that at other frequencies, a fuzzy logic model may be developed which infers SOC unambiguously from the impedance data. We have developed a model which takes the imaginary component of the impedance at 3 frequencies and predicts the SOC of the four Li/SO_2 cells, *independent of the production lot,* to within 10% of the measured SOC. This is despite the fact that each of the two cells from one production lot actually had an 8% lower capacity than the two cells from the other production lot. This shows the robustness of the fuzzy logic technique in practical terms as evidenced by the fact that a single meter is accurate for cells from different production lots. Details of this work may be found in Reference 20.

We have developed a prototype impedance meter to implement this approach. A block diagram of the meter is shown in Figure 13. The impedance measurement begins with a discharge of the battery under a high constant current load for 30 sec. This is followed by the application of a DC voltage to offset the battery voltage and the application of a small AC voltage (~ few mV) to the battery. The ac current response of the battery is fed to a lock-in amplifier together with the ac voltage as a reference. The phase and magnitude of the ac impedance is the output of the lock-in amplifier. The impedance measurement can be performed at several frequencies but we are presently only measuring the cell impedance at two or three frequencies. We have implemented these various circuits in discrete, analog hardware. The impedance measurements agree well with more accurate measurements taken using a Solartron Frequency Response Analyzer. Details of the circuit designs may be found in Reference 19.
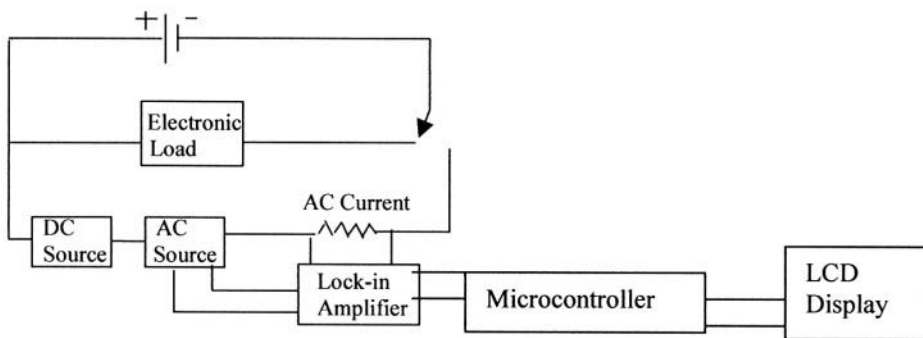
Figure 13. Block diagram of an impedance meter

4.3.3   *SOC Meter for Primary Li/MnO$_2$ Cells*

Li/MnO$_2$ cells are being phased in as replacements to the Li/SO$_2$ cells for military primary cell applications. We have therefore studied the development of a fuzzy logic based SOC meter for the Li/MnO$_2$ cell chemistry. The approach that we are pursuing for the Li/MnO$_2$ cell SOC is the impedance method. Up to this point we have measured eighteen 15 Ah Li/MnO$_2$ primary cells (flat mandrel design, hand crafted. Hawker series) using the Solartron Frequency Response Analyzer and PAR 273 Potentiostat/Galvanostat. By taking the real and imaginary components of impedance at 0.65 Hz and at 650 Hz, and the measured open-circuit voltage as the inputs to a 5-input, 1-output fuzzy logic model, where the output of the model is the SOC of the cell, the SOC of the cells could be determined to within about 10%, even with these hand-crafted, prototype cells! This underscores the power and robustness of the fuzzy logic methodology for determining battery SOC.

4.3.4   *Fuzzy Logic - Summary*

The fuzzy logic methodology offers a powerful and elegant means of determining the SOC of lithium batteries. We have demonstrated that this approach is very robust in that it can be used to measure the SOC of lithium batteries from different production lots as well as prototype cells. Although we have not yet demonstrated it, the fuzzy logic methodology also offers the prospect of taking account of several battery parameters, including self-discharge rate, cycle number, and battery aging in assessing the SOC of a battery. We have described several prototype hardware designs that we have implemented using the fuzzy logic methodology combined with conventional SOC measurement techniques for primary Li/SO_2 cells.

This approach has also been successfully applied to lead acid and NiMH chemistries [21-23] and can be easily extended to determining SOC of Li-ion cells.

5.0   ACKNOWLEDGEMENTS

6.0   REFERENCES

1.   A.W. Swager, *Electronic Design News,* March 2, 1995, p. 47.
2.   D. Friel, "The Importance of Full Smart Battery Data (SBData) Specification Implementation," PowerSmart Inc., 1998.
3.   http://www.sbs-forum.org
4.   M. Isaacson, R. Hollandsworth, P. Giampaoli, F. Linkowsky, A. Salim, and V. Teofilo, The 15th Annaul Battery Conf. On Applications & Advances, IEEE OOTH8490, 11-14 Jan 2000.
5.   U.S. Patent 5,569,259
6.   U.S. Patent 5,828,202
7.   U.S. Patent 5,905,364
8.   U.S. Patent 6,127,804, "Lithium-Ion Charging Means and Method Using Ionic Relaxation Control", J.W. Oglesbee, M.D. Green, J.E. Hermann, October 3, 2000
9.   U.S. Patent Application, "Lithium Ion Rapid Charging System and Method", W.A. van Schalkwijk, and R. Penn, April 2, 2002.
10.   J.O´M. Bockris and A.K.N. Reddy, "Modern Electrochemistry Volume 1: Ionics", 2nd Edition, Plenum Press, New York, 1998, Chapter 4.
11.   U.S. Patent 5,372,898, "Universal Inexpensive Battery State-of-Charge Indicator," T. Atwater and R.M. Dratler, Dec 13, 1994.
12.   U.S. Patent 4,725,784, A. Peled,; A. Peled, *Procs. 34th Power Sources Conf.,* 47 , 1992.

13.   F. Huet, *J. Power Sources,* **70,** 59-69, 1998.
14.   B. Kosko, *Fuzzy Engineering,* Prentice-Hall, NJ, 1997.
15.   E.H. Mamdani and S. Assilian, *International Journal of Man-Machine Studies,* **7,** 1-13, 1975.
16.   The Mathworks, Inc., Natick, MA.
17.   Pritpal Singh, Craig J. Fennie, Jr., Alvin J. Salkind, and David E. Reisner, *Procs. 38th Power Sources Conf.,* Cherry Hill, NJ, June 8-11, 1998, p. 295.
18.   P. Singh, V.R. Gaddam, S. Arey, Z. Yang, C. Fennie, and D.E. Reisner, *Procs. 6th Workshop for Battery Exploratory Development,* Williamsburg, VA, Jun 21-24, 1999.
19.   V.R. Gaddam, X.Q. Wang, S. Arey, Z.J. Yang, P. Singh, C. Fennie, and D.E. Reisner, *Procs. 39th Power Sources Conf.,* Cherry Hill, NJ, June 12-15, 2000.
20.   P.Singh, C.Fennie and D.E.Reisner, *Procs. 15th Ann. Batt. Conf.,* Long Beach, CA, Jan 11-14, 2000.
21.   Pritpal Singh, Craig J. Fennie, Jr., Alvin J. Salkind, and David E. Reisner, *Procs. 33rd IECEC,* Colorado Springs, CO, Aug 2-6, 1998.
22.   S. Arey, V.R. Gaddam, Z. Yang, P. Singh, C. Fennie, and D.E. Reisner, *Procs. EVS-16,* Oct 14-16, 1999, Beijing, PR China.
23.   P. Singh, Y.S. Damodar, C. Fennie, and D.E. Reisner, "Fuzzy Logic-Based Determination of Lead Acid Battery State-of-Charge by Impedance Interrogation *Methods" Procs. EVS-17,* Montreal, Canada, Oct 15-18, 2000

16

Electrochemical Supercapacitors

Marina Mastragostino
Francesea Soavi
University of Bologna
UCI Scienze Chimiche
Via San Donato 15
40127 Bologna
Italy

Catia Arbizzani
University of Bologna
Dip. Chimica "G. Ciamician"
Via F. Selmi 2
40126 Bologna
Italy

1.0   INTRODUCTION

Electrochemical supercapacitors are "novel" energy storage devices, which fill the gap of the Ragone plot between batteries and conventional dielectric capacitors. Supercapacitors, which are assembled like the batteries (two electrodes with a separator in an electrolyte), have much higher power and much longer cycle life (at least two orders of magnitude) but lower energy than batteries [1].

In the last few years the interest in Supercapacitors has increased enormously for applications ranging from the hybrid electric vehicle to consumer electronics. In the electric vehicle, Supercapacitors, operating in parallel with batteries or fuel cells, are expected to provide the power peaks during acceleration and hill climbing, especially with fuel cells, which have lower performance power than batteries. On the other hand, the power requirements for many portable electronic devices have increased dramatically, even to the point of exceeding the capability of conventional batteries, so that great attention is now being focused on Supercapacitors as energy storage systems, particularly on those in which high power density does not result in a drastic reduction in energy. The market for Supercapacitors of high power and energy is thus expected to increase in the future [2].

Research activity, which has been focusing on several classes of electrode materials, is spurring continuous advances in their energy storage capability and has yielded Supercapacitors with greatly improved performance. These devices are divided, on the basis of their energy storage mode, into two categories: the double-layer Supercapacitors and the redox Supercapacitors. In the former, energy storage is electrostatic in origin, the electrodes are high surface area porous carbon materials and the capacitance arises from charge

separation at the interface between the solid electrode surface and the liquid electrolyte. In the latter, fast Faradaic charge transfers take place at the electrode materials, as in a battery, and give rise to what is called pseudocapacitance. Two classes of pseudocapacitive materials have been investigated and developed: the conjugated conducting polymers and the transition metal oxides.

Carbon in its various forms has been the most widely studied electrode material, and the double-layer carbon supercapacitors, which at present are the most advanced version of the supercapacitors are already on the market with high performance products. The science and technology of supercapacitors for a number of electrode materials up to 1999, are excellently reviewed by Burke [3].

In this chapter we review and discuss the most recent advances in: double-layer carbon supercapacitors, with the emphasis on the most recent achievements in activated carbons for preseries supercapacitor prototypes [4-31]; polymer supercapacitors, with particular attention to polymer selection, cell design strategies and polymer cycling stability [32-52]; and metal oxide supercapacitors, with the main accent on ruthenium oxides, which are the most widely investigated inorganic pseudocapacitive materials [53-80]. New hybrid supercapacitor configurations in which one electrode is based on a pseudocapacitive material and the other on capacitive carbons are also reviewed and discussed [51, 81-85]. Finally, we report the most recent advances in nanostructured electrode materials, particularly carbon aerogels and nanotubes, and nanocomposites with ruthenium oxide and conducting polymers [86-99].

2.0   DOUBLE-LAYER SUPERCAPACITORS

Carbon electrodes are readily polarized and, although their electrical conductivity depends on carbon preparation, the carbon electrode materials are extremely attractive for their accessibility, easy processability and relatively low cost; additionally, they are non-toxic materials. They are available under several forms: activated powders, felts and cloths, xerogels and aerogels, and nanotubes. Activated carbon electrodes made by bonding activated carbon particles with a polymeric binder are the most widely used, but binderless activated carbon electrodes based on fiber cloths and felts are also in use. Carbon aerogels, produced by sol-gel processes, are also attractive alternative electrodes for double-layer supercapacitors (DLSs), and their characteristics are discussed in more detail in the last Section of this chapter devoted to nanostructured electrodes [5].

The main research efforts on DLSs have been devoted to the development of porous activated carbons of high specific surface area, and carbon materials

prepared following different procedures with specific surface areas up to 2500 $m^2 \cdot g^{-1}$ are presently available. Based on a double-layer capacitance of 20 $\mu F \cdot cm^{-2}$, very high capacitance values per unit geometric area of supercapacitor can, in principle, be expected: the higher the specific surface area of the carbon is, the higher are the values expected. However, in practice this is not true, and carbons with the same specific surface area do not yield devices with the same capacitance because pore-size distribution is of extreme importance. While the area of all the pores—micropores (pores width less than 2 nm, according to IUPAC classification), mesopores (between 2 nm and 50 nm) and macropores (larger than 50 nm)—contributes to surface area, only a fraction of the pores have suitable size for easy electrolyte access and contribute to electrode material capacitance [6,7]. Pore-size optimization has to take into account the dimensions of solvated ions, which are in different ranges in aqueous and in organic electrolytes. The size of solvated ions generally used in aqueous electrolytes (H^+, K^+, OH^-, SO_4^{2-}) is in the range 0.6-1 nm, and in the 2-5 nm range in organic electrolytes (for example, the size of propylene carbonate-solvated BF_4^- and Et_4N^+ is 2 nm and 5 nm, respectively). Thus, the same carbon material displays lower capacitance value in organic than in aqueous electrolyte.

The optimization of pore-size distribution for easy electrolyte access is an important issue [7-9]. At present, the best activated carbons in organic electrolytes display capacitance values of ca. 120 $F \cdot g^{-1}$, which are lower than those in aqueous electrolytes. On the other hand, only the use of organic electrolytes enables operating voltages above 2.5 V, and the high voltages significantly increase the amount of stored energy according to the equation $E = \frac{1}{2}CV^2$, where V is the voltage and C the capacitance. However, the organic electrolytes display higher specific resistance than the aqueous, and this results in an increase in the device's equivalent series resistance (ESR), which in turn affects the maximum power according to $P_{MAX} = V^2/4R$, where R is the ESR. The main contribution to ESR is the carbon resistance, which includes electronic and ionic components for charging the pores of small size, rather than the ionic resistance between the electrodes. Much effort has been and still is expended in the development of carbon materials with selected pore-size distribution to yield high-capacitance and low-resistance electrodes [10-12].

Impedance spectroscopy provides great insight into carbon electrode performance. For example, Figure 1 shows the impedance spectra of two DLSs with composite electrodes based on different commercial activated carbons (from PICA and Spectracorp) having almost the same composition in terms of activated carbon, binder and conducting additive, and with the same electrode mass loading (ca. 10 $mg \cdot cm^{-2}$) and organic electrolyte (propylene carbonate-Et_4NBF_4) [14]. Although the two carbons have almost the same specific surface area (~2000 $m^2 \cdot g^{-1}$), the two devices display different capacitance and ESR values. At low frequencies the capacitances are 0.28

$F \cdot cm^{-2}$ and 0.48 $F \cdot cm^{-2}$ (corresponding to **80** $F \cdot g^{-1}$ and **130** $F \cdot g^{-1}$ of activated carbon) and the ESRs **7** $\Omega \cdot cm^2$ and **17** $\Omega \cdot cm^2$ for the DLSs based on activated carbon PICA and Spectracorp, respectively. Given that the two devices have the same electrolyte and cell assembly, the bulk resistance, which also includes the electronic resistance of the current collectors, is the same, as demonstrated by the intercept on the Z_{re} axis for $\nu \to \infty$. The differences in the ESR values lie in the different charge resistance of the two carbons.
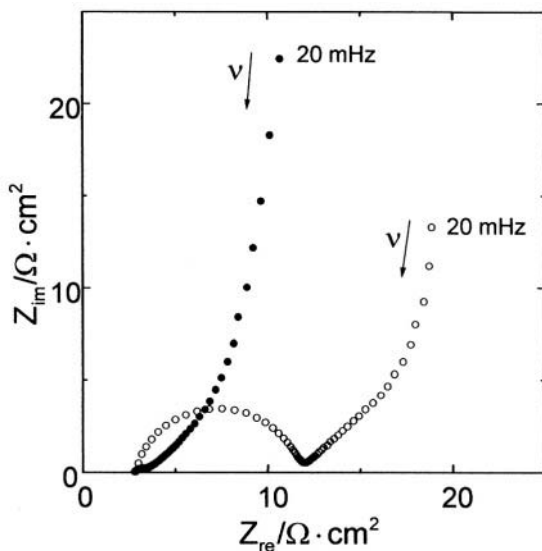
Figure 1. Impedance spectra (40 kHz-20 mHz) of (●) PICA and (○) Spectracorp activated carbon-based DLSs in propylene carbonate (PC)-Et₄NBF₄ [14].

The high-frequency semicircle displayed by the Spectracorp carbon-based DLS, which is due to the ionic and electronic resistance to the interconnecting of the smallest accessible pores in parallel with the capacitance of the macro-pores [15], is absent in the impedance spectrum of the PICA carbon-based DLS, indicating a different pore-size distribution for the two carbons. The impedance response for PICA carbon suggests that a large fraction of pores with easy access by the electrolyte is in the mesopore range, whereas the fraction of pores in the micropore range is not accessible. By contrast, the impedance response for the Spectracorp carbon suggests that a large fraction of pores is in the micropore range but with pore sizes sufficiently wide to be accessible by the electrolyte. The different morphology of the two carbons thus reflects upon the electrode performance, so that the more capacitive carbon is also the more resistive.

It should be noted that a high frequency semicircle can also appear for Faradaic reactions, which take place in the potential range of operation because of the presence on the carbon surface of functional groups that give

rise to a less-than-full electrostatic charge-discharge process of DLS. The presence of these functional groups, derived from certain carbon activation processes, is generally detrimental to device cycling stability [7].

Double-layer carbon supercapacitors on the market use either organic or aqueous liquid electrolyte and are characterized by specific energy and maximum specific power values up to **4 Wh·kg⁻¹** and **4 kW·kg⁻¹**, respectively, and time constants of a few seconds. Table 1 reports voltage (V), capacitance (C), ESR (R) from DC measurements (when not otherwise indicated), the specific energy (E), maximum specific power (**P$_{MAX}$**), weight and time constant (RC) of commercial products from several producers. Data for supercapacitor modules assembled with more cells are also reported. As an example, Figure 2 shows the constant current discharge characteristics of a commercial activated carbon DLS operating in organic electrolyte.

Table 1. Voltage (V), capacitance (C), ESR (R), specific energy (E), maximum specific power (P$_{MAX}$), weight and time constant (RC)

Supercapacitor	V V	C F	R mΩ	E=½CV² Whkg⁻¹	P$_{MAX}$=V²/4R kWkg⁻¹	Weight g	RC s
Single Cell							
EPCOS UltraCap 1200	2.3	1200	1.3	2.2	2.5	400	1.6
EPCOS UltraCap 1200	2.3	3600	3.0	4.1	0.7	650	11
NESS NESSCAP60C	2.3	60	25	3.1	3.8	14	1.5
NESS NESSCAP3500P	2.3	3500	0.4	3.2	4.1	800	1.4
MONTENA BCAP0011A01	2.5	800	2.4	3.3	3.1	210	1.9
MONTENA BCAP0010A03	2.5	2600	0.7	4.3	4.3	525	1.8
Maxwell PowerCache PC2500	2.5	2700	1	3.2	2.2	725	2.7
Matsushita-Panasonic UPB	2.3	1200	2.5*				3.0
Matsushita-Panasonic UPA	2.3	2000	3.0*				6.0
Module							
Maxwell PowerCache PC5.5 (2 cells)	5	1.8	800	0.8	1	8	1.4
Matsushita-Panasonic UPB	12	200	15*				3.0
Matsushita-Panasonic UPA	12	330	18*				5.9
EPCOS UltraCap (6 cells)	14	450	6.5	2.7	1.7	4500	2.9
EPCOS (17 cells)	40	67	23	1.9	2.2	8000	1.5

* ESR measured at 1 kHz

Several products are available from each manufacturer, differing mainly in size, capacitance and ESR and covering different fields of application from consumer electronics, wireless transmission, medical devices (like the MAXWELL PowerCache PC5.5) to UPS, hybrid electric vehicles, and fuel cells. As examples of supercapacitor application to hybrid electric transportation, General Motors and Allison have selected MAXWELL'S PowerCache supercapacitors for their hybrid vehicle, MONTENA has developed with HTA Luzern a hybrid prototype car with a supercapacitor module, and Siemens has manufactured a city bus with supercapacitor as the storage medium for regenerative braking, which enables a reduction of 25% in fuel consumption without compromising drive dynamics. To evaluate the impact of a supercapacitor module on a traction

system, a 1996 European Project within the JOULE III Program was set up to develop a DLS with an electronic control to be integrated into two different full-scale traction systems, supplied respectively by sealed lead batteries and by a fuel cell system [16].
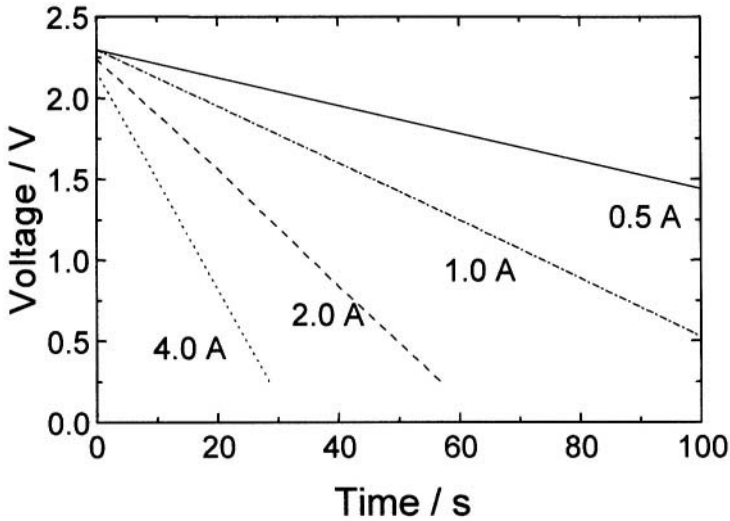
Figure 2. NESSCAP60C constant current discharge characteristics(by permission of NESS Corp., Korea).

Many manufactured carbon structures are available, including activated carbon powders, which yield electrodes via coating processes like those common in battery technology, and cloths, preferred by EPCOS [17] for their higher ESR stability and capacitance despite lower design versatility. The different performance of DLSs is determined not only by the kind of active material but also by electrode design, type of assembly (stack/wound), and lay-out of the terminals and of the current collectors; many research groups are involved in the development of supercapacitor prototypes, with attention being paid to cell design as well as to the selection of active materials and electrolytes [18-25]. By transferring the plastic lithium-ion battery technology to the field of supercapacitors Telcordia Technologies has used bonded microporous separators for ultra-thin design and very low ESR with light packaging material to develop a prototype based on commercial activated carbon NORIT ASupra (90 $F \cdot g^{-1}$), that delivers 6 $Wh \cdot kg^{-1}$ with a time constant of 1 s [18]. Another strategy in developing ultra-thin devices has been pursued using composite electrodes with gel electrolyte as binder material [19].

Studies for the selection of current collectors, the optimization of electrode preparation and electrode composition (in terms of percentage of active material, percentage and type of binder and conducting additive), have made it possible to significantly improve the characteristics of DLSs based on com-

mercial activated carbons and to develop low-cost 294 F module prototypes operating in organic electrolyte [20-24].

To date several commercial carbons have been investigated as electrode materials for supercapacitors: carbon blacks in aqueous electrolyte [26] and activated carbons from Spectracorp in aqueous [7] and from Spectracorp, Kynal Europa, NORIT and PICA in organic electrolyte [20-24,27,28]. Table 2 reports data from ref. [27]: the BET surface area of NORIT and PICA carbons, the carbon electrode capacitance and cell ESR evaluated from galvanostatic cycles in acetonitrile (ACN) or PC-Et$_4$NCH$_3$SO$_3$. These data show that PICACTIF is a very interesting material in that it displays the highest surface area and capacitance and the lowest charge resistance. These are key features in that it is generally reported for activated carbons that an increase in their specific surface area yields an increase in their charge resistance. As noted earlier, the optimization of carbon surface area and pore-size distribution is the goal in the development of high specific energy and power DLSs, and PICACTIF carbon seems to have achieved it.

Since single-cell supercapacitors are relatively low in voltage, most of the commercial products are modules featuring several cells connected in series; some manufacturers are also developing specially designed cell-voltage balancing units for safety reasons and energy content optimization [30, 31].

Table 2. BET surface area of different commercial carbons, carbon electrode specific capacitance and cell ESR values in ACN or PC with Et$_4$NCH$_3$SO$_3$.

Carbons	BET Surface Area m^2·g^{-1}	ACN-Et$_4$NCH$_3$SO$_3$		PC-Et$_4$NCH$_3$SO$_3$	
		Capacitance F·g^{-1}	Resistance Ω·cm^2	Capacitance F·g^{-1}	Resistance Ω·cm^2
Norit SX Ultra	1200	80	5	60	11
PICA B	2100	100	6	75	11
PICACTIF	2315	125	3.5	115	10

3.0 POLYMER SUPERCAPACITORS

Research is also focusing on pseudocapacitive materials such as π-conjugated electronically conducting polymers (ECPs). These display a pseudocapacitive behavior due to fast Faradaic charge processes involving all the polymer mass, called p- and n-doping processes, as in the Scheme 1 (M indicates the monomer unit, and A^- and C^+ indicate the counterions coming from the electrolyte) [32]. The potential values for these doping processes are related to the electronic state of the π–electrons in the conjugated polymers.

$$(M)_n + nyA^- \underset{undoping}{\overset{p\text{-}doping}{\rightleftarrows}} (M^{y+}A_y^-)_n + nye^-$$

Scheme 1

$$(M)_n + nye^- + nyC^+ \underset{undoping}{\overset{n\text{-}doping}{\rightleftarrows}} (M^{y-}C_y^+)_n$$
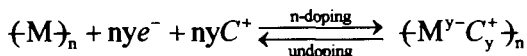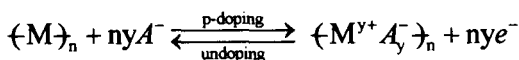
The use of ECP as electrode materials in supercapacitors was introduced in the mid 1990s by Rudge et al. [33, 34]. They suggested that there are different symmetric and unsymmetric types of supercapacitors involving ECPs in the p-doped only and in the p- and n-doped states. In the completely charged state, the p-type supercapacitors have one polymer electrode in the p-doped state and the other one in the undoped, the cell voltage being at the maximum 1 V for symmetric and 1.5 V for unsymmetric devices. Since in the completely discharged supercapacitors both polymer electrodes are in a partial p-doped state, only part of the polymer's total p-doping charge can be delivered by the supercapacitors. The viability of the p-doping/undoping processes of many polymers had already been demonstrated and the ECPs appeared very promising electrode materials for the following reasons: high capacitance (>200 F·g^{-1}), high conductivity in the doped state, fast kinetics of the doping/undoping processes, and low cost, at least for conventional ECPs such polypyrrole, polythiophene and polyaniline when compared to that of the ruthenium oxides and some activated carbons. Even the cycling stability of the ECPs, a much debated key feature for their use in supercapacitor technology, had been widely demonstrated for the p-doping/undoping process of many polymers.

By contrast, n-doping/undoping, is not as easy a process as p-doping and was significantly less studied at the time. Of conventional polymers, only the polythiophenes are n-dopable, in that only in these polymers does the injection of negative charge take place at potentials, which, although very negative, are still compatible with electrolyte and polymer stability. However, very negative potentials require dry and oxygen-free atmosphere, high-purified electrolyte with a wide window at negative potentials.

More recently, and also in view of the development of n/p-type supercapacitors which have n-doped and p-doped polymers as electrode materials, has much attention been devoted to the n-doping of polythiophene derivatives. In fact, the n/p-type supercapacitor is, among the proposed types, that can outperform the activated carbon DLSs as all the doping charge is delivered during discharge and potentials as high as 3.0 V can be reached. In the charged state, the n/p-type supercapacitor has the polymer of the negative electrode in the n-doped state and that of the positive in the p-doped, whereas in the fully discharged state both polymer electrodes are in the undoped state. Scheme 2 shows the charge-discharge reactions for a symmetric device.

$$\underset{n}{(M)} + \underset{n}{(M)} + nyC^+A^- \underset{\text{discharge}}{\overset{\text{charge}}{\rightleftharpoons}} \underset{}{(M^{y+}A_y^-)} + \underset{n}{(M^{y-}C_y^+)} \qquad \textbf{Scheme 2}$$
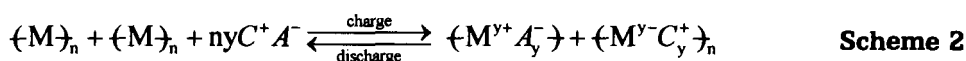
The n/p-type supercapacitors are thus the most promising in terms of specific energy, and they have a further advantage in a high power over the p-type supercapacitors in that the charged device has both electrodes in the

conducting state. High operating potentials up to 3 V are attainable by virtue of the potential separation between the p- and n-doping processes, which is related, when the supercapacitor is symmetric, to the polymer energy gap between conduction and valence bands. Such high potentials are feasible only in organic electrolytes, and electrolyte optimization, even in terms of salt concentration, is an important goal since in the n/p-type supercapacitors, as in the DLSs, the salt is consumed during device charge and it is released during discharge (see Scheme 2).

As Rudge et al. have noted [35], supercapacitors based on ECPs could equally well be described as batteries. Indeed, in the early 1980's Kaneto et al. [36] proposed a polythiophene-based battery in which the electrodes become p- and n-doped upon charge, and undoped upon discharge. A criterion that can be used to distinguish batteries and supercapacitors might be the function they are expected to explicate in terms of specific energy and power. A supercapacitor is required to deliver a high specific power for a short period (10-30 s), whereas the stored energy is significantly lower than that in batteries.

There are many, even recent, examples in the literature of p-type symmetric supercapacitors operating in aqueous [34,37] and in organic electrolytes [34,35,38-41] in which one p-dopable polymer, such as polyaniline, polypyrrole or poly-3,4-ethylenedioxythiopene, is the active material on both electrodes, and p-type unsymmetric supercapacitors [35,38,41] based on two p-dopable conventional polymers (such as polypyrrole, polythiophene, poly-3-methylthiophene and polyaniline) selected by virtue of the difference in potential ranges over which they become p-doped, although their performance is not competitive with that of the DLSs on the market.

In order to facilitate the n-doping process, many polythiophene derivatives have been developed by engineering the thiophene monomer unit to tune the potentials at which the n-doping process takes place [42,43]. Different strategies have been pursued and many interesting monomer units have been prepared, and thus many interesting polymers, but these new tailor-made polymers generally come at a cost that is too high for an industrial application such as in supercapacitors. Furthermore, the addition of substituent groups generally yielded heavy monomer units, so that for the corresponding polymers a larger amount of injected charge is required compared to polythiophene to meet the criterion of high values of the specific parameters, and this can also adversely affect the polymer cycle-life because of the greater mechanical stress affecting the polymer materials.

Symmetric n/p-type supercapacitors based on such non-conventional polymers as polydithienothiophenes [38,44], poly3-phenylthiophene fluorinated derivatives [33,35,44-46], polycyclopentadithiophenone [47], polycyano-substituted-diheteroareneethylenes [48], and unsymmetric n/p devices mainly based on polythiophene, poly-3-methylthiophene and poly-3-*p*-fluorophenyl-

thiophene [49,50] have been developed and, as expected, demonstrated the best performance in terms of specific energy and power among the polymer Supercapacitors, although few cycling stability data for the n/p type super-capacitors are available. It would thus seem opportune to take a closer look at conventional polymers such as poly-3-methylthiophene (pMeT), which is based on a light-weight monomer unit and whose high cycling stability for several thousand galvanostatic charge-discharge cycles in a symmetric n/p-type device has been demonstrated [50]. A conventional polymer like pMeT also has the advantage of low cost: it can be easily prepared both chemically and electro-chemically from the commercial monomer unit.

For the development of supercapacitor prototypes, electrode lamination on current collectors of composite pastes based on ECP, conducting additive and binder has been the preferred route. An optimized cell design is a prerequisite for a well performing, long-life device and it requires the optimization of electrode composition, mass loading and balancing, in addition to that of the electrode active material-to-electrolyte mass ratio [44]. Optimization of this ratio has to take into account (as in the case of activated carbon DLSs) that the electrolyte salt concentration should be sufficiently high so as not to limit the electrode´s capacitance and to assure high conductivity after the device´s charge to minimize the bulk ionic component of its ESR. Electrode mass loading of active material that is too low has poor practical significance and can lead to an overestimation of the device specific energy and power; a total electrode mass loading for both electrodes of ca. $20 \ mg \cdot cm^{2}$ is a value of practical interest. Optimization of elec-trode mass loading and balancing has to take into account the characteris-tics of the charge processes of the polymer electrodes, which, as reported in reference 51, can perform differently in terms of specific capacitance as well as capacity for the p- and n-doping processes.

In reference 51 the performance data of an n/p type pMeT-based super-capacitor operating in $PC-Et_4NBF_4$ with an optimized cell design are reported. Given that pMeT as positive electrode displays a capacitance value per gram of pMeT double that of the pMeT as negative, and the optimized content of pMeT in the composite electrodes is 80% w/w for the positive and 55% for the negative electrode, a mass per cm^2 of the composite negative electrode three times that of the positive was estimated for an optimized cell. Figure 3a shows the voltage profile of a charge-discharge galvanostatic cycle at 5 $mA \cdot cm^{-2}$. To compare the performance of this n/p pMeT supercapacitor with that of a DLS based on activated carbon of high specific area, with 90% w/w activated carbon content, the voltage profile of a DLS tested in the same experimental conditions are in Figure 3b. The total mass loading per cm^2 was almost the same for both Supercapacitors (ca. $20 \ mg \cdot cm^{-2}$). The specific energy (E) and average specific power (P_{av}) of the two Supercapacitors were 13 $Wh \cdot kg^{-1}$ and $700 \ W \cdot kg^{-1}$ for the n/p-type pMeT-based device and $26 \ Wh \cdot kg^{-1}$

and **335 W·kg^{-1}** for the DLS, evaluated from the discharge curves according to

$$E = i \int_{t}^{t+\Delta t} V \, dt / m \quad \text{and} \quad P_{av} = E/\Delta t_d$$

where i is the current density, V the cell potential, m the total mass of the positive and negative composite electrodes per cm^2 and Δt_d the discharge time. Although the n/p-type supercapacitor delivers all the doping charge at high potentials, its specific energy is significantly lower than that of the DLS, mainly because the low conductivity of the pMeT n-doped state does not allow a polymer content higher than 55% for the negative electrodes and because the capacitance of the n-doped form is lower than that of the p-doped.
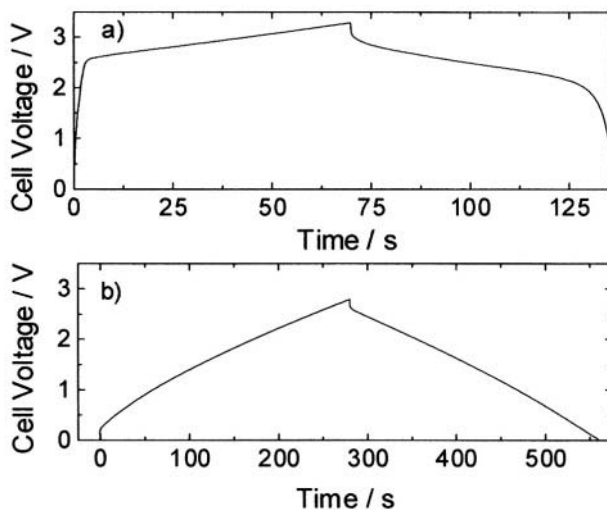
Figure 3. Galvanostatic charge-discharge curves at 5 mA cm^{-2} of
(a) n/p pMeT supercapacitor [negative electrode: 55% pMeT (7.6 mg), 40% SFG44 graphite, 5% binder; positive electrode: 80% pMeT (3.1 mg), 15% SFG44 graphite, 5% binder] and
(b) DLS [negative and positive electrodes: 90% activated carbon (9.0 mg), 5% SFG44 graphite, 5% binder].

In the above ECP-based supercapacitors, the polymer capacity is determined entirely by the electrochemical reaction of the π-conjugated systems. Naoi et al. [52] are pursuing a new polymer engineering strategy to combine the redox process of the π-conjugated system with that of other high specific-capacity electroactive moieties. They have demonstrated that an electroactive moiety such as quinone (Q/Q$^{•-}$/Q^{2-}), when condensed between two aniline moieties, yields a polymer, poly-(l,5-diaminoanthraquinone).

which displays a high specific capacity, high electrical conductivity, wide potential window and fast redox processes. They have also tested the viability of this polymer as both anode and cathode in a "novel" type of supercapacitor and evaluated the device's specific energy and power. These data are of practical interest yet could be further validated by tests on thicker polymer films.

4.0   METAL OXIDE SUPERCAPACITORS

Metal oxides are the other class of pseudocapacitive materials which have been investigated for supercapacitor applications, the ruthenium oxides (RuO_2 and $RuO_2 \cdot xH_2O$) having been especially studied. The pseudo-capacitance in these materials arises from very fast and reversible Faradaic protonation processes on the surface (or in the bulk). The electrochemical reactions for RuO_2-based positive and negative electrodes are

$$HRuO_2 \xrightleftharpoons[\text{discharge}]{\text{charge}} H_{1-\delta}RuO_2 + \delta H^+ + \delta e^-$$

<div align="right">**Scheme 3**</div>

$$HRuO_2 + \delta H^+ + \delta e^- \xrightleftharpoons[\text{discharge}]{\text{charge}} H_{1+\delta}RuO_2$$

and the overall reaction is
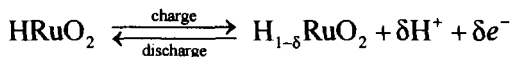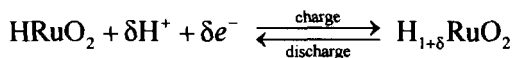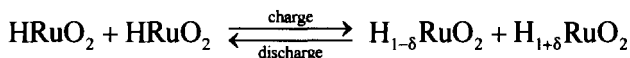
$$HRuO_2 + HRuO_2 \xrightleftharpoons[\text{discharge}]{\text{charge}} H_{1-\delta}RuO_2 + H_{1+\delta}RuO_2 \qquad \textbf{Scheme 4}$$

where $0 < \delta < 1$ (similar reactions take place in $RuO_2 \cdot xH_2O$). The proton moves from one electrode to the other throughout the electrolyte solution, and RuO_2 and H_2RuO_2, respectively, represent the positive and the negative electrodes at the fully charged state of the cell. Unlike the carbon-based DLSs and the n/p-type polymer supercapacitors, the metal oxide supercapacitors keep the salt concentration of the electrolyte constant during the charge and discharge.

Amorphous hydrous ruthenium oxide, $RuO_2 \cdot xH_2O$, prepared by sol-gel process at low temperature, is an especially promising material because of its high capacitance, good conductivity and electrochemical reversibility [53, 54]. The high specific capacitance is due to the fact that the Faradaic reaction can occur not only at the surface of the electrode material but also in the bulk, as the proton can easily enter the bulk of the amorphous $RuO_2 \cdot xH_2O$. In other metal oxides and crystalline RuO_2 itself, only the surface is involved in the charge storage process. While the highest specific capacitance value for crystalline RuO_2 is 380 $F \cdot g^{-1}$ for a surface area of 130 $m^2 \cdot g^{-1}$, a specific capacitance of 768 $F \cdot g^{-1}$ has been reported for an amorphous hydrous RuO_2 of a surface area of 68.6 $m^2 \cdot g^{-1}$ [53].

As the RuO_2-based supercapacitors work in aqueous solution, their maximum working potential is ca. 1 V, and this is a disadvantage for their energy storage capability. A symmetric supercapacitor based on the $RuO_2 \cdot xH_2O$ electrodes with H_2SO_4 as electrolyte, has shown a specific energy of 26.7 Wh·kg^{-1} (only the weight of the electrode materials is included), with good stability over 4000 cycles (10% capacity fade) [53]. Enhanced electrochemical stability has been found with hydrogen-inserted hydrous ruthenium oxide electrodes: these cells exhibited a cycle-life over 60000 cycles with high energy and power [55]. It has been established that in supercapacitors thus far developed with activated carbon-ruthenium oxide composite electrodes, over 50% of the cell's internal resistance is contact-related. Thus, a new preparation method of amorphous RuO_2 films on metallic tantalum substrate has been developed, with the electrodes displaying high performance [56].

Although the amorphous hydrous ruthenium oxide has been shown to be an excellent electrode material because of its high specific capacitance, the high cost of ruthenium is a marked disadvantage for use in such large-scale applications as supercapacitors. Much research effort has thus been directed to enhancing the capacitance of RuO_2 itself, to developing RuO_2-based electrodes with a lower content RuO_2, or to identifying less expensive oxides [57].

Enhanced capacitances have been achieved by preparing extremely fine RuO_2 particles with a porous network in a coated-oxide layer with the addition of salts or rare-earth elements in the dip-coating procedure on Ti substrates, or by preparing ultra fine RuO_2 particles with the addition of a salt catalyst in a sol-gel process [58].

Reduction of the ruthenium content has been pursued in different ways: preparing the Ru-based binary oxide electrodes RuO_2-VO_x/Ti and RuO_2-MoO_x/Ti by dip-coating method [59,60], preparing tungsten and ruthenium oxide composites by precipitation of amorphous ruthenium oxide on the surface of amorphous tungsten oxide [61], doping RuO_2 with Cr (and samples with Cr content y = 0.15 displayed good cyclability with initial capacitance of 740 F·g^{-1} [62]), using strontium ruthenate perovskite [63], and preparing Pb/Ru pyrochlore ($Pb_2Ru_2O_{6.5}$), with which small laboratory-scale prototypes have already been tested [64]. These prototypes have exhibited excellent performance: unpackaged specific energy over 5 Wh·kg^{-1} even at 750 W·kg^{-1} power level.

Another approach that minimizes Ru content is to combine large surface area materials with RuO_2. Supercapacitors based on activated carbon and ruthenium oxides were developed by Zheng et al. in 1996 [65] and recently optimized [66]. They demonstrated that the addition of carbon black with a high surface area (1300 m^2·g^{-1}) increases electrode porosity, a benefit for the proton transfer within the electrode. In addition,

the composite electrode absorbs a great amount of electrolyte, a feature which is also advantageous for the kinetics of the electrochemical process, which yields high capacitances even when the voltage scan rate is high, as shown in Figure 4.

Efforts have also been expended to identify less expensive oxides such as NiO [74, 75], MoN_x [76], Ti-V-W-O/Ti [77], CoO_x xerogels [78] and $H_3PMo_{12}O_{40} \cdot xH_2O$ [79]. A severe limitation of nitrides is that their decomposition or dissolving takes place beyond 0.6 V, NiO and Ti-V-W-O show very low capacitance, whereas the capacitance of CoO_x xerogels is promising (291 $F \cdot g^{-1}$), even if lower than that of RuO_2. Interesting is the study on $H_3PMo_{12}O_{40} \cdot xH_2O$: a comparison of the performance of an unsymmetric supercapacitor based on $H_3PMo_{12}O_{40} \cdot xH_2O$/Nafion 117/$H_\alpha RuO_2 \cdot xH_2O$ and of a symmetric $H_\alpha RuO_2 \cdot xH_2O$/$H_2SO_4$/$H_\alpha RuO_2 \cdot xH_2O$ cell, shows that the energy density of the former (10 $Wh \cdot kg^{-1}$) is 40% that of the latter but it has higher energy and capacitance per unit cost, i.e. 20.8 mWh per US\$ vs. 2.8 mWh per US\$, and 250 F per US\$ vs. 40 F per US\$ [79, Editor´s note: figures are based roughly on 1998 dollars].
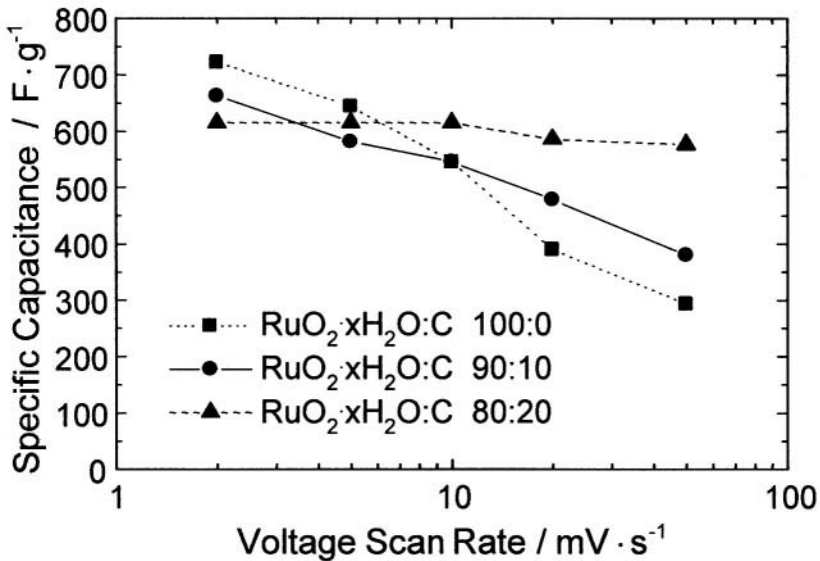
Figure 4. The specific capacitance as a function of voltage scan rate for an electrode made with (■) $RuO_2 \cdot xH_2O$, (●) 90% $RuO_2 \cdot xH_2O$ and 10% carbon black, and (□) 80% $RuO_2 \cdot xH_2O$, and 20% carbon black [66]. Reproduced with permission from The Electrochemical Society, Inc.]

Other oxides, too, can store high charge when highly dispersed and nanosized. Sugimoto et al. have reported that nanosized MoO_3 produce an extremely large pseudocapacitance (ca. 1000 $F \cdot g^{-1}$ at 0.5 $nmol \cdot cm^{-2}$ loading) when highly dispersed on glassy carbon, and that MoO_3-activated carbon composite electrodes, prepared by a simple impregnation method, show a

specific capacitance of **170 F·g⁻¹**, 29% higher than the pristine activated carbon capacitance **(132 F·g⁻¹)**, and a good cycling stability with only an MoO_3 loading of 1% w/w [80].

5.0   HYBRID SUPERCAPACITORS

One successful strategy has been the development of a new super-capacitor design: a hybrid supercapacitor in which the two electrode active materials are charged and discharged with different processes, electrostatic and Faradaic. In other words it is a supercapacitor based on capacitive carbon as negative electrode and pseudocapacitive material as the positive.

The first investigated hybrid configuration derived the positive electrode from a battery technology: the ELIT Co. (Russia) has developed hybrid C/NiOOH supercapacitors with activated carbon and KOH electrolyte for a maximum operating potential of 1.4 V. These supercapacitors have, for current densities in the 1–40 A range, a specific energy from 3.2 to 1.8 Wh·kg⁻¹ and specific power in the **70-2700 W·kg⁻¹** range [81]. The idea of a hybrid C/NiOOH supercapacitor has more recently been developed further, the final goal being a nanostructured cell delivering **15 Wh·kg⁻¹** and **5 kW·kg⁻¹** [82].

Very interesting results have been attained with a hybrid configuration based on activated carbon as negative electrode and electronically conducting polymers as pseudocapacitive positive electrode materials. Undertaken as part of the European JOULE III Programme, this work has led to 1.7 kF module prototypes based on poly-3-methylthiophene, which outperform commercial DLSs in terms of specific energy and power and are competitive with them in terms of cycle-life and materials cost. The development of these polymer hybrid supercapacitors takes into account that p-doped conducting polymers are materials of higher specific capacitance than carbons, their charging resistance is lower, and their cycle-life is generally satisfactory for supercapacitor technology [51, 83-85]. Given that, as noted in Section 3, an n/p-type polymer supercapacitor configuration is not viable because of limitations related to the n-doped negative electrode, a configuration with carbon as negative and polymer as positive appeared a favorable trade-off: it increases device capacitance and reduces cell ESR in order to achieve higher specific energy and power than DLSs.

Scheme 5 reports the charge-discharge processes for the polymer hybrid supercapacitor based on pMeT.
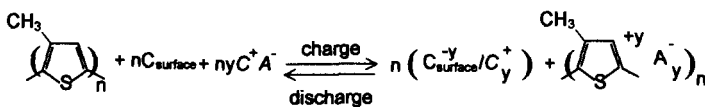
Scheme 5

Particularly for performance of this hybrid system, the optimization of electrode mass loading and balancing is a very important, and intricate, matter. While carbon DLSs are assembled with the same mass loading for both electrodes, and the n/p-type polymer supercapacitors assembled by taking into account the specific capacitance of the two electrodes, the balancing in hybrid supercapacitors must take into account both capacitance and different potential ranges for the charge processes of the two electrode materials. Since the Faradaic charge process of pMeT takes place in a potential range of ca. 0.5 V, a potential excursion of at least 2 V for the charge process of an activated carbon capacitive electrode is required to reach potentials higher than 2.5 V for the charged supercapacitor. Thus, this hybrid supercapacitor was assembled with an active mass loading of the positive electrode higher than that of the negative [83].

Figure 5 shows the voltage profile of the C/pMeT hybrid supercapacitor and of each electrode upon charge-discharge at 5 mA·cm^{-2} between 1.0 and 3.0 V. This supercapacitor, which has a 1.5 mass ratio of positive to negative active electrode material has delivered the promising values of **19 mAh·g^{-1}** of active materials at potentials higher than 1 V and showed a capacitance of **0.62 F·cm^{-2}** (from the discharge curve of plot a), i.e. **39 F·g^{-1}** of total active materials.
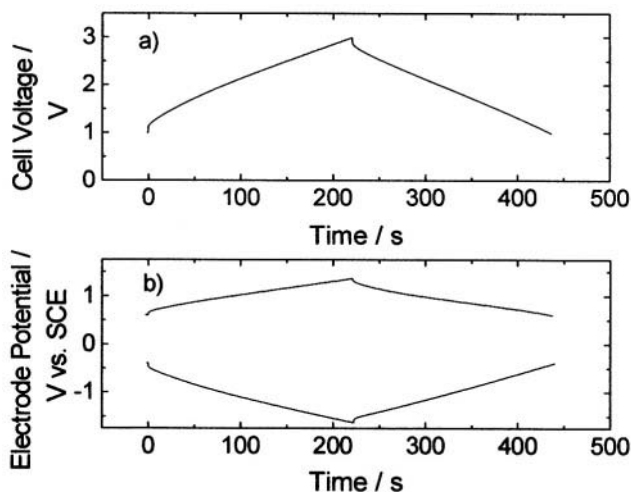
Figure 5. Voltage profile **(a)** of the C/pMeT hybrid supercapacitor and **(b)** of each electrode upon charge-discharge at 5 mA cm^{-2} between 1.0 and 3.0 V. The negative and positive composite electrode compositions were 90% activated carbon, 5% SFG44 graphite, 5% binder, and 80% pMeT, 15% acetylene black, 5% binder, respectively [83]. Reproduced with permission from The Electrochemical Society, Inc.

The advantage of using a p-doped pMeT positive electrode is depicted in Figure 6, which reports the impedance spectra of the C/pMeT hybrid supercapacitor and of its pMeT positive electrode, clearly indicating the low contribution of the polymer electrode to device ESR and its high specific capacitance (**220 F·g^{-1}** of pMeT). These features reflect upon the hybrid supercapacitor's performance in terms of specific energy and power, particularly at high current densities, as confirmed by the data of the Ragone plot in Figure 7, where the specific energy and average specific power (evaluated from the galvanostatic discharges as described in Section 3) of the C/pMeT hybrid supercapacitor and of a DLS with the same cell assembly and total mass loading (~**20 mg·cm^{-2}**) are reported. The maximum specific power values at **5 mA·cm^{-2}** were 9 and **5 kW·kg^{-1}** for the C/pMeT hybrid supercapacitor and DLS, respectively. These data clearly demonstrate that the power performance of this hybrid supercapacitor is higher than that of DLSs of equivalent specific energy.
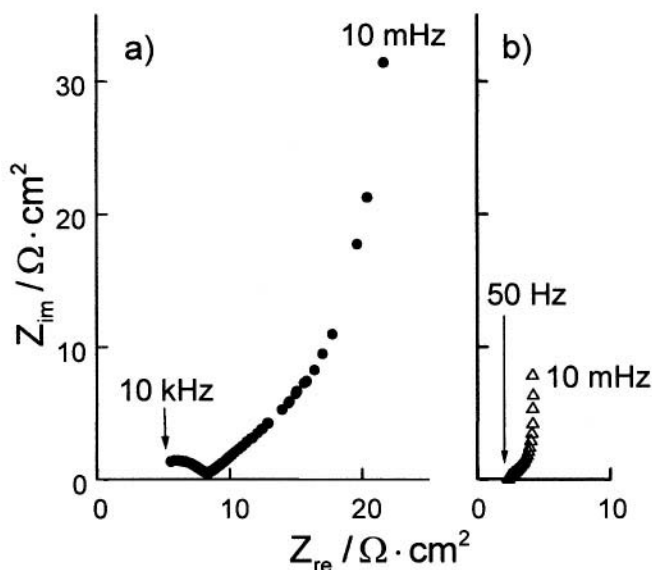
Figure 6. Impedance spectra of (a) C/pMeT hybrid supercapacitor and of its (b) pMeT positive electrode [83]. Reproduced with permission from The Electrochemical Society, Inc.

Furthermore, if the performance of the two systems is compared for working potentials above 1 V and current densities as high as **20 mA·cm^{-2}**, specific energy and power values of **19 Wh·kg^{-1}** and **1.8 kW·kg^{-1}** and 13 **Wh·kg^{-1}** and **1.6 kW·kg^{-1}** are attained for the C/pMeT hybrid supercapacitor and the DLS, respectively. These results clearly show that the hybrid supercapacitor outperforms the double-layer supercapacitor not only in terms of power but also in terms of energy. Even the cycling stability of this hybrid C/pMeT device is demonstrated by repeated galvanostatic cycles over 10000 cycles in reference 83. These hybrid devices can thus

provide a positive response to the market demand for high power super-
capacitors of high specific energy without significantly increasing costs.
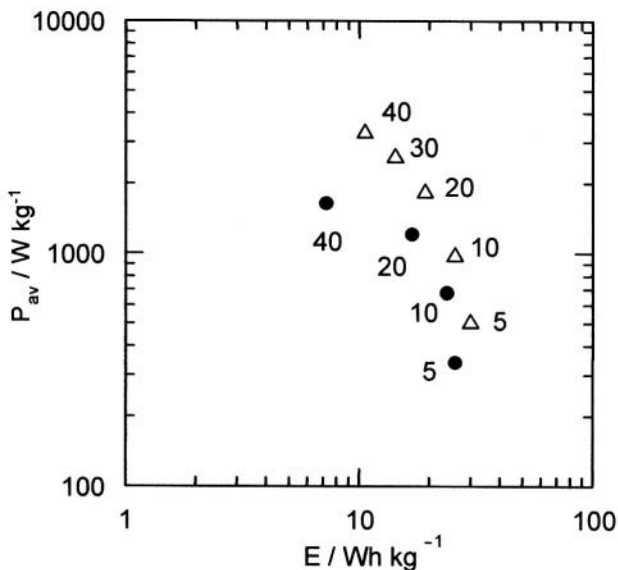
Figure 7. Ragone plot for C/pMeT hybrid supercapacitor (Δ) (cut-off: 1.0-3.0 V) and DLS (•) (cut-off: 0.0-2.8 V) with the same electrolyte, cell assembly and total mass loading. Labels indicate the current density in mA cm^{-2} [83]. Reproduced from with permission from The Electrochemical Society, Inc.

6.0   NANOSTRUCTURED MATERIALS FOR SUPERCAPACITORS

Research efforts of several groups have been devoted to the development of high surface area activated carbon electrodes with optimized performance in terms of capacitance and ionic and electronic resistance, as reported in Section 2. Work is also focusing on nanostructured carbons, such as aerogels and nanotubes, to optimize the interparticle contact resistance and the electrolyte wettability of the pores in carbon electrodes [5].

Carbon aerogel, which is produced by a sol-gel process with "supercritical drying" of the gel, is a monolithic, tridimensional mesoporous network of carbon nanoparticles. Its porosity is due to interconnected carbon nanoparti-cles of the same size, which yield a uniform mesoporous microtexture having specific surface area in the **500-900 m^2·g^{-1}** range and low density. The advantages of carbon aerogels for supercapacitor applications are mainly their low ionic and electronic charging resistance and their potential use as binderless electrodes. Their performance depends greatly on the sol-gel process: by controlling the mass ratio of reactants and the molar ratio of reactants to catalyst, as well as temperature, carbon aerogels with different

microstructures can be prepared, i.e. with different density and grain size [86, 87]. Binderless, monolithic carbon aerogel electrodes reinforced with carbon cloth have recently been tested in button cell supercapacitors of ca. **4 cm²** area: they show a capacitance of 11 F and an ESR of **170 mΩ**, with cyclability performance that is claimed to be even better than that of DLSs based on Maxsorb carbon black or Kynol fiber cloth electrodes [88].

Since their discovery in 1991, carbon nanotubes have received great theoretical and experimental attention for a wide variety of applications, including supercapacitors [5, 89]. Unlike activated carbons, which have a wide pore-size distribution, the catalitically grown carbon nanotubes, because of their unique architecture based on randomly entangled and crosslinked tubes of a diameter of ca. 8 nm, display a narrow distribution of pore size around 2 nm. Since the pores are the open spaces in the entangled network, they are all connected and easily accessible to the electrolyte, i.e. carbon nanotubes are materials having a highly accessible surface area and low charging resistance. Figure 8 shows the transmission electron microscopy (TEM) and scansion electron microscopy (SEM) micrographs of highly dispersed catalitically grown carbon nanotubes and of a nanotube electrode, respectively [89].

Catalitically grown nanotube electrodes have been tested in a single-cell supercapacitor (ca. **1 cm²** area and ca. **25 μm** separator thickness) with H_2SO_4 as electrolyte [89]. The measured ESR was ca. **0.1 Ω**, the specific capacitance was **102 F·g⁻¹** at 1 Hz and, most importantly, **49 F·g⁻¹** at 100 Hz, and the cell's specific power was higher than **8 kW·kg⁻¹**. Data for DLSs built with different kinds of carbon nanotubes and H_2SO_4 are in references 5 and **90-92**. Nanostructured carbons have also been grown by supersonic cluster beam deposition and these nanotubes have already been tested in single cell supercapacitors [93].
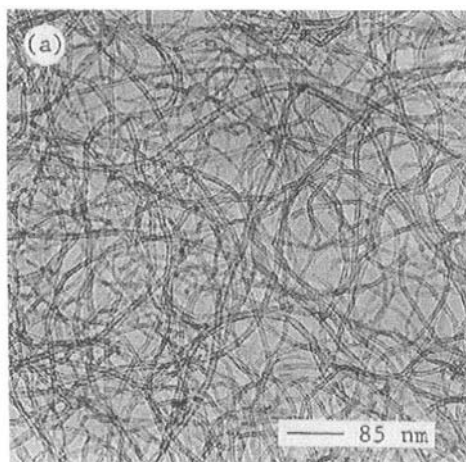
Figure 8a. TEM micrograph of highly dispersed catalitically grown carbon nanotubes
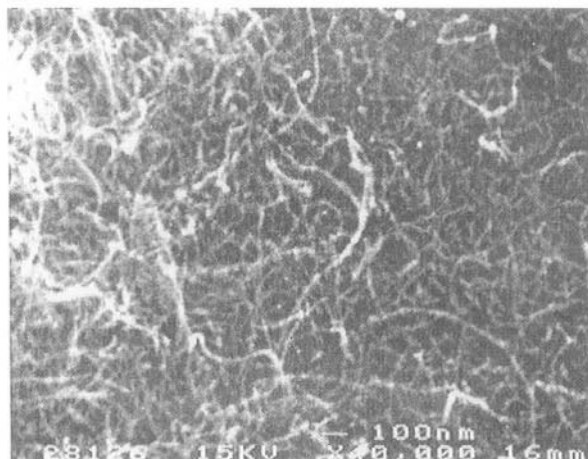
Figure 8b. SEM micrograph of a nanotube electrode [89]. Reproduced with permission from American Institute of Physics]

Nanostructured carbons have also been used in composite electrodes with pseudocapacitive materials to increase their specific capacitance by means of the Faradaic reactions taking place in pseudocapacitive materials like metal oxides and ECPs. One example of this strategy is the preparation of high surface area Ru-carbon aerogel composite electrodes by chemical vapor impregnation of Ru into carbon aerogels to produce a uniform distribution of adherent nanoparticles on the aerogel surface (Ru loading up to 35% to reach **206 F·g^{-1}**) [94]. Improved specific capacitance (**256 F·g^{-1}**) has been attained, however, with lower Ru loading (14%) by a sol-gel route and a conventional drying procedure [67]. Yet, even if this approach is attractive, it does not seem a convenient route from the point of view of cost. The same can be said for the **nanotube-RuO$_2$·xH$_2$O** composites, which reach specific capacitance of **560 F·g^{-1}** with **75% RuO$_2$·xH$_2$O** [95].

By contrast, the use of conducting polymers—the other class of pseudocapacitive materials—in preparing nanostructural composites with carbon is an attractive approach, also taking cost into account. In addition, since it has recently been stressed that the performance of thiophene-based films improves when a porous substrate is used, growing conducting polymers on nanotubes can be seen as an alternative way to improve the performance of the conducting polymer [96]. Indeed, improved characteristics of polyaniline has been achieved when it is grown on carbon nanotubes [97]. Growing polymers like polypyrrole (pPy) on carbon nanotubes has also yielded to very interesting results: a specific capacitance of **170 F·g^{-1}** in aqueous electrolyte, a value much higher than that of pPy alone (**ca. 90 F·g^{-1}**) and of bare carbon nanotubes (**80 F·g^{-1}**) evaluated in aqueous electrolyte. Preliminary results of pPy/carbon nanotube applications in supercapacitors are also reported [98,99].

7.0 CONCLUSIONS

The aim of the authors in writing this chapter on supercapacitors was to highlight the most recent advances in supercapacitor technology and in the basic studies of materials for supercapacitors. This review is also intended to elucidate the factors limiting the power of activated carbon DLSs, which are at present the most advanced version of supercapacitors already on the market with high-performance products. The development of activated carbons with optimized pore-size distribution as well as of electrolytes with higher conductivity and a higher decomposition potential window may lead to further DLS optimization.

For supercapacitors based on ruthenium oxide, despite their high performance and the different approaches taken to overcome the drawback of high cost, there are at the moment no plans to bring them to market at competitive cost. Polymer-based supercapacitors, even in their most promising version with a p-doped polymer and an n-doped one, do not appear competitive with the carbon DLSs because of the intrinsic limitation related to the negative n-doped electrode. On the other hand, the high performance of conducting polymers as positive electrodes indicate that hybrid supercapacitors, in which the positive electrode is a p-doped polymer and the negative an activated carbon, are an excellent strategy as they outperform DLSs and have a reasonable cost-to-performance ratio.

This brings us to nanostructured carbon materials. While they are intrinsically unique because of their particular architecture, which enables controlled porosity, research is still at an early stage with respect to both materials preparation and application in the field of supercapacitors. It is thus difficult to foresee the impact they may have and whether they will lead to "second generation" supercapacitors.

8.0 REFERENCES

1. B. E. Conway, *Electrochemical Supercapacitors,* Kluwer Academic/Plenum Publishers, New York (NY), 1999
2. *Supercapacitors. World Markets, Technologies & Opportunities: 1999-2004,* Paumanok Publications, Inc., Cary (NC), 2000
3. A. Burke, *J. Power Sources,* **91**, 37-50, 2000
4. R. Kotz, M. Carlen, *Electrochim. Acta,* **45**, 2483-2498, 2000
5. E. Frackowiak, F. Béguin, *Carbon,* **39**, 937-950, 2001
6. H. Shi, *Electrochim. Acta,* **41**, 1633-1639, 1996
7. D. Qu, H. Shi, *J. Power Sources,* 74, 99-107, 1998
8. G. Salitra, A. Soffer, L. Eliad, Y. Cohen, D. Aurbach, *J. Electrochem. Soc.,* **147**, 2486-2493, 2000
9. M. Endo, T. Maeda, T. Takeda, Y. J. Kim, K. Koshiba, H. Hara, M.S. Dresselhaus, *J. Electrochem. Soc.,* **148**, A910-A914, 2001

10.   M. Endo, Y. J. Kim, T. Takeda, T. Maeda, T. Hayashi, K. Kashiba, H. Hara, and
       M.S. Dresselhaus, *J. Electrochem. Soc.,* **148**, A1135-A1140, 2001
11.   T.-C. Weng, H. Teng, *J. Electrochem. Soc.,* **148**, A368-A373, 2001
12.   H. Teng, Y.-J. Chang, C.-T. Hsieh, *Carbon,* **39**, 1981-1987, 2001
13.   S. Shiraishi, H. Kurihara, H. Tsubota, A. Oya, Y. Soneda, Y. Yamada,
       Electrochem. and Solid State Lett., **4**, A5-A8, 2001
14.   M. Mastragostino, F. Soavi, *5th International Symposium on Electrochemical
       Impedance Spectroscopy,* Abst. 73, Marilleva (Italy), June 2001
15.   X. Andrieu in *Energy Storage Systems for Electronics,* T. Osaka and M. Datta
       Eds., Gordon and Breach Science Publishers, Amsterdam (NL), 521-547, 2000
16.   E. Faggioli, P. Rena, V. Danel, X. Andrieu, R. Mallant, H. Kahlen, *J. Power
       Sources,* **84**, 261-269, 1999
17.   A. Schwake, C. J. Weber, *10th International Seminar on Double Layer
       Capacitors and Similar Energy Storage Devices,* Florida Educational
       Seminars, Inc., Deerfield Beach (FL), December 2000
18.   A. Du Pasquier, F. Badway, G. G. Amatucci, *10th International Seminar on
       Double Layer Capacitors and Similar Energy Storage Devices,* Florida
       Educational Seminars, Inc., Deerfield Beach (FL), December 2000
19.   T. Osaka, X. Liu, M. Nojima, T. Momma, *J. Electrochem. Soc.,* **146**, 1724-
       1729, 1999
20.   J. F. Sarrau, P. Lailler, P. Simon, J. F. Fauvarque, *10th International
       Seminar on Double Layer Capacitors and Similar Energy Storage Devices,*
       Florida Educational Seminars, Inc., Deerfield Beach (FL), December 2000
21.   L. Bonnefoi, P. Simon, J. F. Fauvarque, C. Sarrazin, A. Dugast, *J. Power
       Sources,* **79**, 37-42, 1999
22.   I. Bispo-Fonseca, J. Aggar, C. Sarrazin, P. Simon, J. F. Fauvarque, *J. Power
       Sources,* **79**, 238-241, 1999
23.   L. Bonnefoi, P. Simon, J. F. Fauvarque, C. Sarrazin, J. F. Sarrau, A. Dugast,
       J. Power Sources, **80**, 149-155, 1999
24.   L. Bonnefoi, P. Simon, J. F. Fauvarque, C. Sarrazin, J. F. Sarrau, P. Lailler, *J.
       Power Sources,* **83**, 162-169, 1999
25.   S. Nomoto, H. Nakata, K, Yoshioka, A. Yoshida, H. Yoneda, *J.Power Sources,*
       97-98, 807-811, 2001
26.   F. Beck, M. Dolata, E. Grivet, N. Probst, *J. Appl. Electrochem.,* **31**, 845-853, 2001
27.   J. Gamby, P. L. Taberna, P. Simon, J. F. Fauvarque, M. Chesneau, *J. Power
       Sources.* **101**, 109-116, 2001
28.   F. Bonhomme, J.C. Lassègues, L. Servant, *J. Electrochem. Soc.,* **148**, E450-
       E458, 2001
29.   B. W. Ricketts, C. Ton-That, *J. Power Sources,* **89**, 64-69, 2000
30.   V. Hermann, A. Schneuwly, R. Gallay, *2001 Joint International Meeting
       ECS-ISE.* Abst. 81, San Francisco (CA), September 2001
31.   H. Michel, A. Schwake, C. J. Weber, *2001 Joint International Meeting ECS-
       ISE,* Abst. 82, San Francisco (CA), September 2001
32.   *Handbook of Organic Conductive Molecules and Polymers,* H. S. Nalwa Ed.,
       John Wiley & Sons Ltd., Chichester (UK), 1997
33.   A. Rudge, J. Davey, S. Gottesfeld, J. P. Ferraris in *New Sealed Rechargeable
       Batteries and Supercapacitors,* Z. Takehara, Y. Matsuda, B. Barnett, E.

Dowgiallo, and G. Halpert Eds., Vol. **93-23**, Honolulu, Hawaii - May 1993, The Electrochemical Soc., Inc., Pennington (NJ), 74-85, 1993

34. A. Rudge, J. Davey, F. Uribe, J. Landeros Jr, S. Gottesfeld, *3rd International Seminar on Double Layer Capacitors and Similar Energy Storage Devices,* Florida Educational Seminars, Inc., Deerfield Beach (FL), December 1993

35. A. Rudge, J. Davey, I. Raistrick, S. Gottesfeld, J. P. Ferraris, *J. Power Sources,* **47**, 89-107, 1994

36. K. Kaneto, K. Yoshino, Y. Inuishi, *Jap. J. Appl. Phys.,* **22**, L567-L568, 1983

37. D. Belanger, X. Ren, J. Davey, F. Uribe, S. Gottesfeld, *J. Electrochem. Soc.,* **147**, 2923-2929, 2000

38. C. Arbizzani, M. Mastragostino, L. Meneghello, *Electrochim. Acta* , **41**, 21-26, 1996

39. S. Ghosh, O. Inganas, *Electrochem. and Solid State Lett.,* **3**, 213-215, 2000

40. F. Fusalba, D. Bélanger, *J. Phys. Chem. B,* **103**, 9044-9054, 1999

41. F. Fusalba, P. Gouérec, D. Villers, D. Bélanger, *J. Electrochem. Soc.,* **148**, A1-A6, 2001

42. J. Roncali, *Chem. Rev.,* **97**, 173-205, 1997

43. C. Arbizzani, M. Mastragostino in *Current Trends in Polymer Science,* vol. 2, Research Trends, Trivandrum (India), 217-239, 1997

44. M. Mastragostino, C. Arbizzani, R. Paraventi, A. Zanelli, *J. Electrochem. Soc.,* **147**, 407-412, 2000

45. J. P. Ferraris, M. M. Eissa, I. D. Brotherston, D. C. Loveday, *Chem. Mater.,* **10**, 3528-3535, 1998

46. A. Laforgue, P. Simon, J. F. Fauvarque, *Synth. Metals,* **123**, 311-319, 2001

47. F. Fusalba, N. El Mehdi, L. Breau, D. Bélanger, *Chem. Mater.,* **11**, 2743-2753, 1999

48. P. Soudan, H. A. Ho, L. Breau, D. Bélanger, *J. Electrochem. Soc.,* **148**, A775-A782, 2001

49. A. Laforgue, P. Simon, C. Sarrazin, J. F. Fauvarque, *J. Power Sources,* **80**, 142-148, 1999

50. M. Mastragostino, R. Paraventi, A. Zanelli, *J. Electrochem. Soc.,* **147**, 3167-3170, 2000

51. C. Arbizzani, M. Mastragostino, F. Soavi, *J. Power Sources,* **100**, 164-170, 2001

52. K. Naoi, S. Suematsu, A. Manago, *J. Electrochem. Soc.,* **147**, 420-426, 2000

53. J. P. Zheng, P. G. Cygan, T. R. Jow, *J. Electrochem. Soc.,* **142**, 2699-2703, 1995

54. J. P. Zheng, J. Huang, T. R. Jow, *J. Electrochem. Soc.,* **144**, 2026-2031, 1997

55. T. R. Jow, J. P. Zheng, *J. Electrochem. Soc.,* **145**, 49-52, 1998

56. Q. L. Fang, D. A. Evans, S. L. Robertson, J. P. Zheng, *J. Electrochem. Soc.,* **148**, A833-A837, 2001

57. Y. Takasu, W. Sugimoto, T. Ohnuma, Y. Murakami, *10th International Seminar on Double Layer Capacitors and Similar Energy Storage Devices,* Florida Educational Seminars, Inc., Deerfield Beach (FL), December 2000

58. Y. Takasu, Y. Murakami, *Electrochim. Acta,* **45**, 4135-4141, 2000

59. Y. Takasu, T. Nakamura, H. Ohkawauchi, Y. Murakami, *J. Electrochem. Soc.,* **144**, 2601-2606, 1997

60. Y. Takasu, T. Nakamura, Y. Murakami, *Chem. Lett.,* 1215-1216, 1998

61. Y. U. Jeong, A. Manthiram, *J. Electrochem. Soc.,* **148**, A189-A193, 2001

62. Y. U. Jeong, A. Manthiram, *Electrochem. and Solid State Lett.,* **3**, 205-208, 2000

63.   P. M. Wilde, T. J. Gunther, R. Oesten, J. Garche, *J. Electroanal. Chem,.* **461**, 154-160, 1999
64.   F. Cao, J. Prakash, *J. Power Sources,* **92**, 40-44, 2001
65.   J. P. Zheng, T. R. Jow, J. Power Sources, **62**, 155-159, 1996
66.   J. P. Zheng, *Electrochem. and Solid State Lett.. 2,* 359-361, 1999
67.   C. Lin, J. A. Ritter, B. N. Popov, *J. Electrochem. Soc.,* **146**, 3155-3160, 1999
68.   J. Zhang, D. Jiang, B. Chen, J. Zhu, L. Jiang, H. Fang, *J. Electrochem. Soc.,* **148**, A1362-A1367, 2001
69.   M. Ramani, B. S. Haran, R. E. White, B. N. Popov, L. Arsov, *J. Power Sources,* **93**, 209-214, 2001
70.   M. Ramani, B. S. Haran, R. E. White, B. N. Popov, *J. Electrochem. Soc.,* **148**, A374-A380, 2001
71.   Y. Sato, K. Yomogida, T. Nanaumi, K. Kobayakawa, Y. Ohsawa, M. Kawai, *Electrochem. and Solid State Lett.,* **3**, 113-116, 2000
72.   R. D. Meyer, T. H. Nguyen, *10th International Seminar on Double Layer Capacitors and Similar Energy Storage Devices,* Florida Educational Seminars, Inc., Deerfield Beach (FL), December 2000
73.   J. Hong, I. Yeo, W. Paik, *J. Electrochem. Soc.,* **148**, A156-A163, 2001
74.   V. Srinivasan, J.W. Weidner, *J. Electrochem. Soc.,* **144**, L210-L213, 1997
75.   K.-C. Liu, M. A. Anderson, *J. Electrochem. Soc.,* **143**, 124-130, 1996
76.   T.-C. Liu, G. Pell, B. E. Conway, S.L. Robertson, *J. Electrochem. Soc.,* **145**, 1882-1888, 1998
77.   Y. Takasu, S. Mizutani, M. Kumagai, S. Sawaguchi, Y. Murakami, *Electrochem. and Solid State Lett.,* **2**, 1-2, 1999
78.   C. Lin, J. A. Ritter, B. N. Popov, *J. Electrochem. Soc.,* **145**, 4097-4102, 1998
79.   A. Yamada, J.B. Goodenough, *J. Electrochem. Soc.,* **145**, 737-743, 1998
80.   W. Sugimoto, T. Ohnuma, Y. Murakami, Y. Takasu, *Electrochem. and Solid State Lett.,* **4**, A145-A147, 2001
81.   A. I. Beliakov, A. M. Brintsev, *7th International Seminar on Double Layer Capacitors and Similar Energy Storage Devices,* Florida Educational Seminars, Inc., Deerfield Beach (FL), December 1997
82.   S. M. Lipka, D. E. Reisner, J. Dai, R. Ge, R. Cepulis, *10th International Seminar on Double Layer Capacitors and Similar Energy Storage Devices,* Florida Educational Seminars, Inc., Deerfield Beach (FL), December 2000
83.   A. Di Fabio, A. Giorgi, M. Mastragostino, F. Soavi, *J. Electrochem. Soc.,* **148**, A845-A850, 2001
84.   A. Laforgue, P. Simon, J. F. Fauvarque, J. F. Sarrau, P. Lailler, *J. Electrochem. Soc.,* **148**, A1130-A1134, 2001
85.   A. Laforgue, P. Simon, J. F. Fauvarque, J. F. Sarrau, P. Lailler, *11th International Seminar on Double Layer Capacitors and Similar Energy Storage Devices,* Florida Educational Seminars, Inc., Deerfield Beach (FL), December 2001
86.   T. Burger, J. Fricke, *Ber. Bunsenges. Phys. Chem.,* **102**, 1523-1528, 1998
87.   J. Wang, S. Q. Zhang, Y. Z. Guo, J. Shen, S. M. Attia, B. Zhou, G. Z. Zheng, Y. S. Gui, *J. Electrochem. Soc.,* **148**, D75-D77, 2001
88.   C. Schmitt, H. Pröbstle, J. Fricke, *J. Non-Cryst. Solids,* **285**, 277-282, 2001
89.   C. Niu, E. K. Sichel, R. Hoch, D. Moy, H. Tennent, *Appl. Phys. Lett.,* **70**, 1480-1482, 1997

90.   R. Z. Ma, J. Liang, B. Q. Wei, B. Zhang, C. L. Xu, D. H. Wu, *J. Power Sources.* **84**, 126-129, 1999

91.   E. Frackowiak, K. Metenier, V. Bertagna, F. Beguin, *Appl. Phys. Lett.,* **77**, 2421-2423 , 2000

92.   K. H. An, W. S. Kim, Y. S. Park, Y. C.Choi, S. M. Lee, D. C.Chung, D. J. Bae, S. C.Lim, Y. H. Lee, *Adv. Mater.,* **13**, 497-500, 2001

93.   L. Diederich, E. Barborini, P. Piseri, A. Podestà, P. Milani, A. Schneuly, R. Gallay, *Appl. Phys. Lett.,* **75**, 2662-2664, 1999

94.   J. M. Miller, B. Dunn, T. D. Tran, R. W. Pekala, *J. Electrochem. Soc.,* **144**, L309-311, 1997

95.   R. Ma, B. Wei, C. Xu, J. Liang, D. Wu, *Bull. Chem. Soc. Jpn..* **73**, 1813-1816, 2000

96.   A. S. Scott, D. S. K. Mudigonda, D. C. Loveday, J. P. Ferraris, 199th *Electrochem. Soc. Meeting,* Abst. 1057, Washington (DC), March 2001

97.   C. Downs, J. Nugent, P. M. Ajayan, D. J. Duquette, K. S. V. Santhanam, *Adv. Mater.,* **11**, 1028-1031, 1999

98.   K. Jurewicz, S. Delpeux, V. Bertagna, F. Béguin, E. Frackowiak, *Chem. Phys. Lett.,* **347**, 36-40, 2001

99.   E. Frackowiak, K. Jurewicz, S. Delpeux, F. Béguin, *J. Power Sources,* **97-98**, 822-825, 2001

Index